

TOPICS IN CURRENT CHEMISTRY

298

Volume Editors R. Naaman • D. N. Beratan • D. H. Waldeck

Electronic and Magnetic Properties of Chiral Molecules and Supramolecular Architectures

 Springer

298

Topics in Current Chemistry

Editorial Board:

A. de Meijere • K.N. Houk • C.A. Hunter • H. Kessler

J.-M. Lehn • S.V. Ley • M. Olivucci • J. Thiem • B.M. Trost

M. Venturi • P. Vogel • C.-H. Wong • H. Wong • H. Yamamoto

Topics in Current Chemistry

Recently Published and Forthcoming Volumes

Electronic and Magnetic Properties of Chiral Molecules and Supramolecular Architectures

Volume Editors: Ron Naaman,
David N. Beratan, David H. Waldeck
Vol. 298, 2011

Natural Products via Enzymatic Reactions

Volume Editor: Jörn Piel
Vol. 297, 2010

Nucleic Acid Transfection

Volume Editors: Wolfgang Bielke,
Christoph Erbacher
Vol. 296, 2010

Carbohydrates in Sustainable Development II

Volume Editors: Amélia P. Rauter,
Pierre Vogel, Yves Queneau
Vol. 295, 2010

Carbohydrates in Sustainable Development I

Volume Editors: Amélia P. Rauter,
Pierre Vogel, Yves Queneau
Vol. 294, 2010

Functional Metal-Organic Frameworks: Gas Storage, Separation and Catalysis

Volume Editor: Martin Schröder
Vol. 293, 2010

C-H Activation

Volume Editors: Jin-Quan Yu, Zhangjie Shi
Vol. 292, 2010

Asymmetric Organocatalysis

Volume Editor: Benjamin List
Vol. 291, 2010

Ionic Liquids

Volume Editor: Barbara Kirchner
Vol. 290, 2010

Orbitals in Chemistry

Volume Editor: Satoshi Inagaki
Vol. 289, 2009

Glycoscience and Microbial Adhesion

Volume Editors: Thisbe K. Lindhorst,
Stefan Oscarson
Vol. 288, 2009

Templates in Chemistry III

Volume Editors: Broekmann, P., Dötz, K.-H.,
Schalley, C.A.
Vol. 287, 2009

Tubulin-Binding Agents: Synthetic, Structural and Mechanistic Insights

Volume Editor: Carlomagno, T.
Vol. 286, 2009

STM and AFM Studies on (Bio)molecular Systems: Unravelling the Nanoworld

Volume Editor: Samorì, P.
Vol. 285, 2008

Amplification of Chirality

Volume Editor: Soai, K.
Vol. 284, 2008

Anthracycline Chemistry and Biology II

Mode of Action, Clinical Aspects and New Drugs
Volume Editor: Krohn, K.
Vol. 283, 2008

Anthracycline Chemistry and Biology I

Biological Occurrence and Biosynthesis,
Synthesis and Chemistry
Volume Editor: Krohn, K.
Vol. 282, 2008

Electronic and Magnetic Properties of Chiral Molecules and Supramolecular Architectures

Volume Editors:

Ron Naaman · David N. Beratan · David H. Waldeck

With Contributions by

J. Autschbach · V. Ben-Moshe · D.N. Beratan · A. D'Urso ·
Y. Inoue · K. Kawai · R. Lauceri · T. Majima · A. Mammana ·
T. Mori · R. Naaman · L. Nitsch-Velasquez · A. Nitzan · R. Purrello ·
R.A. Rosenberg · M. Rudolph · S.S. Skourtis · Z. Vager · Y. Xu ·
G. Yang



Springer

المنارة للاستشارات

Editors

Prof. Dr. Ron Naaman
Department of Chemical Physics
Weizmann Institute of Science
Rehovot 76100
Israel
Ron.Naaman@weizmann.ac.il

Prof. Dr. David N. Beratan
Fitzpatrick Institute for Photonics
Duke University
101 Science Drive
27708 Durham, NC
USA
david.beratan@duke.edu

Prof. David H. Waldeck
University of Pittsburgh
Chevron Science Center
Department of Chemistry
Parkman Avenue 219
15260 Pittsburgh Pennsylvania
USA
dave@pitt.edu

ISSN 0340-1022 e-ISSN 1436-5049
ISBN 978-3-642-18103-0 e-ISBN 978-3-642-18104-7
DOI 10.1007/978-3-642-18104-7
Springer Heidelberg Dordrecht London New York

© Springer-Verlag Berlin Heidelberg 2011

This work is subject to copyright. All rights are reserved, whether the whole or part of the material is concerned, specifically the rights of translation, reprinting, reuse of illustrations, recitation, broadcasting, reproduction on microfilm or in any other way, and storage in data banks. Duplication of this publication or parts thereof is permitted only under the provisions of the German Copyright Law of September 9, 1965, in its current version, and permission for use must always be obtained from Springer. Violations are liable to prosecution under the German Copyright Law.

The use of general descriptive names, registered names, trademarks, etc. in this publication does not imply, even in the absence of a specific statement, that such names are exempt from the relevant protective laws and regulations and therefore free for general use.

Cover design: WMXDesign GmbH, Heidelberg, Germany

Printed on acid-free paper

Springer is part of Springer Science+Business Media (www.springer.com)

المنارة للاستشارات

Volume Editors

Prof. Dr. Ron Naaman

Department of Chemical Physics
Weizmann Institute of Science
Rehovot 76100
Israel
Ron.Naaman@weizmann.ac.il

Prof. David H. Waldeck

University of Pittsburgh
Chevron Science Center
Department of Chemistry
Parkman Avenue 219
15260 Pittsburgh Pennsylvania
USA
dave@pitt.edu

Prof. Dr. David N. Beratan

Fitzpatrick Institute for Photonics
Duke University
101 Science Drive
27708 Durham, NC
USA
david.beratan@duke.edu

Editorial Board

Prof. Dr. Armin de Meijere

Institut für Organische Chemie
der Georg-August-Universität
Tammanstr. 2
37077 Göttingen, Germany
ameijer1@uni-goettingen.de

Prof. Dr. Kendall N. Houk

University of California
Department of Chemistry and Biochemistry
405 Hilgard Avenue
Los Angeles, CA 90024-1589, USA
houk@chem.ucla.edu

Prof. Dr. Christopher A. Hunter

Department of Chemistry
University of Sheffield
Sheffield S3 7HF, United Kingdom
c.hunter@sheffield.ac.uk

Prof. Dr. Horst Kessler

Institut für Organische Chemie
TU München
Lichtenbergstraße 4
86747 Garching, Germany
kessler@ch.tum.de

Prof. Dr. Jean-Marie Lehn

ISIS
8, allée Gaspard Monge
BP 70028
67083 Strasbourg Cedex, France
lehn@isis.u-strasbg.fr

Prof. Dr. Steven V. Ley

University Chemical Laboratory
Lensfield Road
Cambridge CB2 1EW
Great Britain
Svl1000@cus.cam.ac.uk

Prof. Dr. Massimo Olivucci

Università di Siena
Dipartimento di Chimica
Via A De Gasperi 2
53100 Siena, Italy
olivucci@unisi.it

Prof. Dr. Joachim Thiem

Institut für Organische Chemie
Universität Hamburg
Martin-Luther-King-Platz 6
20146 Hamburg, Germany
thiem@chemie.uni-hamburg.de

Prof. Dr. Barry M. Trost

Department of Chemistry
Stanford University
Stanford, CA 94305-5080, USA
bmtrost@leland.stanford.edu

Prof. Dr. Margherita Venturi

Dipartimento di Chimica
Università di Bologna
via Selmi 2
40126 Bologna, Italy
margherita.venturi@unibo.it

Prof. Dr. Pierre Vogel

Laboratory of Glycochemistry
and Asymmetric Synthesis
EPFL – Ecole polytechnique fédérale
de Lausanne
EPFL SB ISIC LGSA
BCH 5307 (Bat.BCH)
1015 Lausanne, Switzerland
pierre.vogel@epfl.ch

Prof. Dr. Chi-Huey Wong

Scipps Research Institute
128 Academia Road, Section 2
Nankang, Taipei
Taiwan
chwong@gate.sinica.edu.tw

Prof. Dr. Henry Wong

The Chinese University of Hong Kong
University Science Centre
Department of Chemistry
Shatin, New Territories
hncwong@cuhk.edu.hk

Prof. Dr. Hisashi Yamamoto

Arthur Holly Compton Distinguished
Professor
Department of Chemistry
The University of Chicago
5735 South Ellis Avenue
Chicago, IL 60637
773-702-5059
USA
yamamoto@uchicago.edu

Topics in Current Chemistry Also Available Electronically

Topics in Current Chemistry is included in Springer's eBook package *Chemistry and Materials Science*. If a library does not opt for the whole package the book series may be bought on a subscription basis. Also, all back volumes are available electronically.

For all customers with a print standing order we offer free access to the electronic volumes of the series published in the current year.

If you do not have access, you can still view the table of contents of each volume and the abstract of each article by going to the SpringerLink homepage, clicking on "Chemistry and Materials Science," under Subject Collection, then "Book Series," under Content Type and finally by selecting *Topics in Current Chemistry*.

You will find information about the

- Editorial Board
- Aims and Scope
- Instructions for Authors
- Sample Contribution

at springer.com using the search function by typing in *Topics in Current Chemistry*.

Color figures are published in full color in the electronic version on SpringerLink.

Aims and Scope

The series *Topics in Current Chemistry* presents critical reviews of the present and future trends in modern chemical research. The scope includes all areas of chemical science, including the interfaces with related disciplines such as biology, medicine, and materials science.

The objective of each thematic volume is to give the non-specialist reader, whether at the university or in industry, a comprehensive overview of an area where new insights of interest to a larger scientific audience are emerging.

Thus each review within the volume critically surveys one aspect of that topic and places it within the context of the volume as a whole. The most significant developments of the last 5–10 years are presented, using selected examples to illustrate the principles discussed. A description of the laboratory procedures involved is often useful to the reader. The coverage is not exhaustive in data, but rather conceptual, concentrating on the methodological thinking that will allow the non-specialist reader to understand the information presented.

Discussion of possible future research directions in the area is welcome.

Review articles for the individual volumes are invited by the volume editors.

In references *Topics in Current Chemistry* is abbreviated *Top Curr Chem* and is cited as a journal.

Impact Factor 2009: 4.291; Section “Chemistry, Multidisciplinary”: Rank 20 of 138

Preface

Chiral molecules, molecules that lack mirror symmetry, have been the focus of attention since it was established that all organisms are built of molecules with specific handedness. The understanding of biological processes that involve intermolecular recognition, including drug interactions with biomolecules, is enhanced by an understanding of the structure and interactions among chiral structures, as well as an ability to synthesize and separate enantiomers and diastereomers. As such, enormous focus has been placed on molecular stereochemistry, beginning with the earliest pioneering studies of van't Hoff, who established the tetrahedral valency of carbon and the consequent origins of molecular chirality. Recent progress in molecular chirality has been recognized for synthetic breakthroughs through the awarding of the 2001 Nobel Prize in Chemistry to Knowles and Noyori for chirally catalyzed hydrogenation and to Sharpless for discoveries on chirally catalyzed oxidation.

When compared to developments associated with the structure and synthesis of chiral structures, less attention has been focused on the electronic and magnetic properties of chiral molecules. Circular dichroism and related optical probes of chirality have been developed mainly as analytical tools and, indeed, they are applied routinely. However, as demonstrated in this volume, the basic physical underpinnings that link structure and chiral properties, including chiro-optical properties, continue to emerge and require the development of physical models and improvement of electronic structure methods before they are fully elucidated.

No apparent ground exists for a “right-handed” structure to be intrinsically more or less stable than a “left-handed” structure, and one might even expect molecules to exist in a superposition of left- and right-handed states. However, chirality in molecules is related to an important symmetry breaking effect in nature, parity violation (PV), so that a very small (of order 10^{-18} eV) energy difference between left- and right-handed molecules is expected. The PV effect is generally considered to be too small to have any significance in chemical systems, and molecules relax into either left- or right-handed states with lifetimes defined by the activation barrier for inversion of the stereochemistry. One consequence of symmetry breaking, *i.e.*, relaxation into long-lived enantiomers or diastereomers, is the

magneto-electric effect. This effect arises when electrons that move through chiral systems are driven by an applied electric field, creating a transient magnetic field. This magnetic field may act on the spin of the mobile electron and align it. In this way, one may envision a relationship between the chiral symmetry and the magnetic and spin characteristics of molecules. When one explores the potential use of organic molecules as components in electronic devices, the novel characteristics derived from chirality require attention. Indeed, these phenomena may help to establish new capabilities that are not available – or are difficult to realize – in more conventional electronic systems.

This volume assembles contributions from researchers investigating novel electronic, magnetic, and spectroscopic properties of chiral molecules and of supramolecular structures made from these molecules. The contributions describe both theoretical and experimental studies, and they aim to provide the reader with a current snapshot of this emerging and rapidly growing field of research into the electronic and magnetic characteristics of chiral systems.

David N. Beratan
Ron Naaman
David H. Waldeck

Contents

Time-Dependent Density Functional Response Theory for Electronic Chiroptical Properties of Chiral Molecules	1
Jochen Autschbach, Lucia Nitsch-Velasquez, and Mark Rudolph	
Recent Theoretical and Experimental Advances in the Electronic Circular Dichroisms of Planar Chiral Cyclophanes	99
Tadashi Mori and Yoshihisa Inoue	
G-C Content Independent Long-Range Charge Transfer Through DNA	129
Kiyohiko Kawai and Tetsuro Majima	
Transfer of Chirality for Memory and Separation	143
Rosaria Lauceri, Alessandro D'Urso, Angela Mammanna, and Roberto Purrello	
Vibrational Circular Dichroism Spectroscopy of Chiral Molecules	189
Guochun Yang and Yunjie Xu	
Spin Selective Electron Transmission Through Monolayers of Chiral Molecules	237
Ron Naaman and Zeev Vager	
Chiral Control of Current Transfer in Molecules	259
Vered Ben-Moshe, David N. Beratan, Abraham Nitzan, and Spiros S. Skourtis	
Spin-Polarized Electron Induced Asymmetric Reactions in Chiral Molecules	279
Richard A. Rosenberg	
Index	307

Time-Dependent Density Functional Response Theory for Electronic Chiroptical Properties of Chiral Molecules

Jochen Autschbach, Lucia Nitsch-Velasquez, and Mark Rudolph

Abstract Methodology to calculate electronic chiroptical properties from time-dependent density functional theory (TDDFT) is outlined. Applications of TDDFT to computations of electronic circular dichroism, optical rotation, and optical rotatory dispersion are reviewed. Emphasis is put on publications from 2005 to 2010, but much of the older literature is also cited and discussed. The determination of the absolute configuration of chiral molecules by combined measurements and computations is an important application of TDDFT chiroptical methods and discussed in some detail. Raman optical activity (ROA) spectra are obtained from normal-mode derivatives of the optical rotation tensor and other linear response tensors. A few selected (ROA) benchmarks are reviewed.

Keywords Chirality · Chiroptical properties · Circular dichroism · Density functional theory · Optical rotation · Optical rotatory dispersion · Quantum theory · Raman optical activity

Contents

1	Introduction	2
2	Time-Dependent Density Functional Theory and Chiroptical Properties	4
2.1	The Optical Rotation Parameter	4
2.2	Optical Rotation and Circular Dichroism	6
2.3	TDDFT Linear Response	9
2.4	Origin Dependence of Chiroptical Properties	12
2.5	Computing Nonsingular Response Near Resonances	15

J. Autschbach (✉), L. Nitsch-Velasquez, and M. Rudolph
Department of Chemistry, University at Buffalo State University of New York, New York, NY, USA
e-mail: jochena@buffalo.edu

2.6	Raman Optical Activity	16
2.7	Considerations Regarding Basis Sets and the Choice of the XC Potentials and the XC Kernel	16
3	Computational Benchmarking	19
4	Beyond Gas Phase and Static Structures	35
4.1	Conformational Averaging mainly of Static Gas Phase Structures	37
4.2	Solvent Effects on Static Structures	39
4.3	Zero-Point and Finite Temperature Vibrational Averaging	41
4.4	Molecular Dynamics with Solvation	44
4.5	ECD Spectra Computed with Vibrational Fine Structure	46
5	Assignments of Absolute Configuration by Comparing TDDFT Computations of ECD and OR/ORD to Experiment	47
6	Analysis of Chiroptical Properties	61
7	Exploring Electronic Chiroptical Properties of a Variety of Systems: Organic Molecules, Fullerenes, and Gold Clusters	67
8	Metal Complexes	81
9	Concluding Remarks	88
	References	89

1 Introduction

Chirality of molecules and molecular aggregates, and the associated *chiroptical properties*, are important in chemistry, biochemistry, physics, and other scientific disciplines [1–7]. Among the chiroptical properties of interest are electronic and vibrational circular dichroism (ECD, VCD), optical rotation (OR) at optical frequencies and its counterpart in the frequency region where vibrational transition occur, Raman optical activity (ROA), as well as induced chiroptical effects such as magnetic circular dichroism and magneto-optical rotation (MCD, MOR). Particularly during the past decade, numerous research studies have demonstrated that molecular chiroptical properties can be computed reliably starting from first principles. For example, the review articles in [8–17] document the progress made in the computational chiroptics field over the past decade.

A major interest from the chemistry and biochemistry community in such computations is the ability to assign the absolute configuration (AC) of a molecule by matching measured chiroptical properties with computations for one particular isomer among a set of possible stereoisomers. In the simplest case, the task is to match the sign of the experimental chiroptical response with that for one of two enantiomers, but the assignment problem can be more complicated if more than one stereocenter is present in the molecule. But there is more to chiroptical properties than AC assignments. Unlike absorption spectra, CD spectra afford positive and negative bands, and thus in some sense they reveal more detail about the excitations than their regular absorption spectra counterparts. The same can be said about ROA vs regular Raman scattering [17]. Monitoring local-structure – CD relationships, for

instance – can reveal much detail about structure and dynamics of a chiral molecule. The assignment of excitation spectra can be aided significantly if a CD spectrum is available in addition to an absorption spectrum. CD induced by a magnetic field is an important tool to assign complicated electronic spectra of chromophores that are of interest in many biochemical applications [18–21]. In materials science, chirality is receiving much interest after it was proposed that a negative refractive index metamaterial can be designed via a chirality-based route [22–24].

Except for small chiral molecules, practically all computational studies of chiroptical properties utilizing first-principles theory have so far employed some form of density functional theory (DFT) [25, 26] and time-dependent DFT (TDDFT) response theory [12, 27–30]. The TDDFT “success story” has its roots in the computational affordability of TDDFT even for relatively large molecules. At the same time, TDDFT includes electron correlation which is important for the response of a molecule to time-dependent electric and magnetic fields. One of us has recently summarized the basic physical principles underlying the computation of ECD, VCD, ROA, and ORD, provided references to pioneering method developments within first-principles theory, discussed a number of representative case studies, and provided a tutorial section with program inputs and outputs [8]. Herein, we aim not to duplicate the material contained in [8], but to focus more closely on TDDFT response theory computations of natural *electronic* CD, and of optical rotation in the optical wavelength region, with an emphasis on recent literature. Somewhat related to optical rotation, the simulation of ROA spectra also entails the computation of mixed electric–magnetic molecular response at optical wavelengths (in this case the derivatives of certain response tensors along the vibrational normal modes). Therefore, we decided to include a brief section on ROA theory and a few benchmark studies in this chapter. Many research papers on the synthesis or characterization of chiral molecules now feature some form of CD or optical rotation calculation, but in some cases the computational part plays only a minor role. We provide a relatively dense coverage of the literature between 2005 and 2010 with an emphasis on papers where the TDDFT computational component is particularly significant. We highlight recent applications of TDDFT to problems related to electronic chiroptical properties, and review not only many successful applications but also cases where TDDFT based on a particular functional or a combination of functionals has revealed difficulties.

In order to render the chapter sufficiently self-contained, the reader will find a theory and methodology section immediately following this introduction (Sect. 2). Literature covering a broad range of applications is reviewed in the subsequent sections, grouped by topics as follows. **Section 3:** Benchmarks of functionals and basis sets, small molecule test cases. **Section 4:** Beyond gas phase and static structures. **Section 5:** (mainly) Assignment of absolute configuration case studies. **Section 6:** Analysis methods for chiroptical properties. **Section 7:** Case studies where a variety of methods was used to probe ECD,

OR, and ORD in detail. [Section 8](#): Metal complexes. [Section 9](#): Concluding remarks.

2 Time-Dependent Density Functional Theory and Chiroptical Properties

2.1 The Optical Rotation Parameter

The usefulness of TDDFT for first-principles theory based computations of chiroptical properties will become obvious after a brief discussion of the basic molecular parameters that describe the response of a molecule to the presence of an electromagnetic (EM) field. Consider, initially, the optical rotation (OR).

A linear polarized EM wave can be represented as a superposition of a left-hand and a right-hand circular polarized wave, with the plane of the linear polarization being defined by the phase shift between the two circular components. As Condon has summarized in a seminal review [31], the rotation of the plane of polarization as the EM wave passes through a chiral medium is caused by a difference of the refractive indices n_L, n_R for its left-hand and right-hand circular components, causing a phase shift between them. The leading-order term describing the difference in the refractive index for left-hand and right-hand circular polarized light for a medium containing freely rotating chiral molecules is governed by the molecular *optical rotation parameter* β . The OR parameter is the isotropic average of a rank-2 tensor, the optical rotation tensor β . We label its elements in a Cartesian coordinate representation as β_{uv} with $u, v, \in \{x, y, z\}$. It follows that $\beta = (1/3) \sum_u \beta_{uu}$.

On a molecular level, β describes the linear response of the electric (\mathbf{d}) and magnetic (\mathbf{m}) dipole moment of a single chiral molecule to the presence of time-dependent electric (\mathbf{E}) and magnetic (\mathbf{B}) fields. We refer the reader to the books by Kauzmann [32] and Barron [1] and the review by Condon [31] for derivations of the following equations for the field-induced dipole moments:

$$\mathbf{d}' = \alpha \mathbf{E} - c^{-1} \beta (\partial \mathbf{B} / \partial t) + \dots \quad (1a)$$

$$\mathbf{m}' = \chi \mathbf{B} + c^{-1} \beta (\partial \mathbf{E} / \partial t) + \dots \quad (1b)$$

Terms of higher order in the field amplitudes or in the multipole expansion are indicated by "...". The other two tensors in (1) are the electric polarizability α and the magnetizability χ . The *linear response* tensors in (1) are molecular properties, amenable to ab initio computations, and the tensor elements are functions of the frequency ω of the applied fields. Because of the time derivatives of the fields involved with the mixed electric–magnetic polarizabilities, chiroptical effects vanish as ω goes to zero (however, β has a nonzero static limit). Away from resonances, the OR parameter is given by [32]

$$\beta = \frac{2c}{3h} \sum_{j \neq 0} \frac{R_j}{\omega_j^2 - \omega^2} \quad (2)$$

where

$$R_j = \text{Im} \left[\sum_u \langle \Psi_0 | \hat{D}_u | \Psi_j \rangle \langle \Psi_j | \hat{M}_u | \Psi_0 \rangle \right] = \text{Im} [\mathbf{D}_j \cdot \mathbf{M}_j^*] \quad (3)$$

is the isotropic *rotatory strength* for excitation number j of the molecule, ω_j is the excitation frequency, $\hat{\mathbf{M}} = -e/(2m_e c) \sum_i (\mathbf{r}_i \times \hat{\mathbf{p}}_i)$ is the electronic magnetic moment operator and \hat{M}_u one of its Cartesian components, $\hat{\mathbf{D}} = -e \sum_i \mathbf{r}_i$ is the electronic dipole moment operator and \hat{D}_u one of its components, and the Ψ are the ground and excited states wavefunctions for the system in the absence of any external fields. Further, $\mathbf{D}_j = \langle \Psi_0 | \hat{\mathbf{D}} | \Psi_j \rangle$ and $\mathbf{M}_j = \langle \Psi_0 | \hat{\mathbf{M}} | \Psi_j \rangle$ are the electric and magnetic transition dipole vectors, respectively, for excitation number j .

Equation (2) is an example of a *sum-over-states* (SOS) expression of a molecular response property. It suggests an easy way of computing β , but in practice the SOS approach is rarely taken because of its very slow convergence, i.e., because of the need to compute many excited states wavefunctions. The summation goes over all excited states and also needs to include, in principle, the continuum of unbound states. As it will be shown below, there are more economic ways of computing β within approximate first-principles electronic structure methods.

For a medium with a standard concentration of identical noninteracting chiral molecules, the molecular OR parameter β can be directly converted to the observed specific rotation via

$$[\alpha]_\omega = 7200 \text{ deg} \frac{\omega^2 N_A}{c^2 M} \beta(\omega) \quad (4)$$

where M is the molecular weight in g mol^{-1} , ω is in units of s^{-1} , β in units of cm^4 , and N_A is Avogadro's number. Equation (4) excludes local field corrections or concentration effects. Another measure of the optical rotation is the *molar rotation* $[\phi]$. The value of the molar rotation, in units of $\text{deg cm}^2 \text{ dmol}^{-1}$, is obtained from the value of $[\alpha]$ in $\text{deg} [\text{dm} (\text{g/cm}^{-3})]^{-1}$, by multiplication of $M/100$ where M is the molar mass in g mol^{-1} :

$$[\phi] = [\alpha] \frac{M}{100} \quad (5)$$

In addition to the optical rotation tensor β , the *gyration tensor* \mathcal{G}' is often used as the basis of computing optical rotations, since it is more straightforward to define working equations for it in the frequency domain. The relation to the OR tensor is

$$\mathcal{G}'(\omega) = -\omega \beta(\omega) \quad (6)$$

The notation G' indicates the isotropic average of the G' tensor, $G' = (1/3) \sum_u G'_{uu}$, which is related to the OR parameter via $G'(\omega) = -\omega\beta(\omega)$. The gyration tensor is the imaginary part of the mixed electric–magnetic dipole response, relating the perturbed dipole moments of (1) in the frequency domain directly to the field amplitudes.

After this brief discussion of the physical significance of the OR parameter, the role of TDDFT in the description of chiroptical effects becomes clear. Chiroptical effects, on a molecular level, are related to perturbations of the electric or magnetic dipole moment by time-dependent magnetic and electric fields, respectively. Since equations (1) establish that the perturbations are linear in the applied field amplitudes, the computational protocol will typically first involve a (static, no external fields) DFT computation of the molecule’s ground state, followed by a *linear response* computation to determine $\beta(\omega)$ from the elements of the β tensor computed for a specific EM field frequency ω . These tensor elements are computed from the first-order perturbations of the dipole moments due to the presence of EM fields of a specified frequency.

For frequencies in the UV–Vis range, one is mainly concerned with the electronic dipole moment perturbations, and therefore frequency-dependent first-order response of the electronic structure is required. It is also possible to solve the time-dependent Kohn–Sham TDDFT equations in the presence of a field directly, and extract the frequency-dependent chiroptical response from the results via Fourier transformations [33]. At the time of writing this chapter this approach appears to have been abandoned in favor of solving frequency-dependent linear response equations directly (see Sect. 2.3), although the time-domain approach is an attractive alternative to investigate molecular response in the presence of very strong fields, or when it becomes necessary to consider pulse shapes. During the past two decades, TDDFT has established itself as the main computational workhorse for linear response computations for all but the smallest molecules, and between the years 2000 and 2010 it has given rise to a “renaissance” [10] in computations of electronic chiroptical properties because of the often very satisfactory performance (such as good agreement with experimental data) at affordable computational cost. For typical problems related to TDDFT see Sect. 2.7.

2.2 Optical Rotation and Circular Dichroism

As a linearly polarized EM wave passes through a chiral medium, and as the relative phase between the circular components changes due to the differing refractive indices n_L and n_R (Sect. 2.1), the absorption coefficients $\varepsilon_L, \varepsilon_R$ of the circular components may also be slightly different (circular dichroism). As a consequence, there is an increasing amplitude difference between the circular components as the wave propagates through the chiral medium, which causes the EM wave to acquire a certain degree of elliptical polarization. This ellipticity, which is actually very small, is a measure of the *circular dichroism* (CD) of the medium [34]. For electronic transitions, we use the acronym ECD.

Experimentally, the CD intensity is often quantified by the differential molar absorption coefficient $\Delta\varepsilon = \varepsilon_L - \varepsilon_R$ for the absorption of left-handed vs right-handed circular polarized light, where $\Delta\varepsilon$ and ε are usually in units of $\text{L mol}^{-1} \text{cm}^{-1}$. The conversion from $\Delta\varepsilon$ in $\text{L mol}^{-1} \text{cm}^{-1}$ to the molar ellipticity in $\text{deg cm}^2 \text{dmol}^{-1}$ is $[\theta] = (18,000 \ln(10)/4\pi)\Delta\varepsilon$. The connection with quantities that can be calculated from first-principles theory is given by the following equation [35]:

$$R_j = \frac{3\hbar c \ln(10) 1000}{16\pi^2 N_A} \int_{\text{CD Band } j} \frac{\Delta\varepsilon(E)}{E} dE \quad (7)$$

which relates the integrated intensity of a band in the CD spectrum that is caused by a single excitation to the rotatory strength of (3).

Thus, the optical rotation, like every dispersive molecular linear response property, has an absorptive counterpart. Fundamentally, based on requirements of causality and general “well-behavedness”, a linear response property such as the molar rotation $[\phi]$ must be accompanied by an imaginary part, which is in this case the molar ellipticity $[\theta]$ quantifying the differential absorption of left-hand vs right-hand circular polarized light. $[\phi]$ and $[\theta]$ are the real and imaginary part of a generalized complex molar rotation, and therefore have the same units (which is convenient for theoretical work). The OR parameter β also has an imaginary counterpart, β' . The real and the imaginary parts are not independent from each other, but related in the form of a Kramers–Kronig (KK) transform pair [34, 36, 37], here written for $[\phi]$ and $[\theta]$:

$$[\phi(\omega)] = \frac{2}{\pi} \text{PV} \int_0^\infty \frac{\mu[\theta(\mu)]}{\mu^2 - \omega^2} d\mu \quad (8a)$$

$$[\theta(\omega)] = -\frac{2\omega}{\pi} \text{PV} \int_0^\infty \frac{[\phi(\mu)]}{\mu^2 - \omega^2} d\mu \quad (8b)$$

“PV” indicates that the principal value of the integral must be taken. Figure 1 shows the behavior of the $[\phi] - [\theta]$ pair (or the real and imaginary part of the OR parameter β) off-resonance (no absorption) and in the vicinity of electronic absorptions. The absence of broadening entails a singular OR at the excitation frequencies of the molecule, where the response becomes purely imaginary.

Herein lies an opportunity for computing excitation spectra (and the actual CD intensity) from TDDFT linear response: Once a response equation for $\beta(\omega)$ (or $[\phi(\omega)]$) has been derived, circular dichroism can be computed from an equation system that determines the poles of β on the frequency axis, just like regular electronic absorption spectra are related to the poles of the electronic polarizability α [27]. Details are provided in Sect. 2.3. We call this the *linear response route* to calculating excitation spectra, in contrast to solving (approximations of) the Schrödinger equation for excited state and explicitly calculating excited state

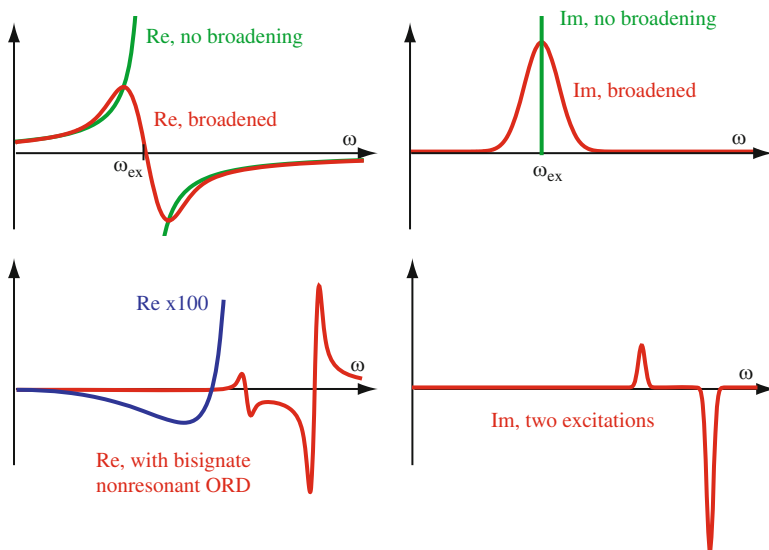


Fig. 1 *Top*: Behavior of the electronic linear chiroptical response in the vicinity of an excitation frequency. Re = real part (e.g., molar rotation $[\phi]$), Im = imaginary part (e.g., molar ellipticity $[\theta]$). Without absorption line broadening, the imaginary part is a line-spectrum (δ -functions) with corresponding singularities in the real part at ω_{ex} . A broadened imaginary part is accompanied by a nonsingular anomalous OR dispersion (real part). A Gaussian broadening was used for this figure [37]. *Bottom*: Several excitations. Electronic absorptions shown as a circular dichroism spectrum with well separated bands. The molar rotation exhibits regions of anomalous dispersion in the vicinity of the excitations [34, 36, 37]. See text for further details

wavefunctions. In the absence of excited state broadening, the divergent real part of the OR parameter as shown in Fig. 1 is given by (2). The corresponding imaginary part is

$$\beta' = \frac{\pi c}{3\omega} \sum_{j \neq 0} R_j [\delta(\omega_j - \omega) + \delta(\omega_j + \omega)] \quad (9)$$

This delta-function term is the “line spectrum” implied in Fig. 1. It was demonstrated elsewhere [8] that β and β' of (2) and (9) represent a KK transform pair satisfying (8).

Figure 1 also shows how low-frequency and higher lying excitations may influence the low-frequency (nonresonant) behavior of the OR. In the example, the low-frequency OR is dominated by the intense second transition, yielding an overall negative sign at low ω despite a positive CD of the first transition. As ω approaches the first transition, its influence eventually becomes dominant (see the frequency denominators in equations (8)), yielding a characteristic *bisignate* ORD off-resonance. Around a resonance, the ORD exhibits a characteristic peak–trough pattern the sign of which indicates the sign of the CD.

2.3 TDDFT Linear Response

This section summarizes the TDDFT linear response approach to compute optical rotation and circular dichroism. For reasons of brevity, assume a closed shell system, real orbitals, and a complete basis set (see Sect. 2.4 for comments regarding basis set incompleteness issues). From solving the canonical ground state Kohn–Sham (KS) equations,

$$\hat{F}_\sigma \varphi_{i\sigma} = \varphi_{i\sigma} \varepsilon_{i\sigma} \quad (10)$$

where \hat{F}_σ is the KS Fock operator for spin σ , and $\varepsilon_{i\sigma}$ one of its eigenvalues, a set of singly occupied molecular spin orbitals (MOs) $\varphi_{i\sigma}$, and a set of unoccupied MOs are available. Per equations (1), to compute the OR parameter in the frequency domain one needs to consider the perturbation of the electric or magnetic dipole moment by a magnetic and electric field of frequency ω , respectively. To compute the dipole moment perturbation, one needs the linear response of the density matrix. We follow the derivations of [38–43]. In the unperturbed MO basis, the linear response (indicated by superscript parentheses) of the density matrix can be written as

$$\gamma_\sigma^{(1)}(\mathbf{r}, \mathbf{r}', \omega) = \sum_{ij} P_{ij\sigma}^{(1)}(\omega) \varphi_{i\sigma}(\mathbf{r}) \varphi_{j\sigma}^*(\mathbf{r}') \quad (11)$$

where the coefficients $P_{ij\sigma}^{(1)}(\omega)$ have to be determined for the perturbation at hand from coupled-perturbed Kohn–Sham equations, or directly from perturbation equations for the density matrix elements [44].

After multiplication with the dipole operators and integration over space, the perturbations of one of the components (u) of the electric and magnetic dipole moment by the v -component of the perturbing field read

$$\begin{aligned} d_u^{(v)} &= \sum_{ai\sigma} (D_{ia\sigma}^u P_{ai\sigma}^{(v)} + D_{ai\sigma}^{u,*} P_{ia\sigma}^{(v)}) = \sum_{ai\sigma} D_{ia\sigma}^u (X_{ai\sigma}^v + Y_{ai\sigma}^v) \\ &= \bar{\mathbf{D}}^u \cdot (\mathbf{X}^v + \mathbf{Y}^v) \end{aligned} \quad (12a)$$

$$\begin{aligned} m_u^{(v)} &= \sum_{ai\sigma} (M_{ia\sigma}^u P_{ai\sigma}^{(v)} + M_{ai\sigma}^{u,*} P_{ia\sigma}^{(v)}) = \sum_{ai\sigma} M_{ia\sigma}^u (X_{ai\sigma}^v - Y_{ai\sigma}^v) \\ &= \bar{\mathbf{M}}^u \cdot (\mathbf{Y}^v - \mathbf{X}^v) \end{aligned} \quad (12b)$$

where $X_{ai\sigma}^v = P_{ai\sigma}^{(v)}(\omega)$; $Y_{ai\sigma}^v = P_{ia\sigma}^{(v)}(\omega)$, and the summation is restricted to $i \in \text{occ}$, $a \in \text{unocc}$. Vectors \mathbf{D}^u and \mathbf{M}^u collect the $(ai\sigma)$ matrix elements of the real electric-dipole and the imaginary magnetic-dipole moment operators (u -component), respectively. A bar indicates the transpose of a matrix or a column vector–row vector transposition. In the previous equation it was considered that the

magnetic moment operator is imaginary, leading to an antisymmetric matrix in the basis of real MOs.

The unknown density matrix coefficient vectors \mathbf{X} and \mathbf{Y} for each of the perturbing field-components can be determined from an equation system that resembles the “random-phase approximation” (RPA) equations [38]:

$$\left[\begin{pmatrix} A & B \\ B & A \end{pmatrix} - \omega \begin{pmatrix} -\mathbb{1} & 0 \\ 0 & \mathbb{1} \end{pmatrix} \right] \begin{pmatrix} \mathbf{X} \\ \mathbf{Y} \end{pmatrix} = \begin{pmatrix} \mathbf{V} \\ \mathbf{W} \end{pmatrix} \quad (13)$$

with

$$A_{ai\sigma,bj\tau} = -\delta_{\sigma\tau} \delta_{ab} \delta_{ij} (\epsilon_{b\tau} - \epsilon_{j\tau}) - K_{ai\sigma,bj\tau}$$

$$B_{ai\sigma,bj\tau} = -K_{ai\sigma,jb\tau}$$

$$W_{bj\tau} = V_{jb\tau} \quad \text{matrix elements of the operator for the external perturbation.}$$

Here, composite vector/matrix indices $(ai\sigma)$, $(bj\tau)$ for pairs of unoccupied (a or b) and occupied (i or j) MOs of spin σ or τ are used. The notation A etc. indicates a matrix with respect to these pairs of composite indices. In TDDFT, the Coulomb and exchange-correlation (XC) elements of the *coupling matrix* K are [38]

$$K_{ai\sigma,bj\tau}^C = \int d^3r d^3r' \cdot \varphi_{a\sigma}^*(\mathbf{r}) \varphi_{i\sigma}(\mathbf{r}) \frac{1}{|\mathbf{r} - \mathbf{r}'|} \varphi_{b\tau}(\mathbf{r}') \varphi_{j\tau}^*(\mathbf{r}') \quad (14a)$$

$$K_{ai\sigma,bj\tau}^{XC} = \int d^3r d^3r' \cdot \varphi_{a\sigma}^*(\mathbf{r}) \varphi_{i\sigma}(\mathbf{r}) f_{XC}^{\sigma\tau}(\mathbf{r}, \mathbf{r}', \omega) \varphi_{b\tau}(\mathbf{r}') \varphi_{j\tau}^*(\mathbf{r}') \quad (14b)$$

The quantity $f_{XC}^{\sigma\tau}(\mathbf{r}, \mathbf{r}', \omega)$ is the frequency-dependent XC kernel for which common approximations are applied: frequency-independent (adiabatic) local density approximations (LDA), adiabatic generalized gradient approximations (GGA), hybrid-DFT variants such as the popular functionals B3LYP and PBE0 in which K^{XC} contains an admixture of Hartree–Fock (“exact”) exchange X ,

$$K_{ai\sigma,bj\tau}^X = -\delta_{\sigma\tau} \int d^3r d^3r' \cdot \varphi_{a\sigma}^*(\mathbf{r}) \varphi_{b\tau}(\mathbf{r}) \frac{1}{|\mathbf{r} - \mathbf{r}'|} \varphi_{i\sigma}(\mathbf{r}') \varphi_{j\tau}^*(\mathbf{r}') \quad (15)$$

Further, there are asymptotically corrected XC kernels available, and other variants (for instance kernels based on current-density functionals, or for range-separated hybrid functionals) with varying degrees of improvements over adiabatic LDA, GGA, or commonly used hybrid DFT XC kernels [45]. *The approximations in the XC response kernel, in the XC potential used to determine the unperturbed MOs, and the size of the one-particle basis set, are the main factors that determine the quality of the solutions obtained from (13), and thus the accuracy of the calculated molecular response properties.* Beyond these factors, the quality of the

computational model (e.g., whether solvent effects are modeled or not, whether vibronic effects are considered, and so on) determines whether good agreement with experiment can be achieved for the right reasons or not.

From (12) it can be seen that either the symmetric ($\mathbf{X} + \mathbf{Y}$) or the antisymmetric ($\mathbf{Y} - \mathbf{X}$) part of the perturbed density matrix is needed. An expression for either one is readily obtained by adding and subtracting the two equations obtained from (13) to yield

$$\left[\begin{pmatrix} A + B & 0 \\ 0 & A - B \end{pmatrix} - \omega \begin{pmatrix} 0 & 1 \\ 1 & 0 \end{pmatrix} \right] \begin{pmatrix} \mathbf{X} + \mathbf{Y} \\ \mathbf{Y} - \mathbf{X} \end{pmatrix} = \begin{pmatrix} \mathbf{V} + \mathbf{W} \\ \mathbf{W} - \mathbf{V} \end{pmatrix} \quad (16)$$

For a perturbing electric field in the ν -direction we have $\mathbf{V} = \mathbf{W} = -\mathbf{D}^\nu$ and $\mathbf{W} - \mathbf{V} = 0$, while for a magnetic field in the ν -direction we have for the imaginary magnetic moment operator $\mathbf{W} = -\mathbf{V} = +\mathbf{M}^\nu$ and $\mathbf{V} + \mathbf{W} = 0$. A nonzero frequency couples the symmetric and the antisymmetric part of the perturbed density matrix, whereas in the static case the two equations in (16) are not coupled. For comments on the apparent lack of symmetry for the perturbation equations for static electric and magnetic fields see [46].

Assume a perturbing electric field of frequency ω in the ν -direction with perturbation matrix elements $(\mathbf{V} + \mathbf{W}) = -2\mathbf{D}^\nu$ in (16), and consider the perturbation of the magnetic dipole moment's u -component. With the help of the definitions

$$\Omega = -\mathcal{S}^{-1/2}(A + B)\mathcal{S}^{-1/2} \quad (17)$$

and

$$\mathcal{S} = -(A - B)^{-1} \quad (18)$$

(used to derive a Hermitean eigenvalue equation below), (16) and (12) yield an expression for the perturbed magnetic dipole moment [42]. Matching the result with (1) yields for the OR parameter [42, 47]

$$\beta(\omega) = -\frac{2c}{3} \text{Im} \sum_u \left(\bar{\mathbf{M}}^u \mathcal{S} \mathcal{S}^{-1/2} [\omega^2 - \Omega]^{-1} \mathcal{S}^{-1/2} \mathbf{D}^u \right) \quad (19)$$

By using the spectral resolution

$$[\omega^2 - \Omega]^{-1} = -\sum_j \frac{\mathbf{F}_j \bar{\mathbf{F}}_j}{\omega_j^2 - \omega^2} \quad (20)$$

($\mathbf{F}_j \bar{\mathbf{F}}_j$ meaning a Kronecker product), with

$$\Omega \mathbf{F}_j = \omega_j^2 \mathbf{F}_j, \quad (21)$$

(19) can be brought to SOS form which allows one to extract TDDFT expressions for the rotatory strength by comparison with (2). The solution of (21) yields the squares of the excitation energies of the molecule, i.e., this equation can be used to compute the electronic excitation spectrum. From a comparison of the TDDFT equation for the OR parameter in (19) with the SOS (2), the TDDFT rotatory strengths are readily computed from the transition moment vectors

$$\mathbf{D}_j = \omega_j^{-1/2} \bar{\mathbf{D}} \mathcal{S}^{-1/2} \mathbf{F}_j, \quad (22a)$$

$$\mathbf{M}_j = -\omega_j^{1/2} \bar{\mathbf{M}} \mathcal{S}^{1/2} \mathbf{F}_j. \quad (22b)$$

Equation (19) for the OR parameter can alternatively be derived from (16) for the case of a perturbing magnetic field, from which the same expressions for the transition dipole moments, (22), are obtained [42]. As long as the matrix Ω does not itself depend on the frequency ω , which is the case for common approximations in TDDFT based on adiabatic LDA, GGA, or hybrid kernels, (21) or a variant thereof can be solved efficiently as an eigenvalue equation. The use of the symmetrized Ω as in (17) is particularly useful in “pure” (nonhybrid) TDDFT because the matrix \mathcal{S} is then diagonal and contains inverses of the orbital energy differences between occupied and unoccupied orbitals on the diagonal. For hybrid XC kernels, this simplification is lost and other approaches involving non-Hermitian eigenvalue solvers and solving (13) for a vanishing right hand side can be more effective [39, 48, 49]. Due to the dimension of the \mathbf{A} , \mathbf{B} matrices, in most cases it is not possible to obtain the complete spectrum defined by a given one-particle basis. Instead, most solvers employ algorithms (Davidson, Lanczos) that allow them to compute a specified number of lowest excitations.

For an alternative formulation of TDDFT response equations starting with a definition of response properties as quasi-energy derivatives, the reader is referred to [50] and references provided therein.

2.4 Origin Dependence of Chiroptical Properties

The electric and magnetic dipole moment operators entering the rotatory strength expression, (3), are dependent on the coordinate origin. If the origin is changed from \mathbf{O} to $\mathbf{O}' = \mathbf{O} - \mathbf{a}$, each electron coordinate changes as $\mathbf{r}'_i = \mathbf{r}_i + \mathbf{a}$. Observable quantities such as the rotatory strength and the optical rotation must not depend on the choice of the coordinate origin. However, in quantum chemical computations with a finite atomic-orbital (AO) basis, computed ORs and rotatory strengths and other response properties involving the magnetic moment are generally origin dependent, i.e., the calculated results may change if an origin shift \mathbf{a} is applied to the coordinates of the molecule. The origin dependence is a manifestation of a more

general problem related to the gauge-freedom of the magnetic vector potential in calculations of magnetic properties with finite basis sets [51]. With good-quality basis sets, which are required anyway to obtain reasonable chiroptical properties, the origin dependence is often small enough such that reliable ORs and CD spectra can be calculated without explicitly fixing the origin dependence. However, it is obviously desirable to eliminate any possible dependence of the computed results on the chosen coordinate origin.

Currently, the two most common ways to circumvent the origin dependence of calculated magnetic and mixed electric–magnetic properties are (1) the use of magnetic-field dependent “gauge-including AOs” (GIAOs, also known as “London-orbitals”) [52–54] and (2) the use of the “velocity-gauge” for the electric dipole moment integrals [55, 56]. The GIAO basis depends explicitly on the magnetic field amplitude which requires the computation of a number of additional terms when solving response equations [54]. Such a basis eliminates the origin dependence of various magnetic properties in DFT/ TDDFT and a number of other variational quantum chemical methods, and also tends to moderately improve convergence of calculated optical rotations with respect to the basis set. Using the velocity gauge is conceptually simpler because it does not introduce a dependence of the basis set on the perturbing fields. Formally, the electric transition dipole moment in the rotatory strength expression (3) can be replaced by its velocity (momentum) form by considering that, in exact theory,

$$\langle \Psi_0 | \hat{\mathbf{D}} | \Psi_j \rangle = i\omega_j^{-1} \langle \Psi_0 | \hat{\mathbf{P}} | \Psi_j \rangle \quad (23)$$

Here, $\hat{\mathbf{P}} = \sum_i \hat{\mathbf{p}}_i$ is the one-electron momentum operator for the N -electron system. Isotropic optical rotations and rotatory strengths that are independent of the choice of the coordinate origin can be calculated in their *velocity form* upon replacing dipole moment matrix elements in TDDFT linear response computations by matrix elements of the momentum operator and division of the result by ω . With incomplete basis sets, (23) is not exactly satisfied but the origin independence of the results is retained, at least for some properties. As Pedersen et al. [56] have shown, optical rotations calculated in a finite basis using the velocity gauge lead to sometimes large values of $G'(\omega = 0)$ although G' has to vanish for zero frequency (see (6)). A modified velocity gauge for the optical rotation tensor [56] involves the subtraction of $G'(\omega = 0)$ from the result calculated for nonzero frequency, with both tensors computed at the same level of theory and using the velocity form of the electric dipole integrals. This procedure yields origin-independent results that compare well with the dipole-length form for large basis sets, and to G' obtained with GIAOs. Pedersen et al. [56] emphasized that using GIAOs does not eliminate the origin dependence within finite basis coupled-cluster methods (nonvariational) whereas the velocity gauge yields origin independent optical rotations for variational and nonvariational methods.

For isotropic media, only the trace of the optical rotation tensor (or of the G' tensor) is relevant for the optical activity. As a necessary requirement for an observable quantity, the isotropic OR is origin independent in exact theory, and in computations where the origin problem is accounted for as outlined at the beginning of this subsection. However, the individual tensor elements of β are origin-dependent even in exact theory, i.e., there is a principal origin dependence which is unrelated to using finite basis sets. The origin dependence of the individual β tensor elements is related to the multipole expansion of the vector potential of the EM field around the origin of the coordinate system [1, 57, 58]. If one includes not only the electric-dipole–magnetic-dipole but also the electric-dipole–electric quadrupole terms, it is possible to define an origin-independent OR tensor which has the same isotropic average as β [1, 59]. The elements of the origin-independent OR tensor read ($u, v, w, t, \in \{x, y, z\}$)

$$\tilde{\beta}_{uv} = \frac{1}{2} \left[\beta_{uv} + \beta_{vu} - \frac{1}{3} \sum_{wt} (\varepsilon_{uwt} A_{wtv} + \varepsilon_{vtw} A_{wtu}) \right] \quad (24)$$

where

$$A_{uvw} = 2 \sum_{j \neq 0} \omega_j \text{Re} \frac{\langle \psi_0 | \hat{D}_u | \psi_j \rangle \langle \psi_j | \hat{\Theta}_{vw} | \psi_0 \rangle}{\omega_j^2 - \omega^2} \quad (25)$$

is an element of the traceless dipole–quadrupole polarizability tensor, with $\hat{\Theta}_{wt}$ being an element of the electronic quadrupole operator. This tensor is also a linear response property and can be obtained during a computation of $\beta(\omega)$ or $G'(\omega)$ at negligible additional cost if the time-dependent electric field is chosen as the perturbation. One can define, in a similar way, origin-independent elements of the rotatory-strength tensor, for calculating the CD of oriented molecules. It is possible to bring the TDDFT analog of (25) to SOS form and derive origin-independent elements of the rotatory strength tensor. Implementations for origin-independent anisotropic CD were carried out within the random phase approximation [60, 61] and coupled cluster theory [62–64]. Regarding TDDFT, see [65].

The focus of this chapter is on isotropic chiroptical properties. Therefore, we briefly mention here some of the few available studies of measurements of ECD and OR tensors, and relevant TDDFT computations. Experimental techniques for measurements of OR tensors have been reported in [66–68]. For an overview see Claborn et al. [69]. Measurements of anisotropic CD in liquid crystals have been reported and reviewed in [70–72]. A measurement of the OR tensor at $\lambda = 670$ nm has been reported for pentaerythritol which crystallizes in the achiral point group S_4 [73]. TDDFT computations were also performed on a single pentaerythritol molecule (B3LYP/aug-cc-pVDZ). The computations yielded good agreement with experiment regarding the orientation of the OR tensor. TDDFT computations of

anisotropic origin-independent OR tensors both for the nonresonant and the resonant case (using a damping technique) were implemented [65]. The imaginary part of the origin-independent OR tensor elements agreed well with experimental oriented CD for the n -to- π^* C=O transition of a steroid molecule [71].

2.5 Computing Nonsingular Response Near Resonances

When written with the help of the Ω matrix as in (19), from (20) the OR parameter and other linear response properties are seen to afford singularities where $\omega = \omega_j$, just like in the SOS equation (2). Therefore, at and near resonances the solutions of the TDDFT response equations (and response equations derived for other quantum chemical methods) yield diverging results that cannot be compared directly to experimental data. In reality, the excited states are broadened, which may be incorporated in the formalism by introducing dephasing constants Γ_j such that $\omega_j \rightarrow \omega_j - i\Gamma_j$ for the excitation frequencies. This would lead to a nonsingular behavior of (20) near the ω_j where the real and the imaginary part of the response function varies smoothly, as in the “broadened” scenario at the top of Fig. 1.

In the absence of information about the Γ_j for individual excited states, and due to the fact that there are various mechanisms that lead to absorption line broadening, consider the following: if all excited states had the same $\Gamma_j = \gamma$, the replacement $\omega_j \rightarrow \omega_j - i\Gamma_j$ is equivalent to replacing ω by $\omega + i\gamma$ in the response equations. The approach has been justified more thoroughly by Norman et al. [74] Damping techniques have been used by us and other groups [36, 37, 74–77] to obtain nonsingular frequency-dependent response functions, including OR dispersion. The linear response equations (13) become complex upon substituting $\omega \rightarrow \omega + i\gamma$, and the solutions have a real and an imaginary part that can be used to calculate the real and the imaginary part of the OR parameter (or of G') simultaneously as a function of the frequency ω . Due to the form of the response equations, the *damping constant* γ takes the role of a finite-lifetime parameter, with an accompanying Lorentzian broadening of the imaginary part of the response function. However, in applications γ is usually used as a more general semiempirical broadening parameter. Information about the magnitude of γ can be obtained, for instance, from the line widths in electronic spectra (UV–Vis range); in applications values on the order of 0.1–0.2 eV have often been found suitable to reproduce experimental dispersion curves. We have recently devised procedures to combine frequency-dependent OR computations including damping with computations of a few excitations and their rotatory strength to significantly speed up the generation of well-resolved ORD curves [37], which is discussed in a later section. Moreover, the procedure allows replacement of the Lorentzian line shape intrinsic in the complex response procedure by other line shapes, for instance by a Gaussian broadening.

2.6 Raman Optical Activity

Although the focus of this chapter is on natural electronic optical activity, there is another chiroptical property for which it is necessary to compute chirality-related molecular response tensors: Raman (vibrational) optical activity (ROA) [17, 78–80]. For TDDFT implementations, see, for example, [81–84]. As for other chiroptical methods, ROA measures a differential intensity with respect to left-hand and right-hand circular polarized light. Underlying the Raman process is not an absorption of a photon, but an inelastic scattering involving the absorption of a photon into a “virtual” state and subsequent emission of a photon of different energy as the molecule returns to the electronic ground state, albeit a different vibrational state from which the absorption occurred. In a backscattering setup, the scattered beam is observed at 180° , the opposite direction to that of the incident laser beam. For a particular vibrational normal mode p , the corresponding isotropic ROA backscattering intensities are [1, 84]

$$I_{\text{R}}(180^\circ) - I_{\text{L}}(180^\circ) = K_p \left[\frac{48(\beta(G')_p^2 + \beta(A)_p^2/3)}{90c} \right], \quad (26)$$

where c is the speed of light, the parameter K_p is independent of the experimental setup but depends on both the incident and scattered frequencies, and $\beta(G')_p^2$ and $\beta(A)_p^2$ are tensor invariants of contractions of different combinations of the dipole–dipole polarizability transition tensor, α^p , the gyration transition tensor, \mathcal{G}'^p , and the electric dipole–electric quadrupole polarizability transition tensor, A^p . In the double harmonic approximation [85] the transition tensors can be computed from derivatives of the polarizability, gyration, and dipole–quadrupole tensors along the normal coordinates. For explicit expressions, see [1, 8, 84]. These derivatives can be computed either by numerical differentiation, which is straightforward but can be resource-consuming and numerically sensitive, or in form of analytic derivatives of the linear response tensors, which entails the solution of a number of quadratic response functions [44]. One of the numerical-differentiation based implementations [84] incorporates damping techniques which also allow for calculations of some of the leading terms of Resonance ROA (RROA) [86, 87] and simulations of surface-enhanced ROA (SERROA).

2.7 Considerations Regarding Basis Sets and the Choice of the XC Potentials and the XC Kernel

Apart from considerations as to how well the computational model represents experimental conditions (e.g., is there solvent present, are there temperature and concentration effects, or partial alignment of molecules?), the accuracy of a

TDDFT computation of chiroptical properties, like computations of other molecular properties, is determined by how well the electronic structure of the molecules of interest is described. In Sect. 2.3 it was emphasized that the one-particle basis set, and the approximations for the XC potential and the XC response kernel, are the major factors that determine the quality of the electronic structure, and response calculations.

Neither are computations with a complete basis set feasible, nor is the true density functional known. The approximations that can be made in a computation are dictated by the nature of the property of interest. For instance, the basis set in computations of CD spectra has to reflect the type of excited states of interest (valence transitions vs diffuse excited states, for example), and the type of operators involved. Diffuse polarization functions and high-angular momentum basis functions are beneficial for computations of properties involving electric and magnetic moment operators and can therefore be required for chiroptical response. A GIAO implementation can improve the basis set convergence, but for optical rotation the effect is less pronounced than, e.g., for magnetizabilities or nuclear magnetic shielding [54, 63, 88–90].

For CD spectra computations of larger molecules in a spectral range where mainly valence transitions are of interest, Gaussian type basis sets with flexibility such as cc-pVDZ and other members of this basis set family, or perhaps 6-311G** or TZVP, appear to offer a good compromise between accuracy and computational cost. Slater-type basis sets suitable for molecular chiroptical response calculations are available at <http://www.scm.com>. In particular for small molecules, where the experimentally accessible spectral range includes excitations into Rydberg states, it is very important that the basis set contains diffuse functions, and therefore basis sets such as aug-cc-pVDZ and 6-311++G**, and other members of these basis set families that incorporate diffuse functions are needed. For optical rotation, diffuse functions are generally beneficial since, from (8), the whole CD spectrum contributes to the OR at a given wavelength. The same considerations apply to ROA computations. For large molecules, diffuse basis sets are often not feasible (and would lead to numerical problems related to over-completeness within the numerical precision of the program). One might argue that, for a large molecule with a large manifold of valence states, the OR at long wavelengths is strongly dominated by transitions that do not require diffuse functions and therefore a valence basis set should be sufficient. In some cases it is possible to augment a valence basis set for a larger molecule with a few carefully selected diffuse functions that are not necessarily atom centered (e.g., to describe a Rydberg series) [91, 92].

Regarding the XC potential and the XC kernel, some of the main issues to be aware of are enumerated below (see recent TDDFT reviews [12, 29, 93] for details and additional references). Future developments in DFT and TDDFT will particularly target the problem how to incorporate into a functional the full exact exchange:

1. GGA functionals afford *self-interaction* errors that can affect computed response properties, including chiroptical response. HF theory is self-interaction free. Hybrid GGA functionals that incorporate typically between 20 and 50% of

HF exchange partially eliminate self-interaction errors and tend to be beneficial for calculations of CD spectra and OR, and to some extent for ROA, too. In response-theory computations, hybrids with a large fraction of HF exchange (50%) are often employed, also to address other common deficiencies listed here.

2. GGA and hybrid functionals do not have the correct *asymptotic behavior* far away from the molecule. As a result, the energies of Rydberg excitations tend to be poorly represented. Shape-corrected XC potentials with the correct asymptotic behavior significantly improve the performance of TDDFT to treat excitations into diffuse states. In recent years, *range-separated* density (long-range corrected, Coulomb-attenuated) functionals [94–96] have become popular. Depending on the parameterization of the functional, the correct asymptotic behavior can be obtained with such a functional. Many excitations relevant to the experimentally accessible spectral range of larger molecules do not go fully into the asymptotic region, in which case an asymptotically correct XC potential might have little impact.
3. *Charge-transfer* (CT) excitations pose difficulties especially for GGA functionals but also for hybrid functionals. The origin of the problem is related to points 1 and 2 [45], generally causing the energies of CT excitations to be significantly underestimated in TDDFT computations. The use of a hybrid with a large fraction of HF exchange, or preferably a range-separated hybrid functional, is beneficial and can in some cases circumvent the CT problem of TDDFT.
4. Approximations made in the XC potential generally also affect the quality of the XC response kernel if it is derived from the potential. In addition, in essentially all applications of TDDFT to computations of molecular response properties, the XC kernel is *adiabatic* (not frequency-dependent), even though it should be a function of frequency. One of the better known consequences of the adiabatic approximation is the inability of TDDFT to describe simultaneous excitations of more than one electron. Due to the sometimes very pronounced effects from the approximations under points 1–3, along with effects from limited basis set flexibility, it is not clear how strongly the adiabatic approximation affects present-day computations of molecular chiroptical response properties in terms of its ability to predict ECD and ORD in the UV–Vis range of frequencies.

If the computational resources available for a particular project allow the use of a hybrid functional, one can generally recommend the hybrid over a nonhybrid GGA functional, except perhaps for metal complexes where the choice of functional is not as straightforward (Sect. 8). Range-separated functionals come with an additional computational cost, but afford the same scaling of the required computational resources with respect to the number of basis functions. Recently proposed double-hybrid functionals that are corrected with a perturbative electron correlation term have been shown to yield better CD band positions than standard hybrid functionals and also afforded fewer “ghost” states (i.e., spurious excited states) [97], but the scaling of these functionals with system size is not as favorable as the scaling with

pure or hybrid GGAs. For computations on large molecules the use of a regular or range separated hybrid is sometimes not feasible, in which case particular care should be taken that the computed results do not suffer excessively from one of the issues 1–3 listed above. However, it needs to be emphasized that there are many successful applications of nonhybrid TDDFT to chiroptical response where these issues were simply not a main source of error. Moreover, the use of hybrid and range-separated hybrid functionals is not the cure for all TDDFT related problems.

3 Computational Benchmarking

It is not always possible to classify a computational study of chiroptical properties as purely theoretical, solely of “benchmarking” character (e.g., testing basis sets, or comparing electronic structure methods), or as being only of the “applications” type where an established method is selected and the main focus is to support the interpretation of experimental data by computations. This section is concerned with theoretical studies that are predominantly of “benchmark” character. These also often involve some method development.

Regarding TDDFT benchmark studies of chiroptical properties prior to 2005, the reader is referred to some of the initial reports of TDDFT implementations and early benchmark studies for OR [15, 42, 47, 53, 98–100], ECD [92, 101–103], ROA [81–84], and (where applicable) older work mainly employing Hartree–Fock theory [52, 55, 85, 104–111]. Often, implementations of a new quantum chemistry method are verified by comparing computations to experimental data for relatively small molecules, and papers reporting new implementations typically also feature comparisons between different functionals and basis sets. The papers on TDDFT methods for chiroptical properties cited above are no exception in this regard. In the following, we discuss some of the more recent benchmark studies. One of the central themes will be the performance of TDDFT computations when compared to wavefunction based correlated ab initio methods. Various acronyms will be used throughout this section and the remainder of this chapter. Some of the most frequently used acronyms are collected in Table 1.

An important development of experimental methods is the cavity ring-down polarimetry (CRDP) developed by Muller, Wiberg and Vaccaro [112]. This method allows for the measurement of optical rotations in the gas phase. High-resolution gas-phase ECD spectra are also available in the literature [91, 113, 114] that allow one to benchmark computational approaches without having to worry about the possible impact of solvent effects. Wilson et al. [115] measured optical rotations at 355 and 633 nm in both gas and solution phase for rigid and nonrigid compounds that are members of terpenoid, epoxide, alkane, and alkene families. Comparison of specific rotations from experiment in gas phase, as well as solution-extrapolated values, with the calculations (B3LYP/pVDZ and B3LYP/pVTZ) demonstrated pronounced solvent effects in some cases.

Table 1 Frequently used acronyms and their definitions

Acronym	Definition
$[\alpha]_D$	Specific rotation at the sodium D line
AC	Absolute configuration
B3LYP	Three-parameter hybrid GGA functional with 20% HF exchange
BHLYP	Hybrid GGA functional with 50% HF exchange
CC	Coupled-cluster theory
CCSD	Coupled-cluster with singles and doubles
CC2	An approximate CCSD method
COSMO	Conductor-like screening solvation model
DFT	Density functional theory
(E)CD	(Electronic) Circular dichroism
GGA	Generalized gradient approximation in DFT
HF	Hartree–Fock
LDA	Local density approximation in DFT
MP2	Møller–Plesset second order perturbative correlation method
OR	Optical rotation
ORD	Optical rotatory dispersion
PCM	Polarizable continuum solvation model
ROA	Raman optical activity
TDDFT	Time-dependent DFT
VCD	Vibrational circular dichroism
ZPVC	Zero-point vibrational corrections

Shcherbin and Ruud [116] explored the robustness of several parametrizations of the Coulomb-attenuated B3LYP functional (CAM-B3LYP) for chiroptical response calculations, with rotatory strengths as their main focus. CAM-B3LYP and other range-separated functionals (see Sect. 2.7) tend to better reproduce excitation energies for charge transfer and Rydberg states than conventional functionals when they satisfy the long-range condition [117]. In [116], the performance of nine CAM-B3LYP parametrizations were evaluated for CD spectra via comparison with more conventional functionals such as B3LYP, BHLYP, and the CC2 and CCSD wavefunction methods. In range-separated functionals, the exchange component is separated into a long-range and a short-range component by partitioning of the r_{12}^{-1} operator. In this study the partitioning proposed by Yanai et al. [95] was used:

$$\frac{1}{r_{12}} = \frac{[\alpha + \beta \operatorname{erf}(\mu r_{12})]}{r_{12}} + \frac{1 - [\alpha + \beta \operatorname{erf}(\mu r_{12})]}{r_{12}} \quad (27)$$

Here, α and β are dimensionless parameters that satisfy $0 \leq \alpha \leq 1$, $0 \leq \beta \leq 1$, and $0 \leq \alpha + \beta \leq 1$. The dimension of parameter μ is an inverse length. The first term in (27) represents the long-range part of the exchange operator, which is used in a modified electron repulsion integral code to calculate HF exchange, while the short-range part is computed using modified expressions for pure DFT exchange. The XC potential calculated this way has the correct asymptotic limit if $\alpha + \beta = 1$.

Table 2 Parametrizations of the CAM-B3LYP functional used by Shcherbin and Ruud [116]

Parameter	CAM1	CAM2	CAM3	CAM4	CAM5	CAM6	CAM7	CAM8	CAM9
α	0.19	0.19	0.19	0.2	0.19	0.19	0.2	0.19	0.2
β	0.46	0.81	0.81	0.3	0.46	0.81	0.3	0.46	0.3
μ	0.33	0.3	0.4	0.4	0.4	0.2	0.33	0.2	0.2

Shcherbin and Ruud explored variations in the μ value, starting with a previous optimized choice of $\mu = 0.33$ au [94]. The test set comprised 14 molecules that had previously been benchmarked for optical activity by a number of groups using TDDFT and CC [47, 98, 99, 101, 118], which included methyloxirane, methylthiirane, methylene-dimethylcyclopropane, methylaziridine derivatives, methylcyclobutene, dimethylallene, and norbornenone. The latter was not included in the statistical analysis because its chiroptical response depended strongly on the method applied, as discussed elsewhere in this review. Geometry optimizations were performed at the B3LYP/cc-pVTZ level of theory. Chiroptical responses were calculated using nine parametrizations optimized by Peach et al. [117]; see Table 2. Three of them had the correct long-range behavior of the XC functional ($\alpha + \beta = 1$). The rotatory strengths of the lowest lying excitation of seven molecules (all the aziridine derivatives and dimethylthiiranes, except for *trans*-2,3-dimethylthiirane) were in agreement between CC and all the functionals studied. However, for *trans*-2,3-dimethylthiirane, CAM1–CAM5 and BLYP yielded the opposite sign when compared with CC, which reflected a potential weakness of these functionals to be used for AC assignments. Pronounced differences between the various computations were observed when comparing the rotatory strengths, particularly those of higher-energy excited states. Through the comparison of the predicted rotatory strengths of the lowest five transitions calculated with the different functionals and CCSD, it was concluded that CAM8 performed the best. For CAM8, the μ parameter of 0.2 was smaller than the recommended value from other studies (0.33 [117], 0.4 [119], 0.47 [120]). The authors remarked that CAM6/7/8 yielded good agreement with CC regarding excitation energies and rotatory strengths, and that CAM6, at the same time, had the correct asymptotic behavior. However, it was also pointed out that it appeared difficult to parameterize the CAM-B3LYP functional both to yield correct excitation energies and have the correct asymptotic behavior, while at the same time yielding accurate and reliable results for the rotatory strengths.

Kowalczyk et al. [121] have investigated the basis set dependence of calculated ORs at four different wavelengths, and of the lowest six states in the ECD spectrum, for (*S*)-2-chloropropionitrile optimized at the B3LYP/6-311++G(d,p) level of theory. The ORD was calculated at 633, 589, 436, and 355 nm. Six basis sets were selected to calculate the specific rotation with an origin-invariant GIAO approach: aug-cc-pVDZ, aug-cc-pVTZ, aug-cc-pVQZ, d-aug-cc-pVDZ, d-aug-cc-pVTZ, and Sadlej-pVDZ (155, 326, 588, 207, 426, and 174 basis functions, respectively). All TDDFT calculations used the B3LYP functional. No solvation models were employed in the calculations. Experimental gas phase measurement

were available at 633 and 355 nm (-6.8 and -37.9 deg mL g⁻¹ dm⁻¹, respectively). Calculations were also carried out with CC2 and CCSD using four of the aforementioned basis sets.

For the singly augmented basis sets at the four wavelengths, going from a double- ζ to a triple- ζ valence basis set changed the specific rotation by up to 12.5 deg mL g⁻¹ dm⁻¹. Going from a triple- to a quadruple- ζ basis set afforded no more than a 0.8 deg mL g⁻¹ dm⁻¹ change. Going from a double- ζ to triple- ζ doubly augmented (d-aug-cc) basis gave a change in specific rotation no larger than 4.8 deg mL g⁻¹ dm⁻¹. It would seem that aug-cc-pVQZ and d-aug-cc-pVTZ are approaching the basis set limit for B3LYP OR calculations of this molecule. However, both B3LYP computed specific rotations at 633 and 355 nm were nearly a factor of two away from experiment for all of the tested basis sets. The CC2 and CCSD calculations agreed well with experiment; particularly calculations with the modified velocity gauge at 633 nm, which were within the experimental error. As the authors noted, however, the low computational cost of DFT allowed the use of the larger d-aug-cc-pVTZ and aug-cc-pVQZ basis sets. Such double augmentation might be necessary for some molecules where Rydberg and other diffuse states contribute much to the OR in the visible wavelength range. Comparing the lowest six calculated excitations from the aug-cc-pVDZ basis (length gauge representation), all B3LYP excitations were lower in energy than the third excitation obtained from CC2 and CCSD. The first B3LYP excitation was approximately 0.68 eV lower than the first CC2 excitation. The underestimation of excitation energies found in [121] appears to be a typical trend seen for TDDFT computations of excitation spectra for organic chromophores with GGA and standard hybrid functionals. Exceptions are known, such as the longest-wavelength transitions in cyanine type chromophores which are overestimated in energy with most density functionals [122, 123].

Using TDDFT and coupled cluster methods, Crawford et al. [124] have calculated the optical rotation at the sodium D line wavelength (589.3 nm) for 13 small rigid organic molecules, all of which have previously determined absolute configurations. The test set included four alkanes, two alkenes, and seven ketones, specifically (1*R*,2*S*,5*R*)-*cis*-pinane, (1*S*,2*S*,5*S*)-*trans*-pinane, (1*S*,3*R*,4*R*)-*endo*-isocamphane, (1*S*,3*S*,4*R*)-*exo*-isocamphane, (1*R*,5*R*)- α -pinene, (1*R*,5*R*)- β -pinene, (1*R*,4*S*)-camphenilone, (1*R*,5*S*)-nopinone, (1*R*,4*S*)-methylnorbornanone, (1*R*,3*S*,6*S*,7*R*)-2-brendanone, (1*R*,3*R*,5*R*,7*R*)-bisnoradamantan-2-one, (1*S*,4*R*)-norbornanone, and (1*S*,4*S*)-norbornenone. It was noted that TDDFT has been known to predict incorrectly the OR sign of six of these molecules at 589.3 nm. (Note that this statement obviously implies a standard functional such as B3LYP.) The geometries were optimized with the B3LYP functional and the 6-31G(d) basis set. TDDFT response calculations were performed using the same functional and the aug-cc-pVDZ basis set, with the molecular center of mass as the coordinate origin. The authors remarked upon the general importance of solvent effects; however, they were not included in the calculations. CCSD computations used the origin dependent length-gauge as well as the origin independent modified velocity-gauge (see Sect. 2.4).

For the four alkanes, B3LYP and CCSD reproduced the correct sign of the optical rotation for *cis*-pinane and *exo*-isocamphane, but not for *endo*-isocamphane and *trans*-pinane. For the two pinenes, both B3LYP and CCSD failed to predict the correct sign for one molecule. Of the seven ketones, B3LYP yielded the correct OR sign for camphenilone, 1-methylnorbornanone, 2-brendanone, and norbornone, while for nopinone, bisnoradamantonone, and norbornanone both DFT and length-gauge CCSD predicted the opposite sign with respect to experiment. Velocity-gauge CCSD yielded the correct OR sign for norbornanone. Experimentally, all of the alkenes and ketones for which TDDFT and CC failed to predict correctly the sign exhibit bisignate ORD. Therefore, for these systems the OR sign is delicately balanced by rotatory strengths of opposite sign, as mentioned in Sect. 2.2 (see Fig. 1). Overall, the study concluded that, surprisingly, CC on average did not perform clearly better than TDDFT when molecules had an experimental bisignate ORD. Improvements in the reproduction of the excitation energies and in antagonistic rotatory strengths of transitions that can lead to a bisignate nonresonant ORD curve should be addressed in future work. As we will often remark, a more reliable AC assignment can be made if the optical rotation is compared for several wavelengths.

Regarding the wrong sign of the OR of β -pinene, an interesting point has been made recently about the basis set convergence of OR calculations. Low-lying Rydberg states can contribute strongly to the OR at long wavelengths [125], and it appears that for bicyclic systems like this the basis set limit is not quickly approached. Baranowska et al. [126, 127] have demonstrated that with very large basis sets the experimental sign of the OR is obtained for β -pinene and *trans*-pinane using the popular B3LYP functional. The agreement with experiment might be fortuitous since vibrational corrections and solvent effects were not considered. However, this work demonstrates that the relative performance of TDDFT and CC methods might not be properly judged based on computations with basis sets such as aug-cc-pVDZ, aug-cc-pVTZ, or Pople basis sets of comparable flexibility in the valence and diffuse regions. Further studies appear to be necessary.

Giorgio et al. [128] have compared the computed ORD of a set of nine small rigid organic molecules with experiment, applying both Hartree–Fock and DFT (B3LYP), along with the 6-31G(d) basis, which is a smaller, more qualitative basis set as compared to the popular aug-cc-pVDZ. The nine molecules studied were (–)-verbenone, (–)-4-methylverbenene, (–)-fenchone, (–)-methylenefenchone, (+)-camphor, (–)-methylenecamphor, (+)-nopinone, (–)- β -pinene, and (–)-Troeger’s base. The optical rotations were measured in hexane, presumably a rather inert solvent with respect to OR measurements, while calculations were for the gas phase. The geometries were optimized at the B3LYP/6-31G(d) level of theory, and optical rotations at a number of wavelengths were calculated between 200 and 650 nm to generate ORD curves for comparison with experiment. The data for (–)-fenchone are shown in Fig. 2 as an example. It is apparent that the calculation of optical rotation without damping techniques diverges around the excitation wavelengths, making a comparison of calculations with experiment somewhat difficult although the sign pattern of the ORD is correctly obtained. Despite this

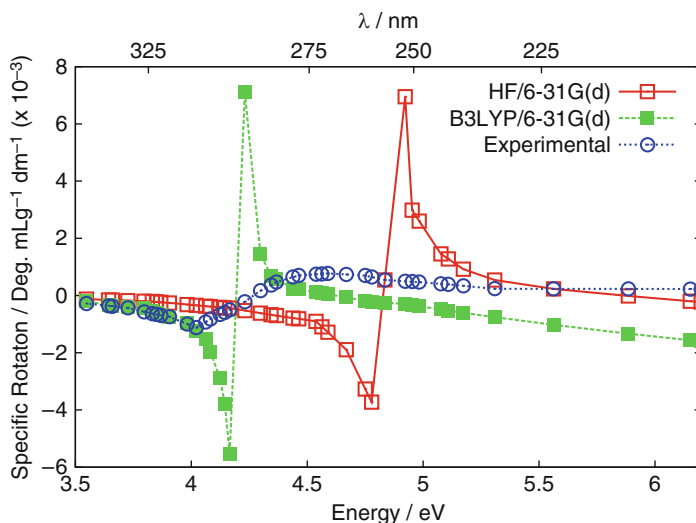


Fig. 2 ORD curves for (–)-fenchone in the resonant and nonresonant regions. Experimental curve measured in hexane. Notice how the ORD diverges around the excitation energies. Data to prepare the plot was taken from [128]

shortcoming, the optical rotation calculations overall compared reasonably well with experiment. At 589.3 nm, B3LYP/6-31G(d) yielded the correct sign for eight out of the nine selected molecules. For the one case of failure, (–)- β -pinene, the calculated dispersion curve as a whole succeeded in matching the trend of the experimental curve in the low energy range (ca. 3.75 eV), as it did for the eight other molecules as well. The Hartree–Fock response calculations failed to reproduce the low energy dispersion trend for Troeger’s base.

Autschbach et al. [75] have used TDDFT to calculate ORD including resonance wavelengths for six rigid organic molecules, five selected from Giorgio et al.’s work [128], as well as the tris-bidentate chiral complex $\text{Co}(\text{en})_3^{3+}$. The organic molecules were verbenone, fenchone, camphor, nopinone, Troeger’s base, and dimethyl-cyclopropane. The experimental ORD of the latter molecule was reported in [129]. A damping technique was implemented into the TDDFT calculations as described in Sect. 2.5. Some authors refer to this method as the complex polarization propagator, or as complex linear response, since the calculations yield both the real and the imaginary part of the OR parameter at a given frequency. Employing an empirical damping factor yields a broadening for calculated optical rotation similar to how calculated CD “stick spectra” are broadened, as illustrated in Fig. 1. The calculated ORD with a damping of γ should yield the same curve as the Kramers–Kronig transformation of the CD Lorentzian-broadened with the corresponding γ (at the same level of theory, assuming all possible excitations were calculated). This was explicitly demonstrated in [36]. All geometries were optimized using revPBE/TZP except for dimethyl-cyclopropane and Δ - $\text{Co}(\text{en})_3^{3+}$, for which geometries

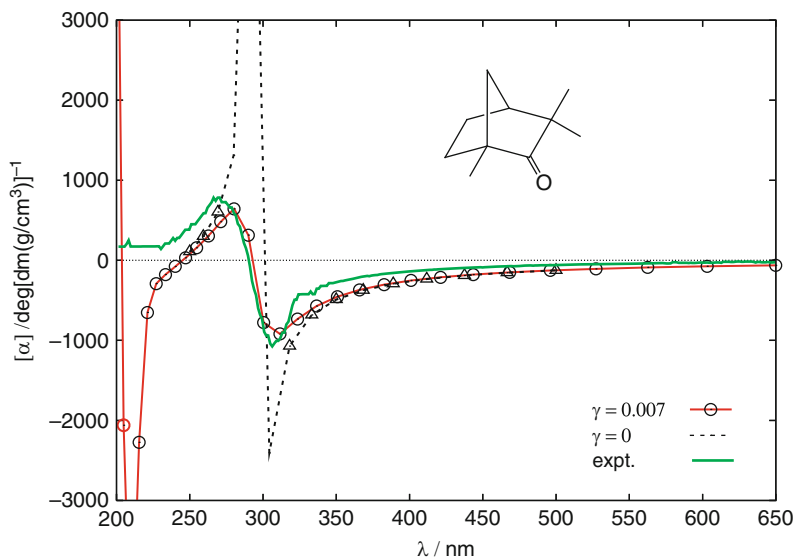


Fig. 3 Optical rotatory dispersion of fenchone as a function of the wavelength λ . Data for figure taken from [75], experimental data from [128]. Damping parameter γ in au

were taken from previous publications [101, 102]. The ORD curves were calculated with polarized diffuse Slater-type basis sets, using a standard GGA functional and, for comparison, an asymptotically corrected XC potential named SAOP [130]. The damped ORD curves matched the experimental trends well in the 200–600 nm range, except for Troeger's base whose agreement was labeled as reasonable. Damped and undamped results for fenchone are presented in Fig. 3 and can be compared to the undamped data obtained by Giorgio et al. [128] shown in Fig. 2. As in that previous work by Giorgio et al., the calculations without damping correctly predicted the pattern of the ORD, but due to the singularities a direct comparison is difficult (and becomes virtually impossible if several excitations overlap). The ORD curve calculated from the damped complex linear response TDDFT method follows the experiment much better. The calculations were also successfully applied to the metal complex for which the computations yielded an OR dispersion curve in the visible wavelength range that matched the experimental data, apart from an overall blue shift caused by an overestimation of the ligand field transition energies by the TDDFT computations. It has been argued elsewhere that this overestimation is mainly caused by self-interaction errors in the functionals [131].

Both [128] and [75] concluded that having more than one frequency/wavelength point to compare to will always lead to a more reliable assessment of the computational data and/or a more reliable AC assignment. Being able to directly calculate the ORD at resonant wavelengths would help to secure an assignment of AC even more so since the ORD then displays information about part of the CD spectrum in a more direct fashion.

Rudolph and Autschbach [37] have investigated the combined use of CD calculations and Kramers–Kronig transformations to aid in the fast generation of optical rotatory dispersion curves. The main goal was to deliver a well resolved rotatory dispersion curve with a minimal number of computed frequency points, even in the resonant regime where the ORD can be rapidly oscillating. It has been known for some time [132] that the KK transformation can be modified to a subtractive form for use with “anchor points.” If one knows the corresponding real/imaginary parts of a response function at a given frequency, it is possible to subtract it from the KK integral transformation in such a way that the transformation is exact at the anchor point. The generally subtractive KK transformation for CD to OR with N anchor points can be written as in equation (28), where $\beta(\omega)$ and $\beta'(\omega)$ are the frequency-dependent real and imaginary parts of the complex optical rotation parameter, respectively:

$$\beta(\omega) = \sum_i^N \beta(\omega_i) \prod_{j \neq i}^N \frac{(\omega^2 - \omega_j^2)}{(\omega_i^2 - \omega_j^2)} + \frac{2}{\pi} \left[\prod_i^N (\omega^2 - \omega_i^2) \right] \int_0^\infty \frac{\beta'(\mu)\mu}{(\mu^2 - \omega^2) \left[\prod_i^N (\mu^2 - \omega_i^2) \right]} d\mu \quad (28)$$

A “chained” doubly subtracted CD transformation (CDKK), where numerous $N = 2$ KK transforms of the ECD spectrum were pieced together to form a complete ORD, was considered superior to a single subtractive transform with $N > 2$. Through the use of a model CD spectrum and its exact KK transform, along with TDDFT computations for fenchone, dimethyloxirane, and [4]triangulane, the authors showed that a smooth ORD curve can be generated through the use of the CDKK of the ECD in the frequency range of interest using a few optical rotation anchor points. An example for fenchone is shown in Fig. 4. It was noted by Crawford et al. [133] that for [4]triangulane, CCSD calculations of the ORD at four frequencies in the nonresonant region required approximately 1 week of CPU time per frequency point. The same ORD curve was obtained in [37] with only two CCSD OR points used in a CDKK with a CD spectrum that came at little additional cost from BHLYP density functional computations.

Stephens and Harada [134] recently pointed out inconsistencies in the literature regarding the broadening of electronic spectra. It was strongly recommended to use Gaussian broadening since it tends to match ECD spectra better than the Lorentzian function. This also has implications regarding the shape of the anomalous OR dispersion around resonance frequencies. The combination of ORD computations with subtractive KK transformations of computed CD spectra of [37] allows for a “lineshape replacement” protocol whereby a calculated ORD corresponding to a Gaussian absorption band can be easily generated. By comparison with unmodified complex response ORD calculations it was shown that the lineshape effects on the

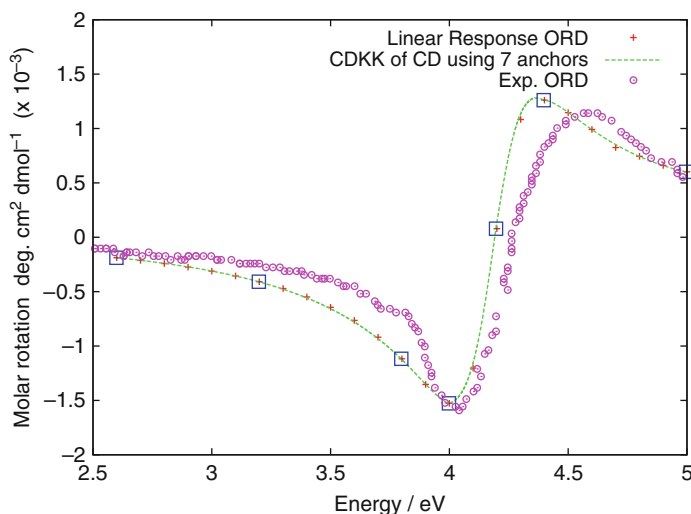


Fig. 4 Comparison of experimental ORD of fenchone with TDDFT calculations of the OR on a fine frequency grid, and with the ORD from a 7-anchor point CDKK (square markers). Data to prepare the plot were taken from [37]

ORD were relatively minor when considering typical differences between calculated and experimental ORD such as seen in Fig. 4.

Wiberg et al. [135] have studied the ORD of 2,3-hexadiene and 2,3-pentadiene. The ORD of 2,3-hexadiene was experimentally measured in gas phase, neat liquid, and in a number of solvents including C_6H_{12} , Bu_2O , MeCN, acetone, benzene, methanol, and CCl_4 . Large differences were observed between the gas phase and condensed phase optical activities. These data are shown in Fig. 5. It is clearly visible that different solvents can affect the optical rotation and therefore care should be taken when comparing experimental data to gas phase calculations. The magnitude of the OR and the magnitude of its dispersion in Fig. 5 appears to be influenced by a solvent-dependent shift in one or more low lying excitations. However, when interpreting the data one should also keep in mind that solvent-solute interactions may not only affect the excitation energies (the denominators in the SOS expression for the OR, (2)), but also the rotatory strengths of individual excitations (the numerators in the SOS). The conformational distribution and solvent effects were investigated computationally at the DFT and CC levels of theory. DFT calculations were performed with B3LYP and both the aug-cc-pVDZ and aug-cc-pVTZ basis sets while the CCSD calculations employed the aug-cc-pVDZ basis. The rotation of the ethyl group as shown in Fig. 6 gave rise to three 2,3-hexadiene conformers: *cis*, *gauche*(+), and *gauche*(-). The structures were optimized with B3LYP/aug-cc-pVDZ. Velocity-gauge, length-gauge, and GIAO specific rotations did not differ from each other by much more than $20 \text{ deg mL g}^{-1} \text{ dm}^{-1}$ for the three conformers with the double- and triple- ζ basis sets (B3LYP). The *gauche*(+) conformer afforded a specific rotation that was approximately twice

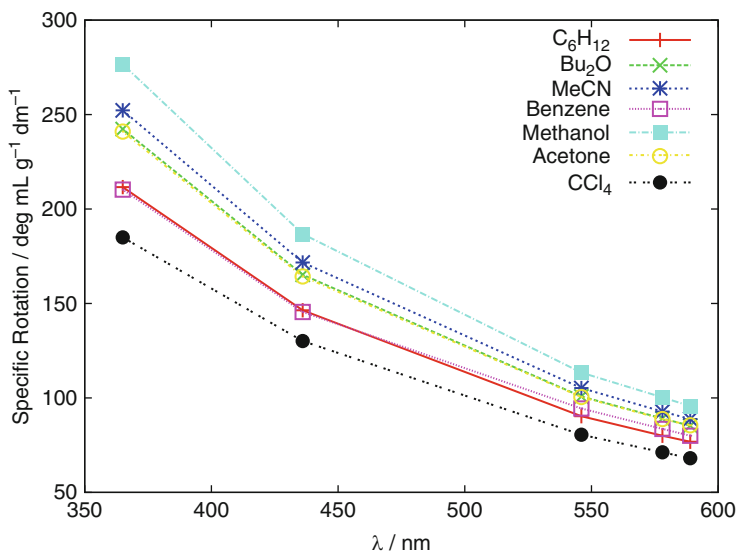
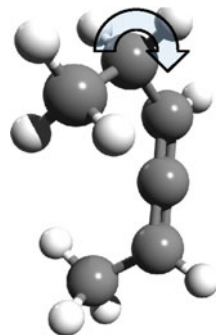


Fig. 5 ORD of 2,3-hexadiene in seven different solvents. Experimental data to prepare the figure were taken from [135]

Fig. 6 A depiction of 2,3-hexadiene illustrating the rotation of the ethyl group responsible for the three conformers. The *cis* conformer was taken as 0° . The *gauche*(+) and *gauche*(-) conformers correspond to 120° and 240° rotations, respectively, as discussed in [135]



that of *cis*, whereas the *gauche*(-) conformer had a magnitude similar to the *cis* conformer, but opposite in sign. This resulted in a Boltzmann averaged specific rotation around $175 \text{ deg mL g}^{-1} \text{ dm}^{-1}$ for aug-cc-pVTZ and between 156 and 173 for aug-cc-pVDZ at 589.3 nm depending on the way the gauge-origin problem was addressed. The Boltzmann averaged specific rotations for CCSD differed by a factor of two with aug-cc-pVDZ between length- and velocity-gauge (87 length, 164 velocity) indicating the extent of basis set incompleteness of the OR computations. Experimentally, the ORD ranged from approximately 70 to $277 \text{ deg mL g}^{-1} \text{ dm}^{-1}$ between 589 and 365 nm depending on which solvent was used. B3LYP/aug-cc-pVDZ yielded ORD that ranged between 108 and 272 over the same wavelength range (GIAOs; length and velocity also afforded similar results). The Boltzmann

averaged ORD curves calculated with the aug-cc-pVDZ basis set (velocity representation) are shown in Fig. 7 along with experimentally measured ORs for selected wavelengths for liquid and gas phase. The computations appear to agree well with the gas-phase measurements, in particular for CCSD, again highlighting the potential importance of solvent effects. The modeling of solvent effects in chiroptical property calculations will be discussed in more detail in Sect. 4.

We note in passing that when Wiberg et al. applied a Sum-Over-States analysis of the OR, the procedure required nearly 2,000 states for the SOS to converge for each of the 3 conformers. This situation appears to be rather typical for optical rotation [136, 137] which suggests that, except in simple cases, the SOS might not be the best tool to rationalize sign and magnitude of the optical rotation at nonresonant wavelengths in chemically intuitive terms.

Cyclopropanes, oxiranes, and thiiranes are small molecules, which makes them attractive for theoretical chemistry. Their small size is suitable for calculations at high levels of theory [115, 138] which also allows one to assess better the accuracy of TDDFT by comparing computational data. Moreover, the three membered ring, common to the three classes of molecules, provides rigidity to the system, thereby reducing the need for considering numerous conformers. At the same time, such rigid systems are suitable to analyze diverse substituent trends [139]. Another attractive feature is that for a number of small molecules, such as the three-ring systems mentioned here, chiroptical properties have been measured experimentally both in gas phase and solution.

Epichlorohydrin, an oxirane derivative, has three thermally accessible rotamers with respect to the C–C–C–Cl dihedral angle. Two of these rotamers contribute

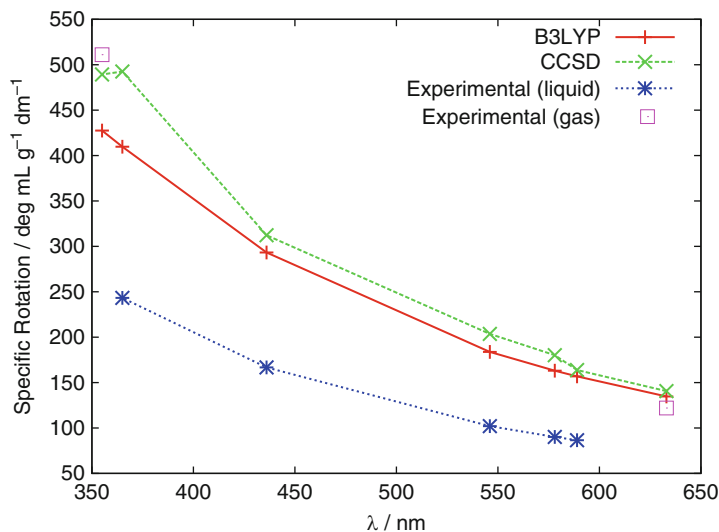


Fig. 7 Boltzmann averaged calculated and experimental ORD of 2,3-hexadiene. Data to prepare the figure were taken from [135]

with a positive sign to the specific rotation and one with a negative sign. Therefore an accurate conformational averaging is necessary to assess the agreement in sign and magnitude with experimental optical rotations ($-55 \text{ deg mL g}^{-1} \text{ dm}^{-1}$ at 633 nm [115]). In order to address this concern, computational studies utilizing different basis sets have been performed where the mole fractions can be compared to experiments in solution and gas phase [140, 141]. Gibbs free energies were calculated including a continuum model (PCM) for solvent effects. Reasonable agreement with experiment was achieved without modeling solvent effects in the OR calculations. It was concluded that the predominant origin of the observed solvent effects can be attributed to the change of rotamer mole fractions with different solvents.

Tam et al. [141] attempted to determine how reliable and accurate CC and DFT/TDDFT calculations are for this conformationally flexible molecule. In addition, they explored the sensitivity of the chiroptical response to two different factors. One was the accuracy of the mole fractions, and another was how different were the ORs of individual rotamers calculated at different levels of theory. It was found that with DFT, at the B3LYP/aug-cc-pVDZ level, the optical rotations were overestimated while CC yielded better agreement with experiment [141, 142]. The predicted gas phase optical rotation, averaged by CC or DFT mole fractions, were not in good agreement with either gas or solution phase experimental measurements. The DFT calculated optical rotations differed between 15 and 65% from experiment.

Methyloxirane is a molecule that has attracted much attention from many different theoretical chemistry groups over the years [16, 47, 53, 56, 98, 99, 107, 138, 143–149]. Its small size allows for the application of high-level ab initio methods. Additionally, this molecule exhibits an experimental bisignate ORD curve which makes it a challenging test case that is sensitive to the computational model used. Moreover, the experimental optical rotation of the S-enantiomer at 589.3 nm has a negative sign in the gas phase and a positive sign in water [112, 115]. This reveals solvent effects that can also be a challenge to reproduce computationally. Although not a TDDFT benchmark, we briefly mention work by Kongsted et al. [146] who explored the ECD of methyloxirane with several approximate CC methods and different basis sets, and obtained overall good agreement with experiment. The authors recommended the study of vibrational effects, especially for ORD curves. Solvent effects computed with the help of continuum models appeared to underestimate the solvent effects seen experimentally. Several attempts to predict the OR dispersion curve of methyloxirane have been made considering different levels of theory for geometry optimization and chiroptical response [138, 145, 146, 150], but more calculations are likely needed. Agreement of experimental and calculated optical rotation achieved using B3LYP at 355 nm [144, 145] has been considered by some as “the right result for the wrong reasons.” Tam et al. found that the lower-lying transitions of methyloxirane CD spectrum involves diffuse Rydberg states that are not well described with B3LYP [145, 147]. The source of errors when using B3LYP lies to some extent in the wrong asymptotic behavior of the functional. The reader is also referred to a comparison of the CD spectrum of dimethyloxirane

calculated with B3LYP and an asymptotically correct XC potential in [8]. The calculations reveal large differences between the spectra and indicate poor performance of B3LYP.

In the aforementioned study, Tam et al. [145] considered the specific rotation depending on the basis set and optimized geometry. In Fig. 8, as viewed from left to right, it can be seen that the quality of the basis set can have a large impact on the calculated specific rotation – a difference of up to 50 deg mL g⁻¹ dm⁻¹ in magnitude. When considering a particular basis set (viewing up-down), one can see the impact of the level of theory used for the geometry optimization. For example, depending on the optimized geometry, B3LYP/6-31G(d) optical rotations varied by about ± 5 deg mL g⁻¹ dm⁻¹ at 589.3 nm. At 355 nm the variation became approximately ± 20 . Figure 9 shows similar information, but for the CC calculations.

In order to determine what interactions dominate the optical rotation of methyloxirane in water, Mukhopadhyay et al. [151] have calculated the optical rotation of the solute–solvent system by including an explicit solvent shell in the calculations. Additional calculations were performed on the solvent shell alone, with the methyloxirane removed. Explicit solvent molecules were modeled by molecular dynamics. Implicit solvation was also considered, modeled by the COSMO continuum model. The optical rotation calculations were performed at the BP86/aug-cc-pVDZ level of theory and did not include zero-point vibrational

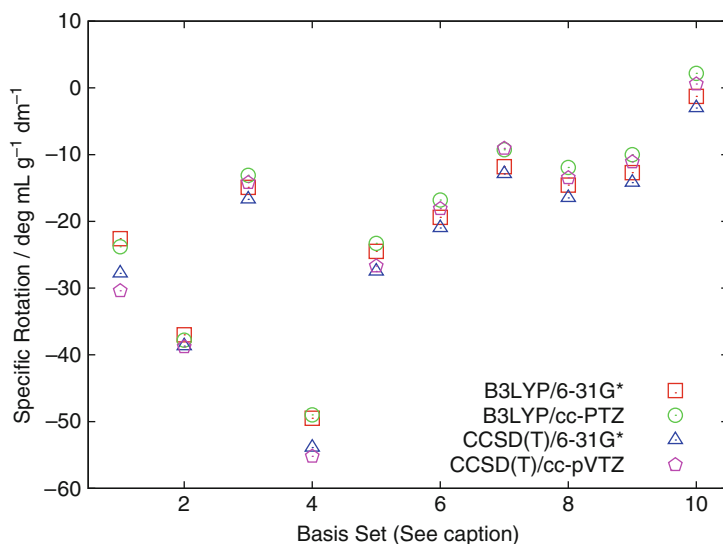


Fig. 8 The effect of basis set on the specific rotation of (*S*)-methyloxirane calculated with the B3LYP functional at 589 nm. The key labels the method of geometry optimization. Basis set numbers correspond to the following: 1 = 6-31G(d), 2 = 6-31++G(d,p), 3 = 6-31++G(2d,2p), 4 = cc-pVDZ, 5 = cc-pVTZ, 6 = aug-cc-pVDZ, 7 = d-aug-cc-pVDZ, 8 = mixed-cc-pVTZ (aug-cc-pVTZ(C,O) and aug-cc-pVDZ(H)), 9 = aug-cc-pVTZ, 10 = Sadlej-pVTZ. Data to prepare the plot were taken from [145]

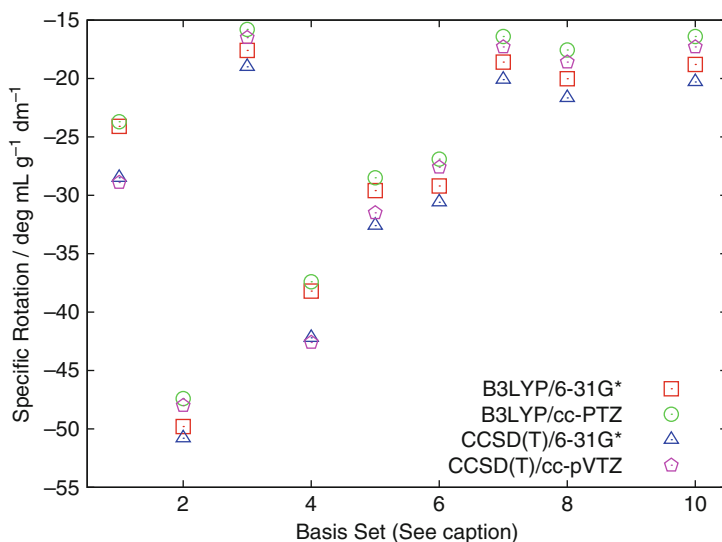


Fig. 9 The effect of basis set size, and geometry dependence, of the specific rotation at 589.3 nm for (*S*)-methyloxirane calculated with CCSD. See Fig. 8 for basis set labeling information. Data to prepare the plot were taken from [145]

effects as in other studies [147, 149, 150]. Since the results from a molecular dynamics trajectory were averaged, classical vibrations of the nuclei and the concomitant effects on the OR are contained in the results, if such an MD approach is used. The implicit solvation model did not reproduce all of the effects seen experimentally; however, the calculations performed with explicit solvation performed very well. The calculations on the solvent shell alone showed little contribution to the computed optical rotation. It was concluded that neither the solvent shell nor the solute alone is the predominant contributor to the ORD, but rather the system as a whole. The physical origin of the positive optical rotation was rationalized by considering the position of water molecules in the first hydration shell around methyloxirane.

Grimme and Goerigk [97, 152] have benchmarked ECD spectra for which the excitation energies were calculated with the double-hybrid functional B2PLYP. The accuracy of excitation energies had been considered as one of the main sources of error in CD spectra. Another source of error can be the transition moments; however, it was argued that the transition moments had sufficient accuracy with standard functionals. A similar point was also made by Autschbach et al. in a TDDFT benchmark study of ECD spectra of Co complexes [102]. The test set of [97] included molecules with varying types of transitions: Rydberg, Rydberg-valence, charge-transfer, and exciton coupling. Six different kinds of chromophores were considered: carbonyl (*R*)-norcamphor), alkene (*S,S*- α -pinene), aromatic (*S*)-2-phenyl-3,3-dimethylbutane), (*M*)-tetramethylpyrrololhellicene, (*S*)-14,17-dimethyl

[2](1,3)-azuleno[2]paracyclophane, and peptide bonds (cyclo-(*S*)-proline-(*S*)-alanine). The double-hybrid functional CD spectra compared well with experiment, and were in better agreement than spectra obtained with conventional functionals for all the molecules except α -pinene. It was also noted that for norcamphor and (*S*)-2-phenyl-1,3-dimethylbutane, the number of “ghost” states was reduced with B2PLYP. However, for (*M*)-tetramethylpyrrololhelicene, the perturbative correction in the double hybrid at high energies broke down, similar to what was seen in a previous study [152]. Grimme et al. concluded that the double functional TD-B2LYP performed better than conventional hybrid functionals since it showed fewer spurious transitions than standard functionals and yielded qualitatively correct CD spectra which were in better agreement with experiment than spectra obtained with B3LYP. The good performance was attributed to a counterbalance effect of the components of B2PLYP. A large fraction of HF exchange reduces the self-interaction error at the expense of reducing some electron correlation. However, the addition of a perturbative correlation correction in the double hybrid has a compensating effect.

We conclude this section with a brief discussion of ROA calculations. In a recent study revisiting the ROA of phenylethanol and phenylethylamine [153], Barron et al. have highlighted how straightforward routine measurements of ROA have become. It was noted that simulations of ROA have been performed for quite some time; however, as both experimental measurement and computational ability advance so must the level of detail in the computational model. It was suggested that the inclusion of effects related to the dynamics of the system, and anharmonicity of the potential energy surface, should be included to yield the most realistic and accurate ROA results.

Reiher et al. [83] have investigated the basis set and TDDFT functional dependence of vibrational ROA for five selected molecules: (*S*)-methyloxirane, (*R*)-epichlorohydrin, (*S*)-glycidol, (*M*)-spiro[2, 2]-pentane-1,4-diene, and (*M*)- σ -[4]-helicene. Three different functionals were used: LDA, BLYP, and B3LYP. For these three functionals, a set of six different basis sets were used, including cc-pVDZ, cc-pVTZ, aug-cc-pVDZ, and aug-cc-pVTZ. Furthermore, Reiher and coworkers used a modified minimal basis proposed for ROA computations by Zuber and Hug [154] (rarefied ROA basis sets) who argued that hydrogens play a critical role in the description of ROA, especially in organic compounds, due to their light weight and likelihood of being at the outermost portion of a molecule because of their monovalent nature. To properly describe the response tensor contributions from these atoms, diffuse p-functions are critical, while the polarizing p-functions found in typical basis sets such as DZP or 6-31G** are not of as high importance (though beneficial, of course). To test the validity of their benchmark calculations, the authors compared experimental backscattering ROA to B3LYP/aug-cc-pVDZ calculations for (*S*)-methyloxirane, (*M*)-spiro[2,2]-pentane-1,4-diene, and (*M*)- σ -[4]-helicene; overall the computations agreed quite well with experiment. See Fig. 10 for an example. It was noted that some of the contributing factors to the differences could be limitations in the computational model, lack of inclusion of solvent effects, as well as the lack of anharmonic contributions. The authors also found that LDA computations performed worse than more

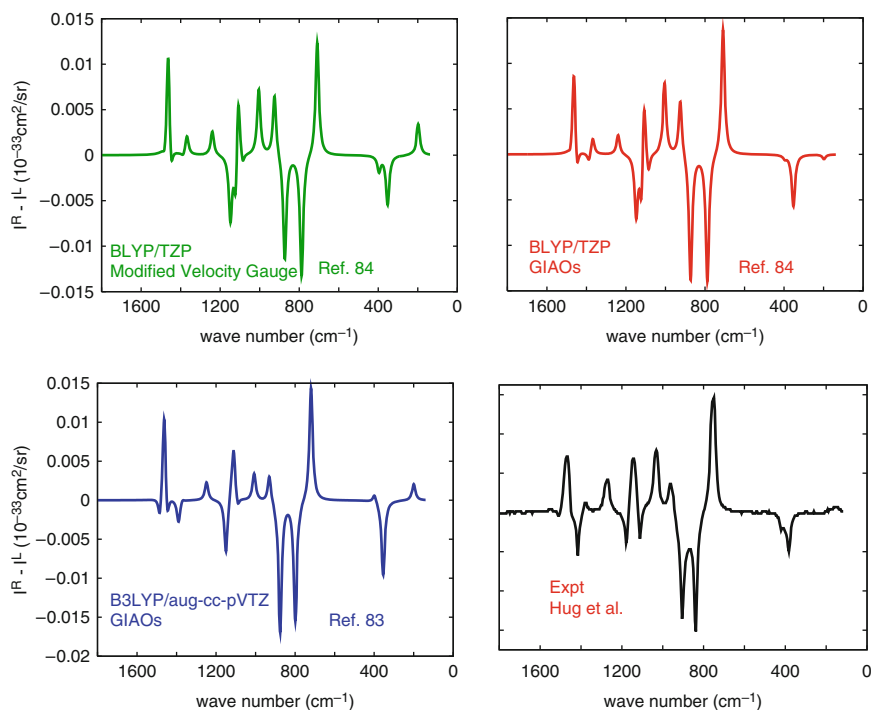


Fig. 10 Computed and experimental ROA for methyloxirane. *Top*: Two spectra computed with Slater-type basis sets and nonhybrid functionals, from [84]. *Bottom*: Computation with a Gaussian-type basis set and the B3LYP hybrid functional, and experimental spectrum. Data to prepare the plots were taken from [83] and [84]

sophisticated functionals, and that the results of the nonhybrid BLYP and the B3LYP hybrid functionals were comparable. Therefore, computational resources can potentially be saved in ROA computations by adopting BLYP and other nonhybrid functionals that do not require to evaluate HF exchange terms in the response steps.

Jensen et al. [84] have developed a TDDFT approach to calculate ROA spectra with a laser frequency far from, but also near and at resonance (resonance ROA, RROA). Experimentally, evidence of RROA has been observed for (+)-naproxene at 514.5 nm [87]. This was not a full resonance situation, as the laser frequency lies in the tail of an intense 325 nm absorption. If an excited state is sufficiently separated from other excitations energetically, a single state approximation [86] predicts that while under resonance the RROA spectrum should become monosignate. Its sign is determined by the negative rotatory strength of the excited state in resonance. This was the observed behavior for naproxene. In their implementation paper, Jensen et al. predicted RROA for hydrogen peroxide as well as (S)-methyloxirane, as they are small molecules which are often used for

benchmark studies. The geometries of both molecules were optimized with BLYP and a Slater-type triple- ζ polarized basis. For response calculations, particularly the ROA of hydrogen peroxide, several Slater-type basis sets were compared: TZP, TZ2P, QZ3P, AZTP, AZ2P, and QZ3Ppol. Comparing the calculated ROA of this molecule for several vibrational modes, the use of basis sets with more diffuse functions yielded results that were similar for both the velocity gauge and those which used GIAOs. The RROA for methyloxirane at full resonance was calculated to be monosignate with the correct sign, which indicated that the single-state approximation provides a viable description of the system. Regarding the nonresonant ROA computations, Fig. 10 also shows two spectra computed with the Slater-type basis sets. They compare well with the Gaussian-type basis set calculations of Reiher et al., and with experiment.

4 Beyond Gas Phase and Static Structures

In order to advance the usefulness of theoretical calculations in broader applications, the computations should be carried out for a system that describes experimental conditions as accurately as possible. To do this, consider the following topics for a description of a system beyond using a single static structure at 0 K: conformational averaging of static gas phase structures (this has been partially addressed already in Sect. 3), solvent effects on static structures, zero-point and finite temperature vibrational averaging, and molecular dynamics (MD) or Monte-Carlo (MC) sampling without and with solvation.

For instance, solvent effects can represent much more than just a small perturbation of the electronic structure of a molecule. Sometimes these effects can be strong enough that the chiroptical response can be dominated by their influence on the chiral solute. For instance, effects that should be considered are how a solvent shell perturbs the electronic structure of the solute (and therefore its chiral response [155]), or the possibility of a solute transferring its chirality to the surrounding solvent shell (influencing one particular solvent molecule [151] or the entire solvent shell [156]). Here and in the following discussions it is assumed that the solvent itself is not chiral, and therefore the only contributions to the chiroptical response of the solution are from the solute or from chirality induced by the solute in the solvent shell.

There are many cases when the molecule of interest is not rigid and has more than one stable conformer under the experimental conditions, and more care has to be taken when interpreting the results. For example, Mazzeo et al. [157] studied three benzotricamphor derivatives. Two of them were rigid and a small basis set (B3LYP/6-31G*) produced optical rotation of the same sign and order of magnitude as found experimentally. However, $[\alpha]_D$ of a benzotricamphor derivative with three benzyldiene moieties added, which was expected to have only one predominant conformer (based on a conformational search performed with a molecular mechanics force field), was overestimated by more than a factor of

two: the calculation in gas phase was $-3,216 \text{ deg mL g}^{-1} \text{ dm}^{-1}$, while the experimental value was $-1,330$ in chloroform. Further study of the OR as function of the twist of the styrene chromophore and the benzylidene moiety showed that there were three related conformers which were within 2 kcal mol^{-1} of the lowest-energy conformer, with specific rotations ranging from -500 to $-3,216 \text{ deg mL g}^{-1} \text{ dm}^{-1}$. In addition, it was noticed that the conformational distribution was sensitive to the method applied (i.e., various semiempirical methods vs DFT). It was concluded that the four thermally accessible conformers should be considered in the calculation in order to improve the OR. Controlling the number of conformers can be simplified experimentally by several approaches, such as locking the structure by chemical derivatization of the molecule of interest and/or adding achiral chromophores that work as chiral probes as has been done in the literature for aliphatic and aromatic diols derivatized with fluorenone [158] (**3**, **10**) (the molecule numbering refers to Figs. 15–17 of Sect. 5 which is concerned with AC assignments). Such an introduction of rigidity in a set of 12 molecules reduced the thermally accessible conformers to one and chiroptical response calculations yielded the correct AC assignment.

The problems of conformational averaging and of considering solvent effects are interconnected. For instance, one of the more obvious effects when going from the gas phase to solution is the resulting change of mole fractions for solutes with multiple conformers [115, 159]. One example of this is epichlorohydrin, which is discussed elsewhere in this chapter. A conformer distribution with several thermally accessible conformers that have considerably different ORs and ECD spectra might also result in a marked temperature dependence of measured and simulated chiroptical properties.

Computationally, the chiral response for conformationally flexible molecules can be obtained by a Boltzmann averaging of thermally accessible conformers, as has been done recently for the OR of helical pentacycles (**41**) [160], oruwacin (**31**) [161], amino acids [136, 155, 162–165], and linarinic acid (**37**) [166], to name just a few examples. As already pointed out, temperature and solvent effects may alter the conformer mole fractions and therefore the averaged chiroptical properties [10, 167]. A difficult situation arises when the response of individual conformers is very different in magnitude and/or in sign. This situation has been investigated for systems such as helical hydrocarbons (**41**) [160], 3-chloro-1-butene [168], a hydrogen peroxide model system [169], amino acids [136, 155, 162–165], and others [10, 141, 167]. See also the examples discussed in Sect. 3. However, if all of the conformers of a given molecule have the same sign of the chiroptical response, as, for instance, in the case of linarinic acid (**37**) [166], a conformational averaging may not even be necessary for an AC assignment. Kundrat and Autschbach have considered a somewhat related situation: a sign change of the OR and the longest-wavelength ECD band occurs for natural amino acids in aqueous solution upon protonation at the carboxylate group [136]. Despite the fact that individual amino acid conformers had, in several cases, different signs of the calculated OR, resulting in considerable difficulties in reproducing the experimental OR in magnitude and sign, the *change* of the chiroptical property upon protonation turned out to

be the same for essentially all conformers of all amino acids that were investigated (which all had the same absolute configuration) and agreed with the experimental sign. It was argued that an AC assignment of organic molecules might be possible if an effect can be exploited where the change in the OR upon protonation, for instance, or a simple derivatization is more reliably reproduced by computations than the conformationally averaged OR itself. A follow-up study on $-OH$ and $-F$ analogs of amino acids indicated that protonation/deprotonation of chiral organic acids might indeed be useful in this context [170].

4.1 *Conformational Averaging mainly of Static Gas Phase Structures*

Wiberg and coworkers investigated the OR temperature dependence of hydrocarbons. Different studies explored how the presence of an alkene chromophore, the conformer distribution, and vibrational modes affected the OR in small molecules.

For example, the specific rotation of three rotamers of 3-chloro-1-butene has been studied computationally [168], accompanied by experimental measurements. The relative energies of the conformers were considered one of the main sources of error when computing the average optical rotation. This encouraged the authors to perform optimizations at various levels of theory including CCD/6-311+G(d) and CCSD(T)/6-311++G(d). The computed optical rotation as a function of the C–C–C=C dihedral angle between 0° and 180° ranged between -526 and $244 \text{ deg mL g}^{-1} \text{ dm}^{-1}$. Further exploration of the vibrational modes of 3-chloro-1-butene showed that four of them had a strong effect on OR. The predicted temperature effects on the OR was in agreement with the experimental trends. The calculations did not include solvent effects, while measurements were performed in cyclohexane solution. Substituent effects were explored by changing the chloro-group to a fluoro-, cyano-, and ethynyl-groups. The trends in both the energies and the specific rotation as a functions of the dihedral angle were qualitatively similar for all the aforementioned substituents, despite the fact that the transition energies were remarkably different. Steric interactions were the predominant factors determining the mole fractions. It was concluded that the ORs of 3-substituted-1-butenes were strongly dependent on the methyl torsion, thus related to the observed temperature dependence. Additionally, it was found that for the substituents considered at the chiral carbon, the nature of the substituent was not a predominant factor.

Wiberg et al. [171] gained information related to the origin of the change in optical rotation as functional of torsional angle, and thus the vibrational/rotational effects on their OR, by exploring a set of six achiral hydrocarbons, alkanes and alkenes from C_2 to C_4 at the B3LYP/6-31++G(d,p) level of theory.

Variations in the alkene C–C–C=C torsional angles caused a positive sign of the specific rotation, while for the alkanes the sign varied. Vibrational modes were explored, and it was found that in the alkenes the terminal CH₂ group had a more dominant effect than =CH–. From a comparison of the transition energies for each conformer, however, it was deduced that these were not the main factors determining the differences in the optical rotation. The authors explored basis set effects on ethane, finding a strong dependence which was attributed to the importance of Rydberg type orbitals.

Wiberg et al. investigated the effect of conformation on the optical rotation of 2-substituted butanes [172]. The potential energy curves of 2-X-butan-2-yls (where X = F, Cl, C, HCC) as a function of the C–C–C–C backbone dihedral angle showed a similar pattern for all substituents analyzed (MP2/6-311+G), with the *trans* rotamer being the most stable. For all the substituents considered, the *trans* rotamer afforded a negative $[\alpha]_D$ when calculated at the B3LYP/aug-cc-pVDZ level of theory. A correlation of the specific rotation and temperature for 2-chloro-butane and 2-methyl-butyronitrile was attributed to a strong effect from the C–C–C–C torsional angle.

Crawford et al. [142] analyzed chloro-butenes, specifically 3-chloro-1-butene, using CC with a triple- ζ basis set and CCSD(T) for energy estimations, which yielded excellent agreement between the experimental and calculated (Boltzmann averaged) specific rotation. Crawford et al. noted substantial differences of the CD and OR of the different conformers of 3-chloro-1-butene when comparing calculations at different levels of theory (CCSD and B3LYP). One of the sources of errors was attributed to the origin dependence related to basis set incompleteness rather than the overall quality of the electronic structure. It was pointed out that 3-chloro-1-butene is an example where problems might arise when a molecule has a global minimum with thermally accessible vibrational modes that overlap with the energy of another local minimum. It was suggested to explore the average over the torsional nuclear wave functions explicitly instead of Boltzmann averaging ORs. We refer the reader to Sect. 4.3 for examples of such procedures.

Pecul et al. [165] have studied the OR of alanine and proline as function of the rotation of the amino, carboxylic, and hydroxy groups in the gas phase using HF and DFT (B3LYP). The zwitterionic structures adopted by amino acids in solution are not stable in gas phase and were not modeled. Seven conformers of (*S*)-alanine (six minima, one transition state), 18 conformers of (*S*)-proline (nine neutral, six cationic, and three anionic) were optimized using B3LYP and the aug-cc-pVDZ basis set. Optical rotation calculations were carried out at the same level of theory. Among the six minimum structures for (*S*)-alanine, the calculated specific rotation varied between 20 and 124 deg mL g⁻¹ dm⁻¹ with the lowest energy conformer around 58. The one transition state afforded a specific rotation of –85. With regards to conformational changes of (*S*)-alanine, the specific rotation varied from 100 to –80 deg mL g⁻¹ dm⁻¹ when considering a rotation of the amino group and approximately 150 to –300 when considering a rotation of the carboxylic group. Rotation of the hydroxyl group afforded a specific rotation between 0 and

180 deg mL g⁻¹ dm⁻¹. For the nine neutral (*S*)-proline conformers, the specific rotations varied from -184 to 48 deg mL g⁻¹ dm⁻¹. For the six cationic (*S*)-proline conformers, the specific rotations varied from -64 to -168 deg mL g⁻¹ dm⁻¹. For the three anionic (*S*)-proline conformers, the specific rotations varied from -623 to +151 deg mL g⁻¹ dm⁻¹. The large magnitudes for the anionic species was rationalized by their low excitation energies which make the system more susceptible to small perturbations (see the SOS equation (2)).

Kundrat and Autschbach considered amino acids in solution by employing the COSMO continuum model and DFT/TDDFT computations using the B3LYP and BHLYP functionals and the aug-cc-pVDZ basis [163, 164]. The main conclusions from this and follow-up work on amino acids by the same authors [36, 136, 155, 162] are discussed elsewhere in this chapter. Of relevance in this subsection is the following aspect: obtaining the correct balance between intramolecular hydrogen bonding in the solute and intermolecular hydrogen bonding between solute and solvent (water) was identified as one of the challenges for the computational model related to obtaining reliable mole fractions for the solution structures (including the zwitterions). The continuum model, with its lack of a discrete description of the solvent, tended to overestimate the stability of conformers with internal hydrogen bonds. As a result, the molar rotation from such conformers tended to contaminate the Boltzmann averaged ORs predicted for the solution.

Grimme et al. [173] have considered the optical rotation of seven different conformers of (*R*)-4-ethyl-4-methyloctane. This particular molecule has a low experimental specific rotation, determined to be about +0.2 deg mL g⁻¹ dm⁻¹. Care has to be taken when computing the response of a molecule with a very small specific rotation due to the approximations in the methods and models used which may easily cause the OR to have the wrong sign. The thermally accessible conformers included the rotamers around the chiral carbon and bond rotations within the substituents. Geometries were optimized at the B97-D/TZV(d,p) level of theory without inclusion of solvent effects. A Boltzmann distribution was used to average the calculated response. The optical rotations were performed using BHLYP/aTZV2P as well as the BLYP/aTZV2P and BLYP/TZVP levels of theory. Depending on the functional/basis set, the individual specific rotations of each conformer varied between about -10 to +50 for the different calculations. The Boltzmann averaged specific rotation of the seven conformers lead to a computed value between 0.7 and 2.2 deg mL g⁻¹ dm⁻¹ at all levels of theory used here. Given the comparatively large specific rotations of the individual conformers, the agreement with experiment can be regarded as good.

4.2 Solvent Effects on Static Structures

For an early benchmark study of OR involving a continuum solvent model, see [174]. More recently, Pecul et al. [175] have implemented a polarizable continuum

model (PCM) which was applied to the calculation of solvent effects on ECD. Benchmarks were performed with methyloxirane, and the bicyclic ketones camphor, norcamphor, norbornenone, and fenchone (all *R* configurations) and dielectric constants corresponding to the solvents *n*-hexane, CF₃CH₂OH, CH₃OH, CH₃CN, and H₂O. Molecular geometries were optimized using B3LYP/TZVP. ECD calculations employed the d-aug-cc-pVDZ basis for methyloxirane and d-aug-cc-pVDZ (aug-cc-pVDZ on hydrogens) for the bicyclic ketones. For methyloxirane, as the dielectric constant ϵ of the continuum solvent increased from 1 to 78, the lowest-energy transition (HOMO to LUMO) blue-shifted approximately by 0.2 eV. All of the CD bands calculated for this molecule exhibited a corresponding shift. For camphor, the HOMO–LUMO transition also blue-shifted upon varying ϵ from 1 to 78, but the magnitude was only on the order of 0.05 eV. The PCM reproduced both the solvent effect independence of the *n*-to- π^* transition and the solvent dependence of the Rydberg type transition. The experimental trend of a reduction in intensity of ECD when comparing gas phase and solution (*n*-hexane) was computationally reproduced with the continuum model. Norcamphor, norbornenone, and fenchone all exhibit carbonyl centered *n*-to- π^* transitions. Similar trends were seen among the respective CD bands, such as blue-shifting in solvents with larger dielectric constant. However, a sign change of the ECD when going from gas phase to solution, with *n*-hexane as a solvent, that is observed experimentally for norcamphor, was not reproduced with the continuum solvation model. Norbornenone is experimentally seen to display an increase in ECD intensity in trifluoroethanol and a decrease in hexane. This trend was not reproduced by the computations. The increase in rotatory strength of the *n*-to- π^* transition with increasing dielectric constant of the medium was correctly predicted for fenchone.

Kundrat et al. [164] have used TDDFT with a continuum solvent model (COSMO) for solvent effects to calculate the ORD of amino acids in protonation states corresponding to neutral solutions (zwitterionic), low pH (cationic, protonated), and high pH (anionic, deprotonated). The authors noted that, as in any study like this, one challenge is the ability to predict the energy of the conformers as accurately as possible to calculate the mole fractions. The amino acids studied were glycine, alanine, proline, and serine. All calculations were performed using B3LYP/aug-cc-pVDZ for optimizations and d-aug-cc-pVDZ for response calculations. The B3LYP, B3LYP, BP86, and HF correctly reproduced the OR dispersion trends for cationic alanine in the 250–600 nm range. The B3LYP calculated specific rotation at the sodium D line for the cationic and zwitterionic forms were 206.4 and 3.9 deg mL g⁻¹ dm⁻¹, respectively, demonstrating the large effect from protonation. Overall, DFT with COSMO did reproduce the sign of the OR at 589.3 nm for cationic, anionic, and zwitterionic amino acids in solution. A consistent underestimation of excitation energies was noted, which resulted in an overestimation of the OR at the sodium D line and an overall red-shift of the dispersion curves. It was already pointed out that such underestimations of excitation energies are often seen for organic molecules with TDDFT computations using standard functionals.

4.3 Zero-Point and Finite Temperature Vibrational Averaging

Under certain conditions it can be expected that vibrational effects play an important role in the chiroptical response of a molecule. For example, vibrational effects might be important when [176]:

1. The molecule becomes chiral by isotopic substitution, which is a challenging case for typical quantum mechanical calculations.
2. The OR or ORD show changes with respect to temperature that are not well explained by changes in Boltzmann averaging. This would certainly include rigid molecules.
3. The ORD exhibits a bisignate nonresonant feature that cannot be explained with the intensity of low lying transitions.
4. Strong solvent effects are observed experimentally that indicate solvent–solute interactions which might in turn alter vibrational effects in the solute.

Ruud et al. [147] performed OR calculations on (*S*)-propylene oxide (methyloxirane) at 355 nm at the B3LYP/aug-cc-pVDZ level of theory including zero point vibrational corrections to investigate the sign change seen in the experimental ORD when approaching lower wavelengths. The computed OR agreed with experiment in sign but was overestimated in magnitude. The authors concluded that the different optical rotation signs at 355 and 589 nm in cyclohexane were a consequence of vibrational effects. In a related study, Kongsted et al. [150] included vibrational contributions to the computed optical rotations at 589.3 and 633 nm. The optical rotation as a function of rotating the methyl group showed that a small geometric deviation can provoke large changes in the OR. However, after vibrational corrections had been incorporated into the calculated optical rotation, an incorrect sign was still obtained. Therefore the authors considered it necessary to add corrections from other vibrational modes. Further investigation showed that TDDFT using the SAOP XC potential and a highly flexible diffuse Slater-type basis strongly overestimated the OR while CC agreed well with experimental gas phase data [146]. Overall, it was concluded that vibrational contributions are important for the OR of methyloxirane and that temperature should be taken into account when calculating vibrational corrections. It was noted that solvent effects on the methyl rotation and on the low-lying CD transitions, as well as deviations from the equilibrium geometry, are factors contributing to the optical rotation sign change from nonpolar to polar solvents.

Kongsted and Ruud [177] revisited the case of (*S*)-methyloxirane and studied solvent effects on zero-point vibrational corrections with regards to optical rotations and NMR shielding constants. A polarizable continuum model (PCM) was used to model solvent effects. (*S*)-Methyloxirane was optimized with B3LYP/cc-pVTZ and all OR calculations used the aug-cc-pVTZ basis set. The OR at three different wavelengths was calculated for the isolated molecule, as well as in cyclohexane, acetonitrile, and water. When going from the gas phase to a high dielectric solvent, the optical rotation at 355 nm changed from 29.6 to

46.5 deg mL g⁻¹ dm⁻¹. Contributions from the zero-point vibrational corrections can also be as large, or larger in magnitude than the OR calculated at the equilibrium geometry. For cyclohexane, the optical rotation at 589.3 nm for the optimized geometry was -1.8 and the ZPVC was calculated as 5.1. At 633 nm the ZPVC to the OR in the gas phase was calculated to be 13.2 deg mL g⁻¹ dm⁻¹. After the inclusion of solvent effects for acetonitrile, the ZPVC dropped to 4.1. Therefore, not only are solvent and vibrational effects important, but there are “cross terms” to be considered as possible effects.

Ruud and Zanasi [147] have studied the effects of ZPVCs on the OR of (*S*)-methyloxirane. Using B3LYP and both aug-cc-pVDZ and aug-cc-pVTZ basis sets, the optical rotations at 355 and 589.3 were calculated, along with the corresponding ZPVCs. The zero-point vibrational corrections can contribute a sizable amount to the optical rotation. For example, the calculated optical rotation for (*S*)-methyloxirane (B3LYP/aug-cc-pVDZ) was -23.2 deg mL g⁻¹ dm⁻¹ and the ZPVC was more than a factor of two larger in magnitude (48.1). For the double- ζ basis, a sign change in the ORD from +10.2 at 355 nm to -26.9 at 589 nm was computed, in agreement with experiment. For the triple- ζ basis, after the inclusion of the ZPVCs, the calculated optical rotation was computed to be positive at both wavelengths. Due to the typical underestimations of excitation energies by B3LYP, the correct sign change is predicted with a smaller basis, but not with the larger one, demonstrating the importance of error balance.

Regarding the overall magnitude of ZPVC for ORs of organic molecules, Mort and Autschbach [148] have considered a set of 22 rigid organic molecules. Computations of ORs and their ZPVCs employed the B3LYP functional and the aug-cc-pVDZ basis set. With regards to the magnitude of the vibrational corrections relative to the equilibrium OR, the individual ZPVC varied between 2% and 155%. It was determined that vibrational corrections contribute on average approximately 20% (median) to the optical rotation. The authors noted that vibrational corrections alone should not be the only factor included when comparing solution phase experimental data, since the overall average agreement of computed and experimental data did not improve when including vibrational corrections. The reason might be the performance of the B3LYP functional used for the ZPV study for the equilibrium ORs. Pedersen et al. [178] recently proposed to combine TDDFT vibrational corrections with CC equilibrium optical rotations in order to obtain more accurate results. It is likely that the same protocol can also be used in conjunction of equilibrium ORs calculated with more modern functionals.

Using an extension of the ZPVC approach of [148], Mort and Autschbach [125] have studied the temperature dependence of the optical rotation. Following an initial report for fenchone [179], a set of six rigid bicyclic organic molecules was considered: (+)- α -pinene, (+)- β -pinene, *cis*-(+)-pinane, (-)-camphene, (+)-camphor, and (-)-fenchone. Geometries were optimized using the B3LYP and the aug-cc-pVDZ basis set. ECD and specific rotation calculations used the same level of theory. The specific rotations were calculated at three wavelengths (365, 546, and 589 nm), with vibrational corrections calculated at six evenly spaced temperatures

between 0 and 100 °C. For four out of the six compounds the temperature dependence seen experimentally was reproduced. A selection of results for fenchone, α -pinene, and camphene is shown in Fig. 11. Two compounds, (+)- β -pinene and *cis*-(+)-pinane, experimentally exhibited the opposite trend to what was predicted by the computations. These cases were analyzed further by considering their ECD spectra, but the analysis was inconclusive. Given the discussion of Sect. 3 regarding the basis set convergence of the OR for bicyclic systems, it is yet unclear whether the disagreement between theory and experiment is caused by basis set incompleteness, deficiencies in the functionals, or simply by the fact that the temperature dependence of the OR for these molecules may not be dominated purely by vibrational effects.

Due to recurring problems with the treatment of methyl rotations in calculations of vibrational averages of optical rotations, Mort and Autschbach [149] have proposed a computational protocol for a separate treatment of hindered rotations. In a nutshell, in this approach a quasi-free rotation of a functional group is treated separately from the vibrational average, with numerically calculated hindered-rotor wavefunctions. With regards to optical activity, the authors studied their protocol on three molecules: (*R*)-methyloxirane, (1*S*)-norbornanone, and

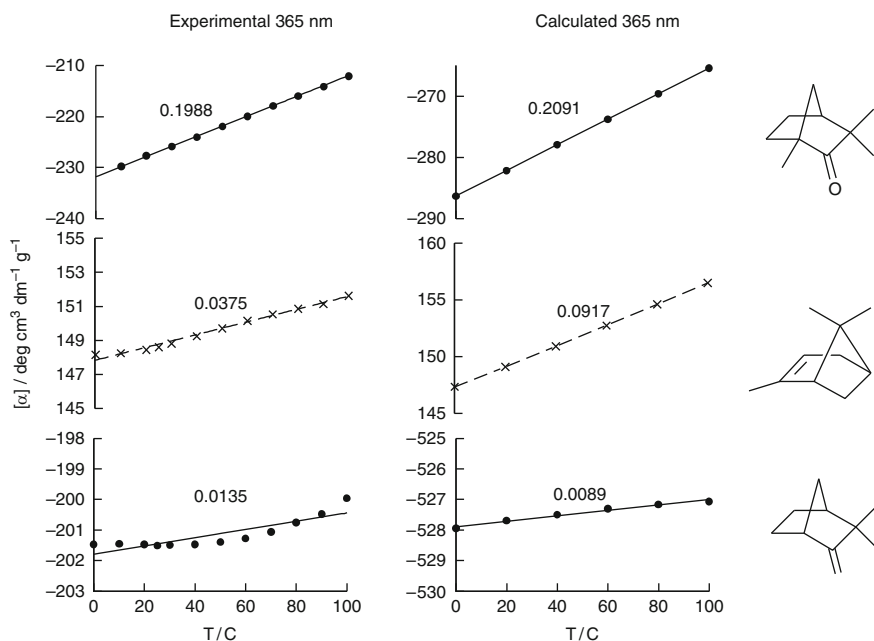


Fig. 11 Selected experimental and calculated results for the temperature dependence of the optical rotation at 365 nm. *Top*: Fenchone. *Center*: α -Pinene. *Bottom*: Camphene. Data to prepare the plots were taken from [125] (experimental data were from Wiberg et al., J. Phys. Chem. A (2005), 109:3405)

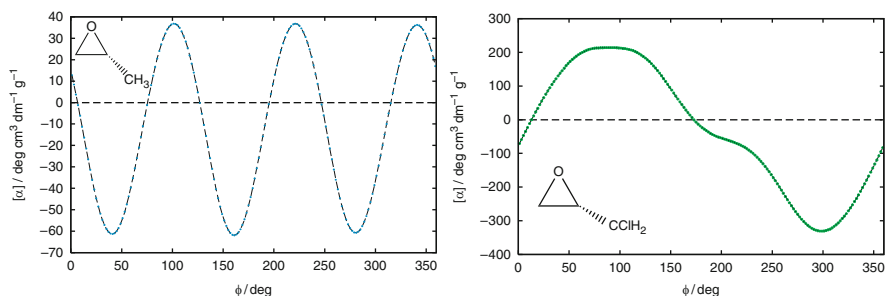


Fig. 12 Specific rotation as a function of rotation of a substituent group. *Left*: Rotation of the CH_3 group in methyloxirane. *Right*: Rotation of the CClH_2 group in epichlorohydrin. A 0° angle corresponds to a minimum-energy geometry. See [149]

(*S*)-epichlorohydrin. Geometries for these molecules were optimized using B3LYP and the aug-cc-pVDZ basis set. Calculations of frequencies, normal modes, and optical rotations were performed at the same level of theory. Typically, the group responsible for the hindered rotation is a methyl group or a Cp ring in organometallic complexes. For testing the method the chloromethyl group in epichlorohydrin was also considered. The computed response showed the expected oscillatory behavior with respect to the local symmetry of the rotating groups, with the OR ranging approximately between -60 and $+35 \text{ deg mL g}^{-1} \text{ dm}^{-1}$ for methyloxirane and -60 to $+40 \text{ deg mL g}^{-1} \text{ dm}^{-1}$ for methylnorbomane. The strong variations led to a pronounced temperature dependence of the conformationally averaged specific rotations, although for these molecules a significant deviation from treating the rotation as a vibrational average would not occur up to around room temperature. The calculations for epichlorohydrin afforded a specific rotation range from approximately 200 to -300 . Each minimum afforded a different calculated specific rotation. A comparison of the $[\alpha]_D$ with respect to the group rotation is shown in Fig. 12 for methyloxirane and epichlorohydrin. The calculations for epichlorohydrin indicated the limits of separating vibrational from rotational modes when there is strong coupling between the modes and a rotation cannot cleanly be separated. It was suggested to compare rotational averages with and without relaxed potentials for the rotations, as deviations are likely to indicate the validity of separating different types of motion. For epichlorohydrin, this separation is not valid.

4.4 Molecular Dynamics with Solvation

A very detailed description of solvent effects, along with temperature effects from nuclear motion (typically with classical nuclei), is obtained from average computed chiroptical response properties computed along the trajectory of a

molecular dynamics (MD) simulation, or using Monte-Carlo (MC) simulations. If solvent molecules are treated as discrete entities, such approaches can provide much detail about the solvent structure around a solute, along with specific solvent solute interactions that a continuum model is not capable of describing. An MD averaging based TDDFT study has been performed for methyloxirane in water [180]. For the polar solvent water, the simulations based on BP86/aug-cc-pVDZ TDDFT calculations were successful in reproducing the OR at wavelengths longer than 400 nm. In aqueous solution, between 355 and 650 nm, the OR remained positive for (*S*)-methyloxirane. Given the difficulties with reproducing the gas phase ORD for methyloxirane, as discussed in previous sections, the reasons for the good agreement with experiment are unclear. It is a possibility that the strong solvent effects in some way suppress delicately balanced OR contributions from higher lying states and cause the system to behave less sensitive to approximations in the electronic structure. A subsequent MC based study, using otherwise similar techniques, considered the possibility of creating a chiral imprint in a nonchiral solvent [159]. See a highlight article [181], and a later section on chiral imprinting.

Following an MD benchmark study for glycine [162], Kundrat and Autschbach [155] have modeled the chiral response of glycine and alanine in aqueous solution using explicit solvation and molecular dynamics. It should be pointed out that glycine is an achiral molecule. However when considering dynamic and solvation effects, distortions of the molecule temporarily induce chiroptical response of large magnitudes. Glycine was therefore used as a test case to determine systematic and statistical errors that would allow one to predict from MD averaging that glycine has a vanishing optical rotation (within the statistical errors). The molar rotations at the sodium D line were calculated using the B3LYP and BHLYP functionals with the aug-cc-pVDZ basis set, while geometry configurations were generated using molecular dynamics. CC2 calculations were performed for comparison, in particular to test the computational TDDFT-based model for artifacts from artificial charge-transfer excitations. A simple point-charge model (SPC) for the solvent was also tested. By plotting the change in molar rotation (see Fig. 13), as well as the change in CD, as a function of solvent distance, it becomes clear that close-by water molecules (both explicit and point-charge models) can cause a sizeable effect in the calculated response. The calculated molar rotation of static (with COSMO) vs dynamic averaging (using SPC) for alanine was 5.4 and $-11 \text{ deg cm}^2 \text{ dmol}^{-1}$ using B3LYP and -1.5 and $-7.8 \text{ deg cm}^2 \text{ dmol}^{-1}$ for BHLYP, respectively. A dynamic averaging with COSMO afforded molar rotations of -16.7 and $-10.9 \text{ deg cm}^2 \text{ dmol}^{-1}$ with the two functionals. A simple point charge representation of water and perhaps other polar solvents can be very efficient at modeling some aspects of explicit solvation without the additional computational cost of treating solvent molecules quantum mechanically. For alanine, however, the use of SPC waters provided only a marginally better agreement with experiment than use of a continuum model alone.

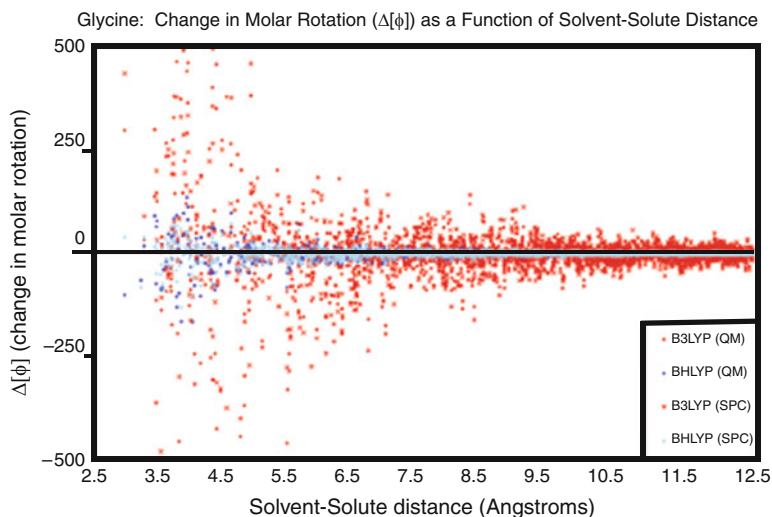


Fig. 13 The change in calculated optical rotation of glycine as a function of inclusion of water molecules (QM or in form of a point-charge model) up to a cut-off distance from the solute. MD data to prepare plot taken from Kundrat and Autschbach [162]

4.5 ECD Spectra Computed with Vibrational Fine Structure

Typically, when ECD spectra are simulated the computed “stick spectra” corresponding to vertical electronic transitions are broadened with Gaussian functions (sometimes Lorentzian broadening is used instead). Band shapes in electronic spectra of large molecules can also be computed more directly, by modeling their vibronic fine structure [182–186]. Several attempts have been made to include vibronic effects in ECD spectra at a first-principles level. Very promising results were obtained for *trans*-(2,3)-dimethyloxirane [183] by computing Franck–Condon (FC) factors from TDDFT. Lin et al. have applied a methodology reported in [185] to calculate the vibronic fine structure in the CD spectrum of (*R*)-(+)-3-methylcyclopentanone [187], also leading to a convincing agreement between simulation and experiment. Both FC factors and vibronic coupling terms were considered in the study of Lin et al. The two approaches are somewhat complementary in the sense that the one used for DMO constructs approximate harmonic excited states potential surfaces from the ground state force field and excited states gradients calculated at the ground state equilibrium geometry. The other approach requires optimized geometries (and ideally also force fields) for the ground state and each electronic excited state. With each method there is a trade-off between accuracy and computational effort, and both have their drawbacks and merits.

Figure 14 shows another example: the absorption, emission, ECD, and the emission counterpart of ECD – circular polarized luminescence (CPL) – for the lowest energy excitation of *d*-camphorquinone, from a recent TDDFT study

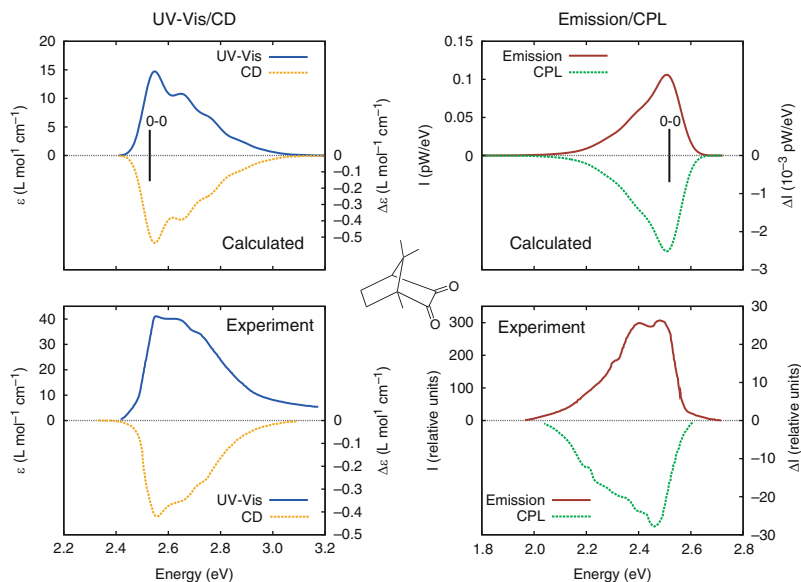


Fig. 14 Calculated and experimental absorption, emission, ECD, and CPL spectrum of *d*-camphorquinone. CAM-B3LYP/TZVP computations vs experiment. Data to prepare the plot were taken from [188]

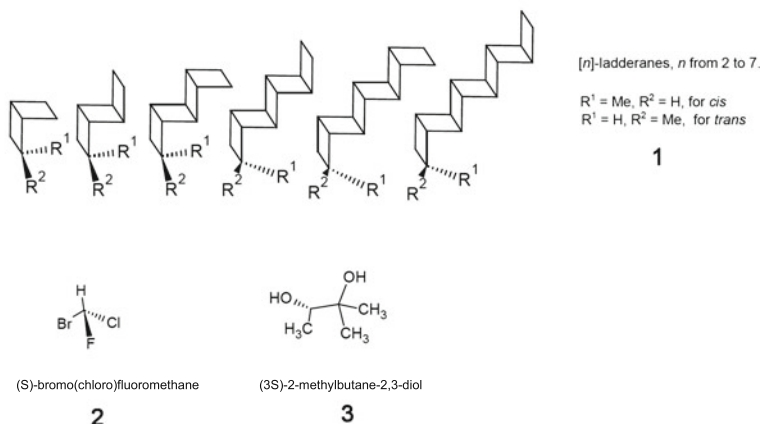
of the CPL spectra of this molecule and (*S,S*)-*trans*- β -hydrindanone [188]. Following ground and excited state optimizations and frequencies calculations for both states, the various bands were obtained from computed FC factors. Each vibronic transition was Gaussian broadened with σ between 0.03 and 0.04 eV. The simulated band shapes and band widths, the red shift of emission vs absorption, as well as the extent of visible fine structure are seen to be in excellent agreement with experiment. The data shown in the figure were obtained with the CAM-B3LYP functional. For the carbonyl centered transition in both molecules, basis set effects and the functional dependence were demonstrated to be relatively modest, allowing simulations of good quality with a nondiffuse basis and standard functionals. To our knowledge, [188] has reported the first computation of vibrationally broadened CPL spectra using modern first principles theory.

5 Assignments of Absolute Configuration by Comparing TDDFT Computations of ECD and OR/ORD to Experiment

This section focuses on AC assignments that were aided by TDDFT computations of electronic chiroptical properties. Figures 15–17 show a selection of molecules whose absolute configuration has been solved during the last five years with the aid of TDDFT calculations utilizing at least one electronic chiroptical response method

a

Chiral centers without chromophore



b

Chiral molecules with formally achiral chromophore

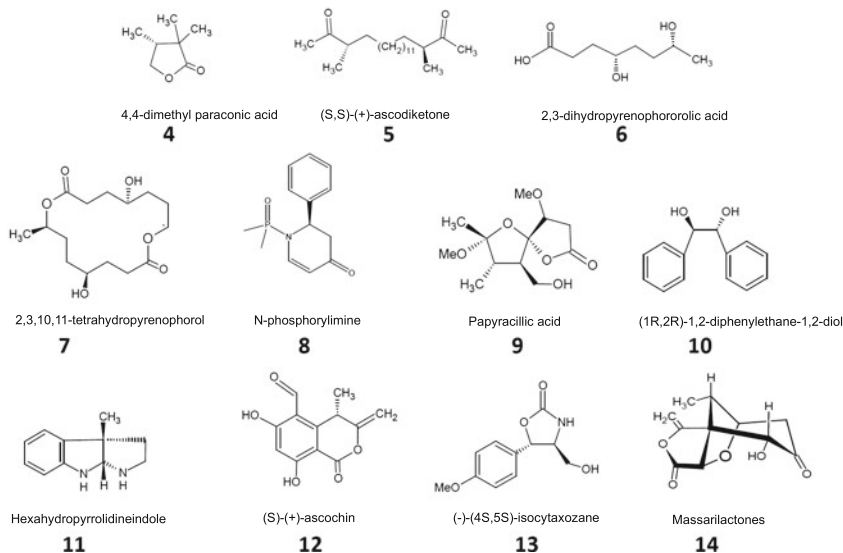


Fig. 15 A selection of molecules for which the absolute configuration has been determined with the help of measurements and computations of chiroptical properties. Part I

(OR, ORD, and/or ECD). The molecules are grouped by the type of chromophore, where applicable, and therefore the numbering is not necessarily in the order of their appearance in the discussion that follows. We will occasionally refer to the molecules of Figs. 15–17 by its number.

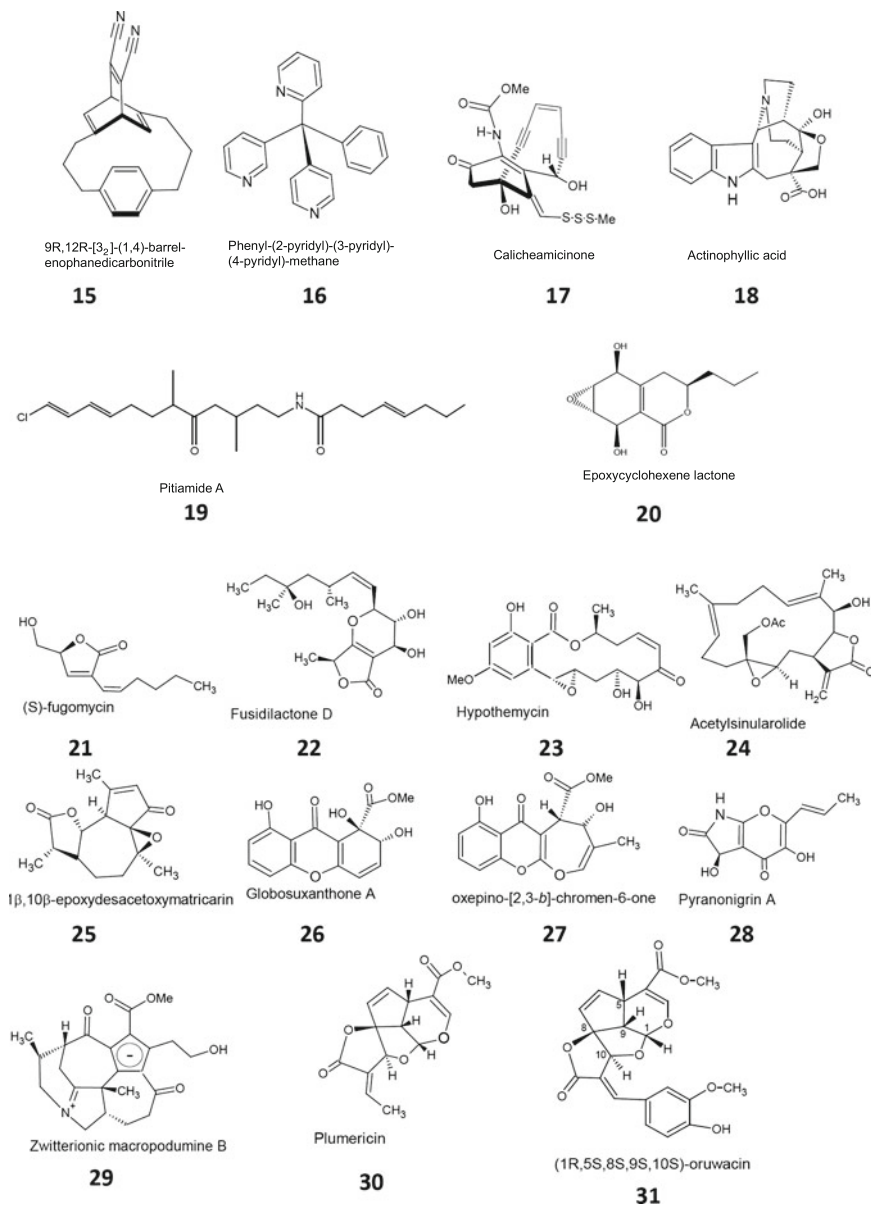


Fig. 16 A selection of molecules for which the absolute configuration has been determined with the help of measurements and computations of chiroptical properties. Part II

The first group contains molecules with only an asymmetric carbon as the stereocenter (**1–3**). Molecules of this type tend to have small optical rotations (i.e., less than $100 \text{ deg mL g}^{-1} \text{ dm}^{-1}$). The second group contains molecules which

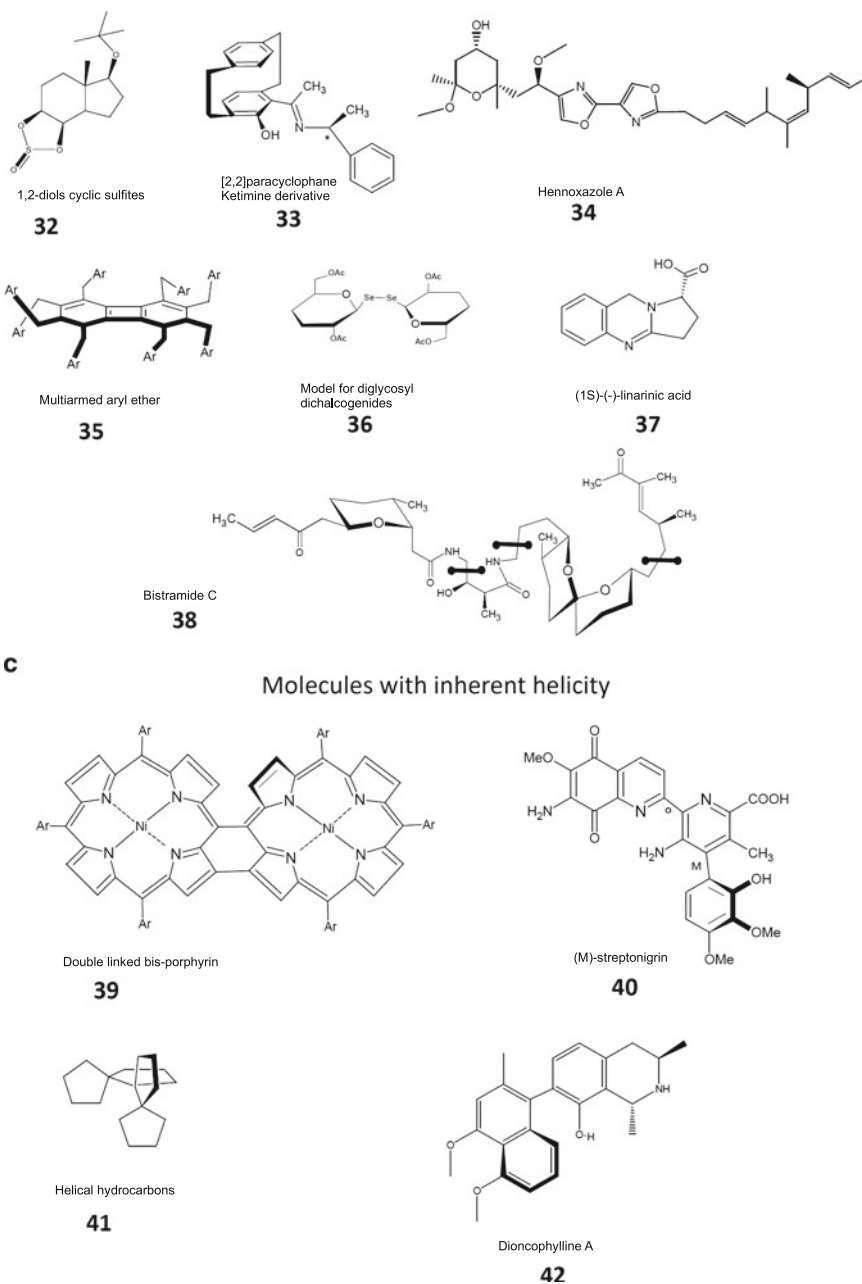


Fig. 17 A selection of molecules for which the absolute configuration has been determined with the help of measurements and computations of chiroptical properties. Part III

have stereocenters plus an otherwise achiral chromophore (4–38). There is typically a π system with low-lying transitions that may contribute strongly to the chiroptical response. Such transitions are n -to- π^* for carbonylic moieties (4–9, 12–14, 17, 18–34) either as ketone, carboxylic acid or lactone forms, and for imine groups (33). It should be noted that in molecules (20–31, 38) there is the presence of an enone type functional group. Other types of transitions are π -to- π^* for the aforementioned moieties and for π systems such as aromatic and conjugated systems. Molecules that contain this kind of chromophore are (10, 11, 15, 16, 35, 37). Another type of transition originates when a metal or heteroatom is present in molecule, such as Se (36) with low-lying σ -to- σ^* transitions. The third group contains molecules with an inherently chiral chromophore (39–42). These systems tend to have strong optical activity.

Rigid molecules have always been of particular interest in the context of chiroptical property computations. Examples of rigid molecules for which ACs have been assigned successfully with the help of TDDFT computations are spirioselenurane [189], *n*-ladderanes (1) [190], paraconic acids (4) [191, 192], pseudo-helical rigid hydrocarbons (41) [160], and other molecules with small specific rotations [15, 16, 193–195]. In comparison, many of the molecules in Figs. 15–17 have a large conformational space which makes it particularly challenging to accurately model their chiroptical properties.

Although it is best to employ a variety of chiroptical methods for a confident AC assignment, the optical rotation at a single wavelength, typically the sodium D line (589.3 nm), has been successfully applied to assign the AC for a number of diverse systems ranging from natural products (18, 31, 37) to spiroannulated rings (41). Systems as simple as having one stereogenic center (1, 2, 37) to as challenging as multiple stereocenters (31) have been investigated. The study of the optical rotation at several wavelengths has been applied to numerous molecules as well, for instance for such systems as paraconic acids (4) [192], cytotoxones (13) [196], and (*l*C)-C₇₆ [197]. Considering not only sign and magnitude of the OR but also the dispersion trend can help to increase confidence in an AC assignment.

Molecules with small specific rotations need to be carefully assigned if the OR at a single wavelength is the only criterion. Even for a conformationally rigid molecule, a small specific rotation (less than about 100 deg mL g⁻¹ dm⁻¹) can be predicted to have the wrong sign by TDDFT gas-phase computations using standard basis sets and standard hybrid functionals [16, 98]. Stephens et al. [16] suggested that for a safe AC assignment, with 95% confidence, the specific rotation should be in the interval of $\pm 2\sigma$ from the experimentally measured value of one of the enantiomers, but not both concurrently. σ is the average uncertainty of the calculated OR. The authors deduced a value of 58 deg mL g⁻¹ dm⁻¹ for 2σ from a TDDFT study of a set of 65 chiral rigid molecules optimized at the B3LYP/6-31G(d) level of theory. The chiroptical response was calculated with the aug-cc-pVDZ basis and a GIAO formalism. The selection of molecules included 17 alkanes, 16 alkenes, 19 ketones and 13 miscellaneous heterocycles. The predicted signs of the (gas phase) specific rotation were in agreement with experiment in different solvents for all but 8 of the 65 rigid molecules. Sources of errors were considered

from both the calculational and experimental point of view, such as errors in the experimental specific rotations related to purity and enantiomeric excess, as well as functional and basis set related errors along with the lack of inclusion of vibrational and solvent effects.

Polavarapu [176] has recently reviewed protocols that have been used for AC assignments based on computed optical rotations. The protocols were classified by four categories:

1. *Single wavelength OR calculations.* As a consequence of the SOS nature of OR, equation (2), the accuracy of OR calculations is influenced by over/under estimations of rotatory strengths and the associated electronic transition energies in the CD spectrum. A way to reduce errors from shifts in the computed excitation energies (which also enter direct linear-response TDDFT computations of the OR that do not employ a SOS) is to introduce wavelength corrections in a SOS. However, the corrections are generally wavelength dependent which makes it difficult to include a simple correction when there are multiple transitions affecting the OR. An example of this type of approach is the study of [3₂] (1,4)-barrelenophanedicarbonitrile (**15**) by Stephens et al. [194], where the SOS optical rotation was calculated with the experimental wavelengths of four low-energy transitions.
2. *Nonresonant monosignate ORD calculations.* An ORD curve can be calculated either directly from the OR parameter (or G') on a frequency or wavelength grid, or from the low-energy part of the CD spectrum through the KK formalism [36, 37, 176, 197] or an SOS equation. However, if the KK or SOS route is used one should be cautious to include a sufficient number of excitations to converge the ORD. When lower-lying CD bands have a different sign to the monosignate ORD curve, it is necessary to include higher lying states. A criterion to eliminate the leading-order cut-off error is to choose a number of excitations in the SOS for which $\sum_j R_j \approx 0$ [36]. Direct linear response methods tend to provide more reliable results, and can be combined with KK and SOS methods in order to reduce the number of frequencies for which the OR has to be computed [37].
3. *Nonresonant bisignate ORD calculations.* Some molecules with a bisignate nonresonant ORD for which computations have been performed are β -pinene [171, 176], spiroseleuranane [176, 189], methyloxirane [176], and *trans*-dimethylcyclopropane [47, 75]. A bisignate nonresonant ORD can be related to different phenomena such as vibrational effects, or the intrinsic electronic optical activity of the molecule. In regards to the latter, the bisignate curve is a consequence of at least one transition higher in energy with an opposite and larger rotatory strength than the lowest-lying energy transition (see Fig. 1). When a bisignate ORD is experimentally observed, one should use as high a level of theory as possible and consider using a more intricate computational model than for a monosignate ORD in order to compute the correct sign [75, 156, 176].
4. *Resonant ORD calculations* For AC assignment based on resonant ORD, it is often sufficient that calculations reproduce the ORD pattern as a function of wavelength [176]. See Sect. 3 for examples.

ECD based assignments of ACs tend to cover the UV–Vis spectral range and often include several excitations. A good match between simulated and measured spectra that cover several well separated excitations can normally be used for a confident assignment of the AC, but care needs to be taken if the CD spectrum is limited to one or very few excitations. In this case a combination of several chiroptical methods would be safer. Polavarapu also pointed out that a comparison of experimental electronic chiroptical properties can help to identify particular instances where the optical rotation in the low energy regime is influenced by higher lying transitions, as was the case for dimethyltartrate [10]. It is advisable to carefully benchmark the basis set when there are apparent inconsistencies between computed ORD and ECD.

In the following paragraphs, work is reviewed where the problem of conformational averaging has been bypassed by working with solids instead of solutions of chiral molecules. For example, Bringmann et al. [199] have investigated dioncophylline A (**42**), a well known naphthylisoquinoline alkaloid, in the solid state by comparing computed and experimental CD. This molecule was chosen because it has previously been studied in forms other than the solid state. The case is challenging because the first four CD bands of the two lowest energy conformers have opposite signs, reducing the reliability of the computed averaged CD spectrum. Bringmann et al. calculated the CD spectra using X-ray crystal structure coordinates, where only one conformer dominates. For the B3LYP/TZVP TDDFT response calculations, the crystal structure was also further optimized at the same level of theory. The ECD from TDDFT calculations matched the spectral features seen experimentally. Effects from neighboring molecules in the solid were also investigated, but at a semiempirical level due to the size of the systems. These effects were explored by analyzing different dimers and an extended system comprised of 16 molecular units. The added contributions from the nearest neighbors did not alter the qualitative agreement between the theoretical and experimental CD. It was pointed out that the chosen approach is promising for situations where intermolecular exciton coupling does not apply or if the chromophores are sufficiently far away of each other. Provided enough computational power, crystal-packing effects can potentially also be studied with *ab initio* methods.

Zhang et al. [200] have studied members of the secalonic acid family, particularly Blennolides A–G. By application of a solid state CD/TDDFT approach, similar to that described above for dioncophylline A, the absolute configuration was assigned. Starting with the (5*S*,6*S*,10*aR*) crystal structure of Blennolide A as the input geometry, the CD was calculated at the B3LYP/TZVP level of theory. Agreement of the computed CD spectrum with the experiment for this molecule was good, both in the solid state (KCl disc) and in solution (dichloromethane), as shown in Fig. 18. The good agreement of the CD spectra suggested the crystal structure is close to the predominant structure seen in solution, which was consequently assigned as (5*S*,6*S*,10*aR*). For blennolides D and E, there were no experimental crystal structures available, and therefore a different approach had to be taken. A conformational search was performed using molecular mechanics (MMFF force field), and the two lowest-energy structures were further optimized with

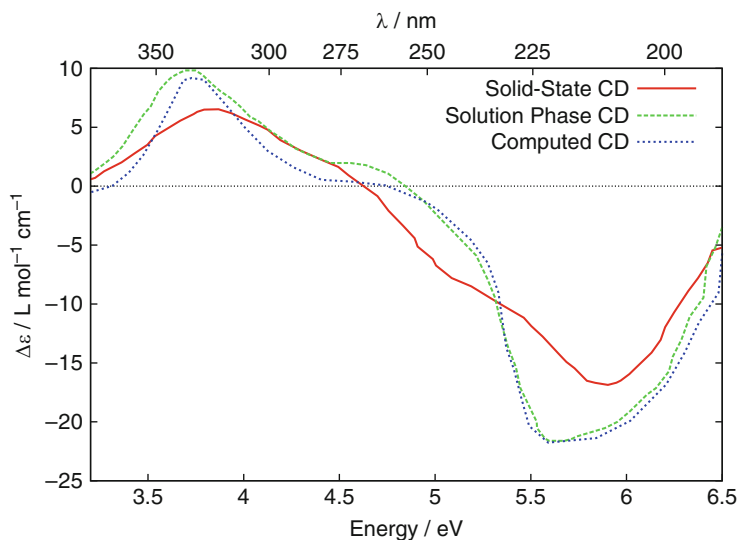


Fig. 18 Comparison of solid state (KCl), solution (dichloromethane) and calculated (B3LYP/TZVP) CD spectrum for the (5S,6S,10aR) Blennolide A. Spectral data to prepare the plot taken from [200]

B3LYP/6-31G(d). The ECD spectra of these were then calculated with the TZVP basis set and Boltzmann averaged. For both conformers, the computed spectra matched well with experimental solution CD spectra (measured in acetonitrile). The spectrum of the lowest energy conformer and the Boltzmann averaged spectrum both agreed qualitatively with the experimental sign pattern. Based on these results, the absolute configurations of blennolides D and E were assigned as (–)-(2S,9S,10S,11R) and (+)-(2R,9S,10S,11R), respectively.

A solid state CD/TDDFT approach was applied to hypothemycin (**23**) by Hussain et al. [201] Hypothemycin is conformationally flexible and has the possibility for excitations to strongly couple in the solid state. X-ray structure coordinates were used for single molecule CD calculations at the B3LYP/TZVP level of theory and compared to experimental solid state measurements. Apparently, intermolecular interactions in the solid state did not give rise to large discrepancies between the spectra. It should be noted, however, that because of possible packing effects one should be cautious when comparing solid state experimental measurements with a single molecular calculation if the importance of packing effects cannot be assessed explicitly by computations.

Hassan et al. have used a solid state CD approach to aid in the absolute configuration assignment of epoxydesacetoxymatricarin (**25**) [202]. The authors of [202] benchmarked several functionals (BP86, B3LYP, and BHLYP) with the TZVP and aug-cc-pVDZ basis sets. The CD computed at the BHLYP/TZVP level of theory based on the experimental X-ray structure was in good agreement with experimental measurements in both solution and solid state. The lowest-energy

excitation was assigned as an n -to- π^* enone chromophore transition. One interesting spectral feature that could not be reproduced computationally was a positive band at 255 nm seen in the solid state that was not seen in solution. The fact that the calculations did not reproduce the transition at 255 nm was attributed to intermolecular interactions in the solid. Hassan et al. hypothesized that the CD band could be due to an enone π -to- π^* transition caused by intermolecular coupling. The importance of determining which CD bands are related to solid state interactions was pointed out. It was suggested that the occurrence of such spectral features may be a tool for investigating chirality due to aggregation in the solid state.

Other examples where solid state CD was utilized to assign absolute configurations are globosuxanthone A [203] (26), papyracillic acids [204] (9), ascochin (12) and ascodiketone [205] (5), massarilactones [206] (14), 2,3-dihydropyrenophorolic acid and 2,3,10,11-tetrahydropyrenophorol [207] (6,7), oxepino[2,3-*b*]chromones [208], 20-acetylsinularolide B [209] (24), fusidilactone D [210] (22), blennolide G [209], tetracyanobutadienes [211], as well as zwitterionic and neutral macropodumines [212] (29).

The absolute configuration assignment of the ten stereocenters of bistramide C (38) by Zuber et al. [213] is an example of how different tools can aid in the prediction of the correct configuration and avoid impractical experimental work. From a starting pool of over 1,000 isomers, the number of structures was reduced by 2 orders of magnitude after calculation of NMR parameters. Comparing the results of computed molar rotations (589.3 nm), the number of isomers was reduced to a selected few, for which the AC assignment was made with the help of CD calculations. This approach was based on van't Hoff's optical superposition principle: dividing molecules into fragments that have weak chiral interactions and then treating each individual fragment. More specifically, Zuber et al. divided bistramide C into four fragments and assigned the relative configuration for nine out of the ten chiral centers via NMR J-couplings. Molar rotations were calculated at the BP86/aug-cc-pVDZ//SVP level of theory. Conformational searches for each fragment were performed with Monte Carlo simulations. Solvent effects for chloroform were included by a continuum model. Calculated optical rotations were added for each possible four-fragment combination. Knowing that the experimental molar rotation was $+70 \text{ deg cm}^2 \text{ dmol}^{-1}$ at 589 nm, the pool of possible isomers was reduced to three. The ECD of each of these fragments was calculated and compared with experiment. Of the three, only one matched the sign pattern of the experimental CD spectra, allowing for an absolute configuration assignment. Similar approaches have been applied with other molecules, too, such as hennoxazole A (34), pitiamide [159] (19), and ladderanes [190].

Studying chiroptical properties can lead to novel ligand design. Mori et al. [214] considered four multiarmed chiral aryl ethers in diverse aromatic skeletons. Two of the molecules, (35) for example, were synthesized with the intent to lock the structure into one of two low-energy conformers. Structures were optimized with dispersion-corrected DFT at the BLYP/TZVP level of theory. Single point energy calculations were performed with a spin component scaled MP2 method and the TZVPP basis. CD spectra were calculated with BHLYP/TZVP. The asymmetric

anti conformers were predominant for the four aryl-ethers, in agreement with X-ray structures. For the locked ethers, the chiroptical response increased as function of temperature (25–95°C). This trend was attributed to the asymmetry of the *anti*-conformers. Regarding the unlocked ethers, the chiroptical response decreased with increasing temperature. This effect was attributed to changes in the mole fractions as function of temperature. With an increase in temperature, the *syn*-conformers become more favored than *anti* due to the freedom of aryl groups in the side chains to rotate and participate in van der Waals interactions.

Crassous et al. [215] have prepared (+)-chlorofluoroiodomethane (**2**) and determined its enantiomeric excess as well as the absolute configuration with the aid of TDDFT calculations of ORs. The ORD was calculated and measured at 589, 577, 546, and 435 nm. Theory at the B3LYP/DGDZVP level reproduced the sign and trend for the ORD seen experimentally. The calculations supported the assignment of (S)-(+), and R(-), for the absolute configuration. In related studies, the absolute configuration of CHFCIBr had previously been assigned with the help of ORD and ROA computations [82, 216].

Stephens et al. [194] have determined the absolute configuration of [3₂](1,4) barrelenophanedicarbonitrile (**15**) with the help of TDDFT computations. A Monte Carlo conformational search was performed which used molecular mechanics and semiempirical methods. The lowest-energy conformers were then further optimized at the B3LYP/6-31G(d) level of theory. ECD and OR calculations were performed with B3LYP and the aug-cc-pVDZ basis set. Experimentally, three conformers were found in the X-ray structure. The geometry of the lowest three conformers found computationally were similar to the experimental structures, and the correct sign of the optical rotation was predicted for all three structures. Comparing the conformational distribution with structures obtained from X-ray crystallography and other experimental measurements, the calculated ECD and OR at the sodium D line aided a safe assignment AC of this molecule as 9S, 12S(+)/9R, 12R(-).

Masullo et al. [217] have isolated several tetracyclic polyisoprenylated xanthenes, including oxy-guttiferone K and guttiferone M. For these molecules, the authors elucidated structures by experimental NMR and mass spectrometry. TDDFT calculations were then performed to help assign the orientation of the cycle formed by one of the isoprenyl chains. Conformers were found by applying MM/MD simulations followed by optimizations at the MPW1PW91/6-31G(d) level of theory. Six conformers were found for oxy-guttiferone K and seven for guttiferone M. ECD spectra were calculated at the same level of theory (see Fig. 19). By comparison of the calculated and experimental CD, it was concluded that the isolated compounds were not the ent-forms (see Fig. 19 for a comparison of oxy-guttiferone K vs its ent-form).

The assignment of absolute configuration based on circular dichroism calculations has become a useful tool in organic synthetic chemistry [218], drug discovery [219, 227], and biochemistry [220–226, 228]. Examples for which the AC has been solved with the help of ECD calculations are *N*-phosphorylimine adducts (**8**) [227], fugomycins (**21**) [229], pyranonigrin (**28**) [231], epoxycyclohexenes (**20**) and isocumarines [230], as well as many other organic molecules [194, 198, 218, 232–251].

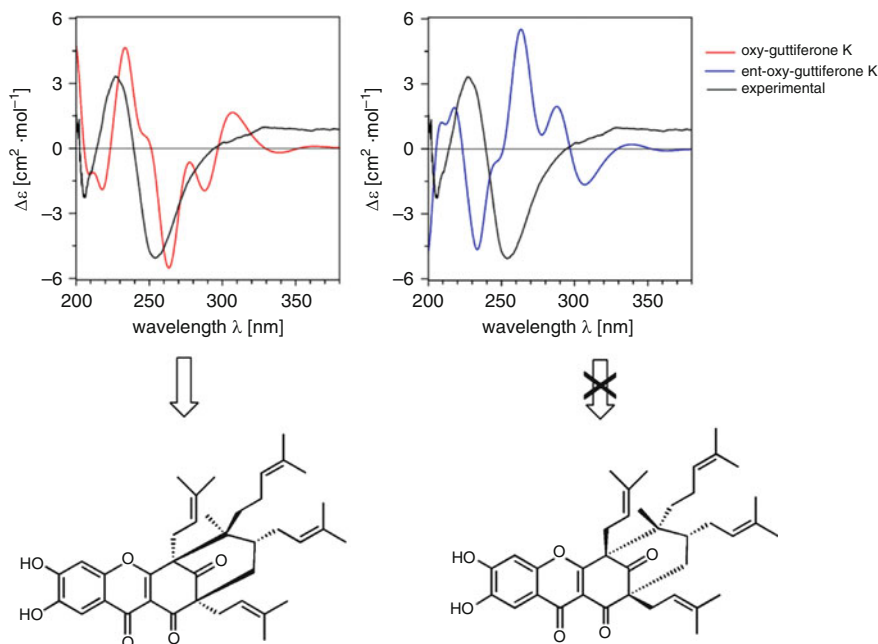


Fig. 19 CD spectra for enantiomers of oxy-guttiferone K (*left*) and its ent-form (*right*). Calculations were performed at the MPW1PW91/6-31G(d) level of theory. Reprinted from [217], with permission from Elsevier

The application of chiroptical methods towards absolute configuration assignment is not limited to natural products, of course. Molecules targeted for their potential application as nano materials have also been studied, such as ladderanes (**1**) synthesized by Zuber et al. [213] which are discussed elsewhere in this chapter.

Chochrek and coworkers [252] developed a protocol for the AC assignment for sulfur centers in cyclic sulfites (**32**). The experimental CD and TDDFT calculations at the B3LYP/6-311++G(2d,2p) level of theory were in very good agreement. It was shown that the ring conformation as well as the configuration around the sulfur atom dominates the CD spectrum to give rise to bands that can be used for reliable AC assignment of the sulfur center. This information allows for the differentiation between sulfur epimers in cyclic sulfites.

Frelek and coworkers [253] studied by TDDFT an empirical helicity rule for AC assignments of the β -lactam moiety present in antibiotics and in synthetic intermediaries of other drugs (see structure in Fig. 20). This work is also an example of a TDDFT-based investigation of ECD spectra for flexible molecules, using an MD protocol. The chirality of the bridgehead carbon in the β -lactam moiety had been experimentally related to a CD band at 220 nm, with a positive Cotton effect corresponding to the *R* configuration at that carbon. The rule was tested with computations on eight molecules: four oxacephams, three carbacephams, and a thio-cepham derivative. Geometry optimizations were performed with PBE0 using

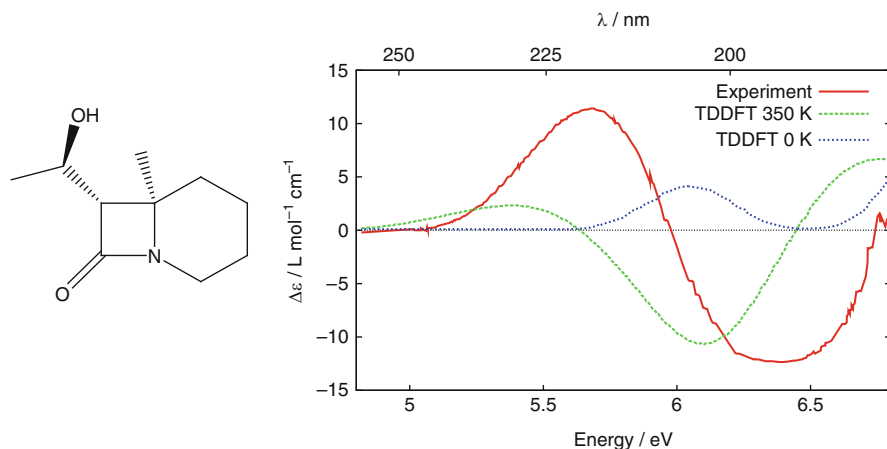


Fig. 20 CD spectra of a carbacephem derivative at different temperatures. The chromophore related to the CD band at 220 nm is the amide group of the azetidin-2-one ring. Data to prepare the plot were taken from [253]

the TZVP basis for nonhydrogen atoms, and a nonpolarized basis for hydrogens. Vertical ECD spectra were simulated based on trajectories obtained from Born–Oppenheimer molecular dynamics. Solvent effects were included with COSMO. The CD spectrum of a carbacephem, as a selected case from the test set, is shown in Fig. 20. The two lowest lying transitions were assigned as n -to- π^* centered on the amide moiety, with a carbonyl centered first transition. A static structure CD spectrum at 0 K showed a blue shift for those transitions, and it was in poor agreement with the experimental spectrum obtained at room temperature. The CD spectrum at 350 K, calculated from the MD average, was red-shifted with respect to the 0 K spectrum, leading to better agreement with experiment.

Kock et al. [254] have isolated two new antimicrobial isochromanes (pseudoanguillosporin A and B; see structure in Fig. 21) and deduced their absolute configuration with support from TDDFT computations. The molecule has three stereocenters. The $6'$ C configuration in the chain was determined by NMR, while the helicity of the isochromane ring and the stereocenter at C_3 were determined by CD TDDFT calculations (Fig. 21). The assignment at C_3 was made with a shortened version of the molecule (Fig. 21) after a conformational search with MMFF and PM3 methods, followed by subsequent geometry optimizations at the B3LYP/6-31G(d) level of theory. ECD spectra were computed for the four lowest energy conformers (B3LYP/TZVP). Experimental and Boltzmann averaged ECD spectra compared well in sign and magnitude for the transitions related to the phenyl chromophore. The AC was assigned as (3R) for both pseudoanguillosporin A and B.

Cheng et al. [166] assigned the absolute configuration of the alkaloid (–)-linarinic acid (37) with the help of theoretical calculations. Via molecular mechanics, a conformational search was performed with the MMFF force field, using water

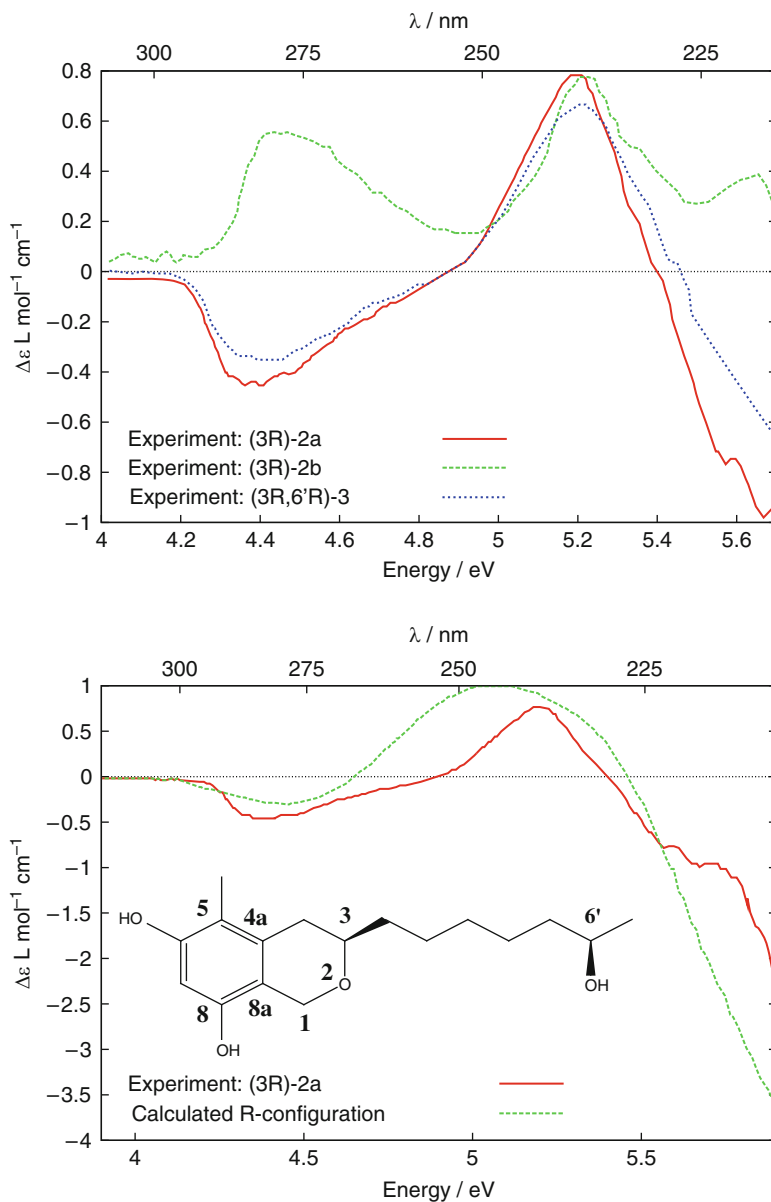
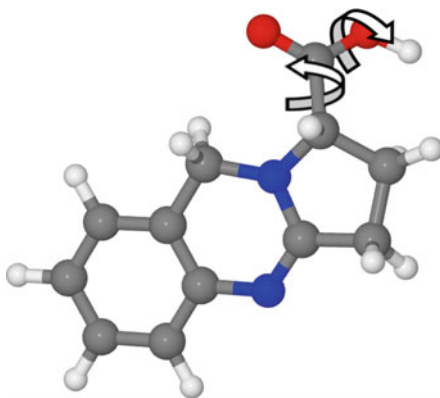


Fig. 21 AC assignment for pseudoanguilsporin A and B. Each stereocenter was analyzed with different strategies. Molecule labels “2a,” “2b,” and “3” are as labeled in [254]. See text for further details. Data to prepare the figures were taken from [254]

Fig. 22 A depiction of the rotations of the carboxylic acid group on (*S*)-linarinic acid responsible for the lowest-energy rotamers found in the conformational search considering water–linarinic acid clusters in Ref. [166]



as solvent. Low-energy conformers that were found all related to a rotation of the carboxylic acid moiety, linked to the stereogenic α -carbon, as shown in Fig. 22. The MM structures were further optimized using HF/6-31G(*d,p*). The geometry of the lowest energy conformer matched well with X-ray crystal structure data. The specific rotation of different conformers of (*S*)-linarinic acid was computed with HF and B3LYP utilizing four different basis sets: 6-31G, 6-31G(*d*), 6-31G(*d,p*), and aug-cc-pVDZ. For the individual conformers, HF and B3LYP (aug-cc-pVDZ) agreed in sign for every case, but not in magnitude. The ORs varied greatly by conformer, spanning a range of approximately 250 deg mL g⁻¹ dm⁻¹. The Boltzmann averaged specific rotation (B3LYP/aug-cc-pVDZ) was -356 deg mL g⁻¹ dm⁻¹, which compared reasonably well with the experimental measurement of -290 deg mL g⁻¹ dm⁻¹ in methanol at the sodium D line wavelength, resulting in the AC assignment as the (*S*) enantiomer.

Matsumoto et al. [246] have used TDDFT to aid in the assignment of the absolute configuration of phenyl-(2-pyridyl)-(3-pyridyl)-(4-pyridyl)methane. Molecular mechanics (MMFF94S) was employed to find a set of low energy conformers, which were further optimized at the B3LYP/6-31G(*d*) level. TDDFT CD calculations were performed with B3LYP/TZVP basis. The conformationally weighted contributions were averaged and compared against experiment. Based on a good match between the calculated and experimental ECD spectra, the molecule was assigned to the (*R*) configuration.

In some cases, theoretical investigations of chiroptical response have been used to reinvestigate previous AC assignments. Through the use of TDDFT calculations, the absolute configuration has been reassigned, for example, for molecules like oruwacin (**31**) [161] and papyracillic acid (**9**) [204]. Previously, the absolute configuration of these two molecules had been assigned by comparison of experimental chiroptical properties with those of similar compounds, which can be problematic. (*M*)-Streptonigrin was also reassigned based on TDDFT computations (B3LYP/TZVP) [255], which helped to decide which of two contradictory previous assignments was correct.

Regarding the oruwacin example [161], Geometry optimizations were performed at the B3LYP/6-31G(d) level of theory, and optical rotation calculations employed B3LYP/aug-cc-pVDZ. No solvation model was applied in the calculations. Due to the size and conformational flexibility of oruwacin, the conformational search was approached by segmentation of the molecule into three subsystems: a plumericin core, phenylplumericin and the *O*-methylcatechol moiety. The ORs of the eight lowest-energy conformers were calculated. It was noted that these eight conformers contribute more than 95% combined to the mole fractions. The weighted specific rotation of (1*R*,5*S*,8*S*,9*S*,10*S*)-oruwacin led to a calculated specific rotation of $-193.3 \text{ deg mL g}^{-1} \text{ dm}^{-1}$ with the experimental value of the natural product being $+193 \text{ deg mL g}^{-1} \text{ dm}^{-1}$. It was thus concluded that the natural product was the enantiomer with the configuration (1*S*,5*R*,8*R*,9*R*,10*R*). The successful reassignment shows that breaking up large conformationally flexible molecules into easier manageable subsystems can be a useful method for analyzing a chiral molecule, and provides a faster way for determining the overall number of conformers. Another useful observation from this work is that comparison of the specific rotations of similar natural products is not always a reliable means of determining the AC.

Kwit et al. [256] reassigned a series of *trans*-diastereomers of cytoxazone (**13**), which are cytokine modulators. Initial calculations of the OR and the ECD spectrum at the B3LYP/6-31G(d) level of theory failed to predict the correct assignment. After switching to a larger basis set, 6-311++G(2d,2p), and including (PCM) solvent effects, the main features of experimental and calculated CD spectra agreed well and led to the assignment as (-)-(4*S*,5*S*)-*trans*-isocytoxazones.

Alonso-Gomez and coworkers [211] studied chirality induction in the allene moiety of 1,1,4,4-tetracyanobuta-1,3-dienes and reconfirmed the AC assignment a diethynylallene. The TDDFT computations of CD spectra employed B3LYP/6-31G(d). Comparing the calculated and experimental CD, the spectra matched regarding the energetic location of the bands and the sign pattern. The allene chirality induction was explained in terms of in-phase and out of phase interactions of the transition dipole moments of the dimethylanilinoacetylene groups.

The AC of a meso-meso β - β doubly linked *bis*-porphyrin (**39**) was reassigned by Muranaka et al. [257] based on TDDFT calculations, which were contrary to a previous assignment that used an exciton coupling model. It was pointed out that this molecule had fused chromophores and therefore the exciton coupling model can be too simplistic and predict the wrong sign, as indeed appeared to be the case for (**39**) [257].

6 Analysis of Chiroptical Properties

With a given basis set and electronic structure method, if all possible excitations (corresponding to physically meaningful transitions, or generated as artifacts from using an incomplete basis and an approximate functional) are included in the SOS for

a dynamic property it should yield the same value of the property calculated directly from linear response using the same level of theory. This applies, for example, to TDDFT spectra vs direct dynamic TDDFT linear response [36, 46]. The SOS might be useful for analyzing the optical rotation in terms of electronic excitations and their rotatory strengths, but, as will be seen shortly, the approach has its limits.

Wiberg et al. [137] have applied an SOS to analyze the specific rotation of substituted oxiranes (X=F, Cl, CN, HCC), chloropropionitrile, ethane, and norbornenone. Calculations were performed with the B3LYP functional and the aug-cc-pVDZ and aug-cc-pVTZ basis sets. The substituted oxiranes required the inclusion of at least 800 states to converge towards the TDDFT linear response-calculated OR at the sodium D line. The SOSs were strongly oscillating. The specific rotations in the first 120 states varied by a few hundred $\text{deg mL g}^{-1} \text{dm}^{-1}$ for some of the oxiranes, and up to 800 $\text{deg mL g}^{-1} \text{dm}^{-1}$ for the HCC substituted molecule. The magnitude of variation was similar for 2-chloropropionitrile, with the SOS requiring nearly 1,000 states to converge. It was concluded that low-lying valence and Rydberg transitions were not dominating the computed nonresonant ORD since a large number of high lying states were required to converge the SOS. A more detailed account of research on 2-chloropropionitrile, including a discussion of the SOS analysis, is given in Sect. 7. Additional information about SOS analyses of other molecules can also be found elsewhere in Sects. 3, 4, and 7.

Attempts to explain the structural and electronic origin of optical rotation in molecules based on a partitioning of ab initio calculated data have been made [107, 136, 159]. Kondru et al. [107] have developed protocols to map out atomic and functional group contributions to optical activity by using a type of Mulliken partitioning. Atomic contribution maps were generated by decomposing the G' tensor calculated for optical rotation into contributions from AO pairs. The analysis allowed for exploration of geometry effects, such as dihedral angles [258] and variation of chiroptical response as a function of distance from the chiral center [159]. The atomic contribution maps can be used to obtain more insight into the results of calculations by finding which atoms contribute most to the calculated OR. An application has been the assignment of a calyculin fragment as A/B depending on the E/Z arrangement of the cyano group [258]. The optical rotation atomic contribution map of this conjugated polyene showed that the chiral carbon centers are conjugated intramolecularly with the cyano group through the π system, resulting in a strong influence of the E vs Z orientation of the cyano group on the optical rotation [159, 258].

TDDFT programs typically determine a set of coefficients $X_{ai\sigma}$, $Y_{ai\sigma}$, or alternatively their sum and difference, for each transition which are used to compute the transition-densities and current-densities, as outlined in Sect. 2.3. We will drop the spin indices here for brevity. The normalization is such that for positive excitation energies [259]

$$\sum_a^{\text{unocc}} \sum_i^{\text{occ}} (X + Y)_{ai} (X - Y)_{ai} = 1 \quad (29)$$

for each transition, where the sums run over the occupied and unoccupied canonical MOs. Therefore, each transition can be analyzed conveniently in terms of occupied–unoccupied MO contributions adding up to 100% per equation (29). Such analysis features are available in many TDDFT codes and have been applied frequently to determine the nature of a transition. Recently, an analysis of transitions in terms of field-free localized MOs (LMOs) has been proposed by Graule et al. [260] In order to quantify contributions to an excitation from a specific “chemist’s orbital”, the canonical MOs φ were transformed into a basis of bonding, lone-pair, core, and unoccupied LMOs λ ,

$$\varphi_j = \sum_k \lambda_k T_{kj} \quad (30)$$

where the transformation matrix T is unitary and diagonal with respect to occupied and unoccupied blocks. Λ_{ck}^S and Λ_{ck}^A are defined in (31a) and (31b) below [260]. These are the symmetric and antisymmetric components of the transition density matrix in the LMO basis:

$$\Lambda_{ck}^S = \sum_{ai} (X + Y)_{ai} T_{ca} T_{ki} \quad (31a)$$

$$\Lambda_{ck}^A = \sum_{bj} (X - Y)_{bj} T_{cb} T_{kj} \quad (31b)$$

The LMO analog of (29) is now

$$\sum_a^{\text{unocc}} \sum_i^{\text{occ}} \Lambda_{ai}^S \Lambda_{ai}^A = 1 \quad (32)$$

The last equation has been used to analyze occupied–unoccupied localized molecular orbital pair contributions for excitations in chiral metal complexes and metallahelicenes [260, 261], as well as in chiral organic acids derived from amino acids by substitution of the amino group with $-\text{OH}$ and $-\text{F}$ [170]. The analyses in terms of canonical MOs and LMOs may be considered complementary tools, with the canonical MO analysis generally leading to fewer contributions since the canonical MOs are well adapted to describe electronic excitations. The analysis in terms of LMOs allows one to focus on selected “chemist’s orbitals” of interest, such as contributions to excitations from a given lone pair or localized π orbital, or from metal-centered orbitals, which can also be very useful.

Chiral-response “sector maps” computed from first principles to describe chiral perturbations of nonchiral chromophores are a tool proposed recently [136, 155, 170] to study CD and OR. The computation of such sector maps has been inspired by the sector rules for ketones that are well known to chemists

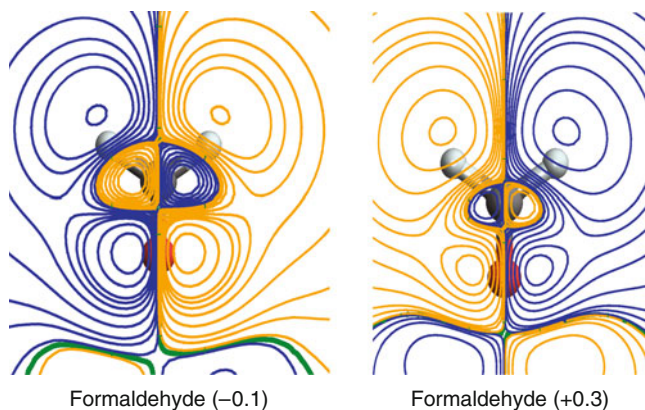


Fig. 23 TDDFT sector maps calculated at the B3LYP/aug-cc-pVDZ level of theory for the circular dichroism induced in the carbonyl centered n -to- π^* transition of formaldehyde. The scan was performed 1.3 Å above the chromophore plane using point charges of $-0.1e$ and $+0.3e$, respectively

[262–264]. The first-principles maps¹ can be constructed by creating a grid around the chromophore of interest, and scanning the chiroptical response induced in the chromophore by a point charge or another perturbing entity on each grid point. The scan can be performed in a plane above a planar chromophore, for example, or on a three-dimensional grid. An example of the carbonyl chromophore is shown in Fig. 23 where the well known octants devised by Moffitt et al. are clearly visible. Similar sectors as for the negative point charge are obtained when a noble gas atom, representing a steric repulsion, is chosen as the perturber [136]. Another example, shown in Fig. 24, is the OR induced by a point charge around a carboxylate chromophore. Both a 3D scan and a map are shown. Sector rules for specific chromophores may be constructed from such computed maps. The success of octant rules [264] and other sector rules discussed elsewhere in this chapter demonstrates that there is a clear need for chirality models with predictive power that are easy to apply. It is now possible to confirm sign, shape, and spatial extension of such sectors by explicit computations of the chiroptical response as a function of the position of an idealized perturber. Sector maps generated for a planar glycine molecule, for example, have shown that the carboxylate chromophore in amino acids cannot be approximated by overlapping sectors of two carbonyl groups at an approximately 120° angle [136], which had previously been used as a model to explain the pH dependence of the OR of amino acids (more on this in Sect. 7).

¹ One should keep in mind that, although the computations are based on first-principles methods, the maps are still models for the corresponding chromophores in chiral molecules. Also, the perturbation is highly simplified.

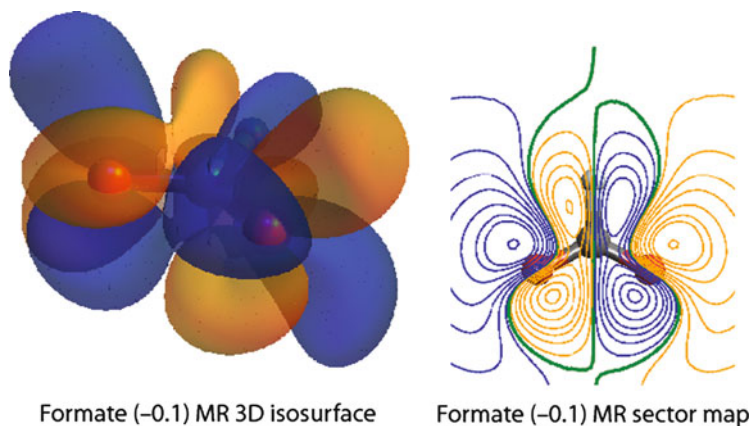


Fig. 24 3D isosurface (*left*) and a sector map (*right*, see also caption of Fig. 23) for the OR induced by a point charge in the $-\text{COO}^-$ chromophore, using B3LYP/aug-cc-pVDZ computations for a formate model. The perturbing charge had a value of $-0.1e$

Another example for an application of computed sector maps is the OR of phenylalanine, as far as contributions from the phenyl group are concerned [155]. Sector maps for benzene were computed as shown in Fig. 25. The findings of [155] were in agreement with a revised sector rule for the phenyl chromophore by Pescitelli et al. who investigated a set of chiral molecules with phenyl substituents ($\text{PhCH}(\text{Me})\text{R}$, with $\text{R} = \text{Et}, ^n\text{Pr}, ^i\text{Pr}, \text{ and } ^t\text{Bu}$) [265].

Neugebauer [266] has implemented a subsystem formulation for the *coupling* of excitations in TDDFT using a frozen density embedding (FDE) scheme. The author remarked upon the usefulness of a subsystem approach for analyzing TDDFT results, since a description of aggregates often includes chromophores that retain their individual properties, to a good approximation, in the aggregate. To test the method, BP86/TZP TDDFT computations were performed for a benzaldehyde dimer at different distances and relative orientations. The distance between the two benzaldehyde units in the dimer was varied from 4 to 10\AA , covering separations where the coupling should be quite strong and rather weak, respectively. The splittings of excitation energies were nearly identical between the coupled FDE calculations and TDDFT computations on the dimer for separations of 5\AA and more. At shorter separations, the differences in the calculated splittings were on the order of 0.05 eV. The short-range deviations were rationalized by deficiencies in the kinetic energy term of the FDE, as well as attributed to problems with charge-transfer like excitations. Considering CD spectra, semiempirical subsystem approaches have been in use for a long time to calculate and analyze CD couplets [14]. Within the FDE approach, Neugebauer noted that for a chiral arrangement of the benzaldehyde dimer uncoupled FDE calculations failed to predict induced CD when the coupled excitations were part of the frozen system. As can be seen in Fig. 26, the coupled FDE faithfully reproduces the CD couplet.

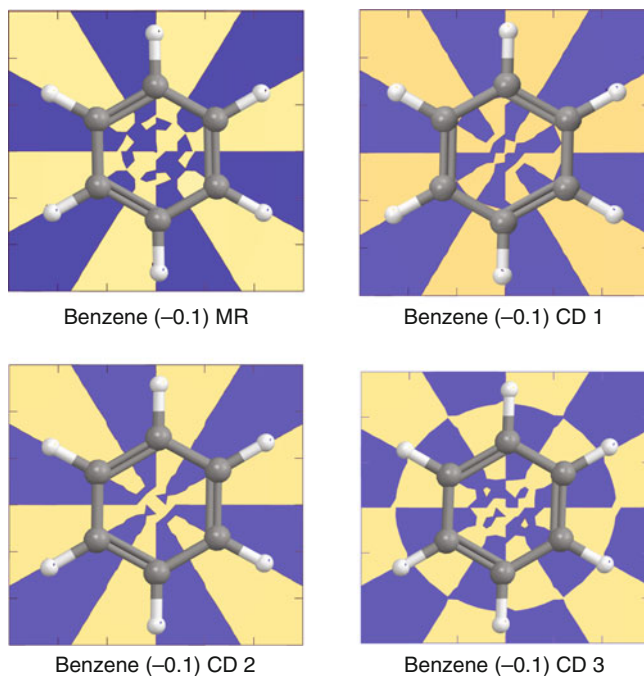


Fig. 25 The sign of the molar rotation (MR) and of the CD of the first three electronic transitions of benzene induced by a point charge of $-0.1e$ located 1.3 \AA above the plane of the ring. The distortions along the edges of the sectors (particularly evident in the center of the ring) are caused by the coarseness of the grid. MR calculated with PBE0/SVP, CD with CC2/SVP. Data to prepare the figure were taken from [155]

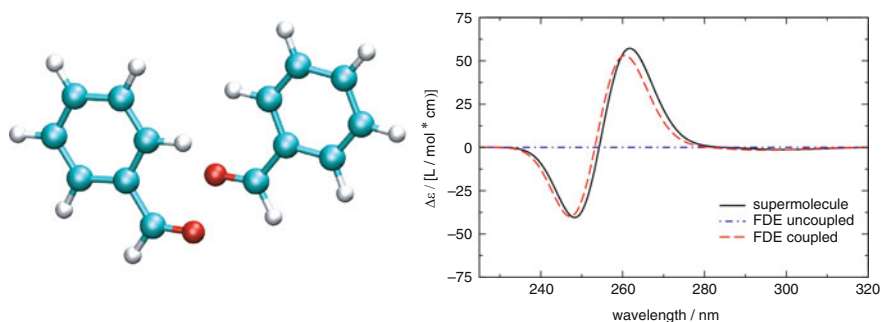


Fig. 26 *Left*: A benzaldehyde dimer at 5 \AA separation. *Right*: CD of the dimer computed with TDDFT for the dimer supermolecule, and using a coupled TDDFT frozen-density embedding subsystem approach [266]. Figures courtesy of Dr. J. Neugebauer

7 Exploring Electronic Chiroptical Properties of a Variety of Systems: Organic Molecules, Fullerenes, and Gold Clusters

In this section we review selected cases where the chiroptical response of a system has been explored in particular detail. This is not to say that no such detailed investigations have been undertaken in the works cited so far – quite the contrary: Many of the research articles that are reviewed above feature detailed analyses of ECD, OR, or ORD, but they are more appropriately discussed in another section.

When computationally investigating general aspects of chirality and chiroptical response of a molecule, it is important to determine the best method or the best combination of methods for its study. Generally, the more chiroptical methods one can use (ORD, ECD, VCD, ROA), the more reliably the results can be interpreted [267]. A combination of methods also aids AC assignments for obvious reasons. When there is access to only one technique experimentally, the selection of computational model should be as reliable as possible and at the highest level of theory feasible. The combination of multiple methods can work as independent verification and when combining the findings, one can gain additional confidence in the AC or in spectral assignments.

An example related to the development of molecular wires is the absolute configuration of the nickel metal complex $\text{Ni}_3[(\text{C}_5\text{H}_5\text{N}_2)_4\text{Cl}_2]$; an “extended metal atom chain” [268]. The AC was solved through the use of experimental and calculated VCD (B3LYP/LANL2DZ), ORD, and ECD (BHLYP/LANL2DZ). All of these individual methods indicated the same absolute configuration. Consequently, the tri-nickel complex was assigned to the (P)-helical structure which had a calculated negative specific rotation.

Another example is a study by Berova et al. [269], which had the goal of assigning the AC of flexible polypyrroloindoline alkaloids (**11**) by combined ORD and ECD calculations. The B3LYP functional was used along with the 6-31G(d) basis set, which is considerably smaller than the aug-cc-pVDZ that is often employed for these types of calculations (but tends to become computationally expensive for larger molecules). When using smaller basis sets for OR calculations, in particular basis sets such as 6-31G(d) that do not include diffuse functions, OR calculations tend to become less reliable. A combination of ECD and ORD calculations might be able to compensate for this if spectral trends and the OR dispersion are reproduced by the small-basis set computations for the right reasons. Due to the flexibility of molecules and number of conformers that had to be considered in [269], for example, the computed ORD alone would likely not have been a sufficiently reliable criterion for the structural assignment.

Isomers of (\pm)-[122]tetramantane, an inherently chiral alkane with a diamond-like cubic framework, were isolated from crude oil, separated, and characterized via X-ray diffraction, IR spectroscopy, ORD, and VCD [270]. The calculated ORD (B3LYP/6-31G(d,p)) is shown in Fig. 27 along with experimental data. Given the size of the basis sets used, and the fact that these alkanes do not have a traditional chromophore with intense valence excitations that can be made responsible for the

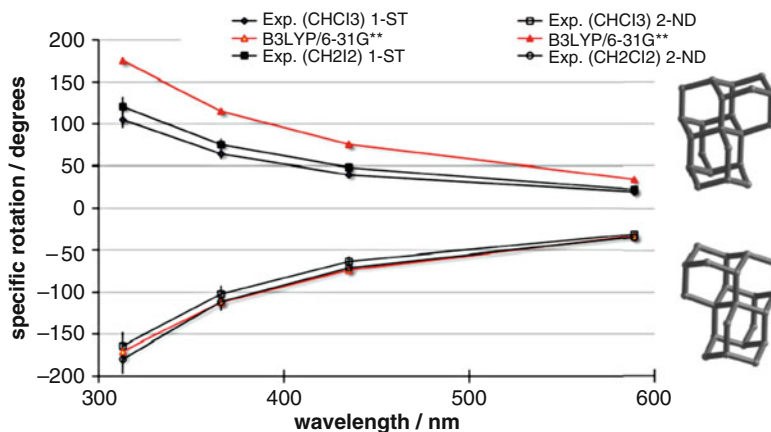


Fig. 27 ORD for enantiomers of (\pm)-[123]tetramantane. Calculations were performed at the B3LYP/6-31G(d,p) level of theory. Experimental data for solutions (CHCl₃ and CH₂Cl₂). Figure reprinted with permission from [270]. Copyright 2009 American Chemical Society

OR dispersion in the transparent region, the agreement between the ORD calculations and experiment is remarkable. To assign the AC of these molecules with single-wavelength OR calculations it would be necessary to carefully benchmark the basis set and check the robustness of the calculated OR with respect to approximations made in the XC potential and response kernel.

Taniguchi et al. [271] used chiroptical properties to determine the absolute configuration of the alkaloid actinophyllic acid (**18**) and its methyl ester form. The authors used multiple methods for an unambiguous AC assignment, by a combination of VCD, ECD, and ORD. As deduced from a proposed biosynthetic pathway, the methyl ester starting structure was built as 15R,16S,19S,20S,21R. A Monte Carlo conformational search with MMFF94 yielded two conformers that were within 10 kcal mol⁻¹ in energy, due mainly to the rigidity of the molecular skeleton. Further optimization of these two conformers, without a solvation model, at the B3LYP/6-31G(d,p) level of theory did not change the geometries significantly and a Boltzmann averaging placed the mole fraction of one conformer at 90%. Chiroptical response was calculated at the B3LYP level of theory using the 6-31G(d,p) and aug-cc-pVDZ basis sets. The AC assignment was attempted by combining information from ECD and VCD. However, the experimental VCD with noncoordinating solvents such as CCl₄ had a low signal to noise ratio, while the calculated and experimental VCD obtained with strongly coordinating solvents (DMSO-*d*₆) were in poor agreement. For this reason, ECD and ORD were employed for the AC assignment. The sign and magnitude of the ORs were in agreement with experiment. Calculated ECD spectra for this structure obtained with both basis sets were also in good agreement with the experimental ECD spectrum of the (-) form, thus confirming the AC assignment by OR. Based on these results, it was concluded

that the (–)-methyl ester form is 15R,16S,19S,20S,21R and the (+) form is the 15S,16R,19R,20R,21S enantiomer.

The study of molecules with more than one chiral center or chromophore, such as [2,2]paracyclophane ketimines (**33**), adds another level of complexity for both theoretical and experimental interpretation. [2,2]Paracyclophane has a relatively restricted conformational space, due to the bridging moieties. The dominant chromophore of (**33**) is in the ketimine moiety. The proximity of the two aromatic groups yields a chiral perturbation with a large optical rotation for some conformers. CD spectra calculated by Warnke et al. [272] at the PBE0/aug-cc-pVSZ//TPSS/SVP level of theory were in good agreement with experiment. The intensity of the first CD band, qualitatively assigned as a π -to- π^* HOMO–LUMO transition, could be used for the assignment of the absolute configuration. Experimental solvent effects were attributed to the chemical isomerism and keto-imine tautomerism. The CD spectra of the keto-imine tautomers were reproduced computationally by Boltzmann averaging of both chemical species. Solvent effects were included via a continuum model. Semiempirical rules for AC assignments for this type of compound were proposed. However, it was pointed out that for more reliable assignments it would be advisable to perform calculations explicitly.

One possible scenario when employing different chiroptical methods is that the comparison of results reveals inconsistencies, whether it be between experiment and calculations or among different calculated properties [267, 273] (e.g., apparent inconsistencies between ECD and ORD). Examples of this are *tert*-butylphenylphosphinoamidate and *tert*-butane sulfinamide [10, 274]. For each of these molecules, possible conformers were computed at the B3LYP/6-31G(d) level of theory. It was also investigated how solvent effects changed the mole fractions for the conformers. In both instances, comparison of calculated ORD and ECD with experiment would have led to inconsistent AC assignments. Through the use of other techniques such as VCD and ROA, the ACs were successfully assigned. These are examples where ORD and ECD combined are not sufficient for an absolute configurational assignment, at the level of theory chosen for the computations. The experimental wavelength range for ORD was not broad enough to show Cotton effects that would have been able to provide a less ambiguous analysis.

Polavarapu et al. [275] have calculated VCD, ECD, and ORD of (aS)-6,6'-dibromo-1,1'-bi-2-naphthol, considering three conformers regarding the OH group orientation. Calculations were performed with B3LYP and three basis sets: 6-31G(d), 6-311G(2d,2p), and 6-311++G(2d,2p) (the latter including diffuse functions). The ECD spectra of the three conformers, utilizing the 6-311++G(2d,2p) basis, showed the same sign pattern and a similar intensity between 200 and 350 nm, both in agreement with experiment. When analyzing the calculated ORD, the 6-31G(d) and 6-311G(2d,2p) calculations exhibited the same trend for the three conformers. The high specific rotations calculated at 355 nm were attributed to the proximity of the first CD band. The conformer-averaged ECD and VCD spectra, along with the ORD, allowed the assignment of the AC. The ECD and ORD did not show enough sensitivity to allow the identification of different conformers. VCD spectra suggested the predominance of only one rotamer.

2-Chloropropionitrile is an interesting molecule for theoretical studies for several reasons. First, because of its small size, 2-chloropropionitrile can be studied at high levels of theory. Second, there are ORD measurements available in gas phase and different solvents. Third, there are pronounced solvent effects that have been experimentally observed. For instance, the specific rotation of the (S)-configuration at the sodium D line in gas phase is -8.3 , in methanol it is -14.06 , and in benzene it is $-34.58 \text{ deg mL g}^{-1} \text{ dm}^{-1}$. Fourth, there is disagreement between experimentally measured gas phase ($[\alpha]_{633} = -55$) and the DC \rightarrow 1 extrapolated solution-phase OR ($[\alpha]_{633} = -30.4$) [115, 172]. Finally, the 2-chloropropionitrile OR is temperature dependent, as observed in the range $0\text{--}100^\circ\text{C}$. Such a dependence was not attributed to solvent effects [172]. Wiberg et al. have investigated the chiroptical response of (S)-2-chloropropionitrile, particularly the aforementioned temperature dependence of the OR, by exploring the effect of the methyl rotation on the energy profile and on the specific rotation, and by analyzing the effect of vibrational modes [115, 172]. For instance, a temperature dependence of the optical rotation may arise from vibrational corrections, to lowest order [125, 148, 168, 276–279],

$$\begin{aligned} \langle [\alpha] \rangle_T &= [\alpha]_e - \frac{1}{4\hbar} \sum_{i,j} \frac{1}{\omega_i} \left(\frac{\partial [\alpha]}{\partial q_i} \right) \coth \left(\frac{\hbar\omega_j}{2kT} \right) k_{ij} \\ &+ \frac{1}{4} \sum_i \coth \left(\frac{\hbar\omega_i}{2kT} \right) \left(\frac{\partial^2 [\alpha]}{\partial q_i^2} \right) \end{aligned} \quad (33)$$

and similarly for the molar rotation or other molecular properties. The term involving the cubic force constants k_{ijj} represents an *anharmonicity* correction while the last term represents a *curvature* correction. In (33), ω_i is the frequency of normal mode i , $[\alpha]_e$ is the property calculated at the equilibrium geometry, T is the temperature, k is the Boltzmann constant, and the q_i are dimensionless vibrational normal coordinates [8].

Wiberg et al. [172] explored such effects of nuclear motion using B3LYP calculations. The basis sets used were 6-31+G*, 6-311++G**, and aug-cc-pVDZ, with and without inclusion of electric field dependent basis functions (EFDs) [280] added to improve the response calculations with respect to basis functions needed to describe an external-field perturbation [171, 172]. ORD calculations in the range of 255–633 nm, with the 6-311++G** and aug-cc-pVDZ basis sets including EFDs yielded very good agreement with experiment (ORs inside the experimental error range). Calculations without EFDs and with smaller basis sets were in considerably less good agreement with experiment. The energy and the OR as function of the H–C–C–Cl dihedral angle (methyl rotation), at the B3LYP/aug-cc-pVDZ level of theory, exhibited neither anharmonicity in the potential energy profile nor a significant curvature of the OR around the equilibrium geometry. It was therefore concluded that effects on the OR from the methyl rotation should not be significant. However, the vibrational modes at 224 and $1,318 \text{ cm}^{-1}$ exhibited OR curvature. The vibrational mode at 224 cm^{-1} involving methyl torsion and C–CN

bending was considered as the main contributor to the ORD temperature dependence of 2-chloropropionitrile.

Kowalczyk et al. [121] studied (*S*)-2-chloropropionitrile to investigate whether the use of EFDFs helps to converge OR computations more rapidly toward the complete basis limit, and whether CC2 or TDDFT would perform better for chiral response calculations. TDDFT calculations were performed at B3LYP level of theory, without including vibrational effects. Optimized geometries were determined with B3LYP/6-311++G** in order to compare with previous calculations [172]. The basis sets considered for chiroptical response were Sadlej's triple- ζ designed for calculating electric-field-dependent properties [281, 282], and the correlation consistent basis sets by Dunning et al. [283–285]. It was concluded that aug-cc-pVQZ and d-aug-cc-pVTZ* OR calculations were close to the B3LYP basis set limit. Here, d-aug-cc-pVTZ* refers to a mixed basis set using d-aug-cc-pVDZ for C, N, and H, and aug-cc-pVDZ for Cl. The B3LYP calculations compared poorly with gas phase experiments. Based on these calculations, it was suggested that the previously mentioned good agreement of experimental and calculated specific rotations of (*S*)-2-chloropropionitrile [172] was perhaps fortuitous [121, 142]. Compared to CC, B3LYP underestimated the energy of excitations and overestimated the rotatory strengths of at least the first six excitations. It was argued that CC calculations were more accurate than TDDFT calculations with the B3LYP functional, and that the differences between CC and experiment can be related to temperature and zero-point vibrational effects as well as to residual correlation effects not included in the approximate coupled cluster model. A sum over states analysis using B3LYP/aug-cc-pVDZ showed that the first 100 excitations did not converge towards the calculated linear response OR and that it afforded strong oscillations even at high excitation energies. Wiberg et al. [137] extended the sum over states study to 1,500 excitations which converged towards the linear response OR. The application of a blue-shift of 0.6 eV to the excitations in the SOS yielded better agreement with the experimental gas phase OR, indicating that a main source of error in the TDDFT calculations might indeed be a global underestimation of the excitation energies. Improved functionals, e.g., from the long-range corrected family, are now available in many programs that should yield overall better excitation spectra and therefore, by virtue of the SOS equation, improved optical rotations.

Norbornenone has a large specific rotation when measured in hexane ($-1,146 \text{ deg mL g}^{-1} \text{ dm}^{-1}$) [168]. To our knowledge there are no gas phase measurement currently available for this molecule. Moscowitz et al. [262] considered this β - γ -unsaturated ketone as an inherently chiral chromophore. Crawford et al. showed that DFT calculations at the B3LYP/aug-cc-pVDZ level of theory yield a specific rotation similar to experiment with a value of $-1,221.8 \text{ deg mL g}^{-1} \text{ dm}^{-1}$, while CC (EOM-CCSD/aug-cc-pVDZ) and HF do not compare as favorably (i.e., that different levels of theory can either strongly over or under estimate the chiroptical response compared to the solution measurements) [142]. Concerning the origin of this particularly strong method dependence, Crawford et al. suggested that neither basis set incompleteness nor vibrational effects were the main culprit.

Treatment of electron correlation at a higher level and considering solvent effects might yield more consistent calculations. Wiberg et al. [168] bisected the skeleton of norbornenone in order to study the effect of the dihedral angle of the α carbon on the specific rotation. It was found that there was a strong effect around 260° (the corresponding angle in norbornenone would be 291°). This indicated that one source of optical activity in this molecule is related to the position of the α carbon. In an SOS analysis of the OR of norbornenone [137], the first transition appeared to be the dominant, in part because it is 1.2 eV lower than the next transition. This HOMO–LUMO transition had an n -to- π^* component as well as a π -to- π^* contribution. Overall, however, Crawford [9a] pointed out that the sensitivity with respect to optical activity for norbornenone to different levels of theory (i.e., CC and DFT) is not yet well understood.

The ORD of the inherently chiral molecule (*P*)-(+)-[4]triangulane was computed employing CCSD, CC2, and TDDFT (B3LYP/aug-cc-pVDZ) [133]. Solvent effects were not taken into account in the computations. Experimentally, in the neat state, the specific rotation ranges from $197.2 \text{ deg mL g}^{-1} \text{ dm}^{-1}$ at 589.3 nm to more than $600 \text{ deg mL g}^{-1} \text{ dm}^{-1}$ at 365 nm . The TDDFT results overestimated the magnitude of the OR somewhat. The CCSD calculations of the ORD yielded better agreement with experiment, albeit at a much higher computational cost. It was noted that both TDDFT and CC methods reproduced the experimental trend correctly. Meijere et al. [286] had previously calculated the ORD of [4]triangulane at the B3LYP/TZVP level of theory employing KK transformations. The calculations matched well with experiment, but only after shifting the ORD curve by 100 nm which was justified by pointing towards unspecific solvent effects that were not considered in the calculations. It was pointed out by Crawford et al. [142] that, despite the good agreement of CCSD/aug-cc-pVDZ with experiment, the reliability of CCSD should be further investigated regarding electron correlation and basis set (in)completeness. Other influences, such as solvent and temperature, should also be investigated.

Chiral disulfide and diselenide chromophores in the diglycosyl dichalcogenides motif were studied by Kurtan et al. [287]. The chirality of R–Z–Z–R (Z = S, Se, Te) had been related to the torsional angle of 90° , resulting in P or M helicity of the molecule. Even though in solution there is a racemic mixture, the crystallization of one enantiomer (either P or M) can be favored. In order to determine the helicity in the crystals, a disulfide quadrant rule was developed which related the helicity and the first CD band (Fig. 28). This rule has been applied to diselenides (36) as well. BP86, B3LYP, and B3LYP TDDFT computations were performed with different basis sets (6-31G(d), 6-311+G(d,p)) to optimize the geometries. For ECD calculations, more flexible basis sets were used, such as TZVP, 6-311+G(d), cc-pVTZ, and a modified TZVP basis which was augmented for C and Se. B3LYP/TZVP afforded the best agreement with experiments (see Fig. 28). The two lowest-lying transitions, which were nonoverlapping and corresponding to the first two bands in the ECD spectrum, were assigned as heteroatom centered n -to- σ^* excitations. Further analysis suggested that the first two CD bands can be attributed to the inherent chirality of the –Z–Z– chromophore. The sign of such bands was found to

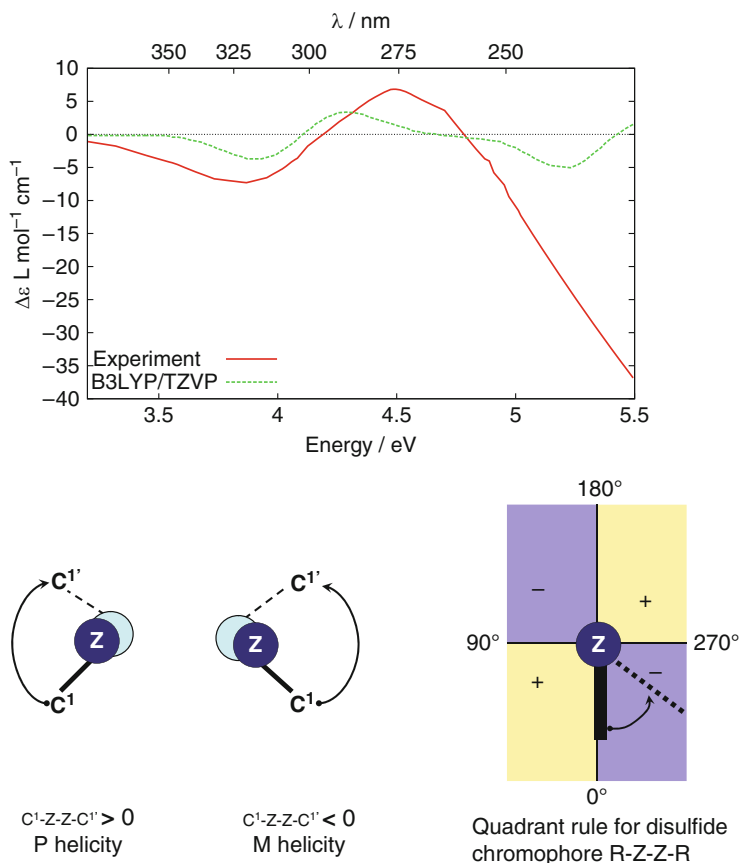


Fig. 28 Quadrant rule for R-Z-Z-R chromophores ($\text{Z} = \text{S, Se, Te}$). *Top*: Experimental and calculated CD spectra of dichalcogenide diselenide. Calculations were performed at the B3LYP/TZVP level of theory. *Bottom*: The quadrant rule for the P/M helicity of dichalcogenides. Data to prepare the figure were taken from [287]

be related to the helicity of the R-Z-Z-R moiety. Kurtan et al. provided theoretical support to the application of quadrant rule for disulfides and diselenides chromophores. The authors recommended focusing on the first two CD bands in order to avoid overlapping transitions and possibly spurious charge transfer transitions calculated with TDDFT at higher energies.

Chiral fullerenes have been challenging molecules to synthesize with significant enantiomeric excess and to assign configurationally [288]. ECD computations have provided support for the assignment of the structure of C_{84} [289, 290]. Polavarapu, Crassous, and Ruud have tackled the (^fC)- C_{76} AC assignment with TDDFT [197]. The ECD spectra for geometries optimized with B3LYP/6-31G were calculated at different levels of theory. All predicted spectra reproduced the main features of the

experimental spectrum. The authors noted that the best agreement was obtained with BHLYP/6-31G(d), particularly for five of the CD bands (see Fig. 29). The B3LYP/6-31G(d) and BLYP/6-31G(d) spectra needed to be blue-shifted for better agreement with experiment. After an applied red-shift, calculations at the HF/6-31G(d) level of theory also matched the experiment. It was noted that the BHLYP functional seems to do well when reproducing lower-lying states for molecules with extended π systems; however its performance for higher-lying states was not as good.

The ORD for $(^f\text{C})\text{-C}_{76}$ was also investigated. Two methods were used: a linear response theory with damping developed by Norman et al. [291] and KK

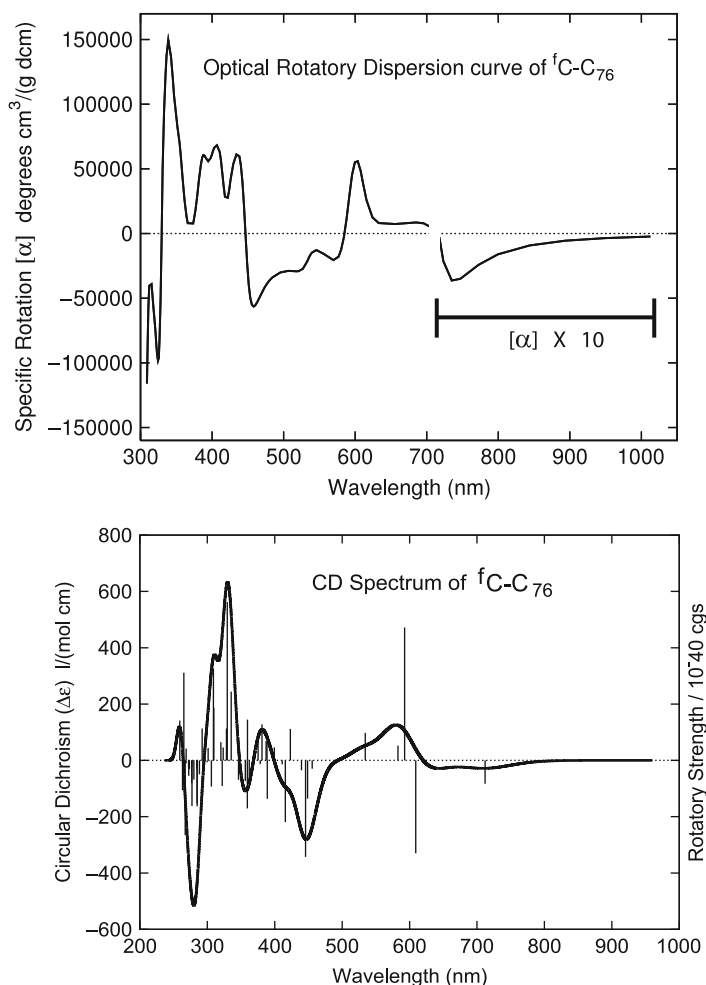


Fig. 29 CD spectrum of $(^f\text{C})\text{-C}_{76}$, and ORD curve from a KK transformation. Data to prepare the plots were taken from [197]

transformations of both computed and experimental CD (See Fig. 29). Linear response calculations at the B3LYP/6-31G* level afforded the best agreement with the KK of the experimental CD at wavelengths above 500 nm. Given the compactness of C₇₆, it can be expected that basis functions on surrounding atoms will effectively act as diffuse polarizing functions for a given atom. A larger basis set would be required for improvements in the calculated response; however the computational resource scaling for a molecule this large would be a concern. Due to the overall performance of the TDDFT calculations in comparison with experiment, with different levels of theory, the authors concluded that the previous structural assignment as (C)-C₇₆ was indeed correct.

A study of [*n*]-ladderanes by Zuber et al. [213] has already been cited. The computations resulted in a successful AC assignment (see (1) in Fig. 15 for *n* = 2–7). ORs at the sodium D line were calculated with the aug-cc-pVDZ basis set and three different electronic structure methods (B3LYP, RI-BP86, and Hartree–Fock). Twelve ladderanes were studied overall: six *trans*-(S)-methyl- and six *cis*-(R)-methyl-[*n*]-ladderanes, with *n* ranging from two to seven. Geometries were optimized with B3LYP/aug-cc-pVDZ. For the *trans*-(S)-ladderanes, the specific rotation was calculated to be positive with all three methods. The predicted HF optical rotations for all molecules were only approximately half of those calculated with B3LYP (which were around 10–15 deg mL g⁻¹ dm⁻¹ lower than the ORs calculated with the BP86 functional). For the *cis*-(R) ladderanes, the calculated optical rotations were lower in magnitude than those of their *trans* analogs. Another marked difference was that the HF optical rotations of the *cis*-ladderanes were much closer to the B3LYP and BP86 calculations, never differing by more than 5 deg mL g⁻¹ dm⁻¹. For these compounds, the trend of decreasing OR for increasing (even) *n* was more apparent across the three methods. The same was true for odd *n*, however the ORs of the [*odd*]-ladderanes were lower than the ORs of [*even*]-ladderanes; i.e., there was an oscillating effect seen in the specific rotations as a function of *n*. The ACs were assigned as (+)-*trans*-(S)-alkyl-[5]-ladderane and (–)-*trans*-(R)-alkyl-[5]-ladderane. Zuber et al. observed a “rung-parity controlled oscillatory” OR phenomenon (see Fig. 30), which can help with the AC assignment of ladderanes without derivatization and when NMR or X-ray structures are not available.

Giorgio et al. [292] studied the ECD of calicheamicinone (the aglycon of calicheamicin), a complex dienocarbamate–enediyne bicyclic antitumoral drug scaffold found in the calicheamicin, esperamicin and shisijimicin A families. These structures afford a main CD band between 310 and 270 nm experimentally that has been attributed to the dienocarbamate and enediyne chromophores. Geometries were optimized with B3LYP/6-31G(d) and response calculations were performed with B3LYP/aug-cc-pVDZ. The optimized and X-ray structures compared well, apart from an uncertainty about the orientation of the carbamate group. Thus, the ECD calculations were performed with the X-ray coordinates as input. The aglycon (see (17) in Fig. 16) was split into three truncated model-complexes which were studied as well, along with calicheamicin aglycon substituting the side chain with sulfur atoms by a methyl group, the dienonecarbamate cycle, and the

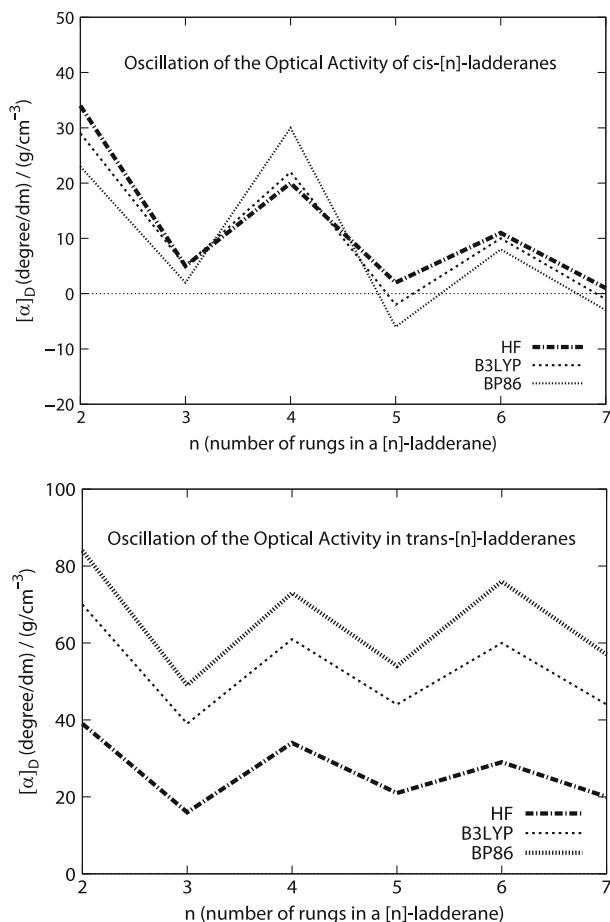


Fig. 30 Rung-parity controlled oscillatory OR phenomenon in $[n]$ -ladderanes. Data to prepare the plot were taken from [213]

enediyne. One moiety (dienonecarbamate) was determined to play a more important role in contributing to the ECD than the other; however the overall ECD did not match well with the experiment unless both chromophores were present, indicating there is an important coupling effect.

CD spectra can be used for an exploration of intermolecular interactions. For example, flavanpentol, a drug for different protein related diseases, has a benzene moiety and three chiral centers. Capelli et al. [293] studied the conformers that this molecule adopts when in close proximity to a proline-rich peptide in aqueous solution. The authors compared ECD spectra of conformers in gas phase and methanol computed with TDDFT at the B3LYP/6-31+G(d) level of theory. Solvent effects were modeled by an integral equation formalism of PCM. The authors noted

that the computed spectral patterns were not affected by different basis sets used. A molecular dynamics conformational search for conformers and a proline-rich protein in aqueous solution was performed with the TIP3P model in order to study how the interaction affects the flavonoids conformation (and therefore its chiroptical response). The simulated spectra matched well with experiment, which lead the authors to their conclusion that flavonoids can self-associate by stacking interactions and hydrogen bond networks. We note in passing a computational study of the coupling of chromophores in rhodopsin [265].

Chiral imprinting in solvent shells appears to have gained interest in recent years [181]. Mukhopadhyay et al. [156] performed computations on a methyloxirane–benzene system. It was argued that the chiral solute methyloxirane leaves a chiral imprint in the solvation shell comprised of rigid nonchiral solvent molecules. MC simulations were used to determine solvent solute configurations. Optical rotations of the solvated methyloxirane were calculated performed with the BP86 and BLYP functionals and the SV/SVP/aug-cc-pVDZ basis sets at four different wavelengths. As in a related study discussed elsewhere in this chapter [180], the optical rotations were computed for the system as a whole, and without the methyloxirane solute. The ORD of the (R) and (S) forms of dimethyloxirane (from MC computations with explicit solvation) were effectively mirror images of each other (BP86/SVP). The ORD of the chiral-imprinted solvent alone, computed from the solute–solvent cluster with dimethyloxirane removed, was of the same magnitude as the ORD of the solvated system; see Fig. 31. The solvent effect dominated the ORD between

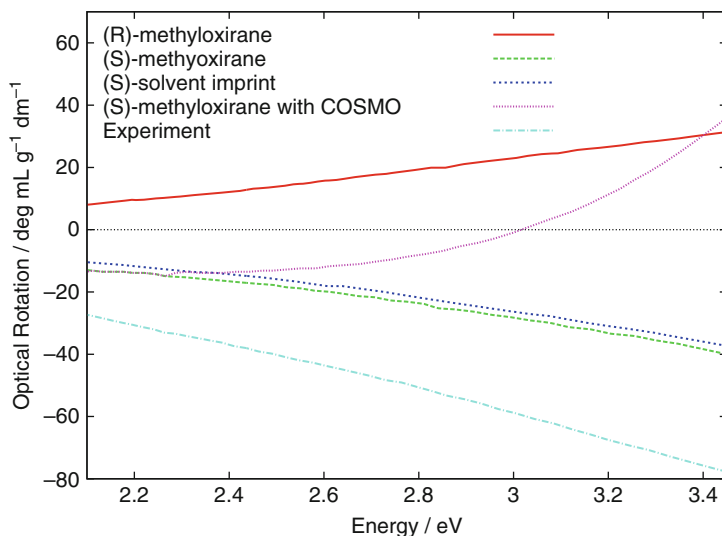


Fig. 31 ORD of methyloxirane in benzene: solute–solvent cluster and solvent imprint. Experimental ORD, computed ORD for gas phase and continuum solvent for (S)-methyloxirane, and computed gas phase ORD of (R)-methyloxirane shown for comparison. Data to prepare the figure were taken from [156]

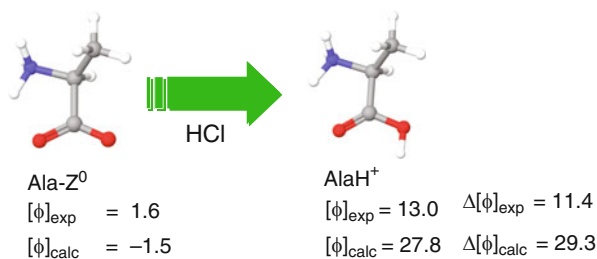
350 and 600 nm. When only implicit solvation was used (continuum model), the calculated ORD predicted the wrong trend (and the wrong sign, depending on the wavelength). It is apparent that for this system implicit solvation cannot model the trends seen experimentally.

Wang and Cann [294] studied the transfer of chirality from a chiral molecule to an achiral solvent utilizing an index of chirality first proposed by Osipov et al. [295]. The importance of the polarizability of the solvent, Boltzmann averaging of conformers, and solvent–solute interactions were evaluated. As a set of chiral test molecules, (*S*)-styrene oxide, (*S*)-*n*-(1(4-bromophenyl)ethyl)pivalamide (PAMD), and (*R*)-acenaphthenol were selected. These molecules allowed the exploration of different aspects of chirality transfer. Explicit solvents considered were ethanol, to explore hydrogen bonding alone, and benzyl alcohol, due to its capability for hydrogen bonds and π -stacking interactions. Some of the following aspects were found important for chirality transfer:

1. It is more probable to occur when there is an opportunity for hydrogen bonding.
2. It involves polarization of the solvent.
3. It might be more pronounced for nonrigid molecular systems. However, the overall optical activity of the solution might be smaller as consequence of cancellation effects of the chirality transfer of different conformers.
4. Chirality indices indicated residual chirality in the solvent as a consequence of the presence of a chiral solute. Wang and Cann proposed the application of such indices for the prediction of the solvent contribution in optical activity [294].

Amino acids are challenging systems for chiroptical response calculations, in part because of their conformational flexibility, the importance of solvent effects on the stability of their conformers and on their ECD and ORD, and the nature of their electronic excitations. Some of the amino acid work from our group and other researchers has already been cited in previous sections. Here, we focus on the pH dependence of the OR. It was observed quite some time ago by Clough, Lutz, and Jirgensons [296–298] (CLJ) that the molar rotation for natural (*S*)-amino acid solutions becomes more positive upon the addition of a strong acid. For the (*R*)-enantiomers, the opposite effect was observed. Kundrat and Autschbach have recently analyzed the CLJ effect for natural amino acids using TDDFT computations [136] (B3LYP and B3LYP, aug-cc-pVDZ basis set) and demonstrated that the molecular origin of CLJ effect can be traced back to a sign change of the CD of the lowest-lying excitation in the carboxylic acid functional group upon protonation. A sum-over-states analysis was also performed, along with calculations of sector maps for the glycine chromophore (see Sect. 6). An illustration of the CLJ effect, and the associated SOS for alanine can be seen in Fig. 32. For both the protonated form (low pH) and the zwitterion (neutral pH) the lowest-energy excitation was assigned as an n -to- π^* type transition centered in the COOH and COO⁻ group, respectively. The molar rotations from just these first excitations would lead to a strongly overestimated CLJ effect, but the converged SOSs demonstrate that this transition is essential [170] since higher lying excitations only dampen the effect. Without these excitations, a negative CLJ behavior would

CLJ effect for Alanine



Sum Over States of Cationic and Zwitterionic Alanine

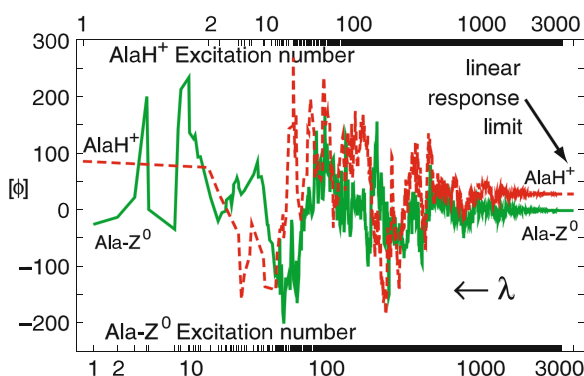


Fig. 32 SOS molar rotation of alanine in the AlaH^{+1} cationic and zwitterionic AlaZ^0 form, as a function of how many states are included in the SOS. Calculations were performed at the B3LYP/aug-cc-pVDZ level of theory. Data to prepare the figure were taken from [136]

be observed. We note in passing the slow convergence of the SOSs which has also been pointed out elsewhere in this chapter (Fig. 33).

The CLJ effect can be generalized to other α -substituted chiral carboxylic acids [170]. With a combination of computed OR, ECD, and sector maps (BHLYP/aug-cc-pVDZ), Nitsch-Velasquez and Autschbach showed that the physical origin of the generalized CLJ effect is the same as for amino acids, linking the absolute configuration directly to the sign of a generalized CLJ effect. The authors noted that for conformationally flexible molecules with small magnitude optical rotations, the presence of a CLJ-type effect might aid the assignment of absolute configurations based on comparing experimental data for structurally closely related molecules with computed *differences* of their chiroptical responses.

Chiral gold clusters have in recent years attracted the interest of researchers [299–304]. Garzón et al. predicted in 2002 and 2003 the circular dichroism of bare

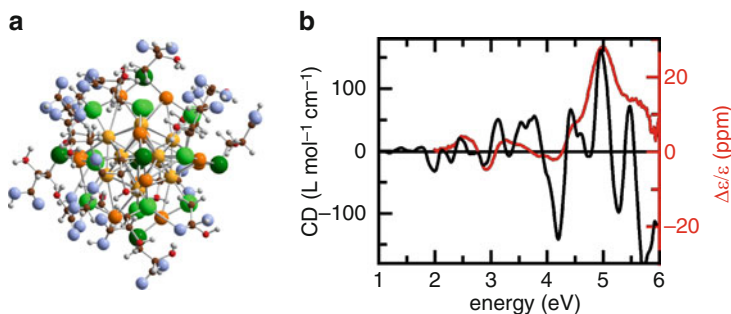


Fig. 33 Optical activity of a chiral ligand-protected gold nanocluster $[\text{Au}_{25}(\text{SR}_{\text{cys}})_{18}]^-$. (a) Optimized geometry. (b) Calculated CD spectrum of the cysteine-protected cluster (black), and experimental spectrum for a glutathione-protected cluster (red). Reprinted with permission from [299]. Copyright 2010 American Chemical Society

and passivated chiral gold clusters [302–304], but at the time a first-principles method was not feasible. Recently Garzón et al. [299] employed TDDFT calculations of ECD spectra, with a split-valence AO basis, the PBE functional, and scalar relativistic pseudopotentials, to investigate the origin of the optical activity for Au_{25} clusters protected by 18 cysteine or glutathione ligands. The computations were performed for the cysteine system, and agreed reasonably well with an experimental ECD spectrum for the glutathione protected cluster. The analysis indicated that both a chiral distortion from the metal atom core and a dissymmetric environment from the ligands act concurrently to generate the ECD, and that these influences cannot easily be considered separately. The calculations also indicated that the CD band shapes should be sensitive to the orientation of the ligand in the layer protecting the cluster.

Goldsmith et al. [305] have investigated a chirality mechanism that may arise in symmetric gold clusters when perturbed dissymmetrically by adsorbates. TDDFT computations of ECD spectra of $\text{Au}_{14}(\text{R-methylthiirane})$ yielded qualitative agreement with a point-charge perturbed particle in a box model for the gold cluster. It was suggested that chiral signatures should be observable in the IR/NIR spectral region for an ensemble of gold clusters passivated with chiral adsorbates.

Provorov and Aikens [306] used TDDFT computations to study gold complexes of the type $[\text{Au}_1\text{L}_4\text{X}_2]^+$ with $\text{X} = \text{Cl}, \text{Br}$, and L representing coordination of the gold cluster by chiral mono- and bidentate phosphine ligands. The computed ECD spectra agreed well with experiment for the first two CD bands. It was observed that the ECD intensity of metal core based transitions dropped significantly when changing ligands from dpb to pairs of PH_3 , driving structural changes in the core which lowered the symmetry from C_2 to C_1 . The lower-lying transitions were related to the delocalization of the metal superatom orbitals, which showed P -like and D -like character. The authors pointed out that their study was the first to demonstrate how the optical activity of the metal core depends sensitively on the

presence and chiral arrangement of surrounding ligands. Such a dependence on the ligands appears to support for the aforementioned work by Goldsmith et al.

8 Metal Complexes

Researchers have shown great interest in chiral metal complexes, and their chiroptical response, for a long time. However, until around 2003 theoretical work on CD spectra of metal complexes has predominantly utilized semiempirical models [307–320]. For instance, much has been learned about the CD of metal-based transitions from theoretical approaches based on crystal field and ligand field models [309, 311, 313–320]. Some of these methods were specifically developed in order to describe the ligand-field (*d-to-d* or *f-to-f*) transitions at the metal center, while the nature of charge-transfer (CT) excitations or of transitions within the ligand system could not be addressed with these methods. Also, “the formidable complexity of these theories has restricted their usage and development to a limited number of specialists” (Kuroda and Saito [310]). Excitations within the ligands of chiral complexes have also been studied with semiempirical models. See [307, 308, 321, 322] for examples. Due to the complexity of OR calculations and the sensitivity of OR to the computational model, direct calculations of the ORD of metal complexes – without involving KK transformations of the CD spectra – have not been undertaken until recently [43].

It is fair to state that direct first-principles computations of ECD spectra and ORD for metal complexes over the UV–Vis frequency range have only become feasible because of the development of the relevant TDDFT techniques. Hartree–Fock theory, although computationally as affordable as TDDFT, usually does not yield reliable ECD spectra for metal complexes and often affords unacceptably large errors for excitation energies. The situation has improved dramatically with the advent of TDDFT, although one should keep in mind that many of the popular functionals have adjustable parameters that were determined from computations on main group atoms and molecules. For a dedicated overview of TDDFT applied to calculate excitation spectra of transition metal systems see [323] by Rosa et al. who concluded that no hybrid nor nonhybrid functional performs consistently well for all metals (range-separated functionals were not considered). Therefore, the selection of the functional is a particularly important aspect of TDDFT computations on metal complexes to ascertain that good results are obtained for the right reasons. The reader is also referred to a recent review of TDDFT methods applied to inorganic systems where additional information about the selection of functionals, along with case studies, can be found [12]. The first TDDFT computations of metal complex CD spectra started to appear in the literature in 2003 [102, 103]. As in previous sections, we focus here on more recent work. A study of a Ni₃ system [268] has already been discussed in Sect. 7

Le Guennic et al. [324] have calculated the ECD of tris-bidentate Fe, Ru, and [Os(phen)₃]²⁺ transition metal complexes (Λ configurations). An example of the

structures for these molecules is depicted in Fig. 34. One aim of this study was the full assignment of the spectra, and the role of the metal in the intense exciton couplets. Another aim of the work was to determine a suitable computational model for the ECD of such complexes. The authors explored the effects of functional, basis set, and solvation on the ECD, and studied the influence of relativistic corrections on the Os and Ru complex. Regarding the basis set, it was found that a split-valence polarized basis on the nonhydrogen ligand atoms along with a polarized metal basis set was sufficient to describe the spectra. Polarization functions on the heavier ligand atoms were important, while adding polarization function on the hydrogens did not change the spectra to a significant degree. Solvent effects were noticeable, but not as pronounced as previously found for a set of Co(III) complexes with +3 charge [102]. Inclusion of relativistic effects, via the zeroth regular approximation (ZORA), had a slight effect on the spectrum of $[\text{Os}(\text{phen})_3]^{2+}$; most notably a red-shift of the lower energy transitions due to the relativistic destabilization of the Os $5d$ orbitals [325, 326]. The nonrelativistic spectrum was strikingly similar to that of the Ru complex. The dependence on the calculated CD spectra with respect to basis set and functional selection, along with solvation and relativistic effects, can be seen in Fig. 35. Calculations on a $(\text{phen})_3$ ligand system with a ghost atom in place of the metal showed that the metal itself does not play a dominant role in the exciton couplet, but that the main reason for the intense CD in the ligand π -to- π^* energy range is indeed a through-space coupling of the ligand π -to- π^* transitions. The lower energy (MLCT and ligand-field) excitations were modeled well for osmium and ruthenium. However, the iron complex did not match the experiment well in this region. Upon further investigation, these low energy transitions were shown to be sensitive to the functional used, as well as to the geometry, and that these transitions likely afforded significant self-interaction errors, similar to the ligand-field transitions in a set of Co(III) complexes that were studied earlier [102].

Marked solvent effects on LMCT bands had previously been predicted for +3 charged Co(III) complexes [102], with less strong effects for complexes with an

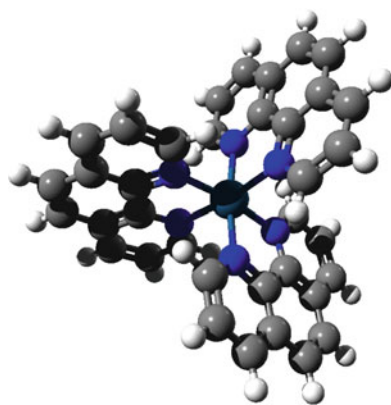


Fig. 34 BP86/TZP optimized Λ - $[\text{Os}(\text{phen})_3]^{2+}$ structure, as an example of the complexes studied in [324]

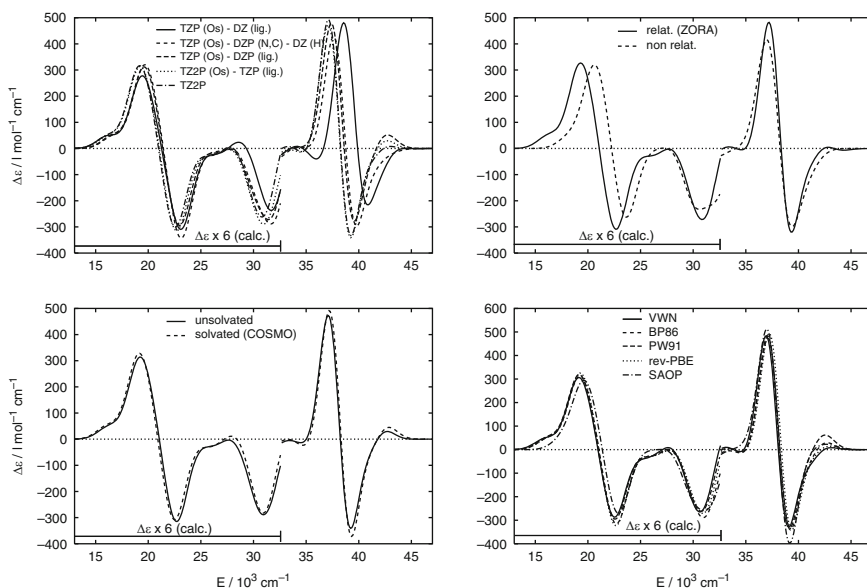


Fig. 35 Dependence of the computed ECD spectrum of $[\text{Os}(\text{phen})_3]^{2+}$ on the computational model. *Top left*: Basis set. *Top right*: Relativistic effects. *Bottom left*: Solvent effects. *Bottom right*: Functional dependence. Figure reproduced from data published in [324]

overall lower charge. The solvent effects were modeled with the COSMO continuum model. Jensen et al. revisited the CD spectrum of $\text{Co}(\text{en})_3^{3+}$ [327]. Solvent effects were treated by a discrete reaction field (DRF), based on a force-field molecular-dynamics simulation. The solvent effects were found to be very similar to those obtained from the COSMO continuum model in static computations. A certain degree of solvent broadening of the LMCT bands was obtained from the DRF computations due to the underlying molecular dynamics.

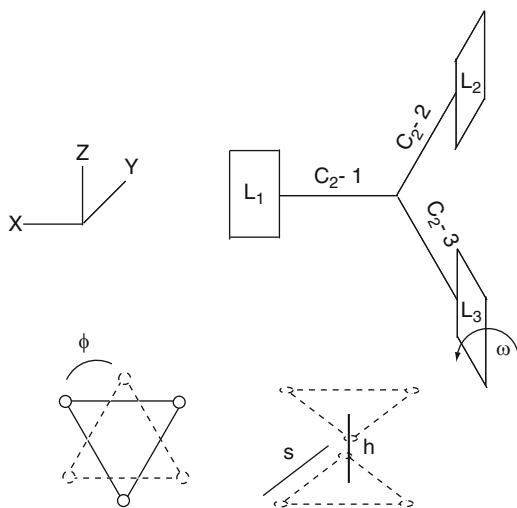
In a series of publications, Jorge et al. have considered the structural and electronic origin of the CD of tris-bidentate transition metal complexes with unsaturated ligands in the d -to- d and in the ligand-to-metal CT (LMCT) region [328, 329]. A detailed analysis of orbital contributions to the transition dipole moments made it possible to relate the TDDFT results to semiempirical models used in the past. Among the findings was that the origin of the CD in the ligand-field transitions involved the mixing of metal with ligand orbitals upon a distortion of the metal environment of octahedral to trigonal-dihedral. Mixing of even with odd metal orbitals (such as nd with $(n+1)p$) provided less than 10% to the optical activity, whereas this would be the only possible contribution in crystal field models.

Fan and Ziegler [330] have recently refined the analysis of the origin of CD in tris-bidentate $\text{M}(\text{L})_3^{n+}$ complexes by analyzing in detail TDDFT ECD data for $\text{Co}(\text{en})_3^{3+}$. Here L is an aliphatic σ -bonding ligand, such as the bidentate ligand ethylenediamine. The authors related s/h and ϕ parameters, traditionally used to describe the

level of polar compression and azimuthal distortion in a system with distorted octahedral symmetry, to a more intuitive ω angle. The ω angle, along with s/h and ϕ parameters are depicted in Fig. 36. Earlier work has been confirmed (see [102, 328, 329] and references therein), showing that the sign and magnitude of s/h relative to a perfect octahedral arrangement determines the ordering and energetic separation of the ligand-field A_2 and E states of D_3 complexes, but does not contribute to the rotatory strengths of these transitions. The magnitude of ϕ , on the other hand, does not contribute to the energy splitting but its sign and magnitude is responsible for the sign and magnitude of the rotatory strengths. By relating the distortion of symmetry to the overlaps of the metal orbitals and the nitrogen σ -coordinating orbitals, it was possible to gain a semiquantitative understanding of the origin of CD on these types of trigonal dihedral complexes. The CD spectrum of Co(en)_3^{3+} computed at the BP86/TZP level of theory showed good agreement with the spectral pattern seen experimentally. Fan and Ziegler were able to interpret the CD bands stemming from ligand-field as well as LMCT transitions in terms of the metal–ligand σ interactions and the magnitude of the overlap of ligand σ combinations with the metal d orbitals.

The analysis has subsequently been extended to other Co(L)_3 complexes [331] as well as M(bipy)_3^{2+} and M(phen)_3^{2+} complexes [332]. In the former study, L represents the unsaturated ligands acetylacetonate (acac), oxalate (ox), malonate (mal), and dithioxalate (diox). In the latter study, M represents the metals iron, ruthenium, and osmium. For the cobalt complexes, BP86/TZP computed spectra were in acceptable agreement with their experimental counterparts. The unsaturated ligands cause more complicated spectra due to the presence of both σ and π orbitals, and therefore the analysis was somewhat more challenging. The distortions of the geometry away from an idealized octahedral metal environment resulted not

Fig. 36 *Top:* Depiction of the ω angle used in [330], and how it reduces D_{3h} symmetry to D_3 . Starting with parallel ligands, rotation of L_n about its C_2 axis by $\omega \neq 0/90/180^\circ$ will result in a chiral structure. *Bottom:* Depiction of how the s , h , and ϕ parameters relate to octahedral complexes and distorted systems with D_3 symmetry



only in an overlap of metal and ligand orbitals yielding $d-d$ and L_o MCT excitations as seen in $\text{Co}(\text{en})_3^{3+}$, but also L_π MCT transitions.

2,2'-Bipyridine, as well as 1,10-phenanthroline, are unsaturated ligands with intense π -to- π^* transitions in the ligand. The main emphasis in [332] was the TDDFT based analysis not of the low-energy $d-d$ transitions but of the exciton CD, which is ascribed to a coupling of π -to- π^* transitions between separate ligands [333, 334], as already briefly mentioned above. The sign pattern of the exciton band was rationalized by the orientation of the transition moments related to the π -to- π^* transitions on the individual ligands. Looking again at Fig. 36, it is apparent that the ω angle will also give a good description of a planar bipy and phen ligand, and how the long-axis polarized ligand π -to- π^* transitions will couple.

Coughlin et al. [335] have synthesized neutral iridium(III) luminophores and have characterized them through the application of circularly polarized luminescence (CPL) and ECD. TDDFT calculations of CPL (see also Sect. 4.5) are not common practice, and therefore the TDDFT computations were restricted to ECD calculations. Among the set of complexes synthesized, calculations were only performed on $(\text{MeOmpy})_2 \text{Ir}(\text{acac})$ at the B3LYP/LANL2DZ level of theory. The comparison of simulated and experimental spectra was favorable, predicting the structure to be a Δ configuration. To strengthen the assignment, calculations were also performed on a complex whose structure had previously been published, $\text{fac-}\Delta\text{-Ir}(\text{ppy})_3$. Calculations on this complex, at the same level of theory, also afforded good agreement with the experimental CD spectrum, especially in the low energy regions, up to 300 nm. In another study by the same group [336] UV-Vis and CD spectra of Fe, Ru, and Zn complexed with the enantiopure hemicage ligand $(-)$ -(5*R*,5'*R*,5''*R*,7*R*,7'*R*,7''*R*,8*S*,8'*S*,8''*S*)-8,8',8''-[(2,4,6-trimethyl-1,3,5-benzenetriyl) tris(methylene)] tris[5,6,7,8-tetrahydro-6,6-dimethyl-3-(2-pyridinyl)-5,7-methano isoquinoline] were computed using TDDFT. The computed excitation energies and intensities agreed well with experimental data, allowing assignment of the configuration around the metal center.

The CD spectra of chiral oxovanadium(IV) phthalocyanines (OVPhTs) were calculated with TDDFT [337]. The starting point for geometry optimizations was the experimentally measured crystal structure of a Ni-phthalocyanine alkoxy system. The first 60 transitions for the CD spectrum were calculated using B3LYP/6-31G(d). The most intense bands of the simulated CD spectrum, including the Q-band, were in agreement with experiment. The authors indicated that these observations were pointing towards an assignment of the system as the right handed isomer. The analogous silicon phthalocyanine was studied as well. Calculations on this system showed that a lack of Q bands for this system was due to the cancellation of these bands among the two lowest-energy conformers [337].

Often, TDDFT studies are targeted at closed-shell systems. However, many metal complexes are paramagnetic, and the open d - or f -shells may pose additional challenges for TDDFT spectral computations. Fan et al. [338] have studied the CD of high-spin trigonal dihedral chromium complexes, and developed a spin-unrestricted TDDFT method for the computations of the CD spectra. When possible, an analogous closed-shell cobalt(III) complex was calculated as well for comparison.

The BP86 functional was used for the response calculations, along with the COSMO solvation model for water and a triple-zeta polarized Slater-type basis set. The authors noted the full use of symmetry, resulting in the fact that only symmetry-allowed transitions of the D_3 complexes had to be computed. For some of the ligands, the spectral trends were similar between Co and Cr, as with $[M(\text{thiox})_3]^{3-}$. This was not the case for other ligands, such as the tris bidentate acac and ox complexes. The ligand field splitting is larger for chromium(III) complexes than for cobalt(III) due to the larger overlap of more diffuse d -orbitals with the ligands for Cr(III). A consequence of this is a blue-shift of $d-d$ and ligand-to-metal-charge-transfer excitations for Cr(III) with respect to Co(III). TDDFT computations of the CD of open-shell metal complexes have also been performed on $[\text{Co}^{\text{II}}(\text{bipy})_3]^{2+}$ [339] and on spin-triplet bis(biuretato) Co^{III} complexes [340].

Tunable chiroptical properties of helicene derivatives containing metal centers have been investigated [260, 261, 341]. Through what was noted as a straightforward synthesis, platinum helicene complexes as well as iridium bis(helicene) complexes have been prepared and their crystal structure determined [261]. The Pt-helicenes were investigated computationally, with structures optimized at the RI-BP86/SV(P) level of theory and spectra computations using BHLYP/SV(P). Experimentally, an absorption band is present in the UV-Vis spectrum around 430 nm that has no corresponding band of noticeable intensity in the CD spectrum. These spectral features were reproduced by the TDDFT computations. The computed UV-Vis spectrum matched well with experiment after a modest red-shift of 0.25 eV, as did the calculated ECD spectrum. See Fig. 37 for a comparison of the CD spectra. Regarding the optical rotation at the sodium D line, the experimental specific rotation was measured as $1,300 \text{ deg mL g}^{-1} \text{ dm}^{-1}$, corresponding to $[\phi] = 8,170 \text{ deg cm}^2 \text{ dmol}^{-1}$ when measured in dichloromethane. The computed gas phase molar rotation, $[\phi]$, was $10.3 \cdot 10^3 \text{ deg cm}^2 \text{ dmol}^{-1}$. For reference, the molar rotation of pristine hexahelicene has been measured to be 11,950 [99] and calculated as $12.0 \cdot 10^3 \text{ deg mL g}^{-1} \text{ dm}^{-1}$ (BHLYP/SV(P)//RI-BP86/TZVP). Inter alia, the calculations for the platinahelicenes revealed significant participation of the metal (in particular Pt $5d$ orbitals) in the excitations in the UV-Vis spectral range. This information helped to rationalize the interesting photophysics of the metallahelicenes. While the organic ligands showed intense fluorescence at room temperature, accompanied by phosphorescence when kept in a glass matrix at low temperature, the metallahelicenes displayed only phosphorescence.

A communication by Graule et al. [341] reported preliminary work on the investigation of the impact on chiral properties by metal variation in metal-bis(helicene) assemblies which incorporated a π conjugated phosphole moiety into a helicene ligand structure (see Fig. 38) which subsequently served as a bidentate ligand of Pd and Cu. At the RI-BP86/SV(P) level of theory, geometry optimizations for the lowest energy conformer of the phosphole-helicene ligand yielded good agreement with X-ray crystal structure parameters. For an optimized Pd-bis(phosphole-helicene) complex the ECD spectrum was calculated at the BHLYP/SV(P) level of theory and compared to experiment. A chemical formula for the Pd complex, as well as the lowest energy conformer of the ligand, are shown in

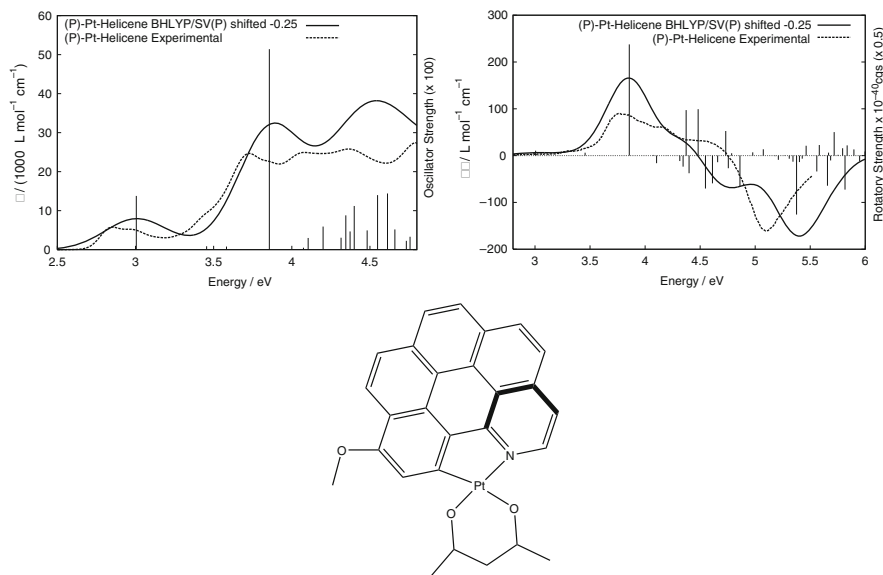


Fig. 37 Calculated and experimental electronic spectra for (P)-Pt-helicene. *Top right:* Experimental and computed ECD. *Top left:* The Experimental and computed UV-Vis spectra. *Bottom:* Structural formula of the Pt-helicene complex. Data to prepare the spectra were taken from [261]

Fig. 38. The agreement between simulated and experimental CD spectra for the Pd complex was very good after a red-shift of 0.25 eV was applied to the excitation energies. Analysis of the computed spectrum showed the intense bands to originate predominately from π -to- π^* transitions within an extended π framework of the phosphole-helicene ligands. Unlike initially expected, the various bands in the CD spectrum cannot be assigned to transitions centered separately on the helicene and phosphole moieties, respectively. The experimentally measured molar rotation of the Pd complex was $23.1 \cdot 10^3 \text{ deg cm}^2 \text{ dmol}^{-1} \pm 2\%$ in dichloromethane. For an analogous Cu complex it was $13.1 \cdot 10^3 \pm 2\%$, a staggering $10^4 \text{ deg cm}^2 \text{ dmol}^{-1}$ lower.

In [260], Graule et al. investigated the reasons for the drastic difference in magnitude for the optical rotation (and ECD intensities) between the Pd and Cu complexes. It turned out that, although the metals hardly participate in the excitations, the nature of the metal dictates the conformation of the ligand in the complexes, and the relative orientations of various chromophore moieties to each other, which was shown to be the main reason for the very different chiroptical response of the Pd vs the Cu system. The most notable effect was when the phosphole phenyl groups were in close proximity to the helicene moiety, a geometry adopted in the Cu system, resulting in a significant drop in the calculated molar rotation along with a decrease in the UV-Vis ECD intensity. These trends aided in the assignment of the Cu bis-helicene complex as a Δ configuration around the metal center. The computed ORs were in good agreement with experiment. Despite the lower ECD intensity of the Cu complexes, a SOS analysis showed that the experimentally known portions of

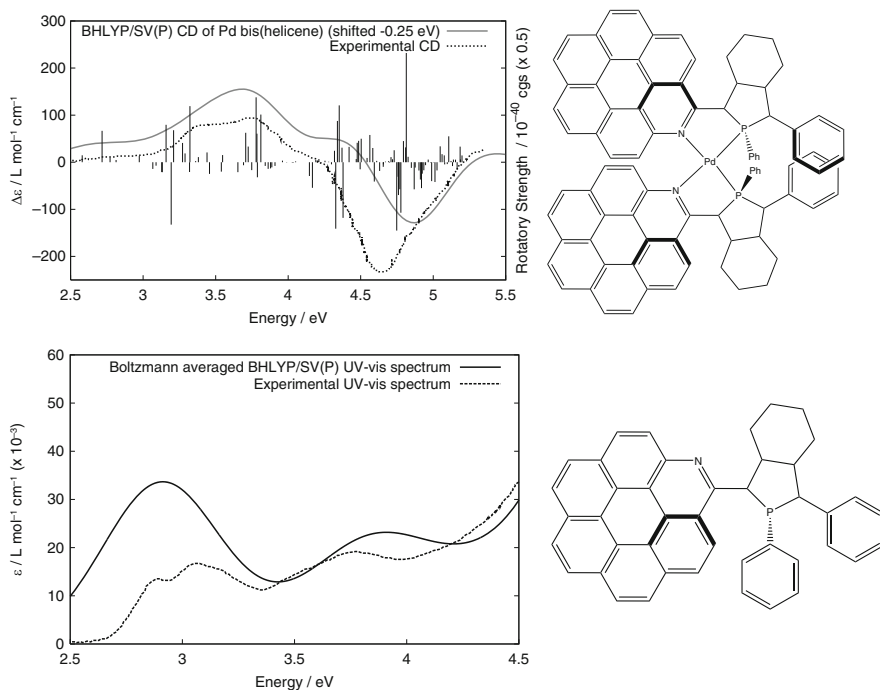


Fig. 38 *Top*: Structure of the Pd-bis(phosphole-helicene) complex and a comparison of the BHLYP/SV(P) computed and experimental CD spectra. *Bottom*: Two-dimensional structure of the phosphole-helicene ligand as well as the experimental UV-Vis vs the Boltzmann averaged spectrum computed at the BHLYP/SV(P) level of theory, red-shifted 0.25 eV. Data to prepare the plots were taken from [260]

the CD spectra did not cause most of the observed OR differences between the two complexes, but that higher lying excitations must be the main contributors.

9 Concluding Remarks

The large number of successful applications of TDDFT to compute ECD spectra and optical rotation demonstrate the maturity of the available methods and their general applicability. Vibrational averaging, the treatment of solvent effects, or the treatment of large conformational spaces remain challenges that require the continued development and careful benchmarking of computational models and protocols. Computing vibronic fine structure and band shapes for ECD spectra is not yet routinely carried out, but the available studies show high promise. The continued development of functionals for TDDFT remains as important as ever. Established (expected) deviations between theory and experiment derived

from numerous B3LYP benchmarks may soon be outdated. As computational methods continue to improve, the calculated chiroptical response will become more accurate and, as a consequence, AC assignments based on matching theoretical with measured ECD, OR, and ORD, assignments of ECD spectra, and investigations into the physical and chemical origin of sign and magnitude of the chiroptical response of a given molecule, will become more reliable.

Acknowledgements The authors acknowledge support of their research by the National Science Foundation (grant no. CHE-447321 and CHE-952253), and by the Center for Computational research (CCR) at the University at Buffalo. We thank Prof. I. Garzón for providing a figure from [299]. We also thank Prof. J. Neugebauer for providing the images in Fig. 26.

References

1. Barron LD (2004) *Molecular light scattering and optical activity*, 2nd edn. Cambridge University Press, Cambridge
2. Berova N, Nakanishi K, Woody RW (eds) (2000) *Circular dichroism. Principles and applications*. VCH, New York
3. Quack M (2002) *Angew Chem Int Ed* 41:4618
4. Zavattini E, Zavattini G, Ruoso G, Polacco E, Milotti E, Karuza M, Gastaldi U, Di Domenico G, Della Valle F, Cimino R, Carusotto S, Cantatore G, Bregant M (2006) *Phys Rev Lett* 96:110406
5. Pályi G, Zucchi C, Caglioti L (eds) (2004) *Progress in biological chirality*. Elsevier Science, Amsterdam
6. Vaccaro PH (2009) *Nature* 458:289
7. Rhee H, June YG, Lee JS, Lee KK, Ha JH, Kim ZH, Jeon SJ, Cho M (2009) *Nature* 458:310
8. Autschbach J (2010) *Chirality* 21:E116
9. (a) Crawford TD (2006) *Theor Chem Acc* 115:227; (b) Pecul M, Ruud K (2005) *Advances in quantum chemistry*, vol 50. Elsevier, San Diego, pp 185–212
10. Polavarapu PL (2007) *Chem Rec* 7:125
11. Polavarapu PL (2002) *Chirality* 14:768
12. Autschbach J (2009) Spectroscopic properties obtained from time-dependent density functional theory (TD-DFT). In: Wiley VCH (ed). *Encyclopedia of inorganic chemistry*, New York
13. Bringmann G, Bruhn T, Maksimenka K, Hemberger Y (2009) *Eur J Org Chem* 2009:2717
14. Berova N, Di Bari L, Pescitelli G (2007) *Chem Soc Rev* 36:914
15. Stephens PJ, Devlin FJ, Cheeseman JR, Frisch MJ, Bortolini O, Besse P (2003) *Chirality* 15: S57
16. Stephens PJ, McCann DM, Cheeseman JR, Frisch MJ (2005) *Chirality* 17:S52
17. Barron LD, Zhu FJ, Hecht L, Tranter GE, Isaacs NW (2007) *J Mol Struct* 834:7
18. Piepho SB, Schatz PN (1983) *Group theory in spectroscopy. With applications to magnetic circular dichroism*. Wiley, New York
19. Seth M, Krykunov M, Ziegler T, Autschbach J, Banerjee A (2008) *J Chem Phys* 128: 144105
20. Seth M, Krykunov M, Ziegler T, Autschbach J (2008) *J Chem Phys* 128:234102
21. Seth M, Ziegler T, Autschbach J (2008) *J Chem Phys* 129:104105
22. Pendry JB (2004) *Science* 306:1353

23. Tretyakov S, Nefedov I, Sihvola A, Maslovski S, Simovski C (2003) *J Electromagn Waves Appl* 17:695
24. *Chemistry and Engineering News* (2005) Dec. 12, 10
25. Parr RG, Yang W (1989) *Density functional theory of atoms and molecules*. Oxford University Press, New York
26. Ziegler T (1991) *Chem Rev* 91:651
27. Gross EKV, Dobson JF, Petersilka M (1996) *Top Curr Chem* 181:81
28. Dobson JF, Vignale G, Das MP (eds) (1998) *Electronic density functional theory. Recent progress and new directions*. Plenum, New York
29. Elliott P, Burke K, Furche F (2009) In: Lipkowitz KB, Cundari TR (eds) *Reviews of computational chemistry*. Wiley, Hoboken, NJ
30. Ziegler T, Autschbach J (2005) *Chem Rev* 105:2695
31. Condon EU (1937) *Rev Mod Phys* 9:432
32. Kauzmann W (1957) *Quantum chemistry*. Academic Press, New York
33. Yabana K, Bertsch GF (1999) *Phys Rev A* 60:1271
34. Moscowitz A (1962) *Adv Chem Phys* 4:67
35. Schellman JA (1975) *Chem Rev* 75:323
36. Krykunov M, Kundrat MD, Autschbach J (2006) *J Chem Phys* 125:194110
37. Rudolph M, Autschbach J (2008) *Chirality* 20:995
38. Casida ME (1995) In: Chong DP (ed) *Recent advances in density functional methods*, vol. 1. World Scientific, Singapore, pp 155–192
39. Bauernschmitt R, Ahlrichs R (1996) *Chem Phys Lett* 256:454
40. van Gisbergen SJA, Snijders JG, Baerends EJ (1999) *Comp Phys Commun* 118:119
41. van Gisbergen SJA, Snijders JG, Baerends EJ (1995) *J Chem Phys* 103:9347
42. Autschbach J, Ziegler T (2002) *J Chem Phys* 116:891
43. Autschbach J (2007) *Comp Lett* 3:131
44. Thorvaldsen AJ, Ruud K, Rizzo A, Coriani S (2008) *J Chem Phys* 129:164110
45. Autschbach J (2009) *ChemPhysChem* 10:1
46. Autschbach J, Seth M, Ziegler T (2007) *J Chem Phys* 126:174103
47. Autschbach J, Ziegler T, Patchkovskii S, van Gisbergen SJA, Baerends EJ (2002) *J Chem Phys* 117:581
48. Stratmann RE, Scuseria GE, Frisch MJ (1998) *J Chem Phys* 109:8218
49. Hirata S, Head-Gordon M, Bartlett RJ (1999) *J Chem Phys* 111:10774
50. Autschbach J (2007) In: Maroulis G, Simos TE (eds) *Computational methods in science and engineering, theory and computation: Old problems and new challenges*, Conference Proceedings 963, vol. 1. American Institute of Physics, New York, pp 138–167
51. McWeeny R (1992) *Methods of molecular quantum mechanics*, 2nd edn. Academic Press, London
52. Bak KD, Hansen AE, Ruud K, Helgaker T, Olsen J, Jørgensen P (1995) *Theor Chim Acta* 90:441
53. Cheeseman JR, Frisch MJ, Devlin FJ, Stephens PJ (2000) *J Phys Chem A* 104:1039
54. Krykunov M, Autschbach J (2005) *J Chem Phys* 123:114103
55. Hansen AE, Bouman TD (1980) *Adv Chem Phys* 44:545
56. Pedersen TB, Koch H, Boman L, Sánchez de Merás AMJ (2004) *Chem Phys Lett* 393:319
57. Caldwell DJ, Eyring H (1971) *The theory of optical activity*. Wiley-Interscience, New York
58. Raab RE, De Lange OL (2005) *Multipole theory in electromagnetism*. Oxford University Press, Oxford
59. Buckingham AD, Dunn MB (1971) *J Chem Soc Appl* 1988–1991
60. Pedersen TB, Hansen AE (1995) *Chem Phys Lett* 246:1
61. Hansen AE, Bak KL (2000) *J Phys Chem A* 104:11362
62. Pedersen TB, Koch H, Ruud K (1999) *J Chem Phys* 110:2883
63. Kongsted J, Pedersen TB, Osted A, Hansen AE, Mikkelsen KV (2004) *J Phys Chem A* 108:3632

64. Kongsted J, Hansen AE, Pedersen TB, Osted A, Mikkelsen KV, Christiansen O (2004) *Chem Phys Lett* 391:259
65. Krykunov M, Autschbach J (2006) *J Chem Phys* 125:034102
66. Moxon JRL, Renshaw AR (1990) *J Phys Condens Matter* 2:6807
67. Moxon JRL, Renshaw AR, Tebbutt IJ (1991) *J Phys D Appl Phys* 24:1187
68. Kaminsky W, Glazer AM (1996) *Ferroelectrics* 183:133
69. Claborn K, Isborn C, Kaminsky W, Kahr B (2008) *Angew Chem Int Ed* 47:5706
70. Kuball HG, Acimis M, Altschuh J (1979) *J Am Chem Soc* 101:20
71. Kuball HG, Höfer T (2000) In: Berova N, Nakanishi K, Woody RW (eds) *Circular dichroism: principles and applications*, chap 5. VCH, New York, pp 133–158
72. Kuball HG (2002) *Enantiomer* 7:197
73. Claborn K, Herreros Cedres J, Isborn C, Zozulya A, Weckert E, Kaminsky W, Kahr B (2006) *J Am Chem Soc* 128:14746
74. Norman P, Bishop DM, Jensen HJA, Oddershede J (2005) *J Chem Phys* 123:194103
75. Autschbach J, Jensen L, Schatz GC, Tse YCE, Krykunov M (2006) *J Phys Chem A* 110:2461
76. Jensen L, Autschbach J, Schatz GC (2005) *J Chem Phys* 122:224115
77. Norman P (2007) *Computational methods in science and engineering, theory and computation: Old problems and new challenges*. In: Maroulis G, Simos TE (eds) *Conference Proceedings* 963, vol. 1. American Institute of Physics, Washington DC, pp 176
78. Barron LD (2007) *Nature* 446:505
79. Bell AF, Hecht L, Barron LD (1998) *J Am Chem Soc* 120:5820
80. Haesler J, Schindelholz I, Riguet E, Bochet CG, Hug W (2007) *Nature* 446:526
81. Ruud K, Helgaker T, Bour P (2002) *J Phys Chem A* 106:7448
82. Polavarapu P (2002) *Angew Chem Int Ed* 41:4544
83. Reiher M, Liegeois V, Ruud K (2005) *J Phys Chem A* 109:7567
84. Jensen L, Autschbach J, Krykunov M, Schatz GC (2007) *J Chem Phys* 127:134101
85. Amos RD (1987) *Adv Chem Phys* 67:99
86. Nafie LA (1996) *Chem Phys* 205:309
87. Vargak M, Freedman TB, Lee E, Nafie LA (1998) *Chem Phys Lett* 287:359
88. Krykunov M, Autschbach J (2007) *J Chem Phys* 126:024101
89. Krykunov M, Banerjee A, Ziegler T, Autschbach J (2005) *J Chem Phys* 122:074105
90. Ruud K, Helgaker T (1997) *Chem Phys Lett* 264:17
91. Carnell M, Peyerimhoff SD, Breest A, Gödderz KH, Ochmann P, Hormes J (1991) *Chem Phys Lett* 180:477
92. Furche F, Ahlrichs R, Wachsmann C, Weber E, Sobanski A, Vögtle F, Grimme S (2000) *J Am Chem Soc* 122:1717
93. Gross EKV, Burke K (2006) In: Marques MAL, Ullrich CA, Nogueira F, Rubio A, Burke K, Gross EKV (eds) *Time-dependent density functional theory*, vol 706, *Lecture Notes in Physics*. Springer, Berlin, pp 1–16
94. Tawada Y, Tsuneda T, Yanagisawa S, Yanai T, Hirao K (2004) *J Chem Phys* 120:8425
95. Yanai T, Tew DP, Handy NC (2004) *Chem Phys Lett* 393:51
96. Livshits E, Baer R (2007) *Phys Chem Chem Phys* 9:2932
97. Goerigk L, Grimme S (2009) *J Phys Chem A* 113:767
98. Stephens PJ, Devlin FJ, Cheeseman JR, Frisch MJ (2001) *J Phys Chem A* 105:5356
99. Grimme S (2001) *Chem Phys Lett* 339:380
100. Ruud K, Helgaker T (2002) *Chem Phys Lett* 352:533
101. Autschbach J, Ziegler T, van Gisbergen SJA, Baerends EJ (2002) *J Chem Phys* 116:6930
102. Autschbach J, Jorge FE, Ziegler T (2003) *Inorg Chem* 42:2867
103. Diedrich C, Grimme S (2003) *J Phys Chem A* 107:2524
104. Hansen AE, Voigt B, Rettrup S (1983) *Int J Quantum Chem* 23:595
105. Amos RD (1982) *Chem Phys Lett* 87:23
106. Amos RD, Rice JE (1989) *Comp Phys Rep* 10:147
107. Kondru RK, Wipf P, Beratan DN (1998) *Science* 282:2247

108. Kondru RK, Wipf P, Beratan DN (1998) *J Am Chem Soc* 120:2204
109. Polavarapu PL (1990) *J Phys Chem* 94:8106
110. Polavarapu PL, Hecht L, Barron LD (1993) *J Phys Chem* 97:1793
111. Helgaker T, Ruud K, Bak KL, Jørgensen P, Olsen J (1994) *Faraday Discuss* 99:165
112. Muller T, Wiberg KB, Vaccaro PH (2000) *J Phys Chem A* 104:5959
113. Breest A, Ochmann P, Pulm F, Goedderz KH, Carnell M, Hormes J (1994) *Mol Phys* 82:539
114. Pulm F, Schramm J, Hormes J, Grimme S, Peyerimhoff S (1997) *Chem Phys* 224:143
115. Wilson SM, Wiberg KB, Cheeseman JR, Frisch MJ, Vaccaro PH (2005) *J Phys Chem A* 109:11752
116. Shcherbin D, Ruud K (2008) *Chem Phys* 349:234
117. Peach MJG, Cohen AJ, Tozer DJ (2006) *Phys Chem Chem Phys* 8:4543
118. Ruud K, Stephens PJ, Devlin FJ, Taylor PR, Cheeseman JR, Frisch MJ (2003) *Chem Phys Lett* 373:606
119. Song J, Hirokawa T, Tsuneda T, Hirao K (2007) *J Chem Phys* 126:154105
120. Fromager E, Toulouse J, Jensen HJA (2007) *J Chem Phys* 126:074111
121. Kowalczyk TD, Abrams ML, Crawford TD (2006) *J Phys Chem A* 110:7649
122. Jacquemin D, Perpète EA, Scuseria GE, Ciofini I, Adamo C (2008) *J Chem Theory Comput* 4:123
123. Calitree B, Donnelly DJ, Holt JJ, Gannon MK, Nygren CL, Autschbach J, Detty MR (2007) *Organometallics* 26:6248
124. Crawford TD, Stephens PJ (2008) *J Phys Chem A* 112:1339
125. Mort BC, Autschbach J (2007) *Chem Phys Chem* 8:605
126. Baranowska A, Laczkowski K, Sadlej A (2009) *J Comput Chem* 31:1176
127. Baranowska A, Sadlej A (2010) *J Comput Chem* 31:552
128. Giorgio E, Viglione RG, Zanasi R, Rosini C (2004) *J Am Chem Soc* 126:12968
129. Moore WR, Anderson HW, Clark SD, Ozretich TM (1971) *J Am Chem Soc* 93:4932
130. Poater J, van Lenthe E, Baerends EJ (2003) *J Chem Phys* 118:8584
131. Le Guennic B, Hieringer W, Görling A, Autschbach J (2005) *J Phys Chem A* 109:4836
132. Ahrenkiel RK (1971) *J Opt Soc Am* 61:1651
133. Crawford TD, Owens LS, Tam MC, Schreiner PR, Koch H (2005) *J Am Chem Soc* 127:1368
134. Stephens PJ, Harada N (2010) *Chirality* 22:229
135. Wiberg KB, Wang YG, Wilson SM, Vaccaro PH, Jørgensen WL, Crawford TD, Abrams ML, Cheeseman JR, Luderer M (2008) *J Phys Chem A* 112:2415
136. Kundrat MD, Autschbach J (2008) *J Am Chem Soc* 130:4404
137. Wiberg KB, Wang YG, Wilson SM, Vaccaro PH, Cheeseman JR (2006) *J Phys Chem A* 110:13995
138. Crawford TD, Tam MC, Abrams ML (2007) *Mol Phys* 105:2607
139. Wiberg KB, Wilson SM, Wang YG, Vaccaro PH, Cheeseman JR, Luderer MR (2007) *J Org Chem* 72:6206
140. Polavarapu PL, Petrovic A, Wang F (2003) *Chirality* 15:S143
141. Tam MC, Crawford TD (2006) *J Phys Chem A* 110:2290
142. Crawford TD, Tam MC, Abrams ML (2007) *J Phys Chem A* 111:12057
143. Ruud K, Åstrand PO, Taylor PR (2001) *J Am Chem Soc* 123:4826
144. Giorgio E, Rosini C, Viglione RG, Zanasi R (2003) *Chem Phys Lett* 376:452
145. Tam MC, Russ NJ, Crawford TD (2004) *J Chem Phys* 121:3550
146. Kongsted J, Pedersen TB, Strange M, Osted A, Hansen AE, Mikkelsen KV, Pawłowski F, Jørgensen P, Hättig C (2005) *Chem Phys Lett* 401:385
147. Ruud K, Zanasi R (2005) *Angew Chem Int Ed* 44:3594
148. Mort BC, Autschbach J (2005) *J Phys Chem A* 109:8617
149. Mort BC, Autschbach J (2008) *Chem Phys Chem* 9:159

150. Kongsted J, Pedersen TB, Jensen L, Hansen AE, Mikkelsen KV (2006) *J Am Chem Soc* 128:976
151. Mukhopadhyay P, Zuber G, Goldsmith M, Wipf P, Beratan DN (2006) *ChemPhysChem* 7:2483
152. Goerigk L, Moellmann J, Grimme S (2009) *Phys Chem Chem Phys* 11:4611
153. Kapitan J, Johannessen C, Bour P, Hecht L, Barron L (2009) *Chirality* 21:E4
154. Zuber G, Hug W (2004) *J Phys Chem A* 108:2108
155. Kundrat MD, Autschbach J (2009) *J Chem Theory Comput* 5:1051
156. Mukhopadhyay P, Zuber G, Wipf P, Beratan DN (2007) *Angew Chem Int Ed* 46:6450
157. Mazzeo G, Giorgio E, Rosini C, Fabris F, Fregonese E, Toniolo U, Lucchi OD (2009) *Chirality* 21:E86
158. Tartaglia S, Padula D, Scafato P, Chiummiento L, Rosini C (2008) *J Org Chem* 73:4865
159. Mukhopadhyay P, Wipf P, Beratan DN (2009) *Acc Chem Res* 42:809A–819A
160. Widjaja T, Fitjer L, Pal A, Schmidt HG, Noltemeyer M, Diedrich C, Grimme S (2007) *J Org Chem* 72:9264
161. Stephens PJ, Pan JJ, Devlin FJ, Cheeseman JR (2008) *J Nat Prod* 71:285
162. Kundrat MD, Autschbach J (2008) *J Chem Theory Comput* 4:1902
163. Kundrat MD, Autschbach J (2006) *J Phys Chem A* 110:12908
164. Kundrat MD, Autschbach J (2006) *J Phys Chem A* 110:4115
165. Pecul M, Ruud K, Rizzo A, Helgaker T (2004) *J Phys Chem A* 108:4269
166. Cheng M, Li Q, Lin B, Sha Y, Ren J, He Y, Wang Q, Hua H, Ruud K (2006) *Tetrahedron Asymmetry* 17:179
167. Petrovic AG, Polavarapu PL, Drabowicz J, Lyzwa P, Mikołajczyk M, Wieczorek W, Balińska A (2008) *J Org Chem* 73:3120
168. Wiberg KB, Vaccaro PH, Cheeseman JR (2003) *J Am Chem Soc* 125:1888
169. Polavarapu PL, Chakraborty DK, Ruud K (2000) *Chem Phys Lett* 319:595
170. Nitsch-Velasquez L, Autschbach J (in press) *Chirality*. DOI 10.1002/chir.20863
171. Wiberg KB, Wang YG, Vaccaro PH, Cheeseman JR, Trucks G, Frisch MJ (2004) *J Phys Chem A* 108:32
172. Wiberg KB, Wang Y, Vaccaro PH, Cheeseman JR, Luderer MR (2005) *J Phys Chem A* 109:3405
173. Grimme S, Mück-Lichtenfeld C (2008) *Chirality* 20:1009
174. Mennucci B, Tomasi J, Cammi R, Cheeseman JR, Frisch MJ, Devlin FJ, Gabriel S, Stephens PJ (2002) *J Phys Chem A* 106:6102
175. Pecul M, Marchesan D, Ruud K, Coriani S (2005) *J Chem Phys* 122:024106
176. Polavarapu PL (2006) *Chirality* 18:348
177. Kongsted J, Ruud K (2008) *Chem Phys Lett* 451:226
178. Pedersen TB, Kongsted J, Crawford TD (2009) *Chirality* 21:E68
179. Mort BC, Autschbach J (2006) *J Phys Chem A* 110:11381
180. Mukhopadhyay P, Zuber G, Goldsmith MR, Wipf P, Beratan DN (2006) *ChemPhysChem* 7:2483
181. Neugebauer J (2007) *Angew Chem Int Ed* 46:7738
182. Grimme S (2004) Calculation of the electronic spectra of large molecules. In: Lipkowitz KB, Larter R, Cundari TR (eds). *Reviews in computational chemistry*, vol 20. Wiley, Hoboken, pp 153–218
183. Neugebauer J, Baerends EJ, Nooijen M, Autschbach J (2005) *J Chem Phys* 122:234305
184. Nooijen M (2006) *Int J Quantum Chem* 106:2489
185. Santoro F, Improta R, Lami A, Bloino J, Barone V (2007) *J Chem Phys* 126:084509
186. Santoro F, Lami A, Improta R, Bloino J, Barone V (2008) *J Chem Phys* 128:224311
187. Lin N, Santoro F, Zhao X, Rizzo A, Barone V (2008) *J Phys Chem A* 112:12401
188. Pritchard B, Autschbach J (2010) *Chem Phys Chem* vol 11, pp 2409–2415
189. Petrovic AG, Polavarapu PL, Drabowicz J, Zhang Y, McConnell OJ, Duddeck H (2005) *Chem Eur J* 11:4257

190. Zuber G, Goldsmith MR, Beratan DN, Wipf P (2005) *Chirality* 17:507
191. Coriani S, Forzato C, Furlan G, Nitti P, Pitacco G, Ringholm M, Ruud K (2009) *Tetrahedron Asymmetr* 20:1459
192. Coriani S, Baranowska A, Ferrighi L, Forzato C, Marchesan D, Nitti P, Pitacco G, Rizzo A, Ruud K (2006) *Chirality* 18:357
193. Stephens PJ, Devlin FJ, Cheeseman JR, Frisch MJ, Rosini C (2002) *Org Lett* 4:4595
194. (a) Stephens PJ, McCann DM, Butkus E, Stoncius E, Cheeseman JR, Frisch MJ (2004) *J Org Chem* 69:1948; (b) Stephens PJ, McCann DM, Devlin FJ, Cheeseman JR, Frisch MJ (2004) *J Am Chem Soc* 126:7514
195. Ren J, Jiang J, Li L, Liao T, Tian R, Chen XL, Jiang S, Pittman CU, Zhu H (2009) *Eur J Org Chem* 2009:3987
196. Giorgio E, Roje M, Tanaka K, Hamersak Z, Sunjic V, Nakanishi K, Rosini C, Berova N (2005) *J Org Chem* 70:6557
197. Polavarapu PL, He J, Crassous J, Ruud K (2005) *ChemPhysChem* 6:2535
198. Petrovic AG, He J, Polavarapu PL, Xiao LS, Armstrong DW (2005) *Org Biomol Chem* 3:1977
199. Bringmann G, Maksimenka K, Bruhn T, Reichert M, Harada T, Kuroda R (2009) *Tetrahedron* 65:5720
200. Zhang W, Krohn K, Flörke U, Pescitelli G, Di Bari L, Antus S, Kurtán T, Rheinheimer J, Draeger S, Schulz B (2008) *Chem Eur J* 14:4913
201. Hussain H, Krohn K, Floerke U, Schulz B, Draeger S, Pescitelli G, Antus S, Kurtán T (2007) *Eur J Org Chem* 2007:292
202. Hassan Z, Hussain H, Ahmad VU, Anjum S, Pescitelli G, Kurtán T, Krohn K (2007) *Tetrahedron Asymmetr* 18:2905
203. Hussain H, Krohn K, Flörke U, Schulz B, Draeger S, Pescitelli G, Salvadori P, Antus S, Kurtán T (2007) *Tetrahedron Asymmetr* 18:925
204. Dai J, Krohn K, Elsässer B, Flörke U, Draeger S, Schulz B, Pescitelli G, Salvadori P, Antus S, Kurtán T (2007) *Eur J Org Chem* 2007:4845
205. Krohn K, Kock I, Elsässer B, Flörke U, Schulz B, Draeger S, Pescitelli G, Antus S, Kurtán T (2007) *Eur J Org Chem* 2007:1123
206. Krohn K, Farooq U, Flörke U, Schulz B, Draeger S, Pescitelli G, Salvadori P, Antus S, Kurtán T (2007) *Eur J Org Chem* 2007:3206
207. Krohn K, Hussain H, Flörke U, Schulz B, Draeger S, Pescitelli G, Salvadori P, Antus S, Kurtán T (2007) *Chirality* 19:464
208. Krohn K, Kouam SF, Kuigoua GM, Hussain H, Cludius-Brandt S, Flörke U, Kurtán T, Pescitelli G, Di Bari L, Draeger S, Schulz B (2009) *Chem Eur J* 15:12121
209. Zhang W, Krohn K, Ding J, Miao ZH, Zhou XH, Chen SH, Pescitelli G, Salvadori P, Kurtan T, Guo YW (2008) *J Nat Prod* 71:961
210. Qin S, Krohn K, Flörke U, Schulz B, Draeger S, Pescitelli G, Salvadori P, Antus S, Kurtán T (2009) *Eur J Org Chem* 2009:3279
211. Alonso-Gómez JL, Petrovic AG, Harada N, Rivera-Fuentes P, Berova N, Diederich F (2009) *Chem Eur J* 15:8396
212. Guo YW, Kurtán T, Krohn K, Pescitelli G, Zhang W (2009) *Chirality* 21:561
213. Zuber G, Goldsmith MR, Hopkins TD, Beratan DN, Wipf P (2005) *Org Lett* 7:5269
214. Mori T, Inoue Y, Grimme S (2007) *J Phys Chem A* 111:4222
215. Crassous J, Jiang Z, Schurig V, Polavarapu P (2004) *Tetrahedron Asymmetr* 15:1995
216. Costante J, Hecht L, Polavarapu PL, Collet A, Barron LD (1997) *Angew Chem Int Ed* 36:885
217. Masullo M, Bassarello C, Bifulco G, Piacente S (2010) *Tetrahedron* 66:139
218. McConnell O, II AB, Balibar C, Byrne N, Cai Y, Carter G, Chlenov M, Di L, Fan K, Goljer I, He Y, Herold D, Kagan M, Kerns E, Koehn F, Kraml C, Marathias V, Marquez B, McDonald L, Nogle L, Petucci C, Schlingmann G, Tawa G, Tischler M, Williamson RT, Sutherland A, Watts W, Young M, Zhang M, Zhang Y, Zhou D, Ho D (2007) *Chirality* 19:658

219. Bringmann G, Gulder TA, Reichert M, Gulder T (2008) *Chirality* 20:628
220. Ding S, Kolbanovskiy A, Durandin A, Crean C, Shafirovich V, Broyde S, Geacintov NE (2009) *Chirality* 21:S231
221. Durandin A, Jia L, Crean C, Kolbanovskiy A, Ding S, Shafirovich V, Broyde S, Geacintov NE (2006) *Chem Res Toxicol* 19:908
222. Castro A, Marques MA, Varsano D, Sottile F, Rubio A (2009) *C R Phys* 10:469
223. Balaz M, Steinkruger JD, Ellestad GA, Berova N (2005) *Org Lett* 7:5613
224. Balaz M, De Napoli M, Holmes AE, Mammana A, Nakanishi K, Berova N, Purrello R (2005) *Angew Chem Int Ed Engl* 44:4006
225. Balaz M, Li BC, Steinkruger JD, Ellestad GA, Nakanishi K, Berova N (2006) *Org Biomol Chem* 4:1865
226. Balaz M, Li BC, Jockusch S, Ellestad GA, Berova N (2006) *Angew Chem Int Ed Engl* 45:3530
227. Di Bari L, Guillarme S, Hermitage S, Jay DA, Pescitelli G, Whiting A (2005) *Chirality* 17:323
228. Di Bari L, Pescitelli G, Salvadori P, Rovini M, Anzini M, Cappelli A, Vomero S (2006) *Tetrahedron Asymmetr* 17:3430
229. Braun M, Hohmann A, Rahematpura J, Bühne C, Grimme S (2004) *Chem Eur J* 10:4584
230. Schlingmann G, Taniguchi T, He H, Bigelis R, Yang HY, Koehn FE, Carter GT, Berova N (2007) *J Nat Prod* 70:1180
231. Hussain H, Akhtar N, Draeger S, Schulz B, Pescitelli G, Salvadori P, Antus S, Kurtán T, Krohn K (2009) *Eur J Org Chem* 2009:749
232. Stephens PJ, Pan J, Devlin FJ, Urbanova M, Julinek O, Hajicek J (2008) *Chirality* 20:454
233. Bodensieck A, Fabian WM, Kunert O, Belaj F, Jahangir S, Schuehly W, Bauer R (2010) *Chirality* 22:308
234. Kwit M, Gawronski J, Sbircea L, Sharma ND, Kaik M, Boyd DR (2009) *Chirality* 21:S37
235. Schuehly W, Crockett SL, Fabian WM (2005) *Chirality* 17:250
236. Petrovic AG, Vick SE, Polavarapu PL (2008) *Chirality* 20:501
237. Seibert SF, Koenig GM, Voloshina E, Raabe G, Fleischhauer J (2006) *Chirality* 18:413
238. Tanaka T, Oelgemoeller M, Fukui K, Aoki F, Mori T, Ohno T, Inoue Y (2007) *Chirality* 19:415
239. Abbate S, Longhi G, Castiglioni E, Lebon F, Wood PM, Woo LWL, Potter BVL (2009) *Chirality* 21:802
240. Brehm L, Greenwood JR, Slok FA, Holm MM, Nielsen B, Geneser U, Stensbol TB, Braeuner-Osborne H, Begtrup M, Egebjerg J, Krogsgaard-Larsen P (2004) *Chirality* 16:452
241. Atodiresei I, Zoellinger M, Lindel T, Fleischhauer J, Raabe G (2007) *Chirality* 19:542
242. Bas D, Buergi T, Lacour J, Vachon J, Weber J (2005) *Chirality* 17:S143
243. Wang Y, Raabe G, Regges C, Fleischhauer J (2003) *Int J Quantum Chem* 93:265
244. Humam M, Christen P, Munoz O, Hostettmann K, Jeannerat D (2008) *Chirality* 20:20
245. Chmielewski M, Cierpucha M, Kowalska P, Kwit M, Frelek J (2008) *Chirality* 20:621
246. Matsumoto K, Inagaki T, Nehira T, Kannami M, Inokuchi D, Kurata H, Kawase T, Pescitelli G, Oda M (2007) *Chemistry* 2:1031
247. Saito H, Mori T, Origane Y, Wada T, Inoue Y (2008) *Chirality* 20:278
248. Kwit M, Sharma ND, Boyd DR, Gawronski J (2007) *Chem Eur J* 13:5812
249. Sallam MAE (2006) *Chirality* 18:790
250. Pham-Tuan H, Larsson C, Hoffmann F, Bergman A, Froeba M, Huehnerfuss H (2005) *Chirality* 17:266
251. Kwit M, Skowronek P, Kolbon H, Gawronski J (2005) *Chirality* 17:S93
252. Chochrek P, Frelek J, Kwit M, Wicha J (2009) *J Org Chem* 74:7300
253. Frelek J, Kowalska P, Masnyk M, Kazimierski A, Korda A, Woznica M, Chmielewski M, Furche F (2007) *Chem Eur J* 6:6732

254. Kock I, Draeger S, Schulz B, Elsässer B, Kurtán T, Kenéz Á, Antus S, Pescitelli G, Salvadori P, Speakman JB, Rheinheimer J, Krohn K (2009) *Eur J Org Chem* 2009:1427
255. Bringmann G, Reichert M, Hemberger Y (2008) *Tetrahedron* 64:515
256. Kwit M, Rozwadowska MD, Gawronski J, Grajewska A (2009) *J Org Chem* 74:8051
257. Muranaka A, Asano Y, Tsuda A, Osuka A, Kobayashi N (2006) *ChemPhysChem* 7:1235
258. Kondru RK, Wipf P, Beratan DN (1999) *J Phys Chem A* 103:6603
259. McLachlan AD, Ball MA (1964) *Rev Mod Phys* 36:844
260. Graule S, Rudolph M, Shen W, Williams JAG, Lescop C, Autschbach J, Crassous J, Reau R (2010) *Chem Eur J* 16:5976
261. Norel L, Rudolph M, Vanthuyne N, Williams JG, Lescop C, Roussel C, Autschbach J, Crassous J, Reau R (2010) *Angew Chem Int Ed* 49:99
262. Moscovitz A (1960) In: Djerassi C. *Optical rotatory dispersion*. McGraw-Hill, New York, pp 150–177
263. Moffitt W, Woodward RB, Moscovitz A, Klyne W, Djerassi C (1961) *J Am Chem Soc* 83:4013
264. Lightner DA (2000) In: Berova N, Nakanishi K, Woody R (eds) *Circular dichroism: principles and applications*, 2nd edn. Wiley, New York, pp 261–304
265. (a) Pescitelli G, Sreerama N, Salvadori P, Nakanishi K, Berova N, Woody RW (2008) *J Am Chem Soc* 130:6170; (b) Pescitelli G, di Bari L, Caporusso AM, Salvadori P (2008) *Chirality* 20:393
266. Neugebauer J (2007) *J Chem Phys* 126:134116
267. Polavarapu PL (2008) *Chirality* 20:664
268. Armstrong DW, Cotton FA, Petrovic AG, Polavarapu PL, Warnke MM (2007) *Inorg Chem* 46:1535
269. Giorgio E, Tanaka K, Verotta L, Nakanishi K, Berova N, Rosini C (2007) *Chirality* 19:434
270. Schreiner PR, Fokin AA, Reisenauer HP, Tkachenko BA, Vass E, Olmstead MM, Bläser D, Boese R, Dahl JEP, Carlson RMK (2009) *J Am Chem Soc* 131:11292
271. Taniguchi T, Martin CL, Monde K, Nakanishi K, Berova N, Overman LE (2009) *J Nat Prod* 72:430
272. Warnke I, Ay S, Bräse S, Furch F (2009) *J Phys Chem A* 113:6987
273. Zhang P, Polavarapu PL (2007) *J Phys Chem A* 111:858
274. Petrovic AG, Polavarapu PL (2007) *J Phys Chem A* 111:10938
275. Polavarapu PL, Jeirath N, Walia S (2009) *J Phys Chem A* 113:5423
276. Sauer SPA, Packer MJ (2000) In: Bunker PR, Jensen P (eds) *Computational molecular spectroscopy*. Wiley, London, pp 221–252
277. Ruud K, Åstrand PO, Taylor PR (2000) *J Chem Phys* 112:2668
278. Åstrand PO, Ruud K (2003) *Phys Chem Chem Phys* 5:5015
279. Mort BC, Autschbach J (2006) *J Am Chem Soc* 128:10060
280. Darling CL, Schlegel HB (1994) *J Phys Chem* 98:5855
281. Sadlej AJ (1988) *Collect Czech Chem Commun* 53:1995
282. Sadlej AJ (1991) *Theor Chim Acta* 79:123
283. Dunning TH Jr (1989) *J Chem Phys* 90:1007
284. Kendall RA, Dunning TH, Harrison RJ (1992) *J Chem Phys* 96:6796
285. Woon DE, Dunning TH (1994) *J Chem Phys* 100:2975
286. de Meijere A, Khlebnikov AF, Kozhushkov SI, Kostikov RR, Schreiner PR, Wittkopp A, Rinderspacher C, Menzel H, Yufit DS, Howard JAK (2002) *Chem Eur J* 8:828
287. Kurtán T, Pescitelli G, Salvadori P, Kenéz A, Antus S, Szilágyi L, Illyés TZ, Szabó I (2008) *Chirality* 20:379
288. Kessinger R, Crassous J, Herrmann A, Ruettimann M, Echegoyen L, Diederich F (1998) *Angew Chem Int Ed* 37:1919
289. Crassous J, Rivera J, Fender NS, Shu L, Echegoyen L, Thilgen C, Herrmann A, Diederich F (1999) *Angew Chem Int Ed* 38:11

290. Furche F, Ahlrichs R (2002) *J Am Chem Soc* 124:3804
291. Norman P, Ruud K, Helgaker T (2004) *J Chem Phys* 120:5027
292. Giorgio E, Tanaka K, Ding W, Krishnamurthy G, Pitts K, Ellestad GA, Rosini C, Berova N (2005) *Bioorg Med Chem* 13:5072
293. Cappelli C, Bronco S, Monti S (2005) *Chirality* 17:577
294. Wang S, Cann NM (2008) *J Chem Phys* 129:054507
295. Osipov MA, Pickup BT, Dunmur DA (1995) *Mol Phys* 84:1193
296. Clough G (1918) *J Chem Soc Trans* 113:526
297. Lutz O, Jirgensons B (1930) *Ber Dtsch Chem Ges B Abh* 448–460
298. Lutz O, Jirgensons B (1931) *Ber Dtsch Chem Ges B Abh* 64:1221
299. Sanchez-Castillo A, Noguez C, Garzón I (2010) *J Am Chem Soc* 132:1504
300. Gautier C, Bürgi T (2006) *J Am Chem Soc* 128:11079
301. Gautier C, Bürgi T (2008) *J Am Chem Soc* 130:7077
302. Garzón IL, Reyes-Nava JA, Rodríguez-Hernández JI, Sigal I, Beltrán M, Michaelian K (2002) *Phys Rev B* 66:073403
303. Román-Velázquez CE, Noguez C, Garzón IL (2003) *J Phys Chem B* 107:12035
304. Garzón IL, Beltrán MR, González G, Gutiérrez-González I, Michaelian K, Reyes-Nava JA, Rodríguez-Hernández JI (2003) *Eur Phys J D* 24:105
305. Goldsmith MR, George CB, Zuber G, Naaman R, Waldeck DH, Wipf P, Beratan DN (2006) *Phys Chem Chem Phys* 8:63
306. Provorse MR, Aikens CM (2010) *J Am Chem Soc* 132:1302
307. McCaffery AJ, Mason SF, Norman BJ (1969) *J Chem Soc A* 1428–1441
308. Mason SF, Norman BJ (1969) *J Chem Soc A* 1442–1447
309. Ballhausen CJ (1979) *Molecular electronic structures of transition metal complexes*. McGraw-Hill, London
310. Kuroda R, Saito Y (2000) In: Berova N, Nakanishi K, Woody RW (eds) *Circular dichroism: principles and applications*, 2nd edn. VCH, New York, pp 563–599
311. Douglas BE, Saito Y (eds) (1980) *Stereochemistry of optically active transition metal compounds*, ACS Symposium Series, vol 119. American Chemical Society, Washington
312. Ziegler M, von Zelewsky A (1998) *Coord Chem Rev* 177:257
313. Volosov A, Woody RW (1994) In: Nakanishi K, Berova N, Woody RW (eds) *Circular dichroism. Principles and Applications*. VCH, New York, pp 59–84
314. Mason SF (1968) *Inorg Chim Acta* 2:89
315. Mason SF, Seal RH (1976) *Mol Phys* 31:755
316. Schipper PE (1978) *J Am Chem Soc* 100(5):1433
317. Richardson FS, Faulkner TR (1982) *J Chem Phys* 76:1595
318. Saxe JD, Faulkner TR, Richardson FS (1982) *J Chem Phys* 76:1607
319. Strickland RW, Richardson FS (1973) *Inorg Chem* 12:1025
320. Evans RS, Schreiner AF, Hauser PJ (1974) *Inorg Chem* 13:2185
321. Král M (1979) *Theor Chim Acta* 50:355
322. Král M, Moscovitz A, Ballhausen CJ (1973) *Theor Chim Acta* 30:339
323. Rosa A, Ricciardi G, Gritsenko O, Baerends EJ (2004) Principles and applications of density functional theory. In: Kaltsoyannis N, McGrady JE (eds) *Inorganic chemistry I, Structure and bonding*, vol. 112. Springer, Heidelberg, pp 49–115
324. Le Guennic B, Hieringer W, Görling A, Autschbach J (2005) *J Phys Chem A* 109:4836
325. Pyykkö P (1988) *Chem Rev* 88:563
326. Autschbach J, Sikierski S, Schwerdtfeger P, Seth M, Schwarz WHE (2002) *J Comput Chem* 23:804
327. Jensen L, Swart M, van Duijnen PT, Autschbach J (2006) *Int J Quantum Chem* 106:2479
328. Jorge FE, Autschbach J, Ziegler T (2005) *J Am Chem Soc* 127:975
329. Jorge FE, Autschbach J, Ziegler T (2003) *Inorg Chem* 42:8902
330. Fan J, Ziegler T (2008) *Chirality* 20:938
331. Fan J, Ziegler T (2008) *Inorg Chem* 47:4762

332. Fan J, Autschbach J, Ziegler T (2010) *Inorg Chem* 49:1355A–1362A
333. Mason SF, Peart BJ (1973) *J Chem Soc Dalton Trans* 9:949
334. Mason SF, Peart BJ (1973) *J Chem Soc Dalton Trans* 9:944
335. Coughlin J, Westrol M, Oyler K, Byrne N, Kraml E, Zysman-Colman C, Lowry M, Bernhard S (2008) *Inorg Chem* 47:2039
336. Coughlin FJ, Oyler KD, Pascal J, Robert A, Bernhard S (2008) *Inorg Chem* 47:974
337. Kobayashi N, Narita F, Ishii K, Muranaka A (2009) *Chem Eur J* 15:10173
338. Fan J, Seth M, Autschbach J, Ziegler T (2008) *Inorg Chem* 47:11656
339. Vargas A, Zerara M, Krausz E, Hauser A, Lawson Daku LM (2006) *J Chem Theor Comput* 2:1342
340. Thulstrup PW, Larsen E (2006) *Dalton Trans* 14:1784
341. Graule S, Rudolph M, Vanthuyne N, Autschbach J, Roussel C, Crassous J, Reau R (2009) *J Am Chem Soc* 131:3183

Recent Theoretical and Experimental Advances in the Electronic Circular Dichroisms of Planar Chiral Cyclophanes

Tadashi Mori and Yoshihisa Inoue

Abstract The chiroptical properties, such as electronic and vibrational circular dichroism and optical rotation, of planar chiral cyclophanes have attracted much attention in recent years. Although the chemistry of cyclophanes has been extensively explored for more than 60 years, the studies on chiral cyclophanes are rather limited. Experimentally, the use of chiral stationary phases in HPLC becomes more popular and facilitates the enantiomer separation of chiral cyclophanes of interest. Almost all chiral cyclophanes can be readily separated, in analytical and preparative scales, most typically on a Daicel OD type column, which is based on cellulose tris(3,5-dimethylphenylcarbamate). The CD spectra of chiral cyclophanes are unique in their fairly large, significantly coupled Cotton effects observed in all the 1B_b , 1L_a , and 1L_b band regions. Theoretically, the time-dependent density functional theory, or TD-DFT, method becomes a cost-efficient, yet accurate, theoretical method to reproduce the electronic circular dichroisms and the absorption spectra of a variety of cyclophanes. The direct comparison of the experimental CD spectra with the theoretical ones readily leads to the unambiguous assignment of the absolute configuration of cyclophanes. In addition, the analysis of configuration interaction and molecular orbitals allows detailed interpretation of the electronic transitions and Cotton effects in the UV and CD spectra. Through the study of the CD spectra of chiral cyclophanes as model systems, the effects of intra- and intermolecular interactions on the chiroptical properties of molecules can be explored, and the results thus obtained are valuable in comprehensively elucidating the structure-chiroptical property relationship. In this review the recent progress in experimental and theoretical investigations of the electronic CD spectra of chiral cyclophanes is discussed.

T. Mori and Y. Inoue

Department of Applied Chemistry, Graduate School of Engineering, Osaka University, 2-1 Yamada-oka, Suita, Osaka 565-0871, Japan
tmori@chem.eng.osaka-u.ac.jp

Keywords Chiroptical properties, Electronic circular dichroisms, Planar chirality, Quantum chemical calculations, Cyclophane

Contents

1	Introduction	100
2	Circular Dichroism of Cyclophanes	102
2.1	Cyclophanes with a Single Chromophore	103
2.2	Cyclophanes Composed of a Pair of Chromophores	107
2.3	Layered Cyclophanes	116
2.4	Bi-Cyclophanes	119
2.5	Dendrimers and Polymers Containing Cyclophanes	121
3	Summary and Outlook	124
	References	125

1 Introduction

The electronic structure of cyclophanes is a subject of continuing research, since the electronic interactions between the two aromatic rings can be sensibly modeled in [2.2]paracyclophane systems. Although their interplane spacing is relatively small (2.6–3.0 Å, as compared with the van der Waals distance of ~3.4 Å), their interactions between the facing two π systems has been extensively investigated by means of absorption, emission, photoelectron, and EPR spectroscopies, as well as electrochemical studies.

The chiroptical properties of molecules are of substantial interest in chemistry and biochemistry and become important tools for the determination of the absolute configuration and conformation of molecular systems. In particular, the circular dichroism [1] is a quantitative measure of the difference in absorption coefficient for left and right circular polarized light:

$$\Delta\varepsilon = \varepsilon_l - \varepsilon_r$$

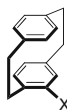
The ellipticity, or the intensity of the circular dichroism (CD) spectrum, is fundamentally characterized by the rotatory strength R , which is given by the imaginary part of the inner product between the electronic and magnetic dipole transition moment vectors:

$$\begin{aligned} R &= \text{Im} \langle \Psi_0 | \hat{\mu} | \Psi_i \rangle \langle \Psi_0 | \hat{m} | \Psi_i \rangle \\ &= |\vec{\mu}_{0i}| \cdot |\vec{m}_{0i}| \cdot \cos(\vec{\mu}_{0i} \cdot \vec{m}_{0i}) \end{aligned}$$

where Ψ_0 and Ψ_i represent the electronic wavefunctions in the ground and excited states, and $\hat{\mu}$ and \hat{m} are the electronic and magnetic dipole transition operators.

Thus, the rotatory strength R is able to be regarded as an analog of the oscillator strength f in UV spectroscopy. Nevertheless, practically no systematic study has been carried out on the effects of electronic and magnetic interactions on the rotatory strength R of cyclophanes.

The planar chirality of [2.2]paracyclophane derivatives was first described by Cram and Allinger in 1955 [2] who successfully resolved the enantiomers of 4-carboxy[2.2]paracyclophane (**1**, X = CO₂H) and reported their specific rotations. The very first CD spectra of chiral cyclophanes were reported in 1969 by Weigang and Nugent for ring-substituted [2.2]paracyclophanes (**1**) [3]. Soon after that, Falk et al. reported the CD spectra of an extended family of substituted [2.2]paracyclophanes and determined their absolute configurations [4]. Since then, the chiroptical properties of chiral cyclophanes, especially the [2.2]paracyclophane derivatives, have been investigated for almost half a century. During that period, a large variety of chiral cyclophanes have been prepared and accordingly the range of available CD data has also been appreciably expanded.



(R_p)-**1**, X = CO₂H, Me, CH₂Br, CH₂OH

Apart from the role of cyclophanes as a model system for studying the electronic interaction between the aromatic moieties, chiral [2.2]paracyclophanes have also been utilized as planar chiral ligands in asymmetric catalysis. Recent advances and applications in this area have been reviewed [5, 6]. The synthesis of heterocyclic compounds based on [2.2]paracyclophane architecture, where the long-distance electronic communication and the planar chirality play significant roles in their application, has also been reported recently [7]. Although the preparation and application of chiral cyclophanes in asymmetric synthesis has attracted much attention for a long time, their chiroptical properties, especially the CD spectra, have rarely been paid attention or even completely ignored.

The optical resolution of racemic cyclophanes can be easily achieved by chiral HPLC, and the measurement of CD spectra of chiral cyclophanes now becomes a routine. The electronic and magnetic interactions between the aromatic rings can be readily examined if the cyclophane architecture is used in the model systems. Despite this experimental and theoretical progress in relevant fields, the chiroptical properties, especially the electronic CD spectra, of chiral cyclophanes have not been systematically studied until very recently.

In this section we will congregate the reported CD spectra of chiral cyclophanes. Some recent examples (from the year 2000 onwards) of chiral cyclophanes of particular interest are selected and the reported spectra are visually reproduced. Classical examples are also cited, mostly with their chemical structures, but the figures of CD spectra are omitted. For ease of viewing, one of the enantiomers is drawn in 3D to underline the stereochemistry (i.e., R_p/S_p , M/P , or

a*R/aS*), even if both of the enantiomers were studied in the original literature. Stereochemical notation of the chiral cyclophanes has been summarized in reviews [5, 6]. Literature dealing with or commenting on the chiral cyclophanes but not reporting on the experimental CD spectra are excluded throughout this review. A cyclophane is principally defined as a compound consisting of an aromatic unit and an aliphatic chain that forms a bridge between two nonadjacent positions of the aromatic ring. Therefore, a large number of complex derivatives (e.g., compounds circulated with multiple aromatic units such as calixarenes or supramolecular systems where bridges form cage structures, and so on) are also categorized as belonging to the cyclophane family. However such complicated systems are beyond the scope of this review.

Recent advances in quantum chemical methods, especially the time-dependent density functional theory (TD-DFT), applying to chiral cyclophanes will also be discussed in this review to explain the experimental CD spectra of cyclophanes [8]. Some of the previous (less accurate, but thought-provoking) theoretical investigations have already been reviewed [9, 10]. In the following sections, we are unable to provide a comprehensive account of the theoretical investigation of the CD spectra of chiral cyclophanes. Rather, the experimental results on the CD spectra of cyclophanes are highlighted and theoretical investigations are provided for a few selected cases to investigate effectively the spectroscopic phenomena where the up-to-date calculations are available.

2 Circular Dichroism of Cyclophanes

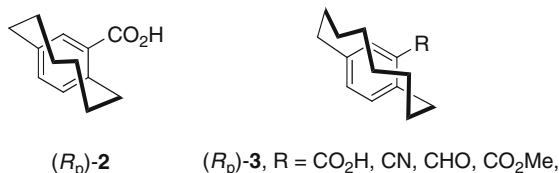
Optical rotation, or more generally the optical rotatory dispersion, is one of the classical chiroptical measures of chiral molecules and hence the specific rotation data of almost all known chiral cyclophanes have accumulated in the literature. For chiral systems lacking chromophores, specific rotations has proven to be of practical value in assigning absolute configurations [11] while the electronic CD spectrum, in general, can provide more information if the chromophoric group is attached in the system of interest. Hitherto, practically no systematic study has been carried out on the optical rotation of chiral cyclophanes. Vibrational circular dichroism (VCD) is another method of choice in recent years in the determination of the absolute configuration and conformation, in particular, of chiral molecules that lack chromophoric group(s) [12, 13]. The VCD studies on chiral cyclophanes, however, are rather limited. Moreover, the method is not applicable a priori to the study of the electronic or magnetic interaction between aromatic systems. At this point, only the recent studies on the VCD spectra of cyclophanes that will not appear in the later sections are cited [14, 15]. Although the data of electronic CD spectra of cyclophanes are still limited, the CD spectra better provide the conformational and configurational information in solution, as well as a solid basis for studying the electronic and magnetic interactions between the π systems, as exemplified in the following sections.

2.1 Cyclophanes with a Single Chromophore

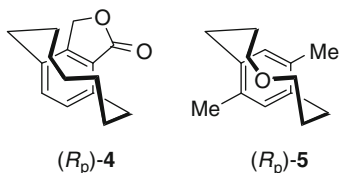
The electronic structure of cyclophanes is reflected in their absorption spectra. As the oligomethylene bridge is shortened in a series of $[n]$ cyclophanes, the bending of the aromatic plane increases. Consequently, the absorption maximum of the UV spectrum gradually red-shifts as the bridging chain becomes shorter [16]. By reducing the number (n) of carbon atoms in the bridge, the vibrational fine structure in the spectrum is gradually diffused and eventually disappears. In sharp contrast, the effect of chain length on the chiroptical properties has not been hitherto investigated systematically. In the following we will briefly summarize the current status of the CD spectral studies of $[n]$ cyclophanes.

2.1.1 $[n]$ Paracyclophanes

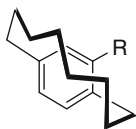
A stereospecific synthesis of [6]paracyclophane-8-carboxylic acid (**2**) was reported, and its CD spectrum was compared with that of [8]paracyclophane-10-carboxylic acid (**3**, R = CO₂H) [17]. The former afforded a pair of bisignate CD patterns in the 200–400 nm region, while only a pair of Cotton effect peaks of the same sign were observed for the latter. The CD intensity ($|\Delta\epsilon|$) of **2** was in the order of $10 \text{ M}^{-1} \text{ cm}^{-1}$ for the main band at $\sim 220 \text{ nm}$. [6]Paracyclophane (**2**) is one of the most strained cyclophanes, and its boat-type deformation of the benzene ring led to the red-shift of ca. 30 nm in its UV and CD spectra. The theoretical spectrum obtained at the TD-DFT-B3-LYP/TZV2P' level well reproduced the experimental spectrum except for the sign of the weak 1L_b band around 320 nm [8]. The CD spectrum of structurally similar methyl 3,6-hexanooxepin-4-carboxylate was also reported [16].



The CD spectra of enantiomerically enriched [7]paracyclophane **4** was also reported. The observed Cotton effects were slightly weaker than those observed for [6]paracyclophane **2** [18]. The CD spectrum of 9,12-dimethyl-4-oxa[7]paracyclophane **5** was measured and compared with the theoretical one calculated with the DFT/SCI method. The $|\Delta\epsilon|$ values at the main band ($40\text{--}70 \text{ M}^{-1} \text{ cm}^{-1}$) are large relative to those of nonoxa-[7]paracyclophane **4** [19]. It is to note that the calculated deformation angle of [7]cyclophane **5** is similar to those of [2.2]paracyclophanes. The theoretical study has been updated by using the more recent TD-DFT method at the B3-LYP/TZV2P' level and all of the four resolved bands in the experimental CD spectra were very well reproduced [8].



The CD spectra of [8]paracyclophane-10-carbonitrile and related compounds (**3**) have been reported and their absolute configurations have been estimated by the theoretical calculations [20]. The bisignate positive and negative Cotton effects were observed at the main band for the (*R_p*)-isomer. The $|\Delta\epsilon|$ values were $10\text{--}20\text{ M}^{-1}\text{ cm}^{-1}$, which are much smaller than those for [7]paracyclophanes, but still larger than those for chiral benzenes substituted by point-chiral substituent(s). The CD spectra of a variety of 12-substituted [10]paracyclophanes (**6**) have been reported [21]. The spectra were significantly different from each other, depending on the substituent. Nevertheless, all of the (*S_p*)-isomers exhibited a pair of negative Cotton effects and the $|\Delta\epsilon|$ values were in the range of $5\text{--}20\text{ M}^{-1}\text{ cm}^{-1}$.



(*R_p*)-**6**, R = Me, NH₂, COMe, CO₂Me
CO₂H, CH₂OH, CHO,
CONH₂, CN, Cl, OH

Imidazole-containing [10]metacyclophane **7** was efficiently synthesized from cyclododecanone and the racemic **7** obtained was effectively resolved to a pair of enantiomers by chiral HPLC (on a Daicel OD-H column) [22]. The absolute configuration of the first-eluted (–)-isomer was determined to be *S_p* by the X-ray crystal structural analysis of (+)-10-camphorsulfonic acid salt of **7**, which displayed a negative Cotton effect at the imidazole band. Unfortunately, the CD intensities are not clear as the concentration of the cyclophane is not stated in the report (Fig. 1).

When a 1:1 mixture of the solid and the liquid diastereomers of bridged [10]cyclophane nicotinamides **8** was heated, the solid (*S_p*,3'*S*)-isomer became predominant over the liquid (*R_p*,3'*S*)-isomer through the fast dynamic (rope-jumping) racemization and the subsequent spontaneous resolution via crystallization [23]. The CD spectra of these cyclophanes exhibit either two positive or two negative Cotton effects at 220 nm and 280 nm, primarily due to the planar chirality (Fig. 2).

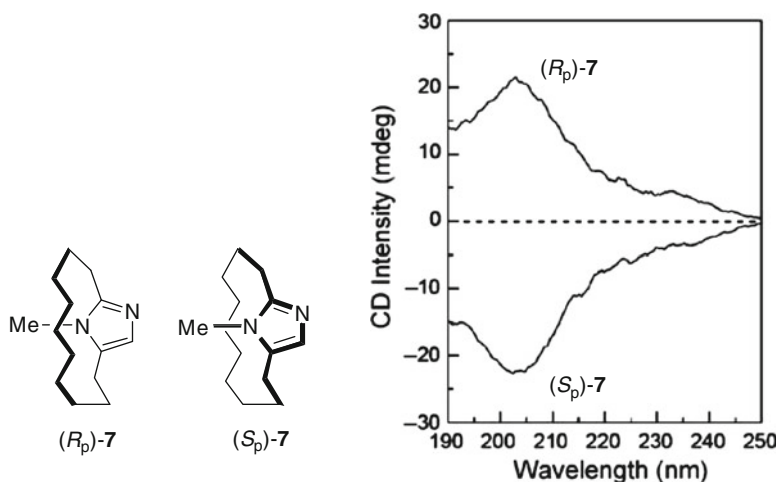


Fig. 1 CD spectra of (*R_p*)- and (*S_p*)-7 in water. Concentration was not reported. Reproduced by permission of [21]. Copyright © 2009 Royal Society of Chemistry

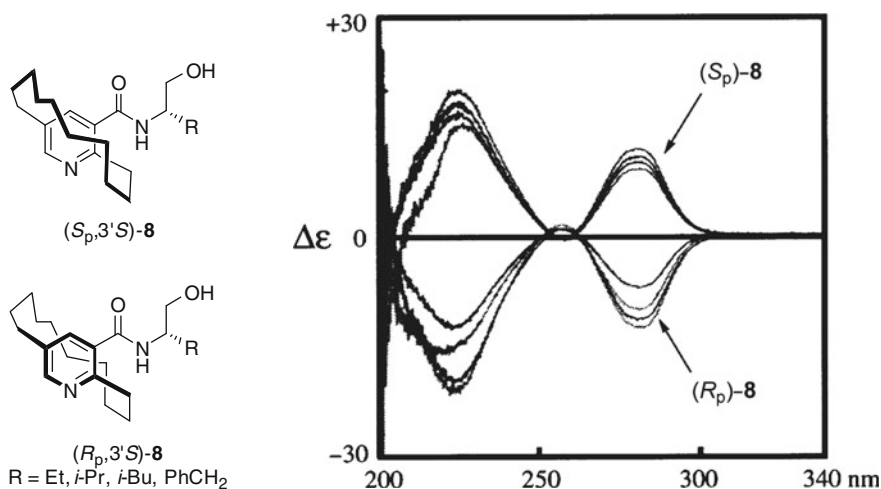
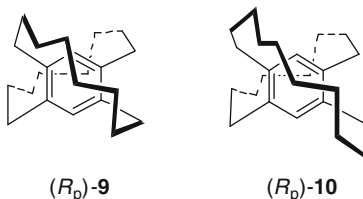


Fig. 2 CD spectra of (*R_p*)- and (*S_p*)-8 in acetonitrile. The both isomers possess the (3'*S*') configuration in the nicotinamide substituent. Reprinted with permission from [22]. Copyright © 2001 Elsevier Ltd

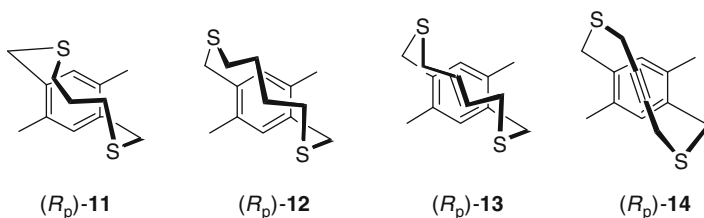
2.1.2 [*m*][*n*]Paracyclophanes

Optically active [8][8]paracyclophane (**9**) and [8][10]paracyclophane (**10**) were prepared and their CD spectra were reported [24]. The pattern and strength of the Cotton effects were almost identical to each other and the $|\Delta\epsilon|$ values were half the magnitude of those for [8]paracyclophane derivatives **3**.

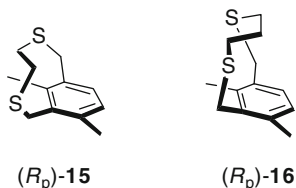


2.1.3 [*n*]Thiacyclophanes

The enantiomer separations of 9,12-dimethyl-2,6-dithia[7]- and 10,13-dimethyl-2,7-dithia[8]paracyclophanes (**11–14**) were achieved by chiral HPLC (on a Daicel OD column) [25]. The CD spectra of these dithiaparacyclophanes exhibited a very similar Cotton effect pattern composed of the first positive, second positive, and third negative peaks (and the opposite pattern for the antipodes). The intensity of the strongest third Cotton effect at 220 nm, assignable to the benzene's π - π^* transition, amounts to 30–45 M⁻¹ cm⁻¹. The stronger Cotton effect for dithia[7]-paracyclophane than for dithia[8]paracyclophane may be ascribed to the difference in deformation angle.



8,12-Dimethyl-2,5-dithia[6]metacyclophane (**15**) and 9,13-dimethyl-2,6-dithia[7]metacyclophane (**16**) were prepared and their enantiomers were (partially) separated by chiral HPLC (on a Daicel OD column) [26]. The CD spectra of these two metacyclophanes were also investigated by the preliminary theoretical calculations. It was shown that the spectra depend strongly on the number of carbon atoms incorporated in the bridging dithiaalane chain, whose dihedral angles play an important role. The electronic excitations of the sulfur's lone-pair electrons were revealed to be critical in theoretically describing the observed Cotton effects.



2.2 Cyclophanes Composed of a Pair of Chromophores

Electronic interactions in [2.2]paracyclophane and its derivatives have been extensively studied [27]. In addition to the original absorption bands, the cyclophanes exhibit the additional “cyclophane” band at longer wavelengths ($\lambda_{\text{max}} = 302$ nm for the parent [2.2]paracyclophane). The existence of the additional bands can be explained in principle by the exciton/charge resonance interaction between the two chromophores. However, the complete assignment of the individual absorption bands in each cyclophane molecule is still a challenging task. It is known that the UV spectra of cyclophanes can be reasonably explained only if the σ - π interaction, or a special type of hyperconjugation, is taken into consideration [28].

Before presenting the actual examples of the CD spectra of chiral [2.2]paracyclophanes, structural features of [2.2]paracyclophane moiety should be briefly discussed here. The parent [2.2]paracyclophane bears a twisted structure with D_2 symmetry at its energy minimum; the twist, or rotation, angle between the facing benzene rings was estimated to be $\sim 6^\circ$ by experiment and $\sim 9^\circ$ by MP2 calculations. The parallel D_{2h} structure is thus the transition between the two enantiomeric D_2 structures. Due to the dynamic interconversion, the parent [2.2]paracyclophane is achiral. A theoretical calculation for one of the enantiomeric forms of D_2 -symmetrical [2.2]paracyclophane at the TD-DFT-B3-LYP/TZV2P' level revealed that the cyclophane induces strong Cotton effects in its CD spectrum, with $|\Delta\epsilon|$ of 20–30 $\text{M}^{-1} \text{cm}^{-1}$ [8]. It is noteworthy that the corresponding sandwich model, in which two benzenes are placed face-to-face at the same distance and twist angle but not connected to each other by the ethano bridges (*note that the bridges are not replaced by methyl groups in this model; when the methyl groups are used in the models, as in the other cases shown below, the spectra were basically reproducible*), only afforded much smaller Cotton effects (as low as $|\Delta\epsilon| = \sim 5 \text{M}^{-1} \text{cm}^{-1}$) and opposite signs for most of the transitions. Thus, the common classification of substituted [2.2]paracyclophanes as planar chiral molecules is itself an arguable point. Although such nomenclatures are used throughout this text (and in other literature), the orbital interactions with the alkyl bridges seem to play a vital role (rather than the distance/angle between the π systems) in the chiroptical properties of cyclophane molecules.

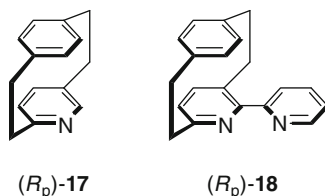
2.2.1 [2.2]Paracyclophanes

Among the cyclophanes bearing a pair of chromophores, [2.2]paracyclophanes are the most extensively studied compounds. Therefore, the studies on the chiroptical properties of cyclophanes have been based strongly on these molecules. Indeed, the first reports on chiral cyclophane dealt with 4-substituted [2.2]paracyclophanes (**1**) [2, 3]. It was reported that the signs of Cotton effects in the longer wavelength region, corresponding to the 1L_b band, were correlated with the Platt's spectroscopic moment, while the signs of the 1L_a band were independent of the substituent.

Thus, for the 1L_b band, bisignate positive-negative Cotton effects were found for 4-carboxy[2.2]paracyclophane (**1**, X = CO₂H), while the opposite negative-positive Cotton effects were found for 4-methyl[2.2]paracyclophane (**1**, X = Me), albeit having the same planar (*S_p*)-chirality. The signs of the Cotton effect at the 1L_a band were, on the other hand, ascribed to the planar chirality of cyclophane moiety [3]. The theoretical CD spectrum of 4-methyl[2.2]paracyclophane at the TD-DFT-B3-LYP/TZV2P' level was in good agreement with experiment [8]. A number of related [2.2]paracyclophanes derivatized from [2.2]paracyclophanecarboxylic acid and 3-([2.2]paracyclophanoyl)propionic acid were also subjected to the CD spectral studies [4].

The CD spectrum of 4-fluoro[2.2]paracyclophane (**1**, X = F) has been repeatedly studied for its structural simplicity with the least hindered substituent [3, 8, 29, 30]. The Cotton effects at the main band are moderately strong, with $\Delta\epsilon$ of 20–30 M⁻¹ cm⁻¹. A previous study with the semiempirical exciton coupling or DeVoe model successfully explained the pattern of CD spectra of 4-amino-, 4-hydroxy-, 4-fluoro-, and 4-iodo[2.2]paracyclophanes [28]. A more recent study on the CD spectra of fluorine-containing 4-X-[2.2]paracyclophanes (**10**, X = F, CH₂F, COCF₃) was combined with the quantum chemical calculations to confirm their absolute configuration. It was found that both F and CH₂F groups do not change the conformational and electronic properties of the parent molecules (e.g., compared with **1**, X = H or Me), while the COCF₃ group causes large perturbations to the [2.2]paracyclophanes, resulting in significant changes in the CD spectra (Fig. 3). The $|\Delta\epsilon|$ value of this compound amounts to 50–60 M⁻¹ cm⁻¹. Thus, the effect of fluorine on the CD spectra was found less important than that of oxygen [29]. The VCD spectra of these cyclophanes were also reported in the same paper.

The CD spectra of enantiopure pyridinophane **17** and bipyridine derivative **18** were reported. Both spectra were relatively complicated compared to those of substituted [2.2]paracyclophanes, apparently showing 6–8 positive/negative Cotton effect peaks. While the $|\Delta\epsilon|$ value for the main band of compound **18** (20–30 M⁻¹ cm⁻¹) was reduced to half that of compound **17** (30–50 M⁻¹ cm⁻¹), the spectrum of planar chiral bipyridine **18** was very sensitive to the added metal salts. The absolute configuration was determined by comparison with the theoretical spectrum at the DFT/SCI level [31].



Several 4,7,12,15-tetrasubstituted[2.2]paracyclophanes were also resolved successfully by chiral HPLC (on a Daicel OD column). The experimental CD spectra were compared with the theoretical ones at a variety of theoretical levels. The simple exciton coupling method [32] was proved to be applied only with careful precautions to the determination of the absolute configuration; in most cases the method

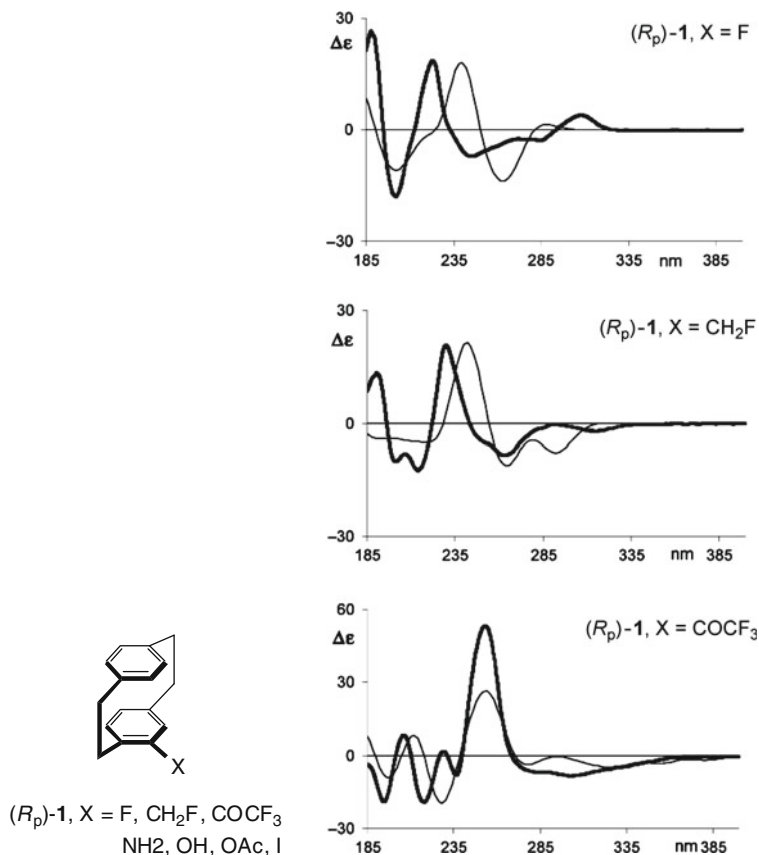


Fig. 3 Comparison of experimental and calculated CD spectra for fluorine containing 4-substituted (R_p) -[2.2]paracyclophanes (**1**, X = F, CH₂F, COCF₃). *Dark lines*: experimental spectra in acetonitrile. *Light lines*: theoretical spectra at the TD-DFT-B3-LYP/TZVP level. Reprinted with permission from [29]. Copyright © 2009 American Chemical Society

failed to predict the accurate configuration. Thus, the CD spectrum of tetramethoxy [2.2]paracyclophane (**19**) was apparently coupled, but the individual CD signals turned out to be composed of several transitions (Fig. 4). Nevertheless, the TD-DFT-BH-LYP calculations well reproduced the experimental CD spectrum and the absolute configuration was indisputably assigned [33].

Donor-acceptor cyclophanes have been extensively investigated as models for intermolecular charge transfer (CT) complexes. The [m.n]cyclophane structure provides the adjustable well-defined distance and orientation for the donor and acceptor units incorporated in its framework. These systems have been systematically investigated by Staab et al. using absorption spectroscopy [34].

Introduction of such additional forces between the π systems afforded interesting effects on the structure and chiroptical properties of the cyclophanes. Thus, some

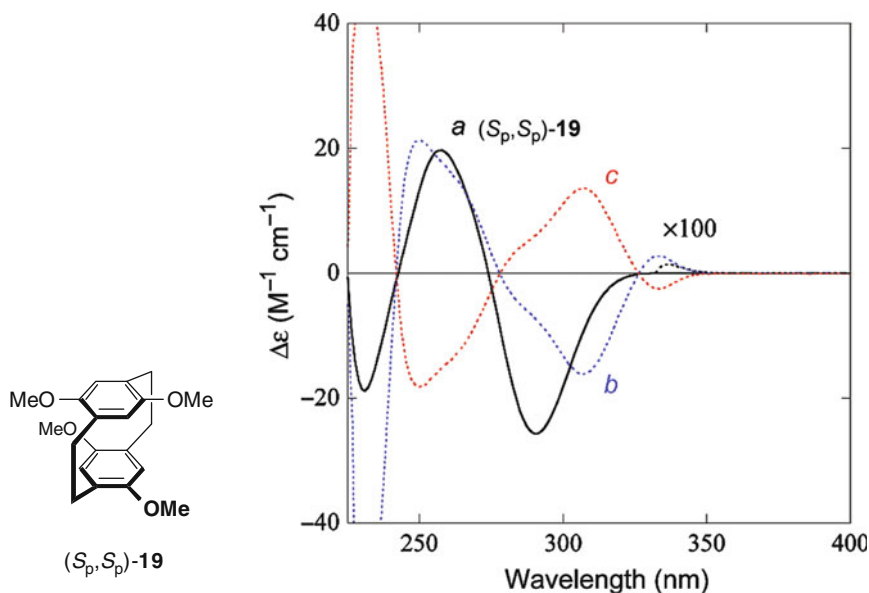


Fig. 4 Comparison of experimental and theoretical CD spectra of (S_p,S_p) -19 in dichloromethane. *Dotted lines*: experimental spectra for both isomers. *Solid lines*: theoretical spectra at the TD-DFT-BH-LYP/TZV2P level. Reprinted with permission from [32]. Copyright © 2007 American Chemical Society

chiral cyclophanes with donor-acceptor interactions were studied [35]. The Cotton effects at the CT band and the relatively strong couplets at the 1L_a and 1L_b bands were apparent for donor-acceptor cyclophanes **20** and **21** (Fig. 5). The maximum $|\Delta\epsilon|$ values for the eclipsed **21** amounted to $\sim 50 M^{-1} cm^{-1}$, while the Cotton effects of staggered **20** were appeared as a couplet in the main band and the $|\Delta\epsilon|$ become as large as 90 – $120 M^{-1} cm^{-1}$. It is also noteworthy that the anisotropy (g) factor of the staggered donor-acceptor cyclophane **20** was 0.01, which is an unusually large value for an allowed transition.

The experimental CD spectra of these donor-acceptor cyclophanes were very well reproduced by the theoretical calculations at the TD-DFT-BH-LYP/TZV2P level [32]. The amount of the exact exchange in the functional to be used turned out to be important for better agreement with experiment. The analysis of the configuration contributions showed that the observed CD spectra essentially resulted from simple overlap of the Cotton effects of pure π - π^* transitions in the donor and acceptor parts, in addition to the CT transitions. Thus, the exciton chirality method cannot be applied to the absolute configuration determination for these cyclophanes. The experimental CD spectrum of more congested donor-acceptor cyclophane **22** was reproduced in a less satisfactory manner compared to the cases of **20** and **21**. The absolute configuration was safely determined by a comparison of the experimental spectrum with the theoretical data at the TD-DFT level; however, the satisfactory reproduction of the whole CD spectrum of **22** was only possible by

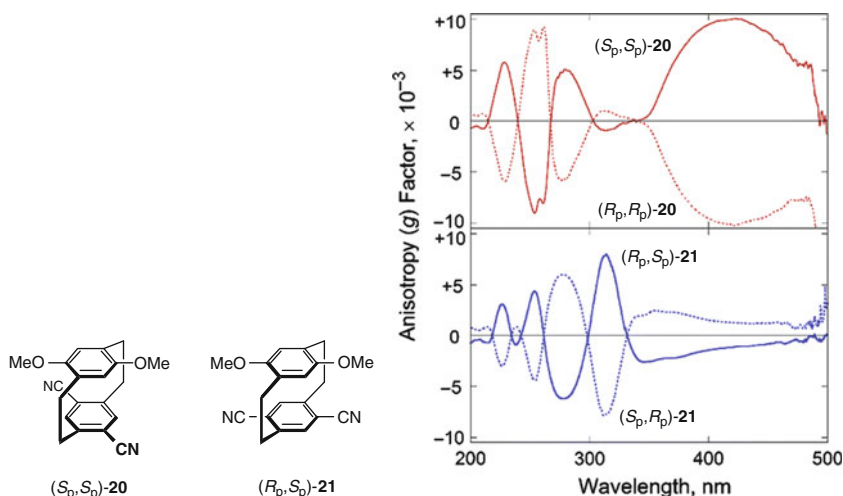


Fig. 5 Anisotropy (g) factors of isomeric paracyclophanes **20** and **21**. Solid lines are for the (S_p,S_p)- and (R_p,S_p)-isomers, respectively. Reprinted with permission from [34]. Copyright © 2005 American Chemical Society

the use of more sophisticated RI-CC2 calculations (Fig. 6). The VCD spectra were also investigated in the same study.

The effects of the interplane distance and the twist angle between the donor and acceptor moieties on the CD spectrum were examined with the intermolecular model systems. The experimental CD spectrum of the cyclophane was well reproduced by the TD-DFT-BH-LYP/TZV2P calculation for the model system, where two aromatic rings are placed at the same spacing and angle as those of the cyclophane and the side chains are replaced by methyl groups. The influence of the distance and angle on the CD spectrum was theoretically investigated. It was demonstrated that both the distance and angle more critically affect the CT transition than the 1L_b transition (Fig. 7). The Cotton effect of the CT band becomes almost zero at an interplane distance of 3.5 Å, which coincides with the equilibrium distances of most of the common intermolecular CT complexes.

[2.2]Paracyclophanes with chiral ketimine side chains constitute a class of highly versatile and enantioselective ligands for catalytic carbon-carbon bond-forming reactions. Proper matching of the side chain and [2.2]paracyclophane configurations induced the cooperative enhancement of the stereoselectivity. The absolute configuration of both stereogenic elements has been successfully resolved by CD spectroscopy combined with theoretical calculation at the TD-DFT-PBE0/SVP level. It is noteworthy that the $|\Delta\epsilon|$ values observed for this compound were rather small ($\sim 10 \text{ M}^{-1} \text{ cm}^{-1}$) compared with the other typical [2.2]paracyclophanes. Cyclophane ($R_p,3'R$)-**23** exhibited unusually strong solvatochromism in its CD spectrum, which was explained in terms of the tautomeric equilibrium between the *ortho*-hydroquinone-imine and *ortho*-quinone-enamine forms (Fig. 8) [36].

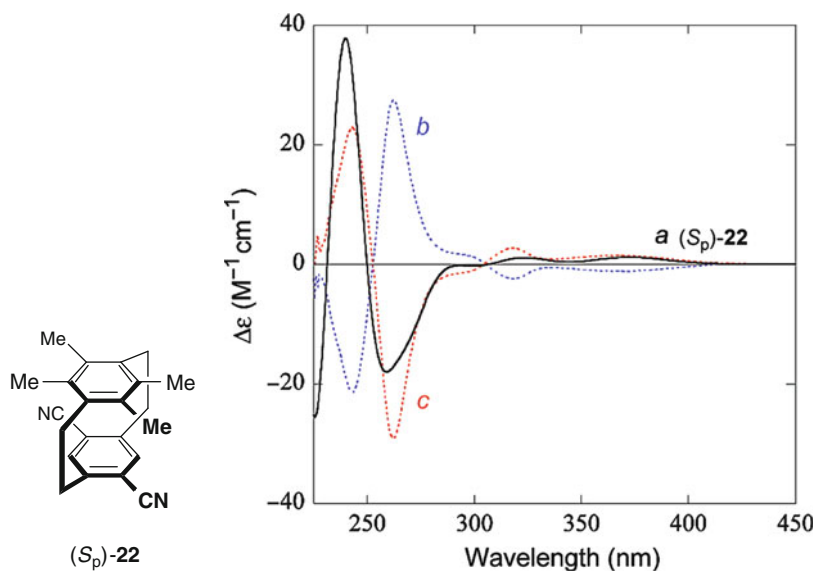


Fig. 6 Comparison of experimental and theoretical CD spectra of **22**. *Dotted lines*: experimental spectra for both isomers in dichloromethane. *Solid lines*: theoretical spectra for $(4S_p)$ -**22** at the RI-CC2/SVP level. Reprinted with permission from [32]. Copyright © 2007 American Chemical Society

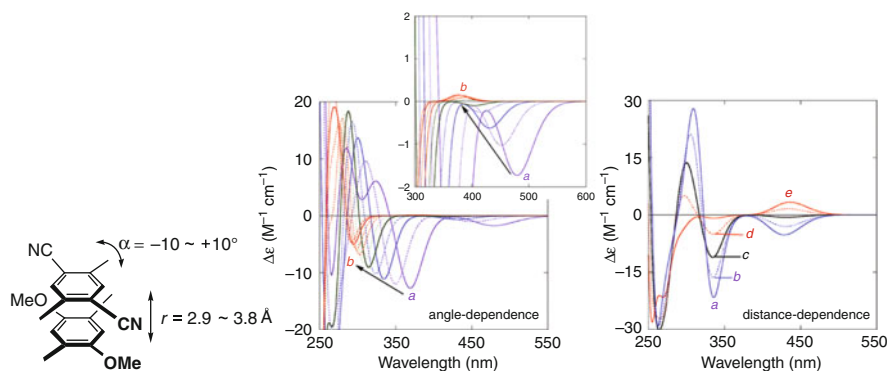


Fig. 7 Theoretical CD spectra of model CT complexes at the TD-DFT-BH-LYP/TZV2P level. *Left*: Effect of interplane distance on the CD spectra. The distance is shifted from (a) 2.9 to (b) 3.8 Å (increment: 0.1 Å). *Inset*: Expansion of the CT band region. *Right*: Effect of inter-ring rotation angle on the CD spectra. The angle is incrementally shifted from (a) -10° , (b) -5° , (c) 0° , (d) $+5^\circ$, and (e) $+10^\circ$ with a constant inter-plane distance of 3.1 Å. Reprinted with permission from [32]. Copyright © 2007 American Chemical Society

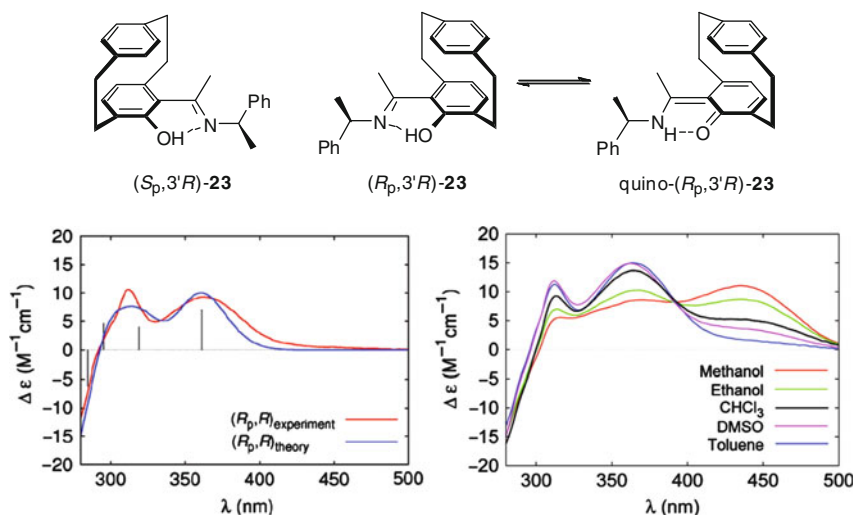
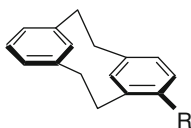


Fig. 8 Theoretical and experimental CD spectra of $(R_p,3'R)$ -23. Reprinted with permission from [35]. Copyright © 2009 American Chemical Society

2.2.2 [2.2]Metacyclophanes

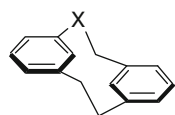
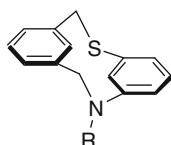
The CD spectra of mono-substituted [2.2]metacyclophanes (**24**) were also reported [37]. All the metacyclophanes exhibited very similar bisignate Cotton effects, except for the acetyl derivative, in which the additional Cotton effect induced by the carbonyl group was observed.



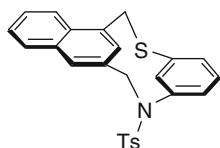
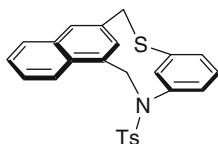
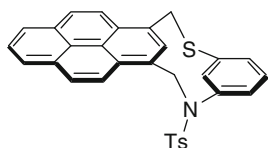
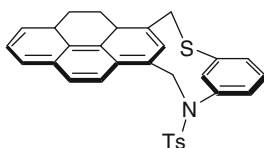
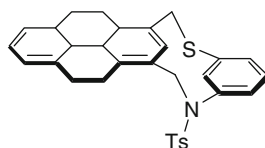
24, R = CO₂H, CO₂Me, CN, Et, Me, COMe, NH₂

Hetera[2.2]metacyclophanes have been more frequently studied by CD spectroscopy, probably due to their facile synthesis. Thus, the experimental and theoretical study of the CD spectra of 1-oxa- and 1-thia-[2.2]metacyclophanes (**25**) was reported [38]. The magnitudes of the Cotton effects do not differ from those of typical [2.2]paracyclophanes, being ca. 25 M⁻¹ cm⁻¹. According to the theoretical investigation using the multireference configuration interaction (MRCI) calculations, the dominant CD transitions of 1-oxa[2.2]metacyclophane (**25**, X = O) was characterized by independent and coupled π - π^* transitions localized in the aromatic rings, while the CD spectrum of 1-thia[2.2]metacyclophane (**25**, X = S) was mainly described by valence-type excitations involving the lone-pair orbitals of the sulfur and/or antibonding σ^* of the C-S bonds. The CD spectra of structurally

similar 1-thia-10-aza[2.2]metacyclophanes (**26**) were also reported [39] and the MRCI calculations were performed for the unsubstituted cyclophane (**26**, R = H) [40]. More recently, the TD-DFT calculations at the TD-DFT-B3-LYP/TZVP level were performed to understand better the CD spectra of these hetera[2.2]metacyclophanes (**25** and **26**, R = H) [8].

(M)-**25**, X = O, S(M)-**26**, R = H, COCF₃, SO₂C₆H₄Me

Analogous 1-thia-10-aza[2.2]metacyclophane derivatives (**27–31**) were prepared and their enantiomers were partially resolved by chiral HPLC (on a Daicel OT(+) column). Their CD spectra were compared in dioxane, but the absolute $\Delta\epsilon$ values were not reported [41].

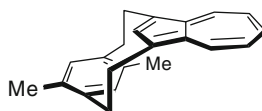
**27****28**Ts = SO₂C₆H₄Me**29****30****31**

Several other [2.2]metacyclophanes were prepared as chiral ligands for complexation with tricarbonylchromium. These ligands formed the corresponding chromium complexes stereoselectively and their CD spectra were also studied [42].

2.2.3 Metaparacyclophane

A variety of arenophanes, such as naphthalenophanes, anthracenophanes, fluorenophanes, phenanthrenophanes, and pyrenophanes, have been reported [26]. Among

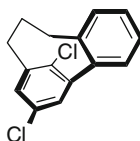
these cyclophanes, chiral azulenophane, 14,17-dimethyl[2](1,3)azuleno[2]paracyclophane (**32**) has been subjected to repeated theoretical investigations. The cyclophane **32** was successfully resolved by chiral HPLC (on a Daicel OD column) and the theoretical investigation was originally performed at the DFT/RPA level [43]. The CD spectrum of **32** was recently reinvestigated by the more sophisticated double-hybrid B2-PLYP method [44].



(*S_p*)-**32**

2.2.4 Orthoparacyclophane

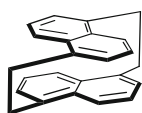
The CD spectrum of 12,15-dichloro[3.0]orthometacyclophane **33** was investigated by the DFT/SCI approach to show that the spectrum differs substantially from that of the corresponding non-linked biphenyl derivative [45]. The observed $|\Delta\epsilon|$ values for **33** were significantly larger ($30\text{--}40\text{ M}^{-1}\text{ cm}^{-1}$) than those for simply substituted biphenyl systems which were extensively investigated very recently ($1\text{--}10\text{ M}^{-1}\text{ cm}^{-1}$) [46].



(*aS*)-*endo*-**33**

2.2.5 Other Cyclophanes

A logical extension of [2.2]paracyclophane may be the corresponding [2.2]naphthalenophanes. Indeed, two chiral naphthalenophanes, (1,5)- and (2,6)-naphthalenophanes (**34** and **35**), have been described [47, 48] but no CD spectral study has been conducted so far.



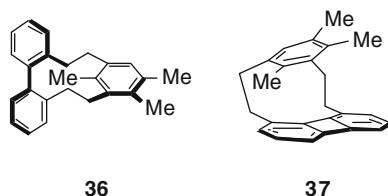
(*R_p*)-**34**



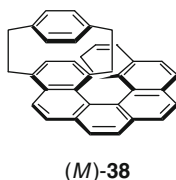
(*R_p*)-**35**

The [2.2]metacyclophane containing biphenyl moiety (**36**) was successfully resolved by chiral HPLC (on a Daicel OD column). Analogous *syn*-[2.2]biphenylenophane (**37**), in which an additional 2,2'-linkage is introduced to **36**, was

enantiomerically enriched under the same HPLC conditions. Upon CD spectral examination, similar Cotton effect patterns were observed in the 180–300 nm region [49].



The chiroptical properties of a hybrid of paracyclophane and helicene, [2.2]paracyclophanohelicene (**38**), were reported [50]. The introduction of [2.2]paracyclophane moiety caused a red shift and intensity enhancement of the absorption in the 240–280 nm regions, which was also reflected in the CD spectrum. It is noteworthy that the (*M*)-helicity was evoked in the hybrid **38** when started from (*R_p*)-[2.2]paracyclophanecarbaldehyde.



A planar chiral naphthalenediimide cyclophane (**39**) and its derivatives were prepared for their tunable intramolecular FRET properties. The enantiomeric enrichment of cyclophane **39** was accomplished by chiral HPLC (on a Daicel IA column) and the CD spectra of enantiomeric **39** were reported (Fig. 9) [51].

2.3 Layered Cyclophanes

Chemistry of multilayered cyclophanes has been reviewed and their physical and chemical properties have also been extensively discussed [52]. The UV spectra are known to show large bathochromic shifts with sizeable hyperchromic effects and become structureless as the number of layers increases. These features are more apparent for up to four-layered cyclophanes. This was explained primarily by the transannular π - π interaction/delocalization, while the effect of deformation of the benzene rings was thought to be rather negligible [53]. Despite the UV spectral study, only a limited amount of effort has been devoted so far to the study of the chiroptical properties of layered cyclophanes.

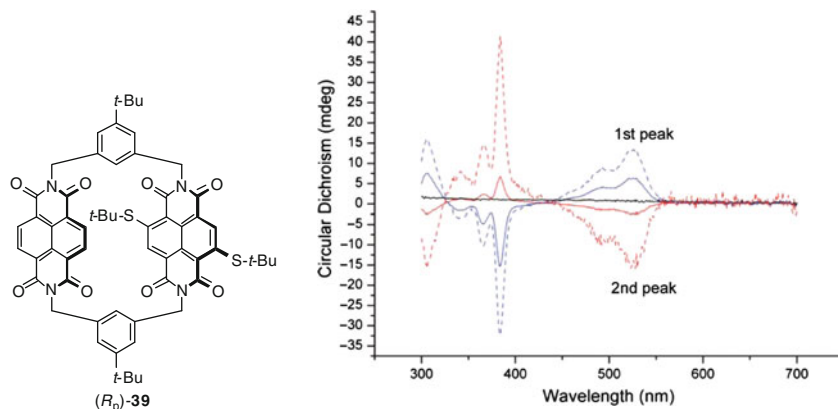
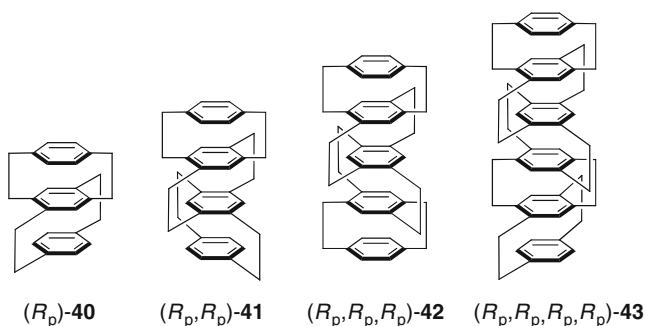
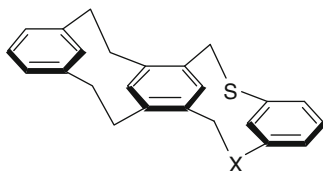


Fig. 9 The CD spectra of chiral naphthalenediimide cyclophane **39** in dichloromethane. *Solid lines*: experimental spectra for enantiomerically enriched samples (concentration: 8.1 and 7.0 μ M for first and second peaks, respectively). *Dotted lines*: spectra of pure enantiomers corrected for the enantiomeric purities of the sample obtained by chiral HPLC. Reprinted with permission from [50]. Copyright © 2009 Royal Society of Chemistry

Optically active triple-, quadruple-, quintuple-, and sextuple-layered [2.2]paracyclophanes (**40–43**) were prepared and their CD spectra were reported [54]. The CD spectra of these multilayered [2.2]paracyclophanes were more complex than those of [2.2]paracyclophanes, exhibiting three bands of the same sign centered at ca. 270, 310, and 350 nm. The observed fine structures were ascribed to the face-to-face interactions between the distorted benzene rings.



Triple-layered [2.2]metacyclophanoarenes (**44**) were also prepared and their enantiomers were enriched by chiral HPLC (on a Daicel OT(+) column). The CD spectra were compared with those of the corresponding two-layered cyclophanes (e.g., **25**, **26**). The major Cotton effect peaks of **44** in the spectra were red-shifted by 20–30 nm, and some additional, but weak, Cotton effects were observed [40].



44, X = O, N-SO₂C₆H₄Me

A racemic mixture of three-layered [3.3]paracyclophane (**45**) was resolved into two enantiomers by chiral HPLC (on a Daicel OD column), and their absolute configuration was determined by a comparison of the experimental CD spectrum with the theoretical one at the TD-DFT-B3-LYP/TZVP level [55]. A simple model, composed of two *p*-xylenes and durene (the side chains were modeled again by methyl groups), was used to explain the origin of the chiroptical properties of the three-layered cyclophane system. Due to the flexibility of the [3.3]paracyclophanes, the solvent effects on the conformer distribution and thus on the chiroptical properties were significant (Fig. 10).

The triple layered tetraazacyclophane (**46**) consisting of the unique crossed meta-meta cyclophane linkage was prepared and the enantiomers were separated by chiral HPLC (on a Daicel OD column). The CD spectrum of **46** was rather complex and seven Cotton effect peaks in the 190–280 nm region were observed [56]. Unfortunately, the four tosyl groups and the ester functions prevented the reasonable theoretical discussion and the assignment of absolute configuration.

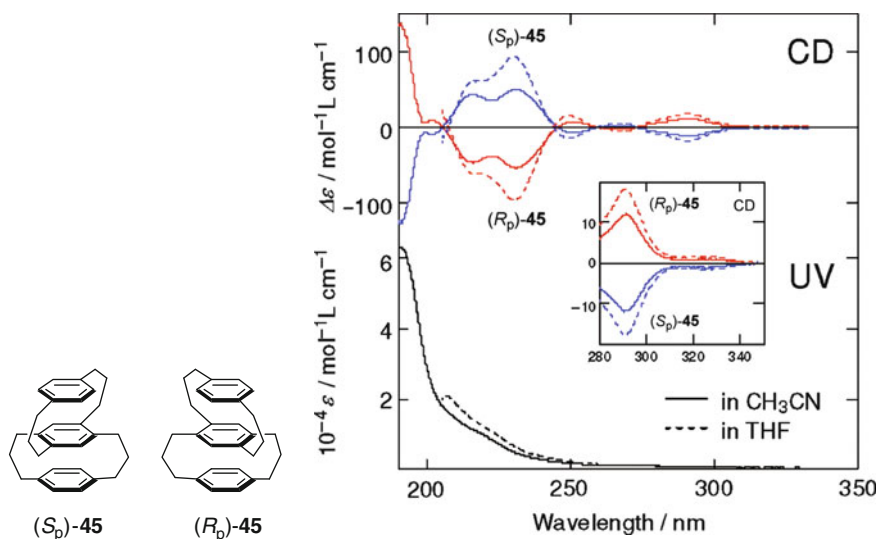
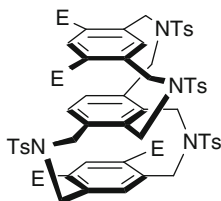


Fig. 10 UV and CD spectra of (*R*_p)- and (*S*_p)-**45**. Reprinted with permission from [54]. Copyright © 2008 American Chemical Society

46, Ts = SO₂C₆H₄Me, E = CO₂Et

2.4 Bi-Cyclophanes

Cyclophane architecture allows us to construct model systems for studying electronic and magnetic interactions by positioning two or more aromatic rings in the desired positions. Further connecting two (or more) cyclophanes either directly (to give biaryls) or with a linker (to give bis-cyclophanes) leads to a variety of unique structural motifs for studying more on such interactions. For instance, axial chirality is introduced to the planar chiral system if two cyclophane components are directly connected to each other, which significantly affects the overall CD spectra. In the following section, recent investigations along this line are presented.

The CD spectral investigation of optically active bi[10]paracyclophanes (**47**), in which two planar and one axial chirality elements are incorporated, was reported in the literature [57]. The experimental CD spectrum of enantiomerically pure (*R_p,S_p*)-**47**, which was derived from the corresponding diastereomeric tetra-(*S*)-camphanoate, was found to be in good agreement with that calculated for the (*aR*)-isomer, but approximately the mirror image of the spectrum computed for the (*aS*)-isomer (Fig. 11). Thus, the CD spectrum can be interpreted mostly in terms of the axial chirality, indicating that the effects from the planar chirality of cyclophane units were more or less cancelled out.

Syntheses and CD spectra of bisnicotinic acid derivatives with two cyclophane units and (*S*)-2-amino-1-butanol linker (**48**) were reported recently. The CD

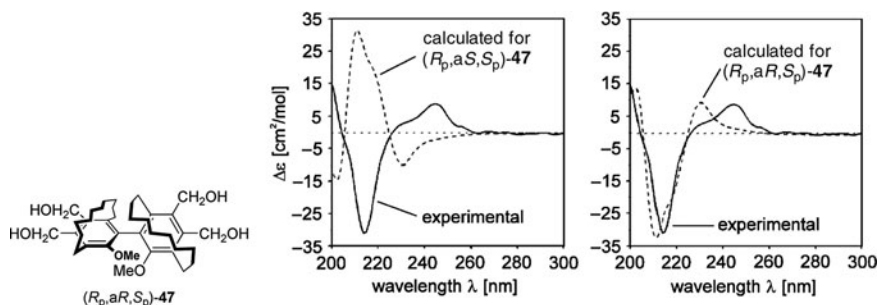


Fig. 11 Experimental CD spectra of (*R_p,S_p*)-**47**, compared with the theoretical ones for (*aR*)- and (*aS*)-rotamers. Reprinted with permission from [56]. Copyright © 2003 Elsevier Ltd

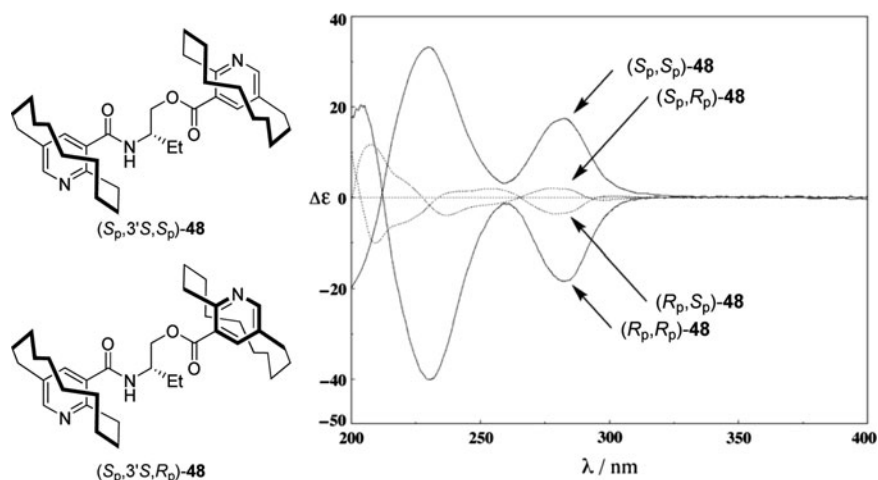


Fig. 12 CD spectra of (S_p,S_p) -, (S_p,R_p) -, (R_p,S_p) -, and (R_p,R_p) -**48**. All isomers possess $(3'S)$ -configuration in the linker. Reprinted with permission from [57]. Copyright © 2009 Elsevier Ltd

spectral comparison of the diastereomeric pair of bi[10]pyridinophane **48** revealed that the chiroptical properties are controlled essentially by the absolute configuration of the planar-chiral cyclophane moieties (Fig. 12). The (S_p,S_p) - and (R_p,R_p) -isomers exhibit two strong Cotton effects of the same signs at 230 and 280 nm, while those with the opposite planar-chiral units merely showed three weak Cotton effects at 210, 250, and 280 nm with the opposite signs. It was also noted that these spectra were nearly superimposable with the sum spectra of the corresponding nicotinamide and nicotinate [58].

The CD spectrum of C_2 -symmetric bipyridinophane (S_p,S_p) -**50** was quite similar to that of [10]cyclophane bipyridine (S_p) -**49**, while the CD spectrum of C_2 -symmetric terpyridine (S_p,S_p) -**51** was similar in shape but the magnitude of Cotton effect was substantially different (Fig. 13) [59].

As unique C_2 -symmetric transition metal complexes, the atropisomeric (R_p,R_p) -2,2'-bi([2]paracyclo[2]-5,8-quinolinophane) (**52**) and (R_p,R_p) -1,1'-bi([2]paracyclo[2]-5,8-isoquinolinophane) (**53**) were prepared from (R_p) -4-amino- and (R_p) -4-carboxy-[2.2]paracyclophanes, respectively. The CD spectra of **52** and **53** were significantly different from each other (Fig. 14) [60]. The bisquinoline moieties are in almost planar orientation in 2,2'-isomer **52** and the origin of chirality is ascribable primarily to the paracyclophane structure. In contrast, the main source of chirality in 1,1'-isomer **53** is the distorted bisquinoline chromophores (i.e., the axial chirality).

The [2]paracyclo[2](5,8)quinolinophane units were tethered with an ethylene linker to afford a unique chiroptical system, *trans*- and *cis*- (R_p,R_p) -1,2-bis(4-methyl-[2]paracyclo[2](5,8)quinolinophan-2-yl)ethenes (**54**) [61]. The *trans* isomer exhibited broad negative/positive Cotton effects at a longer wavelength region, which were followed by a bisignate strong Cotton effect at around 210 nm.

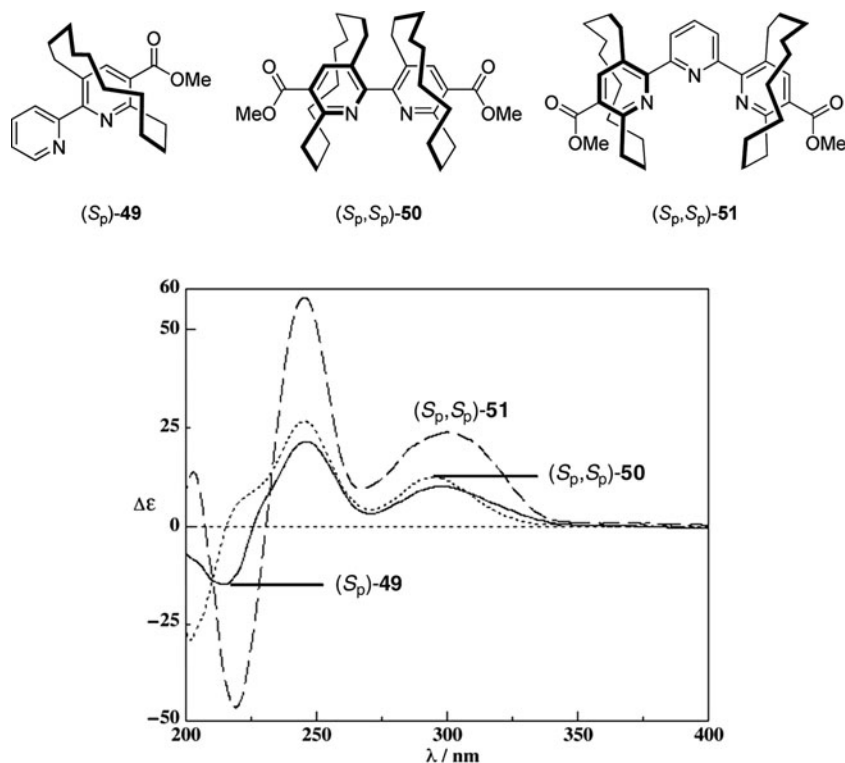


Fig. 13 CD spectra of bipyridines (S_p)-**49** and (S_p,S_p)-**50** and terpyridine (S_p,S_p)-**51**. The solvent was not reported. Reprinted with permission from [58]. Copyright © 2009 Elsevier Ltd

The CD spectrum of the *cis* isomer exhibited appreciably different Cotton effects to that of the *trans* isomer, and most of the CD signals were opposite in sign. In the high-energy region (<250 nm), where the electronic transitions of the cycloquinolinophane chromophore dominate, the Cotton effects observed were almost mirror-imaged (Fig. 15). Accordingly, the cyclophane **54** was considered as a promising chiroptical switching motif. It is also noteworthy that the fairly strong Cotton effects were reported for both *trans*- and *cis*-(R_p,R_p)-**54**, $\Delta\epsilon$ of which amount to -1200 and $+1300$ $M^{-1} \text{ cm}^{-1}$ at ~ 230 nm, respectively.

2.5 Dendrimers and Polymers Containing Cyclophanes

Polymers containing cyclophane-type moieties were also prepared for their unique functionalities and potential applications. Thus, isotactic poly(*para*-phenylene) ladder polymer (**56**) was prepared from the corresponding bromide and borate (**55**) in enantiomerically pure forms and subjected to the CD spectral measurement [62].

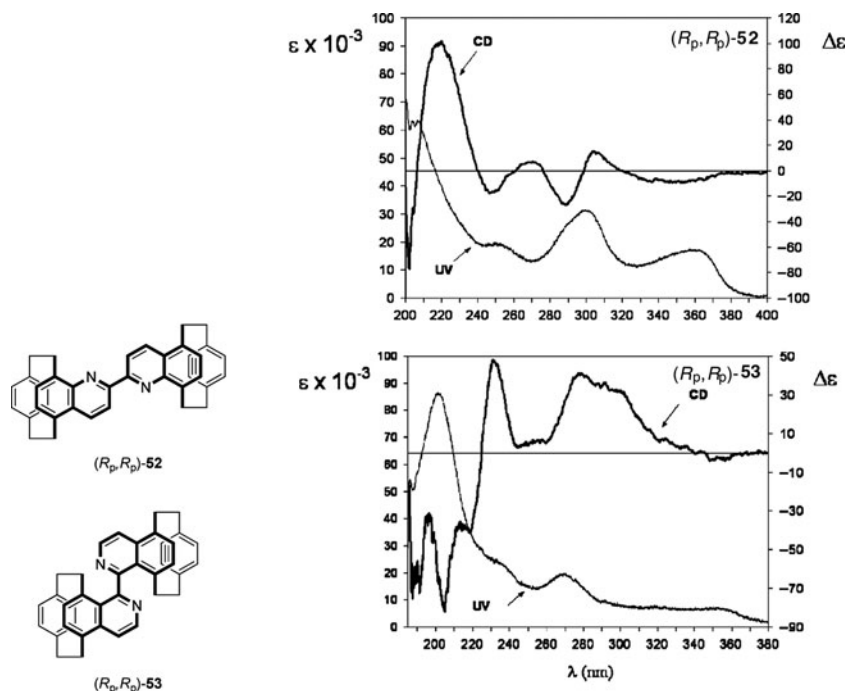


Fig. 14 UV and CD spectra of (R_p,R_p) -52 and (R_p,R_p) -53 in acetonitrile. Reprinted with permission from [59]. Copyright © 2005 American Chemical Society

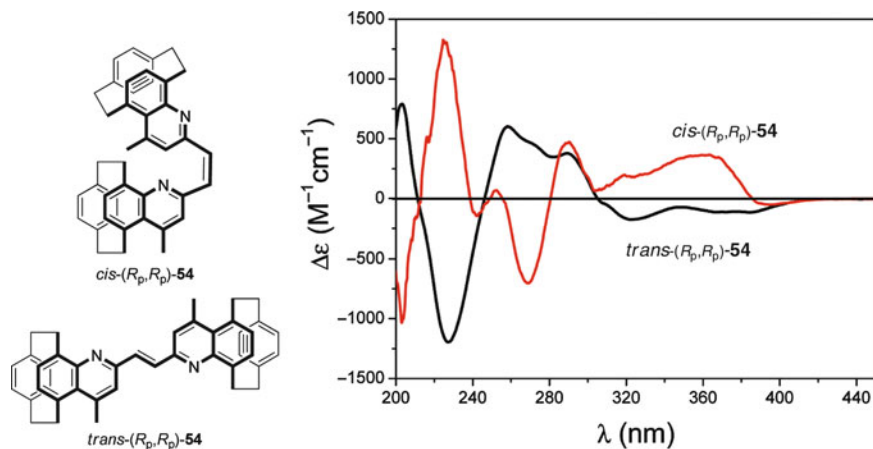
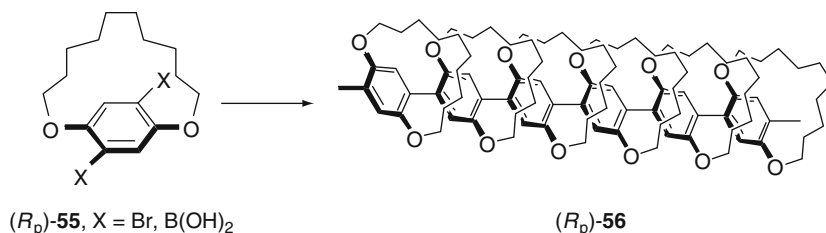
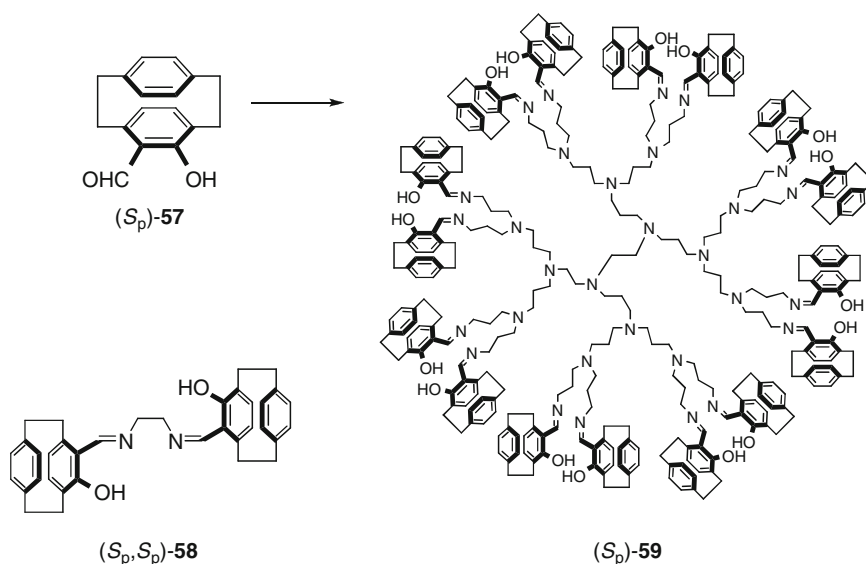


Fig. 15 CD spectra of $trans$ - and cis - (R_p,R_p) -54 in acetonitrile. Reprinted with permission from [60]. Copyright © 2009 American Chemical Society

It was shown that the polymer **56** only affords the relatively weak Cotton effects at 200–300 and 300–400 nm. The preparation and the CD spectra of related ladder polymers were also reported in this paper.



The absolute configuration of 5-formyl-4-hydroxy[2.2]paracyclophane (**57**) was assigned by a comparison of the experimental CD spectrum with the theoretical one using the MRCI calculations. The corresponding dimer or salen analog (**58**), which contains two planar chiral salicylidene units, and the dendrimers bearing up to 16 cyclophane units were prepared from chiral **57** [63]. These compounds were designed for homogeneous catalysts when complexed with metal cations. The CD spectra of the dimer **58** and dendrimer **59** were relatively weaker than the monomeric parent paracyclophane **57**, but significantly altered in the presence of transition metals.



3 Summary and Outlook

The planar chirality of cyclophanes has long been recognized as responsible for their unique chiroptical properties. The CD spectra of cyclophanes provide an additional tool for studying the electronic and magnetic interactions between two aromatic systems. Chiral cyclophanes are also exploited as promising ligands for chiral catalysts; the catalyst's ability can be predicted (at least in part) by the CD spectral examination. As can be seen in this review, the number of available CD spectra of chiral cyclophanes is, however, still quite limited. Obviously, further systematic studies are desired for better understanding the structure-chiroptical property relationship on the basis of the cyclophane architectures and wider applicability to the relevant systems. The modern quantum chemical calculations are useful not only for determining the absolute configuration but also for providing deeper insights into the chiroptical properties of closely located π systems.

The CD spectra of simple [*n*]cyclophanes and their analogs afford relatively strong Cotton effects compared to the simple arenes with point-chiral substituent(s). The [*m.n*]cyclophanes, in which two aromatic rings are stacked in a limited space, afford more complicated CD spectra, generally with higher intensities. The transitions and thus the Cotton effects are significantly coupled to each other and are accompanied by the additional "cyclophane" band. Further effects from the σ and/or *n* orbital of the (hetero)atom in the connecting chain(s) and fused or layered aromatic ring(s) also influence the overall CD spectra of the cyclophanes. The aliphatic chains in cyclophanes generally play a more dominant role in the CD spectra than the distortion of the aromatic planes. The interactions between the cyclophanes (in the connected bicyclophanes and higher homologs) also offer remarkable effects on their chiroptical properties. All of these aspects should be explored in the future study on the electronic/magnetic interaction, which may contribute to the development of novel chiroptical molecules.

Although the challenges for the preparation and the curiosity regarding the properties of [2.2]paracyclophane initiated the chemistry of cyclophanes in its early stage, this eventually led to a wealth of knowledge in the field of electronic interaction, synthesis, and catalysis. We believe that the fundamental studies on the chiroptical properties of cyclophanes, from both the experimental and theoretical viewpoints, will provide further insights into the electronic and magnetic interactions between the phanes and eventually bring us to a bright future in practical applications or devices. We hope this review will draw the reader's attention to, and encourage the studies of, seemingly simple chiral cyclophanes.

Acknowledgments T.M. thanks the Alexander von Humboldt-Stiftung for the fellowship. We thank Prof. Stefan Grimme at Universität Münster for his support at the very beginning of the calculations of CD spectra and fruitful discussion on the theoretical aspects. T.M. offers his thanks for the financial supports of this work by a Grant-in-Aid for Scientific Research (No. 21750044) from the Ministry of Education, Culture, Sports, Science and Technology (MEXT), Japan, Mitsubishi Chemical Corporation Fund, and the Sumitomo Foundation. Y.I. offers his thanks for the support of this work by a Grant-in-Aid for Scientific Research (A) from JSPS (No. 21245011).

References

1. Berova N, Bari LD, Pescitelli G (2007) Application of electronic circular dichroism in configurational and conformational analysis of organic compounds. *Chem Soc Rev* 36: 914–931
2. Cram DJ, Allinger NL (1955) Macro rings XII. Stereochemical consequences of steric compression in the smallest paracyclophane. *J Am Chem Soc* 77:6289–6294
3. Nugent MJ, Weigang OE Jr (1969) [2.2]Paracyclophane system optical activity. II. Circular dichroism of ring-substituted paracyclophanes. *J Am Chem Soc* 91:4556–4558
4. Falk H, Rbich-Rohrwig P, Schlögl K (1970) Absolute Konfiguration Unt Circulardichroismus von Aktiven [2.2]Paracyclophan-derivaten. *Tetrahedron* 26:511–527
5. Gibson SE, Knight JD (2003) [2.2]Paracyclophane derivatives in asymmetric catalysis. *Org Biomol Chem* 1:1256–1269
6. Rozenberg V, Sergeeva E, Hopf H (2004) Cyclophanes as templates in stereoselective synthesis. In: Gleiter R, Hopf H (eds) *Modern cyclophane chemistry*. Wiley-VCH, Weinheim, pp 435–462
7. Aly AA, Brown AB (2009) Asymmetric and fused heterocycles based on [2.2]paracyclophane. *Tetrahedron* 65:8055–8089
8. Grimme S, Bahlmann A (2004) Electronic circular dichroism of cyclophanes. In: Gleiter R, Hopf H (eds) *Modern cyclophane chemistry*. Wiley-VCH, Weinheim, pp 311–336
9. Vögtle F, Pawlitzki G (2002) Cyclophanes: from planar chirality and helicity to cyclochirality. In: Takemura H (ed) *Cyclophane chemistry for the 21st century*. Research Signpost, Kerala, pp 55–90
10. Grimme S, Harren J, Sobanski A, Vögtle F (1998) Structure/chiroptics relationships of planar chiral and helical molecules. *Eur J Org Chem* 1491–1509
11. Mukhopadhyay P, Wipf P, Beratan DN (2009) Optical signatures of molecular dissymmetry: combining theory with experiments to address stereochemical puzzles. *Acc Chem Res* 42:809–819
12. Stephens PJ, Devlin FJ, Pan J-J (2008) The determination of the absolute configurations of chiral molecules using vibrational circular dichroism (VCD) spectroscopy. *Chirality* 20:643–663
13. Freedman TB, Cao X, Dukor RK, Nafie LA (2003) Absolute configuration determination of chiral molecules in the solution state using vibrational circular dichroism. *Chirality* 15:743–758
14. Furo T, Mori T, Origane Y, Wada T, Izumi H, Inoue Y (2006) Absolute configuration determination of donor-acceptor [2.2]paracyclophanes by comparison of theoretical and experimental vibrational circular dichroism spectra. *Chirality* 18:205–211
15. Abbate S, Castiglioni E, Gangemi F, Longhi G, Ruzziconi R, Spizzichino S (2007) Harmonic and anharmonic features of IR and NIR absorption and VCD spectra of chiral 4-X-[2.2]paracyclophanes. *J Phys Chem A* 111:7031–7040
16. Allinger NL, Sprague JT, Liljefors T (1974) Conformational analysis. CIV. Structures, energies, and electronic absorption spectra of the [*n*]paracyclophanes. *J Am Chem Soc* 96:5100–5104
17. Tochtermann W, Vagt W, Snatzke G (1985) Synthese mittlerer und großer Ringe, X. (+)- und (-)-[6]Paracyclophan-8-carbonsäure aus (+)- und (-)-3,6-Hexanooxepin-4-carbonsäure. *Chem Ber* 118:1996–2010
18. Tochtermann W, Olsson G, Mannschreck A, Stühler G, Snatzke G (1990) Synthese mittlerer und großer Ringe, XXVII. Chromatographische Enantiomerentrennung von 3,6-Heptanophthalid – ein Beitrag zur Frage der absoluten Konfiguration von [*n*]Paracyclophancarbon-säuren. *Chem Ber* 123:1437–1439
19. Grimme S, Pischel I, Laufenberg S, Vögtle F (1998) Synthesis, structure, and chiroptical properties of the first 4-oxa[7]paracyclophane. *Chirality* 10:147–153
20. Nehira T, Soutome T, Harada N (2000) Circular dichroism and absolute stereochemistry of [8] paracyclophane-10-carbonitrile and related compounds. *Enantiomer* 5:139–144

21. Eberhardt H, Schlögl K (1972) Darstellung, chiroptische Eigenschaften und absolute Konfiguration von Derivaten des [10]Paracyclophans. *Liebigs Ann Chem* 760:157–170
22. Ishida Y, Iwasa E, Matsuoka Y, Miyauchi H, Saigo K (2009) An enantiopure cyclophane-type imidazole with no central but planar chirality. *Chem Commun* 3401–3403
23. Kanomata N, Ochiai Y (2001) Stereocontrol of molecular jump-rope: crystallization-induced asymmetric transformation of planar-chiral cyclophanes. *Tetrahedron Lett* 42:1045–1048
24. Yamamoto K, Nakazaki M (1974) The absolute configuration of [8][8], [8][10]paracyclophanes and related paracyclophane compounds. *Chem Lett* 1051–1054
25. Pischel I, Nieger M, Archut A, Vögtle F (1996) Chiral dithia[n]paracyclophanes – synthesis, crystal structure, and chiroptical properties. *Tetrahedron* 52:10043–10052
26. Grimme S, Pischel I, Vögtle F, Niegers M (1995) Experimental and theoretical study of dithia [n]metacyclophanes: syntheses, chiroptical properties, and conformational analysis. *J Am Chem Soc* 117:157–162
27. Rademacher P (2004) UV/Vis spectra of cyclophanes. In: Gleiter R, Hopf H (eds) *Modern cyclophane chemistry*. Wiley-VCH, Weinheim, pp 275–310
28. Gleiter R (1969) Consequences of σ - π -interaction in [2.2]-paracyclophane. *Tetrahedron Lett* 10:4453–4456
29. Rosini C, Ruzziconi R, Superchi S, Fringuelli F, Piematti O (1998) Circular dichroism spectra (350–185 nm) of a new series of 4-substituted [2.2]paracyclophanes: a quantitative analysis within the DeVoe polarizability model. *Tetrahedron Asymmetry* 9:55–62
30. Abbate S, Lebon F, Gangemi R, Longhi G, Spizzichino S, Ruzziconi R (2009) Electronic and vibrational circular dichroism spectra of chiral 4-X-[2.2]paracyclophanes with X containing fluorine atoms. *J Phys Chem A* 113:14851–14859
31. Wörsdörfer U, Vögtle F, Nieger M, Waletzke M, Grimme S, Glorius F, Pfaltz A (1999) A new planar chiral bipyridine ligand. *Synthesis* 597–602
32. Weigang OE Jr, Nugent MJ (1969) [2.2]Paracyclophane system optical activity. I. Theory. *J Am Chem Soc* 91:4555–4556
33. Mori T, Inoue Y, Grimme S (2007) Quantum chemical study on the circular dichroism spectra and specific rotation of donor-acceptor cyclophanes. *J Phys Chem A* 111:7995–8006
34. Staab HA (1989) New aspects of organic charge-transfer compounds: syntheses, structures and solid-state properties. In: Yoshida Z, Shiba T, Oshiro Y (eds) *New aspects of organic chemistry I*. VCH, Weinheim, pp 227–236
35. Furo T, Mori T, Wada T, Inoue Y (2005) Absolute configuration of Chiral [2.2]paracyclophanes with intramolecular charge-transfer interaction. Failure of the exciton chirality method and use of the sector rule applied to the cotton effect of the CT transition. *J Am Chem Soc* 127:7995–8006 and 1638
36. Warnke I, Ay S, Bräse S, Furche F (2009) Chiral cooperativity and solvent-induced tautomerism effects in electronic circular dichroism spectra of [2.2]paracyclophane ketimines. *J Phys Chem A* 113:6987–6993
37. Langer E, Lehner H (1973) Circular dichroismus und Elektronenanregungsspektren chiraler [2, 2]Metacyclophane. *Monatsh Chem* 104:644–653
38. Grimme S, Peyerimhoff SD, Bartram S, Vögtle F, Breest A, Hormes J (1993) Experimental and theoretical study of the circular dichroism spectra of oxa- and thia-[2.2]metacyclophane. *Chem Phys Lett* 213:32–40
39. Muller D, Nieger M, Vögtle F (1994) The first [2.2]cyclophane with free N-H in the bridge. *J Chem Soc Chem Commun* 1361–1362
40. Wortmann-Saleh D, Grimme S, Engels B, Müller D, Vögtle F (1995) A study of the N-inversion barrier and the circular dichroism spectra of 1-thia-10-aza[2.2]metacyclophane. *J Chem Soc Perkin Trans 2* 1185–1189
41. Vögtle F, Ostrowicki A, Begemann B, Jansen M, Nieger M, Niecke E (1990) Chirale dreilagige und kondensierte [2.2]Cyclophane. Synthese, Struktur, Chiroptik. *Chem Ber* 123:169–176

42. Schulz J, Bartram S, Nieger M, Vögtle F (1992) Tricarbonylchrom-Komplexe von chiralen [2.2]Metacyclophanen: Darstellung, Struktur und chiroptische Eigenschaften. *Chem Ber* 125:2553–2569
43. Grimme S, Mennicke W, Vögtle F, Nieger M (1999) Experimental and theoretical studies of a chiral azulenophane: synthesis, structure and circular dichroism spectra of 14,17-dimethyl[2](1,3)azulenol[2]paracyclophane. *J Chem Soc Perkin Trans 2*:521–528
44. Goerigk L, Grimme S (2009) Calculation of electronic circular dichroism spectra with time-dependent double-hybrid density functional theory. *J Phys Chem A* 113:767–776
45. Niederal C, Grimme S, Peyerimhoff SD, Sobanski A, Vögtle A, Lutz M, Spek AL, Eis MJ, Wolf WH, Bickelhaupt F (1999) Chiroptical properties of 12,15-dichloro[3.0]orthometacyclophane – correlations between molecular structure and circular dichroism spectra of a biphenylophane. *Tetrahedron Asymmetry* 10:2153–2164
46. Mori T, Inoue Y, Grimme S (2007) Experimental and theoretical study of the CD spectra and conformational properties of axially chiral 2,2'-, 3,3'-, and 4,4'-biphenol ethers. *J Phys Chem A* 111:4222–4234
47. Haenel MW, Staab HA (1973) Transannulare Wechselwirkungen bei [2.2]Phanen, III. [2,2](2,6)Naphthalinophan und [2.2](2,6)Naphthalinophan-1,11-dien. *Chem Ber* 106:2203–2216
48. Haenel MW (1978) Transannulare Wechselwirkungen bei [2.2]Phanen, XI. Chirales und achirales [2,2](1,5)Naphthalinophan. *Chem Ber* 111:1789–1797
49. Laufenberg S, Feuerbacher N, Pischel S, Borsch O, Nieger M, Vögtle F (1997) New biphenylophanes and biphenylophanes – 1,8-dimethylbiphenylene by continuous vacuum pyrolysis. *Liebigs Ann* 1901–1906
50. Nakazaki M, Yamamoto K, Maeda M (1981) Preparation of (–)-(M)-[2.2]paracyclophano-hexahelicene from (–)-(M)-1,4-dimethylhexahelicene and the absolute configuration of 4-substituted [2.2]paracyclophanes. *J Org Chem* 46:1985–1987
51. Gabutti S, Schaffner S, Neuburger M, Fischer M, Schäfer G, Mayor M (2009) Planar chiral asymmetric naphthalenediimide cyclophanes: synthesis, characterization and tunable FRET properties. *Org Biomol Chem* 7:3222–3229
52. Misumi S, Otsubo T (1978) Chemistry of multilayered cyclophanes. *Acc Chem Res* 11:251–256
53. Otsubo T, Mizogami S, Otsubo I, Tozuka Z, Sakagami A, Sakata Y, Misumi S (1973) Layered compounds XV. Synthesis and properties of multilayered cyclophanes. *Bull Chem Soc Jpn* 46:3519–3530
54. Nakazaki M, Yamamoto K, Tanaka S, Kametani H (1977) Syntheses of the optically active multilayered [2.2]paracyclophanes with known absolute configurations. *J Org Chem* 42:287–291
55. Muranaka A, Shibahara M, Watanabe M, Matsumoto T, Shinmyozu T, Kobayashi N (2008) Optical resolution, absolute configuration, and chiroptical properties of three-layered [3.3]paracyclophane. *J Org Chem* 73:9125–9128
56. Harren J, Sobanski A, Nieger M, Yamamoto C, Okamoto Y, Vögtle F (1998) A triple layered helical chiral cyclophane – one-pot synthesis, enantiomer separation and chiroptical properties. *Tetrahedron Asymmetry* 9:1369–1375
57. Tochtermann W, Kuckling D, Meints C, Kraus J, Bringmann G (2003) Bridged bioxepines and bi[10]paracyclophanes – synthesis and absolute configuration of a bi[10]paracyclophane with two chiral planes and one chiral axis. *Tetrahedron* 59:7791–7801
58. Kanomata N, Mishima G, Onozato J (2009) Synchronized stereocontrol of planar chirality by crystallization-induced asymmetric transformation. *Tetrahedron Lett* 50:409–412
59. Kanomata N, Suzuki J, Kubota H, Nishimura K, Enomoto T (2009) Synthesis of planar-chiral bridged bipyridines and terpyridines by metal-mediated coupling reactions of pyridinophanes. *Tetrahedron Lett* 50:2740–2743
60. Ricci G, Ruzziconi R, Giorgio E (2005) Atropisomeric (R, R)-2,2'-bi([2]paracyclo[2](5,8)quinolinophane) and (R, R)-1,1'-bi([2]paracyclo[2](5,8)isoquinolinophane): synthesis, structural analysis, and chiroptical properties. *J Org Chem* 70:1011–1018

61. Gentili PL, Bussotti L, Ruzziconi R, Spizzichino S, Foggi P (2009) Study of the photobehavior of a newly synthesized chiroptical molecule: (E)-(Rp,Rp)-1,2-Bis{4-methyl-[2]paracyclo[2](5,8)quinolinophan-2-yl}ethane. *J Phys Chem A* 113:14650–14656
62. Fiesel R, Hubel J, Apel U, Enkelmann V, Hentschke R, Scherf U, Cabrera K (1997) Novel chiral poly(para-phenylene) derivatives containing cyclophane-type moieties. *Macromol Chem Phys* 198:2623–2650
63. Issberner J, Böhme M, Grimme S, Neiger M, Paulus W, Vögtle F (1996) Dendrimers bearing planar chiral terminal groups – synthesis and chiroptical properties. *Tetrahedron Asymmetry* 7:2223–2232

G-C Content Independent Long-Range Charge Transfer Through DNA

Kiyohiko Kawai and Tetsuro Majima

Abstract The interest in DNA as a building block for nano-electric sensors and devices stemmed from the ability to construct various nanometer-sized two and three-dimensional structures and its amazing positive charge conducting properties. However, since a positive charge migrates along DNA through the HOMO of G-C base-pairs, the conductivity of DNA strongly decreases with the increasing A-T base-pair content hampering the construction of nano-electric circuits in which the use of various sequence patterns is indispensable. In this chapter, we demonstrated that the charge transfer efficiency can be drastically increased in a G-C content independent manner by adjusting the HOMO-level of the A-T base-pair closer to that of the G-C base-pair. This was achieved either by substituting the N7 nitrogen of A with a C-H group (deazaadenine: **Z**) or substituting C2 hydrogen with an amino group (diaminopurine: **D**). Since **Z** and **D** selectively pair with T without significantly perturbing the thermo-stability of the duplex, **Z** and **D** can be used to increase the charge transfer efficiency through DNA while properly maintaining the sequence information carried by DNA.

Keywords Charge transfer, DNA, Electron transfer, HOMO-level

Contents

1	Introduction	130
2	Sequence Dependence of Charge Transfer Rate Through DNA	131
2.1	Method for the Measurement of Charge Transfer Rate in DNA	131
2.2	Sequence Dependence of Charge Transfer Rate Between G-C Base-Pairs	133
3	Sequence Independent and Rapid Long-Range Charge Transfer Through DNA	134
3.1	Replacing Adenine with 7-Deazaadenine (Z)	134

T. Majima (✉) and K. Kawai (✉)
The Institute of Scientific and Industrial Research (SANKEN), Osaka University, Mihogaoka 8–1,
Ibaraki, Osaka 567–0047, Japan
e-mail: majima@sanken.osaka-u.ac.jp; kiyohiko@sanken.osaka-u.ac.jp

3.2	Replacing Adenine with Diaminopurine (D)	137
3.3	Comparison Between Z and D	138
4	Distinguish Between Matched and Mismatched Sequences by Measuring the Charge Transfer Rate Constant Through DNA	139
5	Conclusions	140
	References	141

1 Introduction

DNA consists of four nucleobases, guanine (G), adenine (A), cytosine (C), and thymine (T). Since G selectively pairs with C and so does A with T, DNA can be considered to be constructed by two building blocks, A-T and G-C base-pairs. By programming the sequences of these two building blocks, DNA can be used to form self-assembled nano-structures like cubes as well as two-dimensional molecular sheets [1–3]. The self-assembly of hundreds of well-designed oligonucleotides, so-called DNA origami method, recently made it possible to construct complex surface structures such as smiley faces and a map of north and south Americas [4]. Using the DNA origami method, various two-dimensional and three-dimensional scaffolds for arranging functional molecules have been developed [5–8]. Thus DNA has the potential as a bottom-up material for nano-templates and nano-machines. In particular, the finding that a positive charge (a hole) generated in DNA migrates along DNA over long distances has made it an interesting molecule for the design of nano-electronic sensors and devices [9–14].

A model of a series of the short-range charge transfer processes between G-C base-pairs which have relatively high HOMO-level, i.e., lower oxidation potential than A-T base-pair [15, 16], is the most widely adopted to describe the long-range charge transfer process through DNA [17–25]. Extending of charge delocalized domains over several bases [26, 27] or the formation of the polaron [28–30] during the charge transfer through DNA was also reported by several researchers. The efficiency of the charge transfer through DNA was evaluated by measuring the charge transfer rate. The kinetics of the charge transfer process in DNA was first reported by Lewis and Wasielewski et al., who determined the kinetics of the single-step short-distance charge transfer between G-C base-pairs across A-T base-pair [20, 22, 31]. We have established the method for the observation of the long-range charge transfer through DNA via multistep charge transfer processes and determined the rate constants of the charge transfer through various sequence patterns [23–25]. The charge transfer rate was strongly dependent on the sequence of DNA. Although it was experimentally [32] and theoretically [33, 34] demonstrated that a charge can migrate over long A-T tract sequences between G-C base-pairs via a thermally-induced hopping mechanism, the charge transfer rate sharply decreased with the insertion of a few A-T base-pairs between the G-C base-pairs. For example, the insertion of the three A-T base-pairs between the G-C base-pairs

resulted in a greater than three orders of magnitude decrease in the charge transfer rate [24]. Consistent with the kinetic measurements, Xu and coworkers reported that the conductance decreases exponentially by inserting A-T base-pairs into G-C repeat domains [10, 11]. This is because a positive charge is mainly carried by G-C base-pairs having relatively high HOMO-level and the charge transfer rate between G-C base-pairs strongly depends on the distance or the number of intervening A-T base-pair between G-C base-pairs. As a consequence, the conductivity of the DNA strongly depends on the G-C content and the charge transfer rate becomes insufficiently fast to compete fully with the oxidative degradation of DNA in the presence of A-T base-pairs. A high conductivity was only achieved for the DNA consists solely of G-C base-pairs. This make it difficult to construct the desired DNA nano-electronic sensors and devices in which the use of the various sequence patterns is necessary [14]. By adjusting the HOMO-level of the A-T base-pair closer to that of the G-C base-pair, it would be possible to attain a high conductivity in a G-C content independent manner. In this chapter, we will overview our strategy for increasing the charge transfer efficiency through DNA in a G-C content independent manner, which is based on the increase of the HOMO-level of the A-T base-pair to be closer to that of the G-C base-pair. We also describe our efforts in reading out the sequence information about single nucleotide polymorphisms (SNPs) by measurement of the charge transfer rates through DNA with increased charge transfer efficiency.

2 Sequence Dependence of Charge Transfer Rate Through DNA

2.1 Method for the Measurement of Charge Transfer Rate in DNA

The charge transfer rate through DNA was measured by monitoring the rate that a positive charge traveled from a photosensitizer at one end of the DNA to a charge acceptor at the other end. Transient absorption measurements during the 355-nm laser flash photolysis were employed to investigate the kinetics of the charge transfer process through DNA (Fig. 1). We used naphthalimide (NI) [35, 36] as a photosensitizer to inject a charge into DNA upon the laser flash excitation [23–25, 37–42]. NI was attached to A-stretch sequences, and the irradiation of the NI-site with a 355-nm laser flash triggers the electron transfer between NI in the singlet excited state and adjacent A to give NI radical anion ($\text{NI}^{\bullet-}$) and A radical cation ($\text{A}^{\bullet+}$), respectively. Previously we have demonstrated that the charge transfer between adjacent As proceeds with a rate constant of $>10^9 \text{ s}^{-1}$ and can compete with the charge recombination to produce a long-lived charge-separated state [37]. That is, a part of a charge escapes from the initial charge recombination process between $\text{NI}^{\bullet-}$ and $\text{A}^{\bullet+}$ via rapid sequential charge transfer between As, resulting in the charge trapping at G. Once a charge resides on G, the charge recombination

DNA to the other end can be monitored by the formation of the $\text{PTZ}^{\bullet+}$ with a peak at around 520 nm (Fig. 1) [23–25, 40–44] during the laser flash photolysis measurement. The rate constants of each individual charge transfer steps between G-C base-pairs (k_{ht}) were determined from kinetic modeling. Analysis of time profiles of formation of $\text{PTZ}^{\bullet+}$ via the multistep charge-transfer mechanism was performed with numerical analysis by using Matlab software [25].

2.2 Sequence Dependence of Charge Transfer Rate Between G-C Base-Pairs

The charge transfer through G-C repeat sequences proceeded rapidly, and a kinetic analysis for $(\text{GC})_n$ ($n = 5, 7, 9$) provided a k_{ht} value of $2.2 \times 10^8 \text{ s}^{-1}$ for the charge transfer rate between adjacent G-C base-pairs [25] (G-C/G, Table 1). In order to investigate the effect of intervening A-T base-pairs on the charge transfer rate through DNA, k_{ht} through various intervening A-T base-pairs were measured. When A-T base-pairs were inserted between two G-C base-pairs (G-A_n-G ($n = 1-3$)), the k_{ht} decreased with the increase of the distance between G-C base-pairs, demonstrating that each charge transfer process between G-C base-pairs proceeds by a single-step super-exchange mechanism. Similarly, a significant decrease in k_{ht} with the increase of the distance between G-C base-pairs was observed for G-T_n-G, G-T_n-C, and G-A_n-C sequences (Table 1). These results showed that the charge transfer between G-C base-pairs proceeds by the single-step super-exchange mechanism and the long-range charge transfer proceeds as a consequence of multistep charge transfer processes between G-C base-pairs.

Xu and coworkers measured the conductance for GC repeat sequences by using direct electrical measurements where the conductance decreases exponentially by inserting A-T base-pairs into GC repeat domains [10, 11]. Our results are consistent with the conductance measurements reported by Xu and coworkers, showing that a charge is mainly carried by G-C base-pairs having relatively high HOMO-level and the charge transfer rate between G-C base-pairs strongly depends on the distance or the number of intervening A-T base-pair between G-C base-pairs.

Table 1 Rate constants for charge transfer between G-C base-pairs (k_{ht})

Sequence	$k_{\text{ht}} (\text{s}^{-1})^a$
G-C/G	2.2×10^8
G-A-G	4.8×10^7
G-AA-G	9.7×10^4
G-AAA-G	1.4×10^4
G-T-G	4.6×10^5
G-TT-G	3.6×10^4
G-TTT-G	9.1×10^3

^aRate constants were obtained from the reported values [24, 25]

It was experimentally [32] and theoretically [33, 34] demonstrated that it is possible for a charge to migrate over long A-T tract sequences between G-C base-pairs via a thermally-induced hopping mechanism. However, a high conductivity can only be achieved for the G-C repeat sequences hampering the construction of DNA nano-electric sensors and devices in which the use of various sequence patterns is indispensable [14].

3 Sequence Independent and Rapid Long-Range Charge Transfer Through DNA

The kinetic measurement of the charge transfer in DNA showed that a positive charge migrates through the HOMO of G-C base-pairs and that the presence of A-T base-pairs significantly decreases the charge transfer efficiency. In addition, a charge was demonstrated to migrate rapidly through A-T repeat sequences before a charge is trapped at G-C base-pairs [40]. These results showed that a charge efficiently migrates through the base-pairs of the same HOMO-levels, suggesting that a high conductivity may be attained in a G-C content independent manner by adjusting the HOMO-level of the A-T base-pair closer to that of the G-C base-pair. In order to adjust the HOMO-level of the A-T base-pairs closer to that of the G-C base-pairs, we replaced A with 7-deazaadenine (**Z**) or diaminopurine (**D**).

3.1 Replacing Adenine with 7-Deazaadenine (**Z**)

Z is an analog of A in which the single nitrogen atom of the purine ring is replaced by a C-H group and selectively pairs with T without significantly perturbing the thermo-stability of the duplex (Fig. 2) [47]. Thus, **Z** would be used to construct various DNA nanostructures by maintaining the sequence information of DNA. **Z** has a higher HOMO-level closer to those of G-C base-pairs than of A-T base-pairs. Based on the gel electrophoresis strand cleavage experiments, Nakatani and Saito reported that **Z**-T base-pair in an A-T tract serves as a stepping stone for a positive charge to transfer between two GGG sites [48, 49]. The enhancement of the charge transfer efficiency between two G-C base-pairs upon changing the intervening A-T base-pair to the **Z**-T base-pair was also supported theoretically. Voityuk and Roesch reported that **Z**-T base-pair increases the super-exchange charge transfer efficiency between two G-C base-pairs [50]. Bixon and Jortner demonstrated that a **Z**-T base-pair contribute in the sequential charge transfer process [33].

We first tested whether the charge can go through A-T tract sequences with the assistance of **D**-T base-pairs. In the case of **a0**, no formation of $\text{PTZ}^{\bullet+}$ was observed in the present experimental time window of 200 μs due to the slow charge transfer across the five consecutive A-T base-pairs ($\tau > 100 \mu\text{s}$) [24, 32]. Interestingly, by

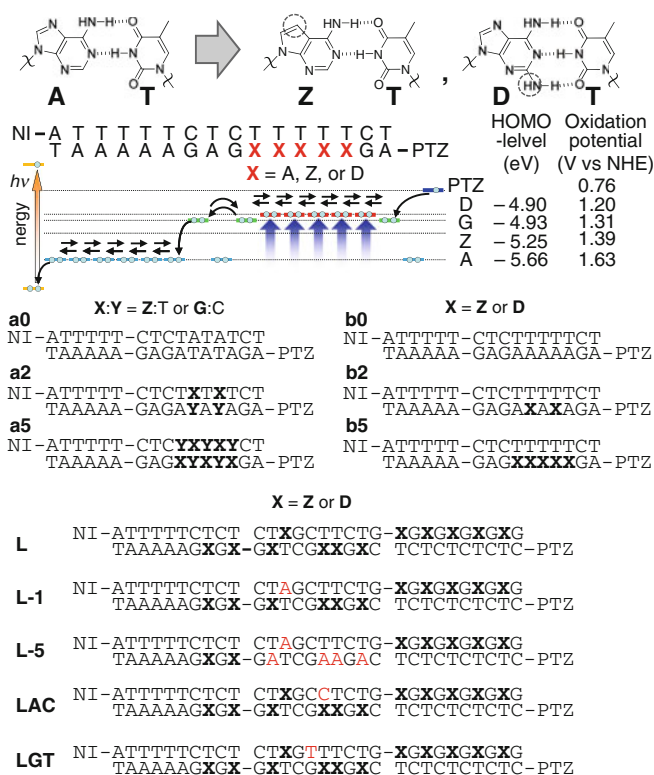


Fig. 2 Long-distance charge transfer through DNA by replacing A-T base-pairs with **Z**-T or **D**-T base-pairs

replacing the A-T base-pairs with **Z**-T base-pairs, an absorption at 520 nm assigned to $\text{PTZ}^{\bullet+}$ emerged upon the charge transfer through DNA along with the immediate formation of the NI radical anion ($\text{NI}^{\bullet-}$) with a peak at 400 nm (Fig. 3). The charge transfer rate dramatically increased with the increasing number of replaced **Z**-T base-pairs (**a2** and **a5** ($X = Z$), Fig. 3a, Table 2). We also investigated the charge-transfer process for a series of DNAs in which the A-T base-pairs in the A-T tract were systematically changed to the G-C base-pairs (**a2**, **a5** ($X = G$), Table 2). Similar to the results observed for DNA replaced with the **Z**-T base-pairs, the replacement of the A-T base-pairs in the A-T tract to the G-C base-pairs resulted in an increase in the charge transfer rate in DNA (Table 2). Interestingly, the charge moved faster through the DNA replaced with **Z**-T than those through the corresponding DNA replaced with the G-C base-pairs, showing that the **Z**-T base-pairs can also serve as charge carriers similar to or even better than the G-C base-pairs. The slower charge transfer rate observed for DNA replaced with G-C base-pairs may be partly explained by the tendency of a charge to localize at the **GG** site as reported by Saito and Sugiyama [51–53]. These results clearly demonstrated that a high charge transfer efficiency through DNA can be achieved in a G-C content

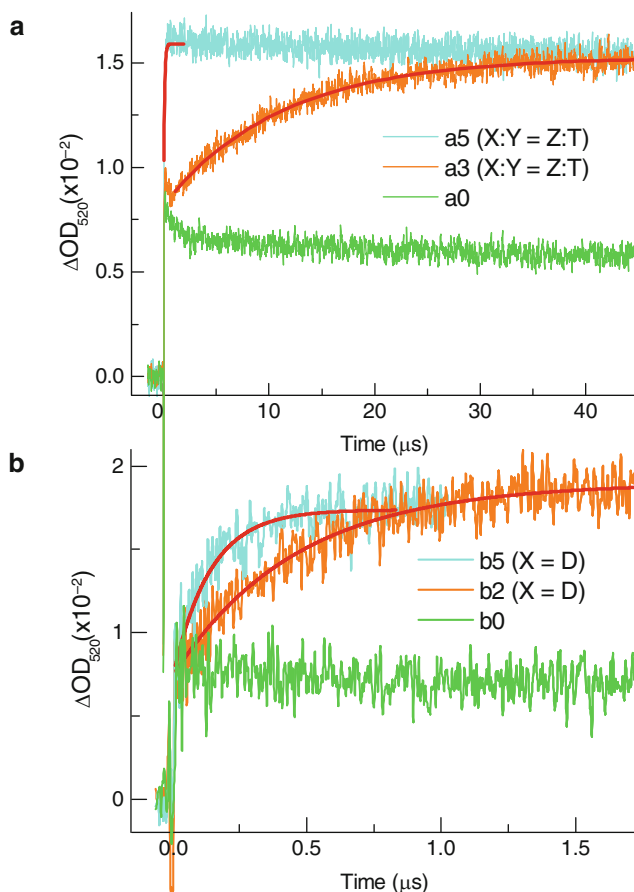


Fig. 3 Time profiles of the transient absorption of PTZ^{•+} monitored at 520 nm during the 355-nm laser flash photolysis of (a) DNA **a0**, **a2** and **a5** (X = Z), and (b) **b0**, **b2**, and **b5** (X = D). The smoothed red curves superimposed on the experimental data are the single exponential fit from which the charge transfer rate through DNA ($1/\tau$) was determined. The sample aqueous solution contained 80 μM DNA and 100 mM NaCl in 10 mM Na phosphate buffer (pH 7.0) purged with Ar

independent manner by replacing the A-T base-pair with the Z-T base-pair. It is also noteworthy that G and Z in both strands increases the charge transfer rate through DNA, showing that a charge migrates through DNA in both an intrastrand and interstrand manner and that the HOMO-level of both strands of the duplex contributes to the charge transfer efficiency through DNA.

We next investigated the charge transfer through the A-repeat sequences in which the charge transfer efficiency was expected to increase due to the direct stacking between purine bases. Similarly, the formation of PTZ^{•+} was not observed for **b0**, and the charge transfer rate increased with the increasing number of Z, and in the case of **b5** (X = Z), in which all the A-T base-pairs in the A-tract was replaced with Z, the charge transfer was accomplished faster than the time resolution

Table 2 Time constants (τ) and rate constants (k_{ht}) for charge transfer through DNA (k_{ht})

DNA	X	τ (μs) ^a	k_{ht} (s^{-1}) ^a
a0	–	>200	$<5 \times 10^3$
a2	Z	12	8.3×10^4
	G	15	6.7×10^4
a5	Z	0.09	1×10^7
	G	0.22	4.6×10^6
b0	–	>200	$<5 \times 10^3$
b2	Z	0.22	4.5×10^6
	D	0.46	2.2×10^6
b5	Z	<0.05	$>2 \times 10^7$
	D	0.14	6.9×10^6
L	Z	0.45	2.2×10^6
	D	11	9.1×10^4
L-1	Z	32	3.1×10^4
	D	110	9.1×10^3
L-5	Z or D	>200	$<5 \times 10^3$
LAC	Z	45	2.2×10^4
	D	59	1.7×10^4
LGT	Z	41	2.4×10^4
	D	110	8.7×10^3

^aThe charge transfer rate through DNA ($1/\tau$) was determined from the single exponential fit of the time profile of the formation of PTZ^{*+} . While it may be inappropriate to analyze the data with single exponential fitting because long-range charge transfer occurs through multistep processes, simple analysis based on single exponential fitting was applied to evaluate approximately the observed long-range charge transfer process. Rate constants were obtained from the reported values [54, 55]

of our experimental setup ($\tau < 50$ ns) (Fig. 3a). Amazingly, the charge transfer rate increased more than three orders of magnitude by merely replacing the N7 nitrogen atom of A with a C-H group.

The charge transfer efficiency through DNA was investigated for DNA with a G-C and A-T mixed random 30-mer sequence longer than 100 Å. Of special interest, the charge transfer occurred as fast as $\tau = 0.45$ μs over 100 Å by replacing the A-T base-pairs with the **Z**-T base-pairs (Fig. 4a, Table 2, **L** (**X = Z**)). The charge transfer rate significantly decreased by converting one **Z**-T base-pair to an A-T base-pair (**L-1** (**X = Z**)) and the charge transfer become too slow to be observed by converting five **Z**-T base-pairs to A-T base-pairs (**L-5** (**X = Z**); $\tau > 100$ μs), showing that a rapid charge transfer through a mixed DNA sequence can be only achieved by replacing the A-T base-pair with the **Z**-T base-pair.

3.2 Replacing Adenine with Diaminopurine (D)

The HOMO-level of **D**-T base-pair was calculated by Nakatani and Saito to be very close to that of G-C [48]; we therefore considered it to be a potential candidate as a charge carrier in DNA [33, 34]. Similar to the strategy for DNA replaced

with **Z-T** base-pairs, we tested whether the charge can go through A-repeat sequences by replacing A-T base-pairs with **D-T** base-pairs [54]. While the formation of $\text{PTZ}^{\bullet+}$ was not observed for **b0** due to the slow charge transfer across the five consecutive A-T base-pairs [24, 55], an absorption at 520 nm assigned to $\text{PTZ}^{\bullet+}$ emerged upon the charge transfer through DNA by replacing the A-T base-pairs in the A-repeat sequences to **D-T** (Fig. 3b, **b2**, **b5** ($\mathbf{X} = \mathbf{D}$)). The charge transfer rate dramatically increased with the increasing number of replaced **D-T** base-pairs. Interestingly, the charge transfer rate increased more than three orders of magnitude by replacing all the A-T base-pairs in the A-tract with **D-T** base-pairs (**b5** ($\mathbf{X} = \mathbf{D}$)). Though the charge moved slightly more slowly through the DNA replaced with **D-T** base-pairs than through the corresponding DNA replaced with **Z-T** base-pairs (Table 2, **b2**, **b5** ($\mathbf{X} = \mathbf{Z}$)), these results clearly demonstrate that the charge transfer efficiency through DNA can be drastically increased by merely replacing the C2 hydrogen atom of A with an amino group.

The charge transfer also occurred over 100 Å through a G-C and A-T mixed random 30-mer sequence by replacing the A-T base-pairs with **D-T** base-pairs (Fig. 4b, **L** ($\mathbf{X} = \mathbf{D}$)). Consistent with the results obtained for DNA with **Z-T** base-pairs, the charge transfer rate significantly decreased in response to converting one **D-T** base-pair to an A-T base-pair **L-1** ($\mathbf{X} = \mathbf{D}$), and the charge transfer rate became too slow to be observed by converting five **D-T** base-pairs to A-T base-pairs **L-5** ($\mathbf{X} = \mathbf{D}$), showing that a fast charge transfer through a mixed DNA sequence can only be achieved by replacing the A-T base-pairs with either **Z-T** or **D-T** base-pairs.

3.3 Comparison Between **Z** and **D**

In the case of the long-distance charge transfer process through G-C and A-T mixed random sequence, the charge transfer rate was approximately 20 times slower for DNA in which A-T base-pairs were replaced with **D-T** base-pairs than that of the corresponding DNA replaced with the **Z-T** base-pairs (Table 2, **L** ($\mathbf{X} = \mathbf{Z}$ vs \mathbf{D})). Although the theoretical calculation suggested the smaller HOMO energy difference between **D-T** and G-C base-pairs than that between **Z-T** and G-C base-pairs, the experimentally derived difference of oxidation potential between **D** and G was much higher than that between **Z** and G [48]. Thus, the actual HOMO energy difference between **D-T** and G-C base-pairs may be higher than that between **Z-T** and G-C base-pairs, resulting in the slower charge transfer rate through DNA replaced with **D-T** base-pairs.

The slower charge transfer rate observed for DNA with **D-T** base-pairs may also be partly explained by the charge localization at the **DD** site, similar to that seen in the GG sites [51–53], because of the higher HOMO-level of **D-T** compared with that of the G-C base-pair.

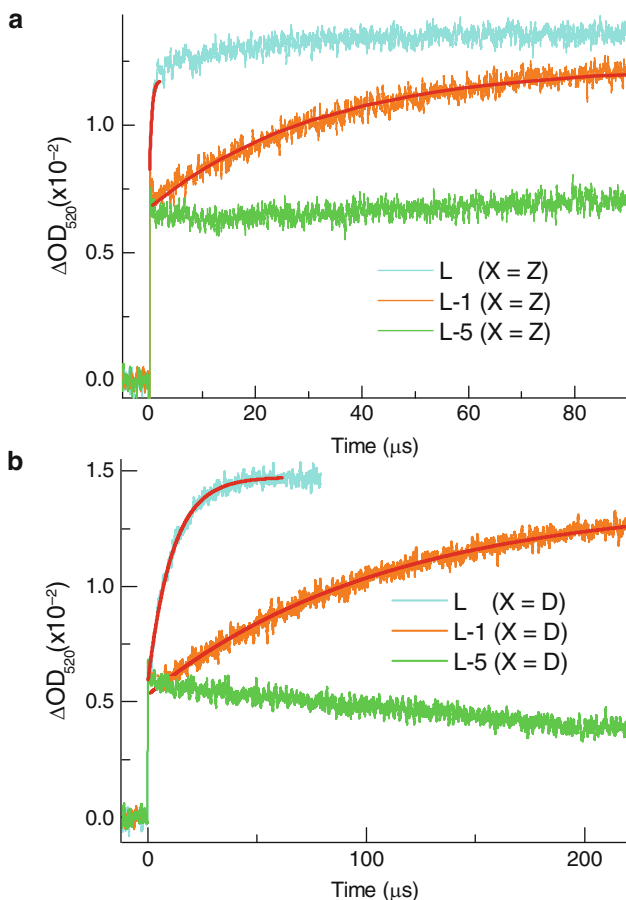


Fig. 4 Time profiles of the transient absorption of PTZ^{•+} monitored at 520 nm during the 355-nm laser flash photolysis of DNA **L**, **L-1** and **L-5** (a) ($X = Z$) and (b) $X = D$. The smoothed red curves superimposed on the experimental data are the single exponential fit from which the charge transfer rate through DNA ($1/\tau$) was determined. The sample aqueous solution contained 80 μM DNA and 100 mM NaCl in 10 mM Na phosphate buffer (pH 7.0) purged with Ar

4 Distinguish Between Matched and Mismatched Sequences by Measuring the Charge Transfer Rate Constant Through DNA

We have measured the charge transfer rate constants for various sequence patterns and it now becomes possible to estimate how fast a charge migrates along DNA of a certain sequence and length based on these rate constants [44]. In other words, this implies that DNA sequence information can be read out by measuring the charge transfer rate constants through DNA. In particular, the presence of a mismatch

causes the perturbation of the π -stacks, resulting in a decrease of charge transfer efficiency and subsequent charge separation yield, making it possible to detect SNPs by measuring the charge transfer rate constants. Indeed, electrochemical detection of the mismatched DNA which depends on the charge transfer efficiency through the π -stack of the DNA has been demonstrated by several groups [11, 44, 56–59]. Kelley and Barton et al. developed a system for the electrochemical detection of a single-base mismatch based on charge transfer through DNA films [60]. They reported that the signal obtained from the redox-active intercalators bound to DNA modified on gold faces exhibits a remarkable sensitivity to the presence of a mismatch within the immobilized duplex. Okamoto and Saito et al. also developed a new SNP photoelectrochemical detection method that relied on the photoinduced charge transfer through a DNA duplex immobilized on a gold electrode [58]. They designed the DNA probes, which contain anthraquinone as a photosensitizer, and hybridized the DNA probe with the target DNA. They reported that the cathodic photocurrent signal markedly changes depending on the presence of the mismatch. However, since the charge transfer rate become too slow to be measured when A-T base-pairs are inserted between G-C base-pairs, SNPs detection was only possible for G-C rich sequences or short DNA.

In order to detect SNPs in various sequence patterns, we next investigated the effect of the mismatch on the charge transfer rate though DNA in which A-T base-pairs are replaced with either **Z**-T base-pairs or **D**-T base-pairs. The presence of an A-C mismatch (**LAC** ($X = \mathbf{Z}$, and \mathbf{D})) or G-T mismatch (**LGT** ($X = \mathbf{Z}$, and \mathbf{D})) in the DNA caused a considerable decrease in the charge transfer rate (Table 2). The charge transfer rate constants obtained for the DNA with a mismatch were on the same order for DNA with **Z**-T and the **D**-T base-pairs, showing that the charge transfer across the mismatch is the major rate-determining step in these DNAs and that it likely reflects the disorder of the DNA π -stack structure caused by the mismatch [44, 56–58, 60–63]. These results clearly show that it is possible to distinguish between matched and mismatched sequences by measurement of their charge transfer rates through DNA in which A-T base-pairs are replaced with either **Z**-T or **D**-T base-pairs. SNP detection requires polymerase chain reaction (PCR) amplification of the genomic region that flanks the SNP site. In particular, while **Z** containing DNA can only be amplified for a specific sequence [64] or in the presence of dATP [65, 66] during the PCR, **D** can fully replace A during PCR [67] and thus would make it possible to detect SNPs in various sequence contexts.

5 Conclusions

In this chapter we have described our approach for increasing the charge transfer efficiency through DNA in a G-C content independent manner which was achieved by adjusting the HOMO-level of the A-T base-pairs closer to that of the G-C base-pairs. The presence of a single mismatch significantly affected the charge transfer rate though DNA in which A-T base-pairs are replaced with either **Z**-T base-pairs or

D-T base-pairs to increase the charge efficiency. Since **D** can fully replace A during PCR, **D** offers us an additional choice in constructing DNA with increased charge transfer efficiency based on the PCR replication and amplification of DNA sequences of interest. By replacing dATP with the triphosphate of **D** (dDTP), PCR amplification of the genomic region that flanks the SNP site may allow us to detect SNPs through the measurement of the charge transfer rates through DNA.

Acknowledgments We are deeply indebted to Ms Haruka Kodera, Dr. Tadao Takada, and Dr. Yasuko Osakada for their contributions to this study during their master and doctor course studies. This work has been partly supported by a Grant-in-Aid for Scientific Research (Project 17105005, 18750148, 21750170, 22245022, and others) from MEXT of Japanese Government. T.M. thanks the WCU (World Class University) program through the National Research Foundation of Korea funded by the Ministry of Education, Science and Technology (R31-10035) for the support.

References

1. Winfree E, Liu FR, Wenzler LA, Seeman NC (1998) *Nature* 394:539
2. Seeman NC (2003) *Nature* 421:427
3. Liao S, Seeman NC (2004) *Science* 306:2072
4. Rothmund PWK (2006) *Nature* 440:297
5. Andersen ES, Dong M, Nielsen MM, Jahn K, Subramani R, Mamdouh W, Golas MM, Sander B, Stark H, Oliveira CLP, Pedersen JS, Birkedal V, Besenbacher F, Gothelf KV, Kjems J (2009) *Nature* 459:73
6. Endo M, Hidaka K, Kato T, Namba K, Sugiyama H (2009) *J Am Chem Soc* 131:15570
7. Steinhauer C, Jungmann R, Sobey TL, Simmel FC, Tinnefeld P (2009) *Angew Chem Int Ed* 48:8870
8. Endo M, Katsuda Y, Hidaka K, Sugiyama H (2010) *J Am Chem Soc* 132:1592
9. Cohen H, Nogues C, Naaman R, Porath D (2005) *Proc Natl Acad Sci USA* 102:11589
10. Xu B, Zhang P, Li X, Tao N (2004) *Nano Lett* 4:1105
11. Hihath J, Xu B, Zhang P, Tao N (2005) *Proc Natl Acad Sci USA* 102:16979
12. Guo X, Gorodetsky AA, Hone J, Barton JK, Nuckolls C (2008) *Nat Nanotechnol* 3:163
13. Okamoto A, Tanaka K, Saito I (2003) *J Am Chem Soc* 125:5066
14. Taniguchi M, Kawai T (2006) *Physica E* 33:1
15. Steenken S, Jovanovic SV (1997) *J Am Chem Soc* 119:617
16. Seidel CAM, Schulz A, Sauer MHM (1996) *J Phys Chem* 100:5541
17. Meggers E, Michel-Beyerle ME, Giese B (1998) *J Am Chem Soc* 120:12950
18. Nakatani K, Dohno C, Saito I (1999) *J Am Chem Soc* 121:10854
19. Bixon M, Giese B, Wessely S, Langenbacher T, Michel-Beyerle ME, Jortner J (1999) *Proc Natl Acad Sci USA* 96:11713
20. Lewis FD, Liu XY, Liu JQ, Miller SE, Hayes RT, Wasielewski MR (2000) *Nature* 406:51
21. Berlin YA, Burin AL, Ratner MA (2001) *J Am Chem Soc* 123:260
22. Lewis FD, Liu J, Zuo X, Hayes RT, Wasielewski MR (2003) *J Am Chem Soc* 125:4850
23. Takada T, Kawai K, Fujitsuka M, Majima T (2004) *Proc Natl Acad Sci USA* 101:14002
24. Takada T, Kawai K, Fujitsuka M, Majima T (2005) *Chem Eur J* 11:3835
25. Osakada Y, Kawai K, Fujitsuka M, Majima T (2006) *Proc Natl Acad Sci USA* 103:18072
26. O'Neill MA, Barton JK (2004) *J Am Chem Soc* 126:11471
27. Zeidan TA, Carmieli R, Kelley RF, Wilson TM, Lewis FD, Wasielewski MR (2008) *J Am Chem Soc* 130:13945

28. Conwell EM, Bloch SM, McLaughlin PM, Basko DM (2007) *J Am Chem Soc* 129:9175
29. Henderson PT, Jones D, Hampikian G, Kan YZ, Schuster GB (1999) *Proc Natl Acad Sci USA* 96:8353
30. Kanvah S, Joseph J, Schuster GB, Barnett RN, Cleveland CL, Landman U (2010) *Acc Chem Res* 43:280
31. Lewis FD, Liu XY, Liu JQ, Hayes RT, Wasielewski MR (2000) *J Am Chem Soc* 122:12037
32. Giese B, Amaudrut J, Kohler AK, Spormann M, Wessely S (2001) *Nature* 412:318
33. Bixon M, Jortner J (2001) *J Am Chem Soc* 123:12556
34. Berlin YA, Burin AL, Ratner MA (2002) *Chem Phys* 275:61
35. Rogers JE, Kelly LA (1999) *J Am Chem Soc* 121:3854
36. Rogers JE, Weiss SJ, Kelly LA (2000) *J Am Chem Soc* 122:427
37. Takada T, Kawai K, Cai X, Sugimoto A, Fujitsuka M, Majima T (2004) *J Am Chem Soc* 126:1125
38. Kawai K, Osakada Y, Takada T, Fujitsuka M, Majima T (2004) *J Am Chem Soc* 126:12843
39. Takada T, Kawai K, Fujitsuka M, Majima T (2006) *Angew Chem Int Ed* 45:120
40. Takada T, Kawai K, Fujitsuka M, Majima T (2006) *J Am Chem Soc* 128:11012
41. Kawai K, Osakada Y, Sugimoto A, Fujitsuka M, Majima T (2007) *Chem Eur J* 13:2386
42. Kawai K, Osakada Y, Fujitsuka M, Majima T (2008) *Chem Eur J* 14:3721
43. Osakada Y, Kawai K, Fujitsuka M, Majima T (2008) *Chem Commun*:2656
44. Osakada Y, Kawai K, Fujitsuka M, Majima T (2008) *Nucleic Acids Res* 36:5562
45. Tierney MT, Sykora M, Khan SI, Grinstaff MW (2000) *J Phys Chem B* 104:7574
46. Tierney MT, Grinstaff MW (2000) *J Org Chem* 65:5355
47. Peng X, Li H, Seela F (2006) *Nucleic Acids Res* 34:5987
48. Nakatani K, Dohno C, Saito I (2000) *J Am Chem Soc* 122:5893
49. Kelley SO, Barton JK (1999) *Science* 283:375
50. Voityuk AA, Roesch N (2002) *J Phys Chem B* 106:3013
51. Saito I, Takayama M, Sugiyama H, Nakatani K, Tsuchida A, Yamamoto M (1995) *J Am Chem Soc* 117:6406
52. Sugiyama H, Saito I (1996) *J Am Chem Soc* 118:7063
53. Saito I, Nakamura T, Nakatani K, Yoshioka Y, Yamaguchi K, Sugiyama H (1998) *J Am Chem Soc* 120:12686
54. Kawai K, Kodera H, Majima T (2010) *J Am Chem Soc* 132:627
55. Kawai K, Kodera H, Osakada Y, Majima T (2009) *Nat Chem* 1:156
56. Boon EM, Ceres DM, Drummond TG, Hill MG, Barton JK (2000) *Nat Biotechnol* 18:1096
57. Schlientz NW, Schuster GB (2003) *J Am Chem Soc* 125:15732
58. Okamoto A, Kamei T, Saito I (2006) *J Am Chem Soc* 128:658
59. Takada T, Lin C, Majima T (2007) *Angew Chem Int Ed* 46:6681
60. Kelley SO, Boon EM, Barton JK, Jackson NM, Hill MG (1999) *Nucleic Acids Res* 27:4830
61. Giese B, Wessely S (2000) *Angew Chem Int Ed Engl* 39:3490
62. Bhattacharya PK, Barton JK (2001) *J Am Chem Soc* 123:8649
63. Okamoto A, Kamei T, Tanaka K, Saito I (2004) *J Am Chem Soc* 126:14732
64. Usdin K (1998) *Nucleic Acids Res* 26:4078
65. Seela F, Roeling A (1992) *Nucleic Acids Res* 20:55
66. Raghavan SC, Houston S, Hegde BG, Langen R, Haworth IS, Lieber MR (2004) *J Biol Chem* 279:46213
67. Suspene R, Renard M, Henry M, Guetard D, Puyraimond-Zemmour D, Billecocq A, Bouloy M, Tangy F, Vartanian J-P, Wain-Hobson S (2008) *Nucleic Acids Res* 36:e72/1

Transfer of Chirality for Memory and Separation

Rosaria Lauceri, Alessandro D'Urso, Angela Mammana,
and Roberto Purrello

Abstract Transfer of chirality is an intriguing issue worth studying to understand better the origin of life and for possible technological applications. In the last few years we have been working in this area studying the chain of events that begins with induction, reaches a permanent transfer (chiral memory) and extends in some cases to a (*quasi*-)reversible situation in which induced and permanently memorized chirality coexists. This can happen thanks to a designed blend of thermodynamics and kinetics.

Keywords Hierarchy · Memory · Porphyrin · Supramolecular chirality · Transfer

Contents

1	Introduction	144
2	Chiral Induction and Memory: Porphyrin (Hetero-) Self-Assemblies in the Presence of Poly-Glutamate	146
3	Porphyry (Hetero-) Self-Assemblies in the Presence of Phenylalanine	154
3.1	Chiral Memory	155
3.2	Reversibility of Chiral Memory	159
4	How Big Must the Template Be in Order to Imprint the Chiral Information?	164
5	Resolution of Chirality by Stirring: The Vortex Effect	174
6	Conclusive Remarks and Perspectives	183
	References	185

R. Lauceri
C.N.R., Istituto di Biostrutture e Bioimmagini-Sezione di Catania, Viale A. Doria 6, 95125 Catania, Italy

A. D'Urso, A. Mammana, and R. Purrello (✉)
Dipartimento di Scienze Chimiche, Università di Catania, Viale A. Doria 6, 95125 Catania, Italy
e-mail: rpurrello@unict.it

Abbreviations

AuT4	Au- <i>meso</i> -tetrakis(4- <i>N</i> -methylpyridyl)porphyrin
CCW	Counter clock wise
CD	Circular dichroism
<i>cis</i> -DPPS	5,10-Bis(4-sulfonatophenyl)-15,20-diphenylporphyrin
CuT4	Cu- <i>meso</i> -tetrakis(4- <i>N</i> -methylpyridyl)porphyrin
CuTPPS	Cu- <i>meso</i> -tetrakis(4-sulphonatophenyl)porphyrin
CW	Clock wise
DLS	Dynamic light scattering
EDXD	Energy dispersive X-ray diffraction
ELS	Elastic light scattering
H ₂ T4	<i>meso</i> -Tetrakis(4- <i>N</i> -methylpyridyl)porphyrin
H ₂ TPPS	<i>meso</i> -Tetrakis (4-sulphonatophenyl)porphyrin
H ₂ TpyP	<i>meso</i> -Tetrakis (4-phenyl)porphyrin
ICD	Induced circular dichroism
LD	Linear dichroism
MnT4	Mn- <i>meso</i> -tetrakis(4- <i>N</i> -methylpyridyl)porphyrin
MT4	<i>meso</i> -Tetrakis(4- <i>N</i> -methylpyridyl)porphyrin metallo derivative
MTPPS	<i>meso</i> -Tetrakis(4-sulphonatophenyl)porphyrin metallo derivative
Mw	Molecular weight
Phe	Phenylalanine
RLS	Resonance light scattering
Ru[(Phen) ₃] ²⁺	Ru[(phenanthroline) ₃] ²⁺
<i>trans</i> -DPPS	5,15-Bis(4-sulfonatophenyl)-10,20-diphenylporphyrin
ZnT4	Zn- <i>meso</i> -tetrakis(4- <i>N</i> -methylpyridyl)porphyrin

1 Introduction

One of the advantages of supramolecular chemistry over the covalent molecular approach resides in the possibility of inducing and/or transferring properties from singular molecules to self-organized multi-molecular assemblies. Chirality is one of these properties: it stems from the electronic level (the helical nature of the electron rearrangement during a transition in chiral chromophores) and spreads up to the three-dimensional spatial disposition of atoms, or molecular components in molecular or supramolecular entities, respectively.

Exploitation of the chiral information at each of these different “levels” might lead to different technological applications: from activation of nonlinear optical effects [1] to synthetic receptors for manifold applications (racemate resolution, chiroptical sensors, etc.).

Yet the design, synthesis and characterization of supramolecular chiral systems are pursued not only in view of their exploitation but also because they represent an

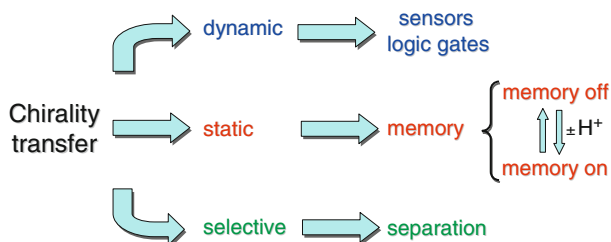
important step to understand better the arising and evolution of chiral bias in living systems [2]. A reasonable scheme to explain the enantiomeric excess of L-amino acids might foresee a chain of events in which a tiny enantiomeric excess, caused from unknown reason(s), has been exponentially amplified up to almost complete predominance of one enantiomer.

The intriguing process of induction (and subsequent transfer and amplification) of chirality from organic or inorganic templates to achiral porphyrin aggregates has been in the focus of our interests for more than a decade. Our studies concern exploitation of the electrostatic interactions as tools to build non-covalent aggregates and have been carried out in aqueous solution.

We will show in this chapter that a designed combination of thermodynamic and/or kinetic control of the self-assembly processes has allowed us to develop various applications all based on the induced chirality in the porphyrin Soret band absorption region. Chiral information transfer has been followed using circular dichroism, a spectroscopic technique particularly useful to characterize (supra) molecular dissymmetry or chirality [3].

Scheme 1 shows that it is possible to distinguish among different kinds of processes leading to chirality transfer. This distinction is mainly based on the possibility of choosing the type of control that self-organization processes have to obey: thermodynamic, kinetic or a designed blend of both.

A dynamic transfer means that the system is exclusively under thermodynamic control: porphyrin aggregation is reversible and induced chirality can be used to get chiroptical sensors or switches (for example for logic gates) [4, 5]. In fact, in these systems chirality is only induced but not permanently transferred; it remains strictly related to the template chirality and is lost when porphyrin-template interaction is disrupted. This particular subject will not be discussed in this chapter. Our attention will be mostly addressed to the other two types of transfer: static and selective. A static transfer is achieved when the system is under kinetic control: the final species is kinetically inert and in this case the chirality induced at the very onset of aggregation becomes an intrinsic property of the porphyrin assembly (see Sect. 2). The rationale design of the latter systems (e.g. the use of the appropriate porphyrins) allows for reversibly switching from a static to a *quasi*-dynamic regime (see Sects. 3 and 4). Finally, a chiral perturbation (such as a vortex, for example)



Scheme 1 Different kind of processes leading to chirality transfer

exerted on a racemate in equilibrium can be selectively transferred to only one enantiomorph: e.g. the transfer of chirality exerted by clockwise (CW) or counter-clockwise (CCW) mechanical vortices on Λ and Δ J aggregates of H_2TPPS (see Sect. 5).

For the sake of simplicity, we have divided this chapter into sections, but, as will be evident, this is just for the sake of tracing a (historical/logical) pathway for the reader. A rigid compartmentalisation is not possible and from time to time we will reconsider subjects discussed in previous paragraphs as logical and natural consequence of the know-how acquired, just as in a feed-back process.

2 Chiral Induction and Memory: Porphyrin (Hetero-) Self-Assemblies in the Presence of Poly-Glutamate

Induction of chiral properties in porphyrin self-assemblies and the following optical activity has been and still is a subject extensively studied and covered from a quite vast literature (some examples are [4–25]).

As presented in Scheme 1, induction of chirality is a necessary and preliminary step leading to its permanent transfer (i.e. memory). For this reason we present first a system which does not show chiral memory but represents a kind of milestone in the development of our research [26]. The rationale behind this study was to investigate systems more complex than those studied in literature at that time (1998). The reason was not simply to do something different or new but to understand if and how chirality transfers and propagates from a chiral template to a first “shell” of achiral guests and from here to a second “shell” of achiral guests.

Working in water we had to design the right combination of charges to build a stable system. The chiral template we chose is poly-glutamate (Fig. 1) (poly-L-glutamate or poly-D-glutamate) which is an ionisable polypeptide ($pK_a \approx 5.0$) having α -helix conformation approximately at pHs below its pK_a and random-coil conformation at pHs above its pK_a (the exact pH of the conformational transition depends on the experimental conditions and the peptide length).

As the first shell of achiral guests we chose various tetracationic porphyrins (Fig. 1), selected on the basis of their peculiar electronic and steric properties: the copper(II), gold(III), zinc(II), and manganese(III) derivatives of *meso*-tetrakis(*N*-methylpyridinium-4-yl)porphyrin (MT4). In particular, CuT4 carries no net charges and no axial ligands on the central metal ion, AuT4 carries a net charge but no axial ligands on the central metal ion, ZnT4 carries no net charges but an axial ligand on the central metal ion, MnT4 carries both a net charge (Mn (III)) and two axial ligands on the central metal ion.

The second shell of achiral guests is built from the tetra-anionic *meso*-tetrakis(4-sulfonatophenyl)porphyrin (H_2TPPS) (Fig. 1). It is worth underlining that protonation of the nitrogen atoms in the inner core of H_2TPPS leads to zwitterionic species prone to self-aggregation. The protonated form of H_2TPPS (H_4TPPS , pK_a

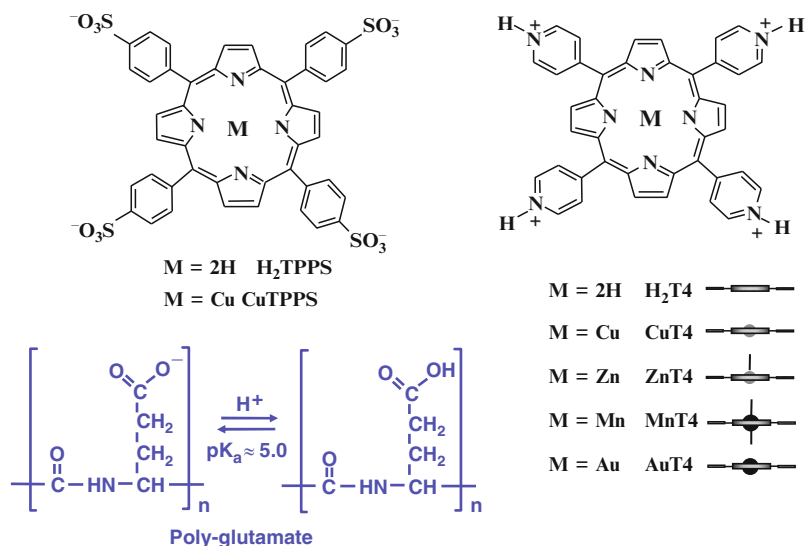


Fig. 1 Schematic structures of anionic (*top left*) and cationic (*top right*) metalloporphyrins. Protonation equilibrium of poly-glutamate (*bottom left*)

Table 1 Visible-absorption and RLS features of J- and H-aggregates of H₂TPPS

	Absorption spectra ^a		RLS spectra ^b
	B-bands	Q-bands	
J-aggregates	489 nm	668 nm, 707 nm	490 nm
H-aggregates	422 nm	575 nm, 625 nm	Not observed

^apH 3.5; $4 \times 10^{-5} \text{ M} \leq [\text{H}_2\text{TPPS}] \leq 5 \times 10^{-4} \text{ M}$; [27]

^bpH 1.2; $I = 0.1 \text{ M}$, $[\text{H}_2\text{TPPS}] = 2.5 \times 10^{-6} \text{ M}$; [29]

≈ 4.8) [27] forms both J-type (edge-to-edge, $\lambda_{\text{max}} \approx 490 \text{ nm}$) and H-type (face-to-face, $\lambda_{\text{max}} \approx 420 \text{ nm}$) aggregates, at pH values close to 2 and sodium chloride concentrations of 0.3 M [27, 28]. The spectroscopic features of these two aggregates can be assigned by means of visible absorption and resonance light scattering (RLS) measurements (Table 1) [28, 29].

In contrast, MT4 porphyrins do not present any strong tendency towards self-aggregation (in the experimental condition used). Their role in this experiment was to act as “spacers” between the negative chiral polymeric matrix and the anionic porphyrins by shielding the electrostatic repulsion between the like-charged molecular components (see Fig. 1). The real intention of the experiment was to understand if the presence of a cationic “layer” on an anionic chiral matrix would permit (1) complexation of anionic porphyrins and (2) a “long-distance” interaction of the matrix with the second shell of guests (i.e. a propagation of chirality from the matrix to H₄TPPS).

Quite unexpectedly, cationic porphyrins showed an additional “role”: an interesting capacity in driving the formation of H- and J-aggregates of H₄TPPS under unusual experimental conditions (i.e. pH close to 3 and no salt addition). This “catalytic” ability depends on steric and/or electronic features of the porphyrins. It is worth noting that, in the absence of MT4, none of the spectroscopic features (see Table 1) associated with aggregation of the protonated form of H₂TPPS was observed and no interaction of the anionic porphyrin with poly-glutamate occurred.

Figure 2a shows, for example, the absorption spectrum (recorded after 1 h of incubation) of a solution of H₂TPPS (5 μM) at pH 2.9 in the presence of poly-L-glutamate (50 μM) and ZnT4 (5 μM). Together with the expected band at 436 nm (due to the absorption of both ZnT4 and H₄TPPS), two additional bands at about 490 and 700 nm are visible. In addition, the RLS spectrum (Fig. 2b) shows a very intense band at about 500 nm and a smaller signal at about 720 nm (not shown). The RLS and absorption bands observed around 500 and 700 nm are diagnostic of the presence of H₄TPPS J-aggregates (Table 1). In the RLS spectrum there is also visible a feature at 420 nm (inset of Fig. 2b) which might be assigned to the formation of H-type aggregates [28].

Moreover, the CD spectrum (Fig. 2c) of the ternary complex shows a very intense *induced bisignate signal* having a maximum at 490 nm, together with smaller conservative features centred at about 420 and 720 nm, testifying that (1) J-aggregate of H₄TPPS is interacting with poly-glutamate and (2) J-aggregate of H₄TPPS is gaining chirality from the polypeptide template. It represents the first observation of a chiral J-aggregate of H₄TPPS at this unusual pH value. Also, the presence of a CD band at 420 nm indicates the formation of a chiral H-type aggregate as well.

Using the same concentrations of H₂TPPS (5 μM) and poly-L-glutamic acid (50 μM) and one-fifth of the stoichiometric amount of ZnT4 (1 μM), the intensity of the CD bands is reduced only by 30%. The observation that the ternary complex concentration does not scale down linearly with the concentration of ZnT4 confirms that anionic and cationic porphyrins are not forming 1:1 hetero-aggregates [30–33] and that ZnT4 serves as a “spacer” to minimize the repulsion between the two

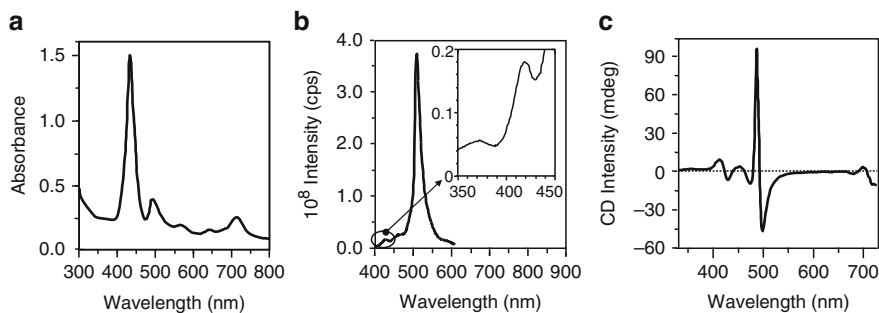


Fig. 2 Absorption (a), RLS (b) and CD (c) spectra at pH 2.9 (citrate buffer 5 mM) of H₂TPPS (5 μM) in the presence of ZnT4 (5 μM) and poly-L-glutamate. Modified from [26]

negative components. This hypothesis is also supported by (1) the observation that a pH increase of only 0.2 units (i.e. a small increase in the number of negative charges on the matrix) causes a 50% reduction of the induced CD signal, most likely because of the stronger repulsion between the anionic porphyrins and the matrix and (2) the fact that in the absence of ZnT4 but at very high salt concentration ($\text{NaCl} > 0.5 \text{ M}$) we observe the same spectroscopic features characteristic of the chiral H- and J-aggregates. The much lower concentration of cationic porphyrins required to induce the formation of these ternary complexes is indicative of their higher efficiency, which must be related to specific molecular recognition processes [20, 24, 34, 35]. Most likely, ZnT4 is mono-dispersed on the matrix, shielding the negative charges. This allows the anionic porphyrins to approach the (partially) anionic chiral polypeptide and gain chirality. Importantly, when poly-D-glutamate is used, the mirror image of the CD features at 422, 490 and 700 nm is observed. This confirms that aggregates of the anionic porphyrin owe their chirality to the polypeptide matrix even though they interact with it only indirectly “through” the cationic porphyrin.

Using axially encumbered porphyrins (MnT4 for the axial ligands and AuT4 for the central positive charge) we have obtained results similar to those found for ZnT4.

CuT4 behaves in a quite different way to the other cationic porphyrins: both the CD and RLS signals characteristic of H₄TPPS H- and J-aggregates are barely detectable for the ternary system poly-glutamate-CuT4-H₄TPPS. A possible explanation is that these two porphyrins form 1:1 hetero-aggregates, not bound to the chiral matrix and competing against the formation of the chiral ternary species. Accordingly, absorption data show that at pH 2.9 in the absence of poly-glutamate, AuT4, MnT4 and ZnT4 still induce the formation of H₄TPPS J-aggregates, whereas CuT4 forms hetero-aggregates in a 1:1 ratio [36]. This different behaviour can be explained considering that (1) penta- and hexa-coordinated porphyrins are not allowed to form “stacked” 1:1 complexes for steric reasons and (2) planar Au(III) porphyrins present a “net” positive charge in the porphyrin core. This causes an electrostatic repulsion between the Au(III)T4 and the protonated H₂TPPS core, thus disfavours the “stacked” interactions and leading to the formation of J H₄TPPS aggregates.

The different “nature” of the interactions between CuT4 and H₂TPPS was underlined from the remarkable sensitivity to small changes in the pH of the solution. In fact, by increasing the pH from 2.9 to 3.2 the J aggregates of H₄TPPS do not form anymore but a 1:1 hetero-aggregate is formed and in the presence of poly-L- or poly-D-glutamate it gains chirality from the matrix. This ternary system is able to retain the chiral information imprinted from the chiral mould, giving rise to the chiral memory phenomenon [37, 38] as will be shown below.

Before discussing the remarkable kinetic inertia of these ternary species it is useful to present the main characteristic of the CuT4-poly-glutamate binary system. The binary complex is chiral and kinetically *labile*. This is shown by (1) the presence of an induced band in the Soret region of the circular dichroism (CD) spectra (inset of Fig. 3, curve a) and (2) the inversion (in about 10 min) of the same

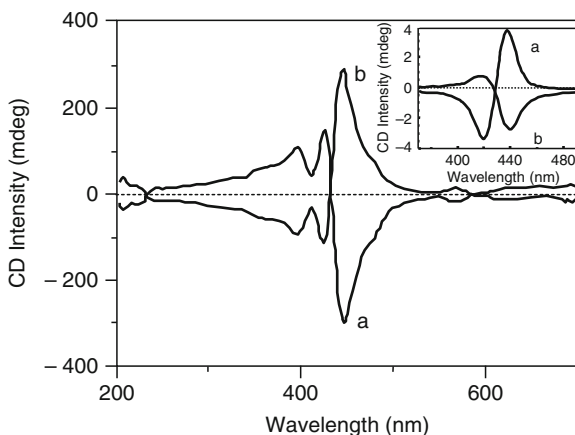


Fig. 3 CD spectra of a solution of CuT4 (4 μM) in the presence of poly-glutamate (200 μM) (a) L- and (b) D-, after addition of H₂TPPS (4 μM). *Inset*: CD spectra of a solution of CuT4 (4 μM) in the presence (a) of poly-L-glutamate (200 μM) at pH 3.6 and (b) the same solution after the addition of fourfold excess of poly-D-glutamate. Modified from [37]

band upon the addition of a fourfold excess of the D-form of the polymer (inset of Fig. 3, curve b). This is in agreement with previous findings [21] where it was shown that the phase of the induced CD signal in the Soret region reflects the helical sense of the matrix; i.e. the complex species formed on the L or D forms are characterized by mirror image CD spectra. Notice that curve b of inset of Fig. 3 is not the perfect mirror image of curve a because both L- and D-supramolecular isomers coexist in equilibrium in solution, with the aggregate on poly-D-glutamate in excess.

Addition of H₂TPPS (in the pH range 3.2–4.0) to the binary complex induces drastic changes in the absorption, fluorescence, and CD spectra, indicating the formation of *chiral ternary complexes* [37, 38]. In particular, the Soret bands of both porphyrins experience quite strong hypochromic effects (~50%), and the fluorescence emission of H₄TPPS is quenched by ~50% (CuT4 is not fluorescent). Also, both the shape (bisignate) and the unusually high intensity of the induced CD features (Fig. 3, curve a) strongly indicate that both porphyrins are extensively aggregated onto the α -helical poly-glutamate [39]. When H₂TPPS is added to a preformed CuT4-poly-D-glutamate binary complex, the mirror images of the CD signals observed with the L-isomer are obtained (Fig. 3, curve b), indicating that the chirality of these assemblies follows the matrix chirality.

However, these supramolecular ternary complexes behave quite differently compared to the parent *binary species*. In fact, the addition of a fourfold excess of poly-L-glutamate to *ternary complexes* “built” on the poly-D-glutamate does *not* lead to the inversion of the induced CD signal in the Soret region (even after 5 days following the addition). The only indication of the L-form excess is the inversion of the helix marker bands at 222 nm and 208 nm (Fig. 4). The same behaviour has been observed for the ternary “L”-supramolecular species upon addition of an excess of

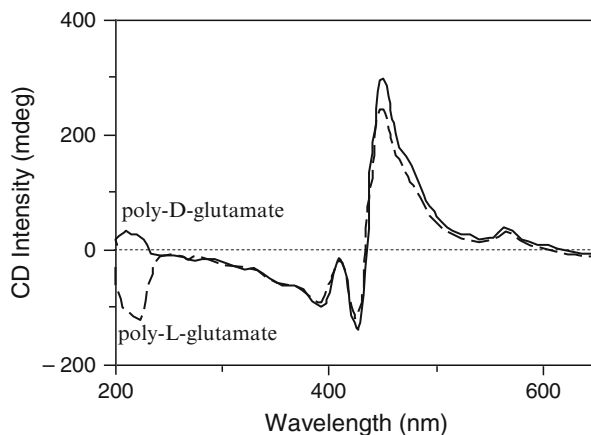


Fig. 4 CD spectra of a solution of CuT4 (4 μ M) and H₂TPPS (4 μ M) in the presence of poly-D-glutamate (200 μ M *black curve*) and the same solution 1 day after the addition of a fourfold excess of poly-L-glutamate (*dashed curve*). Modified from [37]

poly-D-glutamate. The lack of inversion of the *induced* CD bands shows that, in contrast to their *binary* precursors, the poly-glutamate-CuT4-H₄TPPS aggregates are kinetically *inert*.

This behaviour is due to the formation of an extended network of electrostatic interactions (i.e. those between the oppositely charged peripheral groups and the “ π - π ” between the porphine rings) [40].

Another proof of this notable inertia is given by the persistence of the ICD after the poly-glutamate pH-induced helix to coil conformational transition. In fact, since the chirality of the supramolecular complex is transferred from poly-glutamate to porphyrins, the pH-induced helix to coil transition (from pH \sim 4 to 12) should cause the disappearance of the ICD of the ternary species. Surprisingly, increasing the pH to 12 does not perturb the ICD, strongly indicating that these porphyrin assemblies retain their “original” chirality even when the matrix loses it (Fig. 5). Checking the time stability under such critical experimental conditions (pH 12), it turns out that these complexes remain stable for several days, as indicated by the CD intensity in the Soret region which decreases by only 30% over about 4 weeks (Fig. 5) [38].

Notably, hetero-aggregation of the title porphyrins in ultra-pure water, in the absence of poly-glutamate, leads to achiral 1:1 complexes. This aggregation process is also accompanied by a hypochromic absorbance effect and fluorescence quenching similar to that observed in the presence of poly-glutamate, but no CD signal is observed (Fig. 6, black curve). More interestingly, no dichroic signal is observed in the Soret region if poly-glutamate is added after porphyrin self-aggregation (Fig. 6, grey curve) [38]. This behaviour testifies to the relevant kinetic inertia of these porphyrin supramolecular species and suggests that the role of the matrix is crucial only in the very first step of the formation of these ternary chiral species. In fact, once formed, these aggregates seem to have a “life” independent of

Fig. 5 CD spectra of a solution of CuT4 (4 μM) and H₂TPPS (4 μM) in the presence of poly-D-glutamate (200 μM) at pH 3.6 (*black curve*) and at pH \sim 12 immediately (*dashed curve*) and after 2 weeks (*dotted curve*). Modified from [37]

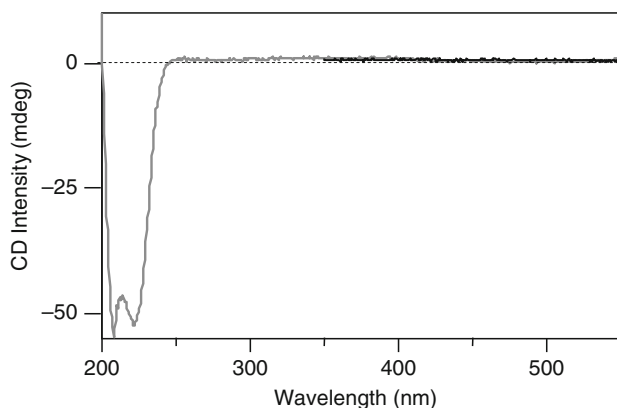
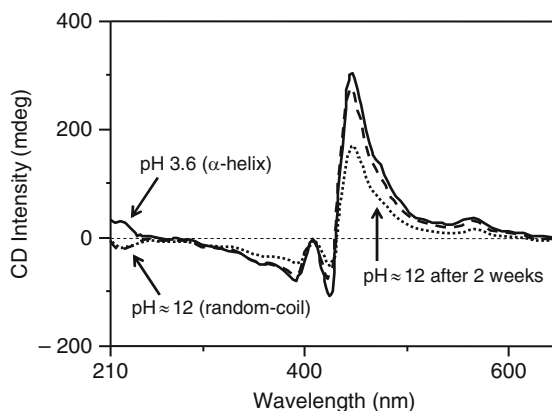


Fig. 6 CD spectra of CuT4 (4 μM) and H₂TPPS (4 μM) aggregated in water at pH 3.6 (*black curve*) and after addition of poly-L-glutamate (*grey curve*). Modified from [45]

the template but retain “memory” of the shape of the “mould” used for their formation.

This is a nice example of hierarchical control over the self-organization process and is related to the thermodynamic stability and kinetic inertia due to the interactions of a convergent stabilization due to all kinds of electrostatic interactions [41].

Neither ZnT4 nor MnT4 or AuT4 form this type of ternary complex under the same experimental conditions. This is due to the presence of, respectively, one or two water molecules axially coordinated to the central metal ions or to the net positive charge in the inner core, which hinders a close contact among porphyrin molecules for steric or electronic reasons.

On the other hand, all the other couples of porphyrins bearing opposite charges H₂T4-H₂TPPS, H₂T4-CuTPPS and CuT4-CuTPPS lead to the formation of supra-molecular species for which the chiral memory phenomenon occurs. All the three

porphyrin systems mentioned earlier follow the same trend presented by the CuT4-H₂TPPS couple [42].

The only significantly different behaviour found was for the CuT4-CuTPPS system. This species exhibits the remarkable inertness and the chiral memory phenomenon presented by the other porphyrin aggregates, but its CD signal is considerably smaller than those exhibited by the other porphyrin couples (H₂T4-H₂TPPS, CuT4-H₂TPPS, H₂T4-CuTPPS) (Fig. 7). These findings suggested to us that the title aggregate is smaller than the others, a hypothesis that was supported by the RLS signals. This particular behaviour could be due to macrocycle distortions following aggregation. Indeed, in the solid state, CuT4 arrangement is characterized by a remarkable distortion of the piled porphyrin macrocycles [43]. This distortion is caused by the π -like interactions between the peripheral pyrrole C _{β} -C _{β} “double bond” and the metal centre (Fig. 8). We hypothesize that similar relevant distortions are also present in the CuT4-CuTPPS aggregate, hindering the formation of extended porphyrin assemblies. Moreover, literature data [40] suggest that distortion caused by the central metal ion affects the attractive interactions between adjacent porphyrins. Aggregates in which only one (or no) copper porphyrin derivative is involved are less affected by the macrocycle distortions and, then, may form larger assemblies.

The study of the aggregation behaviour of the reported systems confirms that net electrostatic interactions are the driving force of the self-assembly process and (due to the large number and strength) lead to the formation of inert ensembles (kinetic inertia, again, turns out to be crucial in determining the memory phenomenon). Yet the aggregation process is also affected by the convergence of all others non-covalent interactions (attractive and repulsive) in tuning the final shape and stability. For example, the central copper ion does not play a trivial role as demonstrated

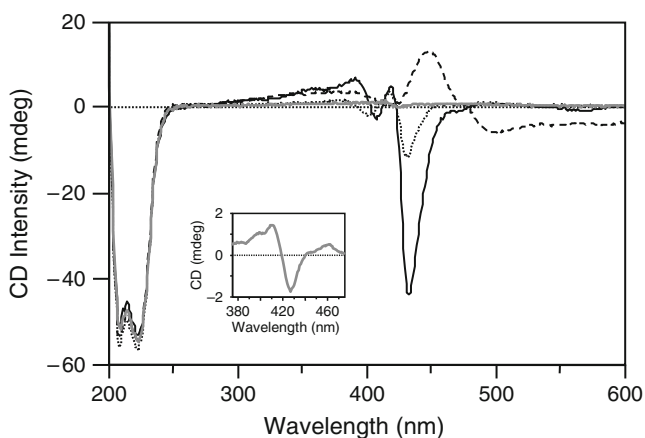


Fig. 7 CD spectra of the couples CuT4-H₂TPPS (*black curve*), H₂T4-H₂TPPS (*dashed curve*), H₂T4-CuTPPS (*dotted curve*) and CuT4-CuTPPS (*grey curve*) (4 μ M each) aggregated in presence of poly-L-glutamate (200 μ M) at pH 4.0. Modified from [45]

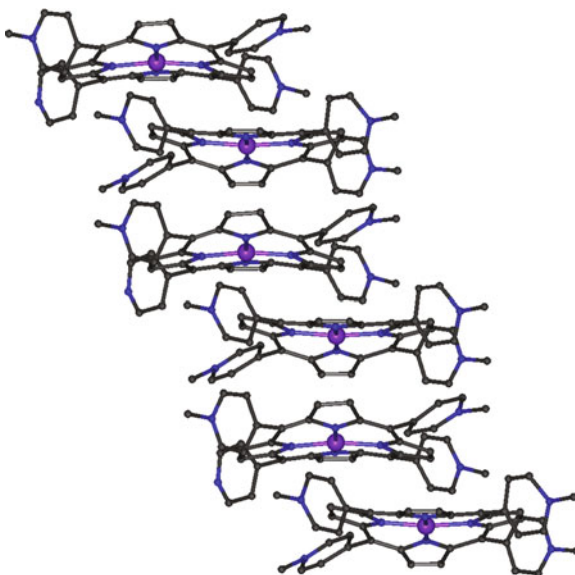


Fig. 8 Structure of the CuT4 “polymeric structure”. Modified from [42]

by its ability in affecting the assembly dimension. This finding may turn out to be useful for modulating the aggregate size, whose control is crucial for the possible applications of these systems.

3 Porphyrin (Hetero-) Self-Assemblies in the Presence of Phenylalanine

An unambiguous demonstration of the memory phenomenon needs to show the survival of the ICD in the Soret region after removal of the chiral mould (e.g. after ultrafiltration). In fact, it is not possible to exclude the possibility that the presence of the cationic N-methylpyridyl groups of porphyrin close to the carboxylate side groups of poly-glutamate could shield electrostatic repulsions (responsible for the α -helix to random coil transition), preserving small regions of the polypeptides from the helix to coil transition. If this would happen it could (partially) explain the persistence of the CD signal of the porphyrin aggregate after the pH jump experiment (see Fig. 5)

However, the removal experiment is not feasible when the mould is a covalent polymer [37, 38, 42, 44, 45] because it could remain trapped in the porphyrin aggregates which are quite extended species (about one million of porphyrins for single aggregate *molecule* as shown by elastic light scattering data).

The “ideal” template (A) for transferring the chirality to the porphyrin assembly and for the following removal experiment is a fluorescent monomeric chiral

molecule (characteristic 1) that, above a given concentration threshold, self-assembles in a chiral fashion (characteristic 2), therefore establishing the equilibrium: n monomers \leftrightarrow (monomer) $_n$ (characteristic 3). The first condition allows us to monitor the residual concentration of the template much more efficiently compared with both the absorption and CD techniques. The second condition is indispensable for transferring chirality from the template to the porphyrin aggregates: induction of chirality (from a template to a supramolecular assembly) has a conformational origin; that is, monomeric A cannot induce chirality onto the achiral porphyrin aggregates, but A aggregates can transfer their handedness. Finally, the third condition helps to reduce the concentration of the template: as soon as the monomeric form of the “template” is removed (e.g. by ultrafiltration), the equilibrium n monomers \leftrightarrow (monomer) $_n$ shifts towards the left and the aggregated form disappears even if traces of the monomers (below the threshold) remain in solution.

We choose, then, as first candidate, “monomeric” phenylalanine (Phe) [46]. In fact, it has a good fluorescence yield in a region where porphyrins only slightly absorb, and its removal from the solution can be easily checked. Moreover, considering that ICD signals, the fingerprint of (extrinsic) chirality, have conformational origin, Phe, due to the hydrophobic character of a large portion of the molecule, ensures greater aggregation tendency than other amino acids.

3.1 Chiral Memory

Indeed, addition of the cationic CuT4 and anionic H₂TPPS to an aqueous solution of L-Phe or D-Phe leads to an ICD in the Soret region (Fig. 9, curves a and b). The

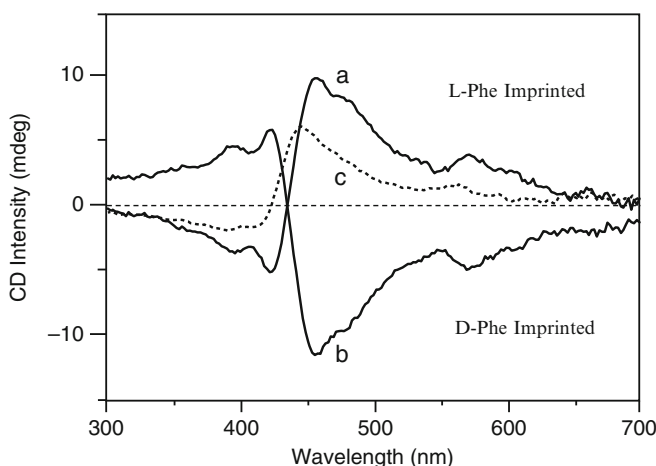


Fig. 9 CD spectra of H₂TPPS and CuT4 (2 μ M) in ultrapure Millipore water in presence of (a) L- and (b) D-phenylalanine (8 mM) and (c) solution (a) after the removal of the L enantiomer. Modified from [46]

threshold concentration of Phe to induce the ICD is about 1×10^{-3} M. Therefore, in contrast to all the previous examples, in this case the preferential conformation of the porphyrin aggregates is borrowed by chiral *non-covalent* polymers. Accordingly, dynamic light scattering data (DLS) of Phe solution show (Fig. 10) the presence at 30°C of large Phe aggregates (~60 nm) whose size decreases with increasing the temperature, levelling off over 60°C (~20 nm) [46].

DLS measurements do not, however, give any insight on Phe clusters chirality. This information can be inferred by using the title assemblies as chirality reporters [46]. This purpose can be accomplished by monitoring the ICD of porphyrins added to various Phe solutions pre-warmed at a given temperature. By increasing the temperature the ICD decreases, paralleling the reduction of Phe mass average molecular weight Mw (Fig. 10). After 60°C the ICD is reduced almost to a noise level, suggesting that there are critical Phe cluster size (about 20 nm) and concentration needed to initiate chiral porphyrin aggregation. In fact, porphyrin assembly formation is not affected by high temperatures. Absorption and RLS measurements confirm that at 80°C CuT4-H₂TPPS aggregates still form.

According to the previous results [37, 38, 42], the title porphyrin aggregates are inert enough to memorize the chirality of polymeric helical templates even after helix disruption. A similar result is also expected here upon Phe removal. Ultrafiltration of the solution leaves, in fact, the CD signal almost unaltered (Fig. 9, curve c), showing that the imprinted aggregates are now intrinsically chiral (they are so stable and inert that their memory lasts for many years) [44–46]. The residual concentration of Phe can be checked by fluorescence, whose remarkable sensitivity allows detecting up to 1×10^{-8} M of Phe. This concentration is far below the concentration threshold necessary to transfer chirality to the porphyrin aggregates (about 10^{-3} M). Dynamic light scattering measurements [46] have shown that, in

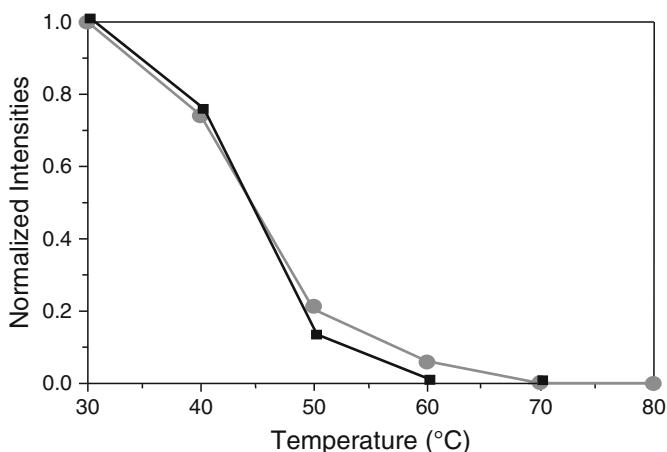


Fig. 10 Intensity variation with temperature of ELS of 80 mM L-phe solution (*circles*) and CD in the Soret region of the imprinted CuT4-H₂TPPS assemblies (*squares*). Modified from [46]

these conditions, the concentration of aggregated Phe is very small, being about 10^{-7} M. Therefore, as soon as most of the monomeric Phe is removed the equilibrium $n\text{Phe} \leftrightarrow (\text{Phe})_n$ can be considered completely shifted towards the monomeric form. Actually, in a 10^{-2} M Phe solution, 10^{-7} M Phe is in aggregate form. The cluster molecular weight being about 10^8 Da, it follows that the Phe cluster concentration able to imprint chirality in the porphyrin aggregate is 10^{-13} M. In this respect the title porphyrin system behaves as a reporter and amplifier of chirality [46].

A direct, fascinating consequence of the “memory” phenomenon is that the title aggregates are inherently chiral and then, in principle, excellent templates for their self-replication. Inset of Fig. 11 shows that when equimolar amounts of CuT4 and H₂TPPS are individually added to solutions containing about 6×10^{-13} M of imprinted-assemblies (each of them formed by about 2×10^6 porphyrin molecules, see [46]) the ICD of the imprinted-aggregates increases and doubles with doubling porphyrins concentration (Fig. 11). The linear increase of the CD with porphyrin concentration shows that the chiral growth process is substantially 100% enantiospecific.

Considering that CuT4 and H₂TPPS strongly interact in water solution forming achiral aggregates in the absence of chiral template, the high efficiency with which sub-picomolar concentration of chiral imprinted aggregate drives the formation of the new one implies that interaction of monomeric cationic and anionic porphyrins with chiral templates leads to chiral self-growth rate much faster than porphyrin assembling as achiral species when they are further away from the chiral template. Kinetic investigations [47] have permitted one to understand the discrimination mechanism and to hypothesize the possible sequence of events hereafter reported and sketched in Fig. 12: after the initial (within the first 10 ms) random distribution of the porphyrin along the template surface (panel a), a second process (within 0.2 s) may lead to a conformational change of the template (panel b) which then favours the formation of a more discrete distribution of porphyrins on the template (panel c). It is only after this event that the interaction of a second porphyrin at

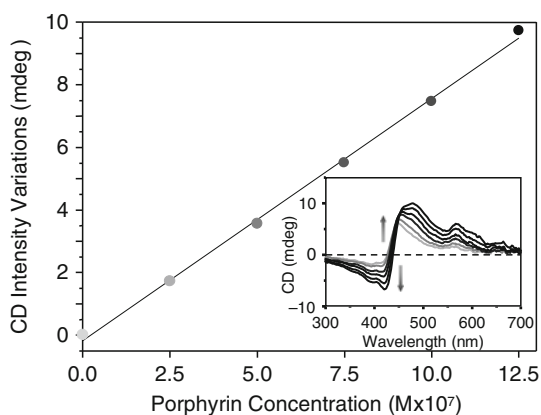


Fig. 11 CD increase of the phenylalanine imprinted aggregates (CD intensity variation) vs the added porphyrin concentration (each aliquots is 0.25 μM). *Inset:* CD spectra before (grey curve) and after five additions of the individual porphyrins. Modified from [45]

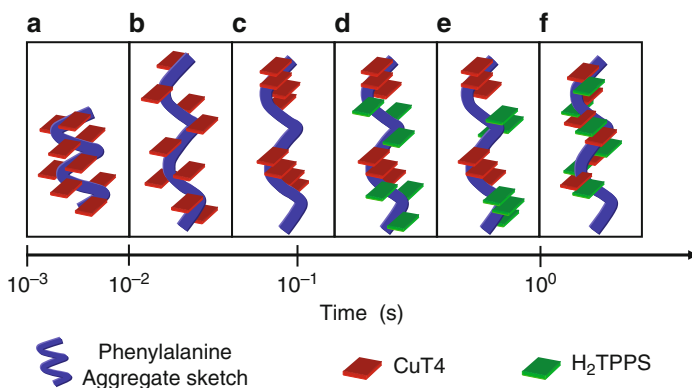


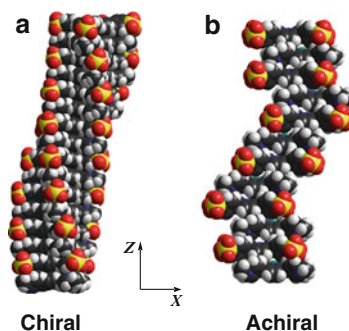
Fig. 12 Stylization of a possible sequence of event. The order of porphyrins addition does not affect the process. Modified from [47]

topologically distinct sites may occur (panel d). At this point, the interaction of the second porphyrin follows the same sequence of events (panel e), followed by a slow hetero-aggregation of the two porphyrins, driven by electrostatic interactions and characterized by a strong chirality (panel f), as suggested by CD.

These kinetic studies show that sub-picomolar concentration of chiral non-covalent polymers plays an efficient catalytic role in the aggregation of opposite-charged porphyrins. The rate of hetero-aggregation onto the chiral surface is, in fact, about two orders of magnitude faster than that measured in its absence, explaining the chiral amplification exerted by porphyrin aggregates. Considering the whole process, the rate limiting step is the diffusion of the two self-aggregates of CuT4 and H₂TPPS (bound at topologically distinct sites) on the Phe cluster surface to form chiral hetero-aggregates. When the imprinted template free chiral hetero-aggregates is used as mould, the singular consecutive addition of the two porphyrins to a 10^{-13} M solution of it determines a self-similar species growth characterized by kinetics too fast to be followed using stopped-flow technique (data not published). This happens because the above-mentioned “slow” diffusion step on the template surface does not verify anymore.

A more complete characterization of this system has been accomplished, determining the solid state structure of the template (L-Phe) free chiral CuT4-H₂TPPS hetero-aggregate through Energy Dispersive X-ray Diffraction (EDXD) analysis [48]. It represents the first structural determination of a porphyrin (chiral) hetero-aggregate. Also, a comparison with the amorphous hetero-aggregate structure that the same porphyrins form in the absence of the chiral template has been reported. In fact, morphology and structure of the porphyrin aggregates are responsible for the porphyrin physical and chemical–physical properties. This relationship is particularly true for the properties of the chiral assemblies. In this perspective, the determination of the supramolecular system structure becomes an essential point

Fig. 13 Molecular packing of the chiral (a) and achiral (b) CuT4-H₂TPPS assembly. Modified from [48]



to clarify the structure-functions relationship in order to increase our ability to design systems having the desired properties.

The syntheses of the CuT4-H₂TPPS chiral hetero-aggregate samples for EDXD analysis need particular care, and were carried out by following a purely non-covalent approach [48].

The structural study of L-Phe-imprinted hetero-aggregates of CuT₄-H₂TPPS compared to the equivalent non-imprinted sample in solid state, performed with EDXD, has shown that the template imprints a helical superstructure responsible for the CD properties (Fig. 13). The lack of template during the onset of the aggregation process leads to a randomly arranged structure and a lack of CD signal in the region of absorbance of the porphyrins. The suprachiral hetero-assembly helical arrangement is, more precisely, characterized by a pitch length of (62.17 ± 0.20) Å, a radius of (5.50 ± 0.30) Å and an interplanar distance of (3.90 ± 0.10) Å. In contrast, the arrangement of the non-template imprinted sample is completely disordered, amorphous and therefore achiral.

3.2 Reversibility of Chiral Memory

As a consequence of their inertness and stability, these aggregates present a lack of reversibility which is in opposition to the fundamentals of supramolecular chemistry which is, in contrast, based on dynamic and reversible behaviour. Static behaviour would lead to the end of the “story”: so let us try to find a possible way to go back and forth with the memorized chirality.

Inertness of the title chiral hetero-porphyrin complexes springs out mainly from the extended network of (strong and weak) electrostatic interactions between the tetra-cationic and tetra-anionic porphyrins. Therefore we can go from a static to a dynamic system (that is we can get reversibility of aggregation) by switching on and off the stronger electrostatic interactions in the network that holds up the non-covalent supramolecular structure: those between net charges [49]. Switching of the electrostatic interactions can be easily achieved by replacing the four

N-methylpyridyl groups (permanently cationic) in the *meso* position of the porphine ring with four pyridyl groups which are *ionisable* (Fig. 14 $pK_a \approx 4$), and can cycle between neutral (deprotonated) and cationic (protonated) states. In order to avoid nitrogen protonation of the inner core of H_2TPPS ($pK_a \approx 5$) we have used CuTPPS instead of the naked anionic parent (Fig. 1). L-Phe and D-Phe are the chiral templates.

In such a design, deprotonation of the four pyridines causes the loss of the positive charges (Fig. 14) and consequently the disassembly of the supramolecular complex: re-protonation would lead to reassembly of the aggregate, but what about the chiral information? Indeed, to reassemble the chiral supramolecular structure after the chiral template removal is the crucial and most tricky step of the whole “erase and rewrite” process. In fact, apparently, “switching on” the electrostatic interactions by re-protonating the four *meso* basic groups (Fig. 14) should lead to the *achiral* complex between the two porphyrins because the chiral information should be lost after the erase reaction (Scheme 2, route *a*).

However, a careful critical analysis of the kinetic properties of these species makes clear that it is possible to store–erase–rewrite the memory of chirality. As previously shown, the storing process is readily accessible: if we have the right molecular components the game is easy.

What about the other two steps: that is, the On–Off procedure? Indeed, the erase and rewrite processes are potentially stored in the properties of the aggregates.

First of all, they are kinetically inert. This means that deprotonation of the four acid groups of the pyridyl moieties would not cause the complete destruction of the chiral complexes but should leave a small amount of chiral seeds (Scheme 2, route *b*). In addition these species are huge: built by one million porphyrins. Therefore, it is conceivable that most water is excluded from the inner part of these species giving rise to families of pK_a values. As a result, pH changes around the pK_a value will not lead to a complete disassembly: a certain small amount of aggregates might resist (condition A).

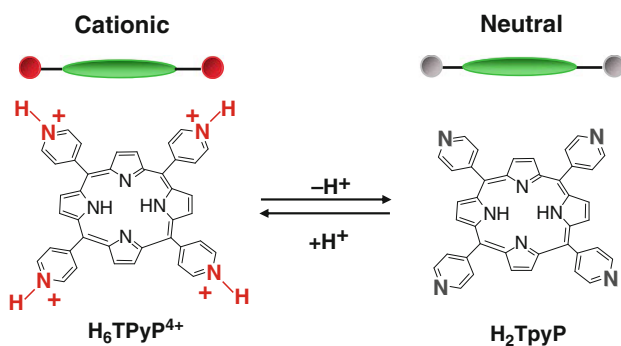
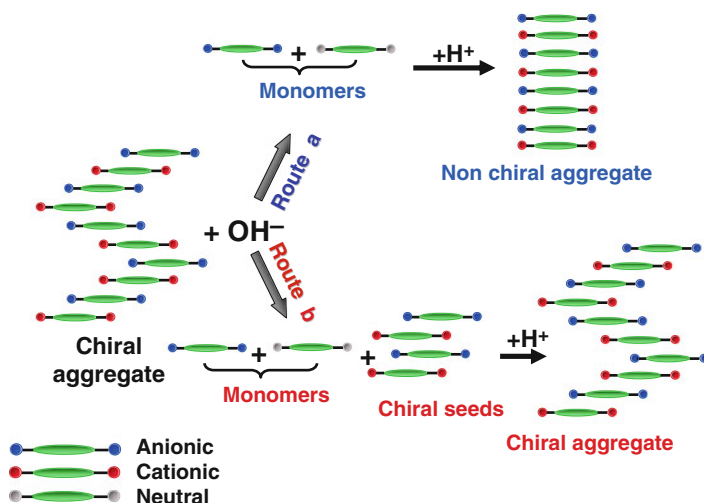


Fig. 14 Protonation equilibrium of the neutral porphyrin H_2TPyP . Modified from [45]



Scheme 2 Picture of the pH-induced disassembly of the chiral porphyrin aggregate and of the two possible reassembling paths. Route a: the chiral aggregate is completely disassembled after the pH-jump. Route b: some undetectable chiral seed survive the pH-jump. Modified from [45]

Second, these assemblies are excellent chiral templates which very efficiently self-catalyse their enantioselective growth [47]. Therefore a lasting small amount of chiral seeds should be enough to promote the formation of the *chiral* supramolecular complex (condition B) (Scheme 2, route *b*). If conditions A and B hold, route *b* of Scheme 2 should be prevalent over route *a*, permitting cycling between a static and a *quasi-dynamic* system.

The concept of *quasi-dynamic* is fundamental to design the erase-rewrite system. It is strictly related to the possible presence of chiral seeds in solution. So we define the system *quasi-dynamic* because part of it should stay in a static condition (the seeds) and part in a dynamic condition (the monomers). From a spectroscopic point of view, at high pH, the “ICD” signal should disappear (in solution there should be achiral monomers plus a spectroscopically undetectable amount of chiral seeds) and reappear at low pH (chiral reassembly) because the chiral reassembly is driven by the seeds.

The reassembly process is, indeed, a nice example of amplification process.

The first and preliminary step is to check that L-Phe or D-Phe are effectively able to imprint a chiral structure in the porphyrin hetero-assembly and to verify the reversible appearance and disappearance of the “induced” CD signal cycling between basic and acidic condition in the presence of the amino acid [49].

The non-covalent synthesis of the chiral porphyrin aggregate has been performed as discussed in the previous paragraph. Addition of an equimolar amount of H_6TPyP^{4+} and CuTPPS (Figs. 14 and 1, respectively) to a solution at pH 2.3 (by HCl) of L-Phe or D-Phe leads to mirror images induced CD signal in the

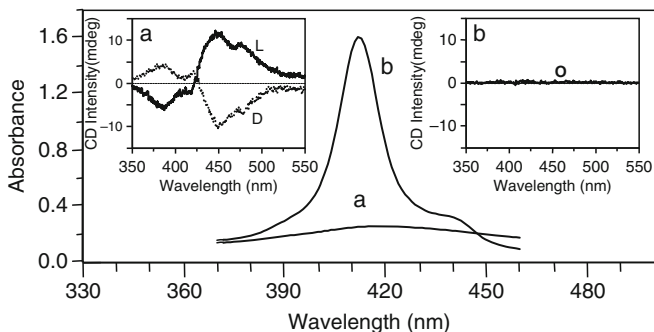


Fig. 15 Absorbance spectra of the couple $H_2TPyP-CuTPPS$ in the aggregated state at pH 2.3 (curve *a*) and in the disassembled state at pH 9.0 (curve *b*). Inset *a*: CD spectra of an aqueous solution of $H_2TPyP-CuTPPS$ ($4 \mu M$ each) aggregated in presence of L- (curve *L*) and D- (curve *D*) phenylalanine at pH 2.3. Inset *b*: CD spectra of an aqueous solution of $H_2TPyP-CuTPPS$ ($4 \mu M$ each) aggregated in simple water at pH 2.3. Modified from [45]

Soret region¹ (inset *a* of Fig. 15) and to about 90% of hypochromicity of the Soret band (Fig. 15, curve *a*). When the pH of the solution is increased from 2.3 to 9.0, the CD of the chiral porphyrin aggregates disappears (inset *b* of Fig. 15) and the absorption spectra experiences quite a strong hyperchromicity (Fig. 15, curve *b*), indicating that most of the porphyrins are in a monomeric state. Decreasing again the pH at 2.3 the CD signal of the porphyrin aggregate is restored (after about 10 min). So the system responds quite well to the external stimuli and, in the presence of phenylalanine, it is able to switch off and on “indefinitely” the supra-molecular chiral information.

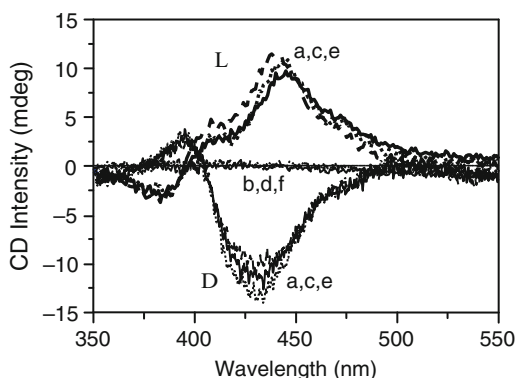
At this point, the most delicate stages of the work have to be performed: (1) removal of the amino acid from the imprinted porphyrin hetero-aggregate solution (in acidic condition) and (2) cycling between acidic and basic conditions to “erase and rewrite” the CD signal (i.e. the chiral information).

Elimination of phenylalanine, by ultra-filtration of the solution, does not affect the chirality of the aggregates, as shown by the persistence of the CD signal in the Soret region. Also, addition of the two porphyrins to the solution containing the supra-molecular chiral assembly leads to the growth of the chiral architectures confirming the remarkable ability of these chiral aggregates to template their own enantio-specific self-propagation [49].

Now the last and most important steps to validate experimentally our hypothesis can be performed: “erase and rewrite” the chiral information using solutions of the amino acid-free chiral porphyrin assemblies.

¹On the contrary, no CD signal is observed when the two porphyrins are mixed in pure water (pH 2.3).

Fig. 16 CD spectra of H_2TPyP -CuTPPS at pH 2.3 (curves *a, b, c*) and pH 9 (curves *b, d, f*) for the L- and D-imprinted aggregates. Modified from [45]



The experiment shown in Fig. 16 [49] demonstrates that, indeed, the “ICD” of the phenylalanine-free chiral aggregate can be cyclically switched “on and off”. The CD for both the L- and D-imprinted aggregates disappears by increasing the pH from 2.3 to 9.0 (Fig. 16, curves *b, d, f*), and it is restored by lowering back the pH at 2.3 (Fig. 16, curves *a, c, e*). No “ICD” is observed for the achiral aggregates when cycling between pH 2.3 and 9.0.

Again, CD changes are parallel to the remarkable absorption variations. Protonation at pH 2.3 of the H_2TPyP peripheral nitrogens leads to aggregation and to about 90% of hypochromicity (Fig. 15, spectrum *a*) whereas deprotonation (at pH 9.0) restores the Soret intensity (Fig. 15, spectrum *b*).

As hypothesized, the remarkable kinetic inertia of the imprinted aggregates allows for the persistence of a spectroscopically undetectable amount of chiral seeds which drives the re-assembly of the chiral structure (Scheme 2, route *b*). Ten consecutive cycles were performed to test the system on-off cycling ability, but, in principle, there are no apparent limitations to the number of cycles that can be performed.

The re-assembly process is time dependent. The CD signal reappears 5 min after the pH driven (from 9.0 to 2.3) aggregation and increases with time. The spectra reported in Fig. 16 have been recorded 10 min after the 9.0→2.3 pH variation [49].

In order to demonstrate that the chiral porphyrin reassembly is due to the presence of the (spectroscopically silent) chiral seeds of the porphyrin aggregate, various solutions of the chiral aggregates were kept at pH 9.0 (that is in the disassembled state) for different time intervals before reassembling them (lowering the pH at 2.3) [49]. In fact, if the chiral reassembly is driven by the presence of inert chiral seeds, then (at pH 9.0) there must be a time interval after which the chiral seeds will disassemble. Then chirality would not be reversible anymore and the system will reassemble in a non-chiral fashion (see route *a* in Scheme 2). Indeed, after about 24 h at pH 9, the CD at pH 2.3 is not restored anymore because the chiral seeds also disassembled.

4 How Big Must the Template Be in Order to Imprint the Chiral Information?

It was previously mentioned that, most likely, there exists a critic template size below which it is no longer possible to transfer the chiral information. DLS measurements suggest that for phenylalanine clusters this size is about 200 Å, [44–46] but, undoubtedly, the subject is worthy of deeper considerations. For this reason, monomeric “small” molecules showing chiral conformation was used as chiral template, i.e. the Λ and Δ enantiomers of ruthenium(II) cationic complexes (≈ 9 Å) (Fig. 17) [50, 51]. In addition, the use of ruthenium(II) cationic complexes turns out to be advantageous because of the possible activation of energy transfer processes from the inorganic to the organic moiety [52]. As the organic part, in fact, anionic porphyrins were used that have absorption bands (Q bands) in the region where the title ruthenium cationic complexes emits (around 600 nm). In particular, the inorganic species are the well-characterized cationic complex of ruthenium(II) with phenanthroline, $[\text{Ru}(\text{phen})_3]^{2+}$ (Fig. 17), while, the anionic porphyrins are tetra-anionic H_2TPPS (Fig. 1) and the *cis*- and *trans*-isomers of the dianionic analogue: 5,10-bis(4-sulfonatophenyl)-15,20-diphenylporphyrin (*cis*-DPPS) (Fig. 17) and 5,15-bis(4-sulfonatophenyl)-10,20-diphenylporphyrin (*trans*-DPPS), (Fig. 17) [50]. These three porphyrins have been particularly chosen for the different number (two or four) and reciprocal (symmetrical, *cis* or *trans*) disposition of the anionic (4-sulfonatophenyl) peripheral groups in the *meso* positions.

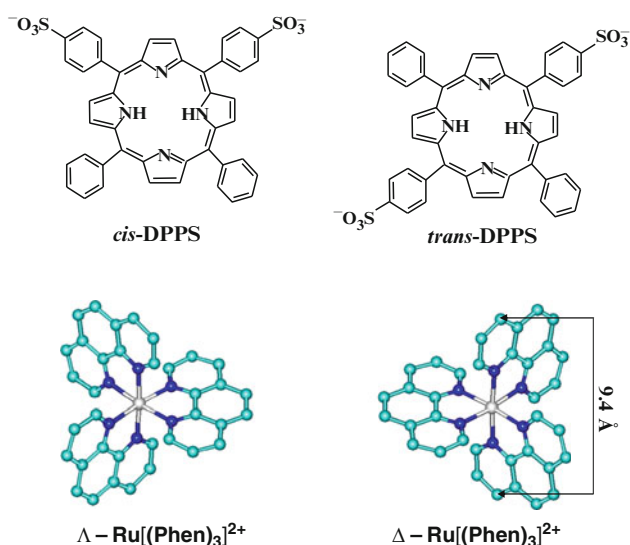


Fig. 17 Structure of the anionic porphyrin *cis*- and *trans*-DPPS and of the Λ - and Δ - enantiomers of $[\text{Ru}(\text{phen})_3]^{2+}$. Modified from [50, 51]

Spectroscopic characterization (through UV-vis absorption, RLS, fluorescence and CD technique) of these systems indicates that $[\text{Ru}(\text{phen})_3]^{2+}$ complexes are effectively able to interact with all the three title porphyrins and to transfer the chiral information [50]. Complexation between the inorganic cationic complex and each porphyrin is confirmed by the appearance of an induced CD signal in the absorption region of the macrocycles (Figs. 18c, 19c and 20c). The sign of the ICD follows the chirality of the inorganic template and the interaction of the three porphyrins with the Λ - and Δ -conformers induces mirror images ICD [53]. The bisignate shape of the CD signal also indicates some electronic communication between porphyrins, indicating their self-aggregation [50].

Moreover, interactions between *cis*-DPPS or *trans*-DPPS with $[\text{Ru}(\text{phen})_3]^{2+}$ reflect the different number and/or position of the anionic groups in the porphyrin macrocycle. In particular, $[\text{Ru}(\text{phen})_3]^{2+}$ forms with H_2TPPS species in 1:2 molar ratio. This finding is in agreement with the formation of a (formally) neutral species because of the 1:2 charge ratio between the two components. RLS data also

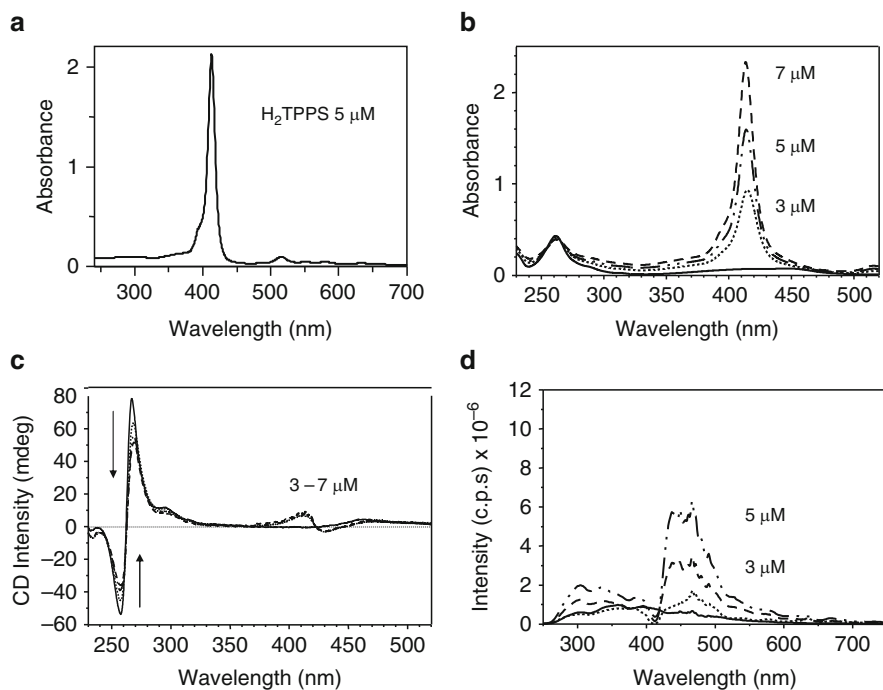


Fig. 18 (a) Absorption spectrum of a 5 μM H_2TPPS aqueous solution. (b) Absorption spectra of a 5 μM Λ - $[\text{Ru}(\text{phen})_3]^{2+}$ aqueous solution in the absence (solid line) and in the presence of different concentrations of H_2TPPS . (c) CD spectra of a 5 μM Λ - $[\text{Ru}(\text{phen})_3]^{2+}$ solution (solid line) in the absence and in the presence of different concentrations of H_2TPPS . (d) RLS spectra of a 5 μM Λ - $[\text{Ru}(\text{phen})_3]^{2+}$ solution (solid line) in the absence and in the presence of different concentrations of H_2TPPS . The RLS spectrum of a 5 μM H_2TPPS aqueous solution (dotted line) is also reported. Modified from [50]

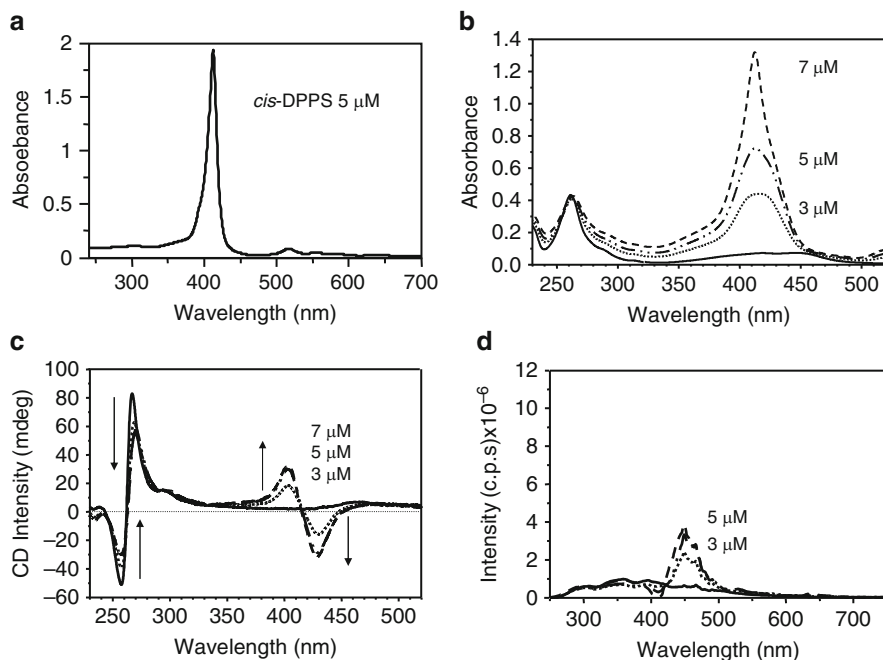


Fig. 19 (a) Absorption spectrum of a $5 \mu\text{M}$ *cis*-DPPS aqueous solution. (b) Absorption spectra of a $5 \mu\text{M}$ $\Lambda\text{-Ru}[(\text{Phen})_3]^{2+}$ aqueous solution (solid line) in the absence and in the presence of different concentrations of *cis*-DPPS. (c) CD spectra of a $5 \mu\text{M}$ $\Lambda\text{-Ru}[(\text{Phen})_3]^{2+}$ solution (solid line) in the absence and in the presence of different concentrations of *cis*-DPPS. (d) RLS spectra of a $5 \mu\text{M}$ $\Lambda\text{-Ru}[(\text{Phen})_3]^{2+}$ solution (solid line) in the absence and in the presence of different concentrations of *cis*-DPPS. The RLS spectrum of a $5 \mu\text{M}$ *cis*-DPPS aqueous solution (dotted line) is also reported. Modified from [50]

(Fig. 18d) confirm the presence of some porphyrin aggregation. *cis*-DPPS instead forms complexes in 1:1 molar ratio. Both the bisignate shape of the ICD signal (Fig. 19c) and the RLS (Fig. 19d) signal intensity evidence of some porphyrin aggregation, even if, to a lower extent with respect to those formed in the $[\text{Ru}(\text{phen})_3]^{2+}\text{-H}_2\text{TPPS}$ system. The most extended aggregation is observed in the $[\text{Ru}(\text{phen})_3]^{2+}\text{-trans-DPPS}$ system (Fig. 20). In this case a more complex behaviour is observed. In fact, the titration of $[\text{Ru}(\text{phen})_3]^{2+}$ solutions with increasing amounts of *trans*-DPPS indicates first the formation of a species with molar ratio ($[\text{Ru}(\text{phen})_3]^{2+}:\text{trans-DPPS}$) 5:6, while, following further additions of porphyrin (beginning from 5:7 molar ratio), a new species is formed. However, it is worth recalling that, because of porphyrins aggregation, the stoichiometric ratio of these systems does not (always) reflect the molecularity of a single species but it is just an average between the stoichiometry of different species.

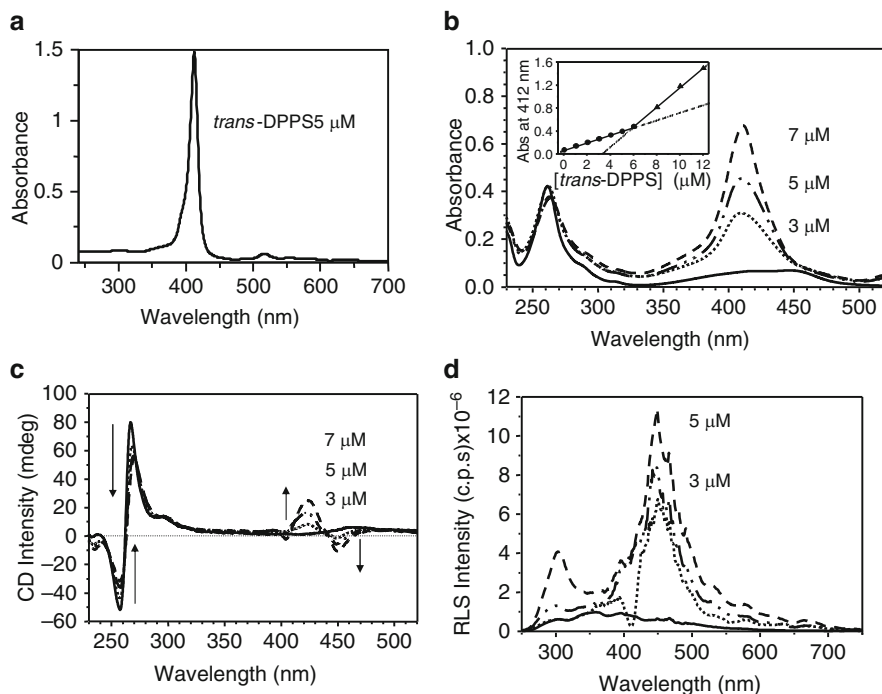


Fig. 20 (a) Absorption spectrum of a 5 μM *trans*-DPPS aqueous solution. (b) Absorption spectra of a 5 μM Λ -Ru[(Phen)₃]²⁺ aqueous solution (*solid line*) in the absence and in the presence of different concentrations of *cis*-DPPS. (c) CD spectra of a 5 μM Λ -Ru[(Phen)₃]²⁺ solution (*solid line*) in the absence and in the presence of different concentrations of *cis*-DPPS. (d) RLS spectra of a 5 μM Λ -Ru[(Phen)₃]²⁺ solution (*solid line*) in the absence and in the presence of different concentrations of *cis*-DPPS. The RLS spectrum of a 5 μM *cis*-DPPS aqueous solution (*dotted line*) is also reported. Modified from [50]

Moreover, fluorescence characterization of these systems indicated, as previously hypothesized, that ruthenium(II) cationic complexes are able to activate energy transfer processes towards the anionic porphyrins [50].

For example, in Fig. 21 the emission spectrum of a solution in which [Ru(phen)₃]²⁺ and *cis*-DPPS are dissolved in a 1:1 ratio (spectrum *c*) together with the emission bands of the two components alone (*a* and *b*, respectively) are shown. The spectra have been recorded by exciting at 262 nm, that is in a region where porphyrin absorption is very weak (about 0.06 absorption units in our experimental conditions) whereas [Ru(phen)₃]²⁺ has the strongest absorption band (about 0.4 absorption units in our experimental conditions). The emission of [Ru(phen)₃]²⁺ alone is centred at 590 nm and, quite interestingly, is completely quenched upon the addition of an equimolar amount of *cis*-DPPS. The emission of free *cis*-DPPS is much weaker than that of [Ru(phen)₃]²⁺ because of the much lower absorbance, yet after the addition of [Ru(phen)₃]²⁺ the porphyrin emission maintains its intensity.

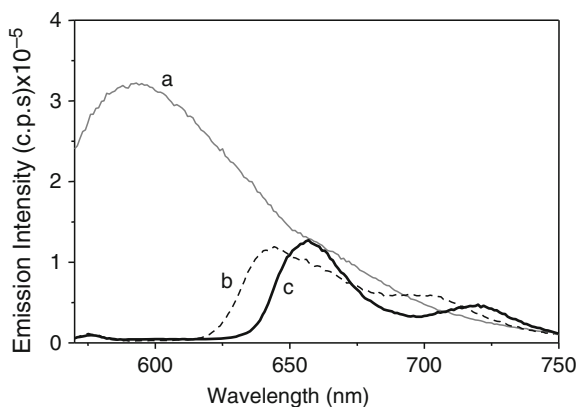


Fig. 21 Emission spectrum of a 5 μM Λ -Ru[(Phen) $_3$] $^{2+}$ aqueous solution in the absence (curve *a*, $\lambda_{\text{ex}} = 262$ nm) and in the presence of 5 μM *trans*-DPPS (curve *c*). Curve *b* is the emission spectrum of a 5 μM *trans*-DPPS aqueous solution ($\lambda_{\text{ex}} = 262$ nm). Modified from [50]

The latter observation suggests some transfer of energy from the ruthenium moiety to the porphyrin. In fact, the presence of [Ru(phen) $_3$] $^{2+}$ (which strongly absorbs at 262 nm) should reduce the number of photons absorbed from the porphyrin and then cause a trivial quenching of the emission. This reduction is further increased by the porphyrin absorption hypochromicity following complexation with [Ru(phen) $_3$] $^{2+}$. In spite of these effects, the emission intensity of *cis*-DPPS is unchanged and allows one to hypothesize that [Ru(phen) $_3$] $^{2+}$ is partially transferring energy to the porphyrin moiety [50].

For both H $_2$ TPPS and *trans*-DPPS we have observed similar but less pronounced effects. This can be rationalized by recalling that the *cis*-isomer forms the smallest aggregates (and then self-quenching due to aggregation is reduced) but, quite likely, also the most organized assemblies (the ICD is the most intense in this series) facilitating the above hypothesized energy transfer.

The behaviour of the systems presented above is, however, even more complex and richer than what we have shown until now. In particular, a deeper study of the tetra-anionic porphyrin–Ru-complexes system has revealed that, using proper experimental conditions, not only the porphyrin J-aggregates show the chiral memory phenomenon, but also that the chiral information can be cyclically erased and rewritten, switching on and off the porphyrin ICD signal by pH variations [51].

We anticipate that this “memory” system also shows a remarkable dependence on the succession of events leading to the final chiral aggregate at pH 2.5: a “wrong” sequence of instructions opens alternatives routes.² The first step of synthesis is the interaction in aqueous solution at pH ≈ 6.0 (and in the presence of NaCl 0.3 M) of

²The formation of the J aggregates is hierarchically controlled. The only way to obtain these species is by allowing porphyrin aggregation with Λ - or Δ -[Ru(phen) $_3$] $^{2+}$ at a pH value of around 6 and then decreasing the pH to 2.5.

H_2TPPS and $[Ru(phen)_3]^{2+}$. Interaction is indicated by variation in the absorption spectra (Fig. 22) and, especially, by the appearance of an induced circular dichroism (Fig. 23) band in the absorption region of the achiral porphyrin. The relationship between chirality of the cationic metal complex and that transferred to the anionic porphyrins is straightforward because interactions of H_2TPPS with the Λ - and Δ - $[Ru(phen)_3]^{2+}$ lead to mirror-image ICD signals (Fig. 23) [51].

The second and final step of the synthesis is accomplished by lowering the pH from ≈ 6.0 to 2.5 (see footnote 2). This leads to spectroscopic variations reporting

Fig. 22 Absorption spectra of $[Ru(phen)_3]^{2+}$ 10 μM at pH = 6.0, NaCl (0.3 M) (*solid curve*) in presence of H_2TPPS 10 μM (*dashed curve*). Spectra were recorded about 1 h after mixing the reagents. Modified from [51]

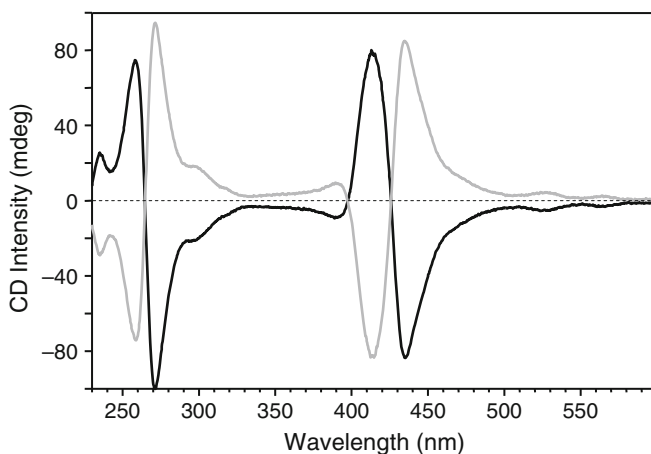
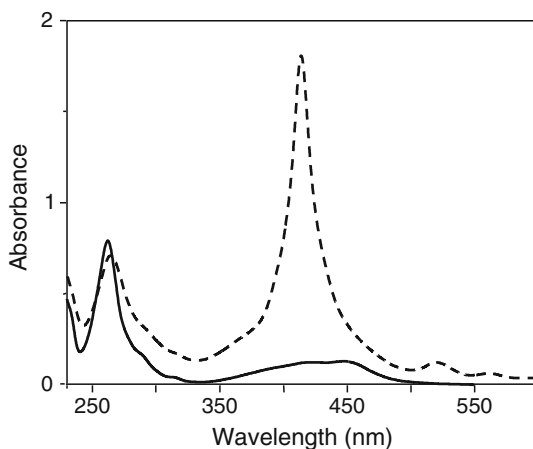


Fig. 23 CD spectra of H_2TPPS 10 μM at pH = 6.0, NaCl (0.3 M) in the presence of Δ - (*solid curve*) and Λ - $[Ru(phen)_3]^{2+}$ (10 μM , *grey curve*) Spectra were recorded about 1 h after mixing the reagents. Modified from [51]

the protonation of the central nitrogen atoms: that is, disappearance of the absorption band at 412 nm (Fig. 24, solid line) and appearance of the band of H_4TPPS at 436 nm (Fig. 24, dashed line). After around 10 min a new absorption band appears at 490 nm and reports the formation of the J aggregates, (Fig. 24, dotted line). The CD spectrum changes accordingly: the exciton-coupled CD band centred at 422 nm disappears soon after the addition of HCl (Fig. 25, solid line) and after around 10 min two new sets of exciton couplet bands centred at 422 nm (H aggregates) and 490 nm (J aggregates) appear (Fig. 25, dotted line). Also in this case it is evident that the chirality of the J aggregates stems from the inorganic

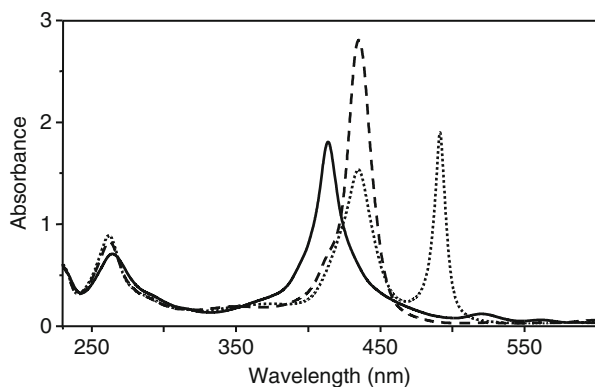


Fig. 24 Absorption spectra of H_2TPPS4 10 μM in NaCl (0.3 M) at pH 7 (solid curve) and at pH 2 (dashed curve) and after 10 min (dotted curve). Modified from [51]

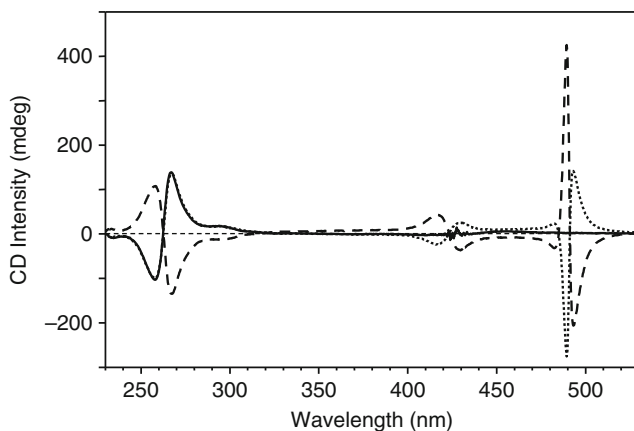


Fig. 25 CD spectra of H_4TPPS4 (10 μM , pH 2.5, NaCl (0.3 M)) in the presence of Δ^- (10 μM , dashed curve) and Λ^- -[Ru(phen) $_3$] $^{2+}$ (10 μM , dotted curve). The solid curve shows the CD spectrum of Λ^- -[Ru(phen) $_3$] $^{2+}$ / H_4TPPS4 system at pH 2.5 soon after the addition of HCl (the spectrum of Δ^- -[Ru(phen) $_3$] $^{2+}$ / H_4TPPS4 is identical and not shown for simplicity). Modified from [51]

template because the exciton bands of H and J aggregates formed with the two enantiomers are, in fact, mirror image one of the other (Fig. 25, dotted line and dashed line) [51].

Memory of chirality is demonstrated by a simple experiment: addition of an excess of Δ -[Ru(phen)₃]²⁺ (15 μ M) to J aggregates preformed in the presence of Λ -[Ru(phen)₃]²⁺ (10 μ M) does not cause inversion of the CD bands in the visible region (where the absorption features of porphyrins dominate) but only in the UV region (the spectroscopic region where absorption of the inorganic complex occurs). This straightforward experiment (Fig. 26) shows that this type of J aggregates “remembers” the chirality imprinted at the very onset of their formation [51].

In order to check the feasibility of switching the memory Off and On, we have performed pH cycles (2.5 \rightarrow 6.0 \rightarrow 2.5) on a solution containing chiral J aggregates of H₄TPPS4 templated on Λ -[Ru(phen)₃]²⁺ but in the presence of an excess of Δ -[Ru(phen)₃]²⁺ (the system discussed in Fig. 26). The absorption changes are predictable: (1) the jump from pH 2.5 (Fig. 27, curve a, dotted line) to around 6.0 (Fig. 27,

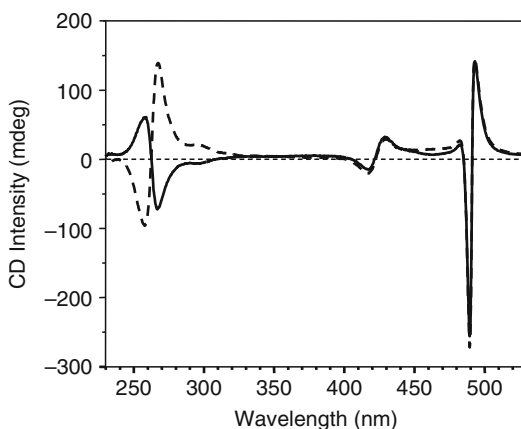


Fig. 26 CD spectra of the H₄TPPS4 J-aggregates formed in the presence of 10 μ M Λ -[Ru(phen)₃]²⁺ before (*dashed curve*) and after (*solid curve*) the addition of an excess (15 μ M) of Δ -[Ru(phen)₃]²⁺. Modified from [51]

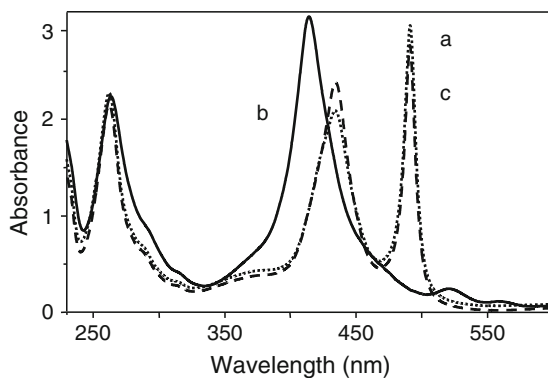
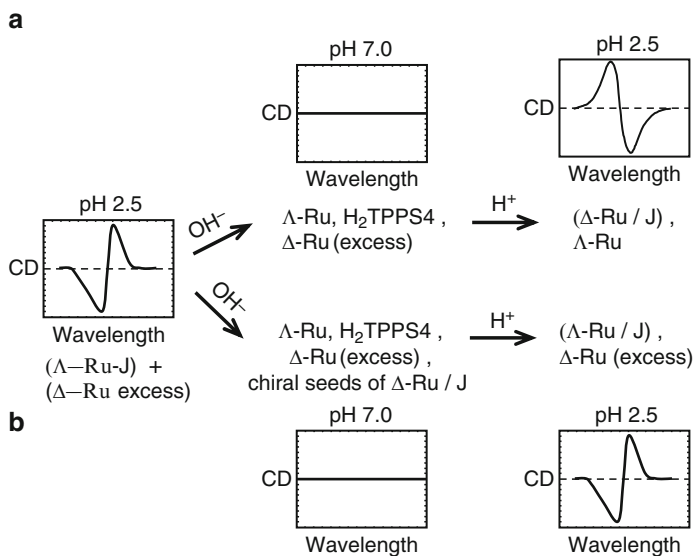


Fig. 27 Absorption spectra of Λ -[Ru(phen)₃]²⁺/H₄TPPS4 (10 μ M, pH 2.5, NaCl (0.3 M)) complex in presence of an excess (15 μ M) of Δ -[Ru(phen)₃]²⁺ (*dotted curve a*) then at pH 6.0 (*solid curve b*) and again at pH 2.5 (*dashed curve c*). Modified from [51]

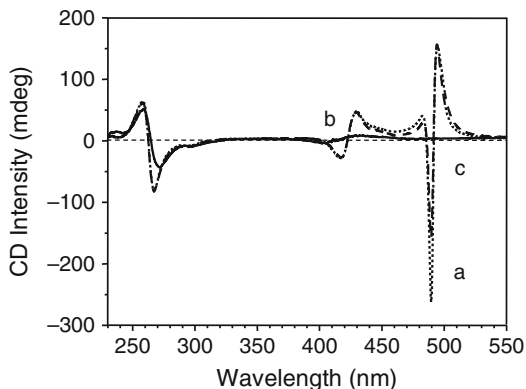
curve b, solid line) will cause porphyrin deprotonation and disassembly of the J aggregates and (2) the following decrease of the pH value to 2.5 (Fig. 27, curve c, dashed line) will lead to (re)protonation of porphyrins and, with time, to the reassembly of the chiral J aggregates [51]. In contrast, the results of the CD experiments are not easily predicted. In fact, in these experimental conditions, two routes are possible (Scheme 3): the first (A) leads to the enantiomeric form (Δ -[Ru(phen)₃]²⁺/J aggregates) of the starting aggregates (Λ -[Ru(phen)₃]²⁺/J aggregates), whilst the second route (B) proceeds with retention of the starting chirality. Route A should be followed if the Λ -[Ru(phen)₃]²⁺/J aggregates are completely destroyed upon porphyrin deprotonation: in this case the excess of the Δ enantiomer will cast the opposite chirality to that initially present. The second route (B) should prevail if the remarkable inertness of the J aggregates (demonstrated by their ability of memorizing the chirality) permits only a partial disassembly to leave a spectroscopically undetectable concentration of Λ -[Ru(phen)₃]²⁺/J aggregates. Here, again, the presence of a quasi-dynamic system is indispensable in order to obtain the reversible amplification of chiral undetectable seeds.

CD data of the pH cycles are shown in Fig. 28 and demonstrate that route B prevails over route A [51]. The absorption spectra (Fig. 27) show that, upon changing the pH value from 2.5 to around 6.0, the spectrum of the non-protonated H₂TPPS is restored: the subsequent decrease of pH to 2.5 leads again (within 5 min) to the J aggregates. The CD spectra are consequently modified in two ways: (1) when the pH is raised from 2.5 (Fig. 28, curve a, dotted line) to around 6.0 the ICD



Scheme 3 Scheme of the two possible reassembly pathways following disassembly of the J aggregates formed for interaction with Λ -[Ru(phen)₃]²⁺ but in the presence of an excess of Δ -[Ru(phen)₃]²⁺. Modified from [51]

Fig. 28 CD spectra of Λ -[Ru(phen)₃]²⁺/H₄TPPS4 (10 μ M, pH 2.5, NaCl (0.3 M)) complex in presence of an excess (15 μ M) of Δ -[Ru(phen)₃]²⁺ (dotted curve a) then at pH 6.0 (solid curve b) and again at pH 2.5 (dashed curve c). Modified from [51]



of the J aggregates disappears to give spectrum b³ (Fig. 28, solid line) and (2) the CD signal of the J aggregates is immediately restored after the pH jump to 2.5 (Fig. 28, curve c, dashed line). Remarkably, the sign of the exciton couplet is the same as that of the starting J complex, confirming the retention of chirality and the remarkable inertness of these chiral aggregates. The same results have been obtained starting from the Δ -[Ru(phen)₃]²⁺/J aggregates. Up to ten consecutive pH cycles were performed without observing any inversion of the CD Soret couplet.^{4,5} After these cycles the same solution was kept at a pH value of about 6.0 for 1, 2, 16, 24, 48 h, and 1 week. After each time interval the pH value was lowered to 2.5 and an identical CD signal shape was obtained, which shows the remarkable stability of these species.⁶

These results can be explained under the light of the experiment shown in the previous section: the inertness and catalytic properties [47] of the initially formed aggregates (seeds), which allow the J species to retain the memory of chirality transferred from Λ - or Δ -[Ru(phen)₃]²⁺ [51]. The increase of the pH value to around 6.0 does not disassemble all the aggregates: a residual concentration of these species remains in solution (the chiral seeds) and is able to drive very efficiently the correct folding of the memorized chirality in spite of the presence of an excess of the template that has an “opposite” handedness. In contrast, memory of chirality is lost if pH value is raised above 8. In these conditions the chiral seeds are destroyed and porphyrin monomers redistribute on the conformers of the metal complex.

³The CD signal of the (Δ -[Ru(phen)₃]²⁺/H₂TPPS) complex is absent because the formation of the complex is slow. The signal appears after 10–15 min.

⁴Memory of chirality is lost if the pH value is raised to 8.

⁵After about five pH cycles the solution becomes milky and scatters because of the formation of extended aggregates: this causes a decrease of the CD intensity.

⁶Melting experiments were also performed: the ICD of Λ - or Δ -[Ru(phen)₃]²⁺/J aggregates disappears at around 90°C. By lowering temperature at 25°C we have obtained the starting signal shape.

This example underlines the central role that hierarchy has in the noncovalent syntheses. It is, in fact, worth emphasizing that addition of chiral metal complexes to pre-formed J aggregates or addition of all components (metal complex, porphyrins, acid, and salt) at pH 2.5 (we have tried all the different combinations) is not effective to obtain the system described above.

5 Resolution of Chirality by Stirring: The Vortex Effect

This last example refers to a selective transfer of chirality. It treats of the action of vortices on a racemate mixture of J-aggregates. The vortex is per se a chiral force and we show that this action is selectively transferred to only one enantiomer. Indeed, the relationship between vortices and chirality of large assemblies is a very intriguing problem which might lead to understanding fundamentals of nature and, from this, to possible technological applications [54]. Since 1990 several different reports have dealt with this topic: some of them describe the formation of one enantiomeric form decided by stirring sense (“static” situation) [55–57]. Others describe a more “dynamic” situation in which clockwise (CW) and counter clockwise (CCW) stirring of solutions containing non-covalent assembly causes an increase of circular dichroism (CD) intensity and a dependence of the CD signs on the stirring sense [58–61]: stopping of stirring restores the initial situation. Interpretation of the dynamic situation results is still quite controversial: is the CD observed under stirring arising from instrumental artefacts, such as fibre alignment into the vortex, or is there also a contribution from real chirality?

Hereafter the behaviour under stirring of previously formed H₄TPPS J-aggregates will be described (Fig. 28) [62]. They respond to mechanical stirring in a dynamic fashion in that their CD signal inverts with stirring sense and the signal intensity increases (Fig. 29), but differently from other examples reported; for this particular system, static and dynamic aspects coexist. Artefacts arising from fibre alignment during stirring are taken for granted [60, 61, 63], even if recent data indicates that the signal contains contributions from chirality [64] as also predicted from theoretical models, foreseeing enantiomeric enrichment in vortices [65].

These premises done, the focus of the following discussion is to understand whether eddies have an impact on supramolecular chirality. Is a vortex able to affect nanoscale chirality? If so, how?

Before analysing the vortex effects on J-aggregates chirality it is worth recalling some peculiarities of this chemical system.

H₂TPPS is not chiral; however, self-aggregation of its protonated (zwitterionic) form (Fig. 29) [10, 28, 66, 67] (for the structure of the chiral aggregates see [68]) induces a split CD (Fig. 30) in the absorption region (Fig. 31) (CD splitting is related to transition moment coupling: positive couplets have the positive intensity at longer wavelengths; negative ones at shorter wavelengths [69]). Both positive (Δ) and negative (Δ) couplets are observed randomly (Fig. 32, black and grey curves, respectively). There are different explanations for the “spontaneous”

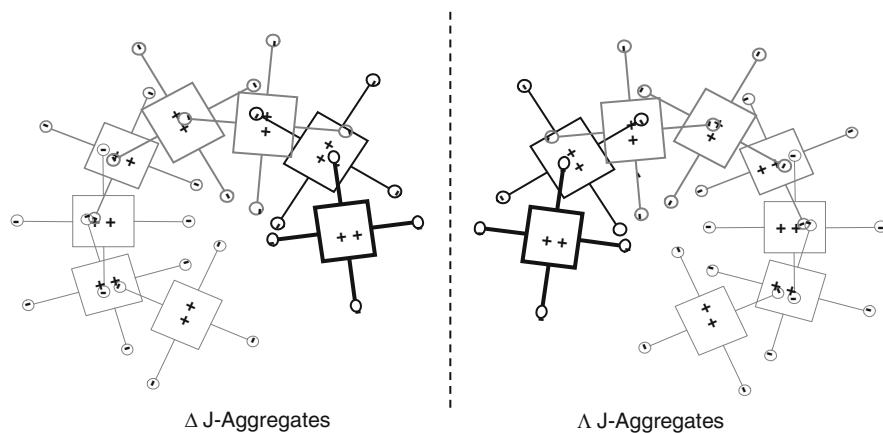


Fig. 29 Possible structure of chiral J-aggregates of H_2TPPS . Modified from [62]

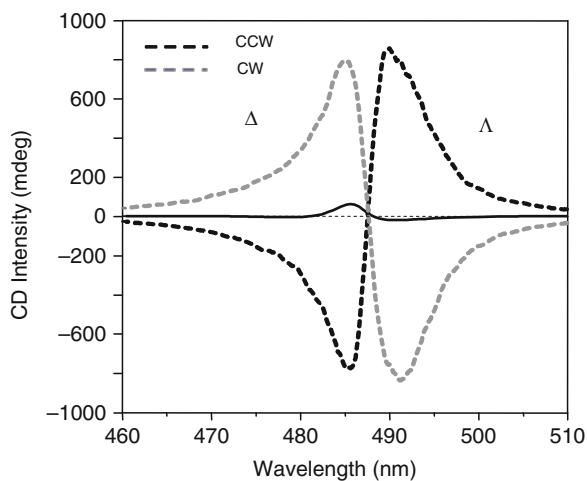


Fig. 30 CD spectra of H_4TPPS (10 μ M, pH 3, $[NaCl] = 0.3$ M) aqueous solutions during CW (grey dashed curve) and CCW (black dashed curve) stirring. The black solid curve shows the spectrum of the standing solution. Modified from [62]

emergence of aggregates chirality: (1) they are not chiral and gain chirality for the presence of picomolar traces of chiral contaminants [70],⁷ (2) they are inherently chiral (Fig. 29) and the 1:1 distribution of enantiomers undergoes to statistical

⁷If chirality is induced at the assembling onset then they will “remember” the shape during their growth leading to chiral amplification [46].

Fig. 31 Absorption spectrum of an aqueous solution of H₂TPPS (at pH 3, [NaCl] = 0.3 M). Modified from [62]

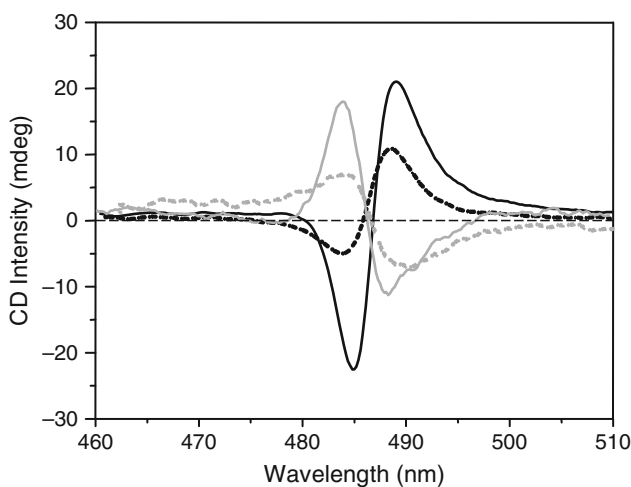
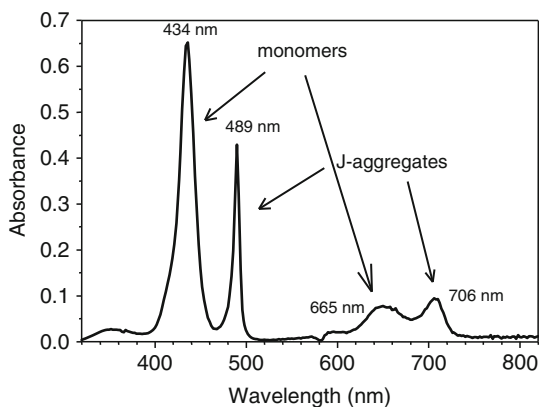


Fig. 32 CD spectra of standing solution soon after J-aggregation (*solid curves*) and empty cuvettes after standing with J-aggregates for 24 h (*dashed curves*) of Λ J-aggregates (*black curves*) and Δ J-aggregates (*grey curves*). Modified from [62]

breaking of parity rule, (3) they are inherently chiral and traces of chiral contaminants shift the 1:1 racemate equilibrium.

In our opinion, the second and the third hypotheses are the most likely. In fact, when working with the J-aggregate in “pure” water, just a small monosignated (negative or positive) CD signal – attributable to a racemate – is observed in the Soret region (Fig. 33).

Also, these aggregates have a tendency to stick onto the cuvette walls [71]; their deposition is revealed from absorption and CD spectra of the empty cuvette after

Fig. 33 CD spectrum of J-aggregate in pure water (racemate). Modified from [62]

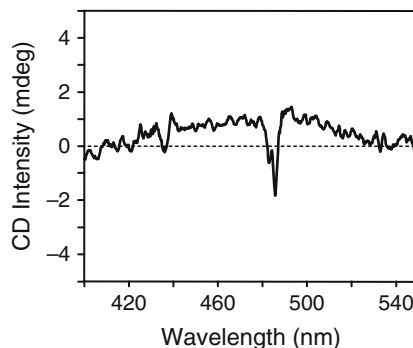
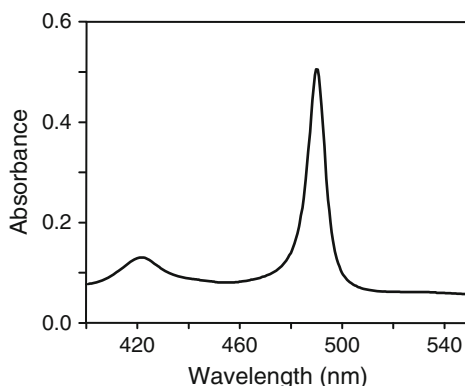


Fig. 34 Absorption spectrum of the species deposited onto the cuvette wall after standing with J-aggregates for 24 h. Modified from [62]



the removal of the J-aggregate solution which had been standing in the cuvette for 24 h. The dashed lines in Fig. 32 show the CD spectra of the empty cuvette, indicating that (1) the species which deposits onto the wall is the enantiomer present in solution at the higher concentration and (2) deposition phenomena do not induce any change in the CD shape (that is, there are no artefacts). Interestingly, the absorption spectrum (Fig. 34) does not show any absorption of the monomeric protonated species: only the bands of the J-aggregates at 489 nm and 422 nm are observed [58]. This result shows that only J-aggregates stick to the wall under these experimental conditions. This information is very important for the interpretation of the experimental data.

Our hypothesis is that J-aggregates are inherently chiral and exist in aqueous solution as racemate. We anticipate that their enantiomorphous distribution can be altered by vortex action: the enantiomer favoured by stirring is deposited on the cuvette wall, the other remains in solution. This is possible because stirring induces a thermodynamic unbalancing in the racemate solution. The situation is complicated because, being a weak thermodynamic force, vortex action competes with other forces, such as, for example, the (stronger) thermodynamic effect exerted by the presence of high concentrations of chiral templates.

To stress the surprising results arising from the effect of stirring, we will first discuss data in which the starting solution has already an excess of one enantiomeric form of J-aggregates⁸: the following data show that CW and CCW eddies allow for deposition (onto the cuvette wall) of the Δ and Λ enantiomer, respectively, independently from the chirality of the enantiomer(s) initially present in solution. Figure 35a shows the CD spectrum of a solution that presents an excess of Λ J-aggregates (solid line). It is worth recalling that standing solutions would show Λ deposition. However, leaving the solution for 24 h in the cuvette under CW stirring (which favours the Δ species) (Fig. 30), we observe, after removal of the solution, a CD signal of the Δ aggregate (Fig. 35a, dashed line) on the cuvette walls. Figure 35b shows that stirring CCW for 24 h, a solution of Δ J-aggregates leads to deposition of Λ aggregates. In both cases (and hereafter in all cases but that shown in Fig. 36) the CD spectrum of the solution after stirring is identical to the initial one (but for the intensity which is lower). For both systems only the absorption bands at 489 nm and 422 nm are detected. The absence of the protonated monomer band at 434 nm indicates that the absorption results from adhesion of the J-aggregates and not from aggregation of the monomers onto the wall.

According to the absorption spectra, and recalling the standing-system indications (the major species sticks onto the wall) (Fig. 32), it is possible to conclude that, under stirring, the major species in solution are the J-aggregates favoured by

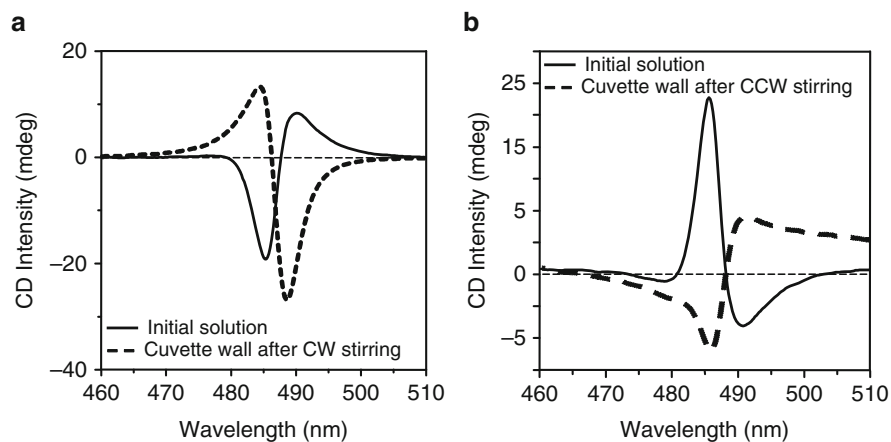


Fig. 35 CD spectra of J-aggregates of H_2TPPS : (a) initial solution of the Λ enantiomer (solid curve), empty cuvette after 24 h of CW stirring in the dark showing deposition of the Δ enantiomer (dashed curve); (b) shows that CCW stirring leads to deposition of Λ aggregates on the cuvette walls (dashed curve) although starting from a Δ initial solution (solid curve). Modified from [62]

⁸This is also the most common situation owing to the “impossibility” to get pure water.

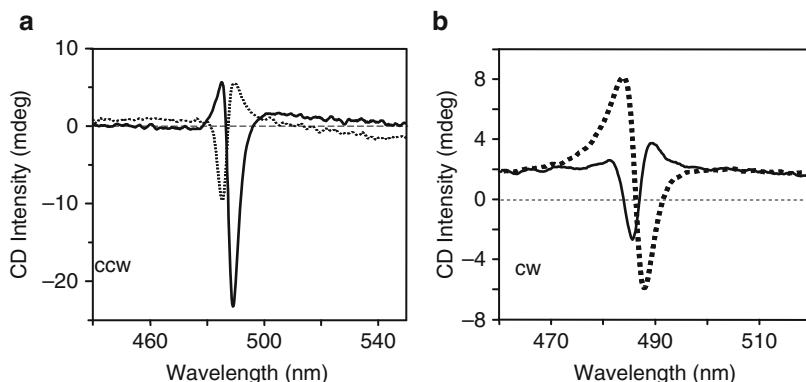
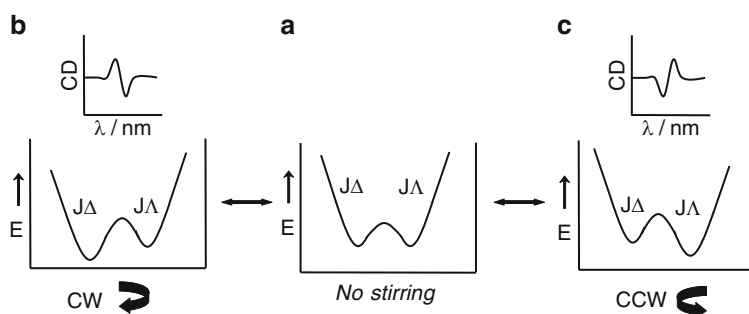


Fig. 36 (a) CD spectra of the inner solution of J-aggregate after 24 h CCW stirring in the dark (*solid curve*), starting from a racemate solution (see Fig. 32), and of cuvette walls (*dashed curve*), showing mirror image CD spectra. (b) The results obtained for CW stirring. Modified from [62]



Scheme 4 Schematic representation of the possible effect of the stirring on a racemate (a). CW (b) and CCW (c) stirring favour Δ and Λ J-aggregates, respectively. Modified from [62]

vortex rotation sense. This means that stirring is inducing a thermodynamic unbalancing in the racemate (Scheme 4).

Starting from the “racemate” in “pure” water (see Fig. 33), the same effect is obtained: the species favoured from stirring is on the wall and the “racemate” remains in solution. Only 4 times in almost 30 experiments with “pure” water was the enantiomer separation observed: the enantiomer “preferred” by stirring onto the wall the other one in solution (Fig. 36). Statistically the latter results might be considered scarcely significant; however, the significance increases taking into account the rare possibility of working with a system 100% free from chiral pollutants (pure water, pure acid and sodium chloride solutions, etc.). In our opinion, these results reinforce the hypothesis that J-aggregates of H_4TPPS exist as racemic mixtures.

To corroborate this point further, J-aggregation was performed in the presence of a racemate of the Λ and Δ enantiomers of $[\text{Ru}(\text{Phen})_3]^{2+}$. These chiral complexes, as previously shown, induce chirality in the aggregates of H_4TPPS : a positive couplet for the Λ -isomer and a negative couplet for the Δ -isomer [51]. Also in this case the J-aggregates respond to stirring by increasing CD intensity and switching couplet sign with stirring sense (Fig. 30). Thus the chiral J-aggregates induced by Λ - or Δ - $[\text{Ru}(\text{Phen})_3]^{2+}$ should respond to mechanical stirring stimuli exactly as the previous racemate system did.

Figure 37a shows that CW stirring indeed induces deposition of Δ aggregates despite the starting solution showing a small Λ CD signal. Analogously, Fig. 37b shows that CCW stirring induces deposition of Λ aggregates even from a starting solution showing a Δ signal. The absorption spectra also show that in this case only J-aggregates deposit onto the wall: porphyrin monomers and ruthenium complexes do not stick onto the walls and remain in solution. This result suggests that the ruthenium complexes are not a constitutive part of the J-aggregates (see footnote 7). The similarity between the data with and without the chiral matrix indicates that the presence of the ruthenium complexes does not induce any significant difference in the response of the J-aggregates towards the macroscopic chirality of vortices.

The next experiment is very useful to compare the stirring effect (which is a weak thermodynamic effect) with a stronger thermodynamic effect, such as that exerted by the presence of high concentrations of chiral templates. The next system, in our design, has to behave differently to the previous ones and helps in delineating a model.

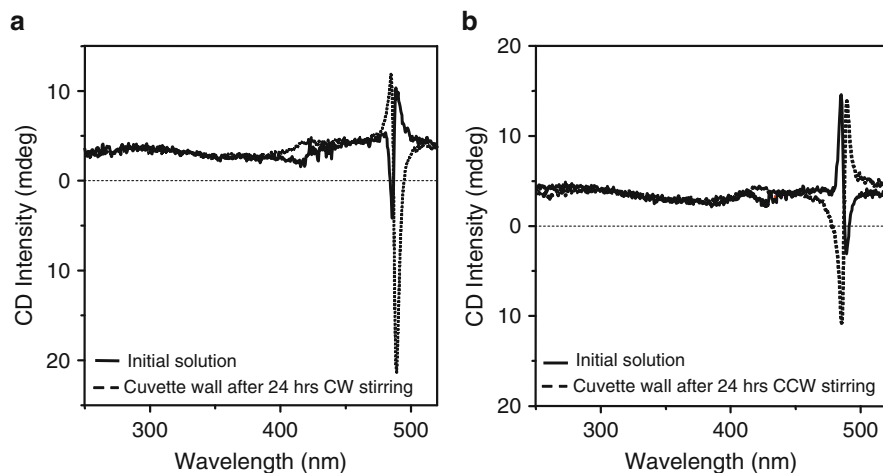


Fig. 37 (a) CD spectra of J-aggregates of H_2TPPS formed in the presence of the racemate of Λ and Δ enantiomers ($10 \mu\text{M}$ each) of $[\text{Ru}(\text{Phen})_3]^{2+}$ ions in which a small excess of Λ -J-aggregates is present. The spectra were recorded before (*solid curve*) and after (*dashed curve*) 24 h of CW stirring in the dark. (b) Data of a solution which initially contains a small excess of Δ -J-aggregates. Initial solution (*solid curve*) and after 24 h CCW stirring in the dark (*dashed curve*). Modified from [62]

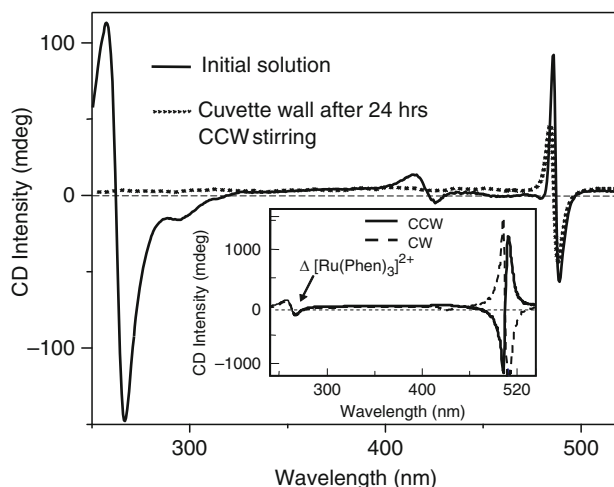


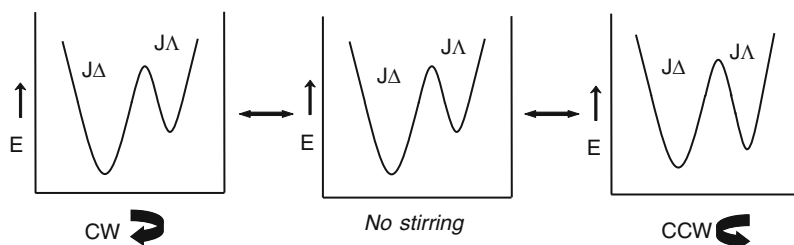
Fig. 38 CD spectra of J-aggregates of H_2TPPS formed in the presence of Δ -[Ru(Phen) $_3$] $^{2+}$ ions (10 μ M): standing solution (*solid curve*), cuvette walls after 24 h CCW stirring in the dark (*dotted curve*). The *inset* shows the effect of stirring on the solution; CCW (*solid curve*), CW (*dashed curve*) stirring. Modified from [62]

Figure 38 shows CD data of a solution in which J-aggregation occurs in the presence of equimolar concentrations of porphyrin and Δ -[Ru(Phen) $_3$] $^{2+}$ ions. In this case not only is the system not racemic but concentration of the chiral matrix is equal to that of porphyrins. Also for this unbalanced system, stirring induces the spectral variations observed for the systems discussed above (inset of Fig. 38).⁹ The prolonged stirring experiment on Δ -[Ru(Phen) $_3$] $^{2+}$ templated J-aggregates (24 h of CCW to favour Λ deposition) shows that, for this thermodynamically unbalanced system, stirring does not cause racemate “resolution”: the starting Δ J-aggregates are in solution and also deposited onto the wall. This indicates that Δ J-aggregates remain the major species in solution (despite the 24 h CCW stirring favouring, in principle, the Λ enantiomer) (Scheme 5) (see footnote 9).

This experiment is also very useful to rule out the possibility that stirring causes deposition of aligned aggregates and to exclude the occurrence of instrumental artefacts such as linear dichroism (LD).¹⁰

⁹The UV part of the CD spectrum, reporting [Ru(Phen) $_3$] $^{2+}$ chirality, is not affected by stirring confirming that ruthenium complexes are free in solution and not part of the J-aggregates. Also for the analogous system with the Λ enantiomer no deposition of the Δ enantiomer is observed in spite of the CW stirring.

¹⁰Following suggestions from a referee we have halved the cuvettes. Both faces show CD signals which have the same shape as that of the empty cuvette: this enables LD contributions to be excluded.



Scheme 5 Schematic representation of the possible stirring effect on a J-aggregate solution in which a thermodynamic “unbalancing” factor is present throughout its formation (Δ -[Ru(Phen)₃]²⁺ in this case). Stirring is unable to overcome the initial unbalancing. Modified from [62]

All these data converge towards a simple thermodynamic model: in a (quasi-) racemic system of non-covalent aggregates, stirring drives a redistribution of (protonated) monomers between the two enantiomeric forms of assemblies and/or drives monomer complexation towards one enantiomer (Δ for CW, Λ for CCW stirring). If a competitive chiral “force” (such as a chiral template) is present in solution, the fate of the system is related to the balance between different forces acting in solution, that is, a low or racemic concentration of chiral template will be overcome by stirring (see examples in Figs. 35–37); however, a high concentration of chiral matrix (see Fig. 38) will drive the system towards the templating chirality (Scheme 5).¹¹

If this model is correct, then there should be a concentration of chiral ruthenium complexes at which they behave as chiral “pollutants”: that is, they will initially template the chirality of the J-aggregates (in standing solutions) but stirring will prevail and drive the system towards the formation of species favoured from the vortex chirality (Scheme 4). Indeed, at a concentration of chiral metal complex of 10 nM (that is 1,000 times more diluted than H₄TPPS), the chirality of the initially formed aggregates is templated by the tiny concentration of chiral complexes (Fig. 39). However, different to the experiment shown in Fig. 38, this time the J-aggregates favoured from a given stirring sense are deposited onto the cuvette wall after 24 h of stirring (broken lines of Fig. 39): thus in this case Λ - or Δ -[Ru(Phen)₃]²⁺ behave like chiral contaminants (Scheme 4).

So we can conclude that for this specific system the action of vortexes is at least twofold causing: (1) fibre alignment in solution (mainly a “mechanical” action leading to increase of the CD signal and inversion of the sign) and (2) enantiomer separation/enrichment (thermodynamic in nature, driven by a chiral field and leading to redistribution and/or enrichment of monomers onto the chiral aggregate favoured by the swirling sense). The cuvette walls represent a kind of “trap” which freezes the deposited J-aggregates in the conformation chosen in solution from the

¹¹ Δ - or Λ -[Ru(Phen)₃]²⁺ are free in solution (10 mM): therefore they can drive a preferential chiral aggregation despite the vortex chirality.

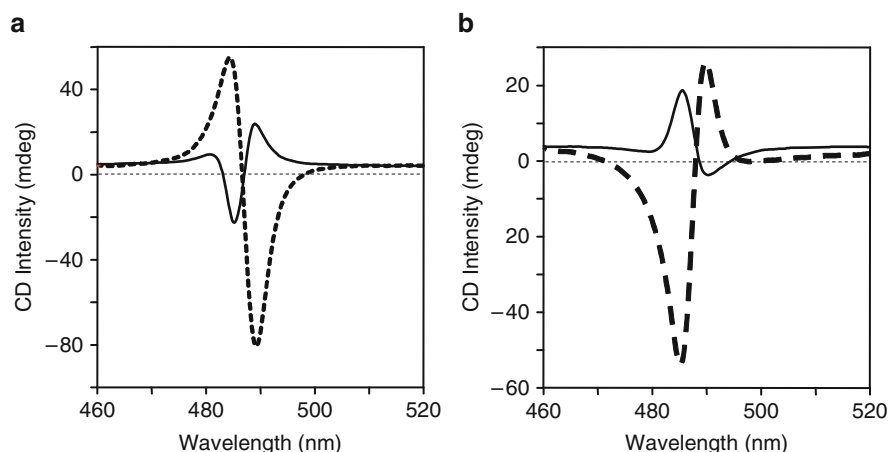


Fig. 39 (a) CD spectra of the J-aggregates of H_2TPPS ($10 \mu M$) formed in the presence of 10 nM of Δ - $[Ru(Phen)_3]^{2+}$: standing solution (*solid curve*) and cuvette walls after 24 h CW stirring (*dashed curve*). (b) CD spectra of J-aggregates templated from 10 nM of Δ - $[Ru-(Phen)_3]^{2+}$ ions: standing solution (*solid curve*) and cuvette walls after 24 h CCW stirring (*dashed curve*). Modified from [62]

vortex chirality: deposition is fundamental in going from a dynamic to a “static” regime.

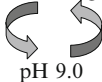

All the reported experimental data strongly support that, for the investigated systems, stirring shifts the equilibrium of a racemic mixture towards the side chosen by the vortex chirality. However, various questions remain open. For example, it is not clear at the moment if, under the effect of a vortex, there is chiral enrichment (monomers caught from the eddy sense and pushed to self-aggregate) and/or a racemate resolution, and it is worthwhile to test other similar chemical systems to discover if this simple scheme is more general.

6 Conclusive Remarks and Perspectives

The results reported here (summarized in Table 2) permit one to outline the general system characteristics necessary to obtain an erasable-rewritable (chiral) memory device. It is quite clear that the driving force of the processes described here is the interaction between net charges. Yet, in our opinion the key point is to exploit hydrophobicity of water-soluble molecules. This dichotomous nature allows molecules to approach each other thanks to attractions between opposite net charges (charges that made them water-soluble) but also drives self-aggregation owing to the very large portion of molecule having a hydrophobic nature.

The overall effect is a convergent action of various binding forces (coulombic, π - π , dispersive, etc.) in promoting self-assembly, leading to very large species

Table 2 Nature and main characteristics of the various chiral supramolecular systems

Components		Relevant chemical-physical conditions	Chiral transfer process
Porphyrin(s)	Chiral template		
H ₂ TPPS + ZnT4, or MnT4, or AuT4	Poly-L-glutamate or poly-D-glutamate (not removable)	pH 2.9	Dynamic (induction, pH reversible)
CuT4	Poly-L-glutamate or poly-D-glutamate (not removable)	pH 3.2–4.0	Dynamic (induction, pH reversible)
CuT4 + H ₂ TPPS	Poly-L-glutamate or poly-D-glutamate (not removable)	pH 3.2–4.0	Static (memory) (chirality permanent transfer in CuT4–H ₂ TPPS aggregate)
CuT4 + H ₂ TPPS	L-Phenylalanine or D-phenylalanine (removable)	Neutral pH	Static (memory) (chirality permanent transfer)
H ₂ TpyP + CuTPPS	L-Phenylalanine or D-phenylalanine (removable)	pH 2.3 assembling  pH 9.0 disassembling	Quasi-dynamic (Memory) (chirality is permanent but pH switchable)
H ₂ TPPS <i>orcis</i> -DPPS or <i>trans</i> -DPPS	Λ -Ru[(Phen) ₃] ²⁺ (not removable)	Neutral pH no salt added	Dynamic (induction of chirality in porphyrin aggregate)
H ₂ TPPS	Λ -Ru[(Phen) ₃] ²⁺ (not removable)	pH 6.0, J-aggregate disruption  pH 2.5, J-aggregate formation	Quasi-dynamic (Memory) (chirality is permanent but pH switchable)
H ₂ TPPS	No template	pH 3.0, NaCl 0.3 M Stirring	Selective (the vortex determines enantiomer enrichment and/or separation. The cuvette walls permit to pass from a dynamic to a “static” regime)

stabilized by an extended network of multiple interactions. We feel that the dimension of the species plays an important role as well, because the core of porphyrin large assemblies is extensively dehydrated and solution changes (as pH) are not easily transmitted to it.

However, thermodynamic forces are not sufficient to explain completely the behaviour of the systems discussed above. Kinetics, acting through hierarchical principles, is of primary importance too. Finally, molecular recognition is facilitated from a very large planar surface which simplifies the growth of species observed during the amplification process.

In fact, only the proper exploitation of thermodynamics, molecular recognition and hierarchy principles in tandem permit one to design complex and functional supramolecular species having the desired properties.

Finally, we feel it is worthwhile to stress one more time the importance of the kinetic inertia in the (reversible) chiral transfer and memory processes of our porphyrin systems. Inertia provides evidence that the system is trapped in an energy minimum. In the above examples the minimum is local: the real minimum is that reached from the achiral system whose formation involves the same enthalpic contribution of the chiral one but a more favourable entropic contribution. In particular, the network of electrostatic interactions ensures a *quite deep* local energy minimum (that is a high value of E_A).

Reversibility (that is, the ability to switch between the imprinted and erased memory) is possible only when the system come out from this deep local minimum. That can be accomplished by changing the “nature” of the system component(s) through photo-, redox- or pH-driven reactions. In this way the thermodynamic energy state of the chiral hetero-aggregates is affected and an alternative, new passage through the energy surfaces, characterized by a low E_A value, is given. The initial system can be reconstituted only if a tiny, but sufficient, amount of seeds survives these thermodynamic variations.

As the reader can see, we are back, as in a cycle, at the concept expressed at the beginning of the paragraph: the importance of the stability and inertness of the *core* of the porphyrin assembly. Stability and inertness of the *core* are ensured, as stated, by the extended dimension of the aggregate and, consequently, by the particular local environment conditions. These are quite different from the conditions of the bulk solution, with which the *core* only partly and indirectly communicates.

Finally, we think that the action of chiral forces is a very intriguing, open scenario which deserves the attention of researchers owing to the possible applications and suggestions on the origin of life.

References

1. Simpson GJ (2004) Molecular origin of the remarkable chiral sensitivity of second-order nonlinear optics. *Chem Phys Chem* 5:1301–1310
2. Purrello R (2003) Lasting chiral memory. *Nat Mater* 2:216–217
3. Mukhopadhyay P, Wipf P, Beratan DN (2009) Optical signatures of molecular dissymmetry: combining theory with experiments to address stereochemical puzzles. *Acc Chem Res* 42:809–819
4. Balaz M, De Napoli M, Holmes AE et al (2005) A cationic zinc porphyrin as a chiroptical probe for Z-DNA. *Angew Chem Int Ed Engl* 44:4006–4009
5. D'Urso A, Mammana A, Balaz M et al (2009) Interactions of a tetra-anionic porphyrin with DNA: from a Z-DNA sensor to a versatile supramolecular device. *J Am Chem Soc* 131:2046–2047
6. Onouchi H, Miyagawa T, Morino K et al (2006) Assisted formation of chiral porphyrin homoaggregates by an induced helical poly(phenylacetylene) template and their chiral memory. *Angew Chem Int Ed Engl* 45:2381–2384

7. Jiang S, Zhang L, Liu M (2009) Photo-triggered J-aggregation and chiral symmetry breaking of an anionic porphyrin (TPPS) in mixed organic solvent. *Chem Commun* 41:6252–6254
8. Zhang L, Liu M (2009) Supramolecular chirality and chiral inversion of tetraphenylsulfonato porphyrin assemblies on optically active polylysine. *J Phys Chem B* 113:14015–14020
9. Zhao L, Wang X, Li Y et al (2009) Chiral micelles of achiral TPPS and diblock copolymer induced by amino acids. *Macromolecules* 42:6253–6260
10. Micali N, Villari V, Castriciano M et al (2006) From fractal to nanorod porphyrin J-aggregates. Concentration-induced tuning of the aggregate size. *J Phys Chem B* 110:8289–8295
11. Jiang S, Liu M (2004) Aggregation and induced chirality of an anionic meso-tetraphenylsulfonato porphyrin (TPPS) on a layer-by-layer assembled DNA/PAH matrix. *J Phys Chem B* 108:2880–2884
12. Lang K, Anzenbacher P, Kapusta P et al (2000) Long-range assemblies on poly(dG-dC)₂ and poly(dA-dT)₂: phosphonium cationic porphyrins and the importance of the charge. *J Photochem Photobiol B-Biol* 57:51–59
13. Pasternack RF (2003) Circular dichroism and the interactions of water soluble porphyrins with DNA – a minireview. *Chirality* 15:329–332
14. Palmans ARA, Meijer EW (2007) Amplification of chirality in dynamic supramolecular aggregates. *Angew Chem Int Ed Engl* 46:2–23
15. Kubat P, Lang K, Kral V et al (2002) Preprogramming of porphyrin-nucleic acid assemblies via variation of the alkyl/aryl substituents of phosphonium tetratolylporphyrins. *J Phys Chem B* 106:6784–6792
16. Pasternack RF, Gurrieri S, Lauceri R et al (1996) Single-stranded nucleic acids as templates for porphyrin assembly formation. *Inorg Chim Acta* 246:7–12
17. Kuciauskas D, Caputo GA (2009) Self-assembly of peptide-porphyrin complexes leads to pH-dependent excitonic coupling. *J Phys Chem B* 113:14439–14447
18. Kokona B, Kim AM, Roden RC et al (2009) Self assembly of coiled-coil peptide-porphyrin complexes. *Biomacromolecules* 10:1454–1459
19. De Luca G, Romeo A, Monsu Scolaro L et al (2010) Conformations of a model protein revealed by an aggregating CuII porphyrin: sensing the difference. *Chem Commun* 46:389–391
20. Monsu Scolaro L, Romeo A, Pasternack RF (2004) Tuning porphyrin/DNA supramolecular assemblies by competitive binding. *J Am Chem Soc* 126:7178–7179
21. Pasternack RF, Giannetto A, Pagano P et al (1991) Self-assembly of porphyrins on nucleic acids and polypeptides. *J Am Chem Soc* 113:7799–7800
22. Purrello R, Gurrieri S, Lauceri R (1999) Porphyrin assemblies as chemical sensors. *Coord Chem Rev* 190–192:683–706
23. Purrello R, Bellacchio E, Gurrieri S et al (1998) pH modulation of porphyrins self-assembly onto polylysine. *J Phys Chem B* 102:8852–8857
24. Lauceri R, Campagna T, Contino A et al (1996) Poly(A A U) triple helix formation promoted by porphyrin assembly. *Angew Chem Int Ed Engl* 35:215–216
25. Bustamante C, Gurrieri S, Pasternack RF et al (1994) Interaction of water-soluble porphyrins with single- and double-stranded polyribonucleotides. *Biopolymers* 34:1099–1104
26. Purrello R, Monsu Scolaro L, Bellacchio E et al (1998) Chiral H- and J-type aggregates of *meso*-tetrakis(4-sulfonatophenyl)porphine on α -helical polyglutamic acid induced by cationic porphyrins. *Inorg Chem* 37:3647–3648
27. Fleischer EB, Palmer JM, Srivastava TS et al (1971) Thermodynamic and kinetic properties of an iron-porphyrin system. *J Am Chem Soc* 93:3162–3167
28. Ribo JM, Crusats J, Farrera J-A et al (1994) Aggregation in water solutions of tetrasodium diprotonated *meso*-tetrakis(4-sulfonatophenyl)porphyrin. *J Chem Soc, Chem Commun* 6:681–682
29. Pasternack RF, Schaefer KF, Hambright P (1994) Resonance light-scattering studies of porphyrin diacid aggregates. *Inorg Chem* 33:2062–2065

30. Shimidzu T, Tomokazu I (1981) Accordion-type aggregate of water-soluble *meso*-tetraphenylporphyrin derivatives. *Chem Lett* 10:853–856
31. Ojadi E, Selzer R, Linschitz H (1985) Properties of porphyrin dimers, formed by pairing cationic and anionic porphyrins. *J Am Chem Soc* 107:7783–7784
32. Hofstra U, Koehorst RBM, Schaafsma TJ (1986) Excited-state properties of water-soluble porphyrin dimers. *Chem Phys Lett* 130:555–559
33. Endisch E, Fuhrhop J-H, Buschmann J et al (1996) β -Tetraethyl- β' -tetrapyrroline-4-yl porphyrins, their *N*-methylated tetracations, and heterodimers with *ms*-tetraphenylsulfonato porphyrins. *J Am Chem Soc* 118:6671–6680
34. Mukundam NE, Pethö G, Dixon D et al (1994) Interactions of an electron-rich tetracationic tentacle porphyrin with calf thymus DNA. *Inorg Chem* 33:4676–4687
35. Schneider H-J, Wang M (1994) DNA interactions with porphyrins bearing ammonium side chains. *J Org Chem* 59:7473–7478
36. Laueri R, Gurrieri S, Bellacchio E et al (2000) J-type aggregates of the anionic *meso*-tetrakis(4-sulfonatophenyl)porphyrin induced by “hindered” cationic porphyrins. *Supramol Chem* 12:193–202
37. Bellacchio E, Laueri R, Gurrieri S et al (1998) Template-imprinted chiral porphyrin aggregates. *J Am Chem Soc* 120:12353–12354
38. Purrello R, Raudino A, Monsù Scolaro L et al (2000) Ternary porphyrin aggregates and their chiral memory. *J Phys Chem B* 104:10900–10908
39. Gibbs EJ, Tinoco I, Maestre M et al (1988) Self-assembly of porphyrins on nucleic acid templates. *Biochem Biophys Res Commun* 157:350–358
40. Hunter CA, Sanders JKM (1990) The nature of π - π interactions. *J Am Chem Soc* 112:5525–5534
41. Laueri R, De Napoli M, Mammana A et al (2004) Hierarchical self-assembly of water-soluble porphyrins. *Synth Met* 147:49–55
42. Mammana A, De Napoli M, Laueri R et al (2005) Induction and memory of chirality in porphyrin hetero-aggregates: the role of the central metal ion. *Bioorg Med Chem* 13:5159–5163
43. Geremia S, Di Costanzo L, Nardin G et al (2004) Assembly of positively charged porphyrins driven by metal ions: a novel polymeric arrangement of cationic metalloporphyrins. *Inorg Chem* 43:7579–7581
44. Laueri R, Purrello R (2005) Transfer, memory and amplification of chirality in porphyrin aggregates. *Supramol Chem* 17:61–66
45. Laueri R, D’Urso A, Mammana A et al (2008) Chiral memory: induction, amplification, and switching in porphyrin assemblies. *Chirality* 20:411–419
46. Laueri R, Raudino A, Monsù Scolaro L et al (2002) From achiral porphyrins to template-imprinted chiral aggregates and further. Self-replication of chiral memory from scratch. *J Am Chem Soc* 124:894–895
47. Laueri R, Fasciglione GF, D’Urso A et al (2008) Kinetic investigation of porphyrin interaction with chiral templates reveals unexpected features of the induction and self-propagation mechanism of chiral memory. *J Am Chem Soc* 130:10476–10477
48. Matassa R, Carbone M, Laueri R et al (2007) Supramolecular structure of extrinsically chiral porphyrin hetero-assemblies and achiral analogues. *Adv Mater* 19:3961–3967
49. Mammana A, D’Urso A, Laueri R et al (2007) Switching off and on the supramolecular chiral memory in porphyrin assemblies. *J Am Chem Soc* 129:8062–8063
50. Randazzo R, Laueri R, Mammana A et al (2009) Interactions of Λ and Δ enantiomers of ruthenium(II) cationic complexes with achiral anionic porphyrins. *Chirality* 21:92–96
51. Randazzo R, Mammana A, D’Urso A et al (2008) Reversible “chiral memory” in ruthenium tris(phenanthroline)-anionic porphyrin complexes. *Angew Chem Int Ed Engl* 47:9879–9882
52. Balzani V, Juris A (2001) Photochemistry and photophysics of Ru(II)-polypyridine complexes in the Bologna group. From early studies to recent developments. *Coord Chem Rev* 21:97–115

53. Castiglioni E, Abbate S, Longhi G et al (2007) Absorption flattening as one cause of distortion of circular dichroism spectra of Δ -[Ru(phen)₃]²⁺-H₂TPPS complex. *Chirality* 19:642–646
54. Amabilino DB (2007) Supramolecular assembly: nanofibre whirlpools. *Nat Mater* 6:924–925
55. Kondepudi DK, Kaufman RJ, Singh N (1990) Chiral symmetry breaking in sodium chlorate crystallization. *Science* 250:975–976
56. Ribo JM, Crusats J, Sague F et al (2001) Chiral sign induction by vortices during the formation of mesophases in stirred solutions. *Science* 292:2063–2066
57. Dzwolak W, Lokszejn A, Galinka-Rakoczj A et al (2007) Conformational indeterminism in protein misfolding: chiral amplification on amyloidogenic pathway of insulin. *J Am Chem Soc* 129:7517–7522
58. Ohno O, Kaizu Y, Kobayashi H (1993) J-aggregate formation of a water-soluble porphyrin in acidic aqueous media. *J Chem Phys* 99:4128–4139
59. Yamaguchi T, Kimura T, Matsuda H et al (2004) Macroscopic spinning chirality memorized in spin-coated films of spatially designed dendritic zinc porphyrin J-aggregates. *Angew Chem Int Ed Engl* 43:6350–6355
60. Tsuda A, Akhtarul Alam Md, Harada T et al (2007) Spectroscopic visualization of vortex flows using dye-containing nanofibers. *Angew Chem Int Ed Engl* 46:8198–8202
61. Wolffs M, George SJ, Tomovic Z et al (2007) Macroscopic origin of CD-effects by alignment of self-assembled fibers in solution. *Angew Chem Int Ed Engl* 46:8203–8205
62. D'Urso A, Randazzo R, Lo Faro L et al (2010) Vortex and nanoscale chirality. *Angew Chem Int Ed Engl* 49:108–112
63. Spada GP (2008) Alignment by the convective and vortex flow of achiral self-assembled fibers induces strong circular dichroism effects. *Angew Chem Int Ed Engl* 47:636–638
64. Arteaga O, Canillas A, Purrello R et al (2009) Evidence of induced chirality in stirred solutions of supramolecular nanofibers. *Opt Lett* 34:2177–2179
65. Kostur M, Schindler M, Talkner P et al (2006) Chiral separation in microflows. *Phys Rev Lett* 96:014502-2–4
66. Pasternack RF, Huber PR, Boyd P et al (1972) Aggregation of meso-substituted water-soluble porphyrins. *J Am Chem Soc* 94:4511–4517
67. Akins DL, Zhu H-R, Guo C (1996) Aggregation of tetraaryl-substituted porphyrins in homogeneous solution. *J Phys Chem* 100:5420–5425
68. Escudero C, Crusat J, Diez-Perez I et al (2006) Folding and hydrodynamic forces in J-aggregates of 5-phenyl-10,15,20-tris(4-sulfophenyl)porphyrin. *Angew Chem Int Ed Engl* 45:8032–8035
69. Berova N, Nakanishi K (2000) In: Berova N, Nakanishi K, Woody RW (eds) *Circular Dichroism, Principles and Applications*. Wiley-VCH, Weinheim, pp 337–382
70. El-Hachemi Z, Escudero C, Arteaga O et al (2009) Chiral sign selection on the J-aggregates of diprotonated tetrakis-(4-sulfonatophenyl)porphyrin by traces of unidentified chiral contaminants present in the ultra-pure water used as solvent. *Chirality* 21:408–412
71. Escudero C, El-Hachemi Z, Crusats J et al (2005) Zwitterionic vs porphyrin free-base structures in 4-phenylsulfonic acid meso-substituted porphyrins. *J Porphyr Phthalocyanines* 9:852–863

Vibrational Circular Dichroism Spectroscopy of Chiral Molecules

Guochun Yang and Yunjie Xu

Abstract In this chapter, new developments and main applications of vibrational circular dichroism (VCD) spectroscopy reported in the last 5 years are described. This includes the determinations of absolute configurations of chiral molecules, understanding solvent effects and modeling solvent–solute explicit hydrogen bonding networks using induced solvent chirality, studies of transition metal complexes and their peculiar and enormous intensity enhancements in VCD spectra, investigations of conformational preference of chiral ligands bound to gold nano particles, and two new advances in applying matrix isolation VCD spectroscopy to flexible, multi-conformational chiral molecules and complexes, and in development of femtosecond laser based VCD instruments for transient VCD monitoring. A brief review of the experimental techniques and theoretical methods is also given. The purpose of this chapter is to provide an up-to-date perspective on the capability of VCD to solve significant problems about chiral molecules in solution, in thin film states, or on surfaces.

Keywords Absolute configuration and conformation determinations · Density functional theory · Induced solvent chirality · Transient VCD measurements · Vibrational circular dichroism

Contents

1	Introduction	190
2	VCD Experiments	192
2.1	VCD Instrumentation and Some Recent Technique Developments	192
2.2	Measurements of VCD Spectra	195

G. Yang and Y. Xu (✉)
Department of Chemistry, University of Alberta, Edmonton, AB, T6G 2G2, Canada
e-mail: yunjie.xu@ualberta.ca

3	VCD Calculations	197
3.1	VCD Theory	197
3.2	Simulations of VCD Spectra	199
4	VCD Applications	201
4.1	AC Determinations	201
4.2	H-bonding Interactions of Chiral Molecules in Solution	207
4.3	Enhancement of VA and VCD Intensities in Transition Metal Containing Chiral Complexes	213
4.4	Conformational Study of Absorbed Chiral Ligands on AuNPs	217
4.5	Matrix Isolation VCD Spectroscopy for Probing Conformational Landscapes of Highly Flexible Chiral Molecules and Chiral Molecular Complexes	222
4.6	Towards Real Time VCD Measurements	225
5	Concluding Remarks	227
	References	228

1 Introduction

The two handed forms of a chiral molecule respond differently to right and left circularly polarized light in absorption, refraction, and scattering. A long-standing challenge in stereochemistry is how to determine the handedness, that is the absolute configuration (AC), of an enantiomerically pure sample using these responses. Vibrational circular dichroism (VCD) is the differential absorbance of left and right circularly polarized light of a molecular vibrational transition in the mid-infrared (IR) fingerprint spectral region [1, 2]. Since its discovery in the mid-1970s [3, 4] and the accompanying theoretical developments [5–15], VCD has matured into a major research area in physical and analytical chemistry, especially in the past decade. The commercialization of the Fourier transform (FT) IR-VCD spectrometer in 1997 and the implementation of density functional theory (DFT) calculations of VCD intensities into the Gaussian suite of programs in 1996, and into other electronic structure software packages later on, have triggered a flourish of VCD related publications. Today, VCD is a very successful spectroscopic technique for determinations of ACs of a wide range of mid-sized chiral molecules which are of fundamental interest and of practical importance [16–20]. The systems investigated include, for example, carbohydrates [21], phosphorus coordination compounds [22], transition metal complexes [23], chiral drugs [19], and natural products [24]. For chiral molecular systems that exist as a single conformer in solution, consistent agreement over more than ten major vibrational bands has been achieved in their AC determination procedures, for example, for mirtazapine, an active pharmaceutical ingredient [16]. One of the largest systems studied with the combined VCD measurement and DFT simulation approach is cryptophane-A, a molecule with 120 atoms and a globular shape, but no stereogenic centers [25].

Compared to other more conventional AC determination tools, such as X-ray crystallography, VCD has the advantage of not requiring a single crystal of

satisfactory size and can be performed directly in solution where a vast number of chemical and biochemical reactions occur. The reliability of AC determinations with the combined VCD spectroscopy and DFT simulation approach has now been solidly established with hundreds of VCD publications related to AC determinations. So far, there are no cases where the ACs, established by a thorough combined VCD and DFT analysis, are found to be false when compared with the ACs established by other methods [24]. In a few documented cases, VCD has, in fact, been used to uncover errors in the AC assignments by other methods, including X-ray crystallography [26]. For this reason, applications of VCD for the determination of ACs of chiral drugs are now also being pursued by major drug companies [27]. Another key advantage of VCD, as an optical spectroscopic method, is its ability to register signals from an individual conformer. Other standard spectroscopic techniques routinely employed for structural determinations, such as nuclear magnetic resonance and X-ray crystallography, on the other hand, cannot register such conformational signatures because of their intrinsic slow response to structural changes. In fact, every AC assignment by the combined VCD and DFT theoretical simulation approach requires a complete analysis of the dominant gas (or solution) phase conformers of the targeted chiral molecule (see below). Therefore the major conformations and the AC of the chiral molecule of interest are determined in the same process.

The maturing of the VCD experimental and theoretical techniques has attracted many new researchers into this exciting research area in the past several years. Many of them have begun to explore the combination of VCD spectroscopic techniques and theoretical modeling to investigate significant chemical problems in solution or on surfaces. At a more fundamental level, they have also applied this new tool to probe the conformational landscapes of flexible chiral molecules and hydrogen (H)-bonded chiral complexes in order to understand solvent effects and chirality recognition. For example, there is significant current interest in intermolecular H-bonding interactions between water and chiral molecules since nearly all biological molecules required for life are chiral and knowledge about their interactions with water is a prerequisite to the understanding of the chemistry of life [28].

In this chapter we focus on a few selective new VCD applications reported in the last 5 years, along with a brief review of the basic experimental techniques and theoretical methods. The remainder of this chapter is organized as follows. In the next section, we will present the VCD experimental technique with a short review of VCD instrumentation and some recent developments, and describe the usual procedure to obtain VA and VCD measurements in solution and in thin film states. In Sect. 3 the associated VCD computational simulations will be illustrated. This includes a brief historical overview of the theory development, and some basics related to VCD calculations, as well as the typical procedure of carrying out VCD simulations. The main part of this chapter deals with the diverse applications of VCD spectroscopy, focusing on the new developments in the last 5 years. Since there are a large number of publications which are dedicated to AC determinations of many interesting and important chiral molecules, a comprehensive review of all

of them is outside the scope of the current chapter. Rather, we will use two recent examples from our own group to illustrate the application of VCD for AC determinations in Sect. 4.1. Readers are referred to a number of excellent reviews from the last few years for an overview of this area [16–18, 20, 24]. In Sect. 4.2, a novel phenomenon termed *chirality transfer* or *induced chirality* will be introduced. In particular, we will use a series of studies from our group to demonstrate how to utilize such chirality transfer signatures to uncover the explicit solvent structures surrounding a chiral solute in solution. The advantages of using VCD spectroscopy to determine ACs and to study intermolecular interactions involving chiral molecules will also be discussed. The study of transition metal complexes and their peculiar VCD intensity enhancements will be described in Sect. 4.3, together with some recent theoretical advances to explain the observed enhancements. In Sect. 4.4 the exciting new applications of VCD by Bürgi and co-workers to unveil the conformational structures of chiral ligands bound to the gold nanoparticles (AuNPs) will be illustrated. In the next two sections we will showcase the recent breakthrough developments in two directions: (1) the combination of matrix isolation with VCD to study conformationally flexible chiral molecules and chiral intermolecular interactions; (2) the coupling of femtosecond lasers into VCD experiments to obtain real time monitoring of, for example, conformational changes of chiral molecules in solution and fast chemical reactions involving chiral molecules. Finally, concluding remarks are given in Sect. 5.

2 VCD Experiments

2.1 VCD Instrumentation and Some Recent Technique Developments

VCD instrumentation has experienced significant growth from its earlier day as a scanning grating instrument [29–32]. Such a grating spectrometer, which works fine for collecting data in a narrow spectral range of one or two key signature bands, is inferior compared to an FTIR instrument where a broad range of spectral frequencies can be covered simultaneously. The first FTIR-VCD spectrometer was demonstrated in 1979 by Nafie and co-workers who placed a photoelastic modulator (PEM) before a sample in an FTIR spectrometer to generate alternating right and left circularly polarized IR light in order to detect the differential absorption [33–35]. A block diagram of the optical-electronic layout of such an FTIR-VCD spectrometer is shown in Fig. 1 [16]. The first commercial VCD spectrometer was marketed by Bomem/BioTools, Inc. in 1997, based on the design from Nafie's laboratory. At present, all major FTIR companies, such as Bruker, Thermo Scientific, and Jasco, carry either VCD modules or stand-alone instrumentation. Nowadays, the vast majority of VCD spectrometers in operation around the world are FTIR-VCD spectrometers which take

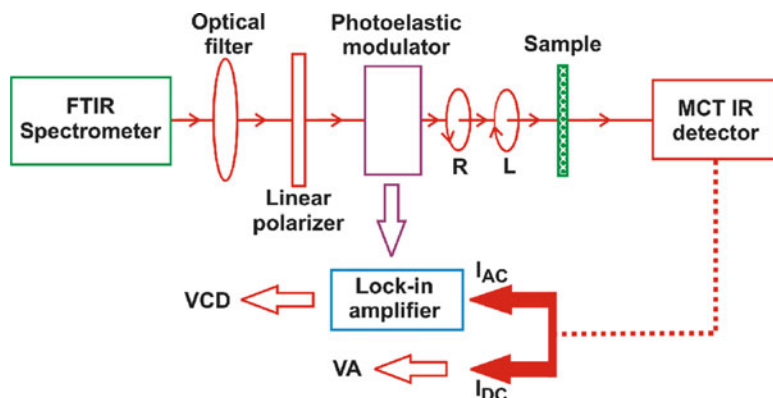


Fig. 1 Block diagram of the optical-electronic layout of an FTIR-VCD spectrometer

advantage of the high-throughput and multiplex characteristics associated with FTIR spectroscopy.

Compared to a typical electronic CD (ECD) signal, a VCD signal is usually quite weak, about 10^4 – 10^6 times lower than the intensity of the corresponding vibrational absorption (VA) band. As such, it is considerably more difficult to obtain good quality VCD spectra. Substantial efforts have been devoted over the years to improve the performance of VCD instruments, noticeably by Nafie and co-workers [36–40]. One primary concern in VCD measurements is the occurrence of optical artifacts which can interfere with the small VCD intensities. In the absence of chirality in a sample, one expects the VCD spectrum to be zero (with low level of noise) across the whole spectral range measured. In practice, this may not be the case because of strain and other imperfections of the optical components employed in the measurement. These can modify the beam polarization state and result in so-called baseline artifacts [36]. VCD spectra in the CH-stretching region of camphor in CCl_4 measured using several different versions of FTIR-VCD spectrometers are depicted in Fig. 2 [41]. Instrumental artifacts are visible in the bottom spectra of Fig. 2a where the raw VCD spectra are given. In principle, the best way to remove such baseline artifacts is to measure the VCD spectrum of the opposite enantiomer of a chiral sample under the identical condition and then obtain the spectrum by subtracting the two raw spectra and dividing the difference spectrum by two. The resulting spectrum after baseline subtraction is depicted in the top part of Fig. 2a. This is taken as the true VCD spectrum. Alternatively, one can measure the racemic mixture under identical condition and subtract it from the raw spectrum of the chiral sample. Very often neither the opposite enantiomer nor the racemic mixture is available, especially when one deals with chiral synthetic products. In those cases, the common practice is to correct the baseline by subtracting the solvent VCD spectrum measured under the same experimental condition. Although this can reduce the VCD baseline artifacts, the VCD spectra thus obtained are often still plagued by artifacts. Such an example is depicted in Fig. 2b where the solvent

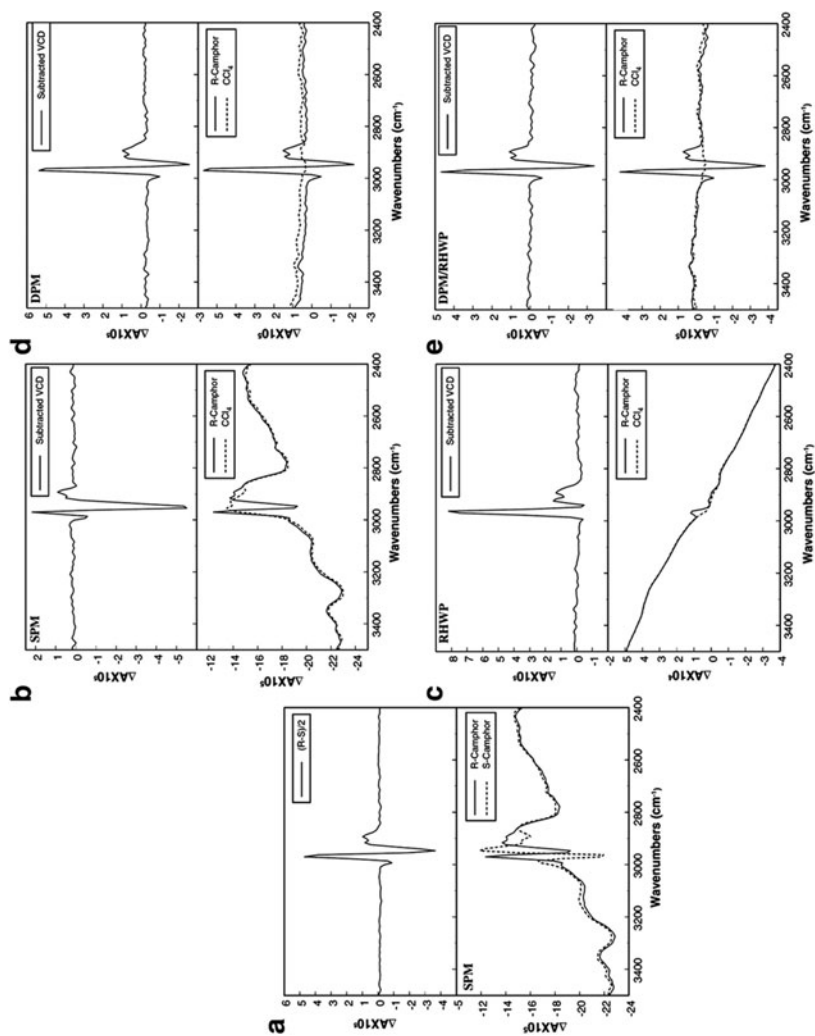


Fig. 2 The VCD spectra of camphor with the anisotropy ratio on the order of magnitude of 10^{-5} are used as examples to illustrate the performance of several generations of FTIR-VCD spectrometers. Raw (*bottom traces*) and subtracted (*top traces*) VCD spectra of 0.6 M R-camphor in CCl_4 in a 0.10 mm CaF_2 cell from 4,000 to $2,000\text{ cm}^{-1}$ are shown: (a) SPM, single PEM only, for a pair of enantiomers. The subtracted spectrum is the true spectrum; (b) SPM, single PEM, with only solvent baseline correction; (c) SPM/RHWP, single PEM (SPM) with RHWP, with only solvent baseline correction; (d) DPM, DPM only, with only solvent baseline correction; (e) DPM/RHWP, with both DPM and RHWP, with only solvent baseline correction. Reproduced with permission from [41]. Copyright (2008) Springer

corrected spectrum shows a very different intensity ratio for the doublet compared to the true spectrum in Fig. 2a.

Significant improvements in baseline stability and artifact suppression were reported in 2000 with a dual-PEM FTIR-VCD spectrometer [36]. This dual polarization modulation (DPM) method involves adding a second PEM between the sample and the detector, in addition to the first PEM which is placed right before the sample in a standard single polarization modulation (SPM) spectrometer. The improvement of a DPM over an SPM spectrometer can be seen by comparing Fig. 2b with Fig. 2d. More recently, Cao et al. added a rotating half-wave plate (RHWP) to the optical train to suppress further the linear birefringence (LB) effects associated with the sample cell in a DPM setup [41]. Their method is based on Hug's *virtual enantiomer* method, originally proposed for Raman Optical Activity (ROA) [42]. With such a setup, these authors achieved basically the same artifact suppression as when using the opposite enantiomer (see Fig. 2a, e). In addition to improving the sensitivity of FTIR-VCD instruments, efforts have also been made to extend the VCD operation into near IR region to as high as $10,000\text{ cm}^{-1}$ by incorporating a dual light source into the DPM FTIR-VCD spectrometer [43–45]. Currently, such an instrument is available commercially from Bomen/Biotoools Inc.

A few scanning dispersive VCD instruments are still in use for biological applications in the mid-IR region [46, 47]. In 2009, a newly designed and optimized dispersive VCD instrument was reported [47]. A collection of spectra for peptides and proteins having different dominant secondary structures (alpha-helix, beta-sheet, and random coil) measured with this new instrument showed substantially improved signal-to-noise (S/N) ratios as compared with the earlier version. The instrument provides protein VCD spectra for the amide I region that are of comparable or better quality than those obtained with a standard commercial FTIR-VCD spectrometer [47].

Besides the continuous improvements of FTIR-VCD instruments described above, some exciting new developments related to VCD measurements have been reported in recent years. These include the developments of matrix isolation FTIR-VCD instruments and of laser based real time VCD spectrometers. These new developments are associated with brand new applications and research directions, such as combining the matrix isolation technique with VCD spectroscopy to probe conformationally flexible chiral molecules and H-bonded chiral molecular complexes, and using femtosecond laser VCD instruments to record time resolved VCD spectra for monitoring fast chemical reactions or folding and unfolding events of peptides and proteins in solution. These will be discussed in more detail in Sects. 4.5 and 4.6.

2.2 Measurements of VCD Spectra

Since VCD measures the differential VA for the left and right circularly polarized light, a reliable VCD spectrum starts with good VA measurements. In our group we

use an FTIR spectrometer (Vertex 70, Bruker) equipped with a VCD module (PMA 50, Bruker) for VCD measurements [48]. First, we determine a suitable solvent depending on the nature of the study and an absorption path length to ensure that an averaged VA intensity, A , is ~ 0.5 in the $1,000\text{--}1,800\text{ cm}^{-1}$ range, the most common region for VCD measurements. In general we try to keep the A values in the range of $0.1\text{--}0.9$ in the frequency region of interest. If this cannot be achieved for all frequency regions of interest simultaneously, separate measurements have to be carried for different regions. If A values are close to 1.0 or more, one often observes severe artifacts which reduce the reliability of the VCD measurements [16, 48]. Details of the measurement and calibration procedures for VCD are well documented for various commercially available FTIR-VCD spectrometers. As discussed in Sect. 2.1, VCD measurements are usually repeated for the opposite enantiomer or the racemic sample or solvent to provide baseline corrections with a standard SPM FTIR-VCD spectrometer. The resulting VA and VCD spectra are usually plotted in stack mode or side by side to allow visual correlation of the VA features with those of VCD (see below). Commonly, a spectral resolution of 4 cm^{-1} is used and often a lower resolution of 8 cm^{-1} or less is used for biomolecular systems or systems with strong intermolecular H-bonds. Typically, samples are held in a variable path length cell with BaF_2 windows which have good transmission down to as low as 800 cm^{-1} . BaF_2 , however, is fairly brittle and is particularly difficult to handle when extremely short path lengths such as $6\text{--}10\text{ }\mu\text{m}$ are required. CaF_2 cells are easier to use and work down to about $1,180\text{ cm}^{-1}$. Data collection times depend strongly on the particular sample. In general, to obtain VCD spectra with good S/N ratios, a few hours of collection time are required for ΔA values in the order of 10^{-5} .

Although the majority of VCD measurements are performed in solution, measurements with cast film samples have also been reported. For example, VCD measurements of amino acids or carbohydrates in aqueous solutions are difficult to make because of the interfering water absorption. Even though successful VCD measurements of carbohydrates in aqueous media have been performed, they require a highly concentrated sample with a concentration of up to 4 M and a very short cell path length of $\sim 6\text{ }\mu\text{m}$ to minimize water absorption [49]. A notable shortcoming of such experiments is the large amount of sample is required, which makes it difficult to apply this method to synthetic materials where often only small amounts of samples are available. Furthermore, some samples may have too low solubility at neutral pH for this approach to be applicable. Polavarapu and co-workers have demonstrated successful usage of the cast film technique for VCD measurements of peptides [50, 51], proteins [52, 53], carbohydrates [54], nucleic acids [55], and viruses [56], and found that their measurements are independent of film orientations and are comparable to the solution phase measurements when available. The use of thin film samples has some significant advantages. First, the removal of the interfering water absorption in the film measurements results in higher light throughput and better S/N ratios for the VCD measurements. Second, the amount of sample used in a film VCD measurement is about one to two orders of magnitude less than that needed for solution phase measurements [54].

For film preparation, the solid sample of interest is dissolved in a suitable solvent and a few drops of the sample solution are cast onto a cell window. The sample window is then placed in a fume hood with a constant dry air (or N₂) flow over the sample at room temperature until the sample is completely dry. The film thickness is optimized in the same fashion as the cell path length in solution phase measurements to attain an averaged VA coefficient of ~0.5. Baseline corrections are done in the same fashion as for the solution measurements discussed above.

It is, however, important to point out that extreme caution should be exercised with cast film VCD measurements because additional macroscopic anisotropies such as LBs may be introduced in the film making process, causing severe artifacts in the observed VCD spectra [57]. For example, Merten et al. found that the VCD measurements of solid polymer films were severely contaminated with LBs [58]. They and others have developed procedures to remove such effects by measuring the film sample under several orientations [58, 59].

3 VCD Calculations

3.1 VCD Theory

The developments of the quantum mechanical calculations of VCD have been summarized before in a number of excellent review articles and books [14–16]. In this section, we briefly describe the basic terms involved, a few key milestones in the development, and the current status.

VA intensity is proportional to the electric dipole strength. In the harmonic approximation, D_{01}^i , the dipole strength for the i th normal mode of a fundamental vibrational transition ($0 \rightarrow 1$) can be expressed as

$$D_{01}^i = |\bar{\mu}_{01}^i|^2 = |\langle \psi_0 | \bar{\mu} | \psi_1^i \rangle|^2 = \frac{\hbar}{2\omega_i} \left| \frac{\partial \bar{\mu}}{\partial Q_i} \right|_0^2. \quad (1)$$

Here ψ_0 is the ground vibrational wave function and ψ_1^i is the wavefunction corresponding to the first excited vibrational state of the i th normal mode; $\bar{\mu}$ is the electric dipole moment operator; Q_i is the normal coordinate for the i th vibrational mode; the subscript “0” at derivative indicates that the term is evaluated at the equilibrium geometry. The related rotational strength or VCD intensity is determined by the dot product between the electric dipole and magnetic dipole transition moment vectors, as given in (2):

$$R_{01}^i = \langle \psi_0 | \bar{\mu} | \psi_1^i \rangle \cdot \text{Im} \langle \psi_1^i | \bar{m} | \psi_0 \rangle = \bar{\mu}_{01}^i \cdot \text{Im}[\bar{m}_{01}^i] = \frac{\hbar}{2} \left(\frac{\partial \bar{\mu}}{\partial Q_i} \right)_0 \cdot \left(\frac{\partial \bar{m}}{\partial Q_i} \right)_0. \quad (2)$$

The new term $\langle \psi_1^i | \vec{m} | \psi_0 \rangle$ is the corresponding magnetic dipole transition moment and \dot{Q}_i is the time derivative of Q_i . The vector $\text{Im} \langle \psi_1^i | \vec{m} | \psi_0 \rangle$ is real since $\langle \psi_1^i | \vec{m} | \psi_0 \rangle$ is purely imaginary. Thus, a prediction of rotational strength requires the calculations of the transition moments of both electric dipole moment operator and magnetic dipole moment operator. Although the calculation of electric dipole transition moments of vibrational transitions within the Born–Oppenheimer (BO) approximation is straightforward, it is not the case for magnetic dipole transition moments. The electronic contribution to a vibrational magnetic dipole transition moment vanishes within the BO approximation [60, 61]. At this stage of theory development, a good number of approximate quantum mechanical methods, such as localized molecular orbital [62, 63], vibronic coupling [64–66], nuclear electric shielding tensor [67, 68], and localized orbital-local origin [69] methods, had been proposed to calculate VCD intensities. The quality of the predicting power of these methods was not nearly satisfactory and further efforts were put into developing a better approximation to evaluate the electronic contribution to a vibrational magnetic dipole transition moment.

Using the so-called magnetic field perturbation method, Buckingham together with his co-workers [6] and Stephens [7] resolved this problem independently by including corrections to the BO approximation. In this approach, the electronic contribution to a vibrational magnetic dipole transition moment can be expressed in a simple form involving only adiabatic electronic wave functions of the ground electronic state. Specifically, it is necessary to calculate the ground state wave function as a function of nuclear displacement and of applied magnetic field. With this method, the electronic part of magnetic dipole moment derivative can be written as [14]

$$\left(\frac{\partial \vec{m}_\alpha^{\text{el}}}{\partial Q} \right)_0 = -\frac{h}{\pi} \text{Im} \left\langle \frac{\partial \psi_0}{\partial B_\alpha} \left| \frac{\partial \psi_0}{\partial Q_i} \right. \right\rangle, \quad (3)$$

where $\frac{\partial \psi_0}{\partial B_\alpha}$ is the derivative of the wave function with respect to the α th component of the magnetic field and $\frac{\partial \psi_0}{\partial Q_i}$ is the derivative with respect to the i th normal coordinate. An analytic procedure for evaluating the normal coordinate derivatives of electric dipole moment was developed in the mid-1980s [70, 71]. Subsequent efforts were directed at finding an analytic procedure for evaluating the normal coordinate derivatives of the magnetic dipole moment. The implementation of magnetic field perturbation theory with DFT for VCD predictions was realized in 1996 [72]. Since then, it has been used to simulate many good quality VCD spectra for comparison with the associated experimental data to determine the molecular conformations and ACs of a wide range of chiral molecules [14–20].

Equation (2) can be rewritten as (4) below where the sign of R_{01}^i is determined by the angle $\zeta(i)$ between the vectors $\vec{\mu}_{01}^i$ and $\text{Im}[\vec{m}_{01}^i]$:

$$\cos \zeta(i) = \frac{\vec{\mu}_{01}^i \cdot \text{Im}[\vec{m}_{01}^i]}{|\vec{\mu}_{01}^i| |\text{Im}[\vec{m}_{01}^i]|} = \frac{R_{01}^i}{|\vec{\mu}_{01}^i| |\text{Im}[\vec{m}_{01}^i]|}. \quad (4)$$

For a certain vibrational mode, if $\zeta(i) > 90^\circ$, then $R_{01}^i < 0$, and if $\zeta(i) < 90^\circ$, then $R_{01}^i > 0$. However, when $\zeta(i)$ is close to 90° even a small perturbation (be it experimental or theoretical), such as solvent, concentration, functional, or basis set can make it larger than 90° . This therefore results in a change of VCD sign. Recently, Baerends et al. systemically investigated the effects of small perturbations on the sign of R_{01}^i [73, 74]. They classify the vibrational modes as either robust where $\zeta(i)$ is far from 90° or non-robust where $\zeta(i)$ is very close to 90° . These authors advocate the use of only robust modes for AC determinations since their VCD signs are not sensitive to small perturbations either of computational or experimental nature and as a result should be predicted correctly by DFT calculations. How well this works in practice has yet to be tested, since current VCD assignments rely largely on an overall pattern recognition in both VA and VCD spectra, rather than one or two peaks [24]. A potential challenge is to assign confidently an observed VCD peak as robust taking into consideration possible overlap of vibrational bands in the experimental spectra and the somewhat limited accuracy of harmonic frequency predictions.

3.2 Simulations of VCD Spectra

Simulation of a VCD spectrum starts with a search for all relevant conformers of the molecular target. It is often beneficial to perform a preliminary search at a semiempirical level such as PM3 and AM1, or to utilize molecular mechanics programs such as Amber, Monte Carlo, and MacroModel for molecules with many potential conformers. The preliminary relative energies and the optimized conformational geometries are then used to identify the most stable conformers within a few kcal/mol and as starting geometries for further optimizations with more desirable functionals and basis sets for DFT calculations, respectively. When a calculation for an entire molecule is impractical, a fragment approach where a suitable portion of the molecule is selected for calculation instead could be used [75]. The geometry optimizations, vibrational frequency, and VA and VCD intensity calculations for the dominant chiral conformers can then be carried out using, for example, the Gaussian 03 program package [76].

VCD calculations are somewhat sensitive to the DFT functionals and basis sets. A large number of VCD studies showed that the hybrid B3LYP or B3PW91 functionals provide predictions in good agreements with the respective experimental data. Bultinck and co-workers investigated the effects of basis sets on VCD calculations and concluded that 6-31G(d) is the minimum basis set for VCD [77]. Calculations of small molecules using large basis sets such as cc-pVTZ and TZ2P were reported to give excellent results [14]. It should be noted that

H-bonded systems may require additional diffuse or polarization functions. For example, the 6-311++G(d,p) basis set had been found to be suitable for H-bonded systems [78–81]. It may be necessary to include Basis Set Superposition Errors (BSSE) [82] and Zero-Point-Energy (ZPE) corrections in evaluating the relative stabilities. Such corrections are often of the same magnitude as the energy differences among the dominant conformers. Moreover, the relative conformer energies may also differ noticeably with the basis sets used. All these factors will affect the Boltzmann factors predicted for different conformers and therefore the appearance of the population weighted VA and VCD spectra. Thus, an appropriate selection of DFT functionals and basis sets is very important for VCD simulations. A scale factor of 0.97–0.98 is usually applied to the calculated harmonic frequencies to account for the fact that the observed frequencies arise from an anharmonic force field instead of a harmonic one. A Lorentzian line shape is typically used in simulations of VA and VCD spectra. The full-width at half maximum (FWHM) used in the spectral simulation is usually based on the experimental VA line widths.

For the VCD studies described in Sects. 4.1 and 4.2, the B3LYP hybrid functional [83, 84] was used because of its proven reliability in predicting VCD intensities [25, 85, 86] and in describing strong H-bonded complexes [87–89]. The initial screening calculations were carried out at a low level of theory such as HF/3-21G or B3LYP/6-31G [90, 91]. The final geometry optimizations of the chiral molecular systems were performed with 6-311++G(d,p) or aug-cc-pVTZ [92].

Although many satisfactory VCD studies based on the gas phase simulations have been reported, it may be necessary to account for solvent effects in order to achieve conclusive AC assignments. Currently, there are two approaches to take solvent effects into account. One of them is the implicit solvent model, which treats a solvent as a continuum dielectric environment and does not consider the explicit intermolecular interactions between chiral solute and solvent molecules. The two most used computational methods for the implicit solvent model are the polarizable continuum model (PCM) [93–95] and the conductor-like screening model (COSMO) [96, 97]. In this treatment, geometry optimizations and harmonic frequency calculations are repeated with the inclusion of PCM or COSMO for all the conformers found. Changes in the conformational structures, the relative energies of conformers, and the harmonic frequencies, as well as in the VA and VCD intensities have been reported with the inclusion of the implicit solvent model. The second approach is called the explicit solvent model, which takes the explicit intermolecular interactions into account. The applications of these two approaches, in particular the latter one will be further discussed in Sect. 4.2.

It should be mentioned that in a number of VCD related studies published, including some examples discussed in this chapter, other chiroptical measurements such as optical rotation (OR) and ECD have also been utilized together with VCD. For example, both OR and VCD have been used to uncover the dominant species responsible for the chiroptical responses of glycidol in CDCl_3 solution in

Sect. 4.2. In the conformational investigations of chiral ligands bound to AuNPs, ECD has been utilized to characterize the properties of the gold metal cores. Although ECD and OR measurements are often easier to obtain, the associated theoretical simulations are generally much less reliable than those of VCD. The related challenges in their theory developments are discussed in several chapters of this volume. At the same time, one should also recognize that these complementary optical activity measurements do contain important new information which is not available with VCD. These joint studies with several chiroptical methods provide solid experimental and theoretical data for further theoretical developments. Very recently, Polavarupa summarized the advantages of using more than one chiroptical methods for AC determinations of chiral compounds in some special cases [98].

4 VCD Applications

4.1 AC Determinations

One of the most common applications of VCD is the AC determinations of chiral compounds. Two recent studies on anthracycline analogs and on pentacoordinate phosphorus complexes from our group are included below as examples.

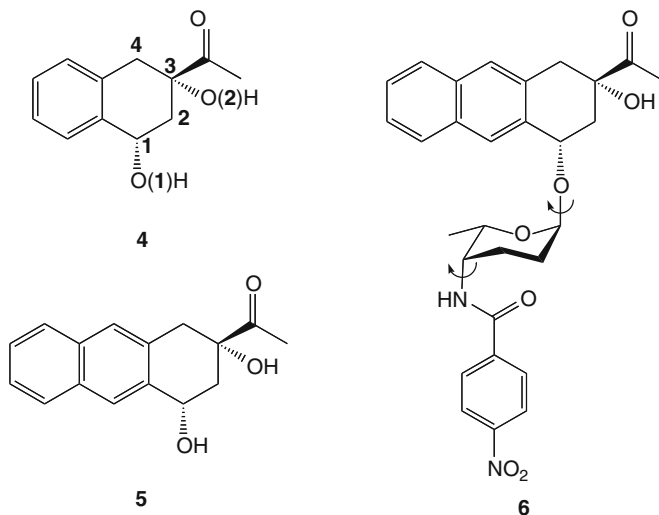


Fig. 3 The structures of the three anthracycline analogs studied. Adapted with permission from [21]. Copyright (2010) Wiley

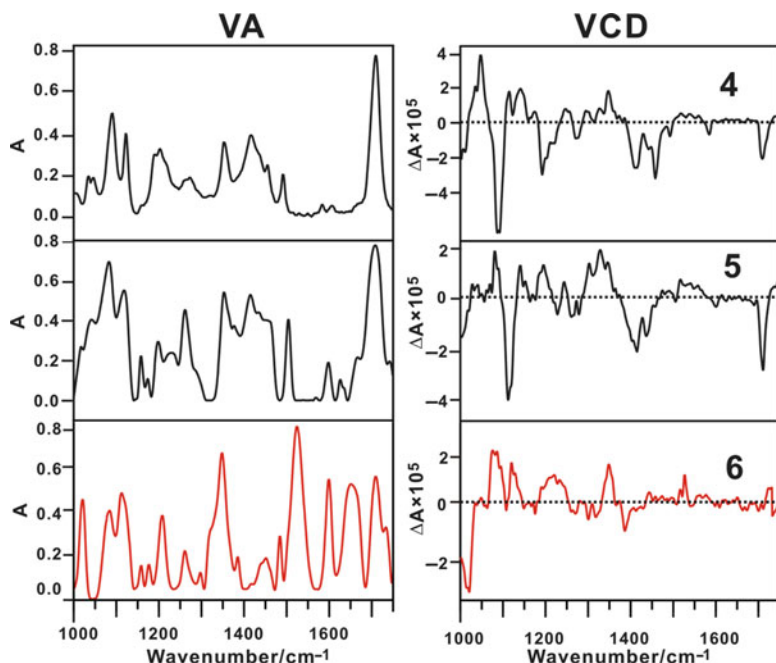


Fig. 4 Experimental VA and VCD spectra of the three anthracycline analogs measured in the thin film state. Adapted with permission from [21]. Copyright (2010) Wiley

4.1.1 Anthracycline Analogs

Daunorubicin and doxorubicin are two natural anthracycline antibiotics and have been used in the clinical treatment of a variety of cancers for more than 40 years [99, 100]. Recently, Lowary and co-workers synthesized anthracycline analogs with truncated aromatic cores, which exhibited modest cytotoxicity by assaying against several cancer cell lines [101]. The three anthracycline analogs studied are shown in Fig. 3 [21]. The experimental VA and VCD spectra (Fig. 4) were measured in the thin film states because of the limited synthetic samples available. Each compound has two stereogenic centers. Thus, there are four possible diastereomers: *SS*, *RR*, *SR*, and *RS* for each of them. Moreover, **4** and **5** each contains two OH groups which can form intramolecular H-bonds leading to conformational complexity or form intermolecular H-bonds leading to aggregates. These possibilities result in a good number of potential isomers. For example, a complete conformational search was carried out for **4**, the resulting *SS* conformers are shown in Fig. 5, and their energies and Boltzmann factors are listed in Table 1. As can be seen in Fig. 5, the most stable conformer forms two intramolecular H-bonds: C=O···HO2 and HO1···HO2 (see Fig. 3 for atom labeling). The experimental and the population weighted VA and VCD spectra of **4** are compared in Fig. 6 and

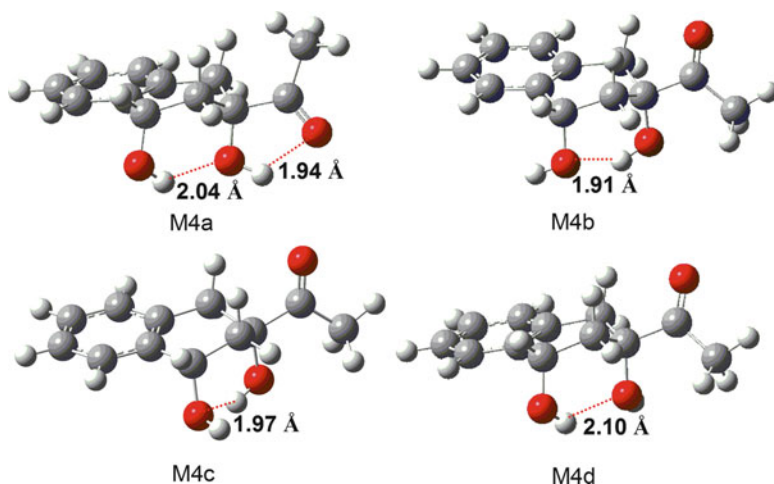


Fig. 5 Optimized geometries of the four most stable *SS* [M4(a–d)] stereoisomers of **4** at the B3LYP/6-311++G** level of theory. Adapted with permission from [21]. Copyright (2010) Wiley

Table 1 The relative Gibbs free energies ΔG (kcal/mol), relative total energies ΔE (kcal/mol), and the normalized Boltzmann factor B_f (in %) at 298.15 K based on the relative Gibbs free energy and the relative total energy of the *SS* conformers of **4** at the B3LYP/6-311++G** level of theory [21]

Monomer	ΔG	$B_f (\Delta G)$	ΔE	$B_f (\Delta E)$
M4a	0	47.56	0	55.45
M4b	0.05	43.71	0.22	38.24
M4c	1.21	6.16	1.48	4.55
M4d	1.76	2.43	2.07	1.68
M4e	3.78	0.08	4.19	0.05
M4f	4.47	0.03	4.87	0.01
M4g	4.54	0.02	4.93	0.01
M4h	6.33	~0	6.66	~0
M4i	7.56	~0	7.78	~0

the good agreement between them allowed us to assign the AC (*SS*) of **4** with high confidence. The further structural search and spectral simulation for the binary **4** complexes confirmed that self-aggregation is of little importance under the current experimental condition. The same AC conclusions were drawn for **5** and **6**. It is interesting to compare the signs of the experimental VCD peaks in the C=O stretching region for these three compounds: the experimental VCD spectra show a negative VCD peak in the C=O region for **4** and **5**, while the corresponding sign is positive for **6** (Fig. 4). This is because the VCD features are also highly sensitive to the dihedral angles of rotatable bonds, in addition to the ACs of chiral molecules. Although the AC of the aglycone of **6** is the same as **5**, the opposite sign observed for **6** vs **5** in the C=O region suggests that the orientation of the C=O group in **6** is different from that in **4** or **5**. Indeed, this was confirmed by examining the dominant

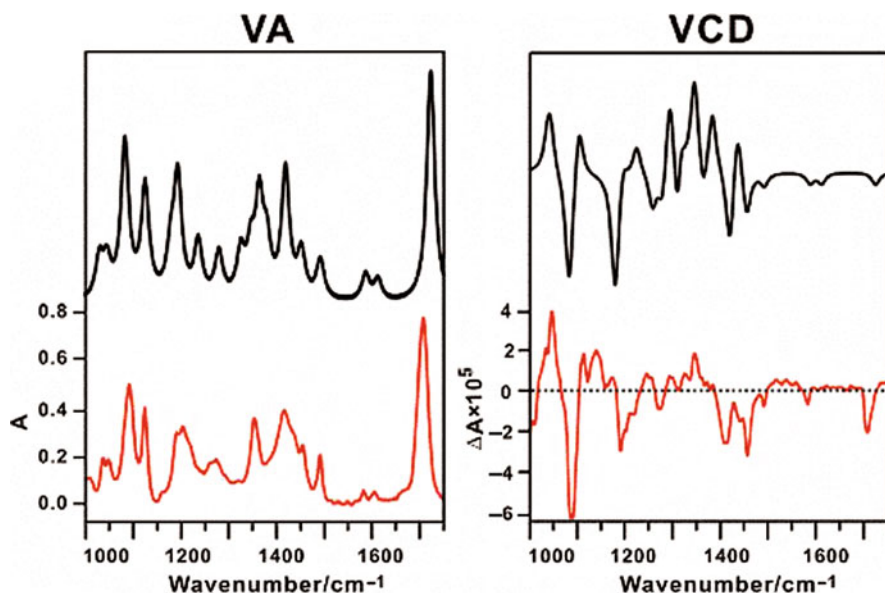


Fig. 6 Comparisons between the experimental (*bottom*) VA (*left*) and VCD (*right*) spectra of **4** and the corresponding calculated spectra (*top*) of **M4a**. Adapted with permission from [21]. Copyright (2010) Wiley

conformers of these three compounds. Besides the different conformational arrangements of the C=O group in **5** and **6**, the addition of the bulky carbohydrate subunit with three additional stereocenters to **6** also introduces other VA and VCD bands in the same frequency region. These factors combined lead to the very different VA and in particular VCD spectra for **5** and **6**. Clearly, a fragment approach [75], as mentioned in Sect. 3.2, is not feasible, i.e., it is not possible to assign the AC of **6** based on the calculation of **5**.

4.1.2 Pentacoordinate Phosphorus Compounds

Pentacoordinate phosphorus compounds have been regarded as intermediates or transition states in many biological processes such as enzymatic phosphoryl transfer reactions [102–107] and hydrolysis or formation of DNA, RNA, c-AMP, and other biologically relevant phosphorus compounds [108, 109]. Pentacoordinate phosphorus compounds with amino acid residues as chiral chelate ligands are of particular interest for their roles as important intermediates in the self-assembly reactions of *N*-phosphoamine acids into peptide [110–116]. Obtaining a single crystal of this type of compounds for solid-state structural characterization is often time consuming and sometimes impossible [117]. So far, very few ACs of pentacoordinate phosphorus compounds have been determined using X-ray

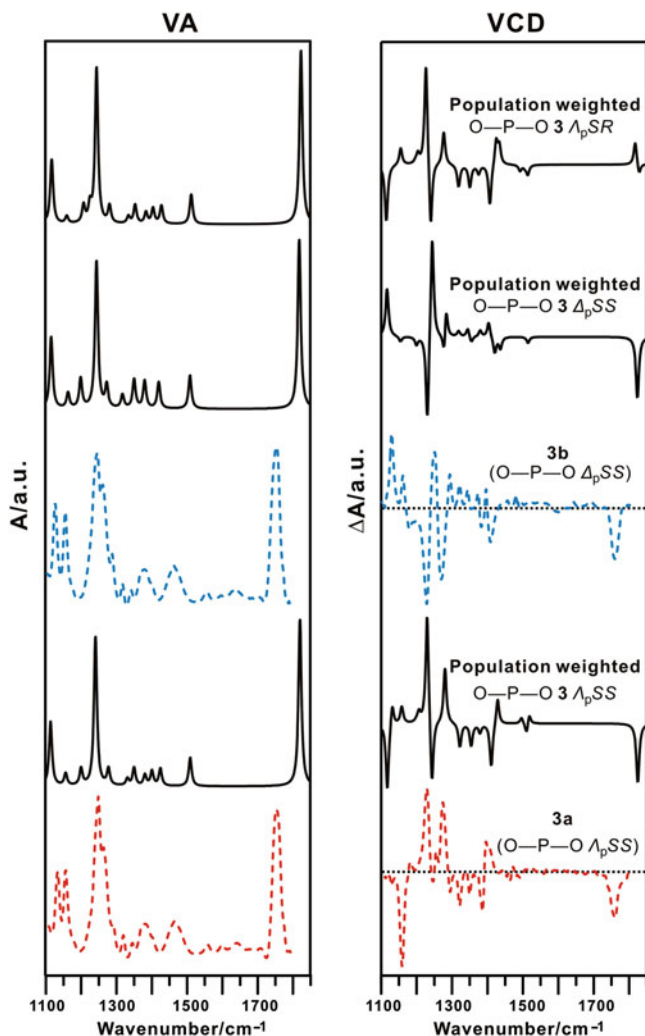


Fig. 8 Comparison of the experimental (dashed line) VA (left) and VCD (right) spectra of **3a** and **3b** with the corresponding calculated population weighted spectra (solid line) of OPO axis A_pSS and Δ_pSS stereoisomers. The calculated VA and VCD spectra of A_pSR are included for comparison. A_pRS is the same as A_pSR because the two chiral ligands are the same except their ACs. Adapted with permission from [22]. Copyright (2010) Wiley

chirality at the phosphorus center while those at the C=O stretching region are determined by the chirality of the amino acid ligands. The analogous AC conclusions were obtained for **5a** and **5b**. The ECD, OR, and VCD measurements obtained

for all four pairs of diastereomers shown in Fig. 7 firmly established that **4a**, **4b**, **6a**, and **6b** are mirror images of **3a**, **3b**, **5a**, and **5b**, respectively.

4.2 *H-bonding Interactions of Chiral Molecules in Solution*

4.2.1 Modeling Chiral Solute–Water H-Bonding Networks by Induced Solvent Chirality

H-bonding interactions between chiral molecules and water molecules play an essential role in life sciences [28, 120–123], since nearly all important biomolecules are chiral and most biological events and reactions take place in an aqueous environment. The structural aspects of water surrounding a chiral molecule and the fundamental roles of water in many important biological processes remain the subjects of intense debate [124–127]. As described in the previous section, for most AC studies with VCD, an inert solvent, such as CCl_4 and CDCl_3 , was chosen whenever possible to avoid complications in simulations due to severe perturbation from the solute–solvent intermolecular interactions. On the other hand, for most biological molecules, such as proteins, peptides, sugars, and amino acids, VA and VCD measurements have been carried out in aqueous solution. To model such measurements adequately, it is necessary to take into account the important intermolecular interactions, such as solute–solvent and solute–solute H-bonding, accurately [128, 129]. Recently, our group has undertaken a series of VCD investigations of the water–solute H-bonding networks in aqueous solution of several basic chiral building blocks such as methyl lactate (ML) [48], lactic acid (LA) [130], propylene oxide (PO) [131], and glycidol [132]. These prototype chiral molecules have been chosen because: (1) they have one, two, or three functional groups, i.e., epoxy O, OH, and C=O, which can act as an H-bond donor or acceptor to form strong H-bonds with water; (2) by sequentially increasing the number of functional groups, one can examine such interactions in an orderly way to better understand the complicated situation with a larger biomolecule with these same functional groups; (3) they are relatively small in size, making them amenable to high level ab initio calculations; (4) these compounds have good solubility in water and in some inert organic solvents, allowing one to perform experimental comparisons directly to uncover the solvent effects due explicitly to the solute–water H-bonding.

In these studies, we focused particularly on the observed VCD features in the water bending vibrational mode region around $1,640\text{ cm}^{-1}$. The experimental VCD spectra of PO, ML, LA, and glycidol in aqueous environments are given in Fig. 9, where the water bending mode regions, showing very distinct VCD spectral features in each case, are highlighted. Water is an achiral molecule. Why should there be such VCD features in its bending mode region? The answer is that some of the water molecules are explicitly H-bonded to a chiral solute and therefore become optically active as part of the super H-bonded chiral complexes. This phenomenon

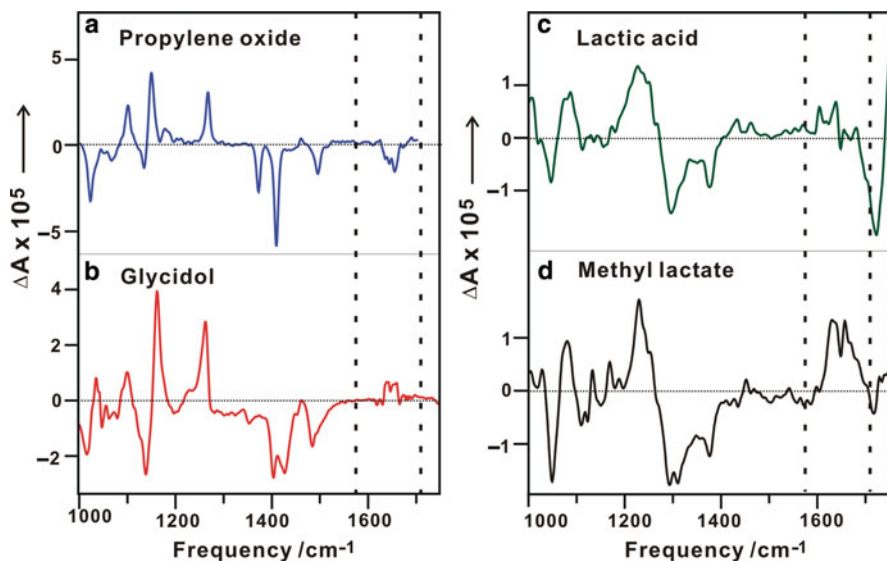


Fig. 9 Comparison of VCD spectra for the S form of (a) propylene oxide, (b) glycidol, (c) lactic acid, and (d) methyl lactate in aqueous solutions. The chirality transfer spectral windows are indicated with dotted lines. Adapted with permission from [132]. Copyright (2009) American Institute of Physics

is termed *induced solvent chirality* or *chirality transfer*. The *induced solvent chirality* is due exclusively to the explicit intermolecular H-bonding interactions between a chiral solute molecule and water molecules. Consequently, these spectral features contain important information about the number of water molecules that are explicitly H-bonded to the chiral solute molecule and the specific binding sites. We called this region *chirality transfer* spectral window which allows one an exclusive view to the chiral solute–water H-bonding networks in solution. The *chirality transfer* spectral features shown in Fig. 9, when compared to the theoretical simulations of the H-bonding network structures, demonstrated a clear preference for a particular type of H-bonding solvation network in each case. It therefore allowed us to arrive at the conclusion that noticeably different H-bonding network structures exist in these solutions (see below).

Similar to the AC determination work illustrated in Sect. 4.1, it is necessary to carry out a complete structural search for all significant chiral species present in order to extract the detailed information contained in the experimental spectra. In addition, one needs to consider solvent effects in these studies. As introduced in Sect. 3.2, currently there are two approaches to model the solvent effects: the implicit solvent model and the explicit model where H-bonding intermolecular interactions are considered explicitly. An example VA and VCD simulation of ML in water with PCM with several different basis sets and functionals is shown in Fig. 10 [48]. Although the calculated VA spectrum with PCM shows a good

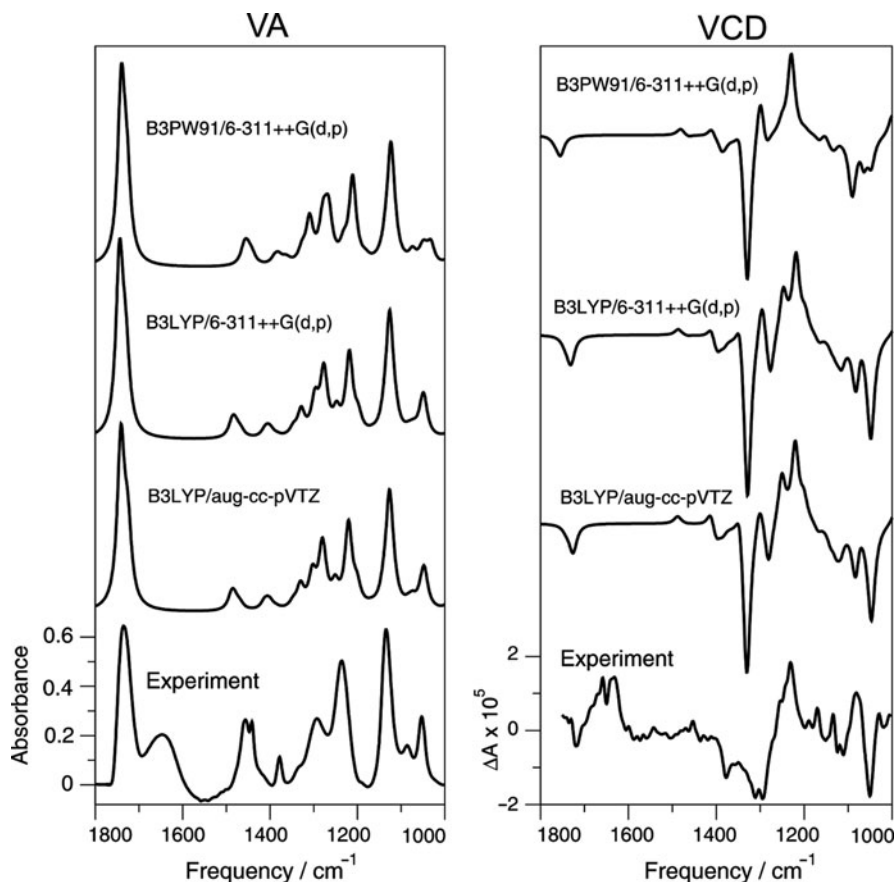


Fig. 10 Comparison of the VA and VCD spectra of ML in water calculated using the PCM model at the three levels of theory (top three traces) with the corresponding experimental spectra in water (bottom trace). Adapted from [48]

correlation with the experimental one, the same cannot be said for the VCD spectrum. In particular, the main features in the *chirality transfer* windows are not captured. This is because PCM does not consider the specific shapes of solvent molecules or the specific H-bonding interactions between water and chiral molecules, rather only the overall dielectric environment associated with water. Therefore, it is necessary to take the explicit intermolecular interactions between the chiral solute and the achiral water solvent molecules into account.

It is often very helpful to apply MD simulations prior to a conformational search in order to gather information about the important H-bonded species in solution [133–136]. In our studies we used the Sander module in the AMBER9 suite of programs [137], the AMBER *ff99* force field based on molecular mechanics, and the TIP3P [138] or TIP4P [139] water model in the simulations. The ratio between

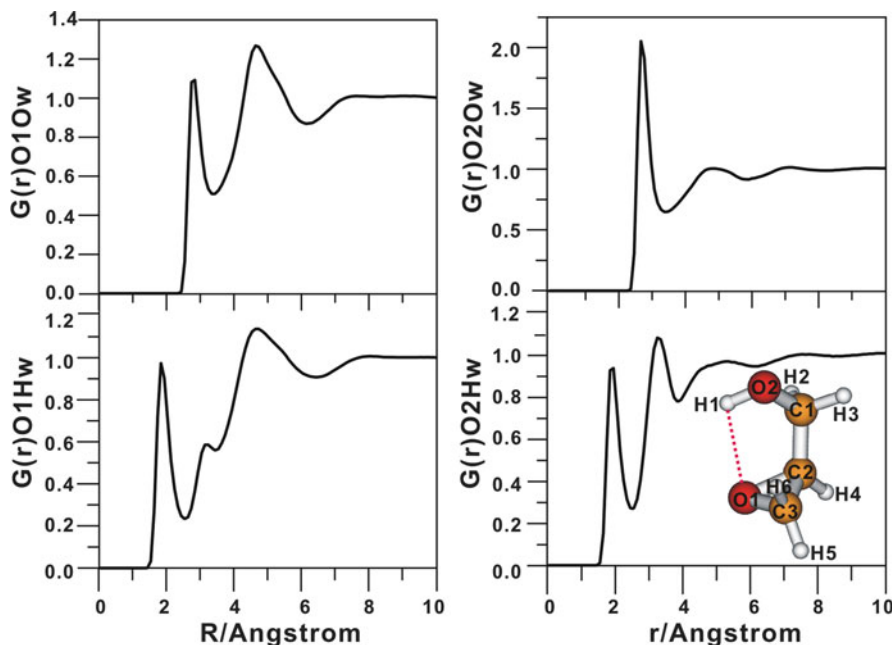


Fig. 11 Radial distribution functions obtained from the MD simulation of glycidol in water. Ow and Hw are the oxygen and hydrogen atoms of water, respectively. The atom labeling of glycidol is given in the *insert*. Adapted with permission from [132]. Copyright (2009) American Institute of Physics

the solute and water molecules in an octahedral box was set to correspond to the actual experimental condition. Information about the short-range structures can be obtained from the analysis of atom–atom radial distribution functions (RDFs). As an example, the RDFs obtained for 6 M glycidol in water are illustrated in Fig. 11. Based on the analysis of RDF results, the number of water molecules explicitly H-bonded to glycidol can be obtained, which was determined to be four in this case. Another important question is what the extent of glycidol self-aggregation is in water. The analysis of the RDF, $g(r)_{O_2O_2}$ (not shown), which provides the information about the distance between the O_2 atoms of two glycidol molecules, confirms that there is little dimer formation. Moreover, the resulting MD snapshots also provide information about the possible H-bonding structures of the glycidol–water clusters. All these results are very informative to guide the conformational search where there are a large number of possible glycidol–water clusters. In total, 34 conformers of the small glycidol–(water) $_N$ clusters with $N = 1, 2, 3,$ and 4 were found with the DFT optimizations. The intermolecular H-bonding distances become shorter and shorter in these clusters with increasing number of water molecules. This is attributed to the cooperative effects of the H-bonding networks. The OH functional group of glycidol can form more intermolecular H-bonds with water than the O atom in the oxirane ring since OH can act as a donor or an acceptor

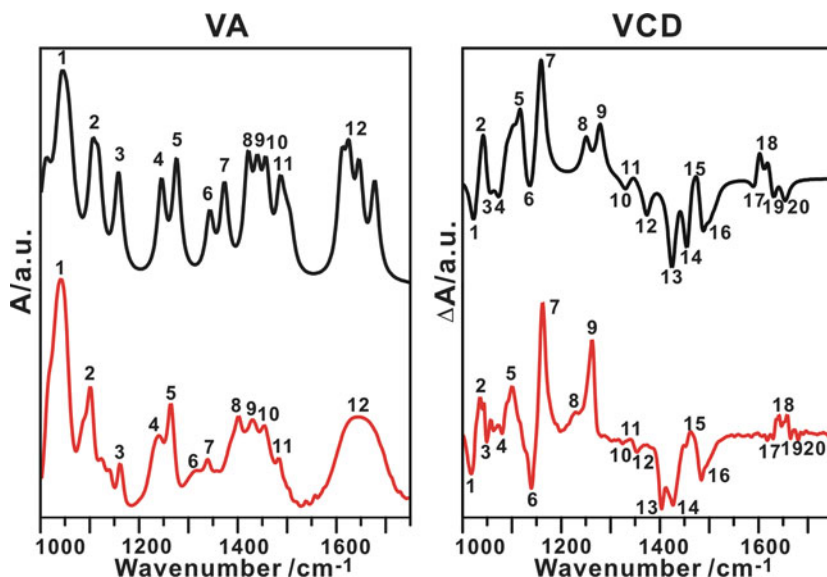


Fig. 12 Comparison of the experimental and simulated VA and VCD spectra of glycidol in water. Adapted with permission from [132]. Copyright (2009) American Institute of Physics

or simultaneously as both. The VA and VCD spectra were simulated by using the population weighted spectra of the 34 conformers. The good agreement between the simulated and the experimental data (Fig. 12) shows that all these clusters make important contributions to the observed spectra and are the important species in the aqueous solution with complicated equilibriums among them.

Although the self-aggregation of glycidol in water is negligible, the situation is different from LA in water. In the 2 M LA aqueous solution, the dominant conformers are the H-bonded clusters between water and the cyclic LA dimer (AA). In other words, water cannot break the strong H-bonds in AA. The VA and VCD spectra simulated using 30% AA-(H₂O)₂, 25% AA-(H₂O)₄, and 45% AA-(H₂O)₆ are in good agreement with the experimental VA and VCD, respectively [130]. In the case of ML in water, the binary ML-H₂O complex was found to be the main contributor, together with some small contribution from ML-(H₂O)₃ [48]. For PO in water, the binary anti-PO-H₂O complex where water binds to PO on the opposite side as the PO methyl group was concluded to be the main species. The contributions from the larger PO-(H₂O)_N (*N* = 2, 3) clusters, on the other hand, were ruled out since they exhibited overwhelmingly strong bisignate and trisignate VCD signals in the *chirality transfer* spectral window which are not visible in the related experimental VCD spectrum [131].

These studies show that the H-bonding network structures depend strongly on the nature of the chiral solute. The *solvent induced chirality* signatures provide significantly more detailed information about the explicit interactions between water and

chiral solute than the corresponding VA features since the latter ones tend to be broad and featureless. They have been employed effectively in the above examples [48, 130–132] as the discriminators to determine the number of water molecules and the specific binding sites for the explicit chiral solute–water H-bonding interactions. One can expect that a combination of this unique spectral window with the matrix isolation technique (see Sect. 4.5) will be a highly sensitive tool to probe these important solute–solvent clusters in great details at a fundamental level.

4.2.2 Self-Aggregation of Chiral Solutes

Some chiral molecules contain both H-bond donor and acceptor functional groups and are capable of forming strong intra- and intermolecular H-bonds. The recent VCD studies of glycidol [140] in CDCl_3 and LA in water [130] demonstrate that such self-aggregations have significant effects on the VA and VCD spectra

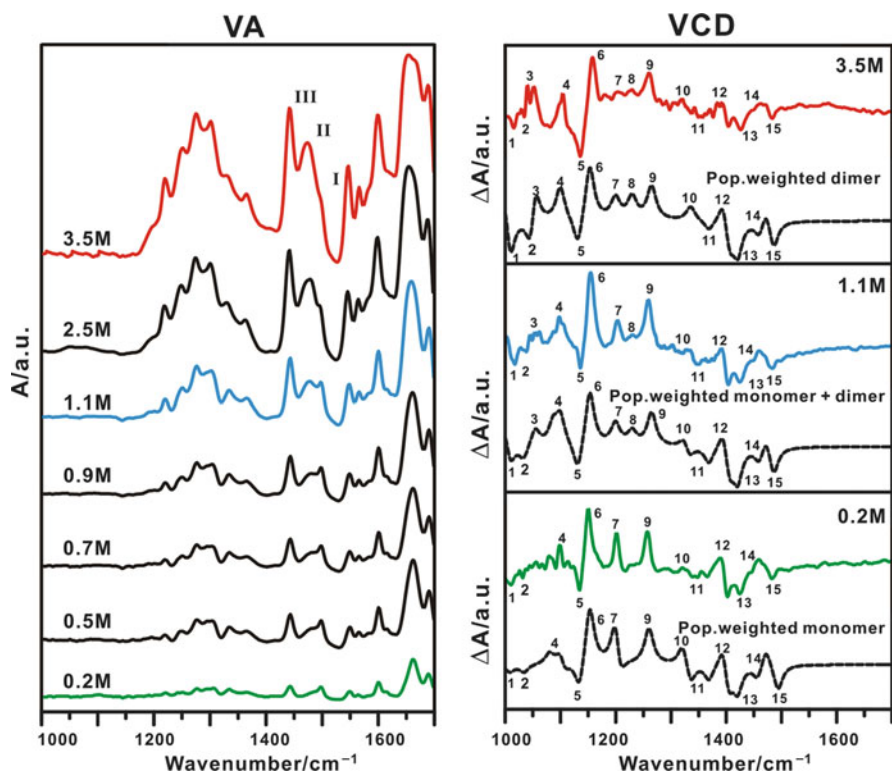


Fig. 13 Experimental VA spectra (*left*) of glycidol in CDCl_3 at seven different concentrations ranging from 0.2 to 3.5 M and the corresponding VCD spectra (*right*) at the three representative concentrations. The simulated VCD spectra (*dashed line*) for these three concentrations are also included. Adapted from [140]

measured. And, vice versa, one can utilize VA and especially VCD techniques to look into this type of intermolecular interactions in solution. Below the study of glycidol in CDCl_3 is used as an example.

Figure 13 shows the concentration dependence of the VA spectra of glycidol in CDCl_3 measured at seven different concentrations ranging from 0.2 to 3.5 M and the related VCD spectra at the three concentrations of 0.2, 1.1, and 3.5 M. The intensity ratio of the three peaks marked with I, II, and III varies noticeably with increasing concentration. When the concentration is ~ 0.2 M, peak II is barely visible and it becomes more obvious, with increasing concentration. At 1.1 M, the intensity of peak II becomes similar to that of peak I. As the concentration increases to 3.1 M, the intensity of peak II becomes much larger than that of peak I. With the increasing concentration, the intensity of peak III becomes larger and larger. Peak I has the smallest relative intensity increase over the whole concentration range, with its main contribution from the glycidol monomer, while peak II, with the largest relative increase, is likely to be dominated by the binary or larger glycidol clusters. The VCD spectral features vary noticeably with increasing concentration, especially, in the $1,000\text{--}1,150\text{ cm}^{-1}$ region. These observations show that the self-aggregation of glycidol in solution occurs with increasing concentration.

Eight stable monomers, 15 dimers, and 6 trimers were obtained after an extensive conformational search based on the MD snapshots. The simulated VA and VCD spectra of these conformers are depicted in Fig. 13 for comparison with the experimental data. The results show that the self-aggregation of glycidol is negligible at 0.2 M or lower concentrations. At 3.5 M the binary conformers dominate, while at the intermediate concentration of 1.1 M both the monomeric and binary conformers are in existence. Complementary OR measurements and simulations (Fig. 14) were also performed for these three representative concentrations. Even with a fairly large basis set such as aug-cc-pVTZ, the magnitudes of the OR values were not predicted exactly at the three concentrations [140]. This alludes to the challenges in obtaining the accurate OR simulations mentioned in Sect. 3.2. On the other hand, both the sign and the trend of variation with concentration observed experimentally were captured by the simulation. The OR results further support the conclusions drawn from the VCD investigation.

4.3 *Enhancement of VA and VCD Intensities in Transition Metal Containing Chiral Complexes*

Transition metal containing chiral complexes exhibit some peculiar VCD behaviors which have fascinated researchers in inorganic chemistry and in spectroscopy. For example, an order of magnitude increase in the VCD intensity, with changes in sign for many VCD transitions, were detected for the open-shell sparteine complexes of Co(II) and Ni(II) as compared to the corresponding closed-shell Zn(II) complex

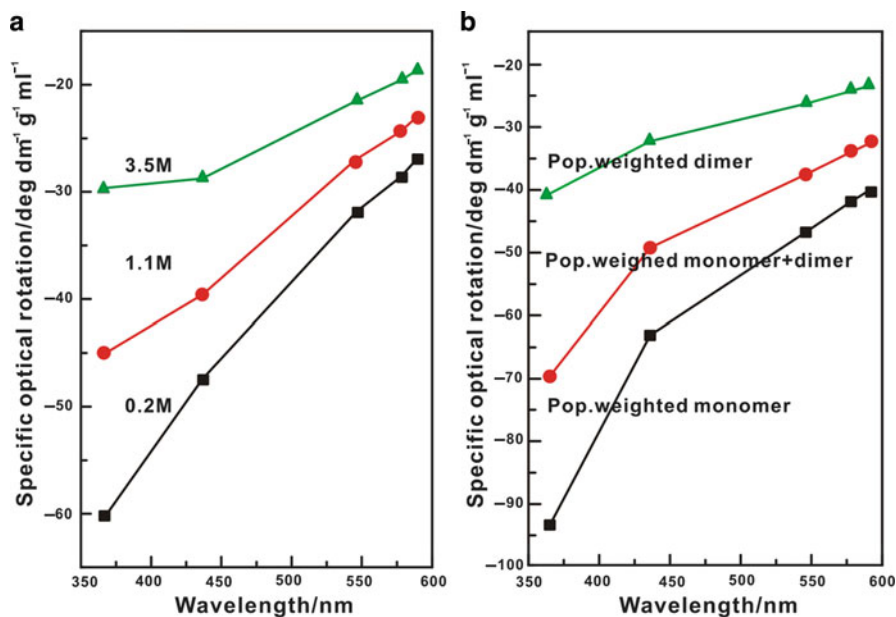


Fig. 14 Comparison of (a) the experimental specific OR values of glycidol at the representative concentrations of 0.2, 1.1, and 3.5 M, recorded at five different wavelengths with (b) the simulated corresponding OR values of the monomeric, monomeric + binary, and binary conformers at the B3LYP/aug-cc-pVTZ level, respectively. The empirical ratio used for these three species are the same as for VCD in Fig. 13. Adapted from [140]

[141, 142]. This observed intensity enhancement had previously been attributed to the presence of large underlying CD intensity from the electronic open-shell d–d transitions [141, 143]. The newer VCD measurements by Nafie, Freedman, and co-workers, however, questioned the validity of such an explanation since the VCD enhancement extends to below 1,000 cm⁻¹ without any diminishing of enhancement or distortion of band shapes, whereas the earlier explanation requires direct overlap with a broad underlying state [142]. The first ab initio VCD calculation for the close-shell Zn(II) complex was reported in the same work, demonstrating very good agreement with the experimental data [142]. This opened the door to further similar VCD/DFT applications to closed-shell transition metal complexes. For the two open-shell complexes, on the other hand, it was found that the atomic axial tensor, and therefore rotational strength, expressions contain low-lying magnetic dipole allowed d–d transitions that are vibronically coupled to the ground state and make large contribution to VCD intensity for all modes due to a small energy denominator [142]. As a result, the current MFP formulation of VCD intensity, used in Gaussian and other software packages, may not be suitable for such open-shell systems because MFP neglects excited-state vibronic details, making it invalid in the presence of small energy denominators. In 2004, Nafie extended the vibronic

theory in the limit of vibrational resonance with low-lying electronic states to account for this [144]. So far it has not been implemented into ab initio programs. And no direct comparison between the simulations incorporating the newly developed theory and the experimental spectroscopic data has been reported so far. More recently, Yamagishi and co-workers examined the effects of central metal ions on the VCD spectra of a series of transition metal complexes [23, 145, 146], and performed DFT simulations of the VCD spectra of several open-shell transition metal complexes such as Λ and Δ -[Ru(acac)₃]. The simulations were found to be in good agreement with the experimental data, in spite of the prevailing view that MFP may not be suitable for the open-shell systems with Jahn–Teller distortion. These authors attributed the observed VCD intensity enhancement to a charge transfer effect, a mechanism invoked to explain a similar enhancement observed in the Co(III) complex discussed below [147].

The tris(ethylenediaminato)cobalt(III) complex, [Co(en)₃]³⁺, is a closed-shell chiral transition metal complex. The achiral ethylenediamine (en) ligand can assume two enantiomeric conformations, with the C–C bond nearly parallel (δ -form) or oblique (λ -form) to the C₃-axis in the Λ -configuration, leading to four conformations for the complex (Fig. 15). A series of VA and VCD experiments were carried out in solution with [Co(en)₃]³⁺ and two different counter ions, i.e., Cl[−] and I[−] [148, 149]. It was discovered that the CH-stretching VA and VCD spectra are highly sensitive to the nature and concentration of the halide counter ions. For example, both VA and VCD intensities in the CH-stretching region increase when the anion is changed from iodide to chloride and with higher halide ion concentrations. It was proposed that the halide anions may exert strong

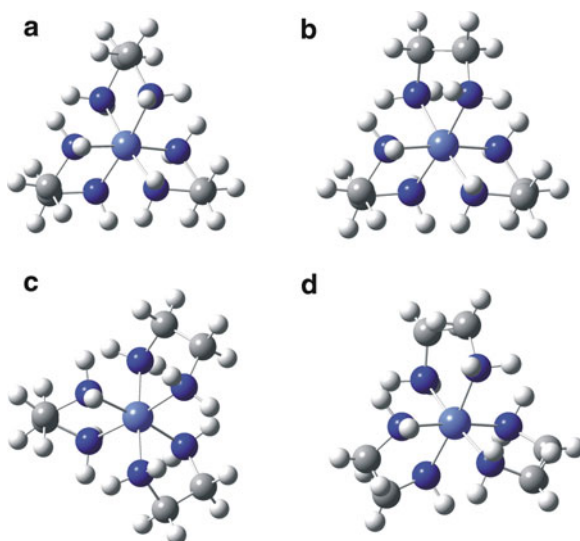


Fig. 15 Λ -[Co(en)₃]³⁺ conformations, viewed along the C₃-axis: (a) $\delta\delta\delta$, (b) $\delta\delta\lambda$, (c) $\delta\lambda\lambda$, and (d) $\lambda\lambda\lambda$

influence on the transition metal complex through H-bonding with the en rings. Computational searches for conformers were performed for $[\text{Co}(\text{en})_3]^{3+}$ with and without Cl^- , with both the LanL2DZ and 6-31G(d) [C, H, N]/Stuttgart ECP [Co] basis sets [149]. Although the $\delta\delta\delta$ form was predicted to be the least stable among

Fig. 16 Geometries of Λ - $[\text{Co}(\text{en})_3]^{3+}$ with two associated chloride ions along the C_3 -axis, $[\text{Co}(\text{en})_3]\text{Cl}_2^+$, and with three associated chloride ions along the three C_2 -axes, $[\text{Co}(\text{en})_3]\text{Cl}_3$

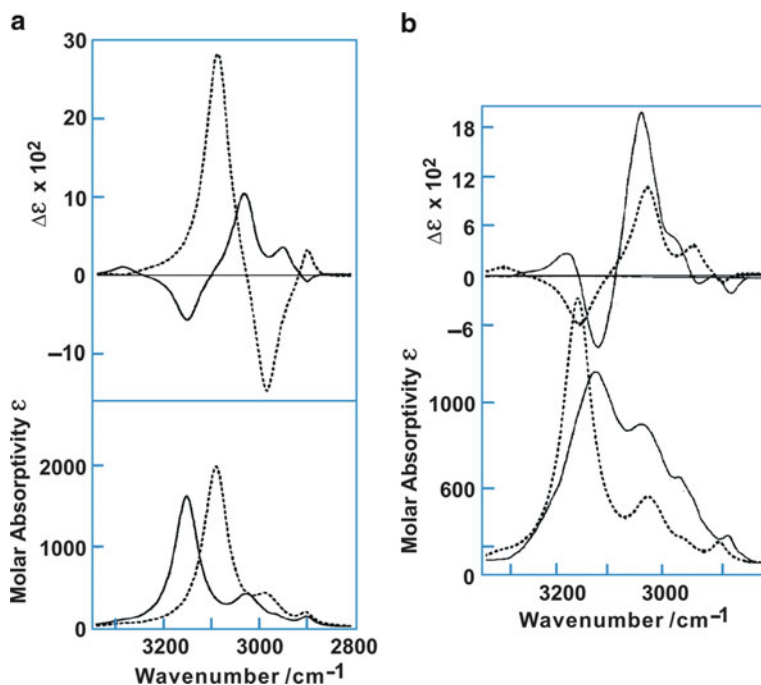
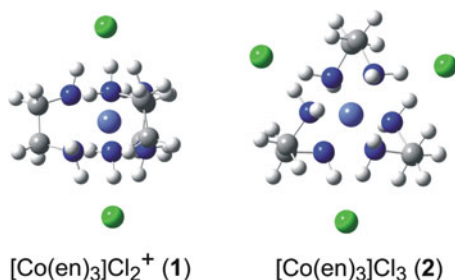


Fig. 17 (a) Calculated NH/CH-stretching VA and VCD spectra (*solid line*) of Λ - $[\text{Co}(\text{en})_3]^{3+}$ with two associated chloride ions, $[\text{Co}(\text{en})_3]\text{Cl}_2^+$ (1), and those (*dashed line*) of three associated chloride ions, $[\text{Co}(\text{en})_3]\text{Cl}_3$ (2). A Lorentzian bandwidth (HWHM) of 30 cm^{-1} is used for the associated NH-stretches and 15 cm^{-1} for the free NH and CH stretches. (b) Comparison of the experimental NH/CH-stretching VA and VCD spectra (*solid line*) of Λ - $[\text{Co}(\text{en})_3]^{3+}$ at 0.06 M with 0.6 M LiCl in DMSO- d_6 with the simulated spectra (*dashed line*) of $[\text{Co}(\text{en})_3]\text{Cl}_2^+$ at the B3LYP/LanL2DZ level of theory. Adapted with permission from [149]. Copyright (2002) American Chemical Society

the four conformers for the free (gas phase) Λ -[Co(en)₃]³⁺, the addition of the Cl⁻ counter ions, which bridge two (or three) NH bonds from the adjacent en rings (see Fig. 16), preferentially stabilizes the $\delta\delta\delta$ -conformation. The simulated VCD spectra for Λ -[Co(en)₃]³⁺ with two and three Cl⁻ counter ions are given in Fig. 17, as well as a comparison between the experimental and calculated spectra. As one can see, the VCD features for Λ -[Co(en)₃]³⁺ with two or three Cl⁻s are drastically different. This allows one to assign the dominant species and their conformers in solution with confidence by correlating the experimental and simulated VCD spectra. Such high sensitivity to the structural details makes VCD an unique and possibly the only spectroscopic technique which can identify the location of the chloride ions interacting with [Co(en)₃]³⁺ in solution.

What is the origin for the intensity enhancement observed when the chloride ions are interacting with [Co(en)₃]³⁺? One may recall that similar enhancements were discussed in Sect. 4.2 where intermolecular H-bonding interactions induce VCD intensity in the water molecules that are H-bonded to a chiral solute. So the answer to this question holds general interest for a number of new research branches. By analyzing the various contributions of the electric and magnetic dipole transition moments of the O \leftrightarrow H...N stretching mode of the benzoylbenzoic acid-NH₃ complex, Nicu and Baerends concluded that the enhancement of the VA and VCD intensities predicted theoretically is due to the donor-acceptor interactions or charge transfer between the NH₃ base and the OH σ^* acceptor [73]. Since the Λ - $\delta\delta\delta$ -[Co(en)₃]³⁺...2Cl⁻ complex has six N \leftrightarrow H...Cl⁻ stretching modes, one may expect a similar mechanism, although the situation is more complicated [147]. Calculations of the complex with and without the chloride ions were performed using the ADF program package with the BP86 and OLYP functionals and the TZP basis set. To locate the origin of the enhancement, these authors looked into the nuclear and electronic contributions of the total electric and magnetic dipole transition moments, and how such contributions vary with and without the presence of the chloride ions. The amount of charge transferred from the associated Cl⁻s into the NH bonds, during the normal mode motion when the H atoms involved in the H-bonds approach the chloride ions, can be estimated by comparing the Mulliken charges of the chloride ions of interest at the equilibrium and the displaced geometries. Through such detailed analyses, it was found that the nuclear and electronic contributions to the dipole transition moments have the same sign in the presence of chloride ions due to the charge transfer, whereas they have opposite sign in the free complex. Consequently, the nuclear and electronic parts reinforce each other in the presence of chloride counter ions. This leads to larger total electric and magnetic dipole transitions moments and therefore results in enhancement of the VA and VCD intensities.

4.4 Conformational Study of Absorbed Chiral Ligands on AuNPs

Monolayer-protected AuNPs are organic-inorganic hybrid material and are of considerable interest for their potential applications in areas such as catalysis,

sensing, and drug delivery [150]. The chemical behavior, such as solubility, molecular recognition, and organization, of these AuNPs is largely controlled by the protected layer. For example, adsorption of a chiral molecule can create a locally chiral environment near the metal surface, leading to a *chiral footprint* on the nonchiral surface [151, 152]. These adsorbed chiral molecules may also transfer chirality onto the electronic structure of the nonchiral metal. Recently, the existence of enantiospecific adsorption of cysteine on the Au₅₅ cluster was demonstrated theoretically [153]. A molecular-level understanding of the interactions between chiral ligands and AuNPs is essential to answer some important questions; for instance: what are the conformations adopted by the chiral ligands and what are the preferred binding sites on the AuNPs? The answers to these fundamental questions can ultimately help with rational designs of functionalized NPs.

Bürgi and co-workers [154–156] have reported a series of conformational investigations of chiral ligands absorbed on AuNPs using VCD spectroscopy complemented with DFT calculations, a powerful spectroscopic tool for conformational studies of condensed matters. Three organic chiral ligands, namely *N*-acetyl-cysteine, *N*-isobutyryl-cysteine, and 1,1'-binaphthyl-2,2'-dithiol (BINAS), were used as chiral ligands in their studies. The details about how to prepare monolayer-protected AuNPs with these ligands can be found in the pertinent references [154–156]. The measured VA and VCD spectra of the AuPNs protected by *N*-isobutyryl-*L/D*-cysteine monolayer are shown in Fig. 18, as examples. As one

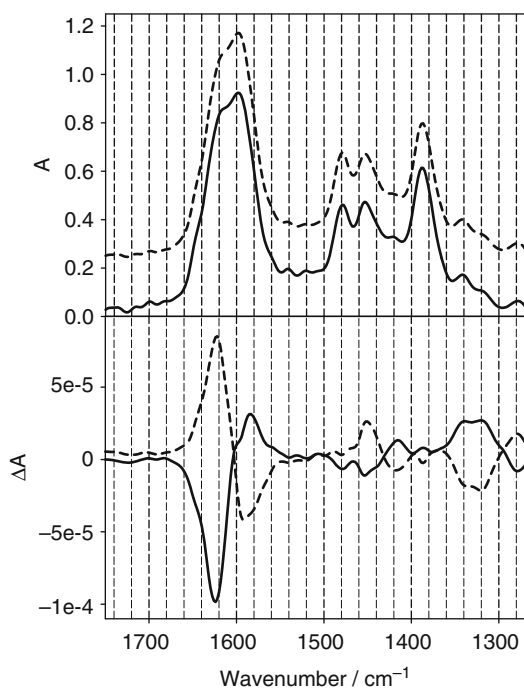


Fig. 18 VA (top) and VCD (bottom) spectra of *N*-isobutyryl-cysteine protected AuNPs in NaOH/D₂O. Solutions were made from 7 mg of sample in 50 μ L of solution. The dashed (solid) lines correspond to the spectra of the particles covered by the *L*-enantiomer (*D*-enantiomer). The VA spectrum of the particles covered with *N*-isobutyryl-*L*-cysteine was offset for clarity. Adapted with permission from [155]. Copyright (2006) American Chemical Society

can see, the VCD spectra show a mirror image relationship for the two enantiomers, whereas the shapes of the related VA spectra are identical. It should be pointed out that the VCD sample used contains different sizes of the monolayer-protected AuNPs. The appearance of relatively strong bands in the VCD spectra suggests that the size of the AuNPs has relatively minor effects on them and that VCD is a local property of the individual adsorbed molecules.

In their latest study with BINAS, a conformationally rigid system, the authors were able to separate the AuNPs protected by BINAS into five different fractions according to their sizes using size exclusion chromatography [157]. They also estimated the particle size for each fraction, for example, fraction 5 AuNPs contain 10–15 gold atoms, fraction 3 about 22–25 gold atoms, and fraction 1 about 30–40 gold atoms [156]. The VCD spectra of the AuNPs protected by BINAS obtained for fraction 1–3 are given in Fig. 19, together with that of free BINAS for comparison. Overall, the VCD spectra of all three fractions look quite similar, but differ from that of the free BINAS. Small differences observed for fraction 3 were attributed to the lower quality of the spectra because of the smaller sample quantity available, rather than to a different conformation of the adsorbed BINAS. These new experiments with improved size resolution clearly demonstrate that the conformation of the adsorbed chiral ligand molecules is not drastically modified by the size of the AuNPs even in the subnanometer range, thus supporting the similar conclusions made in the earlier studies. Very interestingly, they found strong size dependent effects on the UV-vis spectra and even more on the ECD spectra of the AuNPs protected by BINAS [156].

To obtain the conformational information about the chiral ligands bound to the AuNPs from the measured VA and VCD spectra, it is necessary to simulate the VA

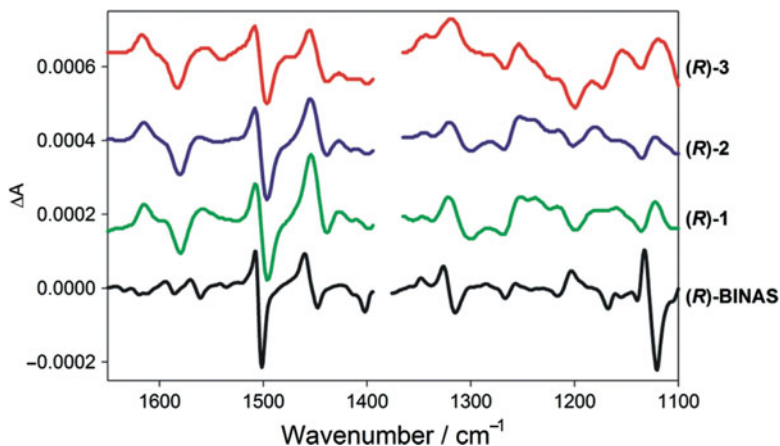


Fig. 19 VCD spectra of the size-separated AuNPs protected with (R)-BINAS with the fraction 1–3 samples obtained using size exclusion chromatography and of free (R)-BINAS in CD_2Cl_2 solution. The spectra of the nanoparticles were scaled by a factor of 4. Adapted with permission from [156]. Copyright (2010) American Chemical Society

and VCD spectra of the protected AuNPs. Since it would be too difficult if not impossible to do a complete conformational search of an actual AuNP covered with chiral ligand molecules, a model which contains a small gold cluster bound to one chiral molecule was used. This approximation is justified by the experimental observation that both VA and VCD are relatively insensitive to the size of AuNPs. Furthermore, some earlier studies showed that the experimental VA spectra of molecules adsorbed on a metal surface can be well reproduced by the calculations of just one single molecule adsorbed on a small metal cluster consisting of a few atoms [158, 159]. In the case of the AuNPs protected by *N*-isobutyryl-L-cysteine, six stable conformers of the adsorbed deprotonated *N*-isobutyryl-L-cysteine on an Au₈ cluster were found and are depicted in Fig. 20. Their corresponding VCD spectra are given in Fig. 21. It is noted that the rotation of isopropyl group has little influence on the VCD spectra, as evidenced by the similar appearance of the VCD spectra of conformers **a** to **c**. The other three conformers exhibit distinctly different VCD patterns. From Fig. 22, one can say that the simulated VCD spectra of **a** (and also **b** and **c**) are in good agreement with the experimental one. Among **a**, **b**, and **c**, **a** is energetically favored with the C–H and

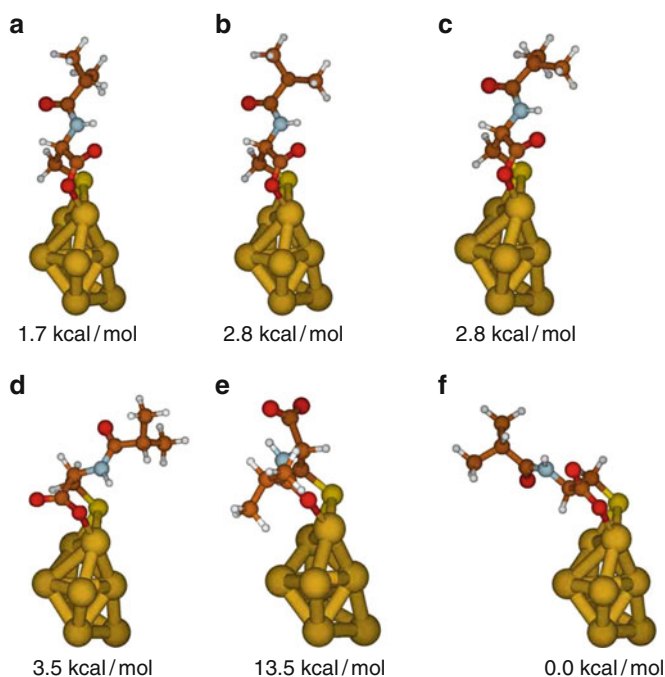
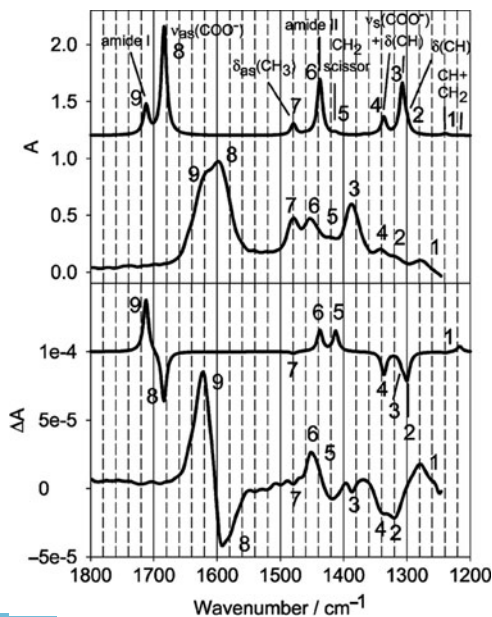


Fig. 20 Calculated conformers of deprotonated *N*-isobutyryl-L-cysteine on a Au₈ cluster. The numbers indicate the calculated relative stability with respect to the most stable conformer **f**. The calculations were performed at the B3PW91 level using a 6-31G(d,p) (LanL2DZ for Au) basis set. Adapted with permission from [155]. Copyright (2006) American Chemical Society

Fig. 21 Calculated VCD spectra for different conformers of *N*-isobutyryl-L-cysteine adsorbed on a Au_8 cluster. The letters correspond to the structures shown in Fig. 21. Adapted with permission from [155]. Copyright (2006) American Chemical Society



Fig. 22 Comparison between calculated and experimental VA and VCD spectra of *N*-isobutyryl-L-cysteine on gold. The calculated spectra are shown for conformer **a** in Fig. 21. Corresponding bands are numbered and the assignment is given in the upper part of the figure. Adapted with permission from [155]. Copyright (2006) American Chemical Society



C=O bonds in the *trans* arrangement. These authors therefore concluded that conformation **a** is the preferred orientation for *N*-isobutyryl-L-cysteine to attach to AuNPs in which the chiral ligand interacts with the AuNPs through the carboxylate and the sulfur atoms. These pioneering studies demonstrate the great potential of VCD spectroscopy for providing insight into the conformations of chiral molecules adsorbed on small metal particles.

4.5 Matrix Isolation VCD Spectroscopy for Probing Conformational Landscapes of Highly Flexible Chiral Molecules and Chiral Molecular Complexes

VCD spectroscopy has been successfully applied to the studies of intermolecular interactions involving several simple basic chiral building blocks such as those discussed in Sect. 4.2. It is, however, still highly challenging to model the solvent–solute interactions adequately for highly flexible chiral molecules, which most of them are. Since the signs of VCD are sensitive to torsional dihedral angles, the corresponding VCD bands of different conformers consequently often have opposite signs. In addition, strong solute–solvent or solute–solute H-bonding interactions can not only shift the band positions but also modify the band intensities and alter the conformational distributions. More importantly, the dominant species contributing to the observed chiroptical measurements may no longer be the isolated chiral solute molecules but rather clusters of solute with solvent molecules or solute self-aggregates. All these effects together may lead to broad, featureless spectra which make it difficult or impossible to extract the information contained in them. In the vast majority of VCD studies, the interpretations rely on the calculations of isolated target molecules. Theoretical VCD modeling that takes into account the solvent–solute interactions has yet to be fully developed. It is therefore strongly desirable to have a spectroscopic technique where one can control spectral contributions of different species and resolve spectral signatures of different conformers in order to test and to benchmark the corresponding theoretical modeling.

The coupling of matrix isolation and VCD techniques provides such an opportunity. Matrix isolation is a mature technique that has been widely used to supply a wealth of structural and dynamical information of various molecular systems. The matrix isolation VCD spectra of two rigid single conformer chiral molecules, i.e., pinene and propylene oxide, were reported in the mid-1980s [160–162]. The potential of such a combination for the study of highly flexible multi-conformational chiral systems and H-bonded chiral molecular complexes was not recognized or pursued at the time, possibly because the theoretical modeling needed to deal with these challenging systems was not available. Such applications were first suggested by Jalkanene and Suhai in 1996 [128]. Because of the very low temperature achieved in a matrix, one has the advantages of minimum interference from an almost non-interacting rare gas matrix and substantially better sensitivity and resolution for the VCD spectra. Indeed, the power of such a combination in the

determination of conformations and the AC of a multi-conformational chiral molecule, i.e., (*R*)-2-amino-1-propanol or (*R*)-alaninol, was demonstrated recently [163]. In Fig. 23, one can compare the VA and VCD spectra of (*R*)-alaninol

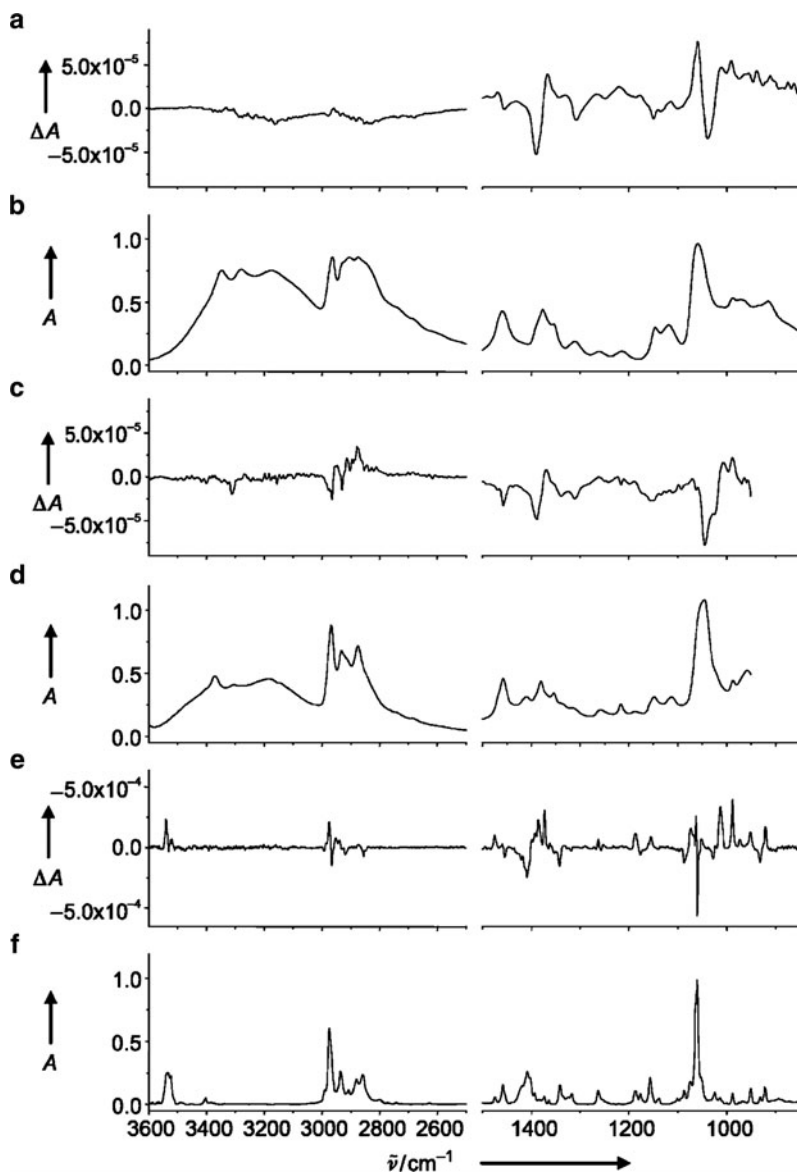


Fig. 23 Spectra of (*R*)-alaninol. (a) VCD spectrum, neat film; (b) VA spectrum, neat film; (c) VCD spectrum of a sample in solution in CDCl_3 ; (d) VA spectrum of a sample in solution in CDCl_3 ; (e) matrix isolation VCD spectrum; (f) matrix isolation-VA spectrum. Copyright Wiley-VCH Verlag GmbH & Co. KGaA. Reproduced with permission from [163]

recorded under three experimental conditions: as a neat film, in CDCl_3 solution, and in a cold Ar matrix. Under the first two conditions, the VA and VCD spectra are broad, unresolved, and with low-intensity. Because of broadening and rotameric averaging, the theoretical calculations did not correlate well with the observed spectra [164]. The matrix isolation VA and VCD spectral features, especially in the O–H and N–H stretching region, on the other hand, are sharp and therefore informative. A further bonus with a matrix is that the absolute intensity and the S/N ratio obtained are about an order of magnitude larger. The superior resolution and S/N ratio allows a decisive comparison between the experimental data and theoretical simulations presented in Fig. 24 (note that labeling of conformers is consistent with reference [165]). Some erroneous assignments made before can now be corrected. For example, the band at $1,316\text{ cm}^{-1}$ has now been determined to (at least partly) belong to the δ -COH transition of the $gG'g$ conformer, thus refuting the original assignment to the γ -CH transition of the $g'Gg'$ conformer since the calculated VCD rotation strength of this γ -CH transition and that of the observed VCD band have opposite signs. Similar investigations have been extended to several flexible natural amino acids and complexes [166–168]. This combination is now also used by other groups, including ours, to study *chirality transfer* effects between chiral solute and achiral solvent molecules and intermolecular interactions in general [169].

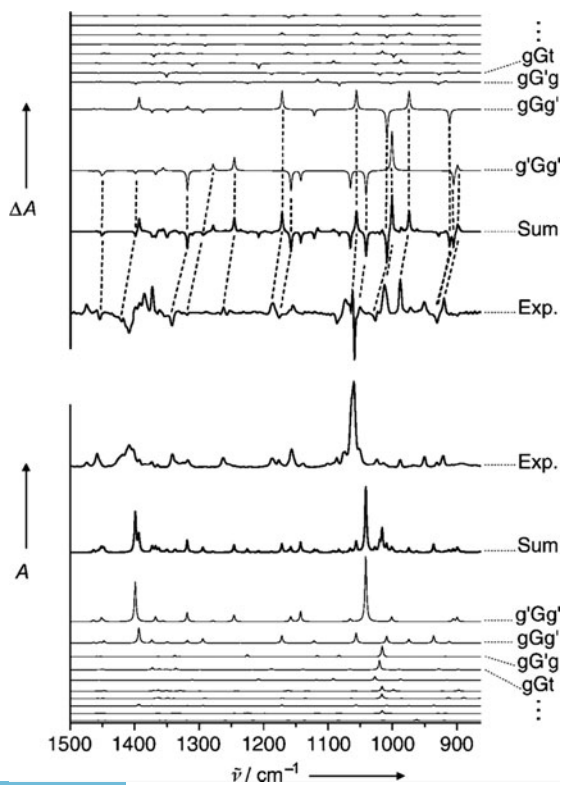


Fig. 24 Experimental (Ar matrix) and calculated (BPW91/TZ2P) VA (*bottom traces*) and VCD (*top traces*) spectra of (*R*)-alaninol. Some assignments are identified by *dashed lines*. Copyright Wiley-VCH Verlag GmbH & Co. KGaA. Reproduced with permission from [163]

4.6 Towards Real Time VCD Measurements

The unique and precious structural information contained in the VCD data has motivated some recent innovations where modern laser technology is coupled into VCD experiments. Vaccaro and co-workers devised a cavity ring down based polarimeter to measure optical rotatory dispersion (ORD) spectra of chiral molecules in the gas phase. The instrument utilizes the extremely high reflectivity (~99.999%) of the ring down mirrors to achieve a very long absorption path, typically several kilometers, to compensate for the low number densities of substances in the gas phase [170, 171]. Their work has provided the much needed benchmarks for theoretical OR calculations. The extension of this technique to measure CD was proposed and proven theoretically [171]. The actual measurements have so far been hampered by the very large background noise. Their work also inspired others including our group to attempt to extend the technique into the mid-IR region for measurements of vibrational optical activities of chiral molecules in the gas phase. So far, this effort has not been fruitful, largely due to lack of suitable optical components in the mid-IR such as high-throughput quarterwave plates needed inside the ring down cavity.

Another direction being pursued with lasers is to substitute the FTIR module with a white light source with a femtosecond laser. The ultimate goal here is to detect *transient* VCD signals and other related vibrational optical activities (VOA) in order to monitor, for example, the folding and unfolding events of polypeptides in solution. Bonmarin and Helbing [172] recently reported a picosecond time resolved VCD spectrometer, which was based on the blueprint of a similar set-up for ECD measurements [173–175]. A femtosecond IR pulse with a 200 cm⁻¹ bandwidth (FWHM) was split into a reference and a probe beam where the latter passed through a wire grid linear polarizer and a PEM before impinging onto a standard sample cell, the same as used in the regular FTIR-VCD experiments. The IR laser signals from both beams were registered by two MCT IR detectors. The laser pulses were synchronized with the reference frequency of the PEM so that the opposite circularly polarized light was generated in two sequential laser pulses. The intensity of each laser pulse was measured individually using gated amplifiers. The static VCD signal was then evaluated using the following expression to account for the laser amplitude fluctuation:

$$\Delta A_{\text{VCD}} = \log_{10} \left(\frac{I_{\text{probe}}^{\text{left}}}{I_{\text{ref}}^{\text{left}}} \right) - \log_{10} \left(\frac{I_{\text{probe}}^{\text{right}}}{I_{\text{ref}}^{\text{right}}} \right). \quad (5)$$

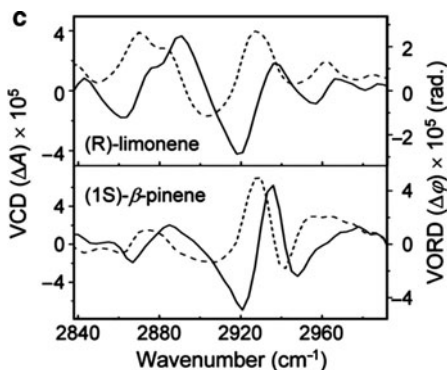
One main challenge to extend this to the mid-IR region is the fact that the corresponding signals such as VA and VCD are orders of magnitude smaller than the electronic transition and ECD signals. These authors reported the static CH-stretching VCD spectra of the Co and Ni metal complexes, i.e., Co(sparteine)Cl₂ and Ni(sparteine)Cl₂ which have quite intense VCD bands due to the enhancement effect discussed in Sect. 4.3. The VCD spectra obtained compare well with the

previously published data collected using a standard FTIR-VCD spectrometer. To perform the first transient VCD measurement, a visible pump beam was focused onto the sample in spatial overlap with the IR probe in order to alter the VCD spectrum of the sample. By varying the delay time on the picosecond scale between the pump and probe beams, the transient VCD responses, which showed recognizable differences from the static spectra, were recorded. This first proof-of-principle experiment [172] demonstrates the feasibility of following fast time scale structural changes using VCD spectroscopy.

Almost in parallel, a different approach to measure VOA using a femtosecond laser was reported by Cho and co-workers [176–178]. These authors showed that one could extract the spectral information of both VCD and vibrational optical rotatory dispersion (VORD) by detecting the coherently emitted optical activity (OA) free-induction-decay (FID) field with a cross-polarization detection scheme. By applying heterodyne-detected FT spectral interferometry (FTSI), a proven method for determining the phase and amplitude of an unknown electric field [179, 180], the authors could then characterize the spectral phase and amplitude of OAFID with respect to a reference field. The VCD and VORD spectra, which correspond to the real and imaginary parts of the linear OA susceptibility, i.e., $\Delta\chi(\omega) = \chi_L(\omega) - \chi_R(\omega)$, were determined subsequently. Details of the scheme involved are somewhat complicated and interested readers are referred to the original articles [176–178] and the references cited for details. Some general points, such as the experimental results obtained, the comparison of this novel technique with the more conventional differential technique for VCD detection, and the exciting potential for monitoring femtosecond events in real time, will be discussed here.

In comparison to the standard VCD measurement methods, including the femtosecond VCD spectrometer by Bonmarin and Helbing [172], which utilize the PM method, their heterodyned FTSI detection scheme has several noticeable advantages. First, the heterodyned FTSI does not rely on a differential measurement and is therefore fairly insensitive to the intensity fluctuation of the incident light beam or laser pulse. Second, the method intrinsically has ultrafast capability because the OA information is obtained from the time domain OAFID field created by a femtosecond pulse. This second advantage is especially important for the real time resolution of VCD measurements. The time resolution with a standard differential method such as the one described before are limited by the PM time of the PEMs used. Moreover, the VORD spectra along with VCD spectra are simultaneously detected with the heterodyned FTSI detection scheme. An example is depicted in Fig. 25 where the VCD and VORD spectra of two small organic molecules (*R*)-limonene and (*1S*)- β -pinene, diluted in CCl_4 , were measured simultaneously for each molecule. Although no explicit time resolved measurements were reported with this instrument, their work established that femtosecond optical pulses can be used to measure simultaneously VCD and VORD spectra with a time resolution that is only limited by the optical activity FID time. This technique is a

Fig. 25 Static VCD (solid curve, left scale) and VORD (dashed curve, right scale) spectra of (*R*)-limonene and (*1S*)- β -pinene obtained simultaneously in the OAFID experiments. Reproduced with permission from [178]. Copyright the Optical Society of America (2009)



promising tool for time resolved VCD studies of chiral chemical reactions and of protein structures and dynamics in solution.

5 Concluding Remarks

VCD spectroscopy and the related DFT theory have advanced tremendously in the last decade. A number of application examples are highlighted in this chapter. This versatile tool has been used to extract valuable information about the ACs of chiral molecules, the H-bonding networks between chiral solute and water, and the conformational properties of chiral ligands bound to AuNPs. The *chirality transfer* VCD features discussed provide a detailed insight into the specific H-bonding configurations taken on by the surrounding water molecules. This, together with step wise solvation studies, which utilize jet-cooled rotational and vibrational spectroscopy to probe small chiral solute–solvent clusters [181–183], will allow one to map out the solvation process in unprecedented details. All these results will further our understanding of structural and functional properties of biomolecules in aqueous solution. The combination of the matrix isolation technique and VCD spectroscopy provides a new tool to tackle the challenge of assigning ACs of highly flexible chiral molecules and to investigate H-bonded chiral complexes. The exciting breakthrough in recording time resolved VCD spectra promises novel VCD applications such as following fast reaction dynamics of chiral molecules and monitoring important biological events in solution in real time.

Acknowledgments We thank Thomas Bürgi and Gyorgy Tarczay for providing the figures in their original publications, Zahra Dezhahang for the structure figures of cobalt complexes. We also thank the University of Alberta, the Natural Sciences and Engineering Research Council of Canada, the Canada Foundation for Innovation, Alberta Ingenuity, and Petro-Canada for funding and the Academic Information and Communication Technology group at the University of Alberta for access to the computing facilities.

References

1. Barron LD (2004) *Molecular light scattering and optical activity*, 2nd edn. Cambridge University Press, Cambridge
2. Polavarapu PL (1998) *Vibrational spectra: principles and applications with emphasis on optical activity*. Elsevier, New York
3. Holzwarth G, Hsu EC, Mosher HS et al (1974) Infrared circular dichroism of carbon-hydrogen and carbon-deuterium stretching modes. *J Am Chem Soc* 96:251–252
4. Nafie LA, Cheng JC, Stephens PJ (1975) Vibrational circular dichroism of 2,2,2-trifluoro-1-phenylethanol. *J Am Chem Soc* 97:3842–3843
5. Galwas PA (1983) On the distribution of optical polarization in molecules. PhD Thesis, University of Cambridge, Cambridge
6. Buckingham AD, Fowler PW, Galwas PA (1987) Velocity-dependent property surfaces and the theory of vibrational circular-dichroism. *Chem Phys* 112:1–14
7. Stephens PJ (1985) Theory of vibrational circular-dichroism. *J Phys Chem* 89:748–752
8. Stephens PJ, Lowe MA (1985) Vibrational circular-dichroism. *Annu Rev Phys Chem* 36:213–241
9. Stephens PJ (1987) Gauge dependence of vibrational magnetic dipole transition moments and rotational strengths. *J Phys Chem* 91:1712–1715
10. Nafie LA (1983) Adiabatic molecular-properties beyond the Born-Oppenheimer approximation – complete adiabatic wave-functions and vibrationally induced electronic current-density. *J Chem Phys* 79:4950–4957
11. Nafie LA (1992) Velocity-gauge formalism in the theory of vibrational circular-dichroism and infrared-absorption. *J Chem Phys* 96:5687–5702
12. Nafie LA (1997) Electron transition current density in molecules.1. Non-Born-Oppenheimer theory of vibronic and vibrational transitions. *J Phys Chem A* 101:7826–7833
13. Freedman TB, Shih M-L, Lee E et al (1997) Ab initio calculations for vibrational transitions in ethylene and formaldehyde. *J Am Chem Soc* 119:10620–10626
14. Stephens PJ, Devlin FJ (2000) Determination of the structure of chiral molecules using ab initio vibrational circular dichroism spectroscopy. *Chirality* 12:172–179
15. Polavarapu PL (2006) Quantum mechanical predictions of chiroptical vibrational properties. *Int J Quantum Chem* 106:1809–1814
16. Freedman TB, Cao XL, Dukor RK et al (2003) Absolute configuration determination of chiral molecules in the solution state using vibrational circular dichroism. *Chirality* 15:743–758
17. Polavarapu PL, He J (2004) Chiral analysis using mid-IR vibrational CD spectroscopy. *Anal Chem* 76:61A–67A
18. Polavarapu PL (2007) Renaissance in chiroptical spectroscopic methods for molecular structure determination. *Chem Rec* 7:125–136
19. Stephens PJ, Devlin FJ, Pan JJ (2008) The determination of the absolute configurations of chiral molecules using vibrational circular dichroism (VCD) spectroscopy. *Chirality* 20:643–663
20. Stephens PJ, Devlin FJ, Aamouche A (2002) Determination of the structures of chiral molecules using vibrational circular dichroism spectroscopy. In: Hicks JM (ed) *Chirality: physical chemistry*. ACS Symposium Series, vol. 810, Chap. 2, Oxford University Press, New York, pp 18–33
21. Yang GC, Ha T, Fan E et al (2010) Determination of the absolute configurations of synthetic daunorubicin analogues using vibrational circular dichroism spectroscopy and density functional theory. *Chirality* 22:734–743
22. Yang GC, Xu Y, Hou JB et al (2010) Determination of the absolute configuration of pentacoordinate chiral phosphorus compounds in solution by using vibrational circular dichroism spectroscopy and density functional theory. *Chem Eur J* 16:2518–2527

23. Sato H, Mori Y, Fukuda Y (2009) Syntheses and vibrational circular dichroism spectra of the complete series of [Ru((-) or (+)-tfac)_n(acac)_{3-n}] (n = 0 ~ 3, tfac = 3-trifluoroacetylcamphorato and acac = acetylacetonato). *Inorg Chem* 48:4354–4361
24. Nafie LA (2008) Vibrational circular dichroism: a new tool for the solution-state determination of the structure and absolute configuration of chiral natural product molecules. *Nat Prod Commun* 3:451–466
25. Brotin T, Cavagnat D, Dutasta JP et al (2006) Vibrational circular dichroism study of optically pure cryptophane-A. *J Am Chem Soc* 128:5533–5540
26. Devlin FJ, Stephens PJ, Besse P (2005) Are the absolute configurations of 2-(1-hydroxyethyl)-chromen-4-one and its 6-bromo derivative determined by X-ray crystallography correct? A vibrational circular dichroism study of their acetate derivatives. *Tetrahedron Asymmetry* 16:1557–1566
27. Nafie LA (2004) New approaches to the determination of absolute configuration for Chiral Pharmaceuticals (Business Briefing – PharmaTech)
28. Jeffrey GA, Saenger W (1991) Hydrogen bonding in biological structure. Springer-Verlag, Berlin
29. Nafie LA, Keiderling TA, Stephens PJ (1976) Vibrational circular-dichroism. *J Am Chem Soc* 98:2715–2723
30. Nafie LA (1988) Polarization modulation FTIR spectroscopy. In: Mackenzie MW (ed) *Advances in applied FTIR spectroscopy*. Wiley, New York, pp 67–104
31. Nafie LA, Long F, Freedman TB et al (1998) The determination of enantiomeric purity and absolute configuration by vibrational circular dichroism spectroscopy. In: de Haseth JA (ed) *Fourier transform spectroscopy: 11th International Conference*, vol. 430, American Institute of Physics. Woodbury, New York, pp 432–434
32. Dukor RK, Nafie LA (2000) Vibrational optical activity of pharmaceuticals and biomolecules. In: Meyers RA (ed) *Encyclopaedia of analytical chemistry: instrumentation and applications*. Wiley, Chichester, UK, pp 662–676
33. Nafie LA, Diem M (1979) Theory of high-frequency differential interferometry – application to the measurement of infrared circular and linear dichroism via Fourier-transform spectroscopy. *Appl Spectrosc* 33:130–135
34. Nafie LA, Diem M, Vidrine DW (1979) Fourier-transform infrared vibrational circular-dichroism. *J Am Chem Soc* 101:496–498
35. Lipp ED, Zimba CG, Nafie LA (1982) Vibrational circular-dichroism in the mid-infrared using Fourier-transform spectroscopy. *Chem Phys Lett* 90:1–5
36. Nafie LA (2000) Dual polarization modulation: a real-time, spectral-multiplex separation of circular dichroism from linear birefringence spectral intensities. *Appl Spectrosc* 54:1634–1645
37. Malon P, Keiderling TA (1988) A solution to the artifact problem in Fourier-transform vibrational circular-dichroism. *Appl Spectrosc* 42:32–38
38. Polavarapu PL (1989) New developments in Fourier-transform infrared vibrational circular-dichroism measurements. *Appl Spectrosc* 43:1295–1297
39. Malon P, Keiderling TA (1996) Spinning quarter-wave plate polarization modulator: test of feasibility for vibrational circular dichroism measurements. *Appl Spectrosc* 50:669–674
40. Malon P, Keiderling TA (1997) Theoretical simulation of a polarization modulator based on mechanical rotation of a polarizing element. *Appl Opt* 36:6141–6148
41. Cao XL, Dukor RK, Nafie LA (2008) Reduction of linear birefringence in vibrational circular dichroism measurement: use of a rotating half-wave plate. *Theor Chem Acc* 119:69–79
42. Hug W (2003) Virtual enantiomers as the solution of optical activity's deterministic offset problem. *Appl Spectrosc* 57:1–13
43. Nafie LA, Buijs H, Rilling A et al (2004) Dual source Fourier transform polarization modulation spectroscopy: an improved method for the measurement of circular and linear dichroism. *Appl Spectrosc* 58:647–654

44. Cao X, Shah RD, Dukor RK et al (2004) Extension of Fourier transform vibrational circular dichroism into the near-infrared region: continuous spectral coverage from 800 to 10 000 cm⁻¹. *Appl Spectrosc* 58:1057–1064
45. Guo C, Shah RD, Dukor RK et al (2006) Fourier transform vibrational circular dichroism from 800 to 10000 cm⁻¹: near-IR-VCD spectral standards for terpenes and related molecules. *Vib Spectrosc* 42:254–272
46. Keiderling TA, Kubelka J, Hilario J (2006) Contribution of transition dipole coupling to amide coupling in IR spectra of peptide secondary structures. *Vibrational Spectroscopy of Biological and Polymer Materials* 253–324
47. Lakhani A, Malon P, Keiderling TA (2009) *Appl Spectrosc* 63:755–785
48. Losada M, Xu Y (2007) Chirality transfer through hydrogen-bonding: experimental and ab initio analyses of vibrational circular dichroism spectra of methyl lactate in water. *Phys Chem Chem Phys* 9:3127–3135
49. Bose PK, Polavarapu PL (1999) Vibrational circular dichroism is a sensitive probe of the glycosidic linkage: oligosaccharides of glucose. *J Am Chem Soc* 121:6094–6095
50. Shanmugam G, Polavarapu PL (2004) Structure of A beta (25-35) peptide in different environments. *Biophys J* 87:622–630
51. Shanmugam G, Polavarapu PL, Gopinath D, Jayakumar R (2005) The structure of antimicrobial pexiganan peptide in solution probed by Fourier transform infrared absorption, vibrational circular dichroism, and electronic circular dichroism spectroscopy. *Biopolymers* 80:636–642
52. Shanmugam G, Polavarapu PL (2004) Vibrational circular dichroism spectra of protein films: thermal denaturation of bovine serum albumin. *Biophys Chem* 111:73–77
53. Shanmugam G, Polavarapu PL (2005) Film techniques for vibrational circular dichroism measurements. *Appl Spectrosc* 59:673–681
54. Petrovic AG, Bose PK, Polavarapu PL (2004) Vibrational circular dichroism of carbohydrate films formed from aqueous solutions. *Carbohydr Res* 339:2713–2720
55. Petrovic AG, Polavarapu PL (2005) Structural transitions in polyriboadenylic acid induced by the changes in pH and temperature: vibrational circular dichroism study in solution and film states. *J Phys Chem B* 109:23698–23705
56. Shanmugam G, Polavarapu PL, Kendall LA et al (2005) Structures of plant viruses from vibrational circular dichroism. *J Gen Virol* 86:2377–2384
57. Haraday T, Kuroday R (2002) Circular dichroism measurement of a protein in dried thin films. *Chem Lett* 326–327
58. Merten C, Kowalik T, Hartwig A (2008) Vibrational circular dichroism spectroscopy of solid polymer films: effects of sample orientation. *Appl Spectrosc* 62:901–905
59. Buffeteau T, Lagugné-Labarthe F, Sourisseau C (2005) Vibrational circular dichroism in general anisotropic thin solid films: measurement and theoretical approach. *Appl Spectrosc* 59:732–745
60. Cohan NV, Hameka HF (1966) Isotope effects in optical rotation. *J Am Chem Soc* 88:2136–2142
61. Faulkner TR, Marcott C, Moscowitz A et al (1977) Anharmonic effects in vibrational circular-dichroism. *J Am Chem Soc* 99:8160–8168
62. Nafie LA, Walnut TH (1977) Vibrational circular-dichroism theory – localized molecular-orbital model. *Chem Phys Lett* 49:441–446
63. Walnut TH, Nafie LA (1977) IR absorption and born-oppenheimer approximation. 2. Vibrational circular-dichroism. *J Chem Phys* 67:1501–1510
64. Nafie LA, Freedman TB (1983) Vibronic coupling theory of infrared vibrational transitions. *J Phys Chem* 78:7108–7116
65. Dutler R, Rauk A (1989) Calculated infrared-absorption and vibrational circular-dichroism intensities of oxirane and its deuterated analogs. *J Am Chem Soc* 111:6957–6966
66. Yang D, Rauk A (1992) Vibrational circular dichroism intensities: ab initio vibronic coupling theory using the distributed origin gauge. *J Chem Phys* 97:6517–6534

67. Hunt KLC, Harris RA (1991) Vibrational circular-dichroism and electric-field shielding tensors – a new physical interpretation based on nonlocal susceptibility densities. *J Chem Phys* 94:6995–7002
68. Lazerretti P, Malagoli M, Zanasi R (1991) Electromagnetic moments and fields induced by nuclear vibrational motion in molecules. *Chem Phys Lett* 179:297–302
69. Hansen AE, Stephens PJ, Bouman TD (1991) Theory of vibrational circular-dichroism – formalisms for atomic polar and axial tensors using noncanonical orbitals. *J Phys Chem* 95:4255–4262
70. Amos RD (1984) Dipole-moment derivatives of H₂O and H₂S. *Chem Phys Lett* 108:185–190
71. Yamaguchi Y, Frisch M, Gaw J et al (1986) Analytic evaluation and basis set dependence of intensities of infrared-spectra. *J Chem Phys* 84:2262–2278
72. Cheeseman JR, Frisch MJ, Devlin FJ et al (1996) Ab initio calculation of atomic axial tensors and vibrational rotational strengths using density functional theory. *Chem Phys Lett* 252:211–220
73. Nicu VP, Neugebauer J, Baerends EJ (2008) Effects of complex formation on vibrational circular dichroism spectra. *J Phys Chem A* 112:6978–6991
74. Nicu VP, Baerends EJ (2009) Robust normal modes in vibrational circular dichroism spectra. *Phys Chem Chem Phys* 11:6107–6118
75. Cichewicz RH, Clifford LJ, Lassen PR, Cao X, Freedman TB, Nafie LA, Deschamps JD, Kenyon VA, Flanary JR, Holman TR, Crews P (2005) Stereochemical determination and bioactivity assessment of (S)-(1)-curcuphenol dimers isolated from the marine sponge *Didiscus aceratus* and synthesized through laccase biocatalysis. *Bioorg Med Chem* 13:5600–5612
76. Frisch MJ, Trucks GW, Schlegel HB, Scuseria GE, Robb MA, Cheeseman JR, Montgomery JA, Jr, Vreven T, Kudin KN, Burant JC, Millam JM, Iyengar SS, Tomasi J, Barone V, Mennucci B, Cossi M, Scalmani G, Rega N, Petersson GA, Nakatsuji H, Hada M, Ehara M, Toyota K, Fukuda R, Hasegawa J, Ishida M, Nakajima T, Honda Y, Kitao O, Nakai H, Klene M, Li X, Knox JE, Hratchian HP, Cross JB, Adamo C, Jaramillo J, Gomperts R, Stratmann RE, Yazyev O, Austin AJ, Cammi R, Pomelli C, Ochterski JW, Ayala PY, Morokuma K, Voth GA, Salvador P, Dannenberg JJ, Zakrzewski VG, Dapprich S, Daniels AD, Strain MC, Farkas O, Malick DK, Rabuck AD, Raghavachari K, Foresman JB, Ortiz JV, Cui Q, Baboul AG, Clifford S, Cioslowski J, Stefanov BB, Liu G, Liashenko A, Piskorz P, Komaromi I, Martin RL, Fox DJ, Keith T, Al-Laham MA, Peng CY, Nanayakkara A, Challacombe M, Gill PMW, Johnson B, Chen W, Wong MW, Gonzalez C, Pople JA (2004) Gaussian 03 C02
77. Kuppens T, Langenaeker W, Tollenaere JP et al (2003) Determination of the stereochemistry of 3-hydroxymethyl-2, 3-dihydro-[1, 4]dioxino[2, 3-b]pyridine by vibrational circular dichroism and the effect of DFT integration grids. *J Phys Chem A* 107:542–553
78. Pacios LF, Galvez O, Gomez PC (2005) Variation of geometries and electron properties along proton transfer in strong hydrogen-bond complexes. *J Chem Phys* 122:214307
79. Sadlej J, Dobrowolski JC, Rode JE et al (2006) DFT study of vibrational circular dichroism spectra of D-lactic acid-water complexes. *Phys Chem Chem Phys* 8:101–113
80. Pathak AK, Mukherjee T, Maity DK (2007) Structure, energy, and IR spectra of I-2(center dot)-.nH(2)O clusters (n = 1-8): a theoretical study. *J Chem Phys* 126:034301
81. Nibu Y, Marui R, Shimada H (2006) IR spectroscopy of hydrogen-bonded 2-fluoropyridine-methanol clusters. *J Phys Chem A* 110:12597–12602
82. Boys SF, Bernardi F (1970) Calculation of small molecular interactions by differences of separate total energies – some procedures with reduced errors. *Mol Phys* 10:553–559
83. Becke AD (1993) Density-functional thermochemistry. 3. The role of exact exchange. *J Chem Phys* 98:5648–5652
84. Lee CT, Yang WT, Parr RG (1988) Development of the colle-salvetti correlation-energy formula into a functional of the electron-density. *Phys Rev B Condens Matter* 37:785–789

85. Stephens PJ, Devlin FJ, Chabalowski CF et al (1994) Ab-initio calculation of vibrational absorption and circular-dichroism spectra using density-functional force-fields. *J Phys Chem* 98:11623–11627
86. Kuppens T, Herrebout W, van der Veken B et al (2006) Intermolecular association of tetrahydrofuran-2-carboxylic acid in solution: a vibrational circular dichroism study. *J Phys Chem A* 110:10191–10200
87. Sander W, Gantenberg M (2005) Aggregation of acetic and propionic acid in argon matrices – a matrix isolation and computational study. *Spectrochim Acta A* 62:902–909
88. Chandra AK, Parveen S, Zeegers-Huyskens T (2007) Anomeric effects in the symmetrical and asymmetrical structures of triethylamine. Blue-shifts of the C-H stretching vibrations in complexed and protonated triethylamine. *J Phys Chem A* 111:8884–8891
89. Demyanov PI, Gschwind RM (2006) Formation of hydrogen bonds in complexes between dimethylcuprate(I) anion and methane, propane, or dimethyl ether. A theoretical study. *Organometallics* 25:5709–5723
90. Scharge T, Emmeluth C, Häber T et al (2006) Competing hydrogen bond topologies in 2-fluoroethanol dimer. *J Mol Struct* 786:86–95
91. Borho N, Xu YJ (2007) Molecular recognition in 1:1 hydrogen-bonded complexes of oxirane and trans-2, 3-dimethyloxirane with ethanol: a rotational spectroscopic and ab initio study. *Phys Chem Chem Phys* 9:4514–4520
92. Krishnan R, Brinkley JS, Seeger R et al (1980) Self-consistent molecular orbital methods. XX. A basis set for correlated wave functions. *J Chem Phys* 72:650–654
93. Tomasi J, Persico M (1994) Molecular-interactions in solution – an overview of methods based on continuous distributions of the solvent. *Chem Rev* 94:2027–2094
94. Cancès E, Mennucci B, Tomasi J (1997) A new integral equation formalism for the polarizable continuum model: theoretical background and applications to isotropic and anisotropic dielectrics. *J Chem Phys* 107:3032–3041
95. Cramer C, Truhlar D (1999) Implicit solvation models: equilibria, structure, spectra, and dynamics. *Chem Rev* 99:2161–2200
96. Klamt A, Schueuermann G (1993) COSMO – a new approach to dielectric screening in solvents with explicit expressions for the screening energy and its gradient. *J Chem Soc Perkin Trans 2* 5:799–805
97. Klamt A (1999) In: Schleyer P v R (ed) *The encyclopedia of computational chemistry*. Wiley, Chichester
98. Polavarapu PL (2008) Why is it important to simultaneously use more than one chiroptical spectroscopic method for determining the structures of chiral molecules? *Chirality* 20: 664–672
99. Kirk JM (1960) The mode of action of actinomycin D. *Biochim Biophys Acta* 42:167–169
100. Di Marco A, Gaetani OP, Scarpinato BM et al (1964) Daunomycin: a new antibiotic of the rhodomycin group. *Nature* 201:706–707
101. Fan E, Shi W, Lowary TL (2007) Synthesis of daunorubicin analogues containing truncated aromatic cores and unnatural monosaccharide residues. *J Org Chem* 72:2917–2928
102. Corbridge DEC (2000) Phosphorus, chemistry, biochemistry and technology, 4th edn. Elsevier, Amsterdam
103. Westheimer FH (1968) Pseudo-rotation in the hydrolysis of phosphate esters. *Acc Chem Res* 1:70–78
104. Buchwald SL, Pliura DH, Knowla JR (1980) Stereochemical evidence for pseudorotation in the reaction of a phosphoric monoester. *J Am Chem Soc* 106:4916–4922
105. Knowles JR (1980) Enzyme-catalyzed phosphoryl transfer-reactions. *Annu Rev Biochem* 49:877–919
106. Vanool PJJM, Buck HM (1984) Trigonal bipyramidal phosphoranes as model compounds for the description of camp-catalyzed reactions. *Traut Chi Pays-Bas* 103:119–122
107. Holmes RR (1980) Pentacoordinated phosphorus, vol. 11. American Chemical Society, Washington, DC, p 87

108. Holmes RR (2004) Phosphoryl transfer enzymes and hypervalent phosphorus chemistry. *Acc Chem Res* 37:746–753
109. Holmes RR (1998) Hexacoordinate phosphorus via donor interaction. Implications regarding enzymatic reaction intermediates. *Acc Chem Res* 31:535–542
110. Fu H, Li ZL, Zhao YF et al (1999) Oligomerization of N,O-bis(trimethylsilyl)- α -amino acids into peptides mediated by o-phenylene phosphorochloridate. *J Am Chem Soc* 121:291–295
111. Lahiri SD, Zhang GF, Dunaway-Mariano D et al (2003) The pentacovalent phosphorus intermediate of a phosphoryl transfer reaction. *Science* 299:2067–2071
112. Leiros I, McSweeney S, Hough E (2004) The reaction mechanism of phospholipase D from *Streptomyces* sp strain PMF. snapshots along the reaction pathway reveal a pentacoordinate reaction intermediate and an unexpected final product. *J Mol Biol* 339:805–820
113. Williams NH (2004) Models for biological phosphoryl transfer. *Biochim Biophys Acta* 1697:279–287
114. Cleland WW, Hengge AC (2006) Enzymatic mechanisms of phosphate and sulfate transfer. *Chem Rev* 106:3252–3278
115. Wittinghofer A (2006) Phosphoryl transfer in Ras proteins, conclusive or elusive? *Trends Biochem Sci* 31:20–23
116. Catrina I, O'Brien PJ, Purcell J et al (2007) Probing the origin of the compromised catalysis of *E. coli* alkaline phosphatase in its promiscuous sulfatase reaction. *J Am Chem Soc* 129:5760–5765
117. Fu H, Xu JH, Wang RJ et al (2003) Synthesis, crystal structure, and diastereomeric transfer of pentacoordinated phosphoranes containing valine or iso-leucine residue. *Phosphorus Sulfur Silicon Relat Elem* 178:1963–1971
118. Timosheva NV, Chandrasekaran A, Holmes RR (2005) Atrane and phosphorane formation with aminotriphenols [1]. *J Am Chem Soc* 127:12474–12475
119. Hou JB, Tang G, Guo JN et al (2009) Stereochemistry of chiral pentacoordinate spirophosphoranes correlated with solid-state circular dichroism and H-1 NMR spectroscopy. *Tetrahedron Asymmetry* 20:1301–1307
120. Ball P (1999) *H₂O: a biography of water*. Weidenfeld & Nicolson, London
121. Yves M (2007) *The hydrogen bond and the water molecule*. Elsevier, New York
122. Hobza P, Zahradnik R (1988) Intermolecular interactions between medium-sized systems – nonempirical and empirical calculations of interaction energies – successes and failures. *Chem Rev* 88:871–897
123. Curtiss LA, Blander M (1988) Thermodynamic properties of gas-phase hydrogen-bonded complexes. *Chem Rev* 88:827–841
124. Ruan CY, Lobastov VA, Vigliotti F et al (2004) Ultrafast electron crystallography of interfacial water. *Science* 304:80–84
125. Wernet P, Nordlund D, Bergmann U et al (2004) The structure of the first coordination shell in liquid water. *Science* 304:995–999
126. Smith JD, Cappa CD, Wilson KR et al (2004) Energetics of hydrogen bond network rearrangements in liquid water. *Science* 304:851–853
127. Bukowski R, Szalewicz K, Groenenboom GC et al (2007) Predictions of the properties of water from first principles. *Science* 315:1249–1252
128. Jalkanen K, Suhai S (1996) N-Acetyl-L-alanine N'-methylamide: a density functional analysis of the vibrational absorption and vibrational circular dichroism spectra. *Chem Phys* 208:81–116
129. Jurgensen VW, Jalkanen K (2006) The VA, VCD, Raman and ROA spectra of tri-L-serine in aqueous solution. *Phys Biol* 3:S63–S69
130. Losada M, Tran H, Xu Y (2008) Lactic acid in solution: investigations of lactic acid self-aggregation and hydrogen bonding interactions with water and methanol using VA and VCD spectroscopy. *J Chem Phys* 128:014508

131. Losada M, Nguyen P, Xu Y (2008) Solvation of propylene oxide in water: vibrational circular dichroism, optical rotation, and computer simulation studies. *J Phys Chem A* 112:5621–5627
132. Yang GC, Xu Y (2009) Probing chiral solute-water hydrogen bonding networks by chirality transfer effects: a vibrational circular dichroism study of glycidol in water. *J Chem Phys* 130:164506
133. Guardia E, Marti J, Garcia-Tarres L et al (2005) A molecular dynamics simulation study of hydrogen bonding in aqueous ionic solutions. *J Mol Liq* 117:63–67
134. Kongsted J, Mennucci B (2007) How to model solvent effects on molecular properties using quantum chemistry? Insights from polarizable discrete or continuum solvation models. *J Phys Chem A* 111:9890–9900
135. Mukhopadhyay P, Zuber G, Goldsmith MR et al (2006) Solvent effect on optical rotation: a case study of methyloxirane in water. *Chemphyschem* 7:2483–2486
136. Malaspina T, Fileti EE, Rivelino R (2007) Structure and UV–vis spectrum of c60 fullerene in ethanol: a sequential molecular dynamics/quantum mechanics study. *J Phys Chem B* 111:11935–11939
137. Case DA, Darden TA, Cheatham TE et al (2006) AMBER 9. University of California, San Francisco, CA
138. Jorgensen WL, Jenson C (1998) Temperature dependence of TIP3P, SPC, and TIP4P water from NPT Monte Carlo simulations: seeking temperatures of maximum density. *J Comput Chem* 19:1179–1186
139. Jorgensen WL, Chandrasekhar J, Madura JD et al (1983) Comparison of simple potential functions for simulating liquid water. *J Chem Phys* 79:926–935
140. Yang GC, Xu Y (2008) The effects of self-aggregation on the vibrational circular dichroism and optical rotation measurements of glycidol. *Phys Chem Chem Phys* 10:6787–6795
141. Cj B, Drake AF, Kuroda R et al (1980) Vibrational electronic interaction in the infrared circular-dichroism spectra of transition-metal complexes. *Chem Phys Lett* 70:8–10
142. He YN, Cao XL, Nafie LA et al (2001) Ab initio VCD calculation of a transition-metal containing molecule and a new intensity enhancement mechanism for VCD. *J Am Chem Soc* 123:11320–11321
143. Fano U (1961) Effects of configuration interaction on intensities and phase shifts. *Phys Rev* 124:1866–1878
144. Nafie LA (2004) Theory of vibrational circular dichroism and infrared absorption: extension to molecules with low-lying excited electronic states. *J Phys Chem A* 108:7222–7231
145. Sato H, Taniguchi T, Monde K, Nishimura S-I, Yamagishi A (2006) Dramatic effects of d-electron configurations on vibrational circular dichroism spectra of tris(acetylacetonato) metal(III). *Chem Lett* 35:364–365
146. Sato H, Taniguchi K, Nakahashi A, Monde K, Yamagishi A (2007) Effects of central metal ions on vibrational circular dichroism spectra of tris(β -diketonato)metal(III) complexes. *Inorg Chem* 46:6755–6766
147. Nicu VP, Autschbach J, Baerends EJ (2009) Enhancement of IR and VCD intensities due to charge transfer. *Phys Chem Chem Phys* 11:1526–1538
148. Young DA, Freedman TB, Lipp ED et al (1986) Vibrational circular-dichroism in transition-metal complexes. 2. Ion association, ring conformation, and ring currents of ethylenediamine ligands. *J Am Chem Soc* 108:7255–7263
149. Freedman TB, Cao XL, Young DA et al (2002) Density functional theory calculations of vibrational circular dichroism in transition metal complexes: Identification of solution conformations and mode of chloride ion association for (+)-tris(ethylenediaminato)cobalt (III). *J Phys Chem A* 106:3560–3565
150. Daniel MC, Astruc D (2004) Gold nanoparticles: assembly, supramolecular chemistry, quantum-size-related properties, and applications toward biology, catalysis, and nanotechnology. *Chem Rev* 104:293–346

151. Humblot V, Haq S, Muryn C et al (2002) From local adsorption stresses to chiral surfaces: (R,R)-tartaric acid on Ni(110). *J Am Chem Soc* 124:503–510
152. Hofer WA, Humblot V, Raval R (2004) Conveying chirality onto the electronic structure of achiral metals: (R,R)-tartaric acid on nickel. *Surf Sci* 554:141–149
153. López-Lozano X, Pérez LA, Garzón IL (2006) Enantiospecific adsorption of chiral molecules on chiral gold clusters. *Phys Rev Lett* 97:233401
154. Gautier C, Bürgi T (2005) Vibrational circular dichroism of N-acetyl-L-cysteine protected gold nanoparticles. *Chem Commun* 5393–5395
155. Gautier C, Bürgi T (2006) Chiral N-isobutryl-cysteine protected gold nanoparticles: preparation, size selection, and optical activity in the UV-vis and infrared. *J Am Chem Soc* 128:11079–11087
156. Gautier C, Bürgi T (2010) Vibrational circular dichroism of adsorbed molecules: binas on gold nanoparticles. *J Phys Chem C*. doi:10.1021/jp910800m
157. Gautier C, Taras R, Gladiali S et al (2008) Chiral 1,1'-binaphthyl-2,2'-dithiol-stabilized gold clusters: size separation and optical activity in the UV-vis. *Chirality* 20:486–493
158. Bürgi T, Bieri M (2004) Time-resolved in situ ATR Spectroscopy of 2-propanol oxidation over Pd/Al₂O₃: evidence for 2-propoxide intermediate. *J Phys Chem B* 108:13364–13369
159. Neurock M (1999) First-principles analysis of the hydrogenation of carbon monoxide over palladium. *Top Catal* 9:135–152
160. Schlosser DW, Devlin F, Jalkanen K et al (1982) Vibrational circular-dichroism of matrix-isolated molecules. *Chem Phys Lett* 88:286–291
161. Polavarapu PL, Hess BA, Schaad LJ (1985) Vibrational-spectra of epoxypropane. *J Phys Chem* 82:1705–1710
162. Lowe MA, Alper JS, Kawiecki R et al (1986) Scaled abinitio force-fields for ethylene-oxide and propylene-oxide. *J Phys Chem* 90:41–50
163. Tarczay G, Magyarfalvi G, Vass E (2006) Towards the determination of the absolute configuration of complex molecular systems: matrix isolation vibrational circular dichroism study of (R)-2-amino-1-propanol. *Angew Chem Int Ed* 45:1775–1777
164. Qu X, Citra M, Raganathan N et al (1993) Proceedings of the 9th International Conference on Fourier Transform Spectroscopy (SPIE vol. 2089, p 142)
165. Fausto R, Cacela C, Duarte ML (2000) Vibrational analysis and structural implications of H-bonding in isolated and aggregated 2-amino-1-propanol: a study by MI-IR and Raman spectroscopy and molecular orbital calculations. *J Mol Struct* 550–551:365–388
166. Pohl G, Perczel A, Vass E et al (2007) A matrix isolation study on Ac-Gly-NHMe and Ac-L-Ala-NHMe, the simplest chiral and achiral building blocks of peptides and proteins. *Phys Chem Chem Phys* 9:4698–4708
167. Pohl G, Perczel A, Vass E et al (2008) A matrix isolation study on Ac-L-Pro-NH₂: a frequent structural element of beta- and gamma-turns of peptides and proteins. *Tetrahedron* 64:2126–2133
168. Tarczay G, Gobi S, Vass E et al (2009) Model peptide-water complexes in Ar matrix: complexation induced conformation change and chirality transfer. *Vib Spectrosc* 50:21–28
169. Sadlej J, Dobrowolski JC, Rode JE (2010) VCD spectroscopy as a novel probe for chirality transfer in molecular interactions. *Chem Soc Rev* 39:1478–1488
170. Muller T, Wiberg KB, Vaccaro PH (2000) Cavity ring-down polarimetry (CRDP): a new scheme for probing circular birefringence and circular dichroism in the gas phase. *J Phys Chem* 104:5959–5968
171. Muller T, Wiberg KB, Vaccaro PH et al (2002) Cavity ring-down polarimetry (CRDP): theoretical and experimental characterization. *J Opt Soc Am B* 19:125–141
172. Bonmarin M, Helbing J (2008) A picosecond time-resolved vibrational circular dichroism spectrometer. *Optics Lett* 33:2086–2088
173. Xie X, Simon JD (1990) Picosecond time-resolved circular-dichroism study of protein relaxation in myoglobin following photodissociation of CO. *J Am Chem Soc* 112: 7802–7803

174. Xie X, Simon JD (1990) Picosecond circular-dichroism spectroscopy – a Jones matrix analysis. *J Opt Soc Am B* 7:1673–1684
175. Xie X, Simon JD (1989) Picosecond time-resolved circular-dichroism spectroscopy – experimental details and applications. *Rev Sci Instrum* 60:2614–2627
176. Rhee H, Ha JH, Jeon SJ et al (2008) Femtosecond spectral interferometry of optical activity: theory. *J Chem Phys* 129:094507
177. Rhee H, June YG, Lee JS et al (2008) Femtosecond characterization of vibrational optical activity of chiral molecules. *Nature* 458:310–313
178. Rhee H, June YG, KZH et al (2009) Phase sensitive detection of vibrational optical activity free-induction-decay: vibrational CD and ORD. *J Opt Soc Am B* 26:1008–1017
179. Lepetit L, Cheriaux G, Joffre M (1995) Linear techniques of phase measurement by femtosecond spectral interferometry for applications in spectroscopy. *J Opt Soc Am B* 12:2467–2474
180. Fittinghoff DN, Bowie JL, Sweetser JN et al (1996) Measurement of the intensity and phase of ultraweak, ultrashort laser pulses. *Opt Lett* 21:884–886
181. Su Z, Wen Q, Xu Y (2006) Conformational stability of the propylene oxide-water adduct: direct spectroscopic detection of O-H...O hydrogen bonded conformers. *J Am Chem Soc* 128:6755–6760
182. Su Z, Xu Y (2007) Hydration of a chiral molecule: the propylene oxide... $(\text{water})_2$ cluster in the gas phase. *Angew Chem Int Ed* 46:6163–6166
183. Zehnacker A, Suhm MA (2008) Chirality recognition between neutral molecules in the gas phase. *Angew Chem Int Ed* 47:6970–6992

Spin Selective Electron Transmission Through Monolayers of Chiral Molecules

Ron Naaman and Zeev Vager

Abstract Self-assembled monolayers (SAMs) of organic dipolar molecules have new electronic and magnetic properties that result from their organization, despite the relatively weak interaction among the molecules themselves. Here we review the origin of this cooperative effect and summarize results obtained on spin selective electron transmission through such monolayers that are made from chiral molecules. We show that SAMs containing chiral dipolar molecules behave like magnetic layers which may serve as spin filters, even without applying an external magnetic field to the layer.

Keywords Dipole Moment, Electron transmission, Monolayer, Spin

Contents

1	Introduction	238
2	Experimental	239
3	Results	244
3.1	Electron Transmission Through SAM of Polyalanine	244
3.2	Temperature Dependence of Spin Transmission	245
3.3	Spin Selectivity in DNA	249
4	Discussion	252
5	Summary	254
	References	255

R. Naaman (✉)

Department of Chemical Physics, The Weizmann Institute, Rehovot 76100, Israel
e-mail: Ron.Naaman@weizmann.ac.il

Z. Vager

Department of Particle Physics, The Weizmann Institute, Rehovot 76100, Israel

1 Introduction

Chiral molecules are defined as those molecules that lack internal plan of symmetry. Molecules that are chiral have two types of enantiomers that can be described as left-handed and right-handed species. Because of broken mirror image symmetry, when a charge moves within a chiral system in one direction it creates a magnetic field. Indeed, the relation between chirality and magnetism has attracted the attention of many, including Pasteur [1] and Lord Kelvin [2]. Recent studies have focused on the related magneto-chiral effect in which the magnetic field can give rise to an enantiomeric excess in photochemical processes [3–6]. Because the electron spin can also interact with a magnetic field, the relation between chirality, the magnetic field, and the electron spin has been discussed in relation to physical as well as chemical processes [7]. It is known that the magneto-electric effect can be found in states of matter which do not have mirror symmetry [8–10]. That effect entails the induction of a magnetic field upon applying an electric field (and vice versa). The interplay between chirality and magnetism also leads to interesting optical phenomena, such as the magnetochiral effect [5, 11–15].

While the mechanism of how charge transport or charge redistribution through chiral systems generates a magnetic field is elementary, this magnetism is transient, ending when the charge flow stops. The only way to transform transient charge flow into permanent magnetism is by spin–orbit coupling that convert the angular momenta of the electrons to spin alignment. However, spin–orbit coupling in hydrocarbons is commonly believed to be very weak and therefore no significant spin alignment is expected. Indeed, the interaction of spin polarized electrons with molecules has been studied [16] and when these electrons were scattered from gas phase chiral molecules only a very small preference of one spin polarization over the other was found [17]. In contrast to gas phase studies, polarized electrons transmitted through organized monolayers of dipolar chiral molecules display very large sensitivity to the handedness of the molecules [18–20]. Several models have been presented for explaining those observations [21, 22], but the phenomenon is not yet explained quantitatively.

Here we will concentrate on the chirality–spin–magnetism relation in chiral molecules that are self-assembled as closed packed organized monolayers on a gold substrate. When dipolar organic molecules are self assembled monolayers (SAMs) on a conducting substrate, they form an electric dipole layer, with a thickness of a few nanometers, over a macroscopic area. In such layers, the original dipole directions are packed parallel to each other at an angle almost perpendicular to the substrate. If each molecule retained its electric dipole moment, the electric field would exceed the dielectric breakdown potential. In order to reduce the electric energy of the assembly, the molecules depolarize, either by charge reorganization within the molecule or by charge transfer between the substrate and the monolayer film [23, 24]. In this way, the average dipole moment per molecule in the layer is reduced. The charge transfer or redistribution can be observed by monitoring the surface contact potential. These measurements indicate that,

even after the charge redistribution, the field across the organic monolayer is large, just below the breakdown voltage.

Both in inorganic–inorganic [25] and in organic–inorganic [26] systems the charge transfer was found to be associated with interesting magnetic properties. The unusual magnetic properties were observed in gold nanoparticles [27] as well as in gold films covered by thiol-terminated SAM [28]. In another interesting study it was demonstrated that it is possible to control the magnetism of thiolated molecules adsorbed as SAM on gold, by photoswitching of the dipole of the adsorbed molecules [29]. For inorganic–organic interfaces this effect was described as the cooperative molecular field effect (COMFET). Namely, the organization of the molecules as a monolayer induces the charge transfer from the substrate, which reduces the field in the monolayer, created by the formation of the dipole layer [30]. A very similar effect was also reported with inorganic interfaces. The recent finding that a TiO_2/LaO interface between the insulating oxides LaAlO_3 and SrTiO_3 can be metallic and has extremely high carrier mobility [31] has triggered a surge of experimental and theoretical studies of this interface [32–41]. This effect arises from charge transfer at the interface, resulting from the large dipole of the LaAlO_3 layers reduced by electrons transferred from the SrTiO_3 substrate. The concentration of these electrons is about $3 \times 10^{14} \text{ cm}^{-2}$. This explanation is in essence identical to that given for the observed reduction in the dipole of self-assembled monolayers of polar organic molecules [42].

Here we will review the results obtained when spin polarized electrons were transmitted through SAM made from chiral molecules and will provide a model that explains how these SAMs may act as a spin filter. The model we present is valid for the case that the chiral molecules form organized layers and it does not relate to charge transfer through a single molecule either isolated or in non-organized media.

2 Experimental

Spin selectivity in electron transmission through self-assembled monolayers (SAMs) of chiral molecules was determined by using circularly polarized light for ejecting spin-polarized electrons from gold substrate covered with the SAM (see Fig. 1) [41]. SAMs were prepared from two molecules – either polyalanine or DNA.

The polypeptide polyalanine was synthesized¹ and characterized by Matrix Assisted Laser Desorption Ionization (MALDI) and amino acid hydrolyses. Monolayers of either L- or D-polyalanine polypeptides, in the form of an α -helix, were prepared by self-assembly on a borosilicate slide that was coated with a 200–300 nm thick gold film (Metallhandel Schroer GmbH). Prior to the adsorption, the gold slides were annealed by flame and only then inserted into a 1 mM peptide solution of

¹ The synthesis was performed by the group of Prof. M. Fridkin, Department of Organic Chemistry, Weizmann Institute.

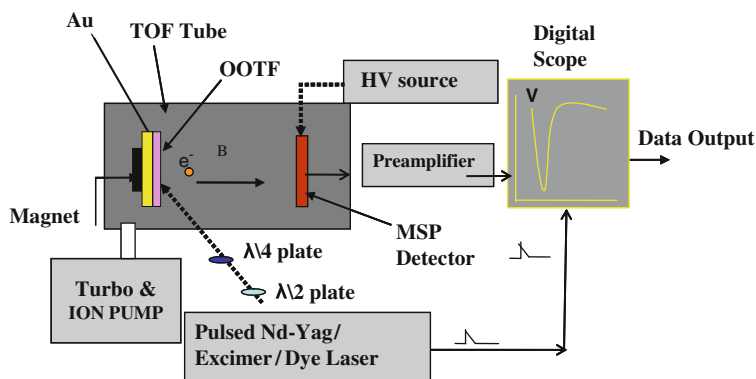


Fig. 1 Scheme of the experimental set-up used for monitoring spin selective electron transmission through organized organic thin films (OOTF)

hexafluoroisopropanol overnight. The slides were then washed with the pure solvent and dried in a stream of nitrogen gas. The peptides are attached to the gold using a sulfide group in the head group of cysteine. By connecting the cysteine either at the C- or N-terminal of the peptide, their dipole moment is pointing either away from the substrate or towards the substrate, respectively. Three films were investigated, monolayers of poly L-alanine and of poly D-alanine consisting of 16 and 22 amino acids, respectively, both connected to the surface at the C-terminal (which will be referred as LC, DC respectively), and a monolayer of poly D-alanine consisting of 22 amino acids and connected to the surface at the N-terminal (DN).

The structure and tilt angle of the molecules relative to the surface normal were determined by their FTIR spectra. In helical peptides, the transition moment of amide-I band lies nearly parallel to the helix axis and that of amide-II perpendicular. Since transition moments, which lie parallel to the gold surface, cannot be detected in grazing angle FTIR, the ratio between the intensities of the amide-I band ($1,665\text{ cm}^{-1}$) and amide-II band ($1,550\text{ cm}^{-1}$) indicates to what extent the molecules in the monolayer are oriented perpendicular to the gold surface. Based on the FTIR spectra it was possible to calculate the tilt angle, namely the angle between the molecular axis and the surface normal. The frequencies of amide-I and amide-II vibrations indicate that the monolayer is indeed in an α helix form (Fig. 2a).

In the α helix there is a hydrogen bond between the carbonyl oxygen of the residue i and the amino group at residue $i + 4$. The helical repeat is $c = 3.6$ residue per turn, which gives a helical angle $\theta = 360^\circ/(3.6\text{ residues/turn}) = 100^\circ/\text{residue}$. The rise is $h = 0.15\text{ nm}$ per residue and, therefore, the pitch is $P = 0.54\text{ nm}$ [43]. Circular dichroism (CD) measurements were performed to verify the handedness of the layers (Fig. 2b). For the CD measurements the polypeptides were deposited on 10 nm thick gold coated quartz slides which are transparent to UV radiation down to 190 nm. The CD spectra indicate a right α helix form for the LC film and a left one for the DC film.

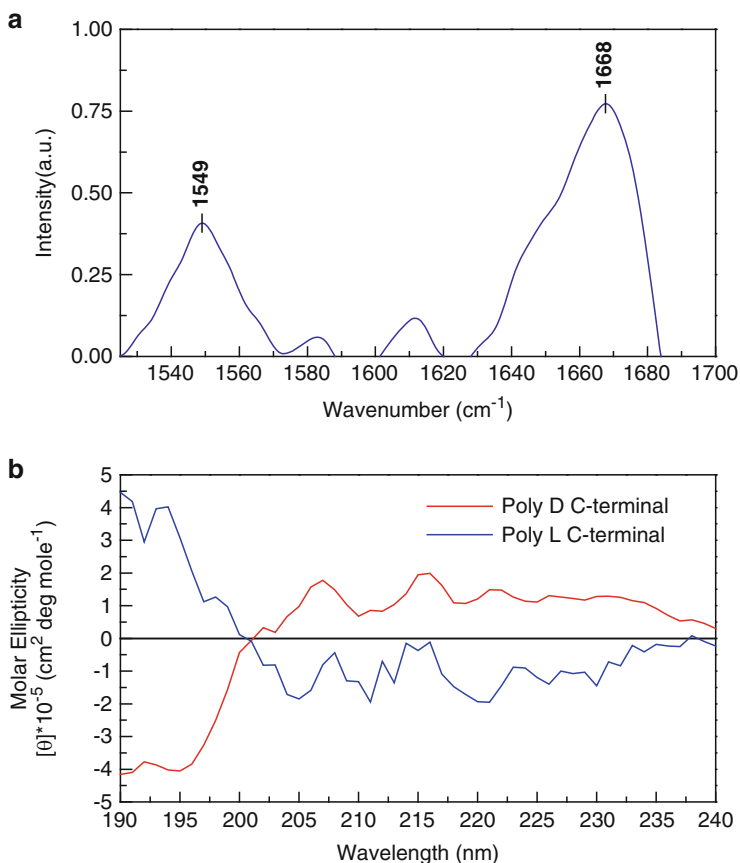


Fig. 2 (a) Grazing angle FTIR spectra of poly L-alanine monolayer on a gold slide. The frequencies of amide-I and amide-II vibrations indicate that the monolayer is in a α helix form. (b) CD spectra of L-polyalanine and D-polyalanine helices (blue and red lines respectively) on 10 nm gold-covered quartz slides. The figure indicates a *right* α helix for L-polyalanine and a *left* one for D-polyalanine

Both AFM and ellipsometry were used to characterize the film thickness. The LC, DC, and DN molecules contained 22 amino acid units and the film thickness was about 4 nm. The LC film was also characterized by atomic force microscopy (Fig. 3). In this case, a surface area of about 500 nm² was removed by scratching (left image). The uncovered area shows a depth of about 4 ± 1 nm relative to the unscratched area from which we conclude that the thickness of the monolayer is about 4 ± 1 nm.

The difference between the values obtained for the thickness of the layers in the two methods may be attributed to the effect the AFM tip has on the molecules or to the fact that, in the ellipsometry measurements, the index of refraction chosen,

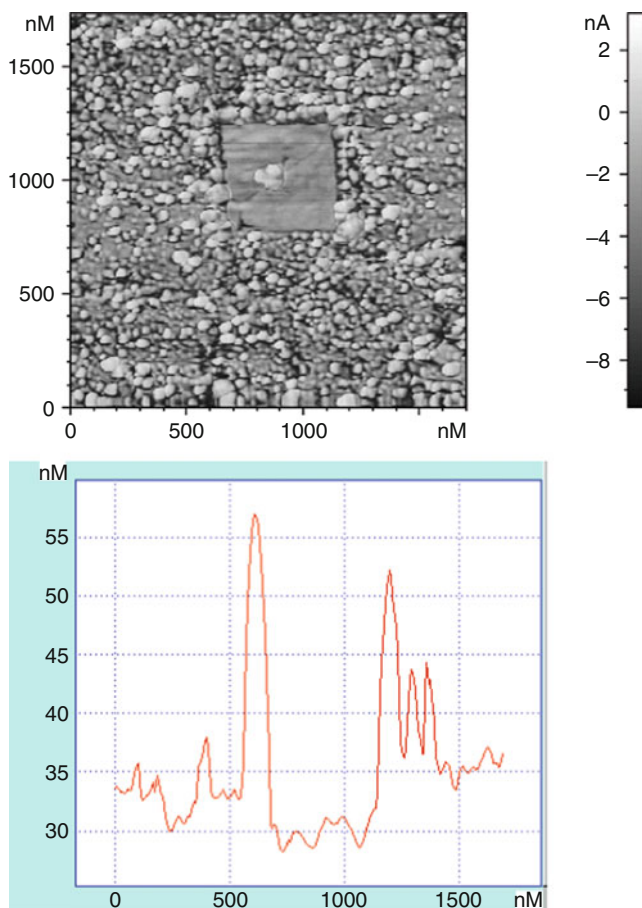


Fig. 3 AFM image of the LC film (*left*). The area in the *middle* was scratched to remove the film, topography of the surface indicating a depth of about 40 Å in the scratched area (*right graph*). The scales in the *right plot* are in nm

which is the index of refraction for the molecules in solution, does not match the refraction index of the molecules after adsorption.

The UV spectrum measured at short wavelengths (200–300 nm) is typical for UV absorption of polyaniline in solution [44] but is about six orders of magnitude higher. The long tail at higher wavelengths is typical for quantum well behavior of large exciton absorption at surfaces [45]. The strong absorption and the exciton tail probably results from mixing of the electronic states of the gold with the electronic states of the molecules.

Self-assembled DNA monolayers were prepared according to a standard procedure [46, 47] by depositing 15-mers of 3' thiolated DNA on clean 200 nm thick polycrystalline gold film evaporated on glass slides. The double-stranded (ds) DNA was produced by hybridization of 3' thiolated single-stranded (ss) DNA ex situ with

its complementary non-thiolated DNA-oligomer by combining equal amounts of the two oligomers in 0.4 M phosphate buffer, pH 7.2, heating the mixture for 10 min at 80 °C, followed by slow cooling to room temperature over several hours. Complete hybridization was determined by non-denaturing gel analysis. The clean Au slide was uniformly covered with the oligomer solution (50 μ M) and kept overnight in a clean and controlled humid environment. After deposition, the slides were washed thoroughly, first in phosphate buffer and subsequently in sterile deionized water (millipore), and then dried in N₂. The thickness of the monolayer, determined by ellipsometry, was 3.7 ± 0.2 nm. ³²P-labeled DNA oligomers were used to characterize the adsorption quantitatively and were found to be about 1×10^{13} molecules/cm².

The samples were inserted into an ultrahigh vacuum chamber at $<10^{-8}$ mbar. The polarized photoelectrons were ejected from the substrate by applying a laser beam at 193 nm (6.4 eV) using a $\lambda/4$ plate to create either left- or right-handed circularly polarized light. It has been established that right-handed circularly polarized light induces positive helicity² in the photoelectrons ejected from the gold substrate and that the reverse is true for left-handed polarized light. The spins of the photoelectrons are polarized by about 15% [48–51]. After having been passed through the organic layers, the electrons' energy distribution is analyzed by using a time-of-flight spectrometer [52].

The laser energy is maintained very low (20 pJ/pulse, energy density ~ 2 nJ/cm²) to avoid any nonlinear processes. To avoid damage from UV radiation, the sample is exposed to the laser beam for only 20 μ s. The photon energy is above that of the gold work-function (~ 5 eV); however, it is less than the ionization potential of the DNA bases (~ 8.4 eV) [53]. Therefore, all the photoelectrons originate from the metal substrate; they are transmitted through the DNA monolayer to the vacuum, where their energy is measured.

The magnetization of the monolayers was measured using an MPMS₂ SQUID-type magnetometer. For these measurements the monolayer was prepared on a pure polycrystalline gold foil. The magnetic response of the slide was measured separately and then subtracted from the signal obtained for the monolayer-coated gold

For the temperature dependence study, samples were inserted into an ultra-high vacuum chamber $<10^{-8}$ Torr. The samples were cooled by flowing liquid nitrogen through a cavity in the sample holder and monitored by a temperature controller device (M.R.C.). After reaching the desired temperature the samples were left to equilibrate for a few minutes. Spin selectivity was recorded at each temperature. Contact potential difference (CPD) measurements were carried out using a commercial Kelvin probe. The CPD was measured between a clean gold substrate and the monolayer by varying the distance between them, hence varying the capacitance of the system [54]. Thus, the method is contact free.

² The helicity is defined for particles with momentum p and spin s as the expectation value of $\frac{s \cdot p}{|s \cdot p|}$.

3 Results

3.1 Electron Transmission Through SAM of Polyalanine

Figure 4 presents the kinetic energy distributions for photoelectrons ejected with a left or right circular polarized laser (solid red and dashed blue lines respectively).

The spectra in panels A and C are obtained for the transmission of electrons through films of L- and D-polyalanine respectively, both bound to the surface through the C-terminal. Panel B corresponds to a film of D-polyalanine bound to

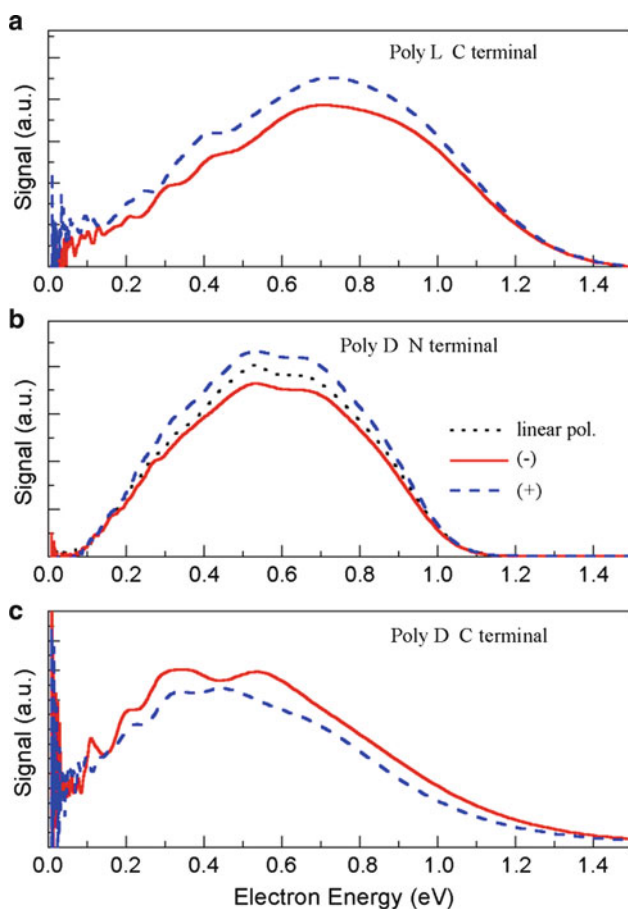


Fig. 4 The energy distribution for photoelectrons ejected with a *left* (negative spin polarization – red, solid) or *right* circular (positive spin polarization – blue, dashed) polarized laser. The electrons are transmitted through films of L- and D-polyalanine both bound to the surface through the carbon terminal (a and c, respectively), and through a film of D-polyalanine bound to the surface through the N-terminal (b). *Angew. Chem. Int. Ed.* 2002, 41, 761 Fig. 2 Copy right permission granted.

the surface through the N-terminal. The results shown in Fig. 4a, c confirm earlier results that showed a large asymmetry for polarized electron transmission through organized film of chiral molecules [20]. The asymmetry parameter is defined as

$$F = \frac{I(+P) - I(-P)}{I(+P) + I(-P)}$$

where $I(+P)$ and $I(-P)$ are the transmission of the electron beam with spin angular momentum oriented parallel (+) and antiparallel (-) to its velocity vector.

The sign of the asymmetry depends on the handedness of the molecules. Surprisingly, for a given handedness of the molecules the sign of the asymmetry switches upon reversing the way the molecules are adsorbed on the surface (from N to C terminated molecules). This is clearly seen in Fig. 8b, c. The observed asymmetry in the transmission through the layer of photoelectrons produced by left and right circular polarization of photons changes from 0.09 ± 0.02 to -0.10 ± 0.02 (Fig. 4b, c respectively). Importantly, the observed 10% effect is induced by merely 15% polarization of the photoelectrons. Thus, the selectivity to the incoming helicity of the electrons is as large as 70% and within experimental error 100% selectivity cannot be ruled out.

3.2 Temperature Dependence of Spin Transmission

The result of the CPD measured on an LC monolayer as a function of temperature, in the range of 300 K to 140 K is shown in Fig. 5a. The CPD at room temperature is about +0.3 V. Upon cooling the CPD signal decreases smoothly, passing through zero at 264 K and continuing to decrease down to -0.3 V. Thus, the layer was found polar, with a negative charge density on the organic surface at room temperature. Upon cooling, the charge density smoothly goes through zero and then to positive charge density at 140 K.

Figure 5b-d presents the kinetic energy distributions for photoelectrons ejected with left and right circularly polarized light from a laser operating at 248 nm ($h\nu = 5.0$ eV). As shown in the figure, both the shape of the spectra and the polarization asymmetry change abruptly at the edges of the temperature range $\Delta = 264 \pm 10$ K. Characteristic spectra within the temperature range above Δ are shown in Fig. 5b. Such broad-band spectra are typical for slow electron transmission through films of polyalanine as shown in Fig. 4. The value of the asymmetry parameter A is 0.09 ± 0.02 . The asymmetry is calculated by comparing the area under the curves corresponding to photoelectrons ejected by right and left handed circular polarized photons. Similarly, spectra within the temperature range below Δ are displayed in Fig. 5d. The typical broad-band spectrum measured here is a bit narrower than at the highest temperatures. Now, the asymmetry parameter is negative with a value of -0.11 ± 0.02 . Notice that the observed $\sim \pm 10\%$ asymmetries are induced by merely 15% polarization of the gold photoelectrons. Thus, the

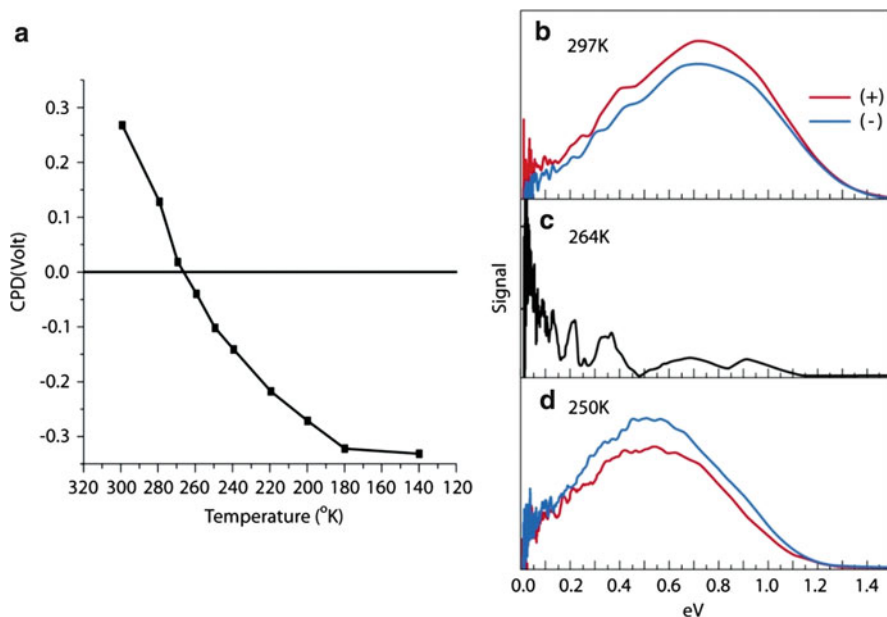
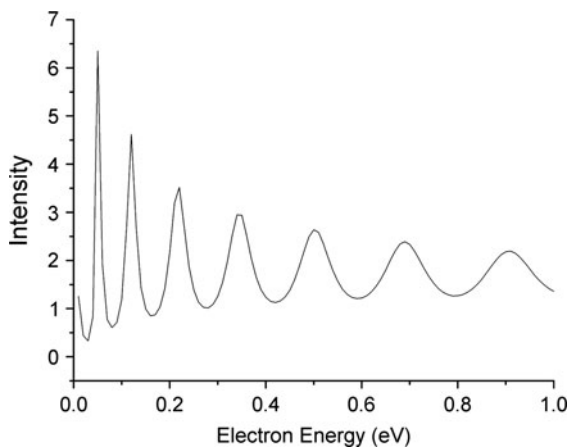


Fig. 5 (a) The contact potential difference (CPD) measured between the gold-coated monolayer of polyaniline and a gold substrate as a function of temperature. (b–d) The photoelectron spectra that were measured at 297 K, 264 K, and 250 K, respectively. The signal intensity is plotted vs the photoejected electrons' kinetic energy. The photon energy used is 5 eV. Separate spectra are shown for a clockwise circularly polarized (+ red curve) photon beam and a counterclockwise circularly polarized (– blue curve) photon beam. (c) The photoelectron spectrum at 264 K, where the CPD is zero (see a). Here the spectrum does not depend on laser polarization and does not exhibit a broad resonance. PHYSICAL REVIEW B 68, 115418 (2003). Copy right permission granted.

selectivity of the monolayer to the helicity of the transmitted electrons is as large as $\pm 70\%$. Spectra measured within the range Δ are illustrated in Fig. 5c. This is the electron transmission spectrum obtained at 264 K, where the CPD passes through zero (Fig. 5a). Several sharp resonances are observed in the figure; however the asymmetry parameter within this temperature range is found to be zero, 0.00 ± 0.01 .

Figure 5c strongly suggests a transmission spectrum through a homogeneous thin layer. This can be simulated by a one-dimensional quantum computation for passage of electrons through an appropriate potential. Such a simulation is shown in Fig. 6. The potential used in the simulation is -5 V at the gold side and zero elsewhere, except for a positive spike (0.1 Å, 7 V) at 50 Å away from the gold. The spike represents the border between the monolayer material and vacuum. Outgoing waves from the monolayer boundary conditions were used. It is known that electron transmission is most efficient along the molecular axis; therefore the effective length used in the simulation is the actual molecular length and not the thickness of the layer.

Fig. 6 Simulation of the transmission spectrum assuming a one dimensional potential of -5 V at the gold substrate side and zero elsewhere, except for a positive spike (0.1 Å, 7 V) at 50 Å away from the gold. The spike represents the border between the monolayer material and vacuum. Outgoing waves from the monolayer boundary conditions are presented



For verifying how the temperature affects the structure of the adsorbed molecules so that the direction of their dipole moment flips, we measured the infrared spectrum of an LC film at two temperatures as shown in Fig. 7. The peaks in Fig. 7a are of the amide-I ($1,668\text{ cm}^{-1}$) and amide-II ($1,544\text{ cm}^{-1}$) bands and those in Fig. 7b are of the amide-III ($3,200\text{--}3,500\text{ cm}^{-1}$) band (N–H stretching). Clearly a dramatic change occurs in the vibrations of the polypeptide upon cooling of the sample. The amide-I vibration is split and shifted to lower wavenumber. The amide-III band also splits but in addition it is shifted to higher wavenumbers.

Further insight about the temperature effect on the monolayer properties was obtained from photoelectron spectra obtained from gold coated with monolayers of LC and DN polyalanine, as shown in Fig. 8 [55]. The ratio between the intensities of the spectra obtained from the LC and DN films at room temperature is 1:5. The photoelectron distribution from the LC film at room temperature is narrow. When the sample is cooled, the intensity of the photoelectron signal decreases and at 260 K a second broader peak starts to appear at higher energies. This peak increases with further decrease of the temperature. The increased yield and broadening of the energy distribution spectra of the LC film, at low temperatures, is an indication for the structural changes occurring in the monolayer when cooled. The energy distribution obtained from the DN film is already broad at room temperature, and decreases in intensity with lowering of the temperature. Comparing the two spectra in Fig. 8a, b, we notice that at room temperature the spectrum taken from DN film is broader and that the decrease in temperature does not cause an abrupt change in the shape of the spectrum, contrary to the observation with the LC film.

The photoelectron signal as a function of the laser intensity was measured at two temperatures for the LC film and is shown in Fig. 9. At room temperature the photoemission signal depends linearly on the laser intensity, indicating a single photon photoemission process. From the high energy cut-off in Fig. 9a we deduce that the workfunction is about 3.9 eV , much lower than the workfunction of the bare

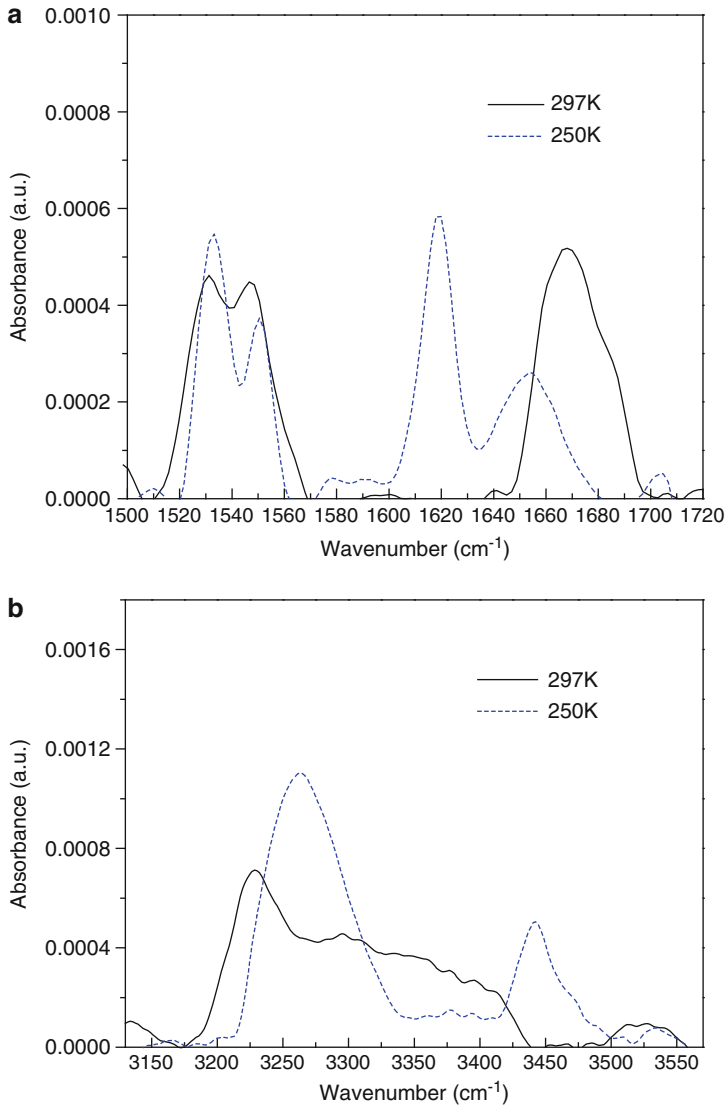


Fig. 7 (a) IR spectra of an LC film measured at two temperatures, showing the amide-I and amide-II vibrations. (b) IR spectra of an LC film measured at two temperatures, showing the amide-III vibrations

gold (about 5 eV). The reduction in the workfunction indicates that the monolayer has a dipole with positive pole pointing *away* from the surface.

The situation is different when the LC film is cooled to 250 K. At this temperature we notice that the slope increases with laser intensity and reaches a value of two at higher laser intensity. This behavior indicates that no single photon emission

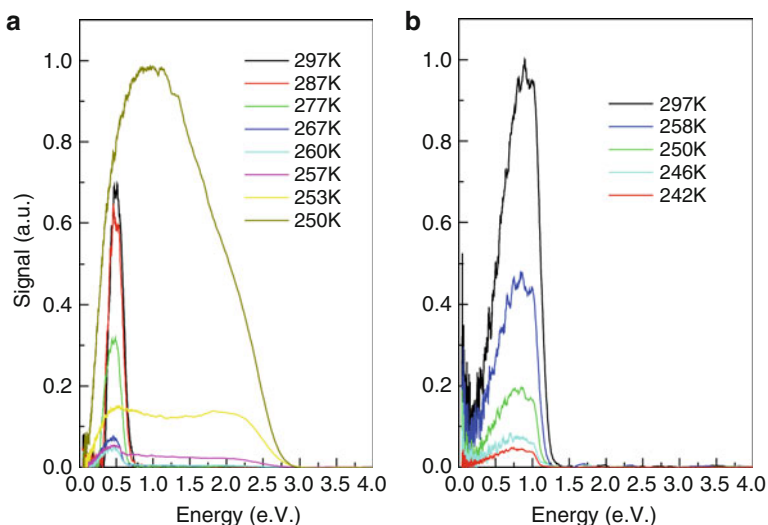


Fig. 8 Normalized temperature dependent photoelectron energy distribution spectra for photoelectrons emitted from gold coated with monolayers of (a) LC polyaniline, and (b) DN polyaniline. The laser wavelength was 266 nm (4.66 eV)

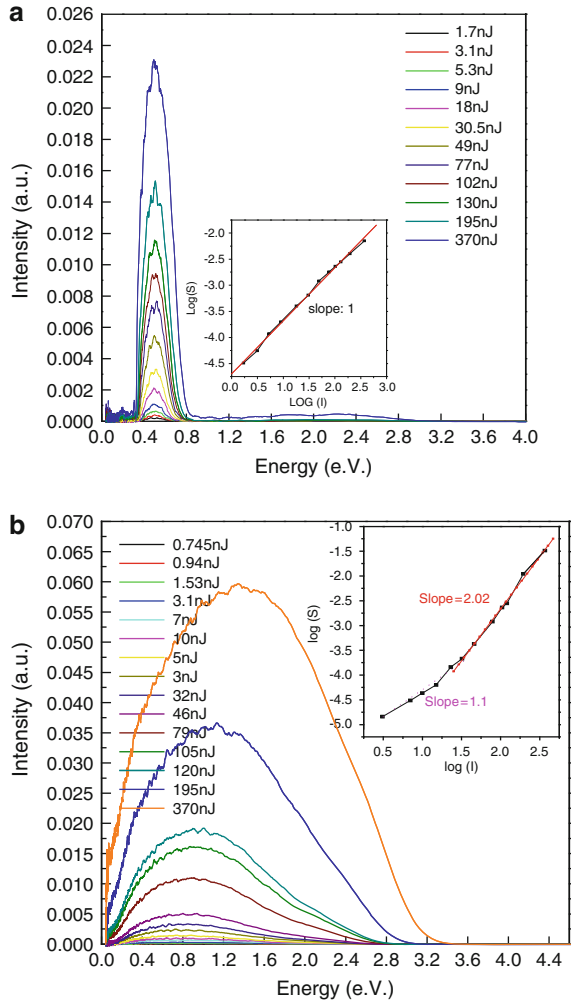
occurs at this temperature; hence the workfunction is much higher and the dipole moment associated with the adsorbed molecules has flipped compared to the room temperature; namely, the positive pole is pointing *towards* the surface.

IR as well as photoelectron spectroscopy prove that in the case of adsorbed polyaniline the molecules are going through a structural change during cooling and this change results in flipping the direction of the electric dipole.

3.3 Spin Selectivity in DNA

Figure 10a, b presents the energy distribution of the transmitted photoelectrons when they are ejected from the gold by either a clockwise (cw) or counter-clockwise (ccw) circularly polarized laser passing through a monolayer made either from single strand (Fig. 10a) or double strand (Fig. 10b) DNA. Within our signal-to-noise ratio, no spin selectivity could be observed in the single-stranded DNA monolayers. In the case of monolayers made from double strand DNA, the transmission is more intense for electrons ejected with a ccw polarized laser, namely these electrons are polarized with their spin pointing anti-parallel relative to their velocity. The transmission selectivity is, with very high confidence, positive. Its exact value varies somewhat from sample to sample and is estimated as $8 \pm 2\%$. The data is based on studying more than 20 samples. Assuming about 15% initial

Fig. 9 Photoelectron emission from an LC film as function of laser intensity, taken at a temperature of (a) 297 K and (b) 250 K. In the *insert* the log of the signal is plotted as a function of the log of the laser intensity



polarization of the electrons, the transmission results indicate a spin selectivity of at least 50%.

Figure 10c, d shows the magnetic moment as measured for DNA adsorbed on 99.999% polycrystalline gold foil after subtracting the diamagnetic contribution of the gold. The foil is made as a $\sim 20 \text{ mm}^2$ disk with a mass of 52.4 mg. While the signal for the ss DNA (Fig. 10c) is very weak, it is very pronounced for the ds DNA monolayer (Fig. 10d). The magnitude of the signal, in this case, varies somewhat from sample to sample, as indicated in the figure. The magnetic moment was found to be temperature independent and showed no hysteresis. At a field of 1 Tesla the signal corresponds to about 90 Bohr magnetons per adsorbed DNA

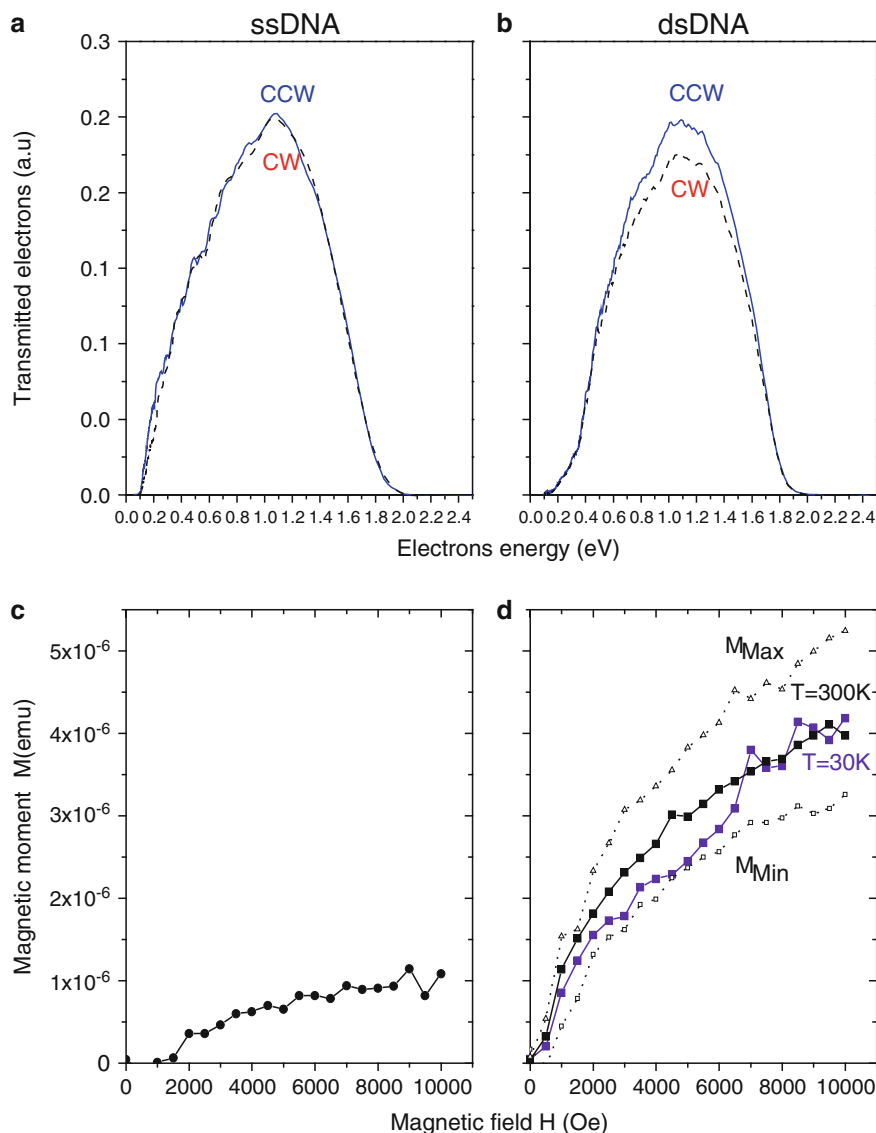


Fig. 10 (a, b) The energy distribution of the transmitted photoelectrons through a monolayer made from single-stranded DNA (a) or from double-stranded DNA oligomers (b). The electrons are ejected from the gold with a clockwise (cw – dotted) or counter-clockwise (ccw – solid) circularly polarized laser. While in the first case the electrons are spin-polarized with the spin parallel to the electrons' velocity for cw circular polarized laser, the spin is polarized anti-parallel to the velocity. (c, d) The magnetic moment as measured for the DNA-coated gold after subtracting the diamagnetic contribution of the gold. The magnetic moment measured for monolayer made from single strands (c) or (d) for monolayers made from double strands measured at 300 (squares – full line) and 30 K (circles – full line). The dotted curves indicate the range of variation in the magnetic measurements obtained for different samples. The extreme values are shown – maximum as triangles and minimum as squares. Copied with permission from PRL 96, 036101 (2006) Fig. 2

molecule,³ and for most of the samples the signal does not reach saturation at this value. These observations are consistent with previous studies performed on layers that were not necessarily chiral [39, 56].

It is important to realize that the spin selective electron transmission cannot be affected by absorption dichroism of the DNA monolayer. This is because the light passes through only a single monolayer resulting in less than 1% absorption of the incident light by the layer [57, 58].⁴ Therefore, absorption cannot account for the 8% difference in the electrons signal observed. In addition, we performed CD absorption experiments at 193 nm and found that, within our signal to noise ratio, no dichroism exists at this wavelength. Hence, one has to conclude that the observed effects are originating from other physical mechanisms.

Two effects were detected in the present study, the spin-selective electron transmission through monolayers made from ds-DNA and the large magnetization measured for these layers. In addition, it has been found that there is a clear difference between monolayers made from ss-DNA and those made from ds-DNA. This difference exists despite the fact that both types of molecules are chiral.

4 Discussion

The results presented above show that, when the dipolar chiral molecules are adsorbed as self-assembled closed packed layer on gold, one obtains a surprising phenomenon of selectively transmitted spin-polarized electrons through the monolayer [18, 26–28]. The photoelectrons ejected from a gold surface are known to preserve about 10–15% of the photon helicity in this energy range [50]. Therefore, if the measured asymmetry factor, $|F|$, is around 10–15%, the transmission selectivity for the electron polarization approaches unity, i.e., full transmission of one spin orientation occurs while there is zero transmission of the other. Hence, the helicity of the emitted photoelectrons from gold has the same sign as the helicity of the impinging photons. The asymmetry factor turns out to be almost independent of energy and, in what follows, only its energy average is quoted.

To understand the symmetry considerations that emerge from the results, we defined a chirality pseudoscalar, c , to have the value +1 for right-handed molecules and –1 for left-handed molecules. For preferred photoemission, the sign of the

³ For a gold foil of area $A = 20 \text{ mm}^2$ and number of molecules per $\text{cm}^2 N = 1.1 \times 10^{13}$ adsorbed on both sides of the foil, and with a magnetic moment of $4 \times 10^{-6} \text{ emu}$ at 1 T, the magnetic moment per molecule is $= \frac{4 \times 10^{-6} \text{ emu}}{2 \times (1.1 \times 10^{13}) (0.2) \text{ molecules}} = 9.09 \times 10^{-19} \text{ emu/molecules} = 98 \mu_B/\text{molecule}$.

⁴ The density of the molecules in the monolayer ($n = 1.4 \times 10^{13} \text{ molecules/cm}^2$) is equivalent to concentration of $7.3 \times 10^{-2} \text{ mol/L}$. For DNA composed from 15 bases the molar extinction coefficient at $\lambda = 260 \text{ nm}$, where the DNA has maximum absorption, is $\epsilon = 122.2 \times 10^3 \text{ L/mol cm}$ and for a path length $\ell = \text{Monolayer thickness} = 3.2 \text{ nm}$, the absorbance $A = -\log(I/I_0) = \epsilon \ell c = 28405.1 \times 10^{-7}$ therefore the amount of light absorbed $\frac{I_0 - I}{I_0} \leq 1\%$.

photons' helicity (+ for clockwise and – for counterclockwise circular polarization) must match the sign of the component of the axial vector E , when E is the electric field, perpendicular to the surface. In the experiments, the electrons originate from the Au substrate and travel through the monolayer to the detector. However, one can perform a “thought experiment” that is time-reversed; the electrons travel from the detector through the monolayer to the Au substrate. Because the dipole field direction will be reversed with respect to the component of the electron spin in its propagation direction, the sign of F will change; i.e., in the time-reversed thought experiment the LN layer will act as an LC layer and vice versa. Time reversal symmetry is broken in this experiment, as it is when the spin is transmitted through a magnetic layer. Thus, the special symmetry found in the table is consistent with that of a magnetic field proportional to E .

The influence of the axial vector cE is shown clearly in Figs. 4 and 5. Specifically, Fig. 5 demonstrates the symmetry very clearly. Figure 5a shows how the surface CPD between gold and a gold substrate covered with the organic monolayer changes with temperature. For this assembly, the CPD changes from 0.3 V at room temperature to -0.3 V at temperatures below 180 K, passing through zero at about 264 K. Thus the direction of the film's electric field can be tuned by the temperature. Figure 5b–d shows the polarization-controlled low-energy photoelectron spectra measured for these films at three different temperatures. These data show that the asymmetry factor F changes its sign as the temperature changes the sign of the CPD, and hence the sign of the postulated magnetic field. It is interesting to note that the symmetry considerations that emerge from the spin-transmission experiments are identical to those obtained based on the magneto-electric effect, which predicts a coupling of the magnetic dipole and the electric field [8, 9].

Evidence that one needs a minimal electric field to create the spin selectivity is clearly seen in Fig. 5c. There, in the vicinity where the contact potential approached zero, the spectrum changed drastically from a broad resonance to a group of sharper resonances and the asymmetry factor dropped to zero. The photoemission yield also dropped. The lack of asymmetry is consistent with time reversal symmetry and the drastic change in the spectrum character indicates that the mechanism governing the electron transmission through the layer has changed. At almost any other temperature the electric field across the layer is high enough to induce a magnetic field in the layer. Consistently, the significant non-zero asymmetry factor indicates the breakdown of time reversal symmetry. This accelerating magnetic field for selected spin polarization is absent under the conditions presented in Fig. 5c. Its absence explains the drastic change in the spectrum and the much lower yield of photoelectrons transmitted through the layer.

Further studies confirmed the importance of having an organized monolayer film for observing this polarization effect [34]. It is important to realize that, when a self-assembled monolayer is formed, the monolayer consists of domains in which the molecules are closely packed. The size of the domains are correlated with the quality of the monolayer (see for example [59]) [60]. Therefore, when one relates to cooperative effects within a self-assembled monolayer, one actually refers to the effects induced by the organization within a domain.

When single-stranded DNA molecules, which do not form a well-organized layer, were adsorbed on a gold substrate, no asymmetry in the photoemission yield for clockwise or counterclockwise circular polarized light could be observed. However, when double-stranded DNA, which formed a well-ordered monolayer, was adsorbed, a large asymmetry was observed.

The high spin selectivity discussed here is reminiscent of spin selectivity in the transmission of electrons through magnetically saturated ferromagnetic thin films such as a cobalt thin layer (for example [61]). There, Pauli exclusion was considered a factor when rationalizing the selectivity. While the magnetization of the ferromagnetic thin layer is induced by an external field, perpendicular to the layer, in the experiments described here, the magnetization in the monolayer is inherent due to its dipolar layer nature and its chirality. The results presented here indicate that the magnetism induced in the chiral organic monolayer must be of the same order of magnitude as the magnetism in the ferromagnetic layers.

The magnetic order in the layer originates in the charge transfer and handedness. Upon charge transfer and because of the molecules' chirality, the spin of the transferred charge is aligned in the direction dictated by the handedness of the adsorbed molecules and the nature of the charge (electron or hole). Note that the spin-orbit interaction responsible for this alignment is small for a single molecule. However, because of the exchange interaction among the transferred electrons, the barrier for flipping the spin to the other direction is given by

$$\Delta_{\text{spin}} = nV_{\text{so}}$$

where n is the number of electrons in a domain and V_{so} is the spin-orbit splitting for a single molecule. V_{so} has been estimated to be on the order of 4 meV, based on recent theory [62] and experiments [63]; therefore, the barrier for spin flip is given by $\Delta_{\text{spin}} \approx 0.1$ eV, assuming that each domain contains about 50 molecules and that the charge density is on the order of 0.5 electron per molecule. Hence, although the alignment of the spin and orbital angular momentum occurs only during the transit of the charge from the substrate into the layer, once all these magnetic moment are co-aligned in the entire domain, the exchange interaction keeps them aligned permanently. Hence the magnetic effect is based on two stages – the first includes transit of charge through chiral molecules which creates a magnetic field that aligns the magnetic dipole of the charge transferred. In the second stage, once the charge is transferred the exchange interaction keeps it aligned in a steady state.

5 Summary

The special symmetry considerations that are associated with chirality are attracting special attention these days, mainly in relation to inorganic interfaces (for a recent review please see [64]). The importance of chirality in biology and its relation to

magnetic properties is another major reason for the attention the subject is attracting. In the present review we have focused on another property of chiral monolayers that emerged unexpectedly. Their action as a “spin filter” is explained here very schematically and no satisfactory microscopic theory for this effect exists, despite numerous efforts to find one.

Nano-objects are becoming the focus of many technologies and research. These objects are typically very sensitive to their surface properties. Therefore, controlling interface properties has emerged as a way to control the electronic and magnetic behavior of nano-objects. Organic self-assembled monolayers are often used for this purpose since they can easily be prepared and controlled. In addition, organic–inorganic interfaces are a key issue vis-a-vis the operation of organic-based electronic devices. Therefore, it is important to realize what new properties emerge from the formation of self-assembled organic monolayers and to apply these new properties for widening the scope of nanotechnology. The new electronic and magnetic properties discussed here offer a new way into production of molecular based spin filters, with no need to apply an external magnetic field. However, there is still a gap in our quantitative theoretical understanding of the phenomena. This type of understanding is required for the field to develop beyond its current stage.

Acknowledgments RN acknowledges the support of the Israel Science Foundation. This research is made possible by the historic generosity of the Harold Perlman family.

References

1. Mason SF (1984) *Nature* 311:19
2. Kelvin L (1904) *Baltimore lectures*. Clay, London
3. Barron L (1994) *Science* 266:1491
4. Kleindienst P, Wagniere G (1998) *Chem Phys Lett* 288:89
5. Rikken GLJA, Raupach E (2000) *Nature* 405:932
6. Rikken GLJA, Raupach E (1997) *Nature* 390:493
7. Wen X, Wilczek F, Zee A (1989) *Phys Rev B* 39:11413
8. Landau LD, Lifshitz EM (1963) *Electrodynamics of continuous media*, 2nd edn. Pergamon, Oxford
9. O'Dell TH (1970) *The electrodynamics of magneto-electric media*. North Holland, Amsterdam
10. Lovesey SW, Staub U (2009) *J Phys Condens Matter* 21:142201 and references cited therein
11. Wagnière GH (2007) *On chirality and the universal asymmetry*. Wiley-VCH, Zürich
12. Barron L (2004) *Molecular light scattering and optical activity*. Cambridge University Press, Cambridge
13. Pinheiro FA, van Tiggelen BA (2002) *Phys Rev E* 66:016607
14. Pinheiro FA, van Tiggelen BA (2003) *J Opt Soc Am A Opt Image Sci Vis* 20:99
15. Train C, Gheorghe R, Krstic V, Chamoreau LM, Ovanesyan NS, Rikken GLJA, Gruselle M, Verdaguer M (2008) *Nat Mater* 7:729
16. Campbell DM, Farago PS (1987) *J Phys B At Mol Phys* 20:5133
17. Nolting C, Mayer S, Kessler J (1997) *J Phys B* 30:5491
18. Ray K, Ananthavel SP, Waldeck DH, Naaman R (1999) *Science* 283:814

19. Carmeli I, Gefen Z, Vager Z, Naaman R (2003) *Phys Rev B* 68:115418
20. Ray SG, Daube SS, Leitus G, Vager Z, Naaman R (2006) *Phys Rev Lett* 96:036101
21. Skourtis SS, Beratan DN, Naaman R, Nitzan A, Waldeck DH (2008) *Phys Rev Lett* 101:238103
22. Yeganeh S, Ratner MA, Medina E, Mujica V (2009) *J Chem Phys* 131:014707
23. Lvov VS, Naaman R, Vager Z, Tiberkevich V (2003) *Chem Phys Lett* 381:650
24. Ito E, Washizu Y, Hayashi N, Ishii H, Matsue N, Tsuboi K, Ouchi Y, Harima Y, Yamashita K, Seki K (2002) *J App Phys* 92:7306
25. Brinkman A, Huijben M, van Zalk J, Huijben M, Zeitler U, Maan JC, van der Wiel WG, Rijnders G, Blank DHA, Hilgenkamp H (2007) *Nat Mater* 6:493
26. Carmeli I, Leitus G, Naaman R, Reich S, Vager Z (2003) *J Chem Phys* 118:10372
27. Crespo P, Litrán R, Rojas TC, Multigner M, de la Fuente JM, Sánchez-López JC, García MA, Hernando A, Penadés S, Fernández A (2004) *Phys Rev Lett* 93:087204
28. Carmeli I, Skakalova V, Naaman R, Vager Z (2002) *Angew Chem Int Ed* 41:761
29. Suda M, Kameyama N, Suzuki M, Kawamura N, Einaga Y (2007) *Angew Chem Int Ed* 46:1
30. Cahen D, Naaman R, Vager Z (2005) *Adv Funct Mater* 15:1571
31. Ohtomo A, Hwang HY (2004) *Nature* 427:423
32. Huijben M, Rijnders G, Blank DHA, Bals S, Aert SV, Verbeeck J, Tendeloo GV, Brinkman A, Hilgenkamp H (2006) *Nat Mater* 5:556
33. Thiel S, Hammerl G, Schmehl A, Schneider CW, Mannhart J (2006) *Science* 313:1942
34. Reyren N, Thiel S, Caviglia AD, Kourkoutis LF, Hammer G, Richter C, Schneider CW, Kopp T, Rüetschid A-S, Jaccard D et al (2007) *Science* 317:1196
35. Herranz G, Basletić M, Bibes M, Carrétéro C, Tafrá E, Jacquet E, Bouzehouane K, Deranlot C, Hamzić A, Broto J-M et al (2007) *Phys Rev Lett* 98:216803
36. Basletić M, Maurice J-L, Carrétéro C, Herranz G, Copie O, Bibes M, Jacquet E, Bouzehouane K, Fusil S, Barthélémy A (2008) *Nat Mater* 7:621
37. Siemons W, Koster G, Yamamoto H, Harrison WA, Lucovsky G, Geballe TH, Blank DHA, Beasley MR (2007) *Phys Rev Lett* 98:196802
38. Willmott PR, Pauli SA, Herger R, Schlepütz CM, Martocchia D, Patterson BD, Delley B, Clarke R, Kumah D, Cionca C et al (2007) *Phys Rev Lett* 99:155502
39. Kalabukhov A, Gunnarsson R, Börjesson J, Olsson E, Claesson T, Winkler D (2007) *Phys Rev B* 75:121404(R)
40. Pentcheva R, Pickett WE (2006) *Phys Rev B* 74:035112
41. Park MS, Rhim SH, Freeman AJ (2006) *Phys Rev B* 74:205416
42. Vager Z, Naaman R (2002) *Chem Phys* 281:305
43. Fasman GD (1967) *Poly- α -amino acids*. Marcel Dekkar, Inc, New York
44. Parrish JR, Blout ER (1972) *Biopolymers* 11:1001
45. Any H, Cheny B, Houy J, Shen Z, Liuy S (1998) *J Phys D Appl Phys* 31:1144 and references cited therein
46. Aqua T, Naaman R, Daube SS (2003) *Langmuir* 19:10573
47. Petrovykh DY, Kimura-Suda H, Whitman LJ et al (2003) *J Am Chem Soc* 125:5219
48. Borstel G, Wohlecke M (1982) *Phys Rev B* 28:1148
49. Kirschner J (1985) *Polarized electrons at surfaces*. Springer, Berlin
50. Meier F, Pescia D (1981) *Phys Rev Lett* 47:374
51. Meier F, Bona GL, Hufner S (1984) *Phys Rev Lett* 52:1152
52. Naaman R, Vager Z (2003) *Acc Chem Res* 36:291
53. Hush NS, Cheung AS (1975) *Chem Phys Lett* 34:11
54. Kronik L, Shapira Y (1999) *Surf Sci Rep* 37:1
55. Carmeli I (2003) PhD Thesis, Weizmann Institute of Science, Israel
56. Venkatesan M, Fitzgerald CB, Coey MD (2004) *Nature* 430:630
57. Fasman GD (1975) *The handbook of biochemistry and molecular biology*, vol 1. CRC Press, Cleveland, OH, p 589

58. Ausubel FM et al. (Eds.) (1990) Current Protocols in Molecular Biology, Vol. 1, Green/Wiley-Interscience, New York
59. Stamou D, Gourdon D, Liley M, Burnham NA, Kulik A, Vogel H, Duschl C (1997) Langmuir 13:2425
60. Suo Z, Gao YF, Scoles G (2004) Trans ASME 71:24
61. Lassailly Y et al (2004) Phys Rev B 50:13054
62. Ando T (2000) J Phys Soc Jpn 69:1757
63. Kuemmeth F, Ilani S, Ralph DC, McEuen PL (2008) Nature 452:448
64. Qi X-L, Zhang S-C (2010) Phys Today 63:33

Chiral Control of Current Transfer in Molecules

Vered Ben-Moshe, David N. Beratan, Abraham Nitzan,
and Spiros S. Skourtis

Abstract Electron transmission through chiral molecules induced by circularly polarized light can be very different for mirror image structures. This behavior is described in terms of *current transfer*: the transfer of both charge and momentum. We review recent theoretical developments on the theory of current transfer and discuss related experimental studies of electron transmission through chiral molecular structures adsorbed on surfaces.

Keywords Chiral control, Current transfer, Dephasing, Molecules, Junctions, Polarized laser pulses, Quantum model simulations

Contents

1	Introduction	260
2	The Transmission of Polarized Electrons Through Chiral Molecular Layers	261
3	Time Dependent Current Transport Analysis	262
3.1	Dephasing	264
4	Steady-State Transport Analysis	268
5	Steady-State Currents and Asymmetry Factors	270
6	Steady-State Current Transfer with Dephasing	274
7	Conclusions	276
	References	277

V. Ben-Moshe (✉) and A. Nitzan
School of Chemistry, Tel Aviv University, Tel Aviv 69978, Israel
D.N. Beratan
Department of Chemistry, Duke University, Durham, NC 27708, USA
Department of Biochemistry, Duke University, Durham, NC 27708, USA
Department of Physics, Duke University, Durham, NC 27708, USA
S.S. Skourtis
Department of Physics, University of Cyprus, Nicosia 1678, Cyprus
e-mail: skourtis@ucy.ac.cy

1 Introduction

Charge transfer between donor and acceptor species mediated by a molecular bridge is of wide interest in chemistry, physics, biology and nanoscience [1–9]. The manipulation of charge transfer, electric currents, and magnetic moments in molecular junctions is of crucial importance in molecular electronics [10–12] and the development of attosecond laser pulses enables exciting new opportunities for the coherent control of electronic motion in atoms and molecules [13–15]. Indeed, novel experiments use attosecond laser pulses to probe and control ultrafast electronic dynamics in atoms and in small molecules [16–27]. Theoretical and computational studies indicate that an important application of attosecond laser pulses will be the generation of currents and induced magnetic moments in molecules. Circularly polarized attosecond laser pulses can be tailored to induce electric currents in linear [28, 29] and ring-shaped molecules such as benzene and Mg-porphyrins [30–32]. Importantly, the laser-generated ring currents and their magnetic moments can be much larger than those generated by static magnetic fields [30–35]. Therefore, the development of theoretical and computational tools for the analysis of current propagation through molecules is central to the fields of molecular electronics and quantum control.

Experiments by Naaman, Waldeck and coworkers [36, 37] show that the relative yield of electron transfer (ET) induced by circularly polarized light (CPL) through helical molecular structures adsorbed on surfaces depends on the relative handedness of the bridge and on the optical circular polarization, in spite of the identical underlying electronic energy spectra. Reversing the direction of the circular polarization or of the molecular handedness has similar effects on the yields, while the transmission of electrons generated by unpolarized light is not influenced by the handedness of the molecule.

Here, we review tight-binding models that account for the above-mentioned ET yield asymmetries in the context of the more general phenomenon of *current transfer* [38–40]. Current transfer is charge transfer where the transferred charge carrier maintains at least some of its linear and/or angular momentum (phase). A recent photoemission experiment [41] demonstrated current transfer: a biased linear momentum distribution on a Cu (100) surface was established based on the angular distribution of the photoemitted current.

As an application of current transfer theory, we examined bridge-mediated electron transport through chiral bridges and we demonstrated that the through-bridge transmission of an electronic state carrying angular momentum or current is affected by the handedness of the bridge [38]. Our model explains the main features of the experimental data in [36, 37] and provides a starting point for understanding how to control through-bridge transmission of electron phase, current, or angular momentum by manipulating the structure of the bridge [38–40].

2 The Transmission of Polarized Electrons Through Chiral Molecular Layers

In [36], unpolarized and polarized photoelectrons are ejected from a Au substrate through Langmuir–Blodgett thin films of chiral molecules, L- or D- stearoyl-lysine, deposited on the substrate. The main observation of [36] is that the handedness of the layer determines the transmission of the photoelectrons generated by right (denoted +) vs left (denoted -) circularly polarized light. The molecular handedness does not affect the transmission of photoelectrons generated by unpolarized light (0). If Y is the relative electron quantum yield scaled to unity for transmission of unpolarized electrons through an enantiomer layer, i.e., $Y[0, L] = 1$, then the measured yields in [36] are $Y[0, D] = 1.07$, $Y[+, L] = 1.11$, $Y[+, D] = 0.92$, $Y[-, L] = 0.89$, and $Y[-, D] = 1.21$, with errors of 1–5%. Therefore, the average asymmetry in transmission through the L layer is $\mathcal{A}[L] = \Delta Y[L] / \bar{Y}[L] = 0.11$, where $\Delta Y[L] = Y[+, L] - Y[-, L]$ and $\bar{Y}[L] = \bar{Y}[+, L] + \bar{Y}[-, L]$, and for the D layer it is $\mathcal{A}[D] = -0.14$. The asymmetry is of the order of 10%, and the yield asymmetry reverses sign when the handedness of the layer is switched.

In [37], monolayers of chirally substituted porphyrins are attached to Au electrodes and are immersed in an electrochemical cell. The Cys end of the molecules is attached to Au and the porphyrin group lies in solution. The porphyrin is excited with right- or left-circularly-polarized light, creating a polarized excited state. The porphyrin excited state is reduced by the Au. The observation in [37] is that the photocurrent induced by right-circularly polarized light differs from the photocurrent induced by left-circularly-polarized light, and this photocurrent asymmetry depends on the handedness of the molecular layer. In particular, for the L monolayer, the average photocurrent asymmetry is $\mathcal{A}[L] = \Delta J[L] / \bar{J}[L] = -0.005 \pm 0.001$, and for the D monolayer it is $\mathcal{A}[D] = 0.004 \pm 0.002$.

Although the transmission asymmetry in the porphyrin system [37] is much lower than the asymmetry in the photoelectron transmission experiment [36], it is surprising that both experiments produce a transmission asymmetry, and that the effect on transmission of reversing the bridge handedness is equivalent to the effect of reversing the polarization of the CPL.

Photoelectrons generated by CPL carry total angular momentum polarization. We propose that the yield asymmetry observed in [36] arises from the change in the orbital angular momentum polarization of the photoelectrons induced by the reversal of the exciting light's polarization [38]. Similarly, the photocurrent asymmetry observed in the porphyrin system [37] arises from the change in the orbital angular momentum of the photogenerated hole.¹ The difference in asymmetry magnitudes

¹Au photoelectrons are spin polarized due to the high spin-orbit coupling of the metal. Therefore, an alternative mechanism for the transmission asymmetry observed in [36] could be based on changes in the photoelectron spin angular momentum. We do not attribute the yield asymmetry to spin polarization because the stearoyl-lysine monolayers in [36] contain only low atomic number atoms that do not scatter spin.

in the two experiments is attributed to a difference in bridge energetics relative to the energy of the photoelectrons (the weak effect in [37] is due to electron transmission via a tunneling mechanism).

3 Time Dependent Current Transport Analysis

A standard model for ET in donor (D)-bridge (B)-acceptor (A) systems describes the donor, bridge, and acceptor species as tight-binding chains [2–9]. The corresponding Hamiltonian is $\hat{H} = \hat{H}_D + \hat{H}_A + \hat{H}_B + \hat{V}_{BA} + \hat{V}_{BD}$, where

$$H_K = \sum_{j_K \in K} E_{j_K}^{(K)} |j_K\rangle \langle j_K| + \sum_{j_K \in K} V_{j_K, j_{K+1}}^{(K)} |j_K\rangle \langle j_K + 1|; \quad K = D, A, B \quad (1)$$

and

$$V_{KK'} = \sum_{j_K \in K} \sum_{j_{K'} \in K'} V_{j_K, j_{K'}}^{(K, K')} |j_K\rangle \langle j_{K'}|; \quad (K, K') = (D, B) \text{ or } (B, A). \quad (2)$$

\hat{H}_D , \hat{H}_B , and \hat{H}_A are the Hamiltonians of D, B, and A. \hat{V}_{BD} and \hat{V}_{BA} describe the D–B and B–A interactions. We will discuss models where *each* of the D, B, and A moieties have identical site energies and inter-site couplings, and where *all* D–B, (A–B) site pairs have identical couplings: $\alpha_K = E_{j_K}^{(K)}$; $\beta_K = V_{j_K, j_{K+1}}^{(K, K)}$; $V_{KK'} = V_{j_K, j_{K'}}^{(K, K')}$ [38–40].

Consider a tight-binding model for a structure with a donor ring, a helical bridge, and a model acceptor (Fig. 1a). In comparison to the system studied in [37], the ring represents the porphyrin moiety, the helical bridge the peptidic linker, and the single atom the gold contact electrode. The model in Fig. 1a is also applicable to the photoelectron experiment [36] in the sense that it incorporates the handedness of the stearoyl-lysine multilayer and the orbital polarization of the incoming (initial) electrons.

For the system in Fig. 1a, we assume that excitation induced by the circularly-polarized light produces a Bloch-type state on the donor:

$$|M_D\rangle = \frac{1}{\sqrt{N_D}} \sum_{j_D=1}^{N_D} \exp[i(j_D - 1)k_{M_D}a] |j_D\rangle, \quad k_{M_D} = 2\pi M_D / (aN_D), \quad (N_D = 6). \quad (3)$$

Since coupling between D and B is assumed to be negligible among all but the nearest two sites of D and B, the bridge-coupled fragment of the $|M_D\rangle$ state is $(|1_D\rangle + \exp[ik_{M_D}a]|2_D\rangle) / \sqrt{6}$ for the right-handed helical bridge and $(|1_D\rangle + \exp[-ik_{M_D}a]|6_D\rangle) / \sqrt{6}$ for the left-handed bridge. Reversing the bridge handedness is equivalent to reversing the current direction ($M_D \rightarrow -M_D$). Indeed, this equal footing for bridge handedness and for the polarization of the excited states is consistent with the ET yields reported in [36, 37].

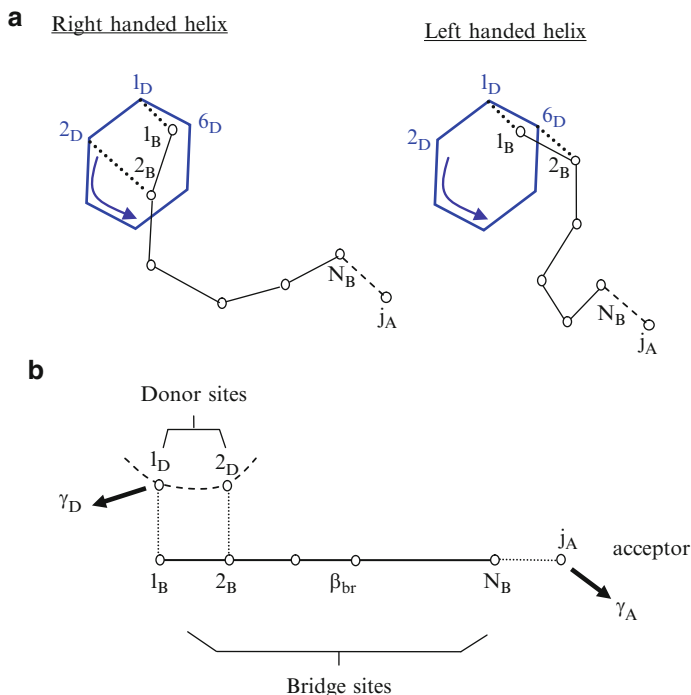


Fig. 1 (a) Tight-binding donor–bridge–acceptor model where the donor moiety is a ring (sites j_D), the bridge is a right- or left-handed helical chain (j_B), and the acceptor (j_A) is an atom connected to the end of the bridge. (b) Simplified representation of the model that emphasizes the different ring-to-bridge tight-binding couplings for left- and right-handed helices. The arrows indicate population relaxation rates for donor and acceptor sites

We use a simplified version of the model in Fig. 1a to examine the effect of donor-current direction reversal on the electron-transfer yield following initial excitation of donor states $|M_D\rangle$ [38] that captures the physics of the electron transmission asymmetry reported in [36, 37] (Fig. 1b). We represent the opposite initial circular currents on the donor by the initial states:

$$|\phi_{in}\rangle = \frac{1}{\sqrt{2}}(|1_D\rangle + e^{i\theta}|2_D\rangle); \quad |\phi_{in}^*\rangle = \frac{1}{\sqrt{2}}(|1_D\rangle + e^{-i\theta}|2_D\rangle). \quad (4)$$

(The phase θ can be thought of as $k_{M_D}a$, but is not restricted to this value, and we have changed the normalization of the state.) In addition, we assume that $|1_D\rangle$ in $|\phi_{in}\rangle$ is characterized by a finite lifetime \hbar/γ_D and that the electron-transfer signal is associated with the decay of the acceptor state $|j_A\rangle$ with rate \hbar/γ_A . These population relaxations are described by replacing E_{jk} by $E_{jk} - i((1/2)\gamma_K)$ in (1) for the corresponding donor and acceptor sites, i.e., $\langle j_K|\hat{H}|j_K\rangle = E_{j_K}^{(K)} - i(1/2)\gamma_K$ $K = D, A$.

Starting from a given initial state $|\phi_{\text{in}}\rangle$, the probability that the acceptor state $|j_{\text{A}}\rangle$ is populated at time t is $P_{j_{\text{A}},\text{in}}(t) = |\langle j_{\text{A}}|e^{-i\hat{H}t/\hbar}|\phi_{\text{in}}\rangle|^2$ (\hat{H} is the (non-Hermitian) Hamiltonian of (1)). The Hamiltonian has site-energies $E_j - i((1/2)\gamma_j)$. The probability can be computed in terms of the right and left eigenvectors, $|X_q^{(R)}\rangle$ and $\langle X_q^{(L)}|$ of \hat{H} , and the corresponding eigenvalues, $\mathcal{E}_q = \varepsilon_q - i\Gamma_q/2$ ($\Gamma_q > 0$):

$$\langle j_{\text{A}}|e^{-i\hat{H}t/\hbar}|\phi_{\text{in}}\rangle = \sum_{q=1}^N \mathbf{R}_{j_{\text{A}},\text{in}}^{(q)} e^{-i\varepsilon_q t/\hbar}; \quad \mathbf{R}_{j_{\text{A}},\text{in}}^{(q)} = \langle j_{\text{A}}|X_q^{(R)}\rangle \langle X_q^{(L)}|\phi_{\text{in}}\rangle. \quad (5)$$

(N is the total number of sites in the DBA system). The yield of the irreversible flux out of the acceptor is

$$Y(\text{in}) = \gamma_{\text{A}} \int_0^{\infty} dt \sum_{j_{\text{A}}} P_{j_{\text{A}},\text{in}}(t). \quad (6)$$

The circularly polarized excitation ($|M_{\text{D}}\rangle$ vs $|-M_{\text{D}}\rangle$) produces asymmetry:

$$\mathcal{A} \equiv \frac{Y(M_{\text{D}}) - Y(-M_{\text{D}})}{Y(M_{\text{D}}) + Y(-M_{\text{D}})}. \quad (7)$$

Reversing the handedness of the bridge produces the same asymmetry. In the model of Fig. 1b, $|M_{\text{D}}\rangle$ corresponds to $|\phi_{\text{in}}\rangle$ in (4) and $|-M_{\text{D}}\rangle$ to $|\phi_{\text{in}}^*\rangle$.

3.1 Dephasing

The current transfer described here is a coherent phenomenon, sensitive to dephasing. To investigate environmental dephasing effects, we incorporate additional relaxation of coherences in the site representation of the Liouville equation for the system's density matrix (DM) $\hat{\rho}$:

$$i\hbar \frac{d}{dt} \rho_{j,l}(t) = \sum_k \left[H_{j,k} \rho_{k,l}(t) - \rho_{j,k}(t) H_{kl} \right] - \{i(\gamma_j/2 + \gamma_l/2) + i\gamma_{jl}\} \rho_{j,l}(t). \quad (8)$$

Here, as above, the population relaxation rates γ_j are nonzero only for donor and acceptor states. The probability $P_{j_{\text{A}},\text{in}}(t) = \rho_{j_{\text{A}},j_{\text{A}}}(t)$ needed in (6) is obtained from (8) using the initial condition $\hat{\rho}(t=0) = |\phi_{\text{in}}\rangle\langle\phi_{\text{in}}|$.

In the model of Fig. 1b, all bridge site-energies are taken equal ($E_{j_{\text{B}}}^{(\text{B})} = \alpha_{\text{B}}$), and similarly for the bridge nearest-neighbor couplings ($V_{j_{\text{B}},j_{\text{B}}+1}^{(\text{B},\text{B})} = \beta_{\text{B}}$), and for the donor-bridge and acceptor-bridge couplings ($V_{1_{\text{D}},1_{\text{B}}}^{(\text{D},\text{B})} = V_{2_{\text{D}},2_{\text{B}}}^{(\text{D},\text{B})} = V_{N_{\text{B}},j_{\text{A}}}^{(\text{B},\text{A})} \equiv V$).

The complex energies of the donor sites (1_D and 2_D) and of the acceptor site (j_A) are taken to be $\alpha_D - i(1/2)\gamma_D$, α_D , and $\alpha_A - i(1/2)\gamma_A$ (where $\alpha_D = \alpha_A$). Using (6) and (7), this leads to

$$\int_0^{\infty} dt P_{j_A, \text{in}}(t) = \hbar \sum_{q=1}^N \frac{|R_{j_A, \text{in}}^{(q)}|^2}{2\Gamma_q} + 2\hbar \sum_{q>q'}^N \text{Im} \left\{ \frac{R_{j_A, \text{in}}^{(q)} \{R_{j_A, \text{in}}^{(q')}\}^*}{(\varepsilon_q - \varepsilon_{q'}) - i(\Gamma_q + \Gamma_{q'})} \right\}, \quad (9)$$

where $\mathcal{E}_q = \varepsilon_q - i\Gamma_q$ are the eigenenergies of the dissipative Hamiltonian, and $R_{fi, \text{in}}^{(q)} = \langle \phi_{fi} | X_q^{(R)} \rangle \langle X_q^{(L)} | \phi_{\text{in}} \rangle$. We solve (8) using $\hat{\rho}(t=0) = |\phi_{\text{in}}\rangle \langle \phi_{\text{in}}|$ or $|\phi_{\text{in}}^*\rangle \langle \phi_{\text{in}}^*|$ with $\gamma_{D(A)}/2 > 0$. Donor coherence relaxation is accounted for by taking $\gamma_{12} > 0$. We calculate the yield asymmetry using (6) and (7).

In Fig. 2, we show the computed asymmetry \mathcal{A} , (7) vs the bridge length for resonant ($\alpha_B - \alpha_{D(A)} = 0$) and nonresonant ($\alpha_B - \alpha_{D(A)} = 3$ eV) bridges, for different donor and acceptor lifetimes, and in the absence of dephasing. The parameters used (donor and acceptor lifetimes in the range 3–30 fs and tight-binding couplings of order 1 eV) are reasonable for nonfluorescing excited electronic states with covalent intersite bonding. It should be emphasized, however, that other values of lifetimes and couplings will generate yield asymmetries. The yield asymmetry

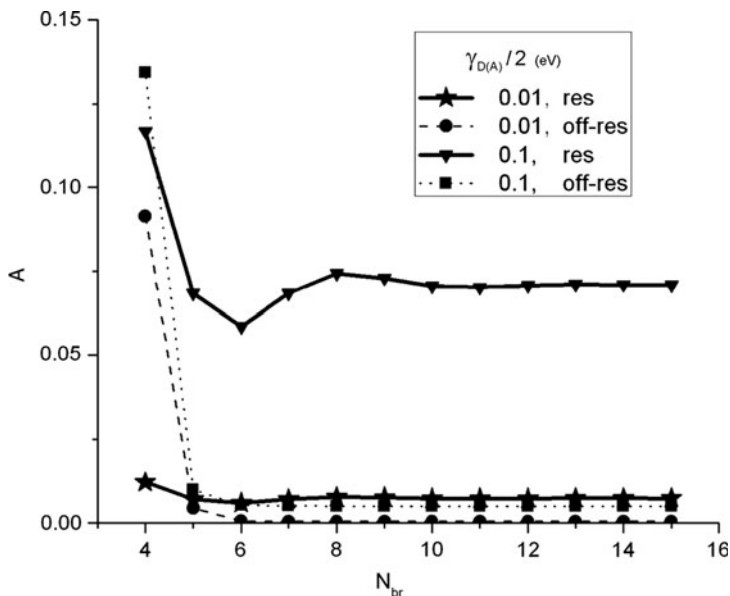


Fig. 2 Yield asymmetry vs bridge length N_{br} , for the model of Fig. 1b, for resonant ($\alpha_B - \alpha_{D(A)} = 0$, squares, solid lines), and off-resonant ($\alpha_B - \alpha_{D(A)} = 3$ eV, circles, dashed lines) bridges. Stars and circles correspond to $\gamma_D = \gamma_A = 0.02$ eV, and triangles and squares correspond to $\gamma_D = \gamma_A = 0.2$ eV. The other parameters are $\beta_B = 0.5$ eV, $V = 1.0$ eV, $\theta = \pi/4$, and $\gamma_{ij} = 0$ for $i \neq j$

becomes independent of length for long bridges and is about an order of magnitude larger in the resonant case compared to the off-resonant case. \mathcal{A} increases with decreasing donor and acceptor lifetimes in both resonant and off-resonant cases. More detailed findings indicate that the donor lifetime effect is dominant in this regard. For parameters in the range studied, and for sufficiently short donor lifetimes, effects are found of the order observed in the experiments ($\sim 10\%$ for a resonant bridge [36] and $< 1\%$ in the off-resonant case [37]). The asymmetry disappears for extremely short donor (acceptor) lifetimes.

Figure 3 shows the effect of dynamic interactions with the thermal environment, in particular the effect of decoherence arising from nuclear motion. Figure 4 shows the effect of donor decoherence. The figure plots \mathcal{A} vs γ_{12} for resonant and nonresonant bridges though increasing decoherence eventually destroys the asymmetry, the loss of yield asymmetry arises only for unphysical large γ_{12} for the resonant-bridge case. Similar results are obtained in the presence of bridge decoherence.

The simple model of Fig. 1b is not expected to reproduce the experimental results of (6) and (7) quantitatively, but it does yield three distinctive and robust features that characterize our model in a relatively large range of system parameters. These include an independence of bridge length for long molecular bridges, an asymmetry that increases as donor lifetime shortens (within physically

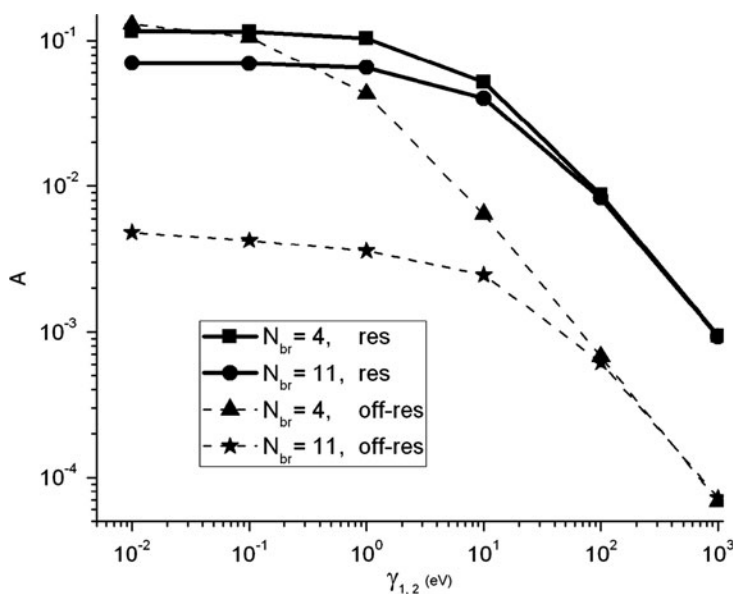
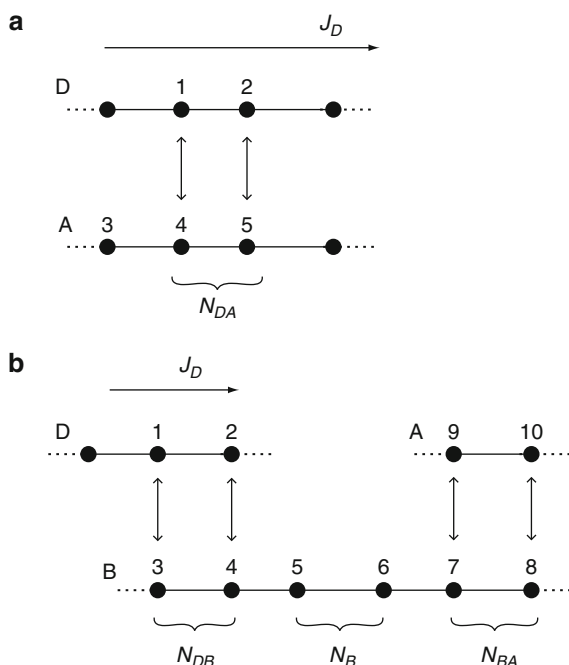


Fig. 3 The yield asymmetry vs donor decoherence (model of Fig. 1b) for resonant and nonresonant bridges of different lengths. Parameters used (except γ_{12}) are the same as in Fig. 2 with $\gamma_D = \gamma_A = 0.2$ eV. The behavior of the asymmetry with respect to donor decoherence shown above is obtained for a wide range of values of $\gamma_{D(A)}$

Fig. 4 Simple models of current transfer. In both models a driving current J_D in wire D is transferred to wire A. In (a) the transfer is direct while in (b) it is mediated by a “bridge” wire B



reasonable values), and an asymmetry of yield that persists in the presence of decoherence. For a reasonable range of system parameters, the calculated asymmetry is of the same order as that seen experimentally for reversed circular polarization. Importantly, the resilience of this asymmetry to decoherence rationalizes the observed behavior in condensed thermal environments. Introduction of site-energy and nearest-neighbor coupling disorder in the Hamiltonian can reduce the magnitude of the asymmetry for resonant transport. Indeed, the experiments of [36] find that the asymmetry disappears when, in a molecular layer of a given handedness, as few as 1% of the molecules are substituted by molecules of the opposite handedness.

The model of Fig. 1b does not rely on the bridge's chiral structure, but rather on the nature of the donor excitation and the proximity effects (derived from the chiral structure) that determine the nature of the donor–bridge coupling. These proximity effects are apparent in chiral molecules and nanostructures. We suggest that electron donor–bridge–acceptor devices could carry electron phase information by optically creating angular-momentum-polarized electron states and by manipulating the bridge's connectivity to the donor and acceptor. Semiconductor nanoparticles linked by DNA or helical polypeptides are particularly promising [42]. In many of these imagined device systems, the experiments involve generation and observation of steady-state currents. It is thus important to extend current-transfer theory to the steady-state regime, as we describe next [39, 40].

4 Steady-State Transport Analysis

In the previous section, we examined the time evolution that follows excitation of a ring current in the donor (Fig. 1a). The ring state $|M_D\rangle$ is an eigenstate of the donor moiety with the eigenvalue $E(K_{M_D}) = \alpha_D + 2\beta \cos(K_{M_D}a)$ and with time evolution $|M_D\rangle e^{-iE(K_{M_D})t/\hbar}$, where $K_{M_D} = 2\pi M_D/(aN_D)$ is quantized. Hence, the injection energy of the electron was determined by the energy of a photo-prepared donor state. We now examine a case where the donor (D) is a wire that is coupled to an acceptor (A) wire directly or through a bridging (B) wire. The D wire is restricted to carry a constant current j_D and we explore the steady state response of the rest of the system. All charge carriers in the system originate from this wire. The injection energy can now take any value within the D-wire energy band.

The models displayed in Fig. 4a, b that respectively represent the direct (DA) and the bridge-mediated (DBA) systems correspond to a tight-binding Hamiltonian with nearest neighbor couplings indicated by the arrows connecting different sites. In the DA system we investigate current transfer from D to A through couplings between N_{DA} pairs of neighboring atoms on different wires. In the DBA system we examine the charge transfer from D to A through B. In this case, N_{DB} , N_{BA} denote, respectively, the number of site pairs connecting the wires D and B and N_B denotes the number of sites on B between these coupling regions.

As in the time-dependent case, the relevant sites on the driver wire are those directly coupled to the A wire of the DA system or to the B wire of the DBA system (e.g., sites 1 and 2 of Fig. 4a, b). The driving conditions on these sites are represented by the Bloch wave:

$$|\psi_D(t)\rangle = c_1(t)|1\rangle + c_2(t)|2\rangle = (\bar{c}_1|1\rangle + \bar{c}_2|2\rangle)e^{-(i/\hbar)Et}, \quad (10a)$$

$$\bar{c}_2 = \bar{c}_1 e^{ik_D a}, \quad (10b)$$

where a is the lattice constant and k_D is the wave vector of the D wire that is related to the injected electron energy E by the dispersion relation

$$E = \alpha_D + 2\beta_D \cos(k_D a). \quad (11)$$

The time dependent Schrödinger equation for the Hamiltonian in (1), (2) of the DBA system (or its equivalent for the DA system) in the site representation is

$$\hbar \frac{dc_n}{dt} = -iE_n c_n - i \sum_{\alpha} V_{n,\alpha} c_{\alpha}, \quad (12)$$

where α sums over all sites that couple with coupling element $V_{n,\alpha}$ to site n .

The infinite extent of the bridge and acceptor wires in Fig. 4a, b provides an effective dissipation mechanism. This mechanism allows the systems to reach a steady state that yields solutions at long times of the form

$$c_n(t) = \bar{c}_n e^{-iEt/\hbar} \quad (13)$$

for all the amplitudes of the A and B wires. Inserting (13) into (12) leads to a set of equations for the steady-state amplitudes \bar{c}_n :

$$0 = -i(E_n - E)\bar{c}_n - i \sum_{\alpha} V_{n,\alpha} \bar{c}_{\alpha}. \quad (14)$$

Equation (14) defines the steady-state wavefunction of the DBA (or DA) system, $|\Psi(t)\rangle = \sum_{n \in B, A} c_n(t) |n\rangle$. Terms involving coefficients on the driving wire appear in the inhomogeneous part of these equations.

In the time-dependent case (Sect. 3), we assigned (real and positive) population-relaxation rates γ_j to some sites by replacing E_j by $(E_j - (1/2)\gamma_j)$ for these sites in (1), (2), and (12). In the steady-state approach, the infinite set of (12) and (13) becomes finite by separating the overall system into interior and exterior parts, and accounting for the effect of the latter on the dynamics of the former by introducing energy-dependent “self energy” terms. In particular, in Fig. 4a, the effect of an exterior part defined as the infinite linear chain extending right to the cut-off site 5 on A is provided by modifying (14):

$$0 = -i(E_A + \Sigma_A(E) - E)\bar{c}_5 - i\beta_A \bar{c}_4 - iV_{AD}\bar{c}_2, \quad (15)$$

where $\Sigma_A(E)$ is the self energy of a one-dimensional tight binding wire, with real and imaginary parts $\Lambda_A(E)$ and $-i(\gamma_A(E)/2)$ respectively,

$$\Sigma_K(E) = \frac{E - E_K - \sqrt{(E - E_K)^2 - 4\beta_K^2}}{2} \equiv \Lambda_K(E) - \frac{i}{2}\gamma_K(E). \quad (16)$$

$K = B, A$

The finite set of steady-state equations for the model in Fig. 4b, for example, is

$$\begin{aligned} 0 &= -i(E_B + \Sigma_B(E) - E)\bar{c}_3 - i\beta_B \bar{c}_4 - iV_{BD}\bar{c}_1 \\ 0 &= -i(E_B - E)\bar{c}_4 - i\beta_B \bar{c}_3 - i\beta_B \bar{c}_5 - iV_{BD}\bar{c}_2 \\ 0 &= -i(E_B - E)\bar{c}_5 - i\beta_B \bar{c}_4 - i\beta_B \bar{c}_6 \\ 0 &= -i(E_B - E)\bar{c}_6 - i\beta_B \bar{c}_5 - i\beta_B \bar{c}_7 \\ 0 &= -i(E_B - E)\bar{c}_7 - i\beta_B \bar{c}_6 - i\beta_B \bar{c}_8 - iV_{BA}\bar{c}_9 \end{aligned}$$

$$\begin{aligned}
0 &= -i(E_B + \Sigma_B(E) - E)\bar{c}_8 - i\beta_B\bar{c}_7 - iV_{BA}\bar{c}_{10} \\
0 &= -i(E_A + \Sigma_A(E) - E)\bar{c}_9 - i\beta_A\bar{c}_{10} - iV_{AB}\bar{c}_7 \\
0 &= -i(E_A + \Sigma_A(E) - E)\bar{c}_{10} - i\beta_A\bar{c}_9 - iV_{AB}\bar{c}_8
\end{aligned} \tag{17}$$

or

$$\mathbf{M}\mathbf{c} = \mathbf{d}, \tag{18}$$

where \mathbf{c} is the column vector transpose $(\bar{c}_3, \bar{c}_4, \bar{c}_5, \bar{c}_6, \bar{c}_7, \bar{c}_8, \bar{c}_9, \bar{c}_{10})$, \mathbf{M} is the matrix multiplying this vector in (17), and \mathbf{d} is the driving vector transpose $(iV_{BD}\bar{c}_1, iV_{BD}\bar{c}_2, 0, 0, 0, 0, 0, 0)$.

Inverting \mathbf{M} in (18) and using (13) produces all of the steady-state coefficients in terms of the steady-state amplitude \bar{c}_1 . In the next section, we use these coefficients to evaluate all of the currents in the system in terms of the driving current J_D .

5 Steady-State Currents and Asymmetry Factors

The steady-state (SS) equation for the population on site n derived from (12)–(14) with $E_n + \Sigma_n(E)$ replacing E_n (when n is an edge site) is:

$$0 = \left(\frac{d|c_n(t)|^2}{dt} \right)_{SS} = \sum_{\alpha} \frac{2V_{n,\alpha}}{\hbar} \text{Im}(c_{\alpha}c_n^*) - \frac{\gamma_n(E)}{\hbar} |c_n|^2 \delta_{n,\text{edge}}. \tag{19}$$

The sum in (19) runs over all sites coupled to site n with coupling $V_{n,\alpha}$ ($V_{n,\alpha} = \beta_K$ if n and α are nearest neighbors (NN) on the same wire K ; $V_{n,\alpha} = V_{K,K'}$ if these sites are NN belonging to different wires K and K'). $\gamma_n(E) = -2\text{Im}\Sigma_n(E)$ contributes only if site n is an edge site on A ($\gamma_n = \gamma_A$) or B ($\gamma_n = \gamma_B$).

Equation (19) implies that the net current from site $n-1$ to site n on wire K is

$$J_{K(n-1 \rightarrow n)} = \frac{2\beta_K}{\hbar} \text{Im}(c_{n-1}c_n^*) \tag{20}$$

and the current out of the system at the edge site n on K is

$$J_{K(n \rightarrow \text{out})} = \frac{\gamma_K(E)}{\hbar} |c_n|^2. \tag{21}$$

We denote current from left to right as positive. In addition, positive assignments are also chosen for the $D \rightarrow A$, $D \rightarrow B$, and $B \rightarrow A$ directions.

The currents out of the A wire to the right and to the left in the DA system are

$$J_A^{right} = \frac{2\beta_A}{\hbar} \text{Im} \left(c_{eright-1} c_{eright}^* \right) = \frac{\Gamma_A(E)}{\hbar} |c_{eright}|^2, \quad (22)$$

$$J_A^{left} = \frac{2\beta_A}{\hbar} \text{Im} \left(c_{eleft+1} c_{eleft}^* \right) = \frac{\Gamma_A(E)}{\hbar} |c_{eleft}|^2, \quad (23)$$

where *eleft* and *eright* denote respectively the left and right edge sites in the interior part of the A wire. Symmetry requires that $J_A^{right}(k_D) = J_A^{left}(-k_D)$. A nonzero current asymmetric factor for the DA model of Fig. 4a denotes current transfer from D to A:

$$\mathcal{A}_1 = \frac{J_A^{left} - J_A^{right}}{J_A^{left} + J_A^{right}} \quad (24)$$

For the DBA model in Fig. 4b, we consider the total charge transmitted to the A wire and measured by $J_A^{total} \equiv J_A^{left} + J_A^{right}$ with regard to the direction of the driving current. Hence, in the case of the DBA system, we examine the following current asymmetric factor:

$$\mathcal{A}_2 = \frac{J_A^{total}(-k_D) - J_A^{total}(k_D)}{J_A^{total}(-k_D) + J_A^{total}(k_D)} \quad (25)$$

that is directly related to the observations in [36, 37].

The following normalized differences are also of use:

$$\overline{\mathcal{A}}_1 = \frac{J_A^{left} - J_A^{right}}{|J_D|}, \quad (26)$$

$$\overline{\mathcal{A}}_2 \equiv \frac{J_A^{total}(-k_D) - J_A^{total}(k_D)}{|J_D|}, \quad (27)$$

where J_D is the donor (driving) current.

The current distribution is shown in Fig. 5 for the A wire of the inset. Here, and below, the coupling between the NN sites on each wire (β_D , β_B , and β_A) are chosen to be 0.1 and all other energy units are determined accordingly. The driving current on the D wire induces left and right going currents at the left and right edge sites, respectively, on the A wire. The current transfer character of the process is expressed by the larger leftward current with respect to the rightward current on A displayed in Fig. 5.

Figure 6 shows the current asymmetry factor \mathcal{A}_1 of (24), displayed vs the number of links, N_{DA} , connecting the D and A wires in a DA system of Fig. 4a. The inset shows the same data, presented in terms of the normalized difference $\overline{\mathcal{A}}_1$ of (26), plotted vs N_{DA} . Figure 7 shows the corresponding property $\overline{\mathcal{A}}_2$ of (25) for the DBA system of Fig. 4b displayed vs. the number of links, N_{DB} , connecting the

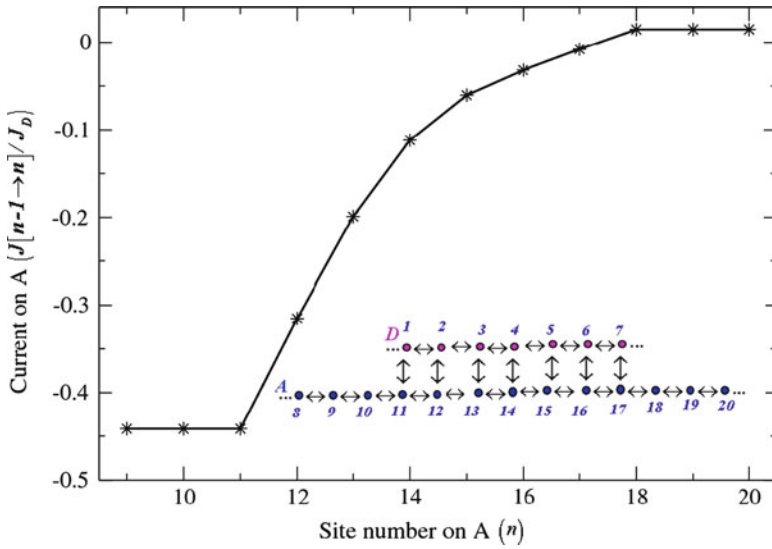


Fig. 5 Wire A current distribution for the DA system shown in the *inset*, characterized by seven-sites coupling between the D and A wires. Here, $|J_D| = 1$, $E_D = E_A = 0$, $\beta_D = \beta_A = 0.1$, $V_{DA} = 0.01$, and the injection energy is $E = -0.17$. The phase $k_{DA} = \arccos[(E - E_D)/2\beta_D]$ is taken positive, implying that the driving current goes from left to right

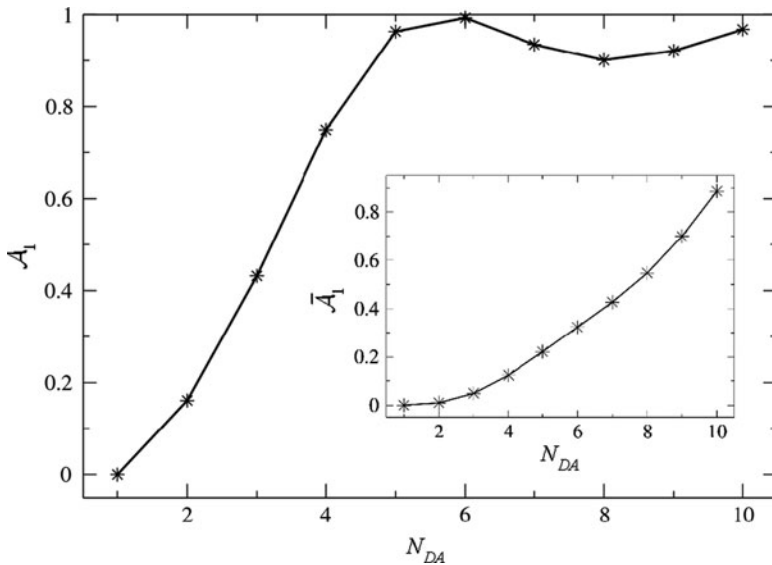


Fig. 6 The current asymmetry factor \mathcal{A}_1 as a function of the number of links, N_{DA} connecting the D and A wires in the DA system displayed in Fig. 4a. The *inset* shows the same data, presented in terms of $\bar{\mathcal{A}}_1$ plotted as a function of N_{DA} . Parameters are similar to those in Fig. 5

D and B wires. The inset shows the same data, presented in terms of the normalized difference $\overline{\mathcal{A}}_2$ of (27), plotted against N_{DB} . In the case that only one site couples directly to the D wire, no information about the direction of the electrons on the D wire is transferred to the A wire in either systems. Hence, in the case of the DA system $\mathcal{A}_1 = \overline{\mathcal{A}}_1 = 0.0$ and in the case of the DBA system, $\mathcal{A}_2 = \overline{\mathcal{A}}_2 = 0.0$. In both systems, asymmetry increases and then saturates near 1 (when the response current becomes nearly unidirectional) as the number of links to the D wire increases.

Substantial current transfer asymmetry is indicated by the large asymmetry factors in Figs. 6 and 7 for both direct and bridge-assisted transfer. The calculated asymmetry factors are much smaller for short bridges. The steady-state scenario is different from the transient process considered in Sect. 3 where, for short pulses, reflection does not set in appreciably during the process lifetime.

An important factor discussed in Sect. 3 [38] is the energy dependence of current transfer. The results displayed in Figs 5–7 correspond to resonant transmission in which site energies in all wires are equal ($E_D = E_B = E_A$). The equivalent superexchange mechanism for nonresonant transfer would be the DBA system where the site energies of the B (“bridge”) wire are different from the site energies of the “donor” and “acceptor” wires, $E_B \neq E_D = E_A$. In the calculation below, we take $E_D = E_A = 0$, $\beta_D = \beta_A = \beta_B = 0.1$, an injection energy $E = -0.17$, and display the current transfer dependence on the B wire energy, E_B . The energy bands in these tight-binding wires range within $E_K \pm 2\beta_K$

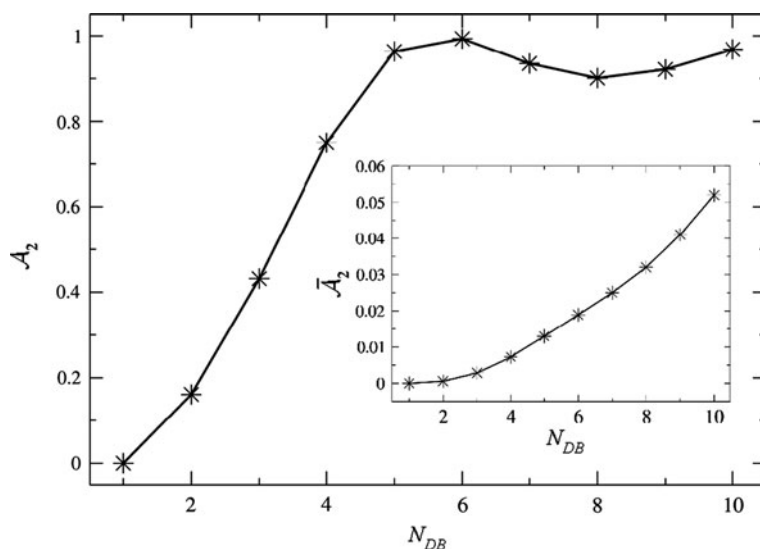


Fig. 7 Current asymmetry \mathcal{A}_2 as a function of the number of links N_{DB} connecting the D and B wires in the DBA system displayed in Fig. 4b. The system parameters are $E_D = E_B = E_A = 0$, $\beta_D = \beta_B = \beta_A = 0.1$, $V_{DB} = V_{BA} = 0.01$, $N_{BA} = 2$, and the injection energy is $E = -0.17$. The same data, presented as $\overline{\mathcal{A}}_2$ vs N_{DB} are shown in the inset

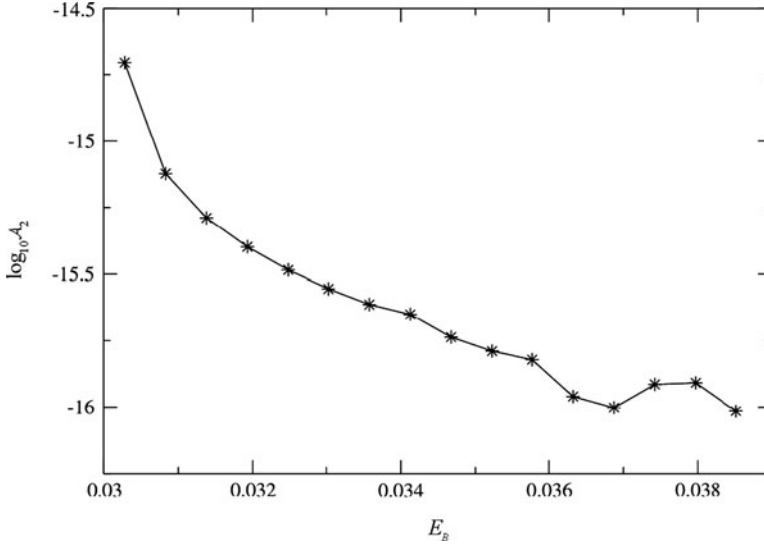


Fig. 8 The current asymmetry factor \mathcal{A}_2 as a function of the bridge site energy E_B for the DBA system in the off-resonance regime, $E_B > 0.03$. The parameters used in this calculation are $E_D = E_A = 0$, $\beta_D = \beta_B = \beta_A = 0.1$, $V_{DB} = V_{BA} = 0.01$, $E = -0.17$, $N_{DB} = 3$, $N_B = 2$, $N_{BA} = 2$. Coarse grained averaging was used to reduce numerical errors that results from computing small differences between relatively large numbers

($K = D, B, A$). Hence, the nonresonant transfer sets in as E_B decreases below $E_B = -0.37$ or increases above $E_B = 0.03$.

Figure 8 shows the current-transfer process in the DBA system for the off-resonance regime, $E_B > 0.03$. In Fig. 8 the current transfer property decays quickly as we go into the off-resonance transfer regime. We find a strong exponential damping of the current transfer property expressed by the asymmetry factor \mathcal{A}_2 .

6 Steady-State Current Transfer with Dephasing

As discussed in Sect. 3, it is of interest to examine the effect of dephasing on the efficiency of current transfer. We assume that the driving wire D remains coherent [i.e., the Bloch wave persists, (10)], and study the effect of dephasing on the “acceptor” (A) wire in the DA system and the “bridge” wire (B) in the DBA system. For this purpose, we shift from the local-site representation of the steady-state analysis to the DM representation and to the ensuing Liouville-space dynamics. Within the DM framework, we can study effects of “pure” dephasing in which nondiagonal elements of the DM are damped while the population (diagonal elements) dynamics is not affected.

The transition from the Schrödinger equation description, $i\hbar d|\Psi\rangle/dt = \hat{H}|\Psi\rangle$, of a closed quantum mechanical system to a Liouville space description, $i\hbar d\hat{\rho}/dt = [\hat{H}, \hat{\rho}]$, is useful. To explore dephasing effects in particular, the DM elements $\rho_{nm} = c_n c_m^*$ of our tight-binding model in the site representation can be obtained using (12). We use (13) to deduce that, at steady state, $d\rho_{nm}/dt = 0$. Furthermore, population damping enters in the time evolution of diagonal density-matrix elements as $d\rho_{nn}/dt = \dots - \gamma_n \rho_{nn}$ and in the corresponding equations for nondiagonal elements as $d\rho_{nm}/dt = \dots - (1/2)(\gamma_n + \gamma_m)\rho_{nm}$ (Sect. 3). This also holds in steady-state situations involving infinite wire systems, where apparent damping results from the imaginary part of the self energy of edge sites, as discussed in Sect. 3, i.e., $d\rho_{nm}/dt = 0 = \dots - (1/2)(\gamma_n(E) + \gamma_m(E))\rho_{nm}$.

We follow the procedure of Segal and Nitzan [43, 44] to implement the driving conditions on the D wire in these steady-state Liouville equations [39, 40]. We now describe results that show the effect of dephasing on current-transfer processes. In these results, we assigned dephasing rates $\gamma_n = \gamma$ to the N_{DA} sites of the A wire that are linked to the D wire in the DA system (Fig. 4a) and to the $N_{DB} + N_B + N_{BA}$ sites on the B wire that connect between the D and A wires in the DBA system (Fig. 4b).

Figure 9 shows the current transfer process in the presence of dephasing in the case of the DA and DBA systems, respectively. As observed above (Sect. 3), while

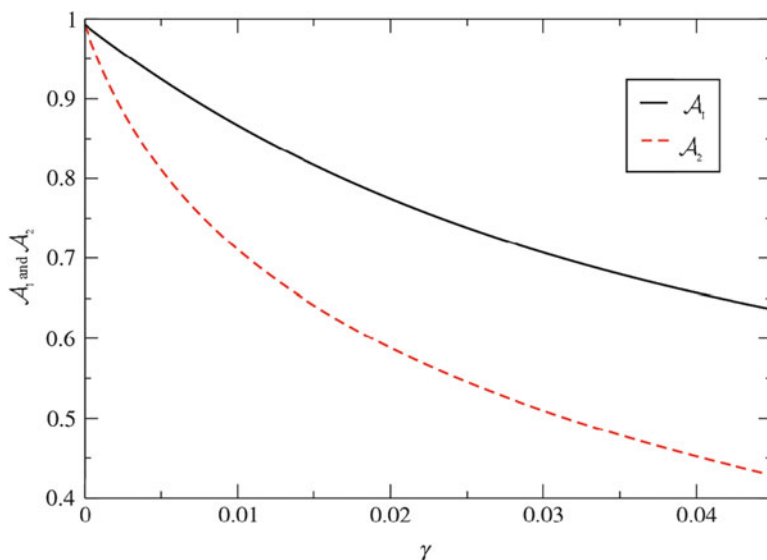


Fig. 9 The current asymmetry factors \mathcal{A}_1 and \mathcal{A}_2 as a function of the dephasing rate γ . The *solid line* is \mathcal{A}_1 for a DA system (Fig. 4a) characterized by the parameters $N_{DA} = 6$, $V_{DA} = 0.01$. The phase $k_{DA} = \arccos\left(\frac{E-E_D}{2\beta_D}\right)$ was taken positive, implying leftward driving current on the D wire. The *dashed line* is \mathcal{A}_2 for a DBA system (Fig. 4b) characterized by the parameters $N_{DB} = 6$, $N_B = 3$, $N_{BA} = 1$, $E_B = 0$, $\beta_B = 0.1$, $V_{DB} = V_{BA} = 0.01$. For both systems, $E_D = E_A = 0$, $\beta_D = \beta_A = 0.1$, and $E = -0.17$

the current transfer efficiency drops with increasing γ , the effect persists up to relatively large values of the dephasing rate (of the order of other energetic parameters in the system such as NN coupling in the wires).

7 Conclusions

Current transfer shifts both charge and momentum from donor to acceptor. We have reviewed time-dependent [38] and steady-state [39, 40] descriptions of current transfer through chiral bridges [36, 37]. In the tight-binding models, current transfer arises from coherent interferences between resonant or tunneling paths. This kind of interference has received attention in recent studies of molecular wires and nanodots [45–50].

In the models reviewed here, one-dimensional chains represent the donor (D), bridge (B), and acceptor (A) moieties. In the first model described here, this current is time dependent, and the time evolution of the system is computed. In the second model, this driving current is constant, and a steady-state current is computed.

In the time-dependent analysis, we address the yield asymmetry of the irreversible flux from the acceptor (A) wire for opposite directions of currents on D. This calculated yield-asymmetry peaks for short bridges and is independent of length for the long bridges. Moreover, the asymmetry is larger in the resonant case, in which the site energies of the D, B, and A wires are equal, compared to the off-resonant case where the B wire site energy is different from the D and A site energies. These results suggest that ET yield asymmetries may be used to distinguish between resonant and superexchange charge-transfer mechanisms. Moreover, the time-dependent calculations indicate that the yield asymmetry increases as the D wire lifetime shortens.

In the steady-state analysis of a donor wire that is coupled directly to an acceptor wire (the DA system), the direction of current on D is transferred to A. In this case, we address the asymmetry in the left and right currents on the A wire. This calculated asymmetry increases with the number of links between the D and A wires and then saturates near 1. In the steady-state analysis of the indirect transfer (the DBA system), we address the asymmetry in total charge transferred from D to A with respect to the direction of the driving current on D. In a similar manner to the case of direct transfer, this asymmetry increases with the number of links between the D and B wires and then saturates near 1. These large asymmetry factors in the steady-state approach indicate substantial current transfer in both the direct and the bridge-assisted transfers. This calculated asymmetry in the total charge transfer in the case of the DBA system damps exponentially with the site energy of the bridge as transport enters the off-resonance regime.

For both time-dependent and steady-state models, coherent dephasing is taken into account by phenomenological terms in the off diagonal time derivatives of the DM elements that appear in the Liouville dynamics. In the time dependent model, increasing the donor or bridge decoherences decreases the yield asymmetry and

eventually destroys it only for unphysically large dephasing constants. In a similar manner, in the steady-state analysis, both the asymmetry in the left and right currents (in the DA system) and the asymmetry in the total charge transferred from D to A (in the DBA system) drop with increasing dephasing. As in the time dependent case, the effect of current transfer in the steady-state approach persists up to relatively large values of dephasing rates.

The time-dependent and steady-state models reviewed here can also be used to analyze the current transfer in a setup of a ring molecule attached to a current carrying molecular wire. In this setup, the current in the linear wire would drive a circular current in the ring molecule that may be detected by its magnetic field [51].

Acknowledgments This research was supported by the National Science Foundation (CHE-1012357, DNB), the Israel Science Foundation, the German-Israel Foundation and the ERC and the US-Israel Binational Science Foundation (AN), the University of Cyprus (SSS) and the Israel Ministry of Science for a fellowship received under the program for Progressing Women in Science (VBM).

References

1. Marcus RA, Sutin N (1985) *Biochim Biophys Acta* 811:265
2. Jortner J, Ratner MA (1997) *Molecular electronics*. Blackwell Science, Oxford
3. Kuznetsov AM, Ulstrup J (1999) *Electron transfer in chemistry and biology*. Wiley, Chichester, UK
4. Jortner J, Bixon M (eds) (1999) *Electron transfer: from isolated molecules to biomolecules*, vol 106–107, *Advances in chemical physics series*. Wiley Interscience, New York
5. May V, Kuhn O (2000) *Charge and energy transfer dynamics in molecular systems*. Wiley-VCH, Berlin
6. Balzani V (ed) (2001) *Electron transfer in chemistry*, vol 1–5. Wiley-VCH, Weinheim
7. Nitzan A (2006) *Chemical dynamics in condensed phases*. Oxford University Press, Oxford
8. Skourtis SS, Waldeck DH, Beratan DN (2010) *Annu Rev Phys Chem* 71:461
9. Beratan DN, Skourtis SS, Balabin IA, Balaeff B, Keinan S, Venkatramani R, Xiao D (2009) *Acc Chem Res* 42:1669
10. Hod O, Rabani E, Baer R (2006) *Acc Chem Res* 39:109
11. Galperin M, Nitzan A (2005) *Phys Rev Lett* 95:206802
12. Galperin M, Nitzan A (2006) *J Chem Phys* 124:234709
13. Pfeifer T (2006) *Nat Phys* 2:297
14. Silberberg Y (2004) *Nature* 430:624
15. Marangos JP (2005) *Nature* 435:435
16. Hentschel M, Kienberger R, Spielmann Ch, Reider GA, Milosevic N, Brabec T, Corkum P, Heinzmann U, Drescher M, Krausz F (2001) *Nature* 414:509
17. Niikura H, Légaré F, Hasbani R, Bandrauk AD, Yu Ivanov M, Villeneuve DM, Corkum PB (2002) *Nature* 417:917
18. Drescher M, Hentschel M, Kienberger R, Uiberacker M, Yakovlev V, Scrinzi A, Westwalbesloh Th, Kleineberg U, Heinzmann U, Krausz F (2002) *Nature* 419:803
19. Niikura H, Légaré F, Hasbani R, Yu Ivanov M, Villeneuve DM, Corkum PB (2003) *Nature* 421:826
20. Itatani J, Levesque J, Zeidler D, Niikura H, Pépin H, Kieffer JC, Corkum PB, Villeneuve PB (2004) *Nature* 432:867

21. Kienberger R, Goulielmakis E, Uiberacker M, Baltuska A, Yakovlev V, Bammer F, Scrinzi A, Westerwalbesloh Th, Kleineberg U, Heinzmann U, Drescher M, Krausz F (2004) *Nature* 427:817
22. Goulielmakis E, Uiberacker M, Kienberger R, Baltuska A, Yakovlev V, Scrinzi A, Westerwalbesloh Th, Kleineberg U, Heinzmann U, Drescher M, Krausz F (2004) *Science* 305:1267
23. Suzuki T, Minemoto S, Kanai T, Sakai H (2004) *Phys Rev Lett* 92:133005
24. Brixner T, Krampert G, Pfeifer T, Selle R, Gerber G, Wollenhaupt M, Graefe O, Horn C, Liese D, Baumert T (2004) *Phys Rev Lett* 92:208301
25. Itatani J, Zeidler D, Levesque J, Spanner M, Villeneuve DM, Corkum PB (2005) *Phys Rev Lett* 94:123902
26. Kanai T, Minemoto S, Sakai H (2005) *Nature* 435:470
27. Mauritsson J, Johnsson P, Mansten E, Swoboda M, Ruchon T, L'Huillier A, Schafer KJ (2008) *Phys Rev Lett* 100:073003
28. Niikura H, Villeneuve DM, Corkum PB (2005) *Phys Rev Lett* 94:083003
29. Barth I, Manz J, Serrano-Andrés L (2008) *Chem Phys* 347:263
30. Barth I, Manz J, Shigeta Y, Yagi K (2006) *J Am Chem Soc* 128:7043
31. Barth I, Manz J (2006) *Angew Chem Int Ed* 45:2962
32. Nobusada K, Yabana K (2007) *Phys Rev A* 75:032518
33. Lazzeretti P (2000) *Prog Nucl Magn Reson Spectrosc* 36:1–88
34. Steiner E, Fowler PW (2001) *J Phys Chem A* 105:9553
35. Steiner E, Soncini A, Fowler PW (2006) *J Phys Chem A* 110:12882
36. Ray K, Ananthavel SP, Waldeck DH, Naaman R (1999) *Science* 283:814
37. Wei JJ, Schafmeister C, Bird G, Paul A, Naaman R, Waldeck DH (2006) *J Phys Chem B* 110:1301
38. Skourtis SS, Beratan DN, Naaman R, Nitzan A, Waldeck DH (2008) *Phys Rev Lett* 101:238103
39. Ben-Moshe V, Nitzan A, Skourtis SS, Beratan DN (2010) *J Phys Chem C* 114:8005
40. Ben-Moshe V (2009) Calculations of electronic conduction properties of molecular junctions. PhD Thesis, Tel Aviv University
41. Güdde J, Rohleder M, Meier T, Koch SW, Höfer U (2007) *Science* 318:1287
42. Naaman R, Sanche L (2007) *Chem Rev* 107:1553
43. Segal D, Nitzan A (2001) *Chem Phys* 268:315
44. Segal D, Nitzan A (2002) *Chem Phys* 281:235
45. Solomon GC, Andrews DQ, Hansen T, Goldsmith RH, Wasielewski MR, Duyne RPV, Ratner MA (2008) *J Chem Phys* 129:054701
46. Andrews DQ, Solomon DC, Goldsmith RH, Hansen T, Wasielewski MR, Duyne RPV, Ratner MA (2008) *J Phys Chem C* 112:16991
47. Ke SH, Yang WT, Baranger HU (2008) *Nano Lett* 8:3257
48. Begemann G, Darau D, Donarini A, Grifoni M (2008) *Phys Rev B* 77:201406
49. Donarini A, Begemann G, Grifoni M (2009) *Nano Lett* 9:2897
50. Xiao DQ, Skourtis SS, Rubtsov IV, Beratan DN (2009) *Nano Lett* 9:1818
51. Ernzerhof M, Bahmann H, Goyer F, Zhuang M, Rocheleau PJ (2006) *Chem Theor Comput* 2:1291

Spin-Polarized Electron Induced Asymmetric Reactions in Chiral Molecules

Richard A. Rosenberg

Abstract Understanding the origin of chirality in nature has been an active area of research since the time of Pasteur. In this chapter we examine one possible route by which this asymmetry could have arisen, namely chiral-specific chemistry induced by spin-polarized electrons. The various sources of spin-polarized electrons (parity violation, photoemission, and secondary processes) are discussed. Experiments aimed at exploring these interactions are reviewed starting with those based on the Vester–Ulbricht hypothesis through recent studies of spin polarized secondary electrons from a magnetic substrate. We will conclude with a discussion of possible new avenues of research that could impact this area.

Keywords Asymmetry · Chemistry · Chirality · Enantiomeric excess · Spin-polarized electrons

Contents

1	Introduction	280
2	Sources of Spin-Polarized Electrons	282
2.1	Parity Violation	282
2.2	Photoemission	282
2.3	Secondary Electrons	284
3	Experimental Studies	287
3.1	High Energy Electrons	287
3.2	Low-Energy Electrons	288
4	Mechanisms	298
5	Conclusion and Future Work	300
	References	301

R.A. Rosenberg

Advanced Photon Source, Argonne National Laboratory, 9700 S. Cass Avenue, Argonne, IL 60439, USA

e-mail: rar@aps.anl.gov

1 Introduction

In 1874 Pasteur wrote

It is inescapable that asymmetric forces must be operative during the synthesis of the first asymmetric natural products. What might these forces be? I, for my part, think that they are cosmological. The universe is asymmetric and I am persuaded that life, as it is known to us, is a direct result of the asymmetry of the universe or of its indirect consequences. The universe is asymmetric [1].

This conclusion stemmed from his initial work on tartaric acid where he observed that naturally occurring materials rotated the plane of polarized light whereas synthetic materials did not. He noticed that the crystals of sodium ammonium tartrate came in two asymmetric forms that were mirror images of one another. By painstakingly sorting the crystals by hand he found that solutions of one form rotated polarized light clockwise, while the other form rotated light counterclockwise. Pasteur correctly deduced the molecule in question was asymmetric and could exist in two forms that differed only by their “handedness” or chirality.

Eighty years later Miller and Urey fascinated the general public with their experiments that showed that an electrical discharge in a mixture of common gases causes reactions leading to important biological molecules such as amino acids [2, 3]. In more recent years the popular literature has showcased other approaches to produce biological molecules such as irradiation of ices found on interstellar dust grains [4, 5]. The great unanswered question, though, is how does chirality arise and how does this process bear on the origin of life? Still, no consensus has arisen as to what is the most likely scenario. In the 125th anniversary issue of Science Magazine in 2005 the editors posed 125 of the most important unanswered questions. Among these was

What is the origin of chirality in nature? Most biomolecules can be synthesized in mirror-image shapes. Yet in organisms, amino acids are always left-handed, and sugars are always right handed. The origins of this preference remain a mystery.

Much of the effort in this area has been summarized in a number of recent reviews [6–12]. Theories may generally be classified as biotic or abiotic. The basic premise of the former is that chiral selection and homogeneity were an inevitable consequence of the evolution of living matter. Abiotic theories are based on the premise that the development of chirality preceded the origin of life and, according to Bonner [7], can be categorized as chance, determinate, and amplification mechanisms. The first two deal with the origin of a small enantiomeric excess (ee), enhancement of one chiral isomer (enantiomer) over the other, while amplification is concerned with the subsequent development of these ees into pure compounds. Chance mechanisms hypothesize that symmetry breaking at the molecular level occurred via a random process that had an equal probability of producing an excess of a particular enantiomer, while determinate mechanisms presuppose that interaction of a chiral physical force [6] with relevant organic molecules led to

an ee. The asymmetry could be induced by direct synthesis of a particular enantiomer or by preferential destruction of a particular isomer in an initially racemic (equal quantities of both enantiomers) mixture.

This chapter deals with one possible determinate mechanism, i.e., the role spin-polarized electrons might play in inducing an ee in chiral compounds. Of all the determinate mechanisms, probably the most discussed is the application of circularly polarized light (CPL) to induce asymmetry in a photolytic reaction. For a detailed discussion of this area the interested reader is recommended to several reviews in this area [13–17] and, in particular, the recent book by Meierhenrich [18]. For comparative purposes we will briefly go over the salient points of asymmetric chemistry induced by CPL.

Chiral-specific photochemistry using CPL depends on the circular dichroism ($\Delta\epsilon = \epsilon_R - \epsilon_L$) of the reactants, i.e., the differences in the absorption coefficients or right and left CPL. The rate of the reaction depends on the amount of light absorbed so if $\Delta\epsilon > 0$, there will be a bias towards one of the enantiomers leading either to its preferential enhancement or destruction and an ee. The enantiomeric purity of the chiral product is determined by the “anisotropy factor,” g , where $g = \Delta\epsilon/\epsilon$ and $\epsilon = 0.5(\epsilon_R + \epsilon_L)$. For optically active compounds g values are fairly small, ~ 0.01 .

There have been four different types of asymmetric CPL induced reactions discussed in the literature. They may be classified as photoequilibration, direct synthesis, photoisomerization, and photolysis. The ee for the first two mechanisms is limited to $g/2$ or less than 1%, while significantly higher ees are theoretically obtainable for the latter two. Asymmetric photoequilibration results from the different rates for photoconversion of D and L enantiomers if CPL is used. The final equilibrium constant is determined by the enantiomer's extinction coefficient so $[D]/[L] = \epsilon_L/\epsilon_D$. In direct synthesis an optically active product is formed from an inactive precursor [7, 19]. Photoisomerization involves the asymmetric CPL induced conversion of an optically active precursor to an achiral isomer [15, 20]. Perhaps the most discussed mechanism is asymmetric photolysis where preferential absorption of CPL by one enantiomer leads to its destruction, thus leading to an ee in the other enantiomer. Depending on the extent of the reaction, relatively high ees can be expected. Using 182-nm circularly polarized synchrotron radiation, Meierhenrich and coworkers obtained a 2.6% ee of D-leucine after irradiating a racemic mixture for 3 h, resulting in decomposition of 70% of the starting material [21].

Since longitudinally spin polarized electrons (SPEs) [6] are truly chiral particles it is reasonable to expect that they could induce asymmetric reactions in chiral molecules analogous to CPL. This chapter is devoted to reviewing this area with emphasis on recent advances in the field. In the next section we will discuss natural occurring sources of SPEs followed by a review of experiments aimed at discovering their role in chiral-selective chemistry. The following section will address possible mechanisms and we will conclude with a discussion of future research in this area.

2 Sources of Spin-Polarized Electrons

2.1 Parity Violation

In 1956 Lee and Yang suggested that the parity principle might be violated for weak interactions like those involved in β decay of radioactive nuclei [22]. This prediction, which resulted in a Nobel prize, was verified the following year by Wu et al. who demonstrated that the electrons emitted from ^{60}Co nuclei during β decay were longitudinally spin polarized with the spins mainly antiparallel to the direction of propagation (left handed) [23]. If parity is conserved there should be equal numbers of left and right handed electrons produced during the β decay process. It is now thought that parity is violated in all the weak interactions mediated by neutral or charged bosons. Thus, all β decaying radioactive elements are a source of longitudinally SPEs. Since there are numerous such elements in nature, this finding stimulated a large research effort aimed at discovering if such electrons could play a role in chiral-selective chemistry. The results of these studies will be summarized in Sect. 3.1.

2.2 Photoemission

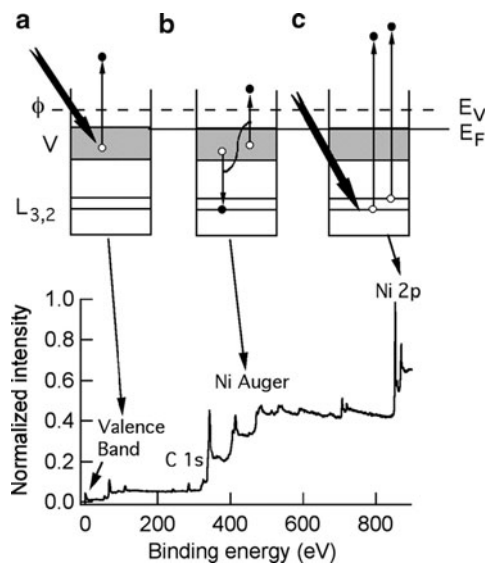
As originally observed by Hertz and later explained by Einstein, electron emission occurs when photons with energy greater than a material's work function irradiate it. The application of this phenomenon led to the development of photoelectron spectroscopy (PES), which is one of the principal methods used to understand chemical and electronic properties of materials. Over the last 40 years advances in technology have also made it possible to determine the spin of the electron and advances in this area have been summarized in several books and reviews [24–28]. A detailed discussion of spin-resolved PES is beyond the scope of this review. The following presents the rudimentary concepts and some illustrative examples.

The basic processes involved in photoemission from a solid are illustrated in Fig. 1. The photon is absorbed by a valence electron (a) or core electron (c) of the N -electron initial state, leading to ejection of that electron into the vacuum and an $(N-1)$ electron final state. By determining the intensity of the emitted electrons as a function of their kinetic energy, one obtains a photoelectron spectrum. The binding energies of the electrons are determined by

$$E_{\text{B}}^{\text{F}} = \hbar\omega - E_{\text{kin}} - \phi,$$

where E_{B}^{F} is the electrons binding energy with respect to the Fermi level, $\hbar\omega$ is the photon energy, E_{kin} is the kinetic energy, and ϕ is the work function. A PE spectrum of a permalloy ($\text{Ni}_{0.8}\text{Fe}_{0.2}$) that had been Ar ion sputtered clean, cooled to 90 K, and

Fig. 1 Top: Basic processes involved in photoemission. The photon is absorbed by a valence electron (a) or core electron (c). In (b) an Auger decay occurs when the core level hole is filled by a valence electron leading to ejection of another valence electron. These processes are illustrated in the XPS spectrum of butanol-dosed permalloy shown below



then dosed with about three monolayers of 2-butanol is shown on the bottom. Process (a) results in the small feature at 0–20 eV binding energy and core level PEs from process (c) are illustrated by the Ni 2*p* electrons as well as the small C 1*s* feature at 285 eV from the adsorbed 2-butanol. Figure 1b shows an Auger decay where the hole in a core level is filled by a valence electron and the excess energy is imparted to another valence electron, which is ejected. The features between 300 and 500 eV arise from such processes.

There are several ways that spin polarization can arise in photoemission of both valence and core level electrons. For crystalline materials the degree of polarization depends on both the energy and angle of observation, i.e., its momentum. Spin polarization arises not only because of initial state effects but also due to spin-dependent interactions among the $N-1$ final-state electrons, spin-orbit effects and spin-dependent elastic exchange scattering. There may also be spin-dependent inelastic scattering leading to spin-polarized secondary electrons, which will be covered in the next section.

The following examples focus on valence level ionization by ultraviolet light, since such processes would produce low energy electrons, which are the most effective at inducing reactions in an adsorbed molecule. There are also many examples of spin-polarized photoemission and Auger electron emission from core levels of both magnetic and nonmagnetic materials [29–35].

The initial state valence electrons of a ferromagnet are unequally populated by majority (\uparrow) and minority (\downarrow) electrons, which result from electron exchange interactions. This can result in fairly substantial spin polarization. For instance, studies of the amorphous alloys $\text{Fe}_{80}\text{B}_{20}$ and $\text{Co}_{77}\text{B}_{23}$ reveal polarization as high as 20% when excited by 35-eV synchrotron radiation [36]. A recent report of Co(100)

films excited by 6.1-eV laser photons showed spin polarizations of up to 35% for electrons with 0.4 eV binding energy [37].

Spin-orbit interactions, resulting from the coupling of the spin to the symmetry of the lattice, can also result in valence level polarized electrons even when there is no net magnetization. Perhaps the best-known example of this is GaAs excited with CPL in the range 1.5–3.6 eV. For σ^+ polarized light only transitions with $\Delta m_j = +1$ are allowed. At the Γ point in the Brillouin zone the sixfold degenerate p band is split into a fourfold degenerate $P_{3/2}$ and a twofold degenerate $P_{1/2}$ band. For light of energy near the bandgap (~ 1.5 eV) the only allowed transitions are from $m_j = -3/2$ (valence band) to $m_j = -1/2$ (conduction band) and from $m_j = -1/2$ to $+1/2$. Polarization arises from the difference in the transition probabilities for these two transitions and is $\sim 40\%$ at threshold (1.5 eV) [38]. This discovery led to the use of GaAs as a source for SPEs for various types of measurements. Polarizations of between 5 and 15% have been measured from gold using CPL in the range 6–9 eV [39]. This property has enabled Naaman and coworkers to study the spin dependence of the transmission of electrons through self-assembled monolayers adsorbed on gold (see chapter by Ron Naaman and Zeev Vager). Spin polarization has also been observed in the case of linear polarized light at normal incidence and normal photoelectron emission for a centrosymmetric cubic crystal, Pt(111). Polarizations of greater than 30% were found in the photon energy range 21–22.4 eV [40]. Spin polarizations approaching 100% have been observed from the outer $P_{3/2}$ levels of adsorbed Kr and Xe excited with circularly polarized synchrotron radiation [41].

2.3 Secondary Electrons

When ionizing radiation interacts with a solid, electrons are produced. The radiation may be in the form of photons, electrons or ions. If these electrons escape into the vacuum without suffering inelastic collisions they are called primary electrons. However, most of the electrons suffer numerous collisions and lose energy in the process. These are the secondary electrons (SEs). The majority of these electrons have very low energy, in the 0–10 eV range. For most materials these electrons are unpolarized. However, if the material is ferromagnetic the SEs can achieve a high degree of polarization. The basic process leading to this is illustrated in Fig. 2a and a typical SE yield curve is shown in Fig. 2b. In a ferromagnet there is an imbalance between the number of majority and minority valence level electrons. For the system in Fig. 2a the majority band is totally filled while the minority band is partially filled. As the electrons scatter in the material there is a higher density of minority band states available for occupation than majority states. Essentially this results in a longer mean free path for majority electrons than minority, which yields a net spin polarization of the former. Although there are subtleties to this model this appears to explain adequately most of the SE polarization results as illustrated in a number of theoretical papers [42–46].

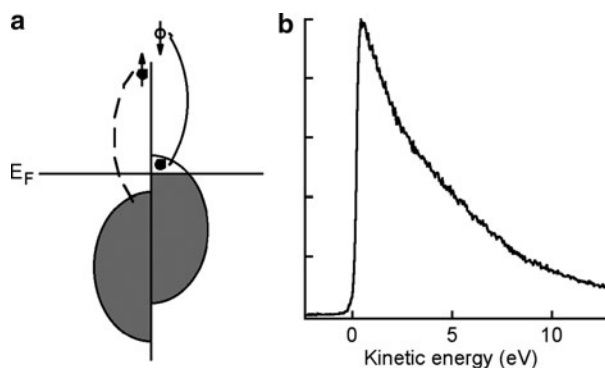
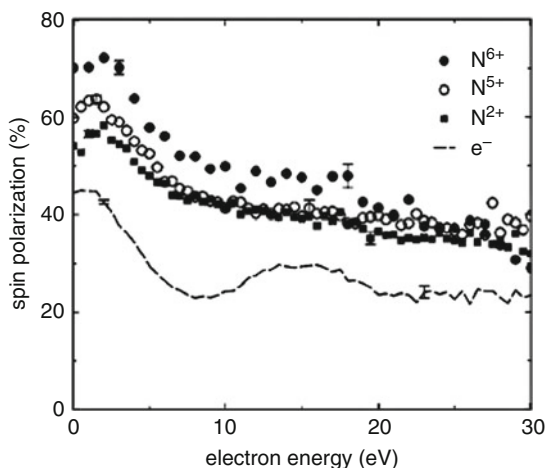


Fig. 2 (a) Schematic illustration of the way preferential scattering of minority electrons leads to a net spin polarization of the majority electrons in the production of secondary electrons in a ferromagnet. (b) Representative secondary electron yield curve from permalloy excited with 1,190 eV X-rays

Fig. 3 Spin polarization of the secondary electrons emitted from an Fe(001) surface following irradiation with 150 keV nitrogen ions in various charge states and 2 keV electrons. Reprinted with permission from [47]. Copyright 2001 by the American Physical Society



There have been numerous experiments performed to measure the SE polarization on a variety of substrates using photons, electrons, or ions. Some results of SE polarization measurements following irradiation of Fe(001) by multicharged nitrogen ions and electrons are shown in Fig. 3 [47]. Note that at higher energies the polarization approaches that of the bcc Fe conduction band electrons (27%) [47] and increases substantially at lower energies as a result of the “spin filter” effect [44]. For ions the polarizations are higher and increase as the charge of the ion increases. As the charge increases more electrons are captured from the conduction band in front of the surface which enhances their contribution to the yield of SEs [47].

It is beyond the scope of this chapter to delve into the details of previous studies on SE polarizations. However, for comparative purposes it is worthwhile to examine the range of experimental results using a variety of projectiles and substrates, which are summarized in Table 1 where the maximum SE spin polarization is presented for a variety of systems. The maximum polarization always occurs at low energies, typically 1–2 eV. Most work has centered on Fe (100) and Fe(110), with maximum polarizations ranging between 17 and 70%. It is worth noting the effect of overlayers on the polarization. For metallic,

Table 1 Summary of experimental studies of secondary electron polarizations

Substrate	Particle (P = photon, E = electron)	Energy (keV)	Maximum SE polarization (%)	Reference
Fe(100)	P	0.06	43	[48]
Co(1010)		0.058	35	
Fe(100)	P	0–10	17	[49]
Fe(100)	N ²⁺ , N ⁵⁺ , N ⁶⁺	150	70	[47]
Fe(100)	E	2	44	[47]
Fe(100)	H ⁺	4–72	65	[50]
Fe(110)	He ⁺	0.5–4	32	[51]
	Ar ⁺		30	
	Xe ⁺		27	
Fe(110)	E	0.05–2.5	30–50	[52]
Fe(110)	E	0.1–1	30–42	[53]
Fe(110)	E	4	50	[54]
FeO			13	
FeO+O ₂			15	
FeO	H ⁺	20	30	[54]
FeO+O ₂			–25	
Fe(110)	E	2	40	[55]
FeO(111)/Fe(110)			–12	
Fe(100)	E	2.5	44	[56]
Fe(100) + Ta			20	
Fe(100)+	E	4	50	[57]
Cr[1–7 ML]			38–20	
Fe(100)+	H ⁺	25	38	[57]
Cr[1–7 ML]			30–22	
Fe _{81.5} B _{14.5} Si ₄	E	0.5	25	[58]
Fe ₈₂ B ₁₂ Si ₆	E	0.4	44	[59]
Fe ₆₀ Ni ₂₀ B ₂₀			44	
Fe ₄₄ Ni ₃₇ B ₁₉			35	
Gd(0001)	E	1	35	[60]
Gd(0001)	P	0.069	22	[61]
+0.2 L O ₂			18	
+3.2 L O ₂			9	
Ni(110)	E	0.4	17	[62]
Permalloy	E	3	17	[63]
Permalloy	E	0.2–2	6–11	[64]

nonmagnetic adsorbates the polarization goes down as expected [56, 57]. Oxygen adsorption can result in a reduction of polarization or even a reversal of it as the result of formation of an FeO layer whose magnetization direction is opposite to that of the substrate [54, 55].

3 Experimental Studies

3.1 High Energy Electrons

3.1.1 The Vester–Ulbricht Hypothesis

Shortly after the discovery of parity violation in nuclear β decay [22, 23], Vester and Ulbricht proposed that these high energy spin-polarized electrons could play an indirect role in chiral-selective chemistry. They hypothesized that the circularly polarized “Bremsstrahlen” photons, produced by impingement of the polarized electrons on matter, could subsequently induce stereoselective synthesis or degradation. Over the next 10–15 years there was a substantial amount of research devoted towards proving whether the “V–U hypothesis” was a viable route for producing chirality in chemical reactions. The general approach was to take a naturally occurring β emitter and use it to irradiate racemic mixtures of chiral molecules and then determine if there was an ee in the products. The activity in this area was surveyed in Bonner’s 1991 review [7] and the overall message was that no compelling evidence could be found to substantiate the V–U hypothesis. Table 2 presents a summary of much of the work discussed by Bonner. For additional details the interested reader should consult this review [7] or the original papers.

Table 2 Summary of experimental work testing the Vester–Ulbricht hypothesis

Reactants	Radioactive source	Irradiation time (years)	Enantiomeric excess?	Reference
D-, L-Tyrosine	$^{90}\text{SrCl}_2$	1.5	Yes	[65]
D-, L-Leucine	$^{90}\text{Sr}-^{90}\text{Y}$	0.3–10.9	No	[66]
D-, L-Tyrosine				
D-, L-Norvaline				
D-, L-Proline				
D-, L-Tryptophan	^{32}P	0.23	Yes	[67]
D-, L-Leucine	^{32}P	0.25–0.34	No	[68]
D-, L-Tryptophan		0.23–1.14	No	
D-, L-Amino acids	^{14}C	12–24	No	[69]
D-, L-Amino acids	^{14}C	17–25	No	[70]
D-, L-Leucine	^{14}C	1	Yes	[71]

3.1.2 Direct Interactions of High-Energy Electrons

Although any irradiation with high energy electrons will produce Bremsstrahlen, some experiments have been conducted which indicated that the electrons themselves could play a direct role in stereoselective chemistry. In research led by Kovacs it was concluded that ^{32}P could induce selective crystallization of L(+)-tartrate in mixtures of sodium ammonium DL-tartrate [72–74]. Akaboshi et al. irradiated crystalline D-, L- and D,L-alanine with β rays/Bremsstrahlen from ^{90}Y and found that radicals were produced at a 14–21% greater rate in D-alanine [75]. These results were confirmed by Conte et al. using ^{90}Y and ^{90}Sr β rays [76, 77]. Akaboshi et al. performed similar experiments using the internal β radiation from ^3H -labeled alanine and also found that radical formation was greater in the D-enantiomer [78].

The first effort to study the direct interaction of artificially produced longitudinally polarized electrons was reported by Bonner et al. who used parallel and antiparallel SPEs, produced in a linear accelerator to study selective degradation in DL-leucine [79]. Although there was some indication of stereoselectivity in some of the measurements, others showed none, so the overall outcome was inconclusive. The effect of Bremsstrahlen radiation was thought not to be a factor [80, 81]. Subsequently Hodge et al. attempted to reproduce the earlier measurements of Bonner, but found no evidence of preferential degradation despite a series of rigorous measurements [82]. The possible reason for the negative results in both sets of measurements was hypothesized to be radioracemization, i.e., the racemization of optically active materials induced by ionizing radiation [83].

The possible role of SEs in conjunction with the above high energy polarized electron experiments was first noted by Walker. He pointed out that any chiral effects of the high energy electrons would be seriously diluted by the unpolarized SEs produced in the samples [84]. Subsequent years saw the research into electron-induced chiral-specific reactions shift to the use of low energy electrons.

3.2 Low-Energy Electrons

3.2.1 Unorganized (Gaseous) Chiral Molecules

In 1980 Farago predicted, on the basis of symmetry arguments, that there should be an asymmetry in the scattering of low energy electrons from chiral molecules that is not due to spin-orbit or exchange interactions [85]. An experimental study followed in which 25 eV unpolarized electrons were scattered from camphor vapor. Spin analysis of the scattered electrons showed no asymmetry within the detection limit ($\sim 0.5\%$) [86]. Subsequent calculations indicated that the cross sections for such scattering would be very small unless spin-orbit or exchange interactions were included [87, 88]. The first successful demonstration of an asymmetry in polarized electron scattering from a chiral molecule came as a result of experiments by

Campbell and Farago [89, 90]. They reported $\sim 0.5\%$ asymmetry in the scattering of 5 eV polarized electrons from camphor. Calculations stimulated by these results pointed out the importance of shape resonances [91] and temporary negative-ion states [92] in the scattering process.

Over the next 15 years considerable theoretical effort was made on the treatment of polarized electron scattering by Thomson, Blum, and coworkers [93–99]. Much of this work is summarized in [100]. Among other things their work identified contributions of true and false chirality for various observables. They predicted large chiral effects (up to 25%) for resonant excitation of oriented molecules containing at least one heavy atom. For randomly oriented molecules chiral effects are on the order of magnitude of 10^{-4} , increasing to 10^{-3} to 10^{-2} in resonance regions. For certain orientations of H_2S_2 their calculations indicated asymmetry parameters of $>1\%$ [96]. They also predicted chiral effects of $\sim 10^{-5}$ in ionization by polarized electrons.

Over the last 15 years considerable advances have been made in experimental studies of low energy polarized electron scattering from chiral molecules. Work by the Munster group [101] indicated that the asymmetry parameter for scattering of 0.9, 4.0, and 5.0 eV polarized electrons from camphor vapor was below their detection limit and cast some doubt on the previous results of Campbell and Farago [89, 90]. They were able to find asymmetries of up to 1.5×10^{-4} in Yb(hfc) a camphor-like molecule containing the heavy Yb atom and 1.7×10^{-4} in bromocamphor and indicated that excitation of temporary negative ion states was responsible for resonances observed in their data [102]. Several years later additional results on camphor, bromocamphor, and dibromocamphor were reported by a group from Nebraska [103]. Their calculations indicated that helical densities were a possible source of chiral asymmetry in the latter two molecules.

3.2.2 Organized (Adsorbed) Molecules

Background

When molecules are adsorbed on a surface their properties can be vastly different from the gas phase. They can dissociate and/or have different geometries (bond angles and bond lengths). Their electrical and magnetic properties can be significantly affected by interaction with the substrate and each other. As shown by the pioneering work of Naaman and coworkers, polarized electron transport through chiral adsorbed layers can be significantly influenced depending on whether the adlayers are organized or not [104–110]. Since this topic will be the subject of several other chapters in this book it will not be pursued further here. In this section we will focus on recent work [111] that showed that spin-polarized SEs can play a significant role in chiral-selective chemistry.

It has long been recognized that electrons and, in particular, SEs can play a major role in X-ray-induced surface chemistry [112]. Because of this, it is important to understand their production, transport, and reactions with molecules. For more

detailed discussion on the production and transport processes, the reader is referred to standard treatments on PES [113–115] and photoyields [116]. For a deeper discussion of electron–molecule reactions, the reader is referred to treatments that deal with electron induced dissociation (EID) of molecules on surfaces and in the gas phase [117–119].

In insulators and semiconductors, many electron–hole pairs are produced by a single core ionization event and resulting cascade. In metals, any holes in the conduction band quickly combine with electrons. For 100-eV photons incident on Si, the number is ~ 50 . Usually the hole–electron pair creation energy is about three times the material's band gap.

Electrons may interact with molecules and cause them to dissociate. These processes are collectively termed EID. EID proceeds via two main pathways. The first arises by the attachment of an electron, where it resides in one of the lowest unoccupied ground state molecular orbitals and forms a negative ion. This state is usually short lived. In many molecules, these temporary negative ion states are dissociative, and produce a neutral and negatively charged fragment species.

A second possible EID process is due to inelastic impact. This occurs when a fast electron, usually a primary or decay electron, collides with an electron in a molecule, leaving the molecule in an excited electronic state. This process, however, is usually not dominant because of the low number of electrons having high enough kinetic energy and because the impact cross section is lower, on the order of the absorption cross section.

Electron attachment is often the dominant surface photochemistry mechanism. The reason for this is a convergence of factors. First, dissociative electron attachment (DEA) cross sections, typically 10^{-16} to 10^{-15} cm², are about a factor of 100 or more higher than absorption cross sections in the soft and hard X-ray regimes. Second, the attachment cross section is maximum for *slow* electrons having kinetic energies less than 10 eV. The secondary electron distribution provides a large number of these electrons, mainly because of inelastic scattering, which peaks the distribution at low energy, but also because the mean free path is such that secondary electrons can travel from within the substrate to an interface region and react.

Transport processes involving electrons and fragments can play important roles in surface photochemistry. Electron–electron scattering dominates the transport of electrons through a solid system. The mean free path length, i.e., the average distance an electron travels before undergoing an inelastic scattering event, is almost material independent. The dependence of the mean free path on electron kinetic energy exhibits a minimum around 20–70 eV, corresponding to path lengths of 0.4–0.7 nm. Both low- and high-energy electrons on either side of the minimum, however, can travel distances of tens of nanometers. The consequence is that there can be a large flux of secondary electrons that is produced by photon absorption relatively far away from the chemical center of interest at an interface.

In Sect. 2.3 we saw that if the substrate is magnetic the SEs may be longitudinally spin polarized. Work by Naaman and coworkers has shown that spin-polarized electrons produced by circularly polarized laser light illumination of an

Au substrate show selectivity in their interaction with adsorbed chiral molecules [104–109]. It is reasonable to expect that low energy spin-polarized SEs should also show preferential scattering with adsorbed chiral molecules. If that scattering leads to a reaction then the products should reflect this preference. The next section shows the approach used in measurements aimed at identifying this process.

Experimental Method

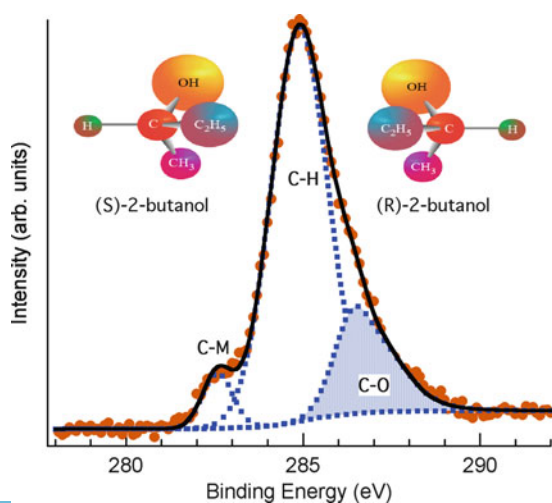
There are four requirements for these experiments: a magnetic substrate, adsorbed chiral molecules, a source of ionizing radiation, and a technique to monitor the reactions or products. If the products are emitted into the gas phase then mass spectroscopy may be employed. However, detection of neutral desorbing species is problematic, particularly if the species are a major component of the residual gas. Detection of ions may be employed and often such photon-stimulated ion desorption measurements can reveal a great deal about the surface reactions [112].

To monitor the surface reaction directly requires a method that is sensitive to the chemical state of the adsorbed molecule. Perhaps the two most sensitive approaches are Fourier transform infrared spectroscopy (FTIR) and X-ray photoelectron spectroscopy (XPS). FTIR directly probes the bonds in the adsorbed molecule by their vibrational signature. It is highly sensitive and has been employed to detect reactions in a variety of laboratory-based experiments of astrochemical relevance. Its main disadvantages for these experiments are that it uses a relatively large beam to probe the reaction and does not directly monitor the region where the SEs are causing the chemistry. XPS has good chemical sensitivity and, since the same radiation is being used to create the SEs and monitor the chemistry, directly probes the region where the reactions are occurring.

Valence level spectroscopy measures the bonding orbitals of a molecule and serves as a fingerprint of intact or reacted molecules. Any changes in bonding are always reflected in the valence spectrum because the valence electronic structure will be altered. Core level photoemission is used to identify specific elements and to distinguish differences in chemical environments for a particular atom. Core level spectroscopy can be used for quantitative analysis because the signal is proportional to the amount of atoms present. This property enables the following of fragmentation reactions species, since individual signals can often be separated and their respective photolysis cross sections determined. The area of a core-level peak is proportional to the number of species, and therefore yields a measure of surface number density as a function of photon exposure. Lineshape analysis can be applied to core electron peaks in photoemission data to give more detailed chemical shift and hence bonding information. Chemical shifts distinguish chemically different sites while the signal intensity for a given core-level component reflects the population of that specific site. In Sect. 3.2.2 we will see how core-level photoemission can be used to distinguish quantitatively reaction rates for C–O bond breaking as a function of chirality.

The choice of substrates was dictated by the need to be able to change the magnetization direction, and thus the secondary electron polarization, with a modest magnetic field. XPS requires accurate measurements of the kinetic energies of the emitted electrons. Any residual magnetic fields in the vicinity of the electron energy analyzer will perturb the electrons trajectory, particularly for lower energy electrons. Permalloy, an iron–nickel alloy, $\text{Fe}_{0.2}\text{Ni}_{0.8}$, has a coercive field of only a few Oersted and thus its magnetization direction can be changed by application of low magnetic fields. By using thin ($<1\ \mu\text{m}$) films the resultant magnetic field from the substrate is negligible. The surfaces of the films can be adequately cleaned, in situ, by Ar ion sputtering which results in an oxygen-free surface and a small amount ($<1\%$) of residual carbon that is intrinsic to the film. The adsorbed chiral molecule, 2-butanol, was chosen for its relatively simple structure and its high vapor pressure (~ 20 Torr at room temperature). The latter property enables one to dose the surface of the permalloy using a calibrated directional gas doser [120] enabling precise and repeatable production of a given coverage. Previous studies have shown that 2-butanol adsorbed on Pt(111) at 80 K remains intact and therefore retains its chirality [121]. It was anticipated that this would also be the case for adsorption on permalloy at 90 K, which was born out by subsequent measurements (see below). The use of a relatively simple molecule was also driven by the need that the chiral carbon should be distinguished from the other carbons by XPS. Figure 4 shows a typical C 1s XPS spectrum of 2-butanol adsorbed on permalloy. In (*R*)- and (*S*)-2-butanol, whose structures are shown in the inset in Fig. 4, the chiral carbon is bound to the OH group so its C 1s core level XPS peak is shifted to higher energies relative to carbons bound to H. By using standard curve fitting techniques it is possible to extract the peak area of carbons bound to H and O. Any reaction that results in C–O bond breaking will result in a decrease in the corresponding peak area (the shaded, blue area in Fig. 4).

Fig. 4 C 1s XPS spectrum of (*R*)-2-butanol adsorbed on permalloy at 90 K obtained at the start of a photolysis series. The points are the raw data; the *dashed lines* are the individual fitted components, and the *solid line* is the synthesized curve. The *filled in region* represents the C–O peak, which directly probes the chiral carbon. Also shown are models of (*S*)- and (*R*)-2-butanol



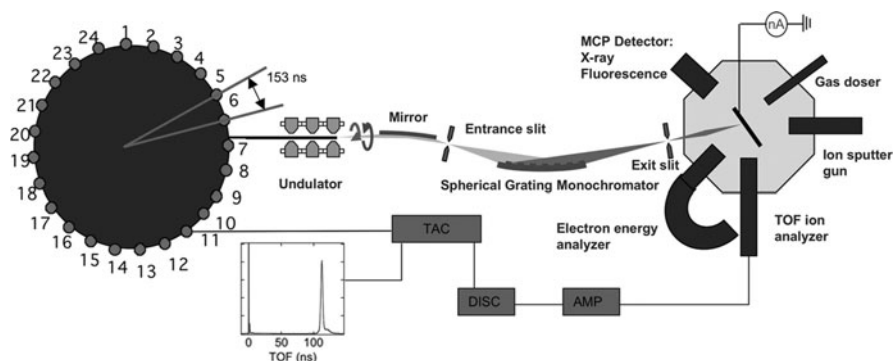


Fig. 5 Schematic diagram of the experimental setup depicting the APS bunched synchrotron radiation, the electromagnetic undulator on beamline 4-ID-C, the spherical grating monochromator and the XPS end station

The X-ray source was synchrotron radiation generated at the Advanced Photon Source (APS) and transmitted by beamline 4-ID-C. A schematic diagram of the beamline and experimental chamber is shown in Fig. 5. Note that in addition to the electron energy analyzer the ultra-high vacuum ($\sim 2 \times 10^{-10}$ Torr) chamber incorporates a microchannel plate detector to measure the total X-ray fluorescence (XRF) and an isolated sample holder so that the restoring current, or total electron yield (TEY), may be determined. Measurement of the XRF as a function of X-ray energy yields a bulk-sensitive X-ray absorption spectrum, while TEY energy dependence yields an absorption spectrum representative of the near surface (< 100 nm) region. Since the X-rays are pulsed with a nominal period of 153 ns it is also possible to detect ions using time-of-flight (TOF) techniques. Use of a specialized electromagnetic undulator insertion device results in a high X-ray flux (3.5×10^{11} photons/s at 1,190 eV), and employment of postmonochromator focusing optics yields a small X-ray spot size ($\sim 3 \times 10^{-4}$ cm²) on the sample. A photon energy of 1,190 eV was used for all XPS measurements. This energy is near the peak of the beamline transmission and also allows C 1s XPS spectra to be obtained without any interference from nearby Auger peaks.

The undulator on beamline 4-ID-C is a special, electromagnetic device, as opposed to the permanent magnet ones used at most facilities. As a result it is able to change the polarization of the X-rays between left and right circular as well as linear. The ability to change the circular polarization rapidly enables one to perform X-ray magnetic circular dichroism (XMCD), which is an elemental-specific technique to measure the magnetic properties of materials [122]. For these experiments XMCD was employed at the Ni L edge to insure that the sample magnetization direction was switched after applying opposing magnetic fields. A typical Ni L XMCD spectrum is shown in Fig. 6. The solid curve is the spectrum with the magnetization direction aligned with the X-ray beam and the dashed curve is the spectrum with the opposite magnetization. The two spectra are mirror images of each other. Since the magnetization direction determines the polarization of the

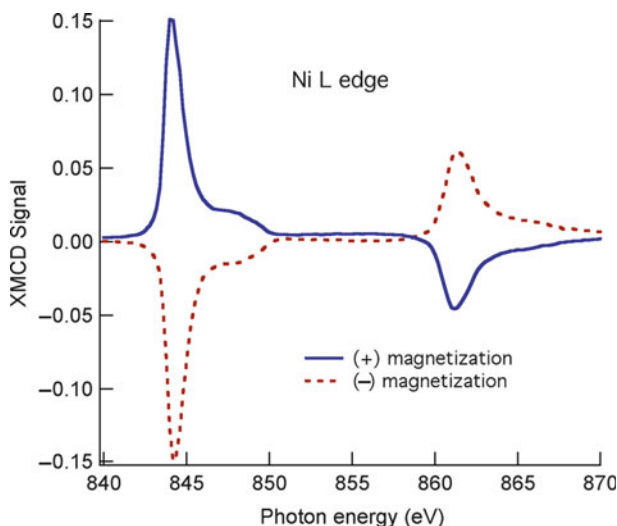


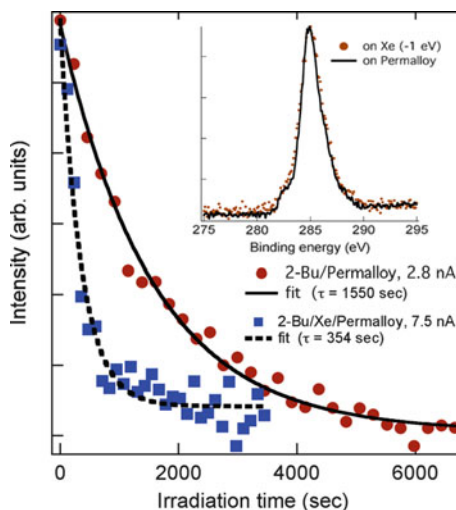
Fig. 6 XMCD spectra of a permalloy sample acquired with the magnetization direction parallel (solid line) and opposite (dashed line) to the X-ray beam propagation vector

secondary electrons, these measurements were an indirect indication of the electron polarization.

The overall approach relies on the determination of accurate rate constants for the reaction of the chiral C–O carbon. The rate equation is $dn/dt = -\sigma fn$, where the reaction cross section is σ (cm^2). Straightforward integration yields $n(\xi)/n(0) = e^{-\sigma\xi}$ where $\xi \equiv \int f(t)dt$ is the photon exposure. Note that in general the photon flux $f(t)$ varies with time so the integral must be used. However, the APS operates in “top-up” mode where the beam current of the stored electrons is kept nearly constant by injection every few minutes. Thus $f(t) = \text{constant} = f$ and the resulting equation is $n(\xi)/n(0) = e^{-\sigma ft}$, where f is the flux density and t is the time. The time constant, τ is defined as $1/\sigma f$, so by using the relationship $n(t) = n(0)\exp(-t/\tau)$, where $n(t) = \text{C–O peak area}$, $n(0) = \text{initial C–O peak area}$, and $t = \text{time}$, we are able to extract the time constant, τ , of the reaction as a function of the chirality of the adsorbed molecule and spin polarization of the substrate secondary electrons.

Previous studies have indicated that adsorption of 2-butanol on a cold metal surface is molecular (there is no adsorption-induced dissociation). To insure that this was the case for 2-butanol adsorbed on a sputter-cleaned permalloy surface, XPS spectra were taken following adsorption on a thick Xe overlayer deposited at ~ 25 K. The inset in Fig. 7 shows a comparison of a C 1s core level spectrum of 2-butanol adsorbed on multilayer Xe and compared with a spectrum of the same amount of 2-butanol adsorbed on permalloy. Other than a rigid shift of the binding energies, due to the lower screening of the C 1s hole by Xe, the two spectra are very similar. Since Xe is chemically inert it is reasonable to expect that 2-butanol remains intact upon adsorption and, therefore, the same appears to be the case following adsorption on permalloy at 90 K.

Fig. 7 Area of the C-O peak of 2-butanol adsorbed on permalloy (*filled circles*) and adsorbed on multilayer Xe (*filled squares*) as a function of irradiation time following exposure to 1,190 eV X-rays. The *solid* and *dashed lines* are fits of an exponential function to the experimental data. The *inset* shows a C 1s XPS spectrum of 2-butanol adsorbed on permalloy (*dots*) and on multilayer Xe (*line*). The Xe data have been shifted by -1 eV to account for the different core-hole screening properties of the two substrates



The general procedure for performing these measurements consisted of the following steps. (1) Prepare a clean permalloy surface by sputtering with 1-kV Ar ions and characterize it with XPS. (2) Adsorb 3.2×10^{15} molecules/cm² of (*R*)- or (*S*)-2-butanol on the clean surface, cooled to 90 K and characterize by XPS. On the basis of previous studies of 2-butanol adsorption on Pt(111) at 80 K [121], this should correspond to around three monolayers. (3) Move to a different position on the sample and photolyze with X-rays with the substrate magnetized in a particular direction. Record ~ 30 XPS spectra sequentially. Following photolysis, record an Ni L-edge XMCD spectrum to characterize the magnetic moment. Repeat 6–10 times at different positions on the sample. (4) Reverse the magnetization direction. (5) Repeat step 3 at a new position. Steps 1–5 were repeated numerous times, following additional sample cleaning steps and dosing. This was necessary to obtain time constants with high accuracy and reproducibility. Note that the small X-ray spot size (0.2×0.15 mm²) permits 10–15 measurements on the same substrate/adsorbate system. This is critical for avoiding systematic errors.

A typical C 1s XPS spectrum obtained at the start of a photolysis series is shown in Fig. 4. Using curve-fitting techniques, the spectrum in Fig. 4 can be decomposed into three main peaks. The small one at ~ 282.5 eV is due to atomic carbon bound to a substrate metal atom (C–M). Some of this intensity is due to residual carbon that remained after sputter-cleaning the surface (< 0.03 monolayer) and some is due to carbon produced from butanol photolysis during the time it took to acquire the spectrum. The most intense peak at ~ 284.9 eV is due to alkyl carbons (C–H), while the peak at ~ 286.5 eV is due to the chiral C atom bound to the OH group [123].

A series of C 1s XPS spectra obtained during irradiation with 1,190 eV X-rays is shown in Fig. 8. Photolysis results in a decrease in intensity of the C–H and C–O peaks and an increase in the C–M intensity. The C–H peak also shifts to lower binding energy. This shift is mainly due to C–O bond cleavage, which lowers the

binding energy of the carbons in the resultant compound. This bond cleavage may also produce additional compounds that contribute to the C–H intensity. Photolysis may also cleave C–C bonds to produce gas phase and/or bound CH_x byproducts. These factors make analysis of the C–H peak complex. Therefore, we focus our kinetic analysis on the C–O peak that directly probes the state of the chiral carbon atom. During the fitting of a photolysis series such as that shown in Fig. 8, the peak shape, width, and position were kept constant for the C–O and C–M structures, while the width and position of the C–H peak was allowed to vary for the reasons mentioned previously. The inset in Fig. 8 shows the C–O component as a function of irradiation time.

A major premise upon which this work is based is that the secondary electrons are responsible for the reaction. To test this hypothesis photolysis experiments were performed for the same coverage of 2-butanol adsorbed on multilayer Xe condensed on permalloy at 25 K. Due to its high bandgap condensed Xe has a much higher electron yield than permalloy. Figure 7 shows the results of the decay of the C–O peak area for 2-butanol adsorbed on the different substrates. By fitting

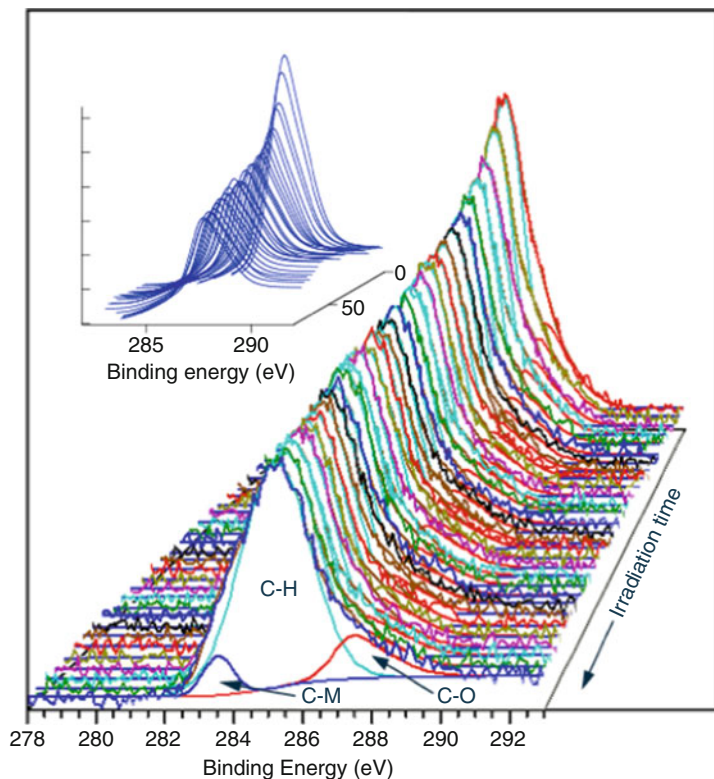


Fig. 8 Series of C 1s XPS spectra of (*R*)-2-butanol adsorbed on permalloy obtained sequentially while irradiating with 1,190-eV X-rays. The *inset* shows the area of the C–O peak component as a function of irradiation time

Fig. 9 Summary of the time constant results. The *squares* are the points for + magnetization, and the *circles* are the points for – magnetization. The *filled points* are for (*R*)-2-butanol and the *open points* are for (*S*)-2-butanol. The *lines* represent the average values: *solid*, (*R*)-2-butanol; *dashed*, (*S*)-2-butanol. The *solid line* in the *inset* shows the enantiomeric excess (*ee*) based on the time constant difference (10%) as a function of time in terms of the time constant, τ . The *dashed line* shows the remaining concentration

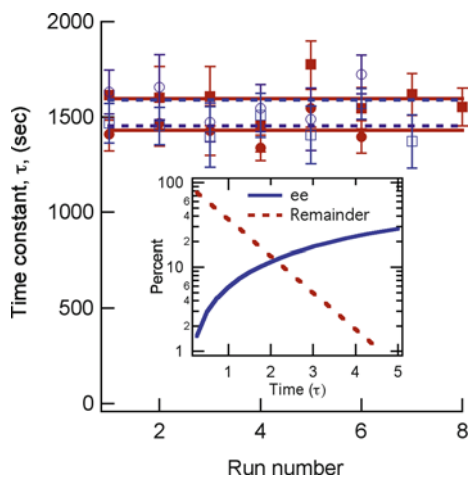


Table 3 Summary of the time constant results

Molecule	Magnetization	Time constant (s)
(<i>R</i>)-2-Butanol	Parallel	1,596 ± 44
(<i>R</i>)-2-Butanol	Antiparallel	1,431 ± 37
(<i>S</i>)-2-Butanol	Parallel	1,453 ± 42
(<i>S</i>)-2-Butanol	Antiparallel	1,589 ± 50

the results to a single exponential function, $n(t) = n(0)\exp(-t/\tau) + B$, where B is the background and τ is the reaction time constant for the two systems are extracted. In the case of the permalloy substrate the time constant is 1,550 s and the corresponding TEY is 2.75 nA. For the Xe substrate the time constant is 354 s and the TEY is 7.5 nA. The reduction in time constant is not inversely proportional to the TEY because evidently a greater proportion of the electrons emitted from the Xe substrate are involved in the reaction than those coming from the Permalloy substrate.

Measurements of the reaction time constant were performed six to eight times for each chirality and magnetization direction. The overall time constant results are summarized in Fig. 9. The individual time constants, with error bars, for the various photolysis series are shown by the data points, and the average value of τ , for each chirality and magnetization direction, are shown by the straight lines and tabulated in Table 3. It was critical that all the data in Fig. 9 were obtained during a single 6-day “run” on the beamline. In between runs the optics are adjusted slightly for other experiments. Thus, it would not be feasible to obtain the same beam profile for a nonconsecutive run, making it impossible to obtain quantitative results. This figure clearly indicates that a reversal of the secondary electron spin polarization results in a dramatic change in the reaction rate for a given chirality. For (*R*)-2-butanol this

difference is $10.9 \pm 3.8\%$, while for (*S*)-2-butanol, it is $8.9 \pm 3.5\%$. The fact that the results for each enantiomer are mirror images of the other is compelling evidence of the validity of the proposed mechanism. It is also interesting to note that these differences in the time constants are approximately the same as the degree of secondary electron spin polarization observed for permalloy (10–15%) (Table 1). To confirm these findings further, a racemic 2-butanol mixture (equal amounts of both enantiomers) was employed. The results obtained indicated that changing the magnetization direction (spin polarization) does not change the reaction time constant of the racemic mixture.

The average difference between the time constants for the two enantiomers is $\sim 10\%$. Using this value we have calculated the ee for an initial racemic mixture as a function of reaction time (Fig. 9, inset). After the time spent acquiring the data in Fig. 8, which equals 6,900 s and represents 4.3 time constants, the ee would be 25% and 1.4% of the initial concentration would be left intact. After a time equivalent to 2 time constants the ee would be 12% with 14% of the initial population remaining. To our knowledge these are the largest values for enantiomeric excesses as the result of circularly polarized light or spin-polarized electron irradiation ever reported. There are several important reasons for the success of the present approach. First of all the measurements were performed under UHV conditions with a well-characterized substrate and carefully controlled, reproducible adsorbate overlayers. Second, the reaction rate constants and thus the ee were all determined in situ. Prior approaches relied on removing the irradiated sample from the reaction vessel and analyzing the chirality using chromatography techniques, which also necessitated processing the sample for analysis. Finally, whereas previous work determined only the ee after a given period of irradiation, our approach yields the reaction time constant, which is a more fundamental value.

4 Mechanisms

Before discussing possible mechanisms that could explain these results, it is worthwhile comparing the time constants to results from previous electron-induced surface chemical reactions. The extracted time constant, τ , equals $1/\sigma f$, where f is the X-ray flux density and χ is the photolysis cross section. Using approximate values of the beam area ($3 \times 10^{-4} \text{ cm}^2$) and X-ray flux ($3.5 \times 10^{11} \text{ ph/s}$), yields a flux density of $1.7 \times 10^{15} \text{ ph/s cm}^2$ and a σ of $\sim 6 \times 10^{-19} \text{ cm}^2$. Our results show that it is the secondary electrons that are inducing the chemical changes. Therefore, it is more applicable to use the secondary electron flux to compute the cross section. An upper bound to this is given by the TEY flux density. This is determined from the measured sample current of 3.8 nA or $2.4 \times 10^{10} \text{ e/s}$, which results in a cross section of $9 \times 10^{-18} \text{ cm}^2$ (9 Mb) This value compares fairly well with reported dissociative electron impact cross sections for CO production from condensed films of acetone (9.6 Mb) [124] or methanol (4.2 Mb) [125] via a DEA mechanism. In the present case a DEA mechanism, in which a temporary negative ion state is formed,

is likely involved since the secondary electron energy distribution and their polarization is highest at low kinetic energies, ~ 2 eV (Fig. 3).

Since there have been no previous studies of spin-polarized electron induced reaction asymmetries in adsorbed chiral molecules, the exact manner by which the enhancement occurs is unclear. If the orbital occupied during DEA is sufficiently diffuse so as to “sample” the regions of the molecule responsible for the chiral structure [92] then enantiomeric specific dissociation will result. On the other hand, it has been theorized that two enantiomers will be ionized at different rates by longitudinally spin-polarized electrons [126]. If there are sufficient numbers of higher energy spin-polarized secondary electrons and the final state reached following ionization is dissociative, then this could lead to chiral enhancement.

Experimental [107] and theoretical [96] studies have shown that relatively large asymmetries exist in the scattering of longitudinally polarized electrons by organized, adsorbed chiral molecules relative to isotropic species. Prior studies of low temperature 2-butanol adsorption on single metal crystal surfaces have shown that the adsorbate overlayer is ordered and the molecule is bound to the surface through the oxygen atom [121, 127]. It is reasonable to assume a similar adsorption behavior of 2-butanol on the polycrystalline metallic permalloy surface used in the present study. Therefore, it is likely that some degree of ordering exists in the first layer, as well as the overlayers (due to hydrogen bonding). Such ordering would enhance the reactive scattering of the polarized electrons by the 2-butanol molecules adsorbed on the permalloy surface.

In the case of organized self-assembled monolayers of DNA and other helical molecules Naaman and coworkers proposed that the observed dichroism in polarized electron scattering resulted from charge transfer from the Au substrate to the adsorbate [104–108]. For dense, ordered chiral molecules the spins of the transferred holes are aligned in the same direction for all domains and act as a “spin filter.” Although such an effect cannot be ruled out in the present case it seems unlikely since coupling of the spins of the transferred holes to the magnetic substrate would tend to align them in the same direction regardless of chirality.

In trying to explain the asymmetric scattering of polarized electrons through organized chiral films, Ray et al. discussed several possibilities to explain their results, which could also apply to the present case [107]. As we have pointed out, the low energy secondary electrons responsible for the reaction are at energies close to the resonant transitions responsible for DEA. Such resonances reflect the underlying chirality and should enhance the asymmetry factor. The alignment of the adlayers restricts angular averaging and could enhance the effect. The most important factor could be that the low energy electrons have a long wavelength and could interact coherently with a large number of chiral centers.

In attempting to explain results from experiments that found positive results for the Vester–Ulbricht Hypothesis [65] (Table 1), Garay et al. hypothesized that the magnetic moment of the electron and the magnetic transition moment of the electronically excited optically active molecules could interact [128]. Thus, the

magnetic transition dipole could influence the probability of the triplet state of the optically active molecules, electron transport, and stereoselectivity.

Finally, in a recent paper, Yeganeh et al. suggest that the large asymmetries seen in polarized electron transmission are partly due to a combination of the presence of a molecule with axial chirality, surface orientation, and cooperative effects in the monolayer [129]. They use scattering theory to show that differences in transmitted intensity arise from the preferential transmission of electrons whose polarization is oriented in the same direction as the sense of advance of the helix.

Whether any or parts of the aforementioned models apply to the results on polarized secondary electron induced chiral reactions is difficult to say. The situation is considerably more complex since it involves reactive scattering and the substrate itself is magnetic. Hopefully, additional experimental and theoretical efforts will lead to a greater understanding of the processes involved.

5 Conclusion and Future Work

The past 50 years have produced a wide range of experimental and theoretical work aimed at determining the possible role of spin-polarized electrons in chiral-selective chemistry. Initial studies, based on the Vester–Ulbricht hypothesis, had some success, but its efficacy is doubtful since most of the chemistry is probably caused by secondary electrons. Subsequent work on low-energy polarized electron scattering from gas-phase chiral molecules showed definite asymmetries which indicated that spin–orbit coupling was an important factor in understanding the results. Recent work in this area has concentrated on understanding the interaction of spin-polarized electrons with adsorbed chiral systems, where collective effects should be important. Many of the chapters in this volume are devoted to this area, while this chapter has concentrated on the role of spin-polarized secondary electrons in producing chiral-selective chemistry.

There is a wide range of research avenues that could be pursued to further understanding in this area. The following list outlines a number of potential areas, some of which we are currently pursuing:

- *Other sources of spin-polarized electrons.* Low-energy SPEs may be produced in other ways such as circularly-polarized UV light irradiation of a surface, spin-polarized electron guns, and spin-polarized tunneling from a magnetic tip. Provided that these sources could be stabilized so that quantitative cross sections could be determined, it should be possible to perform chiral-selective surface chemistry measurements.
- *Other detection methods.* Besides XPS, other chemically sensitive techniques are available to probe the reaction. Surface reflection absorption infrared spectroscopy [130] and electron-energy loss spectroscopy [131] give detailed information on the vibrational states and thus the bonds of surface species. Gas-phase mass spectroscopic techniques provide information about the desorbing species.

In the experimental apparatus shown in Fig. 5 we have recently installed a time-of-flight ion detector, which will be used to analyze anions and cations ejected from the surface. Post-irradiation temperature programmed desorption [132] yields insight into the reaction products and their bonding. If the reactants or products fluoresce then optical spectroscopy could be employed to study them and luminescence circular dichroism would yield information about changes in chirality. If magnetism in the adsorbate layer plays a role then X-ray magnetic circular dichroism [122] (Fig. 6) could determine the magnetic sites with elemental specificity.

- *Other systems.* The 2-butanol adsorbate is one of the simplest chiral molecules. More complex molecules ranging from amino acids to DNA would provide further insight into the chemistry. It would also be beneficial to perform experiments on more well-defined substrates, such as thin films, crystalline magnetic overlayers grown in situ, or single crystal nonmagnetic substrates using other sources of spin-polarized electrons (see above).
- *Theory.* Perhaps this is the one area that would provide the most impact. Although modeling of spin-dependent reactive scattering is certainly challenging, we hope that current and future experimental results will provide motivation for theorists to pursue it.

Acknowledgments I would like to thank Mohammed Abu Haija, Phil Ryan, and Sean Frigo for various contributions to this work. This work was performed at the Advanced Photon Source and was supported by the U.S. Department of Energy, Office of Science, Office of Basic Energy Sciences under Contract No. DE-AC02-06CH11357.

References

1. Pasteur L (1874) C R Acad Sci, Comptes Rendus de l'Académie des Science (1 Jun 1874), Paris
2. Miller SL (1953) A production of amino acids under possible primitive earth conditions. Science 117:528
3. Miller SL, Urey HC (1959) Organic compound synthesis on the primitive earth: several questions about the origin of life have been answered, but much remains to be studied. Science 130:245
4. Bernstein MP, Dworkin JP, Sandford SA et al (2002) Racemic amino acids from the ultraviolet photolysis of interstellar ice analogues. Nature 416:401–403
5. Munoz Caro GM, Meierhenrich UJ, Schutte WA et al (2002) Amino acids from ultraviolet irradiation of interstellar ice analogues. Nature 416:403–406
6. Avalos M, Babiano R, Cintas P et al (1998) Absolute asymmetric synthesis under physical fields: facts and fictions. Chem Rev 98:2391–2404
7. Bonner WA (1991) The origin and amplification of biomolecular chirality. Orig Life Evol Biosph 21:59–111
8. Cintas P (2002) Chirality of living systems: a helping hand from crystals and oligopeptides. Angew Chem Int Ed 41:1139–1145
9. Feringa BL, Rav D (1999) Absolute asymmetric synthesis: the origin, control, and amplification of chirality. Angew Chem Int Ed 38:3418–3438

10. Keszthelyi L (1995) Origin of the homochirality of biomolecules. *Q Rev Biophys* 28:473–507
11. Podlech J (2001) Origin of organic molecules and biomolecular homochirality. *Cell Mol Life Sci* 58:44–60
12. Tsarev V (2009) Physical and astrophysical aspects of the problem of origin of chiral asymmetry of the biosphere. *Phys Part Nuclei* 40:998–1029
13. Bailey J (2001) Astronomical sources of circularly polarized light and the origin of homochirality. *Orig Life Evol Biosph* 31:167–183
14. Griesbeck AG, Meierhenrich UJ (2002) Asymmetric photochemistry and photochirogenesis. *Angew Chem Int Ed* 41:3147–3154
15. Inoue Y, Ramamurthy V (2004) *Chiral photochemistry*. Marcel Decker, New York
16. Jorissen A, Cerf C (2002) Asymmetric photoreactions as the origin of biomolecular homochirality: a critical review. *Orig Life Evol Biosph* 32:129–142
17. Meierhenrich UJ, Thiemann WHP (2004) Photochemical concepts on the origin of biomolecular asymmetry. *Orig Life Evol Biosph* 34:111–121
18. Meierhenrich U (2008) *Amino acids and the asymmetry of life*. Springer, Berlin
19. Buehler O (1974) Photochemistry with circularly polarized light. *Angew Chem Int Ed Engl* 13:179–185
20. Inoue Y, Tsuneishi H, Hakushi T et al (1996) First absolute asymmetric synthesis with circularly polarized synchrotron radiation in the vacuum ultraviolet region: direct photoderacemization of (e)-cyclooctene. *Chem Commun* 2627
21. Meierhenrich UJ, Nahon L, Alcaraz C et al (2005) Asymmetric vacuum UV photolysis of the amino acid leucine in the solid state. *Angew Chem Int Ed* 44:5630–5634
22. Lee TD, Yang CN (1956) Question of parity conservation in weak interactions. *Phys Rev* 104:254
23. Wu CS, Ambler E, Hayward RW et al (1957) Experimental test of parity conservation in beta decay. *Phys Rev* 105:1413
24. Feder R (ed) (1985) *Polarized electrons in surface physics*. World Scientific, Singapore
25. Johnson PD (1997) Spin-polarized photoemission. *Rep Prog Phys* 1217
26. Kessler J (1985) *Polarized electrons*, 2nd edn. Springer, Berlin
27. Kirschner J (1985) *Polarized electrons at surfaces*. Springer, Berlin
28. Osterwalder J (2006) Spin-polarized photoemission. In: Beaurepaire E, Bulou H, Scheurer F, Kappler JP (eds) *Magnetism: a synchrotron radiation approach*. Springer, Berlin, pp 95–120
29. Allenspach R, Taborelli M, Landolt M (1985) Oxygen on Fe(100): an initial-oxidation study by spin-polarized Auger spectroscopy. *Phys Rev Lett* 55:2599
30. De Nadai C, van der Laan G, Dhési SS et al (2003) Spin-polarized magnetic circular dichroism in Ni 2p core-level photoemission. *Phys Rev B* 68:212401
31. Kachel T, Carbone C, Gudat W (1993) Spin polarization of core-level photoelectrons. *Phys Rev B* 47:15391
32. Menchero JG (1996) Spin polarization and magnetic circular dichroism in photoemission from the 2p core level of ferromagnetic Ni. *Phys Rev Lett* 76:3208
33. Sinkovic B, Tjeng LH, Brookes NB et al (1997) Local electronic and magnetic structure of Ni below and above T_c: a spin-resolved circularly polarized resonant photoemission study. *Phys Rev Lett* 79:3510
34. Starke K, Kaduwela AP, Liu Y et al (1996) Spin-polarized photoelectrons excited by circularly polarized radiation from a nonmagnetic solid. *Phys Rev B* 53:R10544
35. Thole BT, van der Laan G (1991) Origin of spin polarization and magnetic dichroism in core-level photoemission. *Phys Rev Lett* 67:3306
36. Matthew JAD, Seddon EA, Xu YBO (1998) Spin polarized photoemission from amorphous alloy surfaces. *J Electron Spectrosc Relat Phenomena* 88–91:171–177
37. Andreyev O, Koroteev YM, Sanchez Albaneda M et al (2006) Spin-resolved two-photon photoemission study of the surface resonance state on Co/Cu(001). *Phys Rev B* 74:195416
38. Pierce DT, Meier F (1976) Photoemission of spin-polarized electrons from GaAs. *Phys Rev B* 13:5484

39. Meier F, Pescia D (1981) Band-structure investigation of gold by spin-polarized photoemission. *Phys Rev Lett* 47:374
40. Schmiedeskamp B, Vogt B, Heinzmann U (1988) Experimental verification of a new spin-polarization effect in photoemission: polarized photoelectrons from Pt(111) with linearly polarized radiation in normal incidence and normal emission. *Phys Rev Lett* 60:651
41. Heinzmann U (1987) Angle-, energy- and spin-resolved photoelectron emission using circularly polarized synchrotron radiation. *Phys Scr* T17:77
42. Koike K, Kirschner J (1992) Primary energy dependence of secondary electron polarization. *J Phys D Appl Phys* 1139
43. Penn DR, Apell SP, Girvin SM (1985) Spin polarization of secondary electrons in transition metals: theory. *Phys Rev B* 32:7753
44. Penn DR, Apell SP, Girvin SM (1985) Theory of spin-polarized secondary electrons in transition metals. *Phys Rev Lett* 55:518
45. Solleder B, Lemell C, Tokesi K et al (2007) Spin-dependent low-energy electron transport in metals. *Phys Rev B* 76:075115
46. Tamura K, Yasuda M, Murata K et al (1999) Analysis of the spin polarization of secondary electrons emitted from permalloy polycrystals. *Jpn J Appl Phys* 38:7173
47. Pfandzelter R, Bernhard T, Winter H (2001) Spin-polarized electrons in collisions of multi-charged nitrogen ions with a magnetized Fe(001) surface. *Phys Rev Lett* 86:4152
48. Kisker E, Gudat W, Schroder K (1982) Observation of a high spin polarization of secondary electrons from single crystal Fe and Co. *Solid State Commun* 44:591–595
49. Boeglin C (1993) Spin-polarized electron emission from Fe(100) by circularly polarized synchrotron radiation. *J Magn Magn Mater* 121:130–133
50. Pfandzelter R, Winter H, Urazgil'din I et al (2003) Spin-polarized electron emission during impact of fast ions on a magnetized Fe(100) surface. *Phys Rev B* 68:165415
51. Kirschner J, Koike K, Oepen HP (1987) Spin polarization of ion-excited secondary electrons from ferromagnets and its application for magnetic sputter depth profiling. *Phys Rev Lett* 59:2099
52. Kirschner J, Koike K (1992) Spin polarization of secondary electrons from Fe(110) excited by unpolarized primary electrons. *Surf Sci* 273:147–159
53. Koike K, Furukawa T, Cameron GP et al (1994) Intensity and polarization oscillation of secondary electrons emitted from Au/Fe(110). *Phys Rev B* 50:4816
54. Busch M, Gruyters M, Winter H (2006) Spin polarization and structure of thin iron oxide layers prepared by oxidation of Fe(110). *Surf Sci* 600:4166–4169
55. Koike K, Furukawa T (1996) Evidence for ferromagnetic order at the FeO(111) surface. *Phys Rev Lett* 77:3921
56. Paul O, Toscano S, Totland K et al (1991) The spatial origin of the spin-polarization of secondary-electron emission from Fe. *Surf Sci* 251–252:27–30
57. Pfandzelter R, Ostwald M, Winter H (2001) Spin-polarized electron emission induced by impact of protons and electrons on Cr/Fe(1 $\bar{1}$ 0 $\bar{1}$ 0). *Surf Sci* 488:90–98
58. Unguris J, Pierce DT, Galejs A et al (1982) Spin and energy analyzed secondary electron emission from a ferromagnet. *Phys Rev Lett* 49:72
59. Hopster H (1987) Spin polarization of secondary electrons from amorphous 3d metallic ferromagnets. *Phys Rev B* 36:2325
60. Tang H, Walker TG, Hopster H et al (1993) Anomalous behavior in the spin polarization of low-energy secondary electrons from Gd(0001). *Phys Rev B* 47:5047
61. Li D, Pearson J, Bader SD et al (1996) Spin polarization of the conduction bands and secondary electrons of Gd(0001). *J Appl Phys* 79:5838–5840
62. Hopster H, Raue R, Kisker E et al (1983) Evidence for spin-dependent electron-hole-pair excitations in spin-polarized secondary-electron emission from Ni(110). *Phys Rev Lett* 50:70
63. Mauri D, Scholl D, Siegmann HC et al (1989) Magnetism in very thin films of permalloy measured by spin polarized cascade electrons. *Appl Phys A* 49:439–447

64. Koike K, Hayakawa K (1984) Spin polarization of electron-excited secondary electrons from a permalloy polycrystal. *Jpn J Appl Phys* 23:L85
65. Garay AS (1968) Origin and role of optical isomery in life. *Nature* 219:338–340
66. Bonner WA (1974) Experiments on the origin of molecular chirality by parity non-conservation during β -decay. *J Mol Evol* 4:23–39
67. Darge W, Laczko I, Thiemann W (1976) Stereoselectivity of [beta] irradiation of D,L -tryptophan in aqueous solution. *Nature* 261:522–524
68. Blair NE, Bonner WA (1980) The radiolysis of tryptophan and leucine with ^{32}P β -radiation. *J Mol Evol* 15:21–28
69. Bernstein WJ, Lemmon RM, Calvin M (1972) In: Rolfing DL, Oparin AI (eds) *Molecular evolution, prebiological and biological*. Plenum, New York, pp 151–155
70. Bonner WA, Lemmon RM, Noyes HP (1978) Beta-radiolysis of crystalline carbon-14-labeled amino acids. *J Org Chem* 43:522–524
71. Tokay R, Nórdén B, Liljenzin J et al (1986) Was natural β radioactivity of carbon-14 the origin of optical one-handedness in life? *J Radioanal Nucl Chem* 104:337–347
72. Kovacs KL (1979) On the physical origin of biological handedness. *Orig Life Evol Biosph* 9:219–233
73. Kovács KL (1981) Beta irradiation may induce stereoselectivity in the crystallization of optical isomers. *Orig Life Evol Biosph* 11:37–52
74. Kovacs KL, Garay AS (1975) Primordial origins of chirality. *Nature* 254:538–538
75. Akaboshi M, Noda M, Kawai K et al (1979) Asymmetrical radical formation in D - and L -alanines irradiated with yttrium-90 β -rays. *Orig Life Evol Biosph* 9:181–186
76. Conte E (1985) Investigation on the chirality of electrons from ^{90}Sr - ^{90}Y beta-decay and their asymmetrical interactions with D - and L -alanines. *Lettere Al Nuovo Cimento* (1971–1985) 44:641–647
77. Conte E, Fanfani G, Pieralice M et al (1986) Investigation on the asymmetrical induced yields in ^{90}Sr - ^{90}Y -beta-irradiated D - and L -alanines. *Orig Life Evol Biosph* 17:51–57
78. Akaboshi M, Noda M, Kawai K et al (1982) Asymmetrical radical formation in D - and L -alanines irradiated with tritium- β -rays. *Orig Life Evol Biosph* 12:395–399
79. Bonner WA, Dort MAV, Yearian MR (1975) Asymmetric degradation of D,L -leucine with longitudinally polarised electrons. *Nature* 258:419–421
80. Keszthelyi L (1976) Asymmetric degradation of D,L -leucine with longitudinally polarised electrons. *Nature* 264:197
81. Walker DC (1976) Polarized bremsstrahlung not the source of optical activity. *Orig Life Evol Biosph* 7:383–387
82. Hodge LA, Dunning FB, Walters GK et al (1979) Degradation of D,L -leucine with longitudinally polarised electrons. *Nature* 280:250–252
83. Bonner WA, Yearian MR, Dort MAV (1979) Degradation of D,L -leucine with longitudinally polarised electrons – reply. *Nature* 280:252
84. Walker DC (1985) Leptons in chemistry. *Acc Chem Res* 18:167–173
85. Farago PS (1980) Spin-dependent features of electron scattering from optically active molecules. *J Phys B* L567
86. Beerlage MJM, Farago PS, Wiel MJVd (1981) A search for spin effects in low-energy electron scattering from optically active camphor. *J Phys B* 3245
87. Rich A, Van House J, Hegstrom RA (1982) Calculation of a mirror asymmetric effect in electron scattering from chiral targets. *Phys Rev Lett* 48:1341
88. Walker DW (1982) Electron scattering from optically active molecules. *J Phys B* 15:L289
89. Campbell DM, Farago PS (1985) Spin-dependent electron scattering from optically active molecules. *Nature* 318:52–53
90. Campbell DM, Farago PS (1987) Electron optic dichroism in camphor. *J Phys B* 20:5133
91. Hayashi S (1988) Asymmetry in elastic scattering of polarised electrons by optically active molecules. *J Phys B* 21:1037

92. Stephen TM, Shi X, Burrow PD (1988) Temporary negative-ion states of chiral molecules: camphor and 3-methylcyclopentanone. *J Phys B* 21:L169
93. Blum K, Thompson D (1989) Spin-dependent electron scattering from oriented molecules. *J Phys B* 22:1823
94. Busalla A, Blum K, Thompson DG (1999) Differential cross section for collisions between electrons and oriented chiral molecules. *Phys Rev Lett* 83:1562
95. Fandreyer R, Thompson D, Blum K (1990) Attenuation of longitudinally polarized electron beams by chiral molecules. *J Phys B* 23:3031
96. Musigmann M, Blum K, Thompson DG (2001) Scattering of polarized electrons from anisotropic chiral ensembles. *J Phys B* 34:2679
97. Musigmann M, Busalla A, Blum K et al (1999) Asymmetries in collisions between electrons and oriented chiral molecules. *J Phys B* 32:4117
98. Smith IM, Thompson DG, Blum K (1998) Chiral effects in electron scattering by molecules using a continuum multiple scattering method. *J Phys B* 31:4029
99. Thompson DG (2004) Chiral effects in the ionization of chiral molecules by electron impact. *J Phys B* 37:1013
100. Blum K, Thompson DG (1997) Chiral effects in electron scattering by molecules. In: Bederson B, Walther H (ed) *Advances in atomic, molecular, and optical physics*. Academic Press, San Diego, pp 39–86
101. Mayer S, Kessler J (1995) Experimental verification of electron optic dichroism. *Phys Rev Lett* 74:4803
102. Mayer S, Nolting C, Kessler J (1996) Electron scattering from chiral molecules. *J Phys B* 29:3497
103. Scheer AM, Gallup GA, Gay TJ (2006) An investigation of electron helicity density in bromocamphor and dibromocamphor as a source of electron circular dichroism. *J Phys B* 39:2169
104. Carmeli I, Leitus G, Naaman R et al (2003) Magnetism induced by the organization of self-assembled monolayers. *J Chem Phys* 118:10372–10375
105. Naaman R, Vager Z (2003) Electron transmission through organized organic thin films. *Acc Chem Res* 36:291–299
106. Naaman R, Vager Z (2006) New electronic and magnetic properties emerging from adsorption of organized organic layers. *Phys Chem Chem Phys* 8:2217–2224
107. Ray K, Ananthavel SP, Waldeck DH et al (1999) Asymmetric scattering of polarized electrons by organized organic films of chiral molecules. *Science* 283:814–816
108. Ray SG, Daube SS, Leitus G et al (2006) Chirality-induced spin-selective properties of self-assembled monolayers of DNA on gold. *Phys Rev Lett* 96:036101
109. Skourtis SS, Beratan DN, Naaman R et al (2008) Chiral control of electron transmission through molecules. *Phys Rev Lett* 101:238103–238104
110. Wei JJ, Schafmeister C, Bird G et al (2005) Molecular chirality and charge transfer through self-assembled scaffold monolayers. *J Phys Chem B* 110:1301–1308
111. Rosenberg RA, Abu Haija M, Ryan PJ (2008) Chiral-selective chemistry induced by spin-polarized secondary electrons from a magnetic substrate. *Phys Rev Lett* 101:178301
112. Rosenberg RA, Frigo SP (2002) Fundamental aspects of synchrotron radiation initiated surface chemistry. In: Sham TK (ed) *Chemical applications of synchrotron radiation, part II: X-ray applications, vol 12A*. World Scientific, Singapore, p 462
113. Cardonna M, Ley L (1978) *Photoemission in solids*. Springer, Berlin
114. Hufner S (1996) *Photoelectron spectroscopy: principles and applications*. Springer, Berlin
115. Prince K (1998) *Photoelectron spectroscopy of solids and surfaces*. World Scientific, Singapore
116. Henke BL, Knauer JP, Premaratne K (1981) The characterization of X-ray photocathodes in the 0.1–10-keV photon energy region. *J Appl Phys* 52:1509–1520
117. Arumainayagam CR, Lee H-L, Nelson RB et al (2010) Low-energy electron-induced reactions in condensed matter. *Surf Sci Rep* 65:1–44

118. Balog R, Langer J, Gohlke S et al (2004) Low energy electron driven reactions in free and bound molecules: from unimolecular processes in the gas phase to complex reactions in a condensed environment. *Int J Mass Spectrom* 233:267–291
119. Sanche L (1990) Low-energy electron scattering from molecules on surfaces. *J Phys B At Mol Opt Phys* 23:1597
120. Frigo SP (1994) The physical aspects of halosilane soft X-ray surface photochemistry. Ph.D. thesis (unpublished), University of Wisconsin, Madison
121. Lee I, Zaera F (2005) Enantioselectivity of adsorption sites created by chiral 2-butanol adsorbed on Pt(111) single-crystal surfaces. *J Phys Chem B* 109:12920–12926
122. Stohr J (1999) Exploring the microscopic origin of magnetic anisotropies with X-ray magnetic circular dichroism (XMDC) spectroscopy. *J Magn Magn Mater* 200:470–497
123. Chen DA, Friend CM (1996) Alcohol chemistry as a probe of mixed-metal phases: reactions of 2-propanol on cobalt-covered Mo(110). *J Phys Chem* 100:17640–17647
124. Lepage M, Michaud M, Sanche L (2000) Low-energy electron scattering cross section for the production of CO within condensed acetone. *J Chem Phys* 113:3602–3608
125. Lepage M, Michaud M, Sanche L (1997) Low energy electron total scattering cross section for the production of CO within condensed methanol. *J Chem Phys* 107:3478–3484
126. Hegstrom RA (1982) β decay and the origins of biological chirality: theoretical results. *Nature* 297:643–647
127. Mulligan A, Lane I, Rousseau GBD et al (2004) Chiral discrimination within disordered adlayers on metal surfaces. *Chem Commun* 21:2492–2493
128. Garay AS, Czégé J, Tolvaj L et al (1973) Biological significance of molecular chirality in energy balance and metabolism. *Acta Biotheor* 22:34–43
129. Yeganeh S, Ratner MA, Medina E et al (2009) Chiral electron transport: scattering through helical potentials. *J Chem Phys* 131:014707–014709
130. Trenary M (2000) Reflection absorption infrared spectroscopy and the structure of molecular adsorbates on metal surfaces. *Annu Rev Phys Chem* 51:381–403
131. Avouris P, Demuth J (1984) Electron energy loss spectroscopy in the study of surfaces. *Annu Rev Phys Chem* 35:49–73
132. Schlichting H, Menzel D (1993) Techniques for wide range, high resolution and precision, thermal desorption measurements: I. Principles of apparatus and operation. *Surf Sci* 285:209–218

Index

A

Absolute configuration, 189
determinations, 201
TDDFT, ECD/OR/ORD, 47
Acenaphthenol, 78
N-Acetylcysteine, 218
Acetylsinularolide, 55
Actinophyllic acid, 68
Adenine, replacement, 134
Adiabatic generalized gradient
approximations (GGA), 10
Alanine, 38, 45, 78, 288
Anthracenophanes, 114
Anthracycline Analogs, 202
Ascochin, 55
Ascodiketone, 55
Asymmetry, 279
Asymmetry factors, 270
AuNPs, absorbed chiral ligands, 217
Azulenophane, 115

B

Barrelenophanedicarbonitrile, 52
Basis set superposition errors (BSSE), 200
Basis sets, 16
Benzotricamphor derivatives, 35
Bi-cyclophanes, 119
Binaphthylthiol (BINAS), 218
Bi[10]paracyclophanes, 119
Bi[10]pyridinophane, 120
Bisnoradamantan-2-one, 22
Bis-porphyrin, 61
Bistramide, 55

Blennolides, 53
Brendanone, 22
Bromophenylethylpivalamide (PAMD), 78
Butanes, 2-substituted, 38

C

Calicheamicin, 75
Calicheamicinone, 75
CAM-B3LYP, 20
Camphene, 42
Camphenilone, 22
Camphor, 23, 24, 40
Camphorquinone, 46
Carbacephams, 57
Cavity ring-down polarimetry (CRDP), 19
Charge transfer, 129
excitations, 81
Charge transfer rate, constant, 139
DNA sequence dependence, 131
Chiral control, 259
Chiral imprinting, 77
Chiral induction, memory, 146
Chiral memory, 155
reversibility, 159
Chiral molecules in solution, H-bonding, 207
Chirality, 1, 279
induced, 192
solvent-induced, 207, 211
stirring, 174
transfer, 145, 192, 208
Chirality-spin-magnetism, 238
Chiroptical properties, 1, 4, 61, 100
origin dependence, 12

3-Chloro-1-butene, 36, 38
 Chlorofluoriodomethane, 56
 Chloropropionitrile, 62, 70
 Circular dichroism, 1, 6, 102, 240
 Circular polarized luminescence (CPL), 46
 Co(III) complexes, 82
 Co(sparteine)Cl₂, 225
 Computational benchmarking, 19
 Conductor-like screening model (COSMO), 200
 Conformation determinations, 189
 Contact potential difference (CPD), 243
 Continuum solvent model (COSMO), 40
 Cooperative molecular field effect (COMFET), 239
 Coupling matrix, 10
 Cryptophane-A, 190
 Cu bis-helice, 87
 Current transfer, 259, 260
 Current transport analysis, time-dependent, 262
 CuT4-poly-glutamate, 149
 Cyclophane nicotinamides, 104
 Cyclophanes, 100
 circular dichroism, 102
 layered, 116
 pair of chromophores, 107
 single chromophore, 103
 Cyclopropanes, 29
 Cytosaxones, 51, 61

D

Daunorubicin, 202
 7-Deazaadenine (Z), 134
 Dendrimers, cyclophanes, 121
 Density functional theory (DFT), 1, 3, 189
 Dephasing, 259, 264
 Diaminopurine (D), 137
 Dibromo-1,1'-bi-2-naphthol, 69
 Diethynylallene, 61
 Dihydropyrenophorolic acid, 55
 Dimethylcyclopropane, 24
 Dimethyloxirane, 46
 Dimethyltartrate, 53
 Dioncophylline A, 53
 Dipole moment, 137
 Diselenides, 72
 Dissociative electron attachment (DEA), 290

DNA, 129
 monolayers, self-assembled, 242, 299
 charge transfer rate, 131
 matched/mismatched sequences, 139
 spin selectivity, 249
 Donor-bridge coupling, 267
 Doxorubicin, 202
 Dual polarization modulation (DPM), 195

E

Electron-electron scattering, 290
 Electron induced dissociation (EID), 290
 Electron transmission, spin-selective, 240
 Electronic chiroptical organic molecules, 67
 Electronic circular dichroisms (ECD), 3, 46, 100
 Electronic circular dichroisms (ECD), spectra, 46
 Electrons, high-energy, 287
 low-energy, 288
 polarized, chiral molecular layers, 261
 secondary, 284
 spin-polarized, 279
 transfer, 129
 transmission, 137
 Enantiomeric excess, 279
 Epichlorohydrin, 33, 36, 44
 Epoxycyclohexenes, 56
 Epoxydesacetoxymatricarin, 54
 Esperamicin, 75
 Ethyl-4-methyloctane, 39
 Explicit solvent model, 200

F

Fenchone, 23, 24, 42
 Flavonoids, 77
 Fluorenone, 36
 Fluorenophanes, 114
 5-Formyl-4-hydroxy[2.2]paracyclophane, 123
 Franck-Condon (FC) factors, 46
 Free-induction-decay (FID), 226
 Frozen density embedding (FDE), 65
 FT spectral interferometry (FTSI), 226
 Fugomycins, 56

Fullerenes, 67
Fusidilactone, 55

G

GaAs, 284
Gas phase, 35
Gauge-including AOs (GIAOs), 13
Globosuxanthone A, 55
Glycidol, 33, 207, 212
Gold clusters, 67, 80
Gold nanoparticles (AuNPs), 192, 217
Gyration tensor, 5

H

H-bonding interactions, 207
Helicenes, 33, 63, 86, 116
Hennoxazole A, 55
2,3-Hexadiene, 27
Hierarchy, 143
HOMO-level, 40, 69, 129, 137
Hydrindanone, 47
Hypothemycin, 54

I

Iridium(III) luminophores, 85
N-Isobutyryl-cysteine, 218
Isocamphane, 22
Isochromanes, 58
Isocoumarines, 56
Isocytosazines, 61

J

Junctions, 259

K

Kramers–Kronig (KK) transform, 7, 24

L

Lactic acid (LA), 207
Ladderanes, 51, 55, 75
Ligand-field transitions, 81
Limonene, 226
Linarinic acid, 36, 58, 60
Linear dichroism (LD), 181

Local density approximations (LDA), 10
London orbitals, 13

M

Magnetic circular dichroism (MCD), 2
Magneto-optical rotation (MOR), 2
Massarilactones, 55
Matrix isolation VCD spectroscopy, 222
Memory, 143, 157
 reversibility, 159
Metacyclophanes, 113
Metal complexes, 81
Metallahelicenes, 63
Metalloporphyrins, 146
Metaparacyclophane, 114
Methyl lactate (ML), 207
O-Methylcatechol, 61
3-Methylcyclopentanone, 46
Methylenecamphor, 23
Methylenefenchone, 23
Methylnorbomanone, 22
Methyloxirane, 30, 33, 40, 77
4-Methylverbenene, 23
Mg-porphyrins, 260
Mirtazapine, 190
Molar rotation, 5
Monolayer, 87, 137, 230, 300

N

Naphthalenediimide cyclophane, 116
Naphthalenophanes, 114
Naproxene, 34
Ni(sparteine)Cl₂, 225
Nonoxa-[7]paracyclophane, 103
Nopinone, 22, 24
Norbomanone, 22, 43
Norbomenone, 22, 62, 71
Norcamphor, 32

O

Optical rotation, 1, 4
Optical rotatory dispersion (ORD), 1, 8, 225
Orthoparacyclophane, 115
Oruwacin, 36, 60
Oxacephams, 57
Oxepino[2,3-*b*]chromones, 55

Oxiranes, 21, 29, 40, 62
 Oxovanadium(IV) phthalocyanines, 85

P

Papyracillic acids, 55, 60
 Paraconic acids, 51
 Paracyclophane ketimines, 69
 Paracyclophane-8-carboxylic acid, 103
 Paracyclophanes, 101
 Paracyclophanohexahelicene, 116
 Parity violation, 282
 Pd-bis(phosphole-helicene) complex, 86
 Pentacoordinate phosphorus compounds, 204
 2,3-Pentadiene, 27
 Phenanthrenophanes, 114
 Phenothiazine (PTZ), 132
 Phenylalanine, 154
 2-Phenyl-3,3-dimethylbutane, 32
 Phenylethanol, 33
 Phenylethylamine, 33
 Phenylplumericin, 61
 Phenyl-(2-pyridyl)-(3-pyridyl)-(4-pyridyl)
 methane, 60
 Phosphole-helicene, 86
N-Phosphorylimine adducts, 56
 Photoelastic modulator (PEM), 192
 Photoelectron spectroscopy (PES), 282
 Photoemission, 282
 Pinane, 22, 24, 42
 Pinene, 22, 42, 226
 Pitamide, 55
 Planar chirality, 100
 Platinum helicene, 86
 Plumericin, 61
 Polarizable continuum model (PCM),
 39, 200
 Polarized laser pulses, 259
 Polyalanine, 239, 241, 249
 SAM, electron transmission, 244
 Polyglutamate, 146
 Polymers, cyclophanes, 121
 Poly(*p*-phenylene) ladder, 121
 Polypyrrroloindoline alkaloids, 67
 Porphyrin, 143, 146
 self-assemblies, 154
 Proline, 38, 39, 76, 287
 Propylene oxide (PO), 41, 207, 222
 Pseudoanguillosporin, 58, 59

Pyranonigrin, 56
 Pyrenophanes, 114

Q

Quantum chemical calculations, 100
 Quantum model simulations, 259
 Quantum theory, 1

R

Radial distribution functions (RDFs), 210
 Raman optical activity (ROA), 1, 16, 195
 Random-phase approximation (RPA), 10
 Rapid long-range charge transfer, DNA, 134
 Resonance ROA (RROA), 16
 Resonances, nonsingular response, 15
 Rhodopsin, 77
 Rotatory strength, 5
 [Ru(phen)₃]²⁺, 165

S

Self-assembled monolayers (SAMs), 238,
 253, 284, 299
 Self-assemblies, 154, 183, 204, 252
 Sequence dependence, charge transfer rate,
 G-C base-pairs, 133
 Shisijimicin, 75
 Simple point-charge model (SPC), 45
 Simulations of surface-enhanced ROA
 (SERROA), 16
 Single polarization modulation (SPM), 195
 Solutes, chiral, self-aggregation, 212
 Solute-water H-bonding networks, 207
 Solvation, molecular dynamics, 44
 Solvent chirality, induced, 189
 Solvent effects, static structures, 39
 Solvent-induced chirality, 207, 211
 Spin, 137
 Spin polarized electrons (SPEs), 281
 Spin transmission, temperature
 dependence, 245
 Spiro[2,2]-pentane-1,4-diene, 33
 Spiroselenurane, 51, 52
 Static gas phase structures, conformational
 averaging, 37
 Static structures, 35
 Steady-state currents, 270
 transfer, dephasing, 274

Steady-state transport analysis, 268
Stearoyl-lysine, 261
Stick spectra, 24, 46
Streptonigrin, 60
Styrene oxide, 78
Sulfonatophenyl-diphenylporphyrin (DPPS), 164
Supramolecular chirality, 143

T

Tartrate, 280, 288
Template size, imprinting chiral information, 164
Tert-butane sulfinamide, 69
Tert-butylphenylphosphinoamidate, 69
Tetraazacyclophane, layered, 118
Tetracyanobutadienes, 55, 61
Tetrahydropyrenophorol, 55
Tetramantane, 67
Tetramethylpyrrolohelicene, 32
Thiacyclophanes, 106
Thiiranes, 29
Time-dependent density functional theory (TDDFT), 1, 4
 linear response, 9
Transition metals, chiral complexes, VA/VCD intensities, 213
Triangulane, 26, 72
Tris(ethylenediaminato)cobalt(III), 215
Troeger's base, 23, 24

V

Verbenone, 23, 24
Vibrational averaging, 41
Vibrational circular dichroism (VCD), 102, 189, 225
 applications, 201
 calculations, 197
 measurements, real time, 225
 spectra, simulations, 199
 theory, 197
 transient, 189
Vibrational fine structure, 46
Vibrational optical activities (VOA), 225
Vibrational optical rotatory dispersion (VORD), 226
Virtual enantiomer method, 195
Vortex effect, 174
V-U hypothesis, 287, 299

X

X-ray magnetic circular dichroism (XMCD), 293
XC kernel, 16
XC potentials, 16

Z

Zero-point-energy (ZPE), 200
Zeroth regular approximation (ZORA), 82